transactions of the ASME

Published Quarterly by
The American Society of
Mechanical Engineers

Volume 92 • Series C • Number 1
FEBRUARY 1970

journal of heat transfer

EDITORIAL OFFICES are at ASME Headquarters, United Engineering Center, 345 East 47th Street, New York, N. Y. 10017. Cable address, "Mechaneer," New York.
PUBLISHED QUARTERLY at 20th and Northampton Streets, Easton, Pa. 18042. Second-class postage paid at Easton.
CHANGES OF ADDRESS must be received at Society headquarters seven weeks before they are to be effective. Please send old label and new address.
PRICES: to members, $2.25 a copy, $7.50 annually; to nonmembers, $4.50 a copy, $15.00 annually.
Add 50 cents for postage to countries outside the U. S. and Canada.

INDEXED by the Engineering Index, Inc.

(Contents Continued on page 213)

CONTENTS

(CONTINUED)

J. H. LIENHARD
Professor of Mechanical Engineering,
University of Kentucky,
Lexington, Ky. Mem. ASME

K. B. KEELING, JR.
Engineer, General Electric Co.,
Louisville, Ky.

An Induced-Convection Effect Upon the Peak-Boiling Heat Flux[1]

An induced-convection effect upon the peak pool-boiling heat flux is identified and described. A method is developed for correlating this effect under conditions of variable gravity, pressure and size, as well as for various boiled liquids. The effect is illustrated, and the correlation verified, with a large number of peak heat-flux data obtained on a horizontal ribbon heater. The data, obtained in a centrifuge, embrace an 87-fold range of gravity, a 22-fold range of width, a 15-fold variation of reduced pressure, and five liquids.

Introduction

THE peak heat flux in saturated pool boiling, q_{max}, is a transition value dictated by the onset of a hydrodynamic instability in the removal of vapor from a heater element. The Zuber-Kutateladze equation for this transition on an infinite flat plate, q_{maxF}, references [1–3][2] is[3]

$$q_{maxF} = 0.131 h_{fg} \rho_g^{1/2} \sqrt[4]{\sigma g(\rho_f - \rho_g)} \sqrt{1 + \frac{\rho_g}{\rho_f}} \qquad (1)$$

Two kinds of parameters are entirely absent from equation (1). There is no characteristic length and there are no transport properties. Accordingly, Lienhard and Schrock [4] were able to use the Law of Corresponding States to write equation (1) in terms of a reduced peak heat flow, $F(p_r)$, such that

$$q_{maxF} = \lambda F(p_r) \qquad (1a)$$

where λ is a complicated function of gravity critical data, and other constants characteristic of the liquid being boiled, and p_r is the reduced pressure.

In 1965, Lienhard and Watanabe [5] found that a previous analytical expression for the minimum heat flux on horizontal wires [6] could be written as the *product* of the minimum heat flux for a flat plate, and a function of the geometric scale parameter, L', defined as

$$L' = L \sqrt{\frac{g(\rho_f - \rho_g)}{\sigma}} \qquad (2)$$

They then provided broad experimental support for the notion that a similar separation would describe the q_{max} in finite geometries. Their correlating equation was

$$q_{max} = \lambda F(p_r) \cdot f(L') \qquad (3)$$

or

$$\frac{q_{max}}{\lambda F(p_r)} = f(L') \qquad (3a)$$

Very little attention has been given to date to the fact that the bubbles rising above a heater of finite size should drag upon the surrounding fluid and induce a secondary flow about the heater. In 1964, the late Costello and his co-workers [7] found that a flat ribbon heater, mounted on a slightly wider block, induced strong side flows. When the side flow was blocked by vertical walls, q_{max} was much lower than it was when the side flows were allowed. Furthermore, they observed an increase of q_{max} with decreasing ribbon width when the side flow was permitted.

Borishanski (see, e.g., [2]) proposed a parameter to describe such an effect as early as 1956. He suggested that his peak heat flux data could be well represented by an expression of the form

$$q_{max} = (0.131 + 4N^{-0.4}) h_{fg} \rho_g^{1/2} \sqrt[4]{\sigma g(\rho_f - \rho_g)} \qquad (4)$$

where

$$N \equiv \frac{\rho_f \sigma}{\mu^2} \sqrt{\frac{\sigma}{g(\rho_f - \rho_g)}} \qquad (5)$$

and μ is the viscosity. We shall see shortly that the parameter, N, characterizes buoyant effects. Borishanski's expression indicates that the influence of the parameter, N, is really pretty small in the flat plate geometry since 0.131 is generally $\gg 4N^{-0.4}$.

The present study is motivated by a specific interest in the in-

[1] This Work was supported under the cognizance of the Lewis Research Center, by NASA Grant NGR-18-001-035.

[2] Numbers in brackets designate References at end of paper.

[3] Symbols not defined in context are explained in the Nomenclature section.

Contributed by the Heat Transfer Division of THE AMERICAN SOCIETY OF MECHANICAL ENGINEERS and presented at the ASME-AIChE Heat Transfer Conference, Minneapolis, Minn., August 3–6, 1969. Manuscript received by the Heat Transfer Division, March 24, 1969; revised manuscript received, May 5, 1969. Paper No. 69-HT-48.

Nomenclature

$f(\ )$ = an arbitrary function of ( )
$F(p_r)$ = a function of p_r equal to q_{maxF}/λ
g = acceleration of gravity or other force field
h_{fg} = latent heat of vaporization
I = induced-convection scale parameter, $\sqrt{\rho_f L \sigma/\mu^2}$
L = characteristic length
L' = dimensionless size, equation (2)
M = molecular weight
N = induced-convection buoyancy parameter, I^2/L'
P = the parachor, $M\sigma^{1/4}/(\rho_f - \rho_g) \simeq$ constant, for any fluid
p_c = critical pressure
p_r = reduced pressure, system pressure $\div p_c$
R = ideal gas constant
T_c = critical temperature
q_{max} = the peak pool-boiling heat flux
q_{maxF} = q_{max} for an infinite horizontal flat plate, as given by Zuber's equation (1)
W = width of horizontal ribbon heaters
W' = dimensionless size based on W
λ = $g^{1/4} p_c (P/M)(8Mp_c/3RT_c)^{3/4}$
μ = liquid viscosity
ρ_f = density of saturated liquid
ρ_g = density of saturated vapor
σ = surface tension between a liquid and its vapor

fluence of variable gravity upon q_{max}. Accordingly the implications of the induced flow observed by Costello, et al., are serious since the effects of this flow stand to be magnified by gravity. We have therefore created a configuration comparable to theirs and studied its performance under variable gravity. Before considering this experiment, however, let us first develop a correlation, similar to equation (3), which accounts for induced flow.

Method of Correlation

The viscosity of the liquid, which has not appeared to be of great importance in prior studies of q_{max}, must now be considered. It is only through the viscous drag exerted by rising bubbles upon the surrounding liquid that flow can be induced. Thus the dependent variable q_{max} will depend primarily upon 7 independent variables[4]: ρ_f, ρ_g, h_{fg}, σ, L, g, and μ. These 8 variables are expressible in four dimensions: Btu, ft, sec, and lb_m. Therefore, we must write down (8-4) or four independent dimensionless groups to describe the phenomenon, in accordance with the Buckingham pi theorem.

The first and most obvious of these groups might be ρ_g/ρ_f. This has generally taken the following form in q_{max} predictions:

$$\sqrt{1 + \rho_g/\rho_f}$$

The second group is a dimensionless *dependent* variable:

$$q_{max}/h_{fg}\rho_g^{1/2}(\rho_f\sigma g)^{1/4}$$

the denominator of which can be combined with $\sqrt{1 + \rho_g/\rho_f}$ to form Zuber's q_{maxF}:

$$\frac{q_{max}}{q_{maxF}} \equiv \frac{q_{max}/h_{fg}\rho_g^{1/2}(\rho_f\sigma g)^{1/4}}{0.131\sqrt{1 + \rho_g/\rho_f}(2 - [\sqrt{1 + \rho_g/\rho_f}]^2)^{1/4}} \quad (6)$$

A third group, $L\sqrt{g\rho_f/\sigma}$, can be multiplied by $(2 - [\sqrt{1 + \rho_g/\rho_f}]^2)^{1/2}$ to get L'.

The fourth group can then be obtained by elimination. The dependent variable, q_{max}, and the only other variable containing the units of Btu, namely, h_{fg}, will be eliminated. So too will ρ_g be deleted as unrelated to the viscous drag problem. If the method of indices is being used to establish the groups, this will leave 4 equations in 5 unknown indices, so one more choice must be made. Setting the index of g equal to zero gives the new parameter

$$I = \sqrt{\rho_f L\sigma/\mu^2} \equiv \sqrt{NL'} \quad (7)$$

We shall call this the "induced-convection *scale* parameter." It is analogous to the ratio of the square root of a Grashof number divided by L', and it characterizes the relevant forces in the following way:

$$I = \frac{[(\text{inertia force})(\text{surface tension force})]^{1/2}}{\text{viscous force}}$$

If gravity is left in this parameter and the size, L, is deleted, the resulting group will be $(\sigma/\mu^2)\sqrt{\sigma\rho_f/g}$. This in turn can be divided by $(2 - [\sqrt{1 + \rho_g/\rho_f}]^2)^{1/2}$ to give Borishanski's N for the fourth group. We shall call N the "induced-convection *buoyancy* parameter" since it replaces L with g. It characterizes the relevant forces in the following rather complicated way:

$$N = \frac{(\text{inertia force})(\text{surface tension force})^{3/2}}{(\text{viscous force})^2(\text{buoyant force})^{1/2}}$$

Combining the four groups, we obtain the desired correlating relation:

$$\frac{q_{max}}{q_{maxF}} = f(L', I, \sqrt{1 + \rho_g/\rho_f}) \quad \text{or} \quad f(L', N, \sqrt{1 + \rho_g/\rho_f}) \quad (8)$$

or, if we choose to use the Law of Corresponding States,

$$\frac{q_{max}}{\lambda F(p_r)} = f(L', I, \sqrt{1 + \rho_g/\rho_f}) \quad \text{or} \quad f(L', N, \sqrt{1 + \rho_g/\rho_f}) \quad (9)$$

Equation (9) implies that the generalized function, $F(p_r)$, should be used to approximate q_{maxF}. This function was established in [4], based upon the flat plate data of Cichelli and Bonilla [8]. Equation (1*a*) is therefore inexact, and equations (8) and (9) represent slightly different means for correlating data.

The choice of I or N as the correlating parameter for induced convection is arbitrary. If one is interested strictly in the influence of gravity, I is probably more convenient because it leaves the influence in the coordinates, q_{max}/q_{maxF} and L', without introducing it in a third parameter. The Borishanski parameter, N, however characterizes the buoyancy forces explicitly.

Equation (3*a*) is of this form. The term $\sqrt{1 + \rho_g/\rho_f}$, which is almost exactly unity for pressures up to the neighborhood of the critical point, appears to be irrelevant at lower pressures and was not needed by Lienhard and Watanabe. Furthermore, their experiments were made on horizontal wires which provided little obstruction to, or interaction with, the movement of any flow that might have been induced. In their case (as in Borishanski's) viscosity was no longer a relevant variable and the fourth-dimensionless group did not appear. Vliet and Leppert [9] found that strong forced-convection currents over cylinders altered q_{max} significantly, but no such evidence has been given for induced convection.

The present dimensional analysis therefore vindicates the separation of q_{maxF} from a function of geometric scale that was assumed to exist in previous studies. It also shows that the previous correlation equation (3*a*) was limited by two implicit assumptions. In the present work we shall retain the assumption that $\sqrt{1 + \rho_g/\rho_f}$ does not contribute, but we shall look for the influence of an additional parameter, I, or N. Our correlation equation will accordingly be

$$\frac{q_{max}}{q_{maxF}} = f(I, W') \quad \text{or} \quad f(N, W') \quad (10)$$

where W' is an L' based upon the width, W, of horizontal heaters, and q_{maxF} is computed from equation (1).

Experiment

At least three things must now be checked experimentally. The first is whether or not equation (8) is based upon the correct physical variables and whether it will succeed in correlating data. The second is whether or not the parameter, I, really will exert significant influence on q_{max}. Finally, experimental evidence will be needed to locate the point at which scale effects vanish as the scale parameters are increased.

Our experiments were made in the University of Kentucky Boiling and Phase-Change Laboratory on a general purpose centrifuge capable of developing as much as 100 earth-normal gravities. The centrifuge facility is described fully in reference [10]. Full details of the experiments, and the raw data, are given in reference [11]. Fig. 1 shows the centrifuge facility. The test capsule appears through an open hatch on the left-hand side. The peak heat-flux transition was observed with the help of a synchronized strobe-light through a plexiglas viewing window on the right-hand side.

Fig. 2 shows a typical flat ribbon heater in place on a special ribbon mount within the test capsule. The inside of the capsule was 7 in. long, by 3 in. high, by $3^3/_4$ in. wide. It is equipped with a vacuum manifold and a vacuum measuring line, a thermo-

[4] *Since the induced flow will act to disrupt the hydrodynamic* process of vapor removal, we are using the word "convection" to describe a fluid mechanical action—not a heat removal process. The transport variables of conductivity or diffusivity are therefore not introduced.

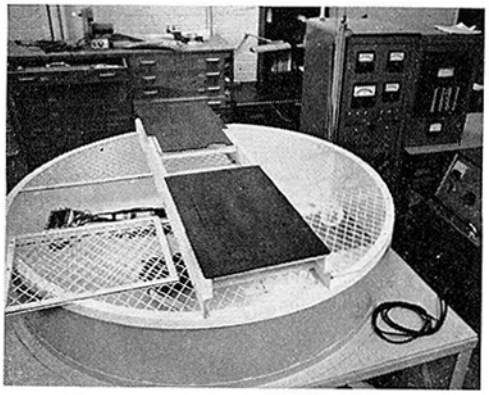

Fig. 1 Gravity-boiling centrifuge facility

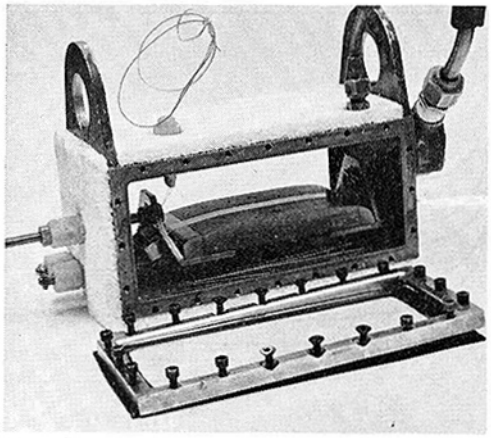

Fig. 2 Test capsule with ribbon heater mount in place

couple to monitor the liquid temperature, and power leads for both the test heater and a preheater on the bottom. These lines pass through appropriate vacuum seals and slip-rings to a pump, a power supply, and a meter panel, outside.

Carefully cleaned nichrome ribbons, between 0.046 and 1.000 in. wide, with a 4.00 heated length, were cut from 0.009, 0.002, or 0.001-in. stock and stretched out on the $2^1/_2$-in-wide mounting block. The capsule was charged with reagent grade acetone, methanol, benzene, isopropanol, or double distilled water, and mounted on the centrifuge. During a run, the liquid level was held in the range 1.0 to 1.5 in. above the ribbon surface and noted to make a hydrostatic head correction, and the temperature held to within a degree of saturation. The angular speed of the centrifuge was read, and (with the preheater turned off) the capsule pressure was recorded. Finally, the power supplied to the ribbon was increased until the peak heat-flux transition was observed, and there it was read.

About 874 observations were made—roughly 419 in acetone, 262 in methanol, 104 in isopropanol, 81 in benzene, and 8 in water. These raw data are tabulated fully in reference [11] and will not be reproduced here. The probable errors of the variables, computed in [11], are about ±6 percent for q_{max}, ±4 percent for W', and ±2 percent for I. The variability of observed q_{max} values was on the order of ±15 percent, as is typical of q_{max} data. Data were measured over a reduced pressure range from 0.0016 to 0.0246, and a range of gravity from 1 to 87 times earth normal gravity.

Results and Correlation

Equation (10) indicates that these data, obtained over a very broad range of conditions, should correlate onto a single surface in q_{max}/q_{maxF}, W', and I or N, coordinates. And if our supposition that induced convection is a significant effect in this configuration, then the surface should show that q_{max}/q_{maxF} varies significantly with either I or N.

To create these surfaces, we plotted all of the present data, and three points for water at one atmosphere and one gravity, from [7], twice: first on q_{max}/q_{maxF} versus W' coordinates for comparatively narrow ranges of I; then on q_{max}/q_{maxF} versus I coordinates for ranges of W'. Fig. 3 shows a typical example of one of these crossplots. An additional 20 crossplots not shown here can be made available on request.[5]

Fig. 3 reveals some things that were generally true of all of the data. The great majority of the data for any substance clustered within ±15 percent of a mean surface through them, and a

[5] The method of correlation used in reference [11] was based on equation (9) instead of (8). This resulted in a doubling of those errors introduced by the Law of Corresponding States and an awkward scaling of q_{max}. The present correlation overcomes these difficulties but required replotting the data instead of using the curves in [11]. The effectiveness of equation (8) was made clear by Sun [12] who used it with great success to correlate cylinder data. The shape of our resulting surface differs somewhat from that plotted in reference [11].

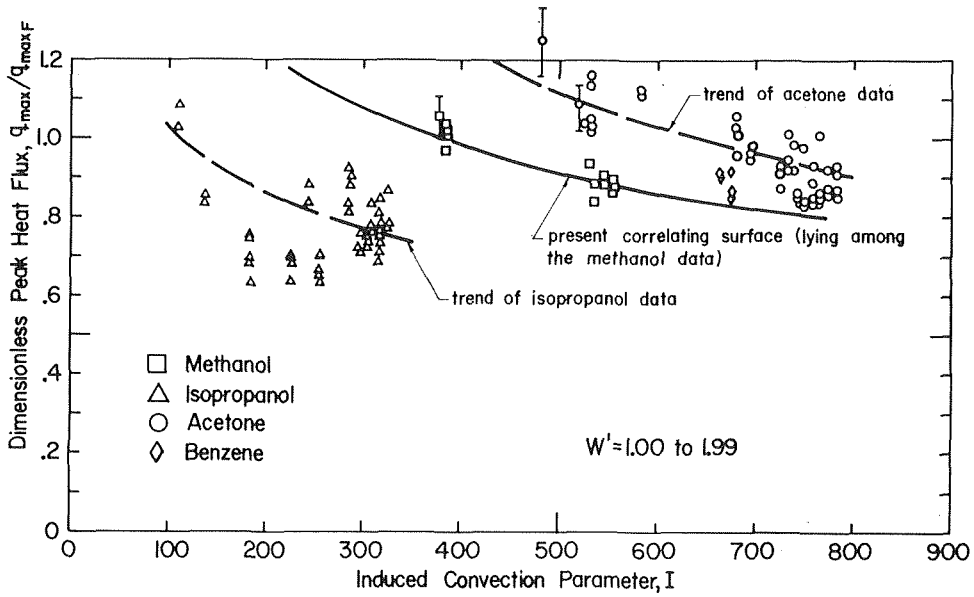

Fig. 3 A typical crossplot for peak heat-flux data in a range of W'

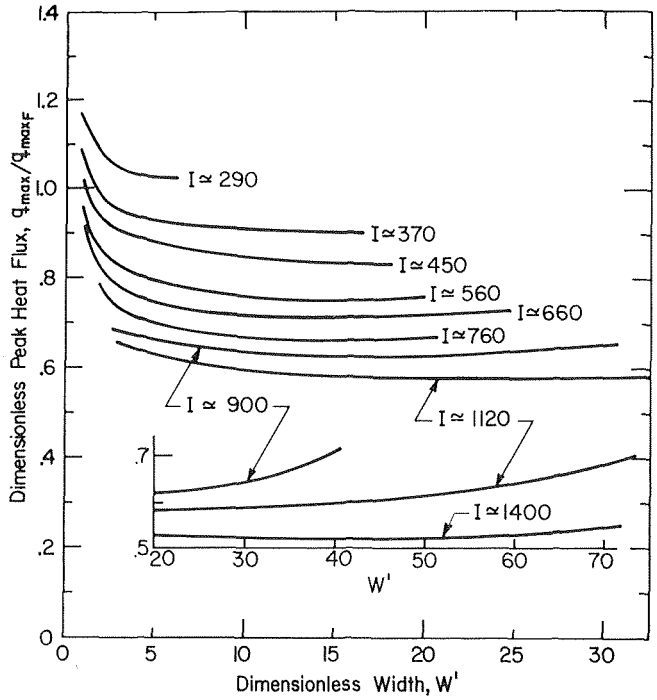

Fig. 4 q_{max}/q_{maxF} versus W' contours for 9 values of I

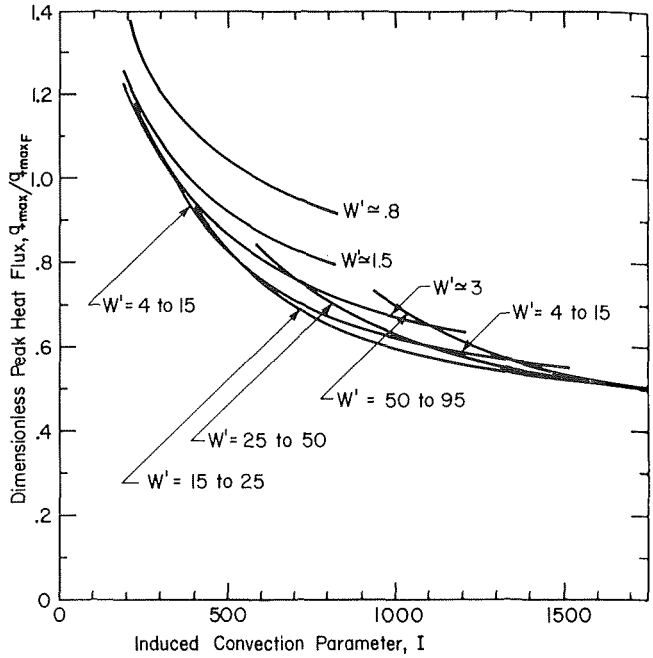

Fig. 5 q_{max}/q_{maxF} versus I contours for 8 values of W'

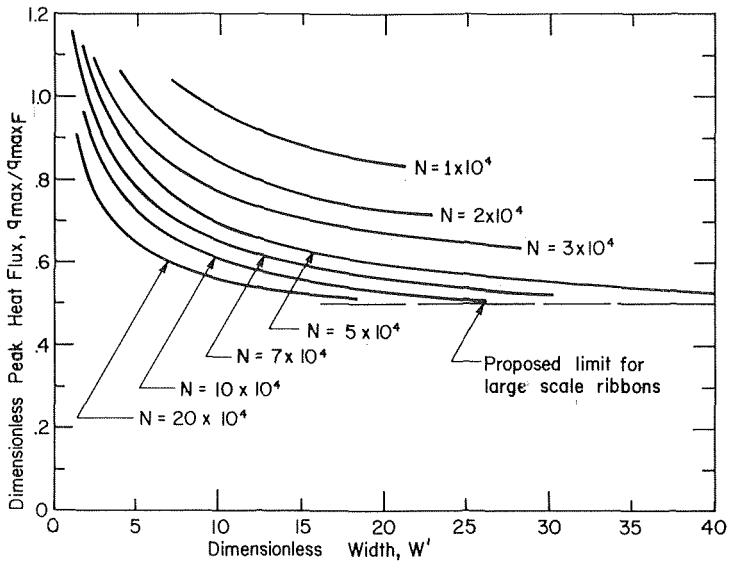

Fig. 6 q_{max}/q_{maxF} versus W' contours for 7 values of N

geometrically similar family of surfaces could be drawn through all of the substances. Methanol was most representative of the substances used. Acetone and water presented the highest q_{max}/q_{maxF} values—about 25 percent above the methanol—and isopropanol the lowest—about 30 percent below the methanol. The benzene data lay between the methanol and acetone data.

The resulting correlating surfaces are each presented here in sets of contours. The correlation function $f(I, W)$ is presented in Figs. 4 and 5 which give q_{max}/q_{maxF} versus W' and q_{max}/q_{maxF} versus I contours, respectively, as obtained from the 21 cross-plots. This surface generally follows the mean of the data for methanol and is consistent with trends that can be identified individually in each of the remaining substances.

The correlation in terms of N was obtained by transforming the curves given in Figs. 4 and 5 with the help of equation (7). It is given in a single plot of q_{max}/q_{maxF} versus W', with N as parameter, in Fig. 6.

Discussion

The correlation surfaces reveal the strong influence of the parameters I and N, that we anticipated, and they also show that this influence vanishes when the *scale* parameters, I and W,' become large. This was to be anticipated since buoyancy completely overbalances both capillary and viscous forces as the scale is increased. Thus

$$\text{limit}\left[\frac{q_{max}}{q_{maxF}}\right] \simeq \frac{1}{2}, \text{ large } I \text{ and } W' \qquad (11)$$

This limit appears to be valid for all $I > 1500$, and W' on the order of 50, depending upon the value of I. Since N is not a scale parameter we cannot propose a proper criterion in terms of it. However, the various lines of constant N seek $q_{max}/q_{maxF} = 1/2$ as an asymptote in Fig. 6.

That this limiting q_{max} is less than the flat plate value might reflect either or both of two factors: (*a*) The finite size of the centrifuge capsule doubtless results in a limiting high Reynolds number circulation which affects the peak heat flux; and/or (*b*) Zuber's equation has not really been subjected to broad testing in a proper flat plate configuration, and some error in the constant, 0.131, could conceivably contribute to a deviation of the present data from the supposed flat plate equation.

When W' falls below unity, surface tension assumes very strong control over the peak heat-flux transition and q_{max} rises sharply. The results of Lienhard and Watanabe, and other authors who have studied q_{max} on cylinders, show a comparable increase of q_{max} as L', based on cylinder diameter, falls below 0.40.

The fact that our data for different substances tend to cluster together, indicates that another parameter is needed to achieve a complete description on the present system. This would have to be a second scale parameter related to the finite size of the capsule. An "I" based upon capsule size, for example, would be smallest for isopropanol and progressively larger for methanol, benzene, acetone, and water—consistent with the order of separation we observed in our crossplotting. Although this effect is a secondary one in the present study, it points up the limitation of the present data to a particular container.

Conclusions

1 Induced (or natural) convection can exert a strong influence on the peak pool-boiling heat flux, if the configuration is one which is susceptible to it.

2 The present data should not be viewed as having broad applicability. They are restricted to a particular configuration of heater and container, and their value lies in that they illustrate the induced-convection effect.

3 Equations (8) and (9) are the appropriate expressions to use to correlate q_{max} data for any heater configuration, in a large container, over ranges of pressure, gravity, and size, and for different liquids.

4 The peak heat flux for a horizontal ribbon heater (and probably for other geometries as well) approaches a constant minimum fraction of q_{maxF} when the scale parameter, I and W', become large. It also approaches this limit as the induced-convection buoyancy parameter, N, increases.

Acknowledgments

Professor R. Eichhorn provided much helpful discussion of this work and K. H. Sun assisted with the apparatus and data reduction.

References

1 Zuber, N., "Hydrodynamic Aspects of Boiling Heat Transfer," PhD thesis, UCLA, Los Angeles, 1959. (Also available as AECU-4439, *Physics and Mathematics.*)

2 Zuber, N., Tribus, M., and Westwater, J. W., "The Hydrodynamic Crisis in Pool Boiling of Saturated and Subcooled Liquids," *International Developments in Heat Transfer*, No. 27, ASME, N. Y., 1963, pp. 230–236.

3 Kutateladze, S. S., "A Hydrodynamic Theory of Changes in the Boiling Process Under Free Convection Changes," *Izv. Akad. Nauk SSSR, Otd. Tekhn. Nauk* No. 4, 1951, p. 529. (Translation is available as AEC-TR-1441.)

4 Lienhard, J. H., and Schrock, V. E., "The Effect of Pressure Geometry, and the Equation of State Upon the Peak and Minimum Boiling Heat Flux," JOURNAL OF HEAT TRANSFER, TRANS. ASME, Series C, Vol. 85, 1963, pp. 261–272.

5 Lienhard, J. H., and Watanabe, K., "On Correlating the Peak and Minimum Boiling Heat Fluxes With Pressure and Heater Configuration," JOURNAL OF HEAT TRANSFER, TRANS. ASME, Series C, Vol. 88, No. 1, Feb. 1965, pp. 94–100.

6 Lienhard, J. H., and Wong, P. T. Y., "The Dominant Unstable Wavelength and Minimum Heat Flux During Film Boiling on a Horizontal Cylinder," JOURNAL OF HEAT TRANSFER, TRANS. ASME, Series C, Vol. 86, 1964, pp. 220–226.

7 Costello, C. P., Bock, C. O., and Nichols, C. C., "A Study of Induced Convective Effects on Pool Boiling Burnout," *CEP Symposium Series*, Vol. 61, 1965, pp. 271–280.

8 Cichelli, M. T., and Bonilla, C. F., "Heat Transfer to Liquids Boiling Under Pressure," *Trans. AIChE*, Vol. 41, 1945, p. 755.

9 Vliet, G. C., and Leppert, G., "Critical Heat Transfer for Nearly Saturated Water Flowing Normal to a Cylinder," JOURNAL OF HEAT TRANSFER, TRANS. ASME, Series C, Vol. 86, 1964, pp. 59–67.

10 Lienhard, J. H., and Carter, W. M., "Gravity Boiling Studies," Technical Report 1-68-ME-1, University of Kentucky, Lexington, Ky., 1968.

11 Keeling, K. B., "Effect of Gravity Induced Convection on the Peak Boiling Heat Flux on Horizontal Strip Heaters," Technical Report 11-69-ME-4, University of Kentucky, Lexington, Ky., 1969.

12 Sun, K. H., "Peak Pool Boiling Heat Flux on Horizontal Cylinders," MS thesis, University of Kentucky. Also available as College of Engineering Bulletin 88, University of Kentucky, 1969.

CHARLES D. JONES
Professor, Mechanical Engineering,
Ohio State University,
Columbus, Ohio

LESTER F. SMITH
Instructor, Engineering Graphics,
Ohio State University,
Columbus, Ohio

Optimum Arrangement of Rectangular Fins on Horizontal Surfaces for Free-Convection Heat Transfer

Experimental average heat-transfer coefficients for free-convection cooling of arrays of isothermal fins on horizontal surfaces over a wider range of spacings than previously available are reported. A simplified correlation is presented and a previously available correlation is questioned. An optimum arrangement for maximum heat transfer and a preliminary design method are suggested, including weight considerations.

Introduction

FREE-CONVECTION heat transfer from finned surfaces, including identification of optimum fin spacings, has been reasonably well established for several geometries including: vertical parallel flat plates [1–3],[1] vertical fins on horizontal tubes [4–8], and fins on vertical surfaces [9, 10]. However, rather limited data are available for an array of rectangular fins on horizontal surfaces [10, 11]. The purpose of this study was the examination of this latter configuration with the prime objective of establishing the optimum spacing of fins for maximum heat transfer from a given surface, in a form which can be conveniently used for preliminary design.

The general nature of the phenomena involved is illustrated by one set of test data presented in Fig. 1. On a given horizontal surface, as the fin spacing is decreased (number of fins increased), the total heat-transfer area per unit base area increases. However, the average heat-transfer coefficient of the array sharply decreases at small fin spacings due to restriction of the free-convective fluid flow. Thus the total heat transferred per unit base area (the product of the previous two parameters for a given temperature difference) exhibits a well-defined maximum value within a rather narrow range of optimum fin spacings. The data from this study permit prediction of optimum fin spacings as a function of fin height and temperature difference, as well as a general correlation of average heat-transfer coefficients for the array.

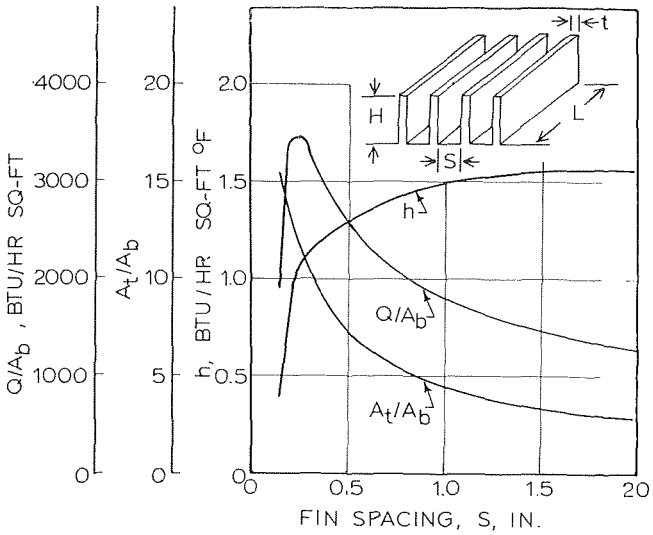

Fig. 1 Typical effects of fin spacing on average heat-transfer coefficients, ratio of total surface area to base surface, and heat transferred per unit base area for 1.94-in-high fins at a temperature difference of 275 deg F

Experimental Method

The experimental apparatus configuration is shown by the

[1] Numbers in brackets designate References at end of paper.

Contributed by the Heat Transfer Division of THE AMERICAN SOCIETY OF MECHANICAL ENGINEERS and presented at the ASME-AIChE Heat Transfer Conference, Minneapolis, Minn., August 3–5, 1969. Manuscript received by the Heat Transfer Division, November 1, 1968; revised manuscript received, April 16, 1969. Paper No. 69-HT-44.

Nomenclature

A_b = base surface area = $(S + t)Ln$, ft²
A_t = total surface area = $(S + t + 2H)Ln$, ft²
a = free-convection modulus = $gB\rho^2c_p/\mu k$, 1/deg F-ft³
B = volumetric expansion coefficient, 1/deg F
c_p = specific heat, constant pressure, Btu/lb-deg F
D = characteristic dimension (general), ft
e = Napierian base of logarithms
Gr = Grashof number = $gB\rho^2D^3\Delta T/\mu^2$
g = local acceleration of gravity, ft/hr²
H = fin height, ft
h = convection heat-transfer coefficient, Btu/hr-ft²-deg F
K_t = temperature correction factor, equation (7)
K_p = pressure correction factor, equation (7)
k = thermal conductivity, Btu/hr-ft deg F
L = fin length, ft
Nu = Nusselt number = hD/k
n = number of fins in an array
P = fin pitch = $S + t$, ft
Pr = Prandtl number = $c_p\mu/k$
p = pressure, lb/in.²
Q = heat transferred, Btu/hr
S = fin spacing, ft
T = temperature, deg F
ΔT = temperature difference = $T_0 - T_a$, deg F
t = fin thickness, ft
w = weight (of fins), lb
μ = viscosity, lb/ft-hr
ρ = density, lb/ft³

Subscripts

a = evaluated at ambient conditions
f = evaluated at film conditions
L = fin length used as characteristic dimension
0 = evaluated at surface temperature
rd = radiation
S = fin spacing used as characteristic dimension
w = fin material property

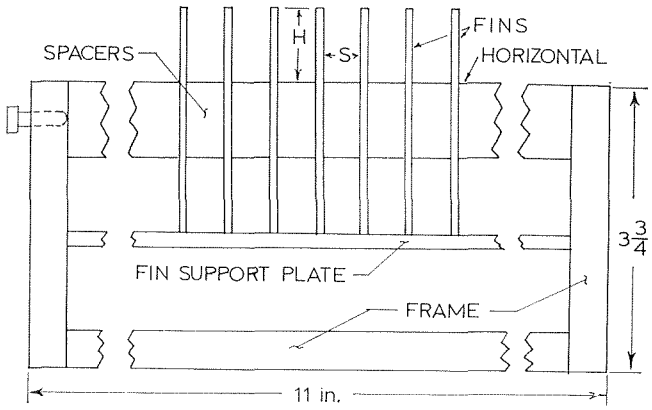

Fig. 2 Sketch of experimental apparatus

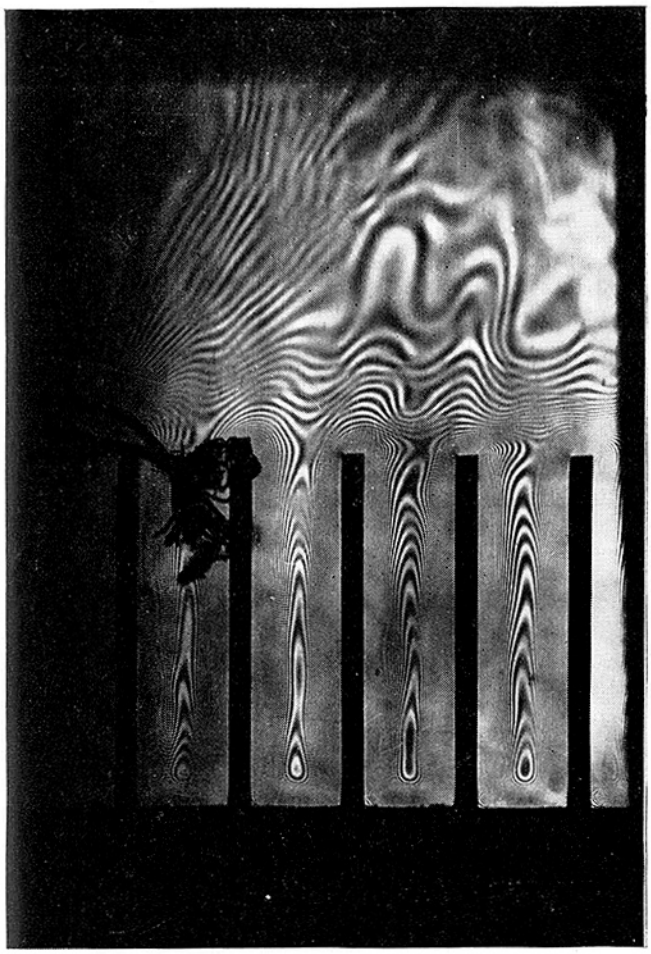

Fig. 3 Interferogram for 1.94-in-high fins, spaced 0.5 in. with a 200 deg F temperature difference

sketch in Fig. 2 and consisted of seven aluminum fins extending through the top horizontal surface of a closed container. Fin height was varied by adjusting the location of the fin support plate and the fin spacing maintained by spacers, the entire assembly being tightly clamped together. The ends of the channels formed by the fins were open; thus ambient air tends to flow horizontally in at the ends. Seventy-two combinations of fin height, spacing, and temperature difference were studied as outlined in Table 1, which also includes principal dimensions.

The apparatus was placed in the light path of a Zehnder-Mach interferometer which gives local temperature gradients averaged over the 10-in. length, and local heat-transfer coefficients were determined by measurement of these local temperature gradients on the interference photographs at 10 equally spaced points on the perimeter of a pair of centrally located fins and the adjacent prime horizontal surface. A typical interference photograph is shown in Fig. 3. Information concerning the interferometer and the techniques used are included in reference [12]. The entire apparatus was sufficiently massive that, after being heated in an electric oven to approximately 350 F, a sequence of interference photographs could be taken during the period of free-convection cooling. The apparatus cooling rate was between 1.0 and 0.1 deg F/min, and the photographic exposure speed 1/50 sec. Measured results with a single fin were in good agreement with available data for vertical flat plates, indicating that quasi-static conditions were established. Temperatures measured by seven thermocouples at a variety of extreme locations on the fins and prime surface (spacers) indicated that the apparatus was isothermal, within a few degrees, at the time each picture was taken. The average heat-transfer coefficient for the array was determined by mechanically integrating the local measured heat-transfer coefficients. Thus the reported value should be applicable to large arrays and do not include an edge effect.

The prime advantage of the interferometric technique is that the heat-transfer coefficients determined are for convection only and are independent of the radiation. The overall experimental error, including end effects associated with the interferometric technique and measured reproducibility of test runs, was determined to be within ± 10 percent. Verification of the experimental method and associated error analysis, in addition to the original experimental data, are contained in reference [13].

Correlation of Data

Average free-convection heat-transfer coefficients for all arrays tested were found to be reasonably correlated by the parameters shown in Fig. 4, using the fin spacing as the characteristic dimension and with all physical properties evaluated at the film temperature. This simple form implies that the heat-transfer coefficient is independent of the fin height. Statistical analysis of the data suggest that a small height effect exists (larger heat-transfer coefficients being associated with larger heights); however, since the size of this effect lies almost within the experimental scatter, it is not included. It should be noted that the fin length, L, is known to be important [10, 11] but was not a variable in this study. These data may be approximated by the empirical equation:

$$(\mathrm{Nu})_S = (6.7 \times 10^{-4})(\mathrm{Gr})_S \mathrm{Pr}\,[1 - e^{(0.746 \times 10^4/\mathrm{Gr}_S\mathrm{Pr})^{0.44}}]^{1.7} \quad (1)$$

which for fin spacings, S, greater than about 2.0 in. reduces to:

$$(\mathrm{Nu})_S = 0.54(\mathrm{Gr}_S\mathrm{Pr})^{0.25} \quad (2)$$

which is commonly accepted for heated flat plates facing upward.

Included in Fig. 4 are the data of Starner and McManus [10], transposed from their Fig. 4 and nondimensionalized for 10-in long fins. These data fall below, but are in fair agreement with,

Table 1 Range of variables studied

Fin height H, in.	Fin spacing, S, in.						
0.94	2.00	1.00	0.50	0.33	0.25	0.16	
1.44			0.50		0.25	0.16	
1.94	1.25	0.75	0.50		0.25	0.16	

Fixed dimensions		Range of relative dimensions
Fin length	$L = 10.0$ in.	$S/H = 0.082$ to 2.13
Fin thickness	$t = 0.125$ in.	$S/L = 0.016$ to 0.20
Number of fins (except $n = 5$ for $S = 2.0$)	$n = 7$	$H/L = 0.094$ to 0.19

Temperature difference, ΔT, from 60 to 280 deg F in six steps

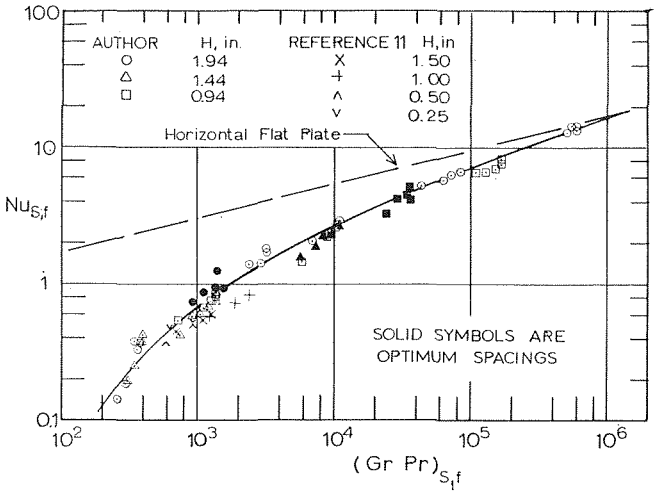

Fig. 4 Recommended correlation of average free convection heat-transfer data using spacing (S) as the characteristic dimension and with the properties evaluated at the film temperature, including the data of reference [11]. Fin length (L) is 10 in.

the authors. It may be noted that the data of Starner and McManus for vertical fin configurations also fell below comparable data reported by Welling and Wooldridge [9]. More recent data by Harahap and McManus [11] for 5-in-long fins on horizontal surfaces fall somewhat above (higher heat-transfer coefficients) the authors' data. It may be concluded that the average heat-transfer coefficients and spacing effects reported in references [10, 11] are in fair agreement with the data presented in this study.

Comparison With Other Correlations

Since the arrays studied by Harahap and McManus [11] were similar to those in this paper, a detailed comparison of the effects of each of the geometric variables may be made. Reference [11] recommends a correlation in the form:

$$(\mathrm{Nu})_L = C[(\mathrm{Gr})_L(\mathrm{Pr})(nS/H)]^a(S/L)^b(H/L)^c \qquad (3)$$

where in the low range:

$$C = 5.22 \times 10^{-3}, \quad a = 0.570, \quad b = 0.412, \quad \text{and} \quad c = 0.656$$

and in the high range:

$$C = 2.787 \times 10^{-4}, \quad a = 0.745, \quad b = 0.412, \quad \text{and} \quad c = 0.656$$

A plot of the authors' data using these coordinates is shown in Fig. 5 to provide a poor correlation with the bulk of the data falling well above the recommended curve. It is also noted that reference [11] recommends evaluation of the physical properties at the surface temperature rather than at the film temperature which causes a considerable distortion at high temperature levels, as illustrated by the inset in Fig. 5. It should be noted that the limited temperature range investigated in reference [11] was sufficiently low that these effects are not significant. Due to the large discrepancy between the correlation parameters recommended by the authors, Fig. 4, and those recommended by Harahap and McManus [11], Fig. 5, examination of each of the geometric parameters will be made to establish areas of agreement. Using equation (3) with the appropriate constants recommended by reference [11] yields, for a given fluid and temperature difference:

$$(h) \text{ proportional to } (L)^{-0.358}(S)^{0.982}(H)^{0.086}(n)^{0.57} \qquad (4)$$

for the low range and

$$(h) \text{ proportional to } (L)^{0.167}(S)^{1.157}(H)^{-0.089}(n)^{0.745} \qquad (5)$$

for the high range. The effects of each geometric dimension may now be compared with the authors' results.

1 Spacing Effects (S). Equations (4) and (5) indicate that the heat-transfer coefficient is proportional to the spacing to about the first power. Fig. 4 shows that the authors' data also has a slope of approximately unity in the range of the data of reference [11].

2 Height Effect (H). Equations (4) and (5) show a very small height effect: for example, a change in height by a factor of two would predict a change in the heat-transfer coefficient of 7 percent. This was approximately the effect observed by the authors which was considered too close to the experimental scatter to include in the correlation.

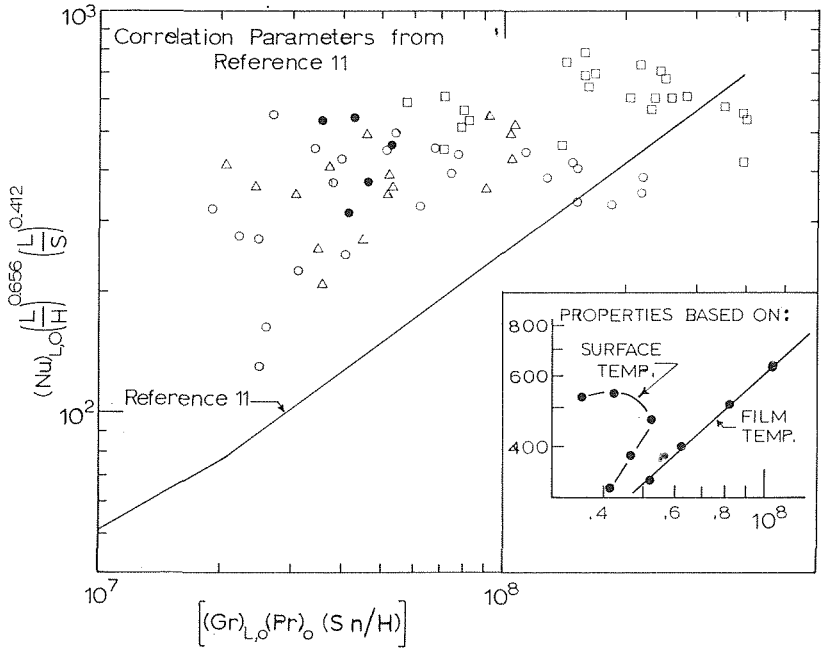

Fig. 5 Author's data using correlation parameters recommended by reference [11]. Inset: typical effects of evaluation of physical properties at surface temperature as compared with film temperature.

3 Length Effect (L). Since the authors did not vary length, no comparison can be made with equations (4) and (5). However, the authors' fin length of 10 in. was identical to that used in a portion of the reference [11] study.

4 Number of Fins (n). Fin numbers varying from 14 to 33 were used by Harahap and McManus [11] compared with 7, and in a few cases 5, used by the authors. Here a specific comparison can be cited between arrays which are almost identical except for number of fins as follows: reference [11] data for $L = 10.0$, $H = 1.50$, $S = 0.25$, and $n = 17$; and authors' data for $L = 10.0$, $H = 1.44$, $S = 0.25$, and $n = 7$ show measured heat-transfer coefficients for all temperature differences tested which agree within 10 percent (triangle and X points in Fig. 4). However, according to equation (5) from reference [11], they are predicted to differ by 94 percent.

The preceding observations suggest that the use of the number of fins (n) in the correlation and employment of fin length (L) as the prime characteristic dimension, is highly questionable. It is recognized that the complex three-dimensional flow field, with flow reversals observed by Harahap and McManus [11], is probably significantly influenced by the fin length (L), and that extensive further studies must be made to quantify this influence. The results of the present study and equations (4) and (5) from reference [11] strongly suggest that spacing (S), is the prime geometric variable.

Optimum Fin Spacing

In most design applications, where weight is not critical, it is usually desirable to maximize the free-convection heat transfer from the finned surface. As shown in Fig. 1, for a given fin height, an optimum fin spacing exists for which the heat transferred will be a maximum. The heat transfer per unit base area for all test data is shown in Fig. 6 as a function of fin spacing and height (for air only with $L = 10.0$ in.). The ordinate is made independent of temperature difference by dividing by the temperature difference to the 1.5 power, since Q varies with the 1.0 power, and h varies as the 0.5 power of the temperature difference in the range of optimum spacings, as shown in Fig. 4. Fig. 6 shows that small optimum spacings are associated with high fins and that with short fins, optimum spacing becomes less well defined and, thus, less critical to design variation. The data, from reference [11], for 10.0-in-long fins, are also shown in Fig. 6. As previously noted, these data for 1.5 and 1.0-in-high fins are in fairly good agreement with the authors. Data and extrapolated (dashed) curves are also shown for the two short fins of reference [11]. It should be noted that all test data from reference [11] were for fin spacings smaller than the optimum. Methods of extending the data of Fig. 6 for use with fluids other than air, or for air at considerably different temperatures and pressures, are described in the next section.

Inspection of fin spacings, which yielded the maximum heat transfer, produced an empirical relation that the optimum spacing occurs when (H) times (S) = 0.56 sq in., which seems to suggest that there exists an optimum cross-sectional area for inflow of air at the ends of the fins. The heat transfer per unit base area as a function of fin height for optimum spacing is shown in Fig. 7. The curve is extrapolated to zero fin height at an ordinate value approximately that of a heated flat plate in air.

Radiation heat transfer may be quite significant in free convection applications. The maximum radiant heat transfer from a large array of fins behaving as a black body would be:

$$Q_{rd}/A_b = 0.173(10)^{-8}(T_0^4 - T_a^4)$$

which by a fortuitous coincidence, in the range of $(T_0 - T_a)$ from 60 to 300 deg F, may be approximated by:

$$Q_{rd} = 0.132(T_0 - T_a)^{1.5} \quad (6)$$

as shown by the long line in Fig. 7. This assumes, of course, that the radiation environment temperature is the same as the ambient air temperature.

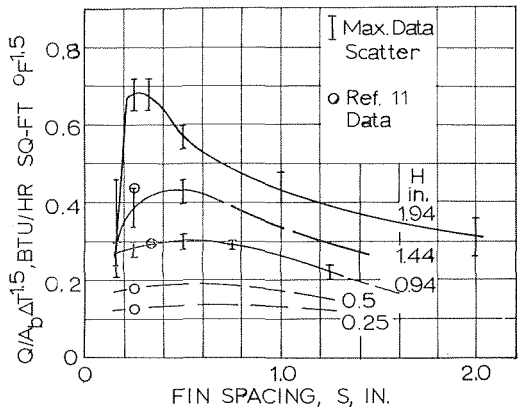

Fig. 6 Heat transfer per unit base area, normalized by temperature difference to the 1.5 power, as effected by fin spacing and fin height, with data from the author and reference [11]. For air, film temperature equal to approximately 160 deg F, and fin length (L) equal to 10 in.

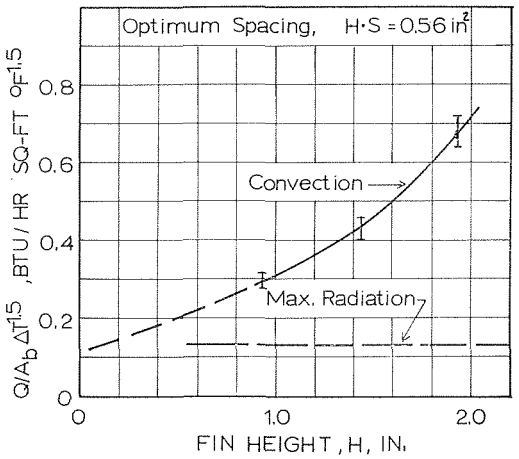

Fig. 7 Maximum heat transfer per unit base area, normalized by temperature difference to the 1.5 power, as a function of fin height for the optimum spacing where the product HS = 0.56 in. squared. For air, film temperature equal to approximately 160 deg F, and fin length (L) equal to 10 in.

Fin Weight Considerations

In applications where the weight of fins added to a surface is important, or the cost of fin material becomes significant, a measure of the heat dissipated per unit fin material weight, in addition to, or to the exclusion of, heat dissipation per unit base area must be considered. The faired curves in Fig. 6 are replotted in Fig. 8 which shows the heat dissipation divided by fin weight (per unit fin thickness, material density, and Δt to the 1.5 power) as a function of fin height and spacing for air. This figure indicates that for a given heat dissipation, light weight arrays will have widely spaced, short fins which is incompatible with maximizing heat dissipation per unit base area. In the range of optimum spacing for maximum heat transfer (values of S between 0.25 and 0.50 in.), tall fins show a slight advantage.

Conclusions

1 Experimental heat-transfer coefficients for arrays of isothermal fins on horizontal surfaces have been established over a reasonably wide range of fin spacings, fin heights, and temperature differences, considerably extending the range of previously available data.

2 Measured values are in fairly good agreement with the limited comparable data of Starner and McManus [10] and Harahap and McManus [11].

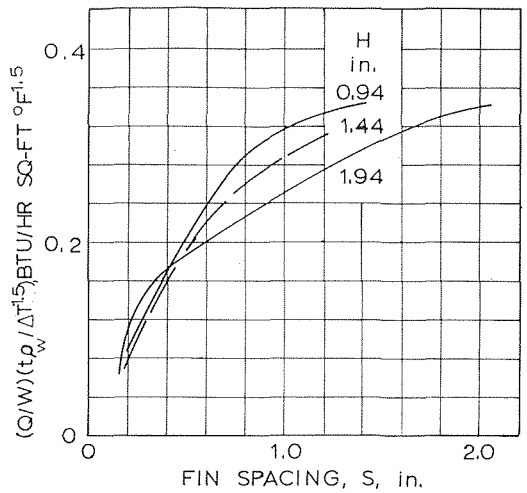

Fig. 8 Heat transfer per unit fin height, which is proportional to heat dissipation per unit fin weight, as a function of fin spacing and fin height. For air, film temperature equal to approximately 160 deg F, and fin length (L) equal to 10 in.

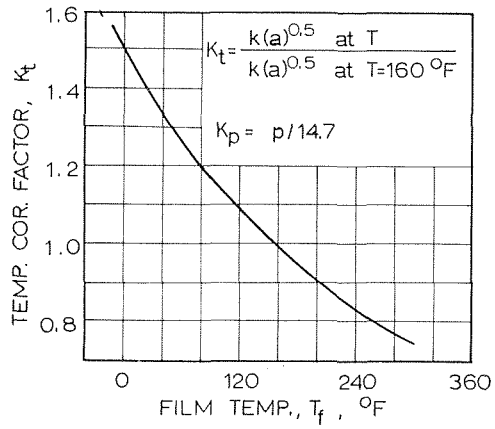

Fig. 9 Temperature and pressure correction factors for air to be used in equation (7)

3 Data correlation suggests that fin spacing is the prime geometric variable, and that the forms of the correlation parameters suggested by reference [11] are questionable.

4 Optimum fin spacings for maximum heat transfer per unit base area have been reasonably established and partially correlated for preliminary design use.

5 The presented data are applicable only to fins approximately 10 in. long. Although reference [11] has identified that fin length has a very significant effect on the heat-transfer coefficient, it is believed that further studies must be made to quantitatively establish these effects.

A Preliminary Design Procedure

A method of utilizing the data presented in this paper to provide a preliminary design estimate of fin requirements is indicated as follows:

1 The following data must be initially known or assumed: Heat to be dissipated through the horizontal surface (Q), dimensions of the surface (A_b), surface temperature (T_0), and ambient fluid temperature (T_a). Calculate $Q/A_b(\Delta T)^{1.5}$

2 Since the design figures are for air, atmospheric pressure, and approximately 160 deg F film temperature, a correction must be applied:

$$Q/A_b(\Delta T)^{1.5} = K_t K_p [Q/A_b(\Delta T)^{1.5}]_{\text{fig}} \qquad (7)$$

the subscript (fig) implies the value to be used in Figs. 6–8. For any fluid,

$$K_t K_p = k(a)^{0.5}/15.1$$

For air, values of the temperature and pressure correction factor are given separately in Fig. 9.

3 The curve in Fig. 7 indicates the fin height (H) and the associated optimum fin spacing is $S = H/0.56$ (in.).

4 A fin thickness (t) and material is now chosen, and fin efficiency (and weight and cost, if appropriate) estimated for the array established, based on maximum heat dissipation per unit base surface area.

5 If the preceding determined values of S, H, weight, or cost are incompatible with other constraints, Fig. 6 can be examined for other combinations of H and S (off-optimum combinations) which may produce the required heat flux. Note that for each fin height there may be two values of fin spacing which produce the required heat flux. In these off-optimum cases, the larger spacing would normally be chosen to minimize the total number of fins.

6 Radiation effects, which increase performance, and fin efficiency effects, which decrease performance, have not been included since they tend to offset each other. Radiation effects can be included by subtracting the value 0.132 from the previously calculated value of $[Q/A_b(\Delta T)^{1.5}]_{\text{fig}}$ before entering the figures. Fin efficiency effects may be approximated by use of equation (7), where the value of the fin efficiency is substituted for $(K_t K_p)$, to obtain a corrected value of $[Q/A_b(\Delta T)^{1.5}]_{\text{fig}}$.

7 It should be noted that these calculations are valid only for fin lengths, L, of 10 in. Shorter fins are known to yield higher heat-transfer coefficients (reference [11]) and longer fins, probably lower heat-transfer coefficients, although this has not yet been established. Also, since the data scatter is approximately 10 percent, some safety factor should be included.

References

1 Elenbaas, W., "Heat Dissipation of Parallel Plates by Free Convection," *Physics*, Vol. 9, No. 1, Jan. 1942.

2 Siegel, R., and Norris, R. H., "Tests of Free Convection in a Partially Enclosed Space Between Two Heated Plates," TRANS. ASME, Vol. 79, 1957, pp. 663–673.

3 Sununu, J. H., "The Effect of Spacing on the Efficiency of Extended Surfaces for Natural Convection Cooling," *Proceedings of the National Electronics Packaging and Production Conference*, New York, June 1963, pp. 30–41.

4 Knudson, J. G., and Pan, R. B., "Natural Convection Heat Transfer From Transverse Finned Tubes," *Chemical Engineering Progress Symposium*, Vol. 61, No. 57, 1965, p. 44.

5 Edwards, J. A., and Chaddock, J. B., "An Experimental Investigation of the Radiation and Free-Convection Heat Transfer From a Cylindrical Disk Extended Surface," *Trans. ASHRAE*, Vol. 69, 1963, pp. 313–322.

6 Edwards, J. A., and Chaddock, J. B., "Free Convection and Radiation Heat Transfer From Fin-on-Tube Heat Exchangers," ASME Paper No. 62-WA-205, 1962.

7 Seigel, L. G., and Bryan, W. L., "Natural Convection Cooling and Dehumidifying," *Heating Piping and Air Conditioning*, Dec. 1957, pp. 129–134.

8 Nwizu, E. I., "An Experimental Investigation of Natural Convection Heat Transfer From Isothermal Horizontal Cylinders With Plain Circular Fins," MSc thesis, The Ohio State University, 1963.

9 Welling, J. R., and Wooldridge, C. B., "Free Convection Heat Transfer Coefficients From Rectangular Vertical Fins," JOURNAL OF HEAT TRANSFER, TRANS. ASME, Series C, Vol. 87, 1965, pp. 439–444.

10 Starner, K. E., and McManus, H. N., "An Experimental Investigation of Free-Convection Heat Transfer From Rectangular-Fin Arrays," JOURNAL OF HEAT TRANSFER, TRANS. ASME, Series C, Vol. 85, 1963, pp. 273–278.

11 Harahap, F., and McManus, H. N., "Natural Convection Heat Transfer From Horizontal Rectangular Fin Arrays," JOURNAL OF HEAT TRANSFER, TRANS. ASME, Series C, Vol. 89, 1967, pp. 32–38.

12 Jones, C. D., and Masson, D. J., "An Interferometric Study of Free Convection Heat Transfer From Enclosed Isothermal Surfaces," TRANS. ASME, Vol. 77, 1955, pp. 1275–1281.

13 Smith, L. F., "An Interferometric Investigation of Optimum Rectangular Fin Geometry for Maximum Free-Convection Heat Transfer From a Finned Horizontal Surface," MSc thesis, The Ohio State University, 1963.

R. H. TIEN

V. KOUMP[1]

Edgar C. Bain Laboratory for Fundamental Research, United States Steel Corp., Monroeville, Pa.

Effect of Density Change on the Solidification of Alloys

During freezing of alloys the difference in densities between the solid and the liquid results in a mass flow throughout the solid-liquid region. This mass flow contributes to transport of mass and heat and hence affects the rate of solidification of the alloy. In this paper an analytical solution is presented on solidification of a semi-infinite slab of a binary alloy at a constant surface temperature and unequal solid and liquid densities. On the basis of an assumed form of the solid fraction distribution within the solid-liquid region, this solution yields the temperature and liquid velocity distribution within the solid-liquid region, the temperature distribution within the solid skin and the rates of propagation of the solidus and the liquidus fronts. A comparison is made with the case of equal solid and liquid densities.

Introduction

Unlike the freezing of pure metals, the solidification of alloys occurs over a temperature range. The freezing of an alloy begins at the liquidus temperature and is completed at solidus (or eutectic) temperature. The one-dimensional solidification of an alloy thus occurs by propagation of two isothermal fronts, the liquidus front and the solidus (or eutectic) front. The region between the two isothermal fronts contains both solid and liquid and will be referred to as the solid-liquid region.

When the densities of the solid and the liquid alloys are equal (simplified case) the liquid within the solid-liquid region does not move with respect to the solid. The transport of mass and heat within the solid-liquid region, under these conditions, occurs by diffusion and thermal conduction, respectively. Solidification of binary alloys for the case of equal solid and liquid densities has been analyzed by the authors in two earlier papers [1, 2].[2]

In general, however, the densities of solid and liquid alloys are not equal, and the liquid-solid transition is accompanied by a change of volume which, in turn, causes the flow of liquid. Since, in the case of freezing a pure metal, the thermal contraction occurs at only one temperature (the freezing point), due to the isothermal freezing process, the flow of liquid toward the freezing front is uniform at any particular time. The nature of the flow of liquid and its effect on the freezing rate for the case of freezing a pure metal were analyzed by Carslaw and Jaeger [3]. During solidification of alloys, however, the change of volume during liquid-solid transition results in a flow of interdendritic liquid throughout the solid-liquid region. In addition to the transport of heat within the solid-liquid region, and hence affecting the rate of solidification of the alloy, this flow of liquid also results in the redistribution of solute. It appears that the nature of the flow of the interdendritic liquid and its effects during solidification of alloys have not been studied by previous investigators.

A mathematical solution of one-dimensional solidification of an alloy is presented in this paper for the case of unequal solid and liquid densities. The surface temperature of the slab is assumed to be constant and lower than the solidus temperature. The physical and thermal properties of the solid and the liquid alloy are assumed to be independent of temperature. It is also assumed that the viscous shear force between the flowing liquid and the solid is completely overcome by the pressure gradient originated from the hydrostatic force exerted by the liquid head. Hence void formation is ignored. Furthermore, the dissipation of heat due to the shear force is assumed to be negligibly small as compared to the latent heat of fusion. The present model consists of conduction equations for both the solidified region and the liquid-solid region, together with proper boundary and initial conditions, equation of continuity to provide the expression of velocity for flowing liquid, and the distribution of solid fraction within the liquid-solid region. An analytical solution is obtained by the use of the error function solution combined with the heat-balance integral method which was originally used by Goodman [4].

Although the result shows that the affect of density change on the solidification rate is only about 10 percent, the other purpose of this investigation is to obtain the analytical expression for the flow of interdendritic liquid throughout the liquid-solid region due to the change of density. Since this flow is the motivation of the redistribution of solute, hence results the nonhomogeneity in the solidified alloy.

The solid fraction distribution within the solid-liquid region is assumed to be cubic form in the example given in the later part of this paper. This is strictly for simplicity purpose. The actual solid fraction distribution can be easily solved from the present model added by a specific relationship between solid fraction and

[1] Presently, Westinghouse Electric Corporation, Pittsburgh, Pa.

[2] Numbers in brackets designate References at end of paper.

Contributed by the Heat Transfer Division of The American Society of Mechanical Engineers and presented at the ASME-AIChE Heat Transfer Conference, Minneapolis, Minn., August 3–6, 1969. Manuscript received by the Heat Transfer Division, January 31, 1969. Paper No. 69-HT-45.

Nomenclature

A = internal heat generation, Btu/ft^3-hr
α = thermal diffusivity, ft^2/hr
c = specific heat Btu/lb-deg F
ϵ = thickness of frozen skin, ft
$\Delta\epsilon$ = thickness of liquid-solid region, ft
f_s = solid fraction
K = thermal conductivity, Btu/ft-hr-deg F
L = latent heat of fusion, Btu/lb
λ = parameter in the expression ϵ and $\Delta\epsilon$, ft/hr$^{1/2}$
ρ_l = density of liquid, lb/ft^3
ρ_s = density of solid, lb/ft^3
t = time, hr
T = temperature, deg F
T_c = surface temperature, deg F
T_s = solidus temperature, deg F
ΔT = temperature difference between liquidus and solidus, deg F
u = velocity, ft/hr
x = distance, ft

Subscripts

1 = solidified region
2 = liquid-solid region

temperature depending on the mode of diffusion of solute, and was demonstrated in a previous analysis [5].

Theoretical Model

Let us consider a semi-infinite region extending in the positive x-direction and occupied by molten alloy at the liquidus temperature. At time zero, the temperature at the surface, $x = 0$ is reduced to T_0, which is constant and lower than the solidus temperature. Thus solidification begins and the two isothermal planes at the solidus and liquidus temperature, respectively, move away from the surface of the slab. These two isothermal planes, defining the boundaries of the solid-liquid region, move with different velocities. Within the solid-liquid region the density of the solid-liquid mass changes at a rate which depends on the difference between the densities of solid and the liquid and the rate of the solid formation. Therefore the liquid within the solid-liquid region flows either toward the solidus front to fill the volume shrinkage due to the solidification, or toward the liquidus front due to volume expansion on freezing, depending on the relative magnitudes of the liquid and solid densities. Since the generation of solid occurs throughout the solid-liquid region, the velocity of the liquid within the solid-liquid region varies not only with time but also with position. The physical representation of the problem and the coordinate system used in the mathematical formulation of the problem are shown in Fig. 1. Assuming constant physical and thermal properties of solid and liquid alloys, the one-dimensional Fourier conduction equations can be written for the solid skin and the solid-liquid region as follows,

$$\frac{\partial^2 T_1}{\partial x^2} = \frac{1}{\alpha_1}\frac{\partial T_1}{\partial t} \qquad 0 \le x \le \epsilon \tag{1}$$

$$K_2\frac{\partial^2 T_2}{\partial x^2} - \rho_l c_2\frac{\partial}{\partial x}(uT_2) + A = \rho_2 c_2\frac{\partial T_2}{\partial t} \quad \epsilon \le x \le \epsilon + \Delta\epsilon \tag{2}$$

The boundary and the initial conditions required in the solution of these equations are

1 $T_1(x = 0) = -(T_s - T_c)$

2 $T_1(x = \epsilon) = 0$

3 $T_2(x = \epsilon) = 0$

4 $T_2(x = \epsilon + \Delta\epsilon) = \Delta T = T_l - T_s$

5 $\dfrac{\partial T_2}{\partial x}(x = \epsilon + \Delta\epsilon) = 0$

6 $K_1\dfrac{\partial T_1}{\partial x}(x = \epsilon) = K_2\dfrac{\partial T_2}{\partial x}(x = \epsilon)$

7 $\epsilon(t = 0) = 0$

8 $\Delta\epsilon(t = 0) = 0$

The first term on the left side of equation (2) represents heat flow by conduction in the solid-liquid region, the second term represents a contribution to the heat flow due to the flow of the liquid, and the last term represents the heat generation due to solid formation within the solid-liquid region. The boundary conditions 1–4 state that the temperature at the surface, $x = 0$, at the solidus front, $x = \epsilon$, and at the liquidus front, $x = \epsilon + \Delta\epsilon$, are constant, independent of time. The fifth boundary condition means that the liquid ahead of the liquidus front is at the liquidus temperature. The sixth boundary condition represents the conservation of energy at the solidus front. The last two initial conditions state that initially the whole region is occupied by the liquid.

The distribution of volume fraction of solid within the solid-liquid region is written as an nth degree polynomial,

$$f_s = 1 - \sum_{i=1}^{n} C_i\bar{x}^i \tag{3}$$

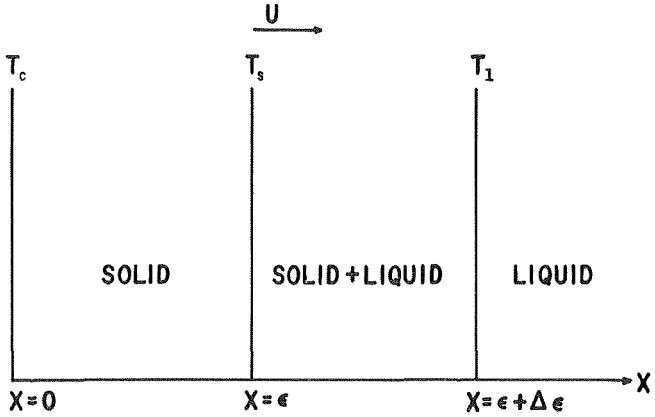

Fig. 1 Physical representation

where $\bar{x} = \dfrac{x - \epsilon}{\Delta\epsilon}$ and C_i's are so chosen that $\sum_{i=1}^{n} C_i = 1$.

The coefficients C_i which represent the distribution of the solid fraction can be calculated from a specific relationship between solid fraction and temperature when the temperature distribution within the solid-liquid region is expressed in terms of a dimensionless space variable such that the functional relationship between them is independent of the form of solid fraction distribution used in the analysis. This procedure to calculate the solid fraction distribution was discussed in detail in reference [5]. However, it is shown in the latter part of this paper that the form of solid fraction distribution is not a dominant factor for the present analysis. Therefore the coefficients, C_i, in the present analysis are assumed to be arbitrary constants for simplicity purposes.

The heat-generation term A can, therefore, be calculated as:

$$A = \rho_2 L\frac{\partial f_s}{\partial t} = \rho_2 L\frac{1}{\Delta\epsilon}\left(\frac{d\epsilon}{dt} + \bar{x}\frac{d\Delta\epsilon}{dt}\right)\left(\sum_{i=1}^{n} iC_i\bar{x}^{i-1}\right) \tag{4}$$

where ρ_2 is the local density within the solid-liquid region, and is equal to

$$\rho_2 = \rho_s f_s + \rho_l(1 - f_s) = \rho_s - (\rho_s - \rho_l)\sum_{i=1}^{n} C_i\bar{x}^i \tag{5}$$

Before applying the concept of continuity to the liquid-solid region to obtain the expression of velocity of flowing liquid, it is necessary to specify the model for the physical construction of the liquid-solid region. The evidence for the dendrite being plate-like which was developed by Flemings [6] and was discussed in reference [1] makes it possible to visualize the liquid-solid region as a collection of rectangular cells which are formed initially at the liquidus front. The solidification takes place merely by thickening of the dendritic plates which form the walls of the individual cells. (The interdendritic branches are assumed to be absent.) The thickness of the cell during one-dimensional solidification is of the order of 100 microns which is quite small in engineering scale. Therefore, any isothermal front within the liquid-solid region can be considered as a porous material with uniform porosity which, in the present model, is obviously a function of solid fraction, and hence depends on temperature. The velocity of flowing liquid, u within the liquid-solid region can thus be expressed by applying the principle of continuity as:

$$u = \left(\frac{\rho_l - \rho_s}{\rho_l}\right)\frac{1}{1 - f_s}\int_0^x \frac{\partial f_s}{\partial t}\,dx$$

$$= \left(\frac{\rho_l - \rho_s}{\rho_l}\right)\left[\frac{d\epsilon}{dt} + \frac{\left(\sum_{i=1}^{n}\frac{i}{i+1}C_i\bar{x}^{i+1}\right)}{\left(\sum_{i=1}^{n}C_i\bar{x}^i\right)}\frac{d\Delta\epsilon}{dt}\right] \tag{6}$$

where u is assumed to be positive when the direction of flow is toward the liquid region.

Solution

Equation (1) with boundary conditions 1 and 2 and initial condition 7 has the following solution

$$T_1(x, t) = (T_s - T_c)\left[\frac{\operatorname{erf}\left(\frac{x}{2\sqrt{\alpha_1}\sqrt{t}}\right)}{\operatorname{erf}\left(\frac{\lambda_1}{\sqrt{\alpha_1}}\right)} - 1\right] \tag{7}$$

$$\epsilon(t) = 2\lambda_1\sqrt{t} \tag{8}$$

where λ_1 is a constant, and will be determined later.

The method of heat-balance integral is now applied to equation (2) by defining the thermal layer as the entire freezing region. After integrating with respect to x between $x = \epsilon$ and $x = \epsilon + \Delta\epsilon$, equation (2) becomes:

$$K_2\frac{\partial T_2}{\partial x}(t = \epsilon + \Delta\epsilon) - K_2\frac{\partial T_2}{\partial x}(x = \epsilon) - \rho_l c_2[(x = \epsilon + \Delta\epsilon)T_2(x = \epsilon + \Delta\epsilon) - u(x = \epsilon)T_2(x = \epsilon)] + \int_\epsilon^{\epsilon+\Delta\epsilon} A\cdot dx = c_2\int_\epsilon^{\epsilon+\Delta\epsilon}\rho_2\frac{\partial T_2}{\partial t}\,dx \tag{9}$$

But

$$\begin{cases} \dfrac{\partial T_2}{\partial x}(t = \epsilon + \Delta\epsilon) = 0 \qquad \text{by B.C. 5} \\ T_2(x = \epsilon + \Delta\epsilon) = \Delta T \qquad \text{by B.C. 4} \\ T_2(x = \epsilon) = 0 \qquad \text{by B.C. 3} \\ u(x = \epsilon + \Delta\epsilon) = \left(\dfrac{\rho_l - \rho_s}{\rho_l}\right) \times\left[\dfrac{d\epsilon}{dt} + \left(\sum_{i=1}^{n}\dfrac{i}{i+1}C_i\right)\dfrac{d\Delta\epsilon}{dt}\right] \qquad \text{by B.C. 6} \\ u(x = \epsilon) = \left(\dfrac{\rho_l - \rho_s}{\rho_l}\right)\dfrac{d\epsilon}{dt} \qquad \text{by B.C. 6} \end{cases} \tag{10}$$

With the aid of equations (4) and (5), the integration of heat-generation term can be expressed as:

$$\int_\epsilon^{\epsilon+\Delta\epsilon} A\cdot dx = L\left\{\left[\rho_s + (\rho_l - \rho_s)\times\left(\sum_{k=2}^{2n}\frac{1}{k}\sum_{\substack{i+j=k\\ i,j=1}}^{n}C_i jC_j\right)\right]\frac{d\epsilon}{dt} + \left[\rho_s\left(\sum_{i=1}^{n}\frac{i}{I=1}C_i\right) + (\rho_l - \rho_s)\left(\sum_{k=2}^{2n}\frac{1}{k+1}\sum_{\substack{i+k=k\\ i,j=1}}^{n}C_i jC_j\right)\right]\frac{d\Delta\epsilon}{dt}\right\} \tag{11}$$

The integration on the right side of equation (9) can be carried out by using equation (5) for the expression of ρ_2.

$$c_2\int_\epsilon^{\epsilon+\Delta\epsilon}\rho_2\frac{\partial T_2}{\partial t}\,dx = c_2\int_\epsilon^{\epsilon+\Delta\epsilon}\frac{\partial}{\partial t}(\rho_2 T_2)dx - c_2\int_\epsilon^{\epsilon+\Delta\epsilon}T_2\frac{\partial\rho_2}{\partial t}\,dx \tag{12}$$

Using Leibniz's formula and the definition of

$$\theta_2 = c_2\int_\epsilon^{\epsilon+\Delta\epsilon}\rho_2 T_2\,dx \tag{13}$$

the first integration on the right side of equation (12) can be reduced to

$$c_2\int_\epsilon^{\epsilon+\Delta\epsilon}\frac{\partial}{\partial t}(\rho_2 T_2)dx = \frac{d\theta_2}{dt} - \rho_l c_2\Delta T\left(\frac{d\epsilon}{dt} + \frac{d\Delta\epsilon}{dt}\right) \tag{14}$$

Substituting equations (10), (11), (12), and (14) into equation (9) provides:

$$-K_2\frac{\partial T_2}{\partial x}(x = \epsilon) - \rho_l c_2\Delta T\left(\frac{\rho_l - \rho_s}{\rho_l}\right)\times\left[\frac{d\epsilon}{dt} + \left(\sum_{i=1}^{n}\frac{i}{i+1}C_i\right)\frac{d\Delta\epsilon}{dt}\right] + L\left\{\left[\rho_s + (\rho_l - \rho_s)\left(\sum_{k=2}^{2n}\frac{1}{k}\sum_{i+j=k}C_i jC_j\right)\right]\frac{d\epsilon}{dt} + \left[\rho_s\left(\sum_{i=1}^{n}\frac{i}{i+1}C_i\right) + (\rho_l - \rho_s)\times\left(\sum_{k=2}^{2n}\frac{1}{k+1}\sum_{i+j=k}C_i jC_j\right)\right]\frac{d\Delta\epsilon}{dt}\right\} = \frac{d\theta_2}{dt} - \rho_l c_2\Delta T\left(\frac{d\epsilon}{dt} + \frac{d\Delta\epsilon}{dt}\right) - c_2\int_\epsilon^{\epsilon+\Delta\epsilon}T_2\frac{\partial\rho_2}{\partial t}\,dx \tag{15}$$

We now let the temperature distribution within the liquid-solid region be in quadratic form,

$$T_2 = A_1(x - \epsilon) + A_2(x - \epsilon)^2$$

which automatically satisfies B.C. 2. Now using B.C. 4 and 5, the coefficients A_1 and A_2 can be calculated

$$T_2 = \Delta T(2\bar{x} - \bar{x}^2), \qquad \text{where } \bar{x} = \frac{x - \epsilon}{\Delta\epsilon} \tag{16}$$

Then

$$-K_2\frac{\partial T_2}{\partial x}(x - \epsilon) = -\frac{2K_2\Delta T}{\Delta\epsilon}$$

$$\frac{d\theta_2}{dt} = \frac{d}{dt}\left[c_2\int_\epsilon^{\epsilon+\Delta\epsilon}\rho_2 T_2 dx\right] = \Delta T c_2\left[\frac{2}{3}\rho_s + (\rho_l - \rho_s)\left(2\sum_{i=1}^{n}\frac{1}{i+2}C_i - \sum_{i=1}^{n}\frac{1}{1+3}C_i\right)\right]\frac{d\Delta\epsilon}{dt}c_2$$

$$\int_\epsilon^{\epsilon+\Delta\epsilon}T_2\frac{\partial\rho_2}{\partial t}\,dx = -(\rho_l - \rho_s)c_2\Delta T\left\{\left[2\left(\sum_{i=1}^{n}\frac{i}{i+1}C_i\right) - \left(\sum_{i=1}^{n}\frac{i}{i+2}C_i\right)\right]\frac{d\epsilon}{dt} + \left[2\left(\sum_{i=1}^{i}\frac{i}{i+2}C_i\right) - \left(\sum_{i=1}^{n}\frac{i}{i+3}C_i\right)\right]\frac{d\Delta\epsilon}{dt}\right\} \tag{17}$$

Combing equations (15) and (17) gives:

$$B_1\frac{d\epsilon}{dt} + B_2\frac{d\Delta\epsilon}{dt} = B_3\frac{1}{\Delta\epsilon} \tag{18}$$

where

$$B_1 = \frac{L}{\Delta T c_2}\left\{\frac{\rho_s}{\rho_l} + \frac{(\rho_l - \rho_s)}{\rho_l}\left[\sum_{k=2}^{2n}\frac{1}{k}\left(\sum_{\substack{i+j=k\\ i,j=1}}^{n}jC_iC_j\right)\right]\right\} + \frac{\rho_s}{\rho_l} - \frac{(\rho_l - \rho_s)}{\rho_l}\left[2\left(\sum_{i=1}^{n}\frac{i}{i+1}C_i\right) - \left(\sum_{i=1}^{n}\frac{i}{i+2}C_i\right)\right] \tag{19}$$

$$B_2 = \frac{L}{\Delta T c_2}\left\{\frac{\rho_s}{\rho_l}\left(\sum_{i=1}^{n}\frac{i}{i+1}C_i\right) + \frac{\rho_l-\rho_s}{\rho_l}\left[\sum_{k=2}^{2n}\frac{1}{k+1}\left(\sum_{\substack{i+j=k\\ i,j=1}}^{n} jC_iC_j\right)\right]\right\} - \frac{(\rho_l-\rho_s)}{\rho_l}\left(\sum_{i=1}^{n}\frac{i}{i+1}C_i\right) - \left[\frac{2}{3}\frac{\rho_s}{\rho_l} + \frac{(\rho_l-\rho_s)}{\rho_l}\left(2\sum_{i=1}^{n}\frac{1}{i+2}C_i - \sum_{i=1}^{n}\frac{1}{i+3}C_i\right)\right] + 1 - \frac{(\rho_l-\rho_s)}{\rho_l}\left[2\left(\sum_{i=1}^{n}\frac{i}{i+2}C_i\right) - \left(\sum_{i=1}^{n}\frac{i}{i+3}C_i\right)\right] \quad (19)$$

(*Cont.*)

$$B_3 = \frac{2K_2}{\rho_l c_2}$$

Now we assume that

$$\Delta\epsilon = 2\lambda_2\sqrt{t}, \quad (20)$$

Substituting equations (7), (8), (16), and (20) into boundary condition (6) yields,

$$\lambda_2 = \Delta T\frac{K_2}{K_1}\frac{\sqrt{\pi\alpha_1}\,\mathrm{erf}\left(\frac{\lambda_1}{\sqrt{\alpha_1}}\right)}{(T_s-T_c)e^{-\lambda_1^2/\alpha_1}} \quad (21)$$

Using the expressions for ϵ and $\Delta\epsilon$ as shown in equations (8) and (20), equation (18) can be rewritten as:

$$B_1\lambda_1 + B_2\lambda_2 = B_3\frac{1}{2\lambda_2} \quad (22)$$

λ_2 can now be eliminated from equations (21) and (22), and a function involving only λ_1 is obtained,

$$B_1\frac{\lambda_1}{\sqrt{\alpha_1}} + B_2\frac{\Delta T}{(T_s-T_c)}\frac{K_2}{K_1}\sqrt{\pi}\frac{\mathrm{erf}\left(\frac{\lambda_1}{\sqrt{\alpha_1}}\right)}{e^{-\lambda_1^2/\alpha_1}} = \frac{(T_s-T_c)}{\Delta T}\frac{K_1}{\rho_l c_2}\frac{1}{\alpha_1\sqrt{\pi}}\frac{e^{-\lambda_1^2/\alpha_1}}{\mathrm{erf}\left(\frac{\lambda_1}{\sqrt{\alpha_1}}\right)} \quad (23)$$

In solution of the problem considered in this paper, the coefficients C_i in equation (3) are assumed to be known. However, these coefficients could be calculated for a specific solid fraction-temperature relationship as described in the Introduction. The parameter λ_1 is evaluated by solving equation (23). The parameter λ_2 is then evaluated from equation (21). With parameters λ_1 and λ_2 now available, ϵ and $\Delta\epsilon$ are evaluated from equations (8) and (20). The velocity and temperature distribution within the solid-liquid region are given by equations (6) and (16), and the temperature distribution within the frozen skin is given by equation (7).

Results and Discussion

In order to illustrate the effect of the heat brought about by the interdendritic liquid flow within the liquid-solid region, we present the results of calculations for one alloy system, with and without density change during solidification. The following physical and thermal properties of the solid and liquid alloys which are close to the Al-Cu system at low concentration of copper are used in the calculations. However the difference between densities of solid and liquid are exaggerated.

$$\begin{aligned} K_1 &= 75 \text{ (Btu/deg F hr)}\\ K_2 &= 45 \text{ (Btu/deg F hr)}\\ c_1 &= 0.25 \text{ (Btu/lb deg F)}\\ c_2 &= 0.3 \text{ (Btu/lb deg F)}\\ \alpha_1 &= 1.507 \text{ (ft}^2\text{/hr)}\\ L &= 170 \text{ (Btu/lb)}\\ \rho_s &= 199 \text{ (lb/ft}^3\text{)}\\ \rho_l &= 160 \text{ (lb/ft}^3\text{)}\\ T_s &= 1018 \text{ (deg F)}\\ \Delta T &= 176 \text{ (deg F)} \end{aligned}$$

In solution of the problem, the solid fraction distribution within the solid-liquid region is assumed to be of cubic form in $\bar{x}$ (it will subsequently be shown that the final result is not strongly affected by this assumption)

$$f_s = 1 - \bar{x}^3$$

i.e., the constants. C_i in equation (3) are,

$$\begin{aligned} C_1 &= 0\\ C_2 &= 0\\ C_3 &= 1\\ n &= 3 \end{aligned}$$

The results of this investigation are presented in dimensionless form for the sake of generality. The dimensionless groups used in the presentation of the results are,

$$\bar{t} = \frac{t\alpha_1}{D^2}$$

$$\bar{x} = \frac{x}{D}, \quad \text{hence } \bar{\epsilon} = \frac{\epsilon}{D};\ \overline{\Delta\epsilon} = \frac{\Delta\epsilon}{D}$$

$$\bar{T} = \frac{T-T_s}{\Delta T}, \quad \text{hence } \bar{T}_c = \frac{T_c-T_s}{\Delta T};$$

$$\bar{T}_1 = \frac{T_1-T_s}{\Delta T}; \quad \bar{T}_2 = \frac{T_2-T_s}{\Delta T}$$

$$\bar{\lambda}_1 = \frac{\lambda_1}{\sqrt{\alpha_1}};\ \bar{\lambda}_2 = \frac{\lambda_2}{\sqrt{\alpha_1}}$$

$$\bar{u} = \frac{uD}{\alpha_1}$$

where D is a characteristic length.

The distribution of velocity within the solid-liquid region is shown in Fig. 2. For the case considered ($\rho_s > \rho_l$) the velocity is negative throughout the solid-liquid region, i.e., the flow of interdendritic fluid is toward the solidus front. The velocity increases (in absolute value) toward the liquidus front to feed the shrinkage due to solidification taking place within the solid-liquid region; and the velocity reaches the highest values at the liquidus front.

For the case shown in Fig. 2, the velocity distribution within the solid-liquid region is approximately linear in $\bar{x}$. This, however, is not generally true. The velocity of interdendritic fluid depends on the solid fraction distribution and, in general, can be represented by a more complex function of $\bar{x}$ as shown in equation (6). The velocity of the interdendritic fluid decreases with the progress of solidification and is inversely proportional to square root of time.

The effect of the flow of interdendritic liquid on the movement of the solidus and the liquidus fronts is shown in Fig. 3. The net

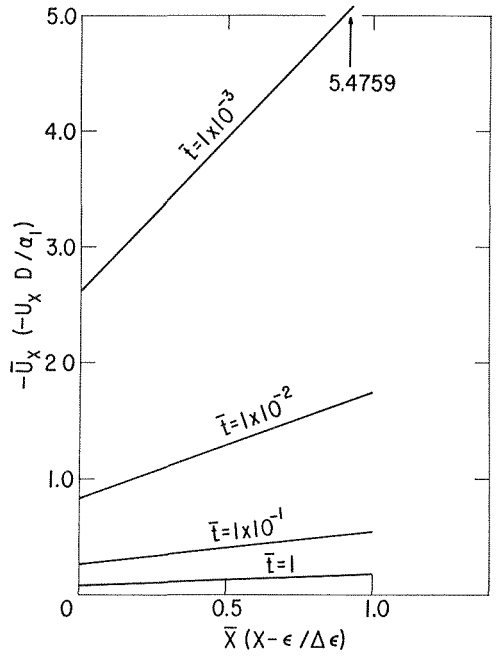

Fig. 2 Velocity distribution

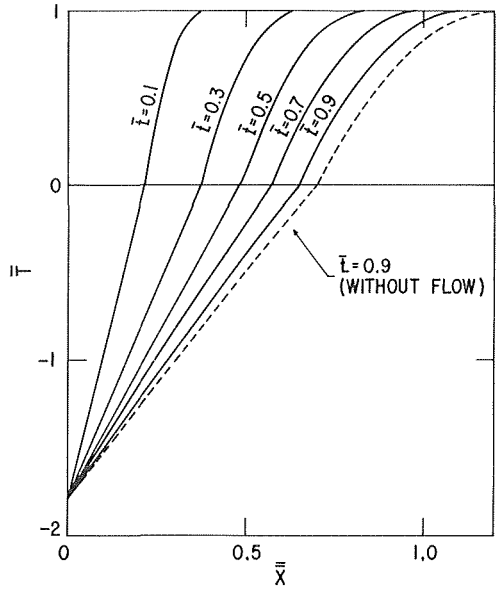

Fig. 4 Temperature distribution

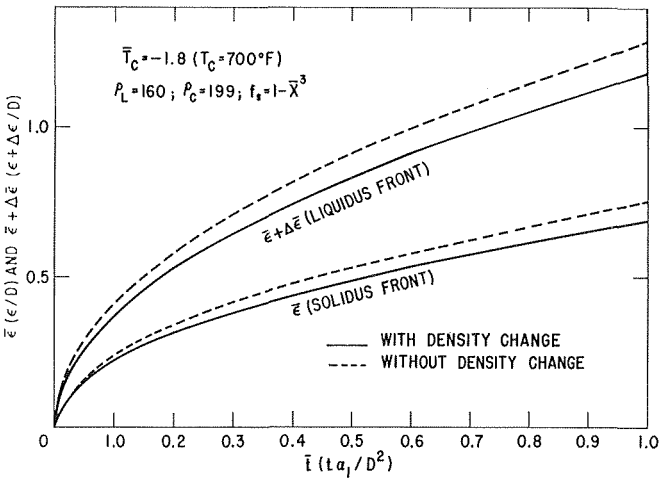

Fig. 3 Growth of liquidus and solidus fronts

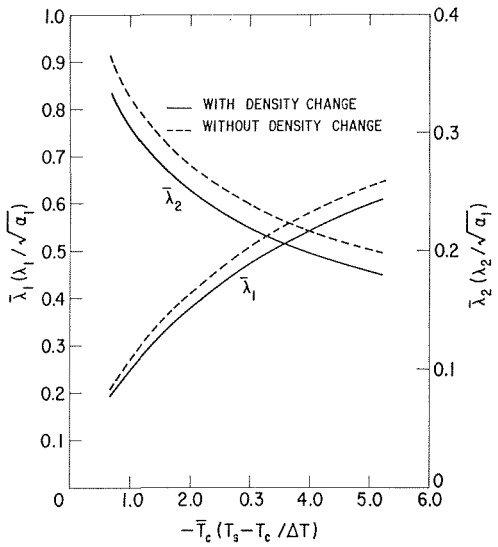

Fig. 5 Parameters $\bar{\lambda}_1$ and $\bar{\lambda}_2$ versus surface temperature $\bar{T}_c$, $f_s = 1 - \bar{x}^3$

effect of the flow (negative velocity) is to slow the solidification process about 10 percent, since additional liquid entering the solid-liquid region also has to be solidified.

A similar conclusion is reached from examination of the temperature distribution within the slab during solidification. The results given in Fig. 4 show that at any given time (for example, $\bar{t} = 0.9$) and position within the slab, the local temperature is higher for the case when $\rho_s > \rho_l$ than for the case of equal solid and liquid densities.

The effect of surface temperature on the movements of the solidus and the liquidus fronts is shown in Fig. 5. These results are expressed as plots of $\bar{\lambda}_1$ and $\bar{\lambda}_2$ versus dimensionless surface temperature. The results presented in Fig. 5 show that in general (at any surface temperature) the solidus and the liquidus fronts move slower when $\rho_s > \rho_l$, than for the case of equal solid and liquid densities (i.e., the conclusion reached previously). But these results also show that as the surface temperature is decreased (i.e., at higher cooling rates) the effect of the flow of interdendritic fluid on the rate solidification becomes more pronounced.

All the results presented so far (i.e. Fig. 2 to Fig. 4) have been calculated using an arbitrary solid fraction distribution within the solid-liquid region,

$$f_s = 1 - \bar{x}^3.$$

In order to test whether the conclusions reached on the basis of these results are affected by the form of the $f_s(\bar{x})$ relation, the calculations have been repeated using linear form of the solid fraction distribution. The parameters $\bar{\lambda}_1$ and $\bar{\lambda}_2$ for this case are plotted versus the dimensionless surface temperature in Fig. 6 which is obviously quite close to Fig. 5. A comparison between the case of linear solid fraction distribution and that of cubic form

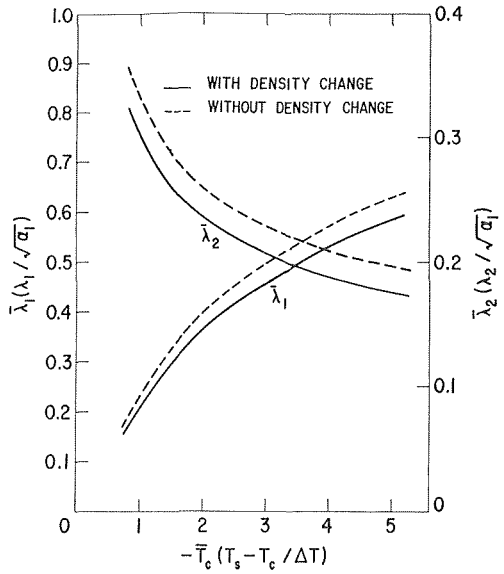

Fig. 6 Parameters $\bar{\lambda}_1$ and $\bar{\lambda}_2$ versus surface temperature $\bar{T}_c$, $f_s = 1 - \bar{x}$

distribution of solid fraction is shown in Table 1. It can be seen that the difference becomes larger when the surface temperature is high, but it still is within 10 percent. Hence, it can be concluded that the effect of the assumed form of the distribution of solid fraction on the solidification rate is small and in no way affects the major conclusions of this investigation.

Table 1 Comparison of solidification rate for different solid fraction distribution $\rho_s > \rho_l$

	λ_1	λ_2	
$f_s = 1 - \bar{x}$	0.7465	0.2211	T_c = 100 deg F
$f_s = 1 - \bar{x}^3$	0.7292	0.2134	
% of difference	2.31	3.48	
$f_s = 1 - \bar{x}$	0.5718	0.2699	T_c = 500 deg F
$f_s = 1 - \bar{x}^3$	0.5516	0.2578	
% of difference	3.53	4.48	
$f_s = 1 - \bar{x}$	0.2367	0.4343	T_c = 900 deg F
$f_s = 1 - \bar{x}^3$	0.2159	0.3944	
% of difference	8.78	9.18	

References

1 Koump, V., Tien, R. H., and Kim, W. J., "Growth of the Solid-Liquid Region During One-Dimensional Solidification of Binary Alloys," *Trans. AIME*, Vol. 259, 1967, pp. 1305–1312.

2 Tien, R. H., and Geiger, G. E., "Heat Transfer Analysis of the Solidification of a Binary Eutectic System," JOURNAL OF HEAT TRANSFER, TRANS. ASME, Series C, Vol. 89, No. 3, Aug. 1967, pp. 230–234.

3 Carslaw, H. S., and Jaeger, J. C., *Conduction of Heat in Solid*, Oxford at the Clarendon Press.

4 Goodman, T. R., "The Heat Balance Integral and Its Application to Problems Involving a Change of Phase," JOURNAL OF HEAT TRANSFER, TRANS. ASME, Series C, Vol. 80, No. 3, Aug. 1958, p. 335.

5 Tien, R. H., and Geiger, G. E., "The Unidimensional Solidification of a Binary Eutectic System With a Time-Dependent Surface Temperature," JOURNAL OF HEAT TRANSFER, TRANS. ASME, Series C, Vol. 90, No. 1, Feb. 1968, pp. 27–31.

6 Bower, T. F., Brody, H. D., and Flemings, M. C., *Trans. AIME*, Vol. 236, 1966, pp. 624–634.

N. VUTZ
Senior Scientist,
Westinghouse Air Brake Co.,
Wilmerding, Pa.
Assoc. Mem. ASME

S. W. ANGRIST
Associate Professor,
Department of Mechanical Engineering,
Carnegie-Mellon University,
Pittsburgh, Pa. Assoc. Mem. ASME

Thermal Contact Resistance of Anisotropic Materials[1]

This work presents an extension of the understanding of thermal contact resistance to include anisotropic materials. The extension involves a mathematical geometric transformation which leaves the thermal currents unchanged while making the temperature distribution in the anisotropic materials soluble by previously published methods. The development of this transformation technique is presented, and the effect of material anisotropy is calculated for a set of interface orientations and material conductivities which characterize typical contact situations. The degree of material anisotropy and the orientation of the contact interface are shown to be important factors affecting the contact resistance in addition to surface roughness, material hardness, and contact load.

Introduction

When two surfaces which are parallel and flat in an engineering sense are pressed together and heat is caused to flow across their interface, one can detect an apparent resistance to heat flow at their interface. This resistance to heat flow commonly called thermal contact resistance arises from the imperfect contact geometry of the mating surfaces. Surfaces which are said to be flat are, in fact, rough and/or wavy. A pressure contact between two such surfaces is imperfect because the two mating surfaces touch only at small and relatively isolated spots. Between these spots, the materials are in very close proximity but there is no direct coupling for the exchange of thermal energy. In a vacuum environment, there will be no interstitial filling material in the regions of close proximity to cause an indirect coupling. Radiant energy coupling is usually negligible compared to the energy transfer through the actual contact spots.

The contact resistance which at first glance seems to be a surface phenomenon is actually a flow constriction phenomenon which occurs in the interior of each of the mating materials. In each of the materials the lines of energy flow change from an even, uniform distribution far away from the contacting surfaces to a set of converging groups, each group converging toward a contact spot. This convergence of the flow lines produces a locally higher heat flow density which requires a locally higher driving potential for the flow. The heat flow lines are constricted in the material in the vicinity of the contact spots.

The size, location, and distribution of the contact spots appear to be the most important factors in the resistance phenomenon. The present work is based on the following ideas: (*a*) The energy transfer in the materials occurs in a continuum. Quantum or atomic effects are not important. (*b*) At the contact spots, the mating bodies are well coupled for thermal energy transfer. Adsorbed layers are punctured or ruptured when the materials yield plastically to form contact spots. Clausing's [6][2] explanation of the dependence of the contact resistance on the direction of heat flow between dissimilar metals in terms of macroscopic phenomena makes prior quantum based explanations seem inappropriate. Holm's [2] work on electric contacts indicates that the second assumption is realistic for moderate contact loads.

Thermal contact resistance effects can be analyzed as conduction problems in a complex three-dimensional geometry. The most serious practical difficulties arise in determining the contact geometry in terms of observable or measurable material and surface properties. Characteristic dimensions of the contact spots are large enough to cause molecular effects to be negligible, but small enough to preclude easy measurement of the important surface and material parameters.

The purpose of the present work is to treat the influence of material anisotropy on the constriction phenomenon and indicate how this influence will manifest itself as the contact resistance. With one exception [7] all work to date on contact resistance has considered isotropic metal-on-metal contacts. Anisotropic materials in contact situations can arise as single crystal semiconductors or in layered materials such as pyrolytic graphite.

The theory describing anisotropic contact resistance is developed by relying on the basic ideas which have found success in describing isotropic material contacts while specifically introducing a technique which makes these descriptions applicable to steady-state heat flow across an interface involving a thermally anisotropic material.

[1] Based on the thesis undertaken in partial fulfillment of the requirement for the degree of Doctor of Philosophy at the Carnegie-Mellon University.

Contributed by the Heat Transfer Division of The American Society of Mechanical Engineers and presented at the ASME-AIChE Heat Transfer Conference, Minneapolis, Minn., August 3–5, 1969. Manuscript received by the Heat Transfer Division, December 19, 1968; revised manuscript received, April 8, 1969. Paper No. 69-HT-47.

[2] Numbers in brackets designate References at end of paper.

Nomenclature

a = contact spot radius
$\hat{a}$ = transformed contact spot radius
A = apparent contact area
c = specific heat
C = correction factor
D = spot diameter
K = transformed conductivity
k_x, k_y, k_z = directional conductivities
k_ξ, k_η, k_ζ = transformed directional conductivities
n = number of contact spots
$\mathbf{q}$ = heat flux vector
$\hat{\mathbf{q}}$ = transformed heat flux vector
R_1 = contact resistance for a single spot
R = total contact resistance
s = surface area
$\hat{s}$ = transformed surface area
T = temperature
x, y, z = coordinates
α = elliptical spot major axis factor
β = elliptical spot minor axis factor
γ = ovalness of elliptical spot
ξ = transformed x
η = transformed y
ζ = transformed z
ρ = material density

Analysis of Constricted Flow in Anisotropic Materials

The theory of conduction in anisotropic materials can be found in Carslaw and Jaeger [1]. The general problem can become quite involved. Fortunately, all materials of potential interest are orthotropic, having differing conductivities in two or three mutually perpendicular directions called the principal conductivity axes. The approach in the following analysis is to mathematically transform the anisotropic constricted flow problem into an equivalent isotropic constricted flow problem for which existing solutions can be used. Conceptually the transformation may be thought of as a stretching of the problem and its boundary conditions in such a way as to make the transformed conductivity uniform in all directions. Care must be exercised to insure that both the temperature and the heat flow are properly transformed. The physical consequences of the limitations on the applicability of this technique are not overly restrictive.

Consider a typical orthotropic solid, pyrolytic graphite, which exhibits a layered structure with a high conductivity in the plane of the layers and a low conductivity perpendicular to the layers. The high conductivity is one hundred to one thousand times greater than the low conductivity [3, 4]. The conductivity ratio depends on the method by which the graphite was produced.

If the boundaries of a conduction problem which involves an orthotropic material are parallel or perpendicular to the principal conductivity axis, the transform previously mentioned may be employed. For contact problem analysis, this requires that the interface plane be either parallel or perpendicular to the principal conductivity directions. For the material mentioned, there is only one critical direction—that of the low thermal conductivity; consequently, Cartesian, cylindrical, or elliptic cylindrical geometries can be used in the analysis.

The conduction equation in rectangular coordinates in an orthotropic material is:

$$\rho c \frac{\partial T}{\partial t} = k_x \frac{\partial^2 T}{\partial x^2} + k_y \frac{\partial^2 T}{\partial y^2} + k_z \frac{\partial^2 T}{\partial z^2}$$

By making the transformation:

$$\xi = x(K/k_x)^{1/2}; \quad \eta = y(K/k_y)^{1/2}; \quad \zeta = z(K/k_z)^{1/2}$$

The conduction equation becomes:

$$\frac{\partial T}{\partial t} = \frac{K}{\rho c}\left(\frac{\partial^2 T}{\partial \xi^2} + \frac{\partial^2 T}{\partial \eta^2} + \frac{\partial^2 T}{\partial \zeta^2}\right)$$

For steady conduction, the foregoing reduces to Laplace's equation and the temperature is independent of K.

If a resistance obtained from the transformed problem is to properly indicate a resistance in the original problem, K must be chosen such that flows are invariant under the transformation. This is necessary because the resistance is a ratio of a flow and a temperature difference. Both must be transformed correctly. This condition may be satisfied by choosing

$$K = (k_x k_y k_z)^{1/3}$$

as derived in the Appendix.

By following the foregoing approach contact situations involving anisotropic materials can be made mathematically equivalent to contact situations in isotropic materials. Though this approach introduces the restriction that the contact interface must be parallel or perpendicular to the principal conductivity directions, it renders previous contact resistance analysis applicable to anisotropic materials.

Constriction effects are conveniently expressed as equivalent lengths for the respective materials. The equivalent lengths for a contact are the extra material thicknesses of each of the contacting bodies, which if in perfect contact, would produce the same overall temperature differences as the imperfect contact situation. This mode of expression displays the geometric properties of the constriction and suppresses the material conductivity dependence. For anisotropic material contacts, the equivalent length depends on the conductivities in directions other than that of the primary heat flow. This dependence can be accounted for by an equivalent length correction factor which depends on the conductivity ratio and interface orientation.

The consequences of material anisotropy on the constriction phenomenon can be analyzed most easily for the case of a single spot on a very large surface. This is a good approximation when the spot size is much smaller than the interspot distances.

Analysis for the Contact Surface Perpendicular to the Principal Axis

Consider small isolated contact spots on an interface which is perpendicular to the direction of low conductivity for one of the typical anisotropic materials as shown in Fig. 1. By using the transforms

$$\xi = x(K/k_1)^{1/2}; \quad \eta = y(K/k_1)^{1/2}; \quad \zeta = z(K/k_2)^{1/2}$$
$$K = (k_1^2 k_2)^{1/3}$$

The problem becomes one of conduction in an isotropic material. The circular contact spots transform to circles because the same factor relates x to ξ and y to η. The isotherms in the transformed constriction resistance problem will be a family of domes nesting over each spot. The constriction resistance for one of these spots according to Holm [2] will be:

$$R_1 = \frac{1}{4K\hat{a}}$$

where $\hat{a}$ is the transformed spot radius, $(K/k_1)^{1/2}a$. For n spots in parallel

$$R = \frac{1}{4nK(K/k_1)^{1/2}a} = \frac{k_1^{1/2}}{4naK^{3/2}}$$

The equivalent length is the constriction resistance multiplied by the contact area and the conductivity in the primary flow direction.

$$l = k_2 A \frac{k_1^{1/2}}{4naK^{3/2}}$$

Recalling that

$$K = (k_1^2 k_2)^{1/3}$$

Then one obtains:

$$l = \frac{A}{4na}\frac{k_2(k_1)^{1/2}}{k_1(k_2)^{1/2}} = \frac{A}{4na}\left[\frac{k_2}{k_1}\right]^{1/2}$$

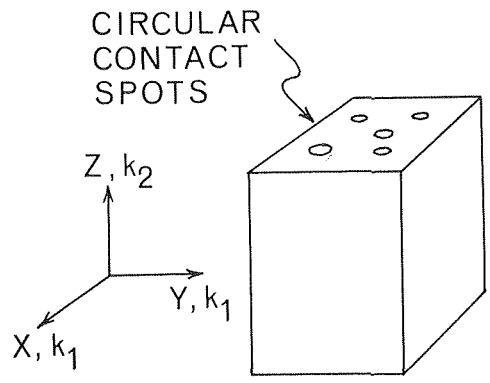

Fig. 1 Anisotropic material with the contact surface perpendicular to the anisotropic direction

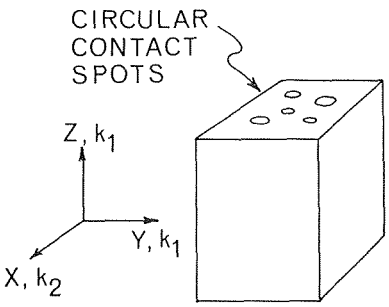

Fig. 2 Anisotropic material with the contact surface parallel to the anisotropic direction

Analysis for the Contact Surface Parallel to the Principal Axis

Consider a small isolated contact spot on an interface parallel to the direction of low conductivity as shown in Fig. 2. Transforming again, this time using

$$\xi = x(K/k_2)^{1/2}; \quad \eta = y(K/k_1)^{1/2}; \quad \zeta = z(K/k_1)^{1/2}$$

$$K = (k_1^2 k_2)^{1/3}$$

One obtains an isotropic conduction problem. The circular spots now become ellipses. Holm's solutions include this situation, but we must obtain the ovalness of the transformed spots. Holm's ellipse solutions are related to equivalent area circular spot solutions by a factor $f(\gamma)$. The ellipse major and minor axes are given by $\alpha = \gamma a$ and $\beta = a/\gamma$. Thus the ratio of the major to the minor axis is γ^2. The ratio of the stretch in the ξ direction to that in the η direction introduced by the transformation is $(k_1/k_2)^{1/2}$. Thus

$$\gamma^2 = \left[\frac{k_1}{k_2}\right]^{1/2}$$

and

$$\gamma = \left[\frac{k_1}{k_2}\right]^{1/4}$$

One can obtain $f(\gamma)$ as a function of γ from Holm [2].

The radius, $\hat{a}$, of the equivalent area circular spot in the transformed problem may be obtained as follows:

$$\text{Ellipse area} = \pi \left[\frac{K}{k_2}\right]^{1/2} a \left[\frac{K}{k_1}\right]^{1/2} a$$

$$\pi \hat{a}^2 = \pi a^2 \frac{K}{(k_1 k_2)^{1/2}}$$

Thus one obtains:

$$\hat{a} = a \frac{K^{1/2}}{(k_1 k_2)^{1/4}}$$

The constriction resistance for a single isolated spot according to Holm is:

$$R_1 = \frac{f(\gamma)}{4K\hat{a}}$$

For n spots in parallel

$$R = \frac{f(\gamma)}{4nK\hat{a}} = \frac{f(\gamma)}{4na} \frac{(k_1 k_2)^{1/4}}{K^{3/2}}$$

The equivalent length, in this case based on conductivity k_1, becomes:

$$l = k_1 A R = \frac{A}{4na} f(\gamma) \frac{k_1 (k_1 k_2)^{1/4}}{k_1 (k_2)^{1/2}}$$

$$l = \frac{A}{4na} \left[\frac{k_1}{k_2}\right]^{1/4} f(\gamma) = \frac{A}{4na} \gamma f(\gamma)$$

The isotherms in the transformed problem will be ellipsoidal domes nesting over the elliptical spots. Upon transforming back to the anisotropic situation, these ellipsoidal domes will become circular domes over circular spots.

Summary and Conclusions

For either interface orientation an anisotropic correction factor, C, may be defined by dividing the equivalent lengths obtained by the isotropic material equivalent length which is $A/4na$. Fig. 3 shows this correction factor as a function of the conductivity ratio for each of the assumed interface orientations.

The analysis has assumed isolated contact spots. If the spot spacing is on the order of the spot size, the constriction effect will be reduced. This could occur at very high contact loads. For a uniform distribution of contact spots on an interface perpendicular to the anisotropic direction, another correction factor obtained by Roess from numerical calculations and presented by Clausing and Chao [5] may be applied. This factor relates the constriction resistance for a spot feeding a concentric finite region to that of a spot feeding an infinite region. The factor which multiplies the resistance obtained from the transformed problem can be used because the spot distribution remains uniform under the transform. Direct numerical calculations appear to be the only good method of analyzing the situation with close spaced contacts on an interface parallel to the anisotropic direction.

Thermal contact phenomena involving orthotropic anisotropic materials can be analyzed by a geometric transformation technique which extends the applicability of solutions of isotropic material contact situations to anisotropic materials. If the size and location of the spots of actual material contact are known or can be accurately estimated from surface profiles and material properties, the interface resistance can be calculated. The resistance depends on the orientation of the anisotropic material and the ratio of its directional conductivities as well as all the parameters which govern isotropic contacts.

In conducting experiments to study this phenomenon, the determination of the size and distribution of the contact spots was

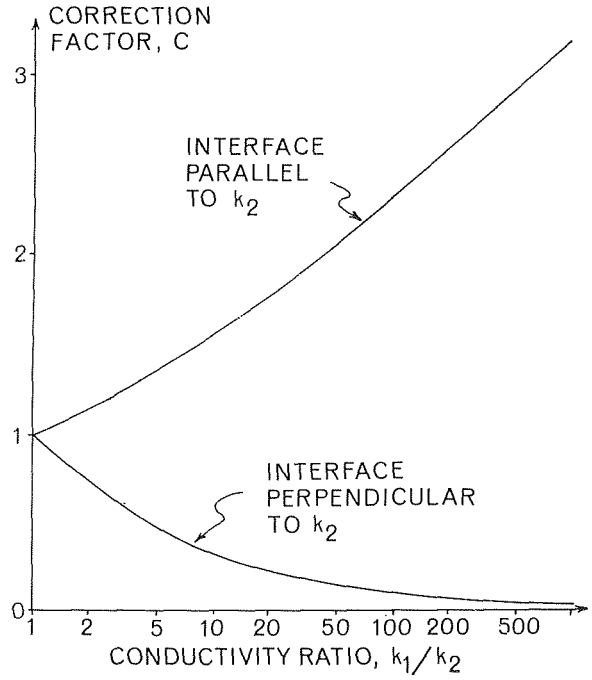

Fig. 3 Equivalent length correction factor, C, versus conductivity ratio for both material orientations

the most difficult task. Interpretation of experiments was radically complicated by the macroscopic constriction effect arising from contact flatness deviation arising during surface preparation, as well as thermal strain. To date no conclusive experimental measurements have been obtained.

References

1 Carslaw, H. S., and Jaeger, J. C., *Conduction of Heat in Solids*, Oxford University Press, 1959.

2 Holm, R., *Electric Contacts*, Almquist and Wiksells, Upsala, Sweden, 1946.

3 General Electric Company, *Pyrolytic Graphite*, May 1963.

4 Stewart, J. D., "Pyrolytic Graphite," ASME Paper 66-MO-54, May 1966.

5 Clausing, A. M., and Chao, B. T., "Thermal Contact Resistance in a Vacuum Environment," University of Illinois Engineering Experiment Station Report ME-TN-2421, Aug. 1963.

6 Clausing, A. M., "Heat Transfer at the Interface of Dissimilar Metals—The Influence of Thermal Strain," *International Journal of Heats and Mass Transfer*, Vol. 9, 1966, pp. 791–801.

7 Powell, R. W., et al., "Heat Transfer at the Interface of Dissimilar Materials," *International Journal of Heat and Mass Transfer*, 1962.

8 Chao, B. T., "A Note on Conduction of Heat in Anisotropic Media," *Applied Scientific Research*, Section A, Vol. 12, 1963, p. 134.

APPENDIX

Examining the invariant flux condition, $\mathbf{q}\cdot\mathbf{ds} = \hat{\mathbf{q}}\cdot\hat{\mathbf{ds}}$, in Cartesian coordinates, we see:

$$q_x dydz + q_y dxdz + q_z dxdy = q_\xi d\eta d\zeta + q_\eta d\xi d\zeta + q_\zeta d\xi d\eta$$

By substituting in $q_x = -k_x \dfrac{\partial T}{\partial x}$, etc., and $q_\xi = -K \dfrac{\partial T}{\partial \xi}$, etc., and multiplying both sides by -1, we obtain:

$$k_x \frac{\partial T}{\partial x} dydz + k_y \frac{\partial T}{\partial y} dxdz + k_z \frac{\partial T}{\partial z} dxdy = K\left(\frac{\partial T}{\partial \xi} d\eta d\zeta + \frac{\partial T}{\partial \eta} d\xi d\zeta + \frac{\partial T}{\partial \zeta} d\xi d\eta\right)$$

Then expressing $d\xi$, $d\eta$, and $d\zeta$ in terms of dx, dy, and dz yields:

$$k_x \frac{\partial T}{\partial x} dydz + k_y \frac{\partial T}{\partial y} dxdz + k_z \frac{\partial T}{\partial z} dxdy = K\left[\left[\frac{k_x}{K}\right]^{1/2}\left[\frac{K}{k_y}\right]^{1/2}\left[\frac{K}{k_z}\right]^{1/2}\frac{\partial T}{\partial x} dydz + \left[\frac{k_y}{K}\right]^{1/2}\left[\frac{K}{k_x}\right]^{1/2}\left[\frac{K}{k_z}\right]^{1/2}\frac{\partial T}{\partial y} dxdz + \left[\frac{k_z}{K}\right]^{1/2}\left[\frac{K}{k_x}\right]^{1/2}\left[\frac{K}{k_y}\right]^{1/2}\frac{\partial T}{\partial z} dxdy\right]$$

Solving for K one obtains:

$$K = (k_x k_y k_z)^{1/3}$$

Several other ways for obtaining K are discussed by Chao in reference [8].

B. K. C. CHAN[1]
Research Scientist,
Engineering Research Division.

C. M. IVEY[2]
Experimental Officer,
Engineering Research Division.

J. M. BARRY
Experimental Officer,
Applied Mathematics and Computing Section.

Australian Atomic Energy Commission
Research Establishment,
Sutherland, New South Wales, Australia

Natural Convection in Enclosed Porous Media With Rectangular Boundaries

Numerical methods are used to solve the field equations for heat transfer in a porous medium filled with gas and bounded by plane rectangular surfaces at different temperatures. The results are presented in terms of theoretical streamlines and isotherms. From these the relative increases in heat transfer rate, corresponding to natural convection, are obtained as functions of three-dimensionless parameters: the Darcy number Da, the Rayleigh number Ra, and a geometric aspect ratio L/D. A possible correlation using the lumped parameter Da Ra is proposed for Da Ra greater than about 40.

Introduction

THE work reported proposes a theoretical model for the motion of a fluid when it is heated in an enclosed porous medium bounded by solid plane surfaces which are different in temperature. The model yields a theoretical rate of heat transfer between these surfaces. This is related to the problem of radial heat transfer from the wall of a nuclear power reactor core, through a multishield structure containing air spaces or porous insulating material, to the pressure vessel.

Most of the studies on natural convection in enclosed spaces have been related to rectangular cavities where an air gap is used for insulation. In these and other cases, it is important to determine the rates of heat transfer across the gap which result from a temperature difference between the opposing faces. Theoretical analysis of the problem usually began with the fundamental differential equations of conservation of mass, momentum, and thermal energy, together with an appropriate equation of state. Where the curvatures of the enclosing surfaces are significant, the problems are generally treated by using cylindrical geometry for which the rectangular geometry is an asymptote. For natural convection in porous media, the problem has been treated similarly by expressing the convective flow in terms of some theoretical model, e.g., Darcy's law.

Early theoretical and experimental studies of convective flow of a fluid in a porous medium were made by Horton and Rogers [1],[3] Morrison, Rogers, and Horton [2], Rogers and Morrison [3], Rogers, Schilberg, and Morrison [4], in 1945–1951, in connection with the distribution of salt in subterranean sand layers. In recent years, in a study of the motion of underground water with particular reference to geothermal activities in New Zealand, Wooding [5–11], Elder [12–15], and McNabb [16], 1957–1967, have reported results on the structure of the flow field and corresponding heat transfer rates for convection of fluid in a porous medium owing to heat generation from below. The criterion for the onset of convective flow was predicted theoretically by Lapwood [17] in 1948, and confirmed experimentally by Katto and Masuoka [18] in 1967. In these studies the term representing viscous forces was neglected in the equation of motion, which was derived from Darcy's law. This may lead to significant errors near the solid boundaries unless a boundary-layer effect is introduced. In a recent paper, two of the present authors, Chan and Ivey [19] 1967, derived the field equations for natural convection in enclosed porous media using a modified form of Darcy's law which takes into account the

[1] Present Address: Department of Chemical Engineering, University of Waterloo, Waterloo, Ontario, Canada.

[2] Present Address: Faculty of Engineering Science, University of Western Ontario, London, Ontario, Canada.

Contributed by the Heat Transfer Division of THE AMERICAN SOCIETY OF MECHANICAL ENGINEERS and presented at the ASME-AIChE Heat Transfer Conference, Minneapolis, Minn., August 3–6, 1969. Manuscript received by the Heat Transfer Division, June 6, 1968; revised manuscript received, April 29, 1969. Paper No. 69-HT-46.

[3] Numbers in brackets designate References at end of paper.

Nomenclature

A = angle of inclination, Fig. 1, rad

C_0 = dimensionless constant

C_p = specific heat of fluid at constant pressure, Btu/lb deg F

D = width of porous bed, ft

$\mathrm{Da} \equiv \frac{K}{D^2}$ = Darcy number, dimensionless

F_c = percentage convergence factor, percent

$\mathrm{Gr} \equiv \frac{\rho^2 g \beta D^3 \Delta T}{\mu^2} = \frac{(T_1 - T_2) g D^3}{T_2 \nu^2}$ = Grashof number

g = gravitational acceleration, ft/hr^2

K = permeability of porous medium, ft^2

k_{ee} = enhanced, or effective, thermal conductivity of gas-filled porous medium, including convective transfer, Btu/hr ft deg F

k_{e0} = effective thermal conductivity of porous medium filled with stagnant gas, Btu/hr ft deg F

k_e = enhanced, or effective, thermal conductivity of fluid in a cavity, including convective transfer, Btu/hr ft deg F

k_g = thermal conductivity of fluid, Btu/hr ft deg F

L = height of porous bed, ft

$\mathrm{Pr} \equiv \frac{\nu}{\alpha} \equiv \frac{\mu C_p}{k_g}$ = Prandtl number, dimensionless

p = pressure of fluid

$\mathrm{Ra} \equiv \frac{(T_1 - T_2) g D^3}{T_2 \alpha \nu}$ = Rayleigh number, dimensionless

T = temperature, deg F; T_1, T_2 = temperatures at hot and cold walls, respectively, Fig. 1

u = the x-component of the superficial fluid velocity, i.e., the volume flow rate per unit cross-sectional area of bed, ft/hr

v = the y-component of the superficial velocity, ft/hr

x = distance along the rectangular coordinate axis which is directed at angle A to the horizontal plane, Fig. 1, ft

(*Continued on next page*)

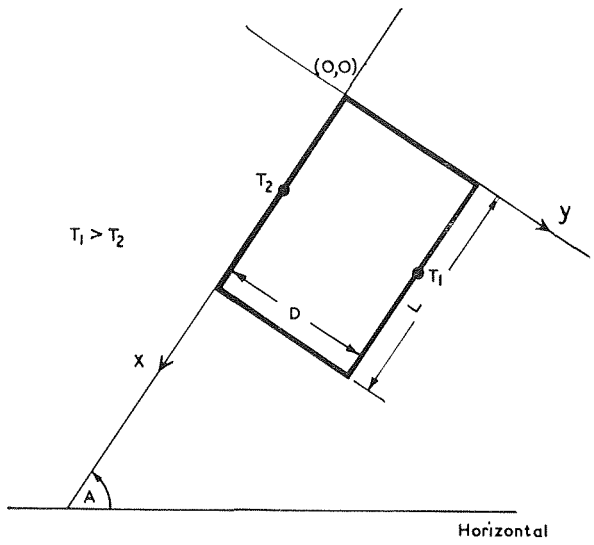

Fig. 1 Coordinates of rectangular geometry notation

viscous forces (Brinkman [20–22], 1947–1949). These equations may be solved numerically, under suitable boundary conditions, to yield useful results and criteria for design.

Theory

The theory is limited throughout to steady state conditions, for which the four equations governing the system are

$$\rho = \rho(T) \tag{1}$$

$$\underline{\nabla} \cdot \underline{u} = 0 \tag{2}$$

$$\underline{u} = \frac{K}{\nu}\left(-\frac{1}{\rho}\underline{\nabla} p + \underline{g} + \nu \nabla^2 \underline{u}\right) \tag{3}$$

$$\underline{u} \cdot \underline{\nabla} T = \alpha_e \nabla^2 T \tag{4}$$

This formulation may be simplified by considering only the two-dimensional motion of the fluid in a space of rectangular cross section filled with unconsolidated particles. T_1 and T_2 in Fig. 1 are the absolute temperatures of the hot and cold boundaries, respectively. The theory is based on the following assumptions: (*a*) the temperature difference $(T_1 - T_2)$ is small compared with T_2; (*b*) the viscosity, density, and thermal conductivity of the fluid are constant except for the effect of density variation in producing buoyancy force; (*c*) the fluid is incompressible, and (*d*) viscous heat dissipation may be neglected.

The superficial velocity $\underline{u}$ in equations (2) to (4) is averaged over a region of space small with respect to macroscopic dimensions in the flow system but large with respect to the pore size. Equation (3), the equation of motion, is the Darcy's law model for the flow regime where the damping force and the viscous force are of the same order of magnitude. In the energy equation, equation (4), the equivalent thermal diffusivity, α_e, is defined by

$$\alpha_e = k_{e0}/\rho C_p \tag{5}$$

where k_{e0} is an equivalent thermal conductivity of the porous medium, for nonflow conditions, taking into account conduction and radiation effects. Methods for estimating k_{e0} have been proposed by Smith [23], 1956, Yagi, et al. [24], 1961, and others. Recently, Katto and Masuoka [18], 1967, verified experimentally that (5) is the correct form for α_e, i.e., the equivalent thermal diffusivity in the energy equation should be defined as the equivalent stagnant thermal conductivity of the porous-medium divided by the specific heat capacity of the fluid.

Boundary conditions of practical interest which are suitable for numerical calculations are: (*a*) uniform temperatures, or heat fluxes, or specified temperature or heat-flux distributions, on the two vertical faces of the space; and (*b*) perfect insulation, or specified temperature distributions, along the horizontal boundaries.

In Cartesian coordinates equations (1) to (4) take the forms

$$\frac{d\rho}{\rho_2} = -\frac{dT}{T_2} \tag{6}$$

$$\frac{\partial u}{\partial x} + \frac{\partial v}{\partial y} = 0 \tag{7}$$

$$\frac{\nu}{K} u = -\frac{1}{\rho_2}\frac{\partial p}{\partial x} - g \sin A \left(\frac{\rho_2 - \rho}{\rho_2}\right) + \nu\left(\frac{\partial^2 u}{\partial x^2} + \frac{\partial^2 u}{\partial y^2}\right) \tag{8}$$

$$\frac{\nu}{K} v = -\frac{1}{\rho_2}\frac{\partial p}{\partial y} - g \cos A \left(\frac{\rho_2 - \rho}{\rho_2}\right) + \nu\left(\frac{\partial^2 v}{\partial x^2} + \frac{\partial^2 v}{\partial y^2}\right) \tag{9}$$

$$u\frac{\partial T}{\partial x} + v\frac{\partial T}{\partial y} = \alpha_e\left(\frac{\partial^2 T}{\partial x^2} + \frac{\partial^2 T}{\partial y^2}\right) \tag{10}$$

The boundary conditions are:

$$u = v = 0, \qquad T = T_1, \quad \text{at} \quad y = 0, \quad \text{for} \quad 0 \le x \le L \tag{11}$$

$$u = v = 0, \qquad T = T_2, \quad \text{at} \quad y = D, \quad \text{for} \quad 0 \le x \le L \tag{12}$$

$$u = v = 0, \qquad \frac{\partial T}{\partial x} = 0, \quad \text{at} \quad x = 0 \text{ and } L, \text{ for } 0 \le y \le D \tag{13}$$

$$0 \le A \le \frac{\pi}{2} \tag{14}$$

Equations (6) to (10) may be made dimensionless by introducing:

1 The relative distances

$$X = \frac{x}{D}, \qquad Y = \frac{y}{D} \tag{15}$$

for $0 \le X \le \dfrac{L}{D}$, $0 \le Y \le 1$.

Nomenclature

$X \equiv \dfrac{x}{D}$ = relative distance on x-axis

y = distance along the rectangular coordinate axis which is directed at angle A to the vertical plane, Fig. 1, ft

$Y \equiv \dfrac{y}{D}$ = relative distance on y-axis

α = thermal diffusivity, ft²/hr

$\alpha_e \equiv \dfrac{k_{e0}}{\rho C_p}$ = equivalent, or effective, thermal diffusivity in porous medium, ft²/hr

β = thermal coefficient of volumetric expansion, ft³/ft³ deg F

$\Delta T \equiv (T_1 - T_2)$ = temperature difference

$\theta \equiv \dfrac{T - T_2}{T_1 - T_2}$ = relative temperature difference, dimensionless; θ_{ij} = elements in the field matrices for θ

μ = viscosity of the fluid, lb/ft hr

$\nu \equiv \dfrac{\mu}{\rho}$ = kinematic viscosity of the fluid, ft²/hr

ρ = density of the fluid, lb/ft; ρ_2 = value of ρ at $T = T_2$

ψ = stream function, dimensionless; ψ_{ij} = elements in the field matrices for ψ

2 The dimensionless stream function ψ, defined by

$$u \equiv \frac{\alpha_e}{D} \cdot \frac{\partial \psi}{\partial Y}, \qquad v \equiv \frac{\alpha_e}{D} \cdot -\frac{\partial \psi}{\partial X}. \tag{16}$$

3 The relative temperature difference

$$\theta \equiv \frac{T - T_2}{T_1 - T_2} \tag{17}$$

for $0 \leq \theta \leq 1$.

4 The dimensionless groups

$$\frac{(T_1 - T_2)gD^3}{T_2 \alpha_e \nu} \equiv \text{Ra} \equiv \text{Gr Pr} \tag{18}$$

$$\frac{K}{D^2} = \text{Da} \tag{19}$$

which the authors will term the Darcy number, after Henry Darcy who laid the foundation for the study of laminar flow through porous media.

The resulant field equations for ψ and θ are

$$\nabla^4 \psi = \frac{1}{\text{Da}} \nabla^2 \psi + \text{Ra} \left(\sin A \frac{\partial \theta}{\partial Y} - \cos A \frac{\partial \theta}{\partial X} \right) \tag{20}$$

$$\nabla^2 \theta = \frac{\partial(\theta, \psi)}{\partial(X, Y)} \tag{21}$$

where

$$\nabla^4 \equiv \nabla^2(\nabla^2)$$

$$\nabla^2 \equiv \frac{\partial^2}{\partial X^2} + \frac{\partial^2}{\partial Y^2}$$

and

$$\frac{\partial(\theta, \psi)}{\partial(X, Y)} \equiv \frac{\partial \theta}{\partial X} \frac{\partial \psi}{\partial Y} - \frac{\partial \theta}{\partial Y} \frac{\partial \psi}{\partial X}$$

with the following boundary conditions:

$$\psi = \frac{\partial \psi}{\partial X} = \frac{\partial \psi}{\partial Y} = 0, \qquad \theta = 1, \qquad \text{at } Y = 0, \qquad \text{for } 0 \leq X \leq \frac{L}{D} \tag{22}$$

$$\psi = \frac{\partial \psi}{\partial X} = \frac{\partial \psi}{\partial Y} = 0, \qquad \theta = 0, \qquad \text{at } Y = 1, \qquad \text{for } 0 \leq X \leq \frac{L}{D} \tag{23}$$

$$\psi = \frac{\partial \psi}{\partial X} = \frac{\partial \psi}{\partial Y} = 0, \qquad \frac{\partial \theta}{\partial X} = 0, \qquad \text{at } X = 0 \text{ and } \frac{L}{D}, \quad \text{for } 0 \leq Y \leq 1 \tag{24}$$

$$0 \leq A \leq \frac{\pi}{2} \tag{25}$$

For given A the solutions of equations (20) and (21) are uniquely determined by the three-dimensionless parameters Da, Ra, and L/D, to give the scalar fields ψ and θ, with the associated streamlines and isotherms.

The case of practical importance is one for which the side surfaces are vertical, i.e., $A = \pi/2$, when equation (20) becomes

$$\nabla^4 \psi = \frac{1}{\text{Da}} \nabla^2 \psi + \text{Ra} \frac{\partial \theta}{\partial Y} \tag{26}$$

The relative increase in heat transfer rate owing to convective flow is given by (Batchelor [25], 1954; Chan and Ivey [19], 1967)

$$\frac{k_{ee}}{k_{e0}} = \frac{1}{L/D} \int_0^{L/D} \left[-\frac{\partial \theta}{\partial Y} \right]_{Y=0} dX \tag{27}$$

where k_{ee} is the enhanced equivalent thermal conductivity which includes the effect of conduction, convection, and radiation. Hence the problem may be expressed parametrically as

$$\frac{k_{ee}}{k_{e0}} = f[\text{Da, Ra, } L/D] \tag{28}$$

Numerical Methods

The two field equations, (26) and (21), are solved subject to the boundary values given by equations (22), (23), and (24). Since Da is small the first of the field equations is transformed to

$$\nabla^2 \psi = \text{Da} \left[\nabla^4 \psi - \text{Ra} \frac{\partial \theta}{\partial Y} \right] \tag{29}$$

Equations (29) and (21) are then solved by representing the finite-difference forms of the derivative components of the right-hand sides by matrix operators (Woodhead and Kettleborough [26], 1963; De Vahl Davis, and Kettleborough [27], 1965).

Since for $L/D > 5.6$, the number of mesh points makes the matrix method prohibitive, the present method is confined to the results for four values of the ratio L/D: 0.2, 0.5, 1, and 5.6.

As the field matrix technique has been described elsewhere, (see [26, 27]) only the main features will be given here. The finite-difference formulas of Bickley ([28–30], 1939–1948) are used to construct differential operators for

$$\frac{\partial^4}{\partial X^4}, \frac{\partial^4}{\partial Y^4}, \frac{\partial^2}{\partial X^2}, \frac{\partial^2}{\partial Y^2}, \frac{\partial}{\partial X}, \frac{\partial}{\partial Y}, \text{ etc.}$$

An initial estimate is made for $[\psi]$ and $[\theta]$, of $\psi_{ij} = 0$ everywhere, and the temperature field is assumed to be linearly distributed, $\theta_{ij} = Y_i$.

The right-hand side of equation (29) is then evaluated using the initial $[\psi]$ and the differential operators. The improved value for $[\psi]$ is found by the inversion of $[\nabla^2]$ and use of the extrapolated Liebman method.

The new estimate of $[\psi]$ together with the old estimate of $[\theta]$ is used to evaluate the right-hand side of equation (21) in a similar manner to that just described, giving a new estimate of $[\theta]$. This completes one iterative cycle. New and old values of $[\psi]$ and $[\theta]$ are compared for satisfactory convergence. Iteration continues until convergence is satisfactory.

Upon completion of solution for a particular Da and Ra, the Ra is increased and the old solution is used as initial values for the new problem. Ra is continually increased until convergence is no longer obtainable.

Computations

The computer used is an IBM 360/50H.

For the square geometry, where $L/D = 1$, a mesh size of $1/10$ is used, giving (11×11) field matrices. This in turn produces operators of order (81×81) and (99×99) to be inverted for solution of equations (29) and (21), respectively.

For the rectangular case, where $L/D = 5.6$, a mesh size of $1/5$ is used on the shorter side, producing field matrices of order (6, 29), and inverse operators of order (108, 108) and (116, 116).

The inversion is performed by the standard Gauss-Jordan method with good results. These are kept on magnetic tape for frequent use.

The criterion used for convergence is

$$\frac{\left[\sum_{ij} \left| \psi_{i,j_{\text{new}}} \right| - \sum_{ij} \left| \psi_{i,j_{\text{old}}} \right| \right]}{\left[\sum_{ij} \left| \psi_{i,j_{\text{old}}} \right| \right]} \times 100 \leq F_c \text{ percent}$$

The value chosen for F_c percent is usually 0.001 percent. This test is also applied to the θ field.

One full iteration cycle takes approximately 2 sec. The

number of iterations required for convergence varies greatly ranging from 1 to about 200, being dependent on the L/D configuration, the value of F_c, the product of Da and Ra, and the weighting factor in the extrapolated Liebman method.

Initial results are obtained for

$$\text{Da} = 10^{-10}, 10^{-9}, 10^{-8}, \ldots . 10^{-1}, 1 \tag{30}$$

at

$$\text{Ra} = 1, 10, 10^2, \ldots . 10^9, 10^{10} \tag{31}$$

For a fixed value of Da, the computation is commenced at Ra = 1, increasing Ra in steps of powers of 10 until convergence is no longer obtainable. For the $L/D = 1$ geometry for the 11 values of Da given by equation (30), convergence is not achieved at Ra = 10^{12}, 10^{11}, 10^{10}, 10^9, 10^8, 10^7, 10^6, 10^5, 1, 1, 1, respectively. Final results are then obtained for small increments of Ra close to values where convergence failed to be achieved.

For a fixed value of Da, if Da Ra $\gtrsim$ 130 and Da is just low enough for convergence, the θ field elements exceed 1 at points corresponding to the upper corner of the hot wall and fall below 0 at those corresponding to the lower corner of the cold wall. These are obviously extraneous results since, from physical considerations, no temperature can be higher than 1 or lower than 0 for constant temperature walls. This apparent anomoly may be due to the use of too few mesh points. Further work employing an iterative numerical technique, incorporating finer mesh, seems to confirm this. Likely localized secondary flow effects, similar to those noted by Elder [13], would first take place at those corners where more mesh points may therefore be required. Moreover, these extraneous results may indicate the onset of physical instability (transition from laminar to turbulent flow) and/or mathematical instability (limit of applicability of the system equations).

Results and Discussion

Since the present numerical method depends largely on the inversion matrix $[\nabla^{-2}]$, this matrix was first established. The determinants of the inversion matrices for all cases studied, L/D = 0.2, 0.5, 1, 2, 5.6, and 10, were also calculated. These had large values of the order of 10^{40}, indicating that the matrix $[\nabla^2]$ is nonsingular which means its inverse exists and that the linear set of equations are well-conditioned. For a given geometry, i.e., fixed L/D, varying the mesh sizes did not appear to have significant effect on the rate of convergence or on the final results.

The theoretical isotherms and streamlines for the square geometry, at Da = 10^{-4} and Ra = 10^4, are compared with the results of Poots [31], 1958, for a square cavity, also at Ra = 10^4. Fig. 2 shows the predicted relative increase in heat transfer rate corresponding to convective flow, as a function of the Rayleigh number, for Da = 10^{-4}. This is compared with the analytical results of Poots up to Ra = 10^4, and with the experimental result of Mull and Reiher (quoted by Jakob [32], 1949) for $10^4 \leq$ Ra $\leq 10^5$, the correlations being

$$\text{Poots:} \quad \frac{k_e}{k_g} = 0.16\ \text{Ra}^{0.25}, \qquad \text{Ra} \leq 10^4 \tag{32}$$

$$\text{Mull and Reiher:} \quad \frac{k_e}{k_g} = 0.18\ \text{Ra}^{0.25}(L/D)^{-0.11}, \qquad 10^4 \leq \text{Ra} \leq 10^5 \tag{33}$$

where k_g is thermal conductivity of the fluid, and k_e is the enhanced, or effective, thermal conductivity on account of convective flow.

The results of Poots were obtained for a square cavity uniformly heated at the right-hand-side vertical wall. Hence the streamlines for the two cases have opposing directions. Also, in Poots' calculations, it was assumed that the temperature distribution along the horizontal end walls is linear. This comparison seems to indicate that for a given geometry and at a given Rayleigh number, the presence of a porous material in an enclosed space would considerably modify the temperature and velocity fields: reducing the rate of convection. Fig. 2 indicates that the present theory predicts the following: (i) for Da = 10^{-4}, below Ra = 10^5 the rate of heat transfer through an enclosed porous medium is substantially the same as pure conductive transfer (in addition to radiation); (ii) above Ra = 10^5, natural convection produces an enhancement of the transfer rate similar to that which occurs at Ra = 10^3 for an enclosed cavity; and (iii) the rate of increase of heat transfer also varies approximately as the one-fourth power of the Rayleigh number.

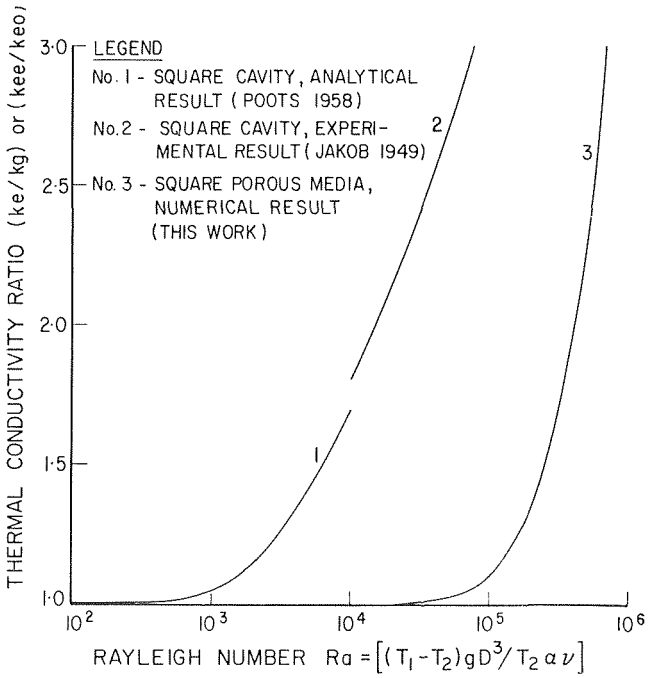

Fig. 2 Variation of heat transfer with Rayleigh number

Figs. 3 and 4 show isotherm and streamline patterns for the square geometry: Da = 10^{-5}, and Ra = 10^7. Figs. 5 and 6 show some of the corresponding patterns for the rectangular geometry, where L/D = 5.6. Clearly the patterns predict that the following occur as Ra increases:

1 A gradual and increasing development of convective motion, accompanied by distortion of the temperature field as compared with that for pure conduction.

2 A gradual development of boundary layers, downward on the cold wall and upward on the hot wall.

These predictions are consistent with the known phenomenon of natural convection in enclosed cavities.

From these ψ and θ maps the following information may also be derived: (i) vertical and horizontal temperature gradients, $\frac{\partial \theta}{\partial X}$ and $\frac{\partial \theta}{\partial Y}$; (ii) vertical and horizontal velocity components u and v (from equation (16)); (iii) the local speed, $(u^2 + v^2)^{1/2}$, and hence localization of stagnation regions; and (iv) the distribution of heat transfer coefficient along the vertical walls, from $\left(\frac{\partial \theta}{\partial Y}\right)_{Y=0 \text{ and } 1}$.

In Fig. 7 the parameter k_{ee}/k_{e0} of equation (27) is plotted against Ra for various values of Da with the square geometry. Similar plots are obtained showing corresponding results for the other geometries. The plots show the following:

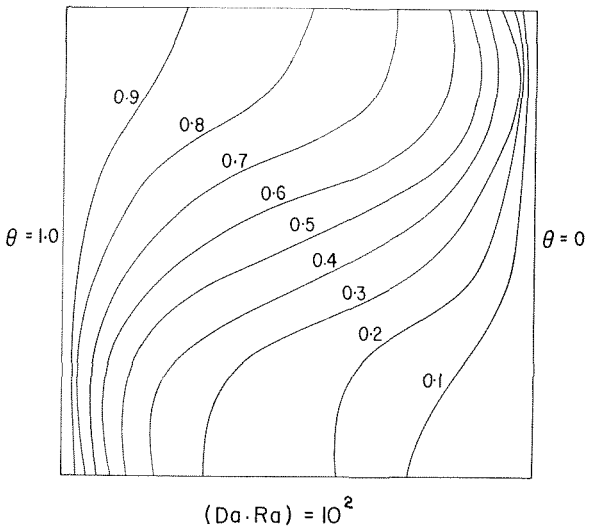

Fig. 3 Isotherms for Da = 10^{-5}, Ra = 10^{7}, L/D = 1.0

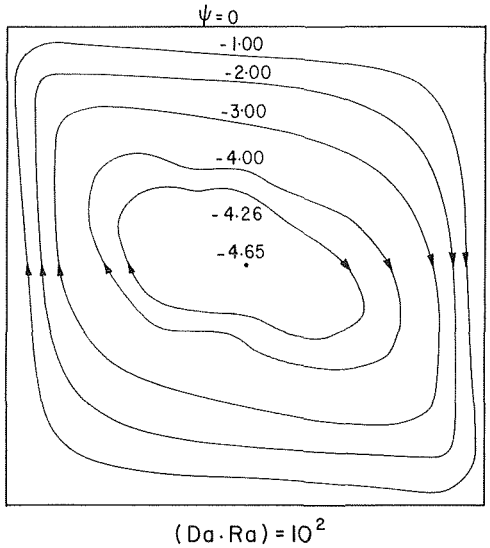

Fig. 4 Streamlines for Da = 10^{-5}, Ra = 10^{8}, L/D = 1.0

1 The curves are approximately parallel and equally spaced, so that for fixed k_{ee}/k_{e0}, Da decreases by powers of 10 as Ra increases by powers of 10. Hence, for a given value of k_{ee}/k_{e0}, Ra = constant/Da. This implies that k_{ee}/k_{e0} is uniquely determined by Da Ra, or $k_{ee}/k_{e0} = f$ (Da Ra) for given L/D which is predicted by equation (28).

2 The critical value of Ra, i.e., the value at which the onset of convection occurs, increases exponentially with exponentially decreasing Da.

3 For fixed values of Da, the ratio k_{ee}/k_{e0} varies exponentially, with Ra; and for fixed Ra, it varies exponentially with Da.

It would seem therefore that, for fixed L/D, the ratio k_{ee}/k_{e0} varies exponentially with Da Ra. This is verified in Fig. 8 in which k_{ee}/k_{e0} is plotted against Da Ra on logarithmic coordinates. For Da Ra > 40, the k_{ee}/k_{e0} values increase beyond unity, generating unique curves which are approximately linear and parallel for each of the six geometries studied. Hence an equation expressing a tentative correlation with these parameters may take the form:

$$\frac{k_{ee}}{k_{e0}} = f(L/D)(\text{Da Ra})^{C_0}, \qquad \text{for Da Ra} > 40 \tag{34}$$

where C_0 is a dimensionless constant ($C_0 \simeq 0.7$). This confirms equation (28).

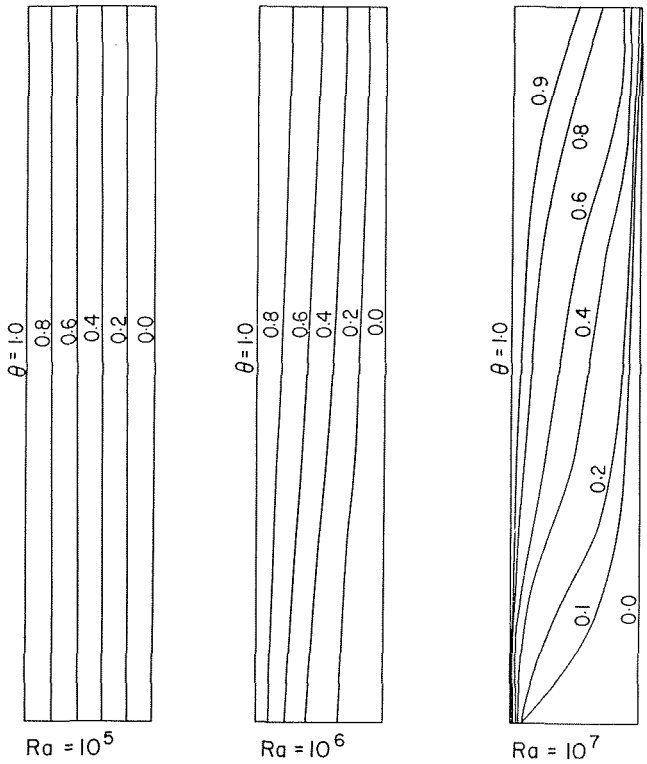

Fig. 5 Isotherms for Da = 10^{-5}, Ra = 10^{5}, 10^{6}, and 10^{7}, L/D = 5.6

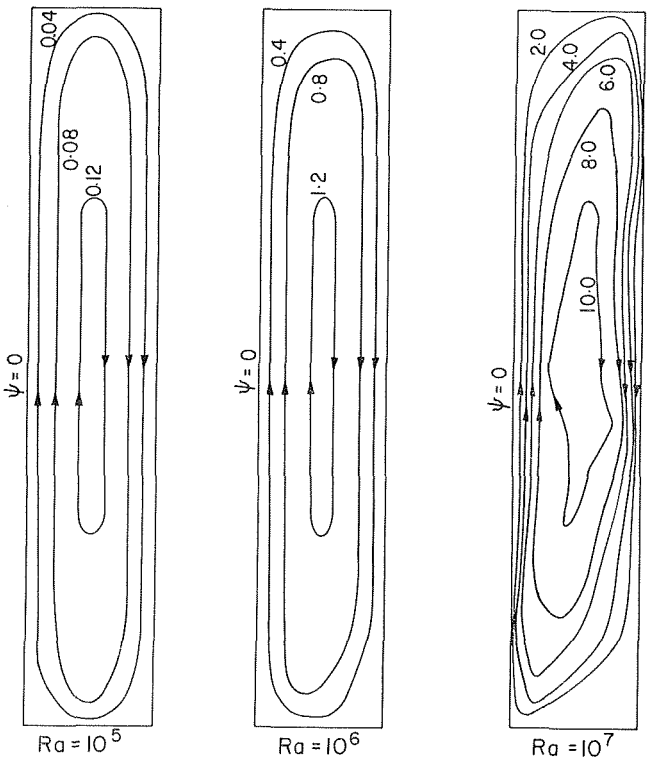

Fig. 6 Streamlines for Da = 10^{-5}, Ra = 10^{5}, 10^{6}, and 10^{7}, L/D = 5.6

That Da Ra would be an approximate criterion of heat transfer in the present system may be seen from equation (26). The left-hand-side of this equation represents the viscous forces which may be small. If they are neglected, the equation becomes

$$\nabla^2\psi + \text{Da Ra}\,\frac{\partial\theta}{\partial Y} = 0 \tag{35}$$

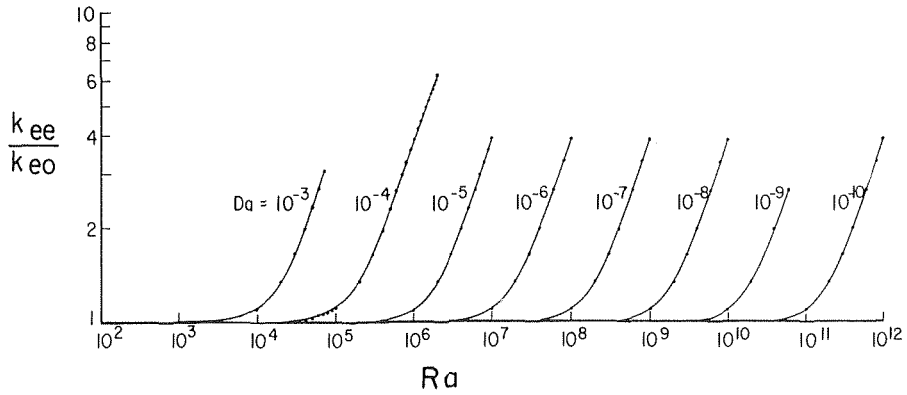

Fig. 7 Variation of thermal conductivity ratio k_{ee}/k_{e0} with Ra for various values of Da, square geometry ($L/D = 1.0$)

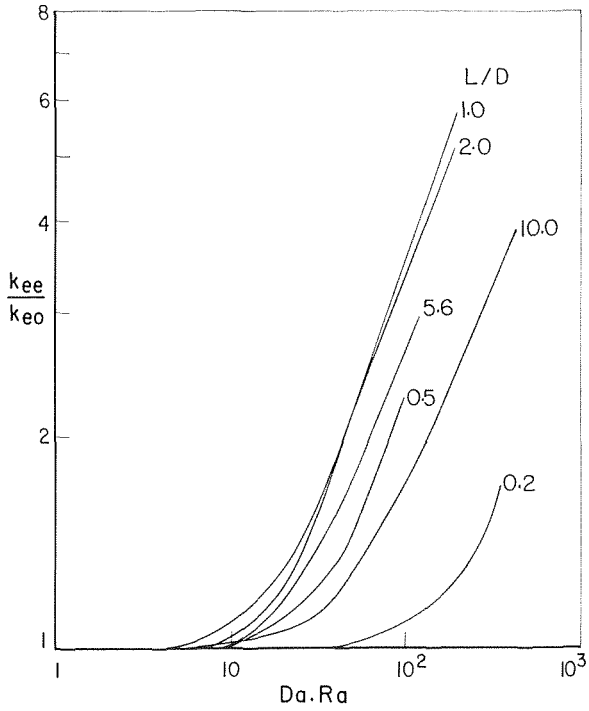

Fig. 8 Correlation of thermal conductivity ratio k_{ee}/k_{e0} with lumped parameter Da Ra

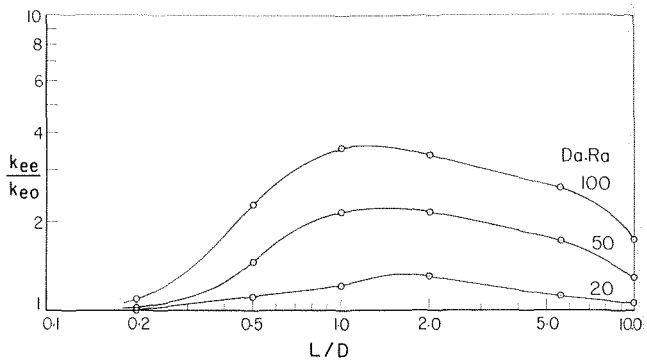

Fig. 9 Variation of thermal conductivity ratio k_{ee}/k_{e0} with L/D for various values of the lumped parameter Da Ra

It may be of interest to note that the criterion for the onset of convective flow of fluid in a porous medium, heated from below, is given by:

$$\text{Da Ra} = 4\pi^2 = 39.5 \tag{36}$$

a result deducible from the analysis of Lapwood [17] who used equation (35), and from the experimental work of Katto and Masuoka [18].

The function $f(L/D)$ may be examined by a plot of k_{ee}/k_{e0} versus L/D for fixed values of Da Ra, Fig. 9. It appears that the relative increase in the heat transfer rate has a maximum value in the vicinity of the L/D ratio of 1.5, a result which is similar to the case of the enclosed cavity (Hirata, et al. [33] 1967). At the two limits of the L/D ratio: as $L/D \to \infty$ ($L \to \infty$, or $D \to 0$), and $L/D \to 0$ ($L \to 0$, or $D \to \infty$), natural convection is either suppressed owing to increasing resistance to flow (for the cases $L \to 0$, and $D \to 0$), or it is dominated by pure conduction (for the cases $L \to \infty$, and $D \to \infty$). Hence the ratio k_{ee}/k_{e0} approaches unity at these limits, when it may have a maximum value between them. At $L/D = 1.5$, it seems reasonable to expect that a balance of these effects occur and hence the relative increase in the heat transfer rate reaches a maximum.

Conclusion

The analysis presented suggests a correlation of heat transfer rate in a porous medium bounded by surfaces at different temperatures. Theoretical flow patterns for an enclosed fluid, and temperature distributions within the medium, were obtained by a numerical method. These patterns are at least qualitatively consistent with known convective phenomenon. Rapid convergence for the numerical technique may be achieved by using field matrices and an inversion matrix.

Acknowledgments

Acknowledgments are due to G. W. K. Ford, Chief of Engineering Research Division, for encouragement and support during the course of this work; to our colleagues in the Engineering Research Division, in particular to F. A. Rocke who reviewed this work and made many comments and criticisms; and to Prof. J. J. Thompson, Head of the School of Nuclear Engineering, University of New South Wales, for some helpful discussions.

References

1 Horton, C. W., and Rogers, F. T., Jr., "Convective Currents in a Porous Medium," *Journal of Applied Physics*, Vol. 16, 1945, p. 367.

2 Morrison, H. L., Rogers, F. T., Jr., and Horton, C. W., "Convective Currents in Porous Media, II. Observation of Conditions at Onset of Convection," *Journal of Applied Physics*, Vol. 20, 1949, p. 1027.

3 Rogers, F. T., Jr., and Morrison, H. L., "Convective Currents in a Porous Media, III. Extended Theory of the Critical Gradient," *Journal of Applied Physics*, Vol. 21, 1950, p. 1177.

4 Rogers, F. T., Jr., Schilberg, L. E., and Morrison, H. L., "Convective Currents in Porous Media, IV. Remarks on the Theory," *Journal of Applied Physics*, Vol. 22, 1951, p. 1476.

5 Wooding, R. A., "Steady-State Free Thermal Convection of

Liquid in a Saturated Permeable Medium," *Journal of Fluid Mechanics*, Vol. 2, 1957, p. 273.

6 Wooding, R. A., "An Experiment on Free Thermal Convection of Water in Saturated Permeable Material," *Journal of Fluid Mechanics*, Vol. 3, 1958, p. 582.

7 Wooding, R. A., "The Stability of a Viscous Liquid in a Vertical Tube Containing Porous Material," *Proceedings of the Royal Society*, London, Series A, Vol. 252, 1949, p. 120.

8 Wooding, R. A., "Instability of a Viscous Liquid of Variable Density in a Vertical Hele-Shaw Cell," *Journal of Fluid Mechanics*, Vol. 7, 1960, p. 501.

9 Wooding, R. A., "Rayleigh Instability of a Thermal Boundary Layer in Flow Through a Porous Medium," *Journal of Fluid Mechanics*, Vol. 9, 1960, p. 183.

10 Wooding, R. A., "Free Convection of Fluid in a Vertical Tube Filled With Porous Material," *Journal of Fluid Mechanics*, Vol. 13, 1962, p. 129.

11 Wooding, R. A., "Convection in a Saturated Porous Medium at Large Rayleigh Number or Peclet Number," *Journal of Fluid Mechanics*, Vol. 15, 1963, p. 527.

12 Elder, J. W., "Laminar/Turbulent Free Convection in a Vertical Slot," *Journal of Fluid Mechanics*, Vol. 23, 1965, p. 77.

13 Elder, J. W., "Numerical Experiments With Free Convection in a Vertical Slot," *Journal of Fluid Mechanics*, Vol. 24, 1966, p. 823.

14 Elder, J. W., "Steady Free Convection in a Porous Medium Heated From Below," *Journal of Fluid Mechanics*, Vol. 27, 1967, p. 29.

15 Elder, J. W., "Transient Convection in a Porous Medium," *Journal of Fluid Mechanics*, Vol. 27, 1967, p. 609.

16 McNabb, A., "On Convection in a Porous Medium," *Proceedings of the Second Australian Conference on Hydraulics and Fluid Mechanics*, University of Auckland, N. Z., 1965, p. C161.

17 Lapwood, E. R., "Convection of Fluid in a Porous Medium," *Proceedings of the Cambridge Philosophical Society*, Vol. 44, 1948, p. 508.

18 Katto, Y., and Masuoka, T., "Criterion for the Onset of Convective Flow in a Fluid in a Porous Medium," *International Journal of Heat and Mass Transfer*, Vol. 10, 1967, p. 297.

19 Chan, B. K. C., and Ivey, C. M., "Natural Convection in Enclosed Cavities and Porous Media: Part I. Formulation of Field Equations for Rectangular and Cylindrical Geometries," Australian Atomic Energy Commission Report: AAEC/E, 1967.

20 Brinkman, H. C., "A Calculation of the Viscous Force Exerted by a Flowing Fluid on a Dense Swarm of Particles," *Applied Science Research*, Vol. A1, 1947, p. 27.

21 Brinkman, H. C., "On the Permeability of Media Consisting of Closely Packed Porous Particles," *Applied Science Research*, Vol. A1, 1948, p. 81.

22 Brinkman, H. C., "Calculations on the Flow of Heterogeneous Mixtures Through Porous Media," *Applied Science Research*, Vol. A1, 1949, p. 333.

23 Smith, J. M., *Chemical Engineering Kinetics*, McGraw-Hill, New York, 1956, p. 384.

24 Yagi, S., Kunii, D., and Wakao, N., "Radially Effective Thermal Conductivities in Packed Beds," *International Development in Heat Transfer, Proceedings, Heat Transfer Conf., London—Colorado*, ASME, 1961, p. 742.

25 Batchelor, G. K., "Heat Transfer by Free Convection Across a Closed Cavity Between Vertical Boundaries at Different Temperatures," *Quarterly of Applied Mathematics*, Vol. 12, 1954, p. 209.

26 Woodhead, R. W., and Kettleborough, C. F., "Solution of Navier-Stokes Equations for the Non-Linear Hydrodynamic Slider by Matrix Algebra Methods," *Journal of Mechanical Engineering Science*, Vol. 5, 1963, p. 163.

27 De Vahl Davis, G., and Kettleborough, C. F., "Natural Convection in an Enclosed Rectangular Cavity," *Mechanical and Chemical Engineering Transactions, Institution of Engineers, Australia*, Vol. MC1, 1965, p. 43.

28 Bickley, W. G., "Formulae for Numerical Integration," *Mathematics Gazette*, Vol. 23, 1939, p. 352.

29 Bickley, W. G., "Formulae for Numerical Differentiation," *Mathematics Gazette*, Vol. 25, 1941, p. 19.

30 Bickley, W. G., "Finite Difference Formulae for the Square Lattice," *Quarterly Journal of Mechanics and Applied Mathematics*, Vol. 1, 1948, p. 35.

31 Poots, G., "Heat Transfer by Laminar Free-Convection in Enclosed Plane Gas Layers," *Quarterly Journal of Mechanics and Applied Mathematics*, Vol. 11, 1958, p. 257.

32 Jakob, M., *Heat Transfer*, Vol. 1, Wiley, N. Y., 1949.

33 Hirata, M., et al., "Heat Transfer Across an Enclosed Vertical Layer of Relatively Low Height/Thickness Ratio," Paper No. 203, *Proceedings of the JSME Semi-International Symposium*, Sept. 1967, pp. 13–18

I. S. HABIB[1]
R. GREIF
Department of Mechanical Engineering,
University of California,
Berkeley, Calif.

Nongray Radiative Transport in a Cylindrical Medium

The problem of determining the radiative transport in a nongray cylindrical medium is considered. Nongray effects are included through use of the total band absorptance. Exact and approximate formulations and results are presented and very good agreement is obtained.

Introduction

THE DETERMINATION of the radiative transport in nongray media represents a complex problem which has forced various investigators to simplify the basic equations before attempting to obtain a solution [1–12].[2] The problem is further complicated when there is a strong interaction between the thermal radiation and other modes of energy transport. A useful simplification in the planar geometry has been achieved by replacing the exponential integral, $E_2(x)$, by an exponential function; that is, $E_2(x) \simeq ae^{-bx}$, where a and b are arbitrary constants. A detailed comparison between the exact and the approximate results in the planar geometry showed that very good agreement was obtained with this approximation. The particular values of $a = 0.9$ and $b = 1.8$ were recommended [13].

The purpose of the present study is to determine the radiative transport in a nongray medium in the cylindrical geometry. The system considered is a tube at a constant temperature with uniform heat generation in the gas. Nongray effects are included by using the total band absorptance [3, 14, 15] and both exact and approximate results are obtained.

Radiative Flux

The radiative heat flux in the radial direction in cylindrical coordinates in a tube at constant temperature may be written in the following form [16–19]

$$q_\omega = 4\int_0^{\pi/2}\left\{B_{\omega,0}\cos\gamma\left(D_3\left[\frac{2}{\cos\gamma}\int_{r\sin\gamma}^{r}k_\omega(\eta)d\eta + \frac{1}{\cos\gamma}\int_r^R k_\omega(\eta)d\eta\right] - D_3\left[\frac{1}{\cos\gamma}\int_r^R k_\omega(\eta)d\eta\right]\right)\right.$$
$$+\int_{r\sin\gamma}^{r}B_\omega(r')k_\omega(r')D_2\left[\frac{1}{\cos\gamma}\int_{r'}^{r}k_\omega(\eta)d\eta\right]dr'$$
$$-\int_r^R B_\omega(r')_\omega k(\eta)D_2\left[\frac{1}{\cos\gamma}\int_{r'}^{r}k_\omega(\eta)d\eta\right]dr'$$
$$\left.+\int_{r\sin\gamma}^{R}B_\omega(r')k_\omega(r')D_2\left[\frac{1}{\cos\gamma}\int_{r\sin\gamma}^{r}k_\omega(\eta)d\eta + \frac{1}{\cos\gamma}\int_{r\sin\gamma}^{r'}k_\omega(\eta)d\eta\right]dr'\right\}d\gamma \quad (1)$$

where r is the physical coordinate in the radial direction, R is the radius of the cylinder, ω is the wave number, k_ω is the spectral absorption coefficient, and B_ω is the blackbody radiation intensity. Equation (1) is valid for a nonscattering medium in local thermodynamic equilibrium bounded by black tube walls. The exponential integral function $D_n(x)$ is defined by

$$D_n(x) \equiv \int_0^{\pi/2}(\cos^{n-1}\alpha)\exp\left(\frac{-x}{\cos\alpha}\right)d\alpha = \int_0^1 \frac{\mu^{n-1}e^{-x/\mu}}{(1-\mu^2)^{1/2}}d\mu \quad (2)$$

Using the recurrence relation for $D_n(x)$, namely,

$$D_n'(x) = -D_{n-1}(x) \qquad n > 1 \quad (3)$$

where $D_n'(x)$ is the derivative of $D_n(x)$ with respect to x, yields the following result for equation (1) [19][3]:

[1] Presently, Assistant Professor, University of Michigan, Dearborn Campus, Dearborn, Mich.

[2] Numbers in brackets designate References at end of paper.

Contributed by the Heat Transfer Division of THE AMERICAN SOCIETY OF MECHANICAL ENGINEERS and presented at the ASME-AIChE Heat Transfer Conference, Minneapolis, Minn., August 3–6, 1969. Manuscript received by the Heat Transfer Division, January 2, 1969; revised manuscript received, April 28, 1969. Paper No. 69-HT-38.

[3] We have taken k_ω to be independent of temperature. However, for the case when k_ω is a function of the temperature according to $k_\omega = fcn(\omega)\cdot fcn(T)$ the same procedures can be carried out [2].

Nomenclature

A = total band absorptance
A_0 = bandwidth parameter
B_ω = blackbody radiation intensity
$B_{\omega,0}$ = blackbody radiation intensity evaluated at T_0
$B_{\omega c}$ = blackbody radiation intensity evaluated at band center
C_0 = correlation parameter
E_ω = blackbody flux density equals πB_ω
$E_{\omega c}$ = blackbody flux density evaluated at band center
F = radiative flux
H = wall radiosity
I = total radiation intensity
k_ω = absorption coefficient
P = pressure
Q = uniform heat source
q_r = total radiative flux
R, r_0 = tube radius
r = local radius
t = pressure broadening parameter
u = nondimensional optical depth $= C_0^2 Pr$
u_0 = defined as $C_0^2 PR$

Superscripts

$+$ = directed toward wall
$-$ = directed away from wall
$'$ = differentiation, dummy variable of integration

Subscripts

0 = evaluated at T_0
ω = wave number
ωc = evaluated at band center

$$q_\omega = 4\int_{\gamma=0}^{\pi/2}\left\{\int_{r\sin\gamma}^{r}(B_\omega(r') - B_{\omega,0})k_\omega \times D_2\left[\frac{k_\omega(r + r' - 2r\sin\gamma)}{\cos\gamma}\right]dr' - \int_{r}^{R}(B_\omega(r') - B_{\omega,0})k_\omega \times D_2\left[\frac{k_\omega(r' - r)}{\cos\gamma}\right]dr' + \int_{r\sin\gamma}^{r}(B_\omega(r') - B_{\omega,0})k_\omega \times D_2\left[\frac{k_\omega(r - r')}{\cos\gamma}\right]dr' + \int_{r}^{R}(B_\omega(r') - B_{\omega,0})k_\omega \times D_2\left[\frac{k_\omega(r + r' - 2r\sin\gamma)}{\cos\gamma}\right]dr'\right\}d\gamma \quad (4)$$

The specific medium we now consider is one comprised of an infrared radiating gas. For infrared radiating gases the bandwidth is sufficiently narrow so that the blackbody radiation intensity, B_ω, may be approximated by its value at the center of the band, $B_{\omega c}$. Thus the total radiative flux for one band, which is obtained by integrating the spectral radiative flux over the bandwidth, $\Delta\omega$, is given by

$$q_r = \int_{\Delta\omega} q_\omega d\omega \quad (5)$$

$$q_r = 4\int_{\gamma=0}^{\pi/2}\left\{\int_{r\sin\gamma}^{r}(B_{\omega c}(r') - B_{\omega c,0})\left(\int_{\alpha=0}^{\pi/2}\cos\alpha\int_{\Delta\omega}k_\omega \times \exp\left[-k_\omega\left(\frac{r + r' - 2r\sin\gamma}{\cos\gamma\cos\alpha}\right)\right]d\omega d\alpha\right)dr' - \int_{r}^{R}(B_{\omega c}(r') - B_{\omega c,0})\left(\int_{0}^{\pi/2}\cos\alpha\int_{\Delta\omega}k_\omega\exp\left[\frac{-k_\omega(r' - r)}{\cos\gamma\cos\alpha}\right]d\omega d\alpha\right)dr' + \int_{r\sin\gamma}^{r}(B_{\omega c}(r') - B_{\omega c,0})\left(\int_{0}^{\pi/2}\cos\alpha\int_{\Delta\omega}k_\omega \times \exp\left[\frac{-k_\omega(r - r')}{\cos\gamma\cos\alpha}\right]d\omega d\alpha\right)dr' + \int_{r}^{R}(B_{\omega c}(r') - B_{\omega c,0})\left(\int_{0}^{\pi/2}\cos\alpha\int_{\Delta\omega}k_\omega \times \exp\left[-k_\omega\left(\frac{r + r' - 2r\sin\gamma}{\cos\gamma\cos\alpha}\right)\right]d\omega d\alpha\right)dr'\right\}d\gamma \quad (6)$$

Equation (6) is the "exact" relation subject to the conditions previously stated. We have used the definition for the exponential integral $D_n(x)$ given in equation (2).

The nongray effects may be included in the total band absorptance [3, 13, 14] defined by

$$A(y) = \int_{\Delta\omega}(1 - e^{-k_\omega y})d\omega \quad (7)$$

and

$$A'(y) = \int_{\Delta\omega}k_\omega e^{-k_\omega y}d\omega \quad (8)$$

where $A'(y)$ is the derivative of $A(y)$ with respect to y. Hence, equation (6) may be written in terms of the derivative of the band absorptance

$$q_r = 4\int_{\gamma=0}^{\pi/2}\left\{\int_{r\sin\gamma}^{r}(B_{\omega c}(r') - B_{\omega c,0}) \times \left[\int_{\alpha=0}^{\pi/2}\cos\alpha\left(A'\left[\frac{r + r' - 2r\sin\gamma}{\cos\gamma\cos\alpha}\right] + A'\left[\frac{r - r'}{\cos\gamma\cos\alpha}\right]\right)d\alpha\right]dr' - \int_{r}^{R}(B_{\omega c}(r') - B_{\omega c,0}) \times \left[\int_{0}^{\pi/2}\cos\alpha\left(A'\left[\frac{r' - r}{\cos\gamma\cos\alpha}\right] - A'\left[\frac{r' + r - 2r\sin\gamma}{\cos\gamma\cos\alpha}\right]\right)d\alpha\right]dr'\right\}d\gamma \quad (9)$$

(*Cont.*)

It is preferable to formulate the problem directly in terms of the band absorptance [13]. This can be accomplished by integrating equation (9) by parts which yields the following (exact) expression for the total radiative flux

$$q_r = 4\int_{\alpha=0}^{\pi/2}\cos^2\alpha\int_{\gamma=0}^{\pi/2}\cos\gamma\left\{\int_{r\sin\gamma}^{r}A\left[\frac{r - r'}{\cos\gamma\cos\alpha}\right] \times \frac{d}{dr'}(B_{\omega c}(r') - B_{\omega c,0})dr' + \int_{r}^{R}A\left[\frac{r' - r}{\cos\gamma\cos\alpha}\right] \times \frac{d}{dr'}(B_{\omega c}(r') - B_{\omega c,0})dr' - \int_{r\sin\gamma}^{R}A\left[\frac{r + r' - 2r\sin\gamma}{\cos\gamma\cos\alpha}\right] \times \frac{d}{dr'}(B_{\omega c}(r') - B_{\omega c,0})dr' - (B_{\omega c}(R) - B_{\omega c,0}) \times \left(A\left[\frac{R - r}{\cos\gamma\cos\alpha}\right] - A\left[\frac{r + R - 2r\sin}{\cos\gamma\cos\alpha}\right]\right)d\gamma d\alpha \quad (10)$$

The determination of the radiative flux from equation (10) is a complex calculation involving numerical integration of three integrals. In almost all problems the temperature profile is unknown so that an iterative procedure involving triple integrals must be used to obtain the solution.

To simplify this problem we introduce the approximation[4]

$$D_2(x) \approx ae^{-bx} \quad (11)$$

which is similar to the approximation used in the planar geometry for the exponential integral, $E_2(x)$. The constants a and b are arbitrary and are chosen to give the best agreement with the exact results as obtained from equation (10). Substituting this approximation into the relation for the radiative flux, equation (6), and using the definition of the band absorptance yields the following *approximate* expression for the radiative flux

$$q_r = 4a\int_{\gamma=0}^{\pi/2}\left\{\int_{r\sin\gamma}^{r}(B_{\omega c}(r') - B_{\omega c,0}) \times \left(A'\left[b\,\frac{(r + r' - 2r\sin\gamma)}{\cos\gamma}\right] + A'\left[\frac{b(r - r')}{\cos\gamma}\right]\right)dr' - \int_{r}^{R}(B_{\omega c}(r') - B_{\omega c,0})\left(A'\left[\frac{b(r' - r)}{\cos\gamma}\right] - A'\left[\frac{b(r + r' - 2r\sin\gamma)}{\cos\gamma}\right]\right)dr'\right\}d\gamma \quad (12)$$

Integrating by parts, we obtain

$$q_r = \frac{4a}{b}\int_{\gamma=0}^{\pi/2}\cos\gamma\left\{\int_{r\sin\gamma}^{r}A\left[\frac{b(r - r')}{\cos\gamma}\right] \times \frac{d}{dr'}(B_{\omega c}(r') - B_{\omega c,0})dr' + \int_{r}^{R}A\left[\frac{b(r' - r)}{\cos\gamma}\right]\frac{d}{dr'}(B_{\omega c}(r') - B_{\omega c,0})dr' - \int_{r\sin\gamma}^{R}A\left[\frac{b(r + r' - 2r\sin\gamma)}{\cos\gamma}\right] \quad (13)$$

[4] In response to a referee's comment, it should be emphasized that this approximation was not used in obtaining the exact relations, equations (6), (9), and (10).

$$\times \frac{d}{dr'}\,(B_{\omega c}(r') - B_{\omega c,0})dr' - (B_{\omega c}(R) - B_{\omega c,0})$$

$$\times \left(A\left[\frac{b(R-r)}{\cos\gamma}\right] - A\left[\frac{b(r+R-2r\sin\gamma)}{\cos\gamma}\right]\right)\Bigg\}\,d\gamma \quad (13)$$

(*Cont.*)

Radiative Heat Transfer With a Uniform Source

We now consider the problem of a uniform heat source in a radiating medium contained in a long circular cylinder at a constant temperature T_0. The equation for the conservation of energy is given by

$$\frac{1}{r}\frac{d}{dr}\,(rq) = Q \quad (14)$$

so that the radiative flux is given by

$$q = Qr/2 \quad (15)$$

Combining equation (15) with the exact expression for the radiative flux, equation (10), yields the following integral equation[5]

$$\frac{u}{2} = \frac{4}{\pi}\int_{\alpha=0}^{\pi/2}\cos^2\alpha\int_{\gamma=0}^{\pi/2}\cos\gamma\left\{\int_{u\sin\gamma}^{u}\bar{A}\left[\frac{u-u'}{\cos\gamma\cos\alpha}\right]\times\frac{d\phi}{du'}\,du' + \int_{u}^{u_0}\bar{A}\left[\frac{u'-u}{\cos\gamma\cos\alpha}\right]\frac{d\phi}{du'}\,du' - \int_{u\sin\gamma}^{u_0}\bar{A}\left[\frac{u+u'-2u\sin\gamma}{\cos\gamma\cos\alpha}\right]\frac{d\phi}{du'}\,du' + \phi(u_0)\left[\bar{A}\left[\frac{u+u_0-2u\sin\gamma}{\cos\gamma\cos\alpha}\right] - \bar{A}\left[\frac{u_0-u}{\cos\gamma\cos\alpha}\right]\right]\right\}d\gamma\,d\alpha \quad (16)$$

where

$$\bar{A} = \frac{A}{A_0}, \qquad u = C_0^2Pr, \qquad u_0 = C_0^2PR$$

and

$$\phi = \frac{B_{\omega c}(T) - B_{\omega c,0}}{Q/A_0C_0^2P}. \quad (17)$$

A_0 is a bandwidth parameter and C_0^2 is a correlation quantity.

To evaluate the band absorptance we use the following correlation of Tien and Lowder [15] based on the results of Edwards and Menard [14]

$$A = A_0\ln\left\{\frac{uf(t)[u+2]}{[u+2f(t)]} + 1\right\} \quad (18)$$

where

$$f(t) = 2.94[1 - e^{-2.6t}]. \quad (19)$$

The variable t is a line structure parameter.

The solution to equation (16) was obtained by assuming a third-order polynomial distribution for ϕ with unknown constants. The constants were determined by satisfying equation (16) at equally spaced intervals of u. The number of intervals varied from 5–10. Equation (16) was considered to be solved when the resulting simultaneous equations yielded virtually the same results over the entire optical path as the number of intervals was increased. A quartic profile for ϕ was also used and the results were in very good agreement with those obtained from the cubic profile and are presented in Fig. 1.

Using the approximate relation for the radiative flux, equation (15), with equation (13) we obtain the following integral equation

$$\frac{u}{2} = \frac{4a}{\pi b}\int_{\gamma=0}^{\pi/2}\cos\gamma\left\{\int_{u\sin\gamma}^{u}\bar{A}\left[\frac{b(u-u')}{\cos\gamma}\right]\frac{d\phi}{du'}\,du' + \int_{u}^{u_0}\bar{A}\left[\frac{b(u'-u)}{\cos\gamma}\right]\frac{d\phi}{du'}\,du' - \int_{u\sin\gamma}^{u_0}\bar{A}\left[b\,\frac{(u+u'-2u\sin\gamma)}{\cos\gamma}\right]\frac{d\phi}{du'}\,du' + \phi(u_0)\times\left(\bar{A}\left[b\left(\frac{u+u_0-2u\sin\gamma}{\cos\gamma}\right)\right] - \bar{A}\left[\frac{b(u_0-u)}{\cos\gamma}\right]\right)\right\}d\gamma \quad (20)$$

The solution to equation (20) was obtained in the manner just described and the results are also presented in Fig. 1. It is seen that a value of a equal to unity and b equal to $^5/_4$ in the approximate formulation yields results that are in excellent agreement

[5] The gas is assumed to have only one band. For a multiband medium, the radiative flux is given by $q_r = \sum_{i=1}^{n} q_{r,i}$ where n is the number of bands.

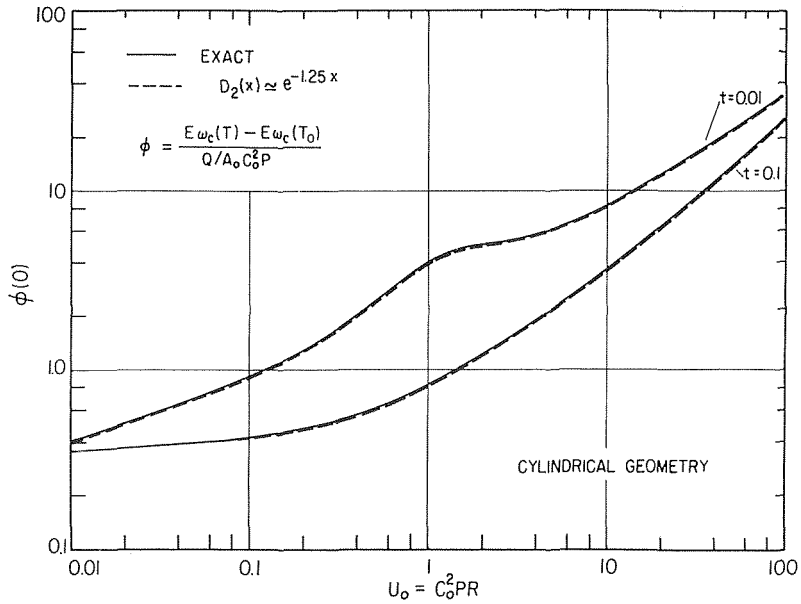

Fig. 1 Center-line temperature of radiating gas with a heat source

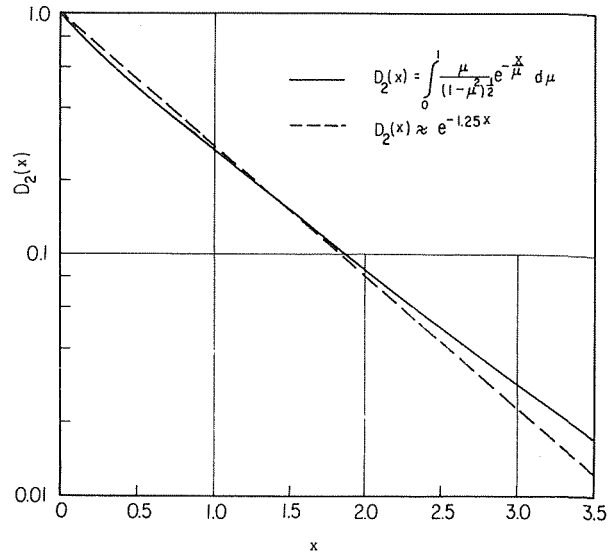

Fig. 2 Comparison of exponential integral function and approximation

with the exact results as obtained from equation (16).[6] In Fig. 2 the comparison between $D_2(x)$ and $e^{-5x/4}$ is presented.[7]

Conclusions

The problem of determining the radiative transport in the cylindrical geometry has been carried out. The inclusion of nongray effects was made through use of the total band absorptance in both the exact and an approximate formulation. The approximate formulation, corresponding to the approximation $D_2(x) \simeq e^{-5x/4}$, yields results which are in very good agreement with the exact calculations.

Acknowledgments

This research was supported in part by the National Science Foundation under Grant NSF GK 1297.

References

1 Cess, R. D., Mighdoll, P., and Tiwari, S. N., "Infrared Radiative Heat Transfer in Non-Gray Gases," *International Journal of Heat and Mass Transfer*, Vol. 10, 1967, pp. 1521–1532.

2 Wilson, K. H., and Greif, R., "Radiation Transport in Atomic Plasmas," *Journal of Quantitative Spectroscopy and Radiative Transfer*, Vol. 8, 1968, pp. 1061–1086.

3 Tien, C. L., "Thermal Radiation Properties of Gases," *Advances in Heat Transfer*, Vol. V, Academic Press, New York, 1967.

4 Viskanta, R., "Radiation Transfer and Interaction of Convection With Radiation Heat Transfer," *Advances in Heat Transfer*, Vol. III, 175, Academic Press, New York, 1966.

5 Sparrow, E. M., and Cess, R. D., *Radiation Heat Transfer*, Brooks/Cole, Belmont, Calif., 1966.

6 De Soto, S., and Edwards, D. K., "Radiative Emission and Absorption in Non-Isothermal Non-Gray Gases in Tubes," *Heat Transfer and Fluid Mechanics Institute*, Stanford University Press, 1965, p. 358.

7 Edwards, D. K., et al., "Radiant Heat Transfer in Nonisothermal Nongray Gases," JOURNAL OF HEAT TRANSFER, TRANS. ASME, Series C, Vol. 89, 1967, pp. 219–229.

[6] We note that for a gray gas, the total radiative flux is given by equation (4) with the wave number dependence omitted. Equation (4) was integrated to obtain the radial radiative flux in a gray gas with a specified linear radial temperature profile. The results are presented in Fig. 3. The exact and the approximate results are seen to be in very good agreement. The temperature profile is the same as that used by Kesten [18] in his gray-gas calculations. However, both our exact results and our approximate results do not agree with those presented in reference [18].

[7] We note that the presence of nonblack walls greatly increases the complexity of the problem. Fortunately, for many problems the effects of nonblack walls are small and may be neglected [19]. For completeness, we have presented the approximate formulation of the problem of nonblack walls in the Appendix.

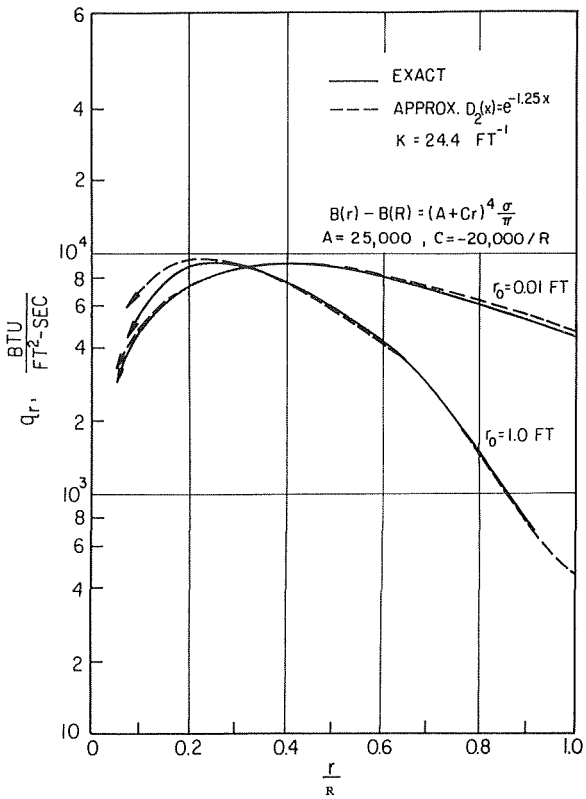

Fig. 3 Radial radiative heat flux for a gray gas

8 Novotny, J. L., and Kelleher, M. D., "Conduction in Nongray Radiating Gases," *International Journal of Heat and Mass Transfer*, Vol. 10, 1967, pp. 1521–1532.

9 De Soto, S., "Coupled Radiation, Conduction, and Convection in Entrance Region Flow," *International Journal of Heat and Mass Transfer*, Vol. 11, 1968, pp. 39–54.

10 Cess, R. D., and Tiwari, S. N., "Heat Transfer to Laminar Flow of an Absorbing-Emitting Gas Between Parallel Plates," SUNY Report No. 90, 1967.

11 Landram, C. S., Greif, R., and Habib, I. S., "Heat Transfer in Turbulent Pipe Flow With Optically Thin Radiation," JOURNAL OF HEAT TRANSFER, TRANS. ASME, Series C, Vol. 91, Aug. 1969, pp. 330–336.

12 Greif, R., "Nongray Radiation Heat Transfer in the Optically Thin Region," JOURNAL OF HEAT TRANSFER, TRANS. ASME, Series C, Vol. 90, 1968, pp. 363–365.

13 Greif, R., and Habib, I. S., "Infrared Radiation Transport: Exact and Approximate Results," JOURNAL OF HEAT TRANSFER, TRANS. ASME, Series C, Vol. 91, 1969, pp. 282–284.

14 Edwards, D. K., and Menard, W. A., "Comparison of Models for Correlation of Total Band Absorption," *Applied Optics*, Vol. 3, 1964, pp. 621–625.

15 Tien, C. L., and Lowder, J. E., "A Correlation for Total Band Absorptance of Radiating Gases," *International Journal of Heat and Mass Transfer*, Vol. 9, 1966, pp. 698–701.

16 Geffcken, W., "Radiale Strahlungsleitung in langer Zylindern," *Glastechn*, Berichte, Sonnderband, 32K, Heft VII, 1959, pp. 23–39.

17 Kuznetsov, Ye. S., "Temperature Distribution in an Infinite Cylinder and in a Sphere in a State of Non-Monochromatic Radiation Equilibrium," *Zhur. Vych. Mat. i Mat. Fiz. 2*, No. 2, 1962, pp. 217–246; English translation in USSR *Computational Mathematics and Mathematical Physics*, Vol. 2, No. 2, 1963, pp. 230–254.

18 Kesten, A. S., "Radiant Heat Flux Distribution in a Cylindrically Symmetric Nonisothermal Gas With Temperature-Dependent Absorption Coefficient," *Journal of Quantitative Spectroscopy and Radiation Transfer*, Vol. 8, Pergamon Press, 1968, pp. 419–434.

19 Habib, I. S., "Heat Transfer to a Radiating Gas Flowing Turbulently in a Tube: An Experimental and Theoretical Study," PhD dissertation, University of California, Berkeley, Calif., Dec. 1968.

APPENDIX

Radiative Heat Flux in Cylindrical Geometry With a Wall Emittance

For diffuse nonblack walls equation (1) can be written as follows

$$q_\omega = 4\int_0^{\pi/2}\Bigg\{I_\omega(0)\frac{\cos\gamma}{b}ae^{-\frac{bk_\omega}{\cos\gamma}(r+R-2r\sin\gamma)} - \frac{I_\omega(0)\cos\gamma}{b}ae^{-\frac{bk_\omega(R-r)}{\cos\gamma}} + \int_{r\sin\gamma}^{r}\left[\frac{E_\omega(r')-E_{\omega,0}}{\pi}\right] \times k_\omega a e^{-\frac{bk_\omega(r-r')}{\cos\gamma}}dr' + \frac{aE_{\omega,0}}{\pi b}\cos\gamma - \frac{aE_{\omega,0}}{\pi b} \times \cos\gamma e^{\frac{-bk_\omega(r-r\sin\gamma)}{\cos\gamma}} - \int_r^R\left[\frac{E_\omega(r')-E_{\omega,0}}{\pi}\right] \times k_\omega a e^{\frac{-bk_\omega(r'-r)}{\cos\gamma}}dr' + \frac{aE_{\omega,0}}{\pi b}\cos\gamma e^{\frac{-bk_\omega(R-r)}{\cos\gamma}} - \frac{aE_{\omega,0}}{\pi b}\cos\gamma + \int_r^R\left[\frac{E_\omega(r')-E_{\omega,0}}{\pi}\right]k_\omega a e^{\frac{-bk_\omega(r+r'-2r\sin\gamma)}{\cos\gamma}}dr' - \frac{aE_{\omega,0}\cos\gamma}{\pi b}e^{-\frac{bk_\omega}{\cos\gamma}(r+R-2r\sin\gamma)} + \frac{aE_{\omega,0}\cos\gamma}{\pi b}e^{-\frac{bk_\omega}{\cos\gamma}(r-r\sin\gamma)}\Bigg\}d\gamma \quad (21)$$

where $I_\omega(0) = H_\omega(0)/\pi$ and $H_\omega(0)$ is the radiosity of the wall. The approximation $D_2(x) \simeq ae^{-bx}$ has been used in equation (21). Equation (21) can be rewritten in the following form

$$q_\omega = \frac{4}{\pi}\int_0^{\pi/2}\Bigg\{\int_{r\sin\gamma}^{r}[E_\omega(r')-E_{\omega,0}]k_\omega a e^{-\frac{bk_\omega}{\cos\gamma}(r-r')}dr' - \int_r^R[E_\omega(r')-E_{\omega,0}]k_\omega a e^{-\frac{bk_\omega}{\cos\gamma}(r'-r)}dr' + \int_{r\sin\gamma}^{R}[E_\omega(r')-E_{\omega,0}]k_\omega a e^{-\frac{bk_\omega}{\cos\gamma}(r+r'-2r\sin\gamma)}dr' + (H_\omega(0)-E_{\omega,0})\frac{a}{b}\cos\gamma\left[e^{-\frac{bk_\omega}{\cos\gamma}(r+R-2r\sin\gamma)} - e^{-b\frac{k_\omega(R-r)}{\cos\gamma}}\right]\Bigg\}d\gamma \quad (22)$$

The radiosity of the surface is expressed as

$$H(0) = \epsilon E_0 + (1-\epsilon)F^+(R) \quad (23)$$

where $F^+(R)$ is the irradiation of the surface. We have for the reflected energy F^- the following relation

$$F^- = (1-\epsilon)F^+$$

where $F_\omega{}^+$ is represented by the following expression

$$F_\omega{}^+(R) = 4\int_{\alpha=0}^{\pi/2}\cos^2\alpha d\alpha\int_{\beta=0}^{\pi/2}I_\omega{}^+\cos\beta d\beta \quad (24)$$

or

$$F_\omega{}^+(R) = 4\int_{\beta=0}^{\pi/2}\cos\beta\int_{\alpha=0}^{\pi/2}I_\omega{}^+\cos^2\alpha d\alpha d\beta \quad (25)$$

From references [18, 19] equation (25) can be written in the following form

$$F_\omega{}^+(R) = 4\int_0^{\pi/2}\cos\gamma\Bigg\{I_\omega(0)D_3\left[\frac{2k_\omega}{\cos\gamma}(R-R\sin\gamma)\right] + \int_{R\sin\gamma}^{R}k_\omega\frac{B_\omega(r')}{\cos\gamma}\left(D_2\left[\frac{k_\omega}{\cos\gamma}(R+r'-2R\sin\gamma)\right] + D_2\left[\frac{k_\omega}{\cos\gamma}(R-r')\right]\right)dr'\Bigg\}d\gamma \quad (26)$$

Substituting equation (26) into equation (23) and using the exponential function approximation for D_3 yields

$$I_\omega(0) = \frac{\epsilon E_{\omega,0}}{\pi} + \frac{(1-\epsilon)}{\pi}\frac{4a}{b}I_\omega(0)\int_0^{\pi/2}\cos\gamma e^{\frac{-2k_\omega b(R-R\sin\gamma)}{\cos\gamma}} + \frac{4a(1-\epsilon)}{\pi}\int_0^{\pi/2}\cos\gamma\int_{R\sin\gamma}^{R}\frac{k_\omega B_\omega(r')}{\cos\gamma} \times\left(e^{-\frac{bk_\omega}{\cos\gamma}(R+r'-2R\sin\gamma)} + e^{\frac{-bk_\omega}{\cos\gamma}(R-r')}\right)dr'd\gamma \quad (27)$$

Solving equation (27) for $I_\omega(0)$ and setting $H_\omega(0) = \pi I_\omega(0)$ for a diffuse surface we obtain

$$H_\omega(0) = \epsilon E_{\omega,0} + 4a(1-\epsilon)\int_0^{\pi/2}\int_{R\sin\gamma}^{R}k_\omega B_\omega(r') \times\left[e^{\frac{-bk\omega(R+r'-2R\sin\gamma)}{\cos\gamma}} + e^{\frac{-bk\omega(R-r')}{\cos\gamma}}\right]dr'd\gamma/\text{den} \quad (28)$$

where

$$\text{den} = 1 - \frac{4(1-\epsilon)}{\pi}\frac{a}{b}\int_0^{\pi/2}\cos\gamma e^{\frac{-2k\omega b}{\cos\gamma}(R-R\sin\gamma)}d\gamma$$

Equation (28) represents the expression for the surface radiosity to be used in equation (22).

Turbulent Heat Transfer in Concentric Annuli With Constant Wall Temperatures

ALAN QUARMBY

R. K. ANAND

University of Manchester Institute of Science and Technology, Manchester, England

The problem of turbulent heat transfer in concentric annuli is analyzed for the case in which one wall has a constant temperature while the other is insulated. The solution is given for both the thermal entrance region and the fully developed situation with heating at either one of the annular surfaces. The description of the velocity profile properly takes into account the Reynolds number and radius ratio dependence of the nondimensional turbulent velocity profile in concentric annuli. Results are presented for radius ratios 2.88, 5.625, and 9.37 with the Reynolds number range from 20,000 to 240,000 and for Prandtl numbers 0.01, 0.7, and 1000. The calculated Nusselt numbers for the constant wall temperature boundary condition are smaller than the corresponding result for a uniform heat-flux boundary condition. The available experimental evidence for concentric annuli is insufficient to provide a direct test of the analysis. However some calculated results for the radius ratios 1.05 and 50 are in agreement with available theory and experiments for the parallel plate channel and circular tube, respectively. There is also good agreement between the calculated results for the extension of the analysis to the case of a linear rise in wall temperature and experiments for a uniform heat-flux boundary condition for the annuli considered.

Introduction

THE annular configuration is of considerable importance in the design of heat exchangers and has attracted much theoretical and experimental effort. Like the circular tube and parallel plate channel, a theoretical analysis may be made of turbulent heat transfer in concentric annuli from the energy equation. Such analyses have been presented for concentric annuli in previous work only for the case in which there is a uniform heat flux at the annular surfaces and the situation is fully developed. The analysis of the thermal entrance region, which is of importance unless the duct is very long, requires the solution of a partial differential equation and may be an eigenvalue problem. With a uniform wall heat-flux boundary condition the fully developed solution may be obtained without considering the thermal entrance region. However, with a constant-wall-temperature boundary condition, the asymptotic value of the Nusselt number may only be calculated from the thermal entrance region solution. Such analyses have been given by Sleicher and Tribus [1][1] for the circular tube and by Hatton and Quarmby [2] for the parallel plate channel.

The value of such solutions depends very much upon the accuracy of the description of the turbulent velocity profile and the variation of eddy diffusivity across the duct. Previous formulations of these quantities for concentric annuli, e.g., Leung, Kays,

Contributed by the Heat Transfer Division of THE AMERICAN SOCIETY OF MECHANICAL ENGINEERS and presented at the ASME-AIChE Heat Transfer Conference, Minneapolis, Minn., August 3–6, 1969. Manuscript received by the Heat Transfer Division, April 4, 1969. Paper No. 69-HT-51.

[1] Numbers in brackets designate References at end of paper.

Nomenclature

A = cross-sectional area of annulus
b = radius ratio r_0/r_i
C_n = eigenconstant
C = coefficient in eddy diffusivity equation
c_p = specific heat at constant pressure
D = annular characteristic dimension $2(r_0 - r_i)$
h = heat transfer coefficient
K = von Karman's constant in similarity hypothesis
k = thermal conductivity
k^1 = k/lb'
l = mixing length
n = index in sublayer profile
Nu = Nusselt number hD/k
Pr = Prandtl number $\mu c_p/k$
Re = Reynolds number u_bD/ν
R = nondimensional radius $r/(r_0 - r_i)$
r = radius
$r_0^+ = r_0\sqrt{\tau_0/\mu}/\nu$
$r_i^+ = r_i\sqrt{\tau_i/\mu}/\nu$
t = temperature
T = nondimensional temperature $\dfrac{t - t_\omega}{t_e - t_\omega}$
u = fluid velocity
u^+ = nondimensional turbulent velocity $u/\sqrt{\tau/\zeta}$
u_b = bulk velocity $\int_A u\,dA/A$
v' = fictitious velocity of turbulent eddy
x = axial distance
x^+ = nondimensional axial distance x/D
y = radial distance from annular wall
$y^+ = y\sqrt{\tau/\mu}/\nu$
α = thermal diffusivity
β = $1 - y^+/y_m{}^+$
λ = eigenvalue
ρ = density
τ = shear stress
μ = viscosity
ν = kinematic viscosity μ/ρ
ν^1 = $\nu/\rho v'$
ϵ_m = eddy diffusivity of momentum
ϵ_H = eddy diffusivity of heat

Subscripts

i = inner
o = outer
m = at position of maximum velocity
l = at edge of sublayer
e = entrance value at $x = 0$
b = bulk value

and Reynolds [3] and Lee and Barrow [4], have included certain assumptions which recent experimental work by Quarmby [5] has shown to be incorrect. It has been shown by reference [5] that the nondimensional velocity profile in concentric annuli is dependent on the radius ratio and Reynolds number. In particular, the radius of maximum velocity is a function of these parameters and is not the same as in laminar flow. An analysis of turbulent flow in concentric annuli from von Karman's similarity hypothesis has been given by Quarmby [6] which is in good agreement with the findings of [5].

This analysis is used here, together with descriptions of the eddy diffusivities of momentum and heat which are believed accurate, to provide the solution of the energy equation for turbulent heat transfer in the thermal entrance region of concentric annuli with a boundary condition of constant wall temperature.

General Energy Equation

With the usual assumptions of constant fluid properties and negligible axial conduction and introducing the concept of eddy diffusivity of heat, the energy equation becomes,

$$\frac{1}{r}\frac{\partial}{\partial r}\left[(\alpha + \epsilon_H) r \frac{\partial t}{\partial r}\right] = u\frac{\partial t}{\partial x} \tag{1}$$

It is further assumed that the temperature is uniform, t_e, and the turbulent velocity profile is fully developed at the start of the heated section at $x = 0$. Using the nondimensional variables

$$T = \frac{t - t_w}{t_e - t_w}, \qquad x^+ = \frac{x}{D}$$

and

$$R = \frac{r}{r_o - r_i}, \qquad r_0{}^+ = \frac{r_0\sqrt{\tau_0/\rho}}{\nu}$$

equation (1) becomes

$$\frac{1}{R}\frac{\partial}{\partial R}\left[\left(\frac{\epsilon_H}{\nu} + \frac{1}{\Pr}\right) R \frac{\partial T}{\partial R}\right] = \frac{b-1}{2b} r_o{}^+ u_o{}^+ \frac{\partial T}{\partial x^+} \tag{2}$$

The subscript w refers to the heated wall so that for heating on the inner wall $T_i = \dfrac{t - t_i}{t_e - t_i}$ and for heating on the outer wall $T_o = \dfrac{t - t_o}{t_e - t_o}$. Since T is defined relative to the wall temperature it is clear that the asymptotic value of T must be zero since this corresponds to the condition that the fluid temperature is everywhere equal to that of the heated wall. Accordingly, the temperature T has only a developing part which may be given by a variables-separable solution as

$$T = \phi(R)\psi(X) \tag{3}$$

Equation (3) is substituted into equation (2) and each side multiplied by 8/Re and equated to the constant $-\lambda^2$. On rearranging we have

$$T = \sum_1^\infty C_n \phi_n(R)\psi_n(X) \tag{4}$$

where $\lambda^2{}_n$ are the eigenvalues and

$$\psi_n = \exp\left[-\frac{8\lambda_n{}^2 x^+}{\mathrm{Re}}\right] \tag{5}$$

The eigenfunctions ϕ_n are determined from

$$\frac{1}{R}\frac{d}{dR}\left[R\left(\frac{\epsilon_H}{\nu} + \frac{1}{\Pr}\right)\frac{d\phi_n}{dR}\right] + 4\frac{b-1}{b}\frac{r_o{}^+ u_o{}^+ \lambda_n{}^2}{\mathrm{Re}}\phi_n = 0 \tag{6}$$

The boundary conditions on equation (6) are that $T = 1$ at $x = 0$ and $T = 0$ at the heated wall for all values of x^+. At the unheated wall $\dfrac{\partial T}{\partial R} = 0$ for all values of x^+. The eigenvalues are determined from these boundary conditions and the constants C_n from the Sturm-Liouiville condition, so that

$$C_n = \frac{\int_{R_i}^{R_o} u_0{}^+ R\phi_n(R)dR}{\int_{R_i}^{R_o} u_o{}^+ R\phi_n(R)^2 dR} \tag{7}$$

It is clear from equations (4) and (7) that an arbitrary multiplicative factor may be associated with ϕ_n or, equivalently, that the magnitude of $\dfrac{d\phi_n}{dR}$ at the heated wall may be taken as unity. Thus, for heating at the inner wall $\left(\dfrac{dT_i}{dR}\right)_{R_i} = 1$ and for heating at the outer wall $\left(\dfrac{dT_o}{dR}\right)_{R_o} = -1$.

The Nusselt number is defined by

$$\mathrm{Nu} = \frac{hD}{k} = -\left(\frac{\partial t}{\partial r}\right)_w \frac{D}{t_o - t_b} \tag{8}$$

From the expression for t_b given by

$$t_b = \frac{\int_{r_i}^{r_o} urtdr}{\int_{r_i}^{r_o} urdr} \tag{9}$$

and use of equation (6)

$$T_{ib} = \frac{1}{\Pr(b+1)}\sum_1^\infty \frac{C_n}{\lambda_n{}^2}\left(\frac{d\phi_n}{dR}\right)_w \exp\left[-\frac{8\lambda^2{}_n}{\mathrm{Re}}x^+\right] \tag{10a}$$

and

$$T_{ob} = \frac{b}{\Pr(b+1)}\sum_1^\infty \frac{C_n}{\lambda^2{}_n}\left(\frac{\partial\phi_n}{\partial R}\right)_\omega \exp\left[-\frac{8\lambda^2{}_n}{\mathrm{Re}}x^+\right] \tag{10b}$$

Differentiating equation (4) and since the magnitude of $\left(\dfrac{dT}{dR}\right)_w$ is taken as unity in the solution we have

$$\mathrm{Nu}_i = \frac{2\Pr(b+1)\sum_1^\infty C_n \exp\left[-\dfrac{8\lambda_n{}^2}{\mathrm{Re}}x^+\right]}{\sum_1^\infty \dfrac{C_n}{\lambda_n{}^2}\exp\left[-\dfrac{8\lambda^2{}_n}{\mathrm{Re}}x^+\right]} \tag{11a}$$

and

$$\mathrm{Nu}_o = \frac{2\Pr\dfrac{b+1}{b}\sum_1^\infty C_n \exp\left[-\dfrac{8\lambda_n{}^2}{\mathrm{Re}}x^+\right]}{\sum_1^\infty \dfrac{C_n}{\lambda_n{}^2}\exp\left[-\dfrac{8\lambda_n{}^2}{\mathrm{Re}}x^+\right]} \tag{11b}$$

These expressions reduce, correctly, to the parallel plate limit given by reference [2] as b becomes unity, i.e.,

$$\mathrm{Nu} = \frac{4\Pr\sum_1^\infty C_n \exp\left[-\dfrac{8\lambda_n{}^2}{\mathrm{Re}}x^+\right]}{\sum_1^\infty \dfrac{C_n}{\lambda_n{}^2}\exp\left[-\dfrac{8\lambda_n{}^2}{\mathrm{Re}}x^+\right]} \tag{11c}$$

Unlike the circular tube and parallel plate channel the problem is not symmetric with respect to the center line of the annular space. Accordingly, the eigenvalues and constants for the case

of heating at the outer wall are different to those for heating at the inner wall. Thus two sets of λ_n and C_n must be determined for each radius ratio-Reynolds number-Prandtl number combination.

Velocity Profile and Eddy Diffusivity Variation

The solution of equation (6) requires an accurate description of the velocity profile and of the variation of eddy diffusivity across the duct. In the present work the velocity profile is given by an analysis due to reference [6] which is described in the Appendix. This analysis is based on the von Karman similarity hypothesis and may also be used to give a description of the eddy diffusivity of momentum, ϵ_m. However, the value of ϵ_m thus given by the similarity hypothesis is zero at the radius of maximum velocity. Since the eddy diffusivity of heat is to be obtained from ϵ_m by an expression for ϵ_H/ϵ_m such a value is not acceptable since heat is being transferred across the plane of the radius of maximum velocity in the present unsymmetrically heated case. Accordingly the eddy diffusivity of momentum is given in the center of the duct by an expression developed from that given by reference [3] which fits the data of reference [5] for ϵ_m. In the region close to the annulus wall the expression for ϵ_m given by Deissler [7] is used. Thus ϵ_m is described as follows, for $0 < y_o^+ < y_{to}^+$

$$\frac{\epsilon_m}{\nu} = n^2 u_o^+ y_o^+ [1 - \exp(-n^2 u_o^+ y_o^+)] \tag{12}$$

and for $y_{to}^+ < y_o^+ < y_{mo}^+$

$$\frac{\epsilon_m}{\nu} = \frac{1}{15}\left(1 - \frac{a}{b}\right) r_o^+ (1 - \beta_o^2)(1 + 2\beta_o^2) \times [1 + 0.6\beta_o(1 - \beta_o)] - C_o \tag{13}$$

where $\beta_o = 1 - y_o^+/y_{mo}^+$

In the inner sublayer, $\frac{\epsilon_m}{\nu}$ is given by replacing the subscript o in equation (12) by i, while for $y_{ti}^+ < y_i^+ < y_{mi}^+$.

$$\frac{\epsilon_m}{\nu} = \frac{1}{15}\left(1 - \frac{a}{b}\right) r_o^+ (1 - \beta_2^2)(1 + 2\beta_1^2) \times \left[1 + 0.6\sqrt{\frac{\tau_o}{\tau_i}}\,\beta_i(1 - \beta_i)\right]\left[1 - \left(1 - \frac{y_{mi}^+}{y_{mo}^+}\right)\beta_i\right] - C_i \tag{14}$$

where $\beta_i = 1 - y_i^+/y_{mi}^+$.

Leung, Kays, and Reynolds [3] used equation (13) with $C_o = 0$. The value of $\frac{\epsilon_m}{\nu}$ at y_{to}^+ thus calculated is not the same as that obtained from equation (12) at the same point. The coefficients C_o and C_i are introduced to eliminate these discontinuities in the eddy diffusivity profile and are defined as follows. If the difference, at y_{to}^+, in ϵ_m between equations (12) and (13) with C_o zero is $\delta(\epsilon_m)_o$ then

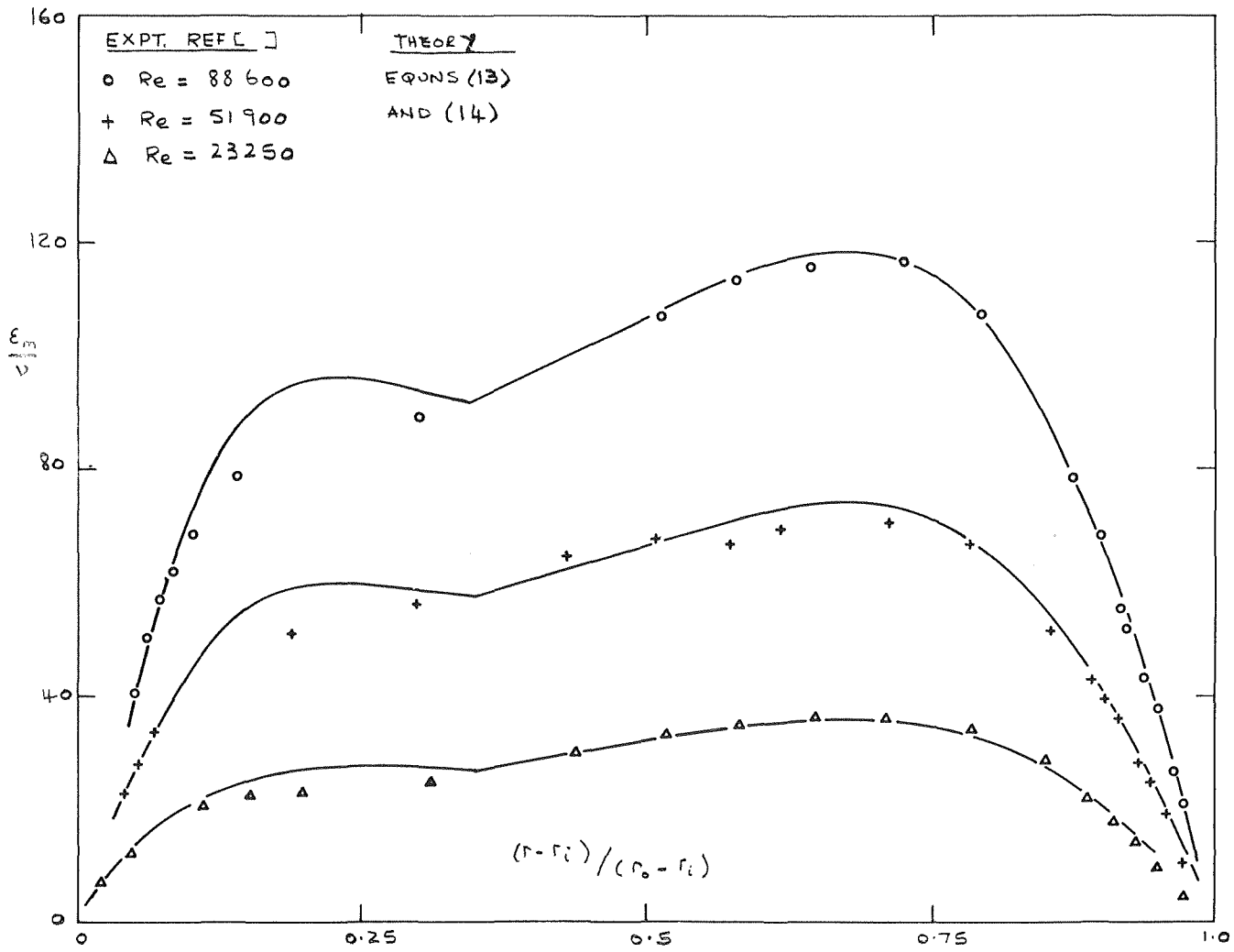

Fig. 1 Eddy diffusivity in concentric annuli $b = 5.62$

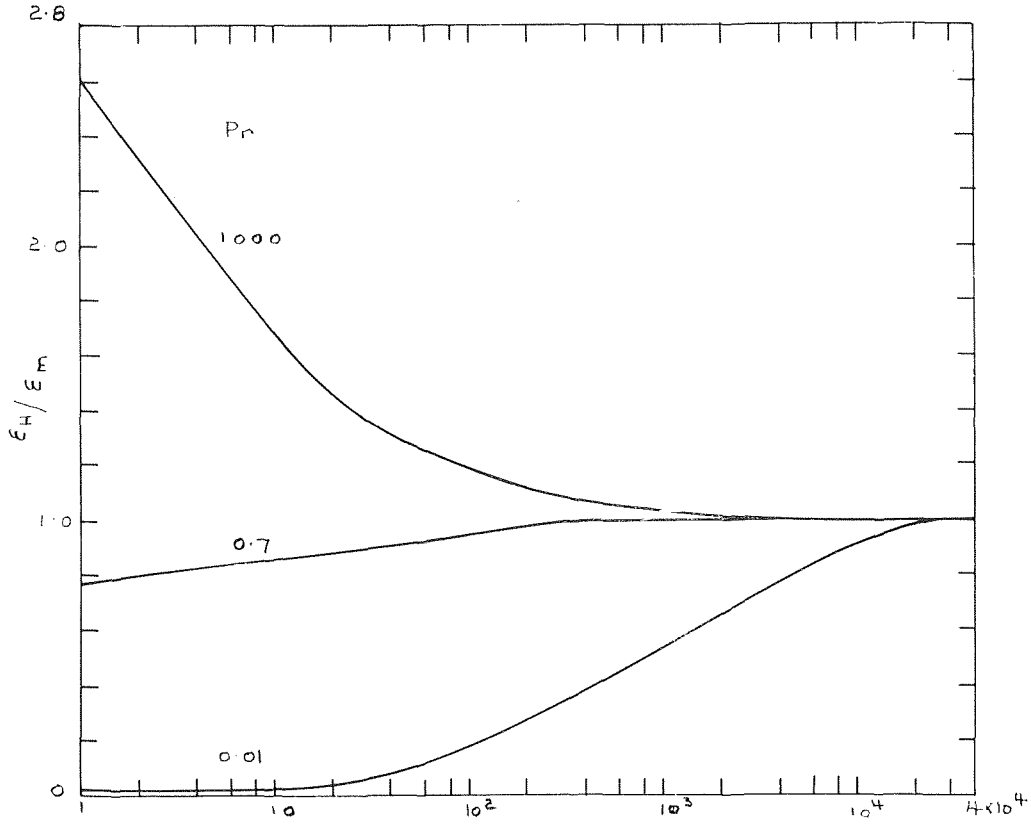

Fig. 2 Ratio of ϵ_H/ϵ_m from Jenkins' expression

$$C_o = \delta(\epsilon_m)_o(y_{mo}{}^+ - y_o{}^+)/(y_{mo}{}^+ - y_{lo}{}^+)$$

Similarly,

$$C_i = \delta(\epsilon_m)_i(y_{mi}{}^+ - y_i{}^+)/(y_{mi}{}^+ - y_{li}{}^+)$$

Fig. 1 shows the agreement between the present description of ϵ_m and measured values given by reference [5]. Similar good agreement has been shown for equations (13) and (14) by reference [3] for radius ratios up to 19 and Reynolds numbers as high as 700,000.

The ratio of the eddy diffusivity of heat to that of momentum is taken from the expression due to Jenkins [8]; namely,

$$\frac{\epsilon_H}{\epsilon_m} = \mathrm{Pr}\,\frac{1 - \dfrac{90}{\pi^6}\dfrac{1}{k^1}\displaystyle\sum_{n=1}^{6}\frac{1}{n^6}\,1 - \exp\,(-n^2\pi^2k^1)}{1 - \dfrac{90}{\pi^6}\dfrac{1}{\nu^1}\displaystyle\sum_{n=1}^{6}\frac{1}{n^6}\,1 - \exp\,(-n^2\pi^2\nu^1)} \qquad (15)$$

This ratio has been evaluated by reference [3] as a function of ϵ_m/ν and the values for Pr = 1000, 0.7, and 0.01 are given in Fig. 2.

Calculations and Results

For a given radius ratio, the Reynolds number is determined by choice of the parameter $r_o{}^+$ since $\mathrm{Re} = u_bD/\nu$ may be expressed as

$$\mathrm{Re} = \frac{4}{b+1}\frac{1}{r_i{}^+}\int_0^{y_{mi}{}^+} u_i{}^+(y_i{}^+ + r_i{}^+)dy_i{}^+ + \frac{b}{r_o{}^+}\int_0^{y_{mo}{}^+} u_o{}^+(r_o{}^+ - y_o{}^+)dy_o{}^+ \qquad (16)$$

The relationship between $r_o{}^+$ and Re for the radius ratio 1.05, 2.88, 5.625, 9.37, and 50 is given in Table 1. These ratios were chosen since they were used in the flow study of reference [6] and correspond with the experimental results of reference [5]. The results for $b = 1.05$ and 50 are comparable with results for a parallel plate channel and a circular tube, respectively.

Table 1 Relation between Re and $r_o{}^+$ for concentric annuli

b =	1.05		2.88		5.625		9.37		50	
r_o^+	Re	r_o^+	Re	r_o^+	Re	r_o^+	Re	r_o^+	Re
6000	9050	485	10180	360	9456	325	9243	295	9088
11100	17550	882	19560	820	23560	875	28040	1000	36310
25600	52900	1600	38530	1950	63250	2210	80460	2210	89640
50000	96650	5000	141340	5000	184400	3000	113900	2500	103140
100000	212200	7500	223200	7300	290900	5000	202700	5000	225600
150000	334600	1000	308400	10000	401200	10000	440800	10000	488900

The integration of the equations was effected by using a Runge-Kutta technique and accuracy was insured by suitable choice of the step length. The eigenvalues were determined by a trial and error method which consisted of integrating equation (6) from the heated wall with arbitrary values given to the λ_n and establishing which values fulfilled the correct boundary condition at the unheated wall. The constants C_n were then found by direct integration of equation (7). The eigenvalues and constants for $b = 2.88$, 5.625, and 9.37 for a constant wall temperature on the inner wall are given in Table 2 and for a constant wall temperature on the outer wall in Table 3. Since the radius ratios $b = 50$ and 1.05 were investigated merely to provide a comparison with experimental work for the circular tube and parallel plate channel, the eigenvalues and constants for Pr = 0.7 only were calculated. These are given in Table 4.

Table 2 Constant wall temperature at inner wall; eigenvalues and constants

b	Re	n	Pr = 0.01 λ_n	Pr = 0.01 C_n	Pr = 0.7 λ_n	Pr = 0.7 C_n	Pr = 1000 λ_n	Pr = 1000 C_n
2.88	20363	1	9.075083	-2.899786	3.091883	-26.13537	0.320858	-399.8196
		2	32.80151	-2.184740	14.08061	-10.32470	14.47666	- 15.66066
		3	55.55759	-1.566498	25.03239	- 2.722456	27.61772	12.02237
		4	78.05885	-2.157974	35.48164	- 5.277310	39.23275	- 11.94325
		5	100.5745	-1.220921	45.66055	- 1.238206	49.75455	6.560319
		6	123.0365	-2.229934	55.91421	- 4.664812	56.96660	- 2.983221
		7	145.4938	-0.950982	65.98038	- 0.270775	-	-
	73035	1	9.416890	-3.139316	5.069913	-68.70389	0.556746	-1202.379
		2	34.42458	-2.140490	24.18967	-18.36254	24.01419	- 2.586613
		3	58.09132	-1.921002	43.11542	- 9.218279	45.8849	- 1.035307
		4	81.64276	-1.846881	61.02498	- 7.824075	65.88311	- 0.863087
		5	105.1252	-1.809663	78.41138	- 6.750022	85.51508	- 0.788957
		6	128.5867	-1.781055	95.96298	- 6.040550	105.2247	- 0.848930
		7	152.0325	-1.757175	113.2700	- 5.557072	124.5951	- 1.016885
	122275	1	9.894949	-3.481402	6.169168	-101.8846	0.696367	-1881.199
		2	36.55422	-2.331768	30.03570	- 25.80744	29.41814	- 4.169436
		3	61.55557	-2.013125	53.64464	-12.81945	56.16238	- 1.594658
		4	86.54685	-1.923808	75.91237	-10.91440	80.62271	- 1.238183
		5	111.3810	-1.895964	97.52171	- 9.406338	104.6599	- 1.020585
		6	136.2241	-1.864430	119.3548	- 8.400775	128.8666	- 0.953958
		7	161.0496	-1.852537	140.8829	- 7.723904	152.7554	- 0.957475
	170415	1	10.37975	-3.847055	7.014179	-131.8325	0.805328	-2516.153
		2	38.69533	-2.526060	34.59894	- 32.25595	33.54718	- 5.714979
		3	65.08417	-2.106454	61.87580	-15.92151	64.01264	- 2.147616
		4	91.53173	-2.004531	87.54783	-13.58441	91.87436	- 1.622690
		5	117.7368	-1.983785	112.4494	-11.70796	119.2518	- 1.285538
		6	143.9828	-1.947898	137.6165	-10.44894	146.8418	- 1.138684
		7	170.2076	-1.943638	162.4331	- 9.599539	174.0882	- 1.069480

b	Re	n	Pr = 0.01 λ_n	Pr = 0.01 C_n	Pr = 0.7 λ_n	Pr = 0.7 C_n	Pr = 1000 λ_n	Pr = 1000 C_n
5.625	30226	1	7.992251	-3.991700	3.006043	-41.53817	0.290471	-590.1611
		2	32.43244	-2.177867	17.44283	- 8.604550	18.24873	- 0.901330
		3	55.36463	-1.938196	30.53339	- 4.739451	33.61881	- 0.517312
		4	78.01522	-1.846164	43.26135	- 3.992748	48.04803	- 0.627029
		5	100.5791	-1.770317	55.58452	- 3.669077	61.74534	- 0.987041
		6	123.1472	-1.718124	67.91099	- 3.269371	74.71682	- 1.795102
		7	145.6580	-1.680681	80.25847	- 3.034592	83.32550	- 1.575629
	65116	1	8.208116	-4.216823	4.016382	-74.23870	0.414489	-1137.877
		2	33.78839	-2.270990	24.23021	-14.08323	24.80260	- 1.709988
		3	57.42224	-1.996290	42.43878	- 7.789196	45.59228	- 0.821534
		4	80.90392	-1.899412	60.08606	- 6.631848	65.28998	- 0.736744
		5	104.2955	-1.850289	77.12644	- 6.179343	84.35160	- 0.761381
		6	127.6499	-1.816304	94.12569	- 5.952280	103.4471	- 0.854037
		7	150.9754	-1.788706	111.1633	- 5.172300	122.3952	- 1.115195
	125267	1	8.722900	-4.784154	5.125125	-120.9990	0.549439	-1999.309
		2	36.70451	-2.476832	32.00075	- 21.28122	32.14804	- 3.092469
		3	62.09195	-2.110161	56.08750	- 11.71480	58.98238	- 1.405441
		4	87.47004	-1.982941	79.37752	- 10.04015	84.43577	- 1.144173
		5	112.7423	-1.950942	101.8479	- 9.389511	109.1080	- 1.030665
		6	137.9151	-1.929277	124.2736	- 8.439301	133.9183	- 0.956326
		7	163.0917	-1.907136	146.7614	- 7.840364	158.7204	- 0.978241
	236822	1	9.69456	-5.953074	6.537680	-226.7880	0.725608	-3487.521
		2	42.16597	-2.868571	42.19933	-112.6053	41.65225	- 5.627407
		3	70.99961	-2.319742	74.01814	51.78292	76.20928	- 2.490315
		4	99.98238	-2.149568	104.7114	-100.5854	108.9599	- 1.953745
		5	128.7981	-2.145444	134.2894	72.86839	140.7483	- 1.654222
		6	157.4228	-2.137264	163.8059	-100.5410	172.7960	- 1.405361
		7	186.1126	-2.116600	193.4264	66.53570	204.8621	- 1.293330

b	Re	n	Pr =0.1 λ_n	Pr =0.1 C_n	Pr = 0.7 λ_n	Pr = 0.7 C_n	Pr = 1000 λ_n	Pr = 1000 C_n
9.37	42945	1	7.326682	-5.346613	2.973056	-63.88097	0.284069	-836.6941
		2	32.46807	-2.428282	21.07102	- 9.210693	22.24966	- 0.873264
		3	55.59644	-2.085337	36.55989	- 5.477274	39.99339	- 0.516435
		4	78.53718	-1.956305	51.69166	- 4.662476	57.05247	- 0.542383
		5	101.3551	-1.879692	66.40976	- 4.492097	73.50250	- 0.715022
		6	124.1450	-1.815596	80.93133	- 4.226783	89.61274	- 1.052817
		7	146.9168	-1.772007	95.52910	- 3.907540	105.1524	- 1.740639
	80016	1	7.585646	-5.748278	3.711728	-99.67655	0.369121	-1413.317
		2	34.28466	-2.521136	24.41801	-13.19182	28.48552	- 1.472657
		3	58.46403	-2.143681	47.55374	- 7.852744	51.08216	- 0.799316
		4	82.53197	-2.001491	67.22472	- 6.734451	72.86677	- 0.719205
		5	106.5018	-1.939238	86.34033	- 6.537745	93.99648	- 0.759391
		6	130.4060	-1.902128	105.1649	- 6.202879	114.9322	- 0.830831
		7	154.2773	-1.875041	124.0504	- 5.776935	135.9150	- 0.984349
	157789	1	8.203973	-6.753652	4.768409	-164.5326	0.494325	-2533.635
		2	38.41610	-2.757374	36.76948	- 19.93419	37.35043	- 2.717795
		3	65.10658	-2.283110	63.76188	- 11.89856	66.84202	- 1.417726
		4	91.82073	-2.106159	90.06481	- 10.31336	95.28862	- 1.183148
		5	118.4713	-2.055428	115.6049	- 10.10213	122.9029	- 1.121113
		6	144.9895	-2.044937	140.7481	- 9.614570	150.3124	- 1.058839
		7	171.4501	-2.029921	165.9868	- 8.940345	177.8989	- 1.034234
	231996	1	8.784331	-7.771293	5.518450	-220.4155	0.584899	-3547.008
		2	42.31814	-2.980203	43.61477	- 25.37930	43.93415	- 3.881036
		3	71.45661	-2.409200	75.62531	- 15.18009	78.37564	- 2.003972
		4	100.6980	-2.206836	106.7835	- 13.23217	111.6075	- 1.645538
		5	129.8855	-2.169354	137.0169	- 13.02506	143.9172	- 1.511811
		6	158.8802	-2.180982	166.7686	- 12.42693	176.0272	- 1.362212
		7	187.8014	-2.174664	196.6387	- 11.54948	208.3624	- 1.255906

Table 3 Constant wall temperature at outer wall; eigenvalues and constants

b	Re	n	Pr = 0.01 λ_n	Pr = 0.01 C_n	Pr = 0.7 λ_n	Pr = 0.7 C_n	Pr = 1000 λ_n	Pr = 1000 C_n
2.88	20363	1	13.28325	-1.834183	4.895039	- 21.57020	0.522454	-367.7152
		2	34.65226	-1.885824	14.21774	- 9.296906	14.47746	- 6.227211
		3	56.64096	-1.630964	25.31622	- 3.972633	27.62350	4.851804
		4	78.92202	-1.817647	35.57417	- 4.134452	39.24599	- 5.331832
		5	101.2323	-1.446870	45.80004	- 2.357333	49.87949	2.813525
		6	123.5740	-1.781653	56.00696	- 3.282394	58.00810	- 2.706227
		7	145.9693	-1.299235	66.09829	- 1.600982	76.26263	- 21.78299
	73035	1	13.97642	-2.047283	8.143507	- 59.67937	0.914452	-1126.332
		2	36.10625	-1.965480	24.37149	- 18.69831	24.01474	- 2.476077
		3	59.29361	-1.817168	43.56329	- 10.27337	45.88888	- 1.153948
		4	82.52081	-1.766783	61.14153	- 7.784162	65.88442	- 0.846964
		5	105.8165	-1.738139	78.57743	- 6.781996	85.51825	- 0.806826
		6	129.1498	-1.713352	96.04529	- 5.896312	105.2294	- 0.864743
		7	152.5093	-1.691267	113.3448	- 5.382809	124.6058	- 1.068564
	122275	1	14.82584	-2.324203	9.951011	- 89.50058	1.146056	-1769.282
		2	38.10563	-2.166809	30.23145	- 26.31512	29.41866	- 3.985931
		3	62.86456	-1.922032	54.17890	- 14.39880	56.16674	- 1.769743
		4	87.42396	-1.853610	76.04051	- 10.88266	80.62350	- 1.196264
		5	112.0975	-1.830149	97.70816	- 9.471152	104.6617	- 1.014519
		6	136.8026	-1.802637	119.4431	- 8.218484	128.8681	- 0.930630
		7	161.5180	-1.788587	140.9592	- 7.493423	152.7579	- 0.943543
	170415	1	15.66785	-2.620234	11.34112	-116.5589	1.326834	-2371.650
		2	40.14063	-2.368487	34.80461	- 32.90321	33.54769	- 5.462482
		3	66.49384	-2.028501	62.47536	- 17.96062	64.01755	- 2.384324
		4	92.40850	-1.942479	87.68502	- 13.55954	91.87507	- 1.563865
		5	118.4780	-1.922669	112.6518	- 11.80169	119.2534	- 1.271219
		6	144.5740	-1.890629	137.7098	- 10.23445	146.8429	- 1.101982
		7	170.6696	-1.880715	162.5105	- 9.319703	174.0897	- 1.039835

b	Re	n	Pr = 0.01 λ_n	Pr = 0.01 C_n	Pr = 0.7 λ_n	Pr = 0.7 C_n	Pr = 1000 λ_n	Pr = 1000 C_n
5.625	30226	1	14.46964	-1.862939	6.268068	-30.75390	0.662449	- 516.8081
		2	35.65612	-1.797933	17.90387	- 9.254864	18.25292	- 1.019198
		3	57.53934	-1.717540	31.13099	- 5.617130	33.62685	- 0.673969
		4	79.66570	-1.672252	43.61935	- 4.263844	48.06026	- 0.745806
		5	101.9489	-1.626293	55.80325	- 3.628838	61.78367	- 1.217318
		6	124.2505	-1.585645	68.13511	- 3.213319	74.99613	- 2.800970
		7	146.6134	-1.553730	80.42125	- 2.883351	85.88324	- 5.490860
	65116	1	15.07970	-2.028908	8.490866	-56.80974	0.927873	-1013.742
		2	36.86019	-1.901848	24.83839	-15.63620	24.80781	- 1.945516
		3	59.71320	-1.782306	43.21680	- 9.494701	45.59952	- 1.041106
		4	82.64930	-1.740444	60.54474	- 7.236186	65.29541	- 0.8066845
		5	105.6884	-1.714439	77.38267	- 6.197319	84.35784	- 0.795683
		6	128.7931	-1.690685	94.38067	- 5.536550	103.4605	- 0.940667
		7	151.9488	-1.668144	111.3252	- 4.968934	122.4255	- 1.272868
	125267	1	16.32410	-2.415349	10.94189	-94.86330	1.235954	-1798.632
		2	39.63510	-2.133389	32.74275	-23.98258	32.15476	- 3.534336
		3	64.56743	-1.922274	57.05892	-14.55812	58.99075	- 1.766283
		4	89.34820	-1.855023	79.93314	-11.06415	84.44035	- 1.215655
		5	114.1606	-1.832402	102.1323	- 9.442392	109.1110	- 1.014893
		6	139.1085	-1.815154	124.5611	- 8.428532	133.9227	- 0.960494
		7	164.0934	-1.796299	146.9375	- 7.564538	158.7259	- 0.975470
	236622	1	18.57346	-3.218728	14.07381	-157.7191	1.639299	-3164.603
		2	44.93661	-2.561151	43.10654	- 36.73990	41.66084	- 6.415408
		3	73.80227	-2.184752	75.22734	- 22.28590	76.22028	- 3.168512
		4	102.0729	-2.072201	105.3869	- 16.90572	108.9650	- 2.064554
		5	130.2490	-2.051479	134.6056	- 14.39932	140.7505	- 1.596420
		6	158.6847	-2.038173	164.1290	- 12.85162	172.7990	- 1.375544
		7	187.1388	-2.015898	193.6126	- 11.51405	204.8647	- 1.242404

b	Re	n	Pr = 0.01 λ_n	Pr = 0.01 C_n	Pr = 0.7 λ_n	Pr = 0.7 C_n	Pr = 1000 λ_n	Pr = 1000 C_n
9.37	42945	1	15.31560	-1.939132	7.568563	-42.38570	0.798245	-705.0760
		2	36.69157	-1.815440	21.98638	-11.30336	22.25825	- 1.270078
		3	58.83514	-1.729585	37.53048	- 7.236891	40.00402	- 0.783866
		4	81.07431	-1.691031	52.42856	- 5.612073	57.06527	- 0.722132
		5	103.4552	-1.659917	66.86289	- 4.736754	73.52361	- 0.882977
		6	125.9207	-1.623360	81.28564	- 4.224132	89.67696	- 1.411074
		7	148.4192	-1.589611	95.83479	- 3.801155	105.51222	- 2.910468
	80016	1	16.13696	-2.176337	9.596857	-68.56517	1.046148	-1211.604
		2	38.45544	-1.942557	28.54705	-16.83746	28.49637	- 2.177536
		3	61.84821	-1.810976	48.76199	-10.77944	51.09333	- 1.198011
		4	85.23766	-1.764113	68.12504	- 8.326993	72.87622	- 0.906773
		5	108.6938	-1.740480	86.87617	- 7.015186	94.00505	- 0.837965
		6	132.2360	-1.721529	105.5727	- 6.287613	114.9449	- 0.915241
		7	155.8436	-1.703650	124.4018	- 5.711760	135.9401	- 1.136126
	157789	1	17.92158	-2.753387	12.50075	-116.9076	1.410559	-2201.778
		2	42.54364	-2.233665	38.19248	- 26.30077	37.36503	- 4.079571
		3	68.81453	-2.004007	65.28569	- 16.85143	66.85567	- 2.119952
		4	94.85010	-1.929800	91.18638	- 12.98980	95.29813	- 1.453833
		5	120.8137	-1.900982	116.2351	- 10.90787	122.9088	- 1.170224
		6	146.8957	-1.888802	141.2041	- 9.759193	150.3180	- 1.065081
		7	173.0960	-1.875413	166.3813	- 8.863960	177.9061	- 1.045427
	231996	1	19.54425	-3.347630	14.57425	-159.3378	1.676155	-3108.772
		2	46.45371	-2.502758	45.24382	- 34.09554	43.95141	- 5.844285
		3	75.45973	-2.184107	77.37047	- 21.83574	78.39197	- 3.043570
		4	104.0000	-2.084261	108.0571	- 16.80992	111.6181	- 2.021642
		5	132.3402	-2.049520	137.7106	- 14.09673	143.9228	- 1.557139
		6	160.8301	-2.041556	167.2537	- 12.60549	176.0319	- 1.349933
		7	189.4915	-2.029360	197.0583	- 11.44853	208.3679	- 1.248994

Table 4 Eigenvalues and constants for Pr = 0.7

b	Re	n	INNER WALL HEATED		OUTER WALL HEATED	
			λ_n	C_n	λ_n	C_n
1.05	10678	1	2.944155	- 10.46659	3.007009	- 11.76624
		2	10.05278	- 2.262412	10.05470	- 4.751257
		3	18.20843	- 2.247138	18.21802	- 2.313879
		4	25.67910	- 1.230020	25.68116	- 1.893671
		5	33.03450	- 3.018416	33.04621	- 1.714579
		6	40.04762	- 1.548232	40.05076	- 1.810220
		7	46.96938	- 5.445581	46.98126	- 1.929662
	96652	1	7.240922	- 68.82003	7.405079	- 72.15285
		2	25.46487	- 19.00285	25.46372	- 25.61173
		3	46.58816	- 10.98803	46.60933	- 12.01722
		4	65.59459	- 6.927203	65.59188	- 9.604351
		5	84.81447	- 7.275717	84.82822	- 7.967276
		6	103.5769	- 5.018644	103.5708	- 7.146268
		7	122.5735	- 5.810152	122.5903	- 6.304283
	212171	1	9.862065	-128.5516	10.08330	-134.5867
		2	35.41606	- 33.41325	35.41048	- 43.94293
		3	65.17389	- 18.58598	65.20776	- 20.23612
		4	91.75025	- 11.98334	91.74477	- 16.15252
		5	118.6343	- 12.28446	118.6531	- 13.42941
		6	144.8566	- 8.646678	144.8465	- 11.98347
		7	171.4395	- 9.740605	171.4569	- 10.68851
50	9088	1	1.110350	- 37.68120	4.257759	- 12.27092
		2	11.34677	- 1.371425	12.34525	- 5.304203
		3	19.59091	- 2.346650	20.71190	- 2.287193
		4	27.52957	- 0.624688	28.89519	- 2.050347
		5	35.14898	- 3.726741	36.72904	- 2.108870
		6	42.64025	- 3.461220	44.06288	- 2.255732
		7	50.19726	- 18.52956	50.95560	- 2.302626
	89645	1	2.286086	-165.9140	10.69343	- 76.72818
		2	31.45926	- 3.990712	34.0658	- 16.95477
		3	54.01127	- 4.599720	56.59003	- 11.58012
		4	76.20086	- 2.083965	78.69905	- 9.157637
		5	98.03957	- 4.282116	100.5468	- 7.714342
		6	119.5247	- 1.878516	121.5715	- 6.768916
		7	140.7451	- 5.265772	142.5174	- 6.120657
	222160	1	3.120907	-311.5185	15.29109	-162.5556
		2	47.20071	- 6.316225	50.73081	- 31.41073
		3	80.86743	- 7.156884	84.50112	- 21.51259
		4	113.9925	- 3.389476	117.5294	- 17.02338
		5	146.5960	- 6.931484	149.8517	- 14.29809
		6	178.6144	- 3.169523	181.4380	- 12.46519
		7	210.1332	- 9.192922	212.4908	- 11.22363

The fully developed Nusselt numbers for the inner and outer walls are shown in Figs. 3 and 4, respectively. These may be obtained by evaluating equations (11a) and (11b) for large values of x^+ or by taking the approximation that only the first term need be considered. Thus the fully developed Nusselt Numbers are

$$\mathrm{Nu}_i = 2\ \mathrm{Pr}\ (b + 1)\lambda_1^2 \tag{17}$$

and

$$\mathrm{Nu}_o = 2\ \mathrm{Pr}\ (b + 1)\lambda_1^2/b \tag{18}$$

It may be noted in Fig. 4 that the results for Nu_o for $b = 50$ and $b = 9.37$ are indistinguishable as are the results for $b = 2.88$ and $b = 1.05$. As is to be expected there is a much greater radius ratio effect on Nu_i than on Nu_o.

Fig. 5 shows the variation of Nu_i and Nu_o in the thermal entrance region for $b = 5.625$ with Re = 30,200 and 125300. Similar results may be obtained for the other radius ratios from equations (11).

Discussion and Comparison With Experiment

The authors are not aware of any experimental results for annuli in the literature in which the boundary conditions are the same as the present analysis. Some results for a uniform heat flux have been given by reference [3] and Quarmby [9]. The present analysis may only be directly compared for $b = 50$ with the experimental results of Boelter, et al. [10], for a steam-heated circular tube with air flowing. Fig. 4 shows the good agreement between the results of Boelter, et al., for the fully developed case and the calculated values of Nu_o for $b = 50$.

There is also very good agreement in the entrance region, where a comparison may be made with the results for $b = 9.37$ which, as mentioned, are indistinguishable from those for $b = 50$. This is shown in Fig. 6.

A further comparison of the analysis with experiment may be made, which also illustrates the use of the entrance region solution to provide results for cases in which the wall temperature has an arbitrary axial variation. If the wall temperature varies linearly with x, i.e., $t = Ax$ then by the principle of superposition it may be shown that

$$\mathrm{Nu}_i = 2\ \mathrm{Pr}\ (b + 1)\frac{\sum_1^\infty \frac{C_n}{8\lambda_n^2}\left[1 - \exp\left(-\frac{8\lambda_n^2}{\mathrm{Re}}x^+\right)\right]}{\sum_1^\infty \frac{C_n}{8\lambda_n^4}\left[1 - \exp\left(-\frac{8\lambda_n^2}{\mathrm{Re}}x^+\right)\right]} \tag{19}$$

$$\mathrm{Nu}_o = 2\ \mathrm{Pr}\ \frac{(b + 1)}{b}\frac{\sum_1^\infty \frac{C_n}{8\lambda_n^2}\left[1 - \exp\left(-\frac{8\lambda_n^2}{\mathrm{Re}}x^+\right)\right]}{\sum_1^\infty \frac{C_n}{8\lambda_n^4}\left[1 - \exp\left(-\frac{8\lambda_n^2}{\mathrm{Re}}x^+\right)\right]} \tag{20}$$

These expressions reduce correctly to the parallel plate channel results given by reference [2] if b is unity.

The boundary condition of linear rise in wall temperature is exactly that of the fully developed situation with a uniform wall heat flux. Accordingly, equation (19) for Nu_i for large x^+ may be compared with the uniform wall-heat-flux experimental results of references [3, 9]. This is shown in Fig. 7. The agreement is quite satisfactory. Also Nu_o calculated from equation (20) for $b = 50$ may be compared with results for a uniformly heated circular tube and this is shown in Fig. (8) where a comparison is made with the results of Deissler [7] and reference [3]. The two results for $b = 1.05$ from equations (19) and (20) are indistinguishable and either may be compared with the experimental results for Barrow [11] for a parallel plate channel, Fig. 8. There is good agreement between the solution for a linear rise in wall temperature and experiment for uniform heat flux in both Figs. 7 and 8. Also it may be noted that the fully developed Nusselt numbers for a linear rise in wall temperature or, equivalently, for a uniform wall heat flux are slightly greater than those for a constant wall temperature. This is in agreement with previous calculations in the literature for the circular tube and parallel plate channel.

Conclusion

There is good agreement between the predictions of the analysis and the experimental evidence. This is true both for a direct comparison with experimental results for a plain tube having a constant wall temperature and also for an indirect comparison

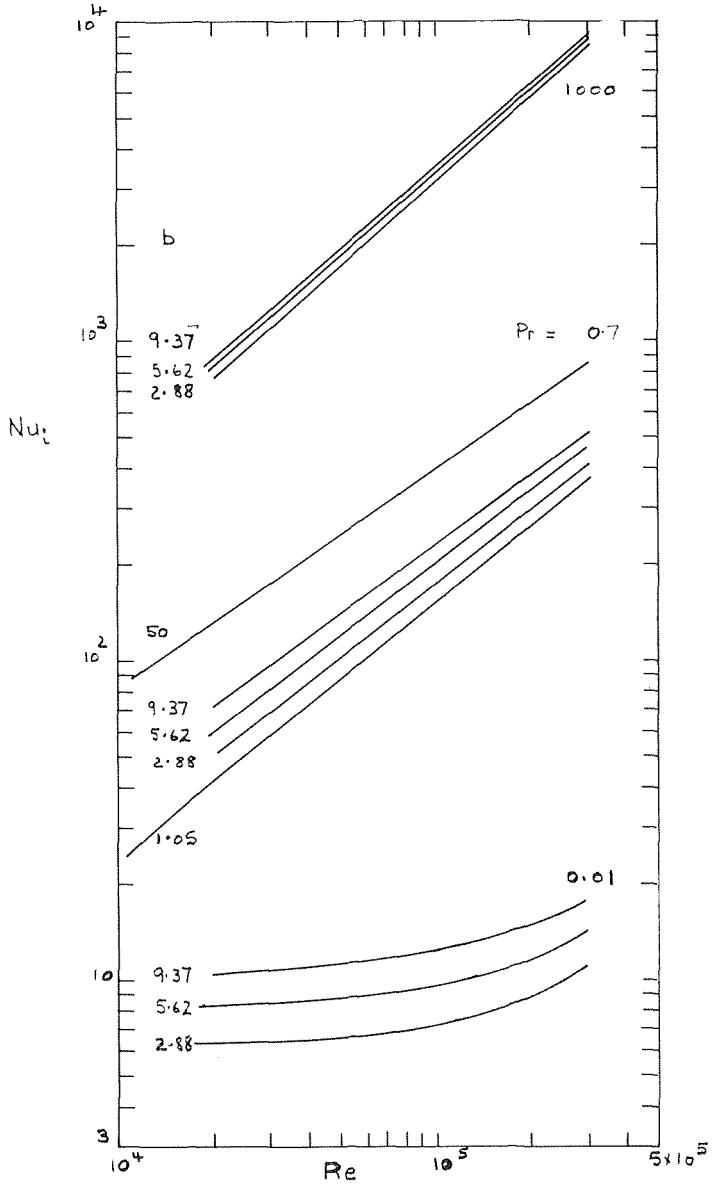

Fig. 3 Fully developed Nusselt numbers for heating on the inner wall

between an extension of the analysis for annuli to the case of linear wall temperature rise and experiments for a uniform wall heat flux. The good agreement indicates that the descriptions of the velocity profile and eddy diffusivities of heat and momentum employed are accurate.

The results show that the radius-ratio effect on the Nusselt number is much less with the outer wall heated than with the inner wall heated. Also the constant wall temperature boundary condition gives lower Nusselt numbers than with uniform heat flux. Both these effects hold true over all the range of radius ratio Reynolds number and Prandtl number investigated.

References

1 Sleicher, C. A., and Tribus, M., "Heat Transfer in a Pipe With Turbulent Flow and Arbitrary Wall Temperature Distribution," Heat Transfer and Fluid Mechanics Institute, Stanford, 1956, pp. 59–78.

2 Hatton, A. P., and Quarmby, A., "The Effect of Axially Varying and Unsymmetrical Boundary Conditions on Heat Transfer With Turbulent Flow Between Parallel Plates," *International Journal of Heat and Mass Transfer*, Vol. 6, 1963, pp. 903–914.

3 Leung, E. Y., Kays, W. M., and Reynolds, W. C., "Heat Transfer and Turbulent Flow in Concentric and Eccentric Annuli With Constant and Variable Heat Flux," Engineering Report, AHT 4, Stanford University, 1962.

4 Lee, Y., and Barrow, H., "Turbulent Flow and Heat Transfer in Concentric Annuli," *Proceedings of the Institute of Mechanical Engineers*, Vol. 3, 1963, p. 178.

5 Quarmby, A., "An Experimental Study of Turbulent Flow Through Concentric Annuli," *Internal Journal of Mechanical Science*, Vol. 9, 1967, p. 205.

6 Quarmby, A., "An Analysis of Turbulent Flow in Concentric Annuli," *Applied Scientific Research*, Vol. 19, 1968, p. 250.

7 Deissler, R. G., "Analysis of Turbulent Heat Transfer, Mass Transfer, and Fluid Friction in Smooth Tubes at High Prandtl and Schmidt Numbers," NACA Report 1210, 1955.

8 Jenkins, R., "Variation of Eddy Conductivity With Prandtl Modulus and Its Use in Prediction of Turbulent Heat Transfer Coefficients," Heat Transfer and Fluid Mechanics Institute, Stanford, Vol. 147, 1951.

9 Quarmby, A., "Some Measurements of Turbulent Heat Transfer in the Thermal Entrance Region of Concentric Annuli," *International Journal of Heat and Mass Transfer*, Vol. 10, 1967, pp. 267–276.

10 Boelter, L. M. K., Young, G., and Iverson, H. W., "An Investigation of Aircraft Heaters—Distribution of Heat Transfer Rate in the Entrance Section of a Circular Tube," NACA Report 1451, 1948.

11 Barrow, H., "An Analytical and Experimental Study of Turbulent Gas Flow Between Two Smooth Parallel Walls With Unequal

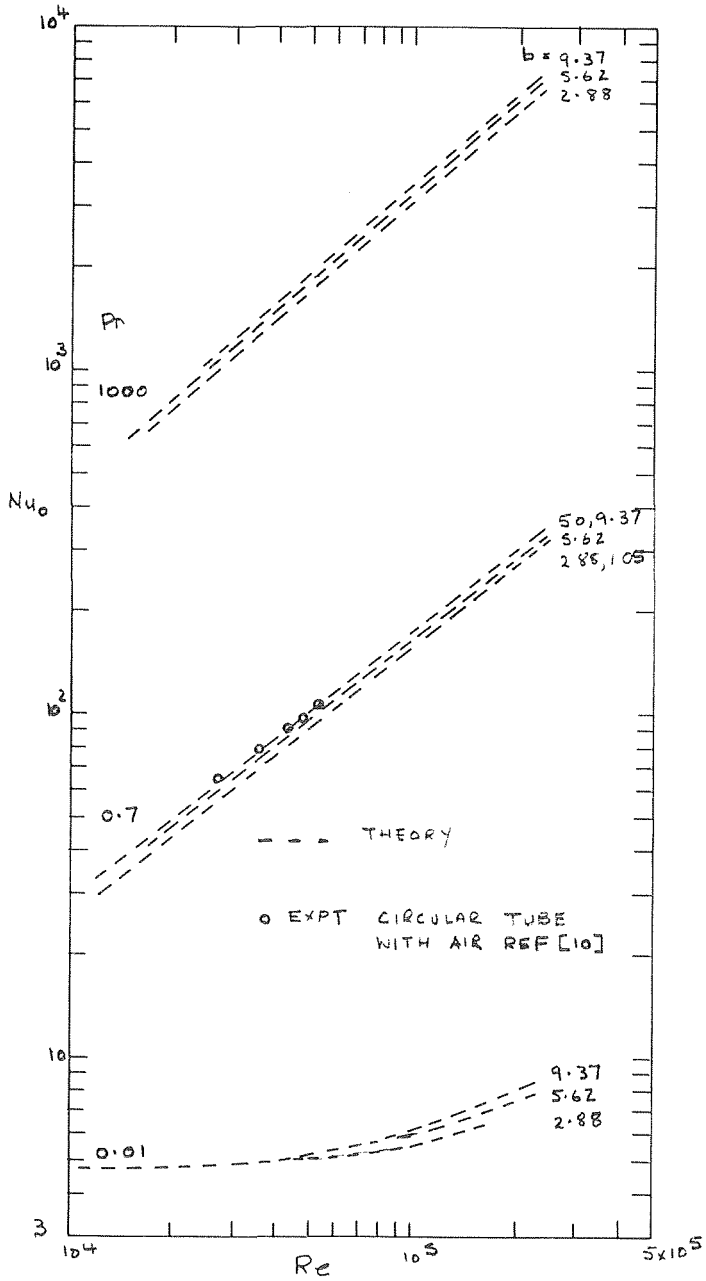

Fig. 4 Fully developed Nusselt numbers for heating on the outer wall

Heat Fluxes," *International Journal of Heat and Mass Transfer*, Vol. 1, 1962, p. 306.

APPENDIX

The turbulent velocity profile in the concentric annulus may be described by the following equations. These are developed from von Karman's similarity hypothesis for the center region of the annulus. Deissler's [7] expression for ϵ_m/ν, equation (12), is used to deduce the velocity profile in the sublayer region which extends up to y_l^+.

In the inner sublayer region for $0 < y_i^+ < y_{li}^+$

$$\frac{du_i^+}{dy_i^+} = \frac{\tau/\tau_i}{1 + n^2 u_i^+ y_i^+ [1 - \exp(-n^2 u_i^+ y_i^+)]} \tag{21}$$

with $u_i^+ = 0$ at $y_i^+ = 0$, while for $y_{li}^+ < y_i^+ < y_{mi}^+$

$$\frac{d^2u_i^+}{dy_i^{+2}} = \frac{-K(du_i^+/dy_i^+)^2}{\left[\frac{\tau}{\tau_i} - \frac{du_i^+}{dy_i^+}\right]^{1/2}} \tag{22}$$

with the boundary condition at y_{li}^+ that both u_i^+ and $\frac{du_i^+}{dy_i^+}$ are taken equal to the corresponding values given there by the sublayer profile.

For the outer profile, for $0 < y_o^+ < y_{lo}^+$

$$\frac{du_o^+}{dy_o^+} = \frac{\tau/\tau_o}{1 + n^2 u_o^+ y_o^+ [1 - \exp(-n^2 u_o^+ y_o^+)]} \tag{23}$$

and for $y_{lo}^+ < y_o^+ < y_{mo}^+$

$$\frac{d^2u_o^+}{dy_o^{+2}} = \frac{-K(du_o^+/dy_o^+)^2}{\left[\frac{\tau}{\tau_o} - \frac{du_o^+}{dy_o^+}\right]^{1/2}} \tag{24}$$

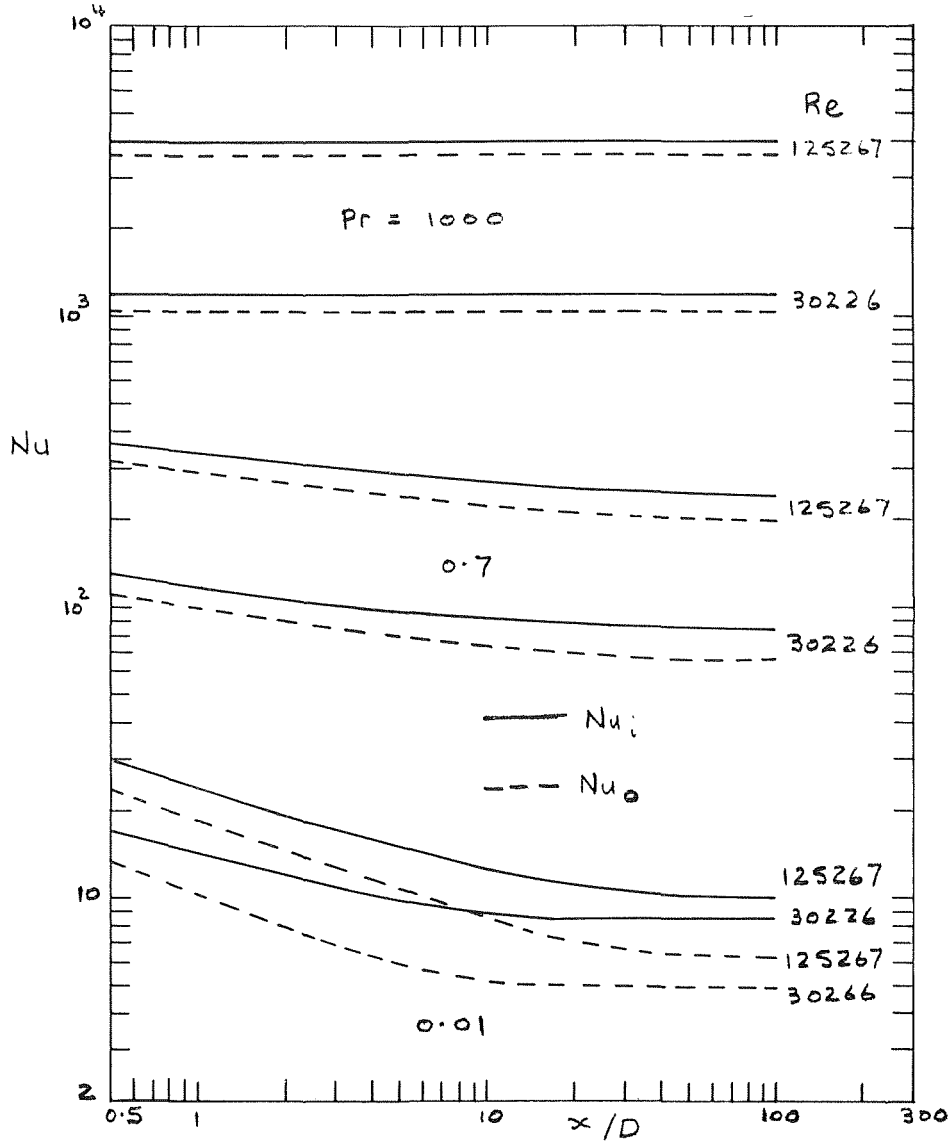

Fig. 5 Entrance region heat transfer $b = 5.625$

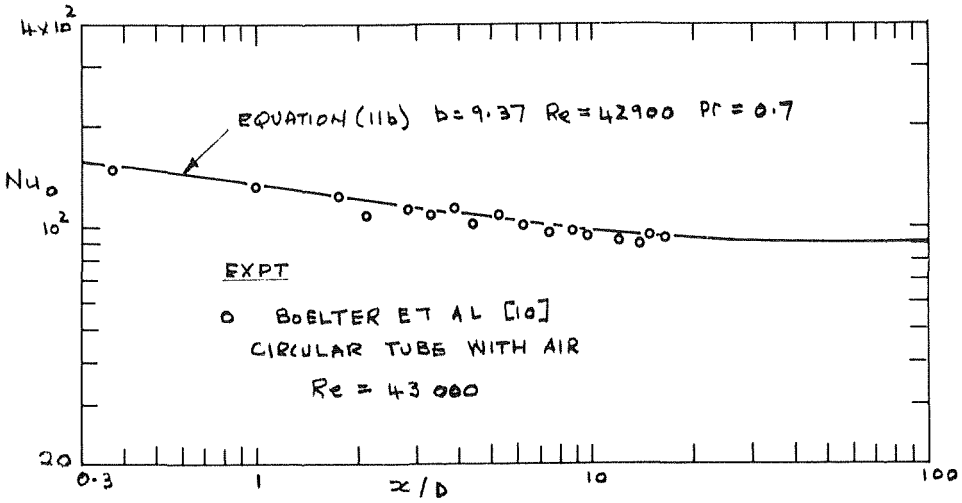

Fig. 6 Entrance region heat transfer with outer wall heated, $b = 9.37$

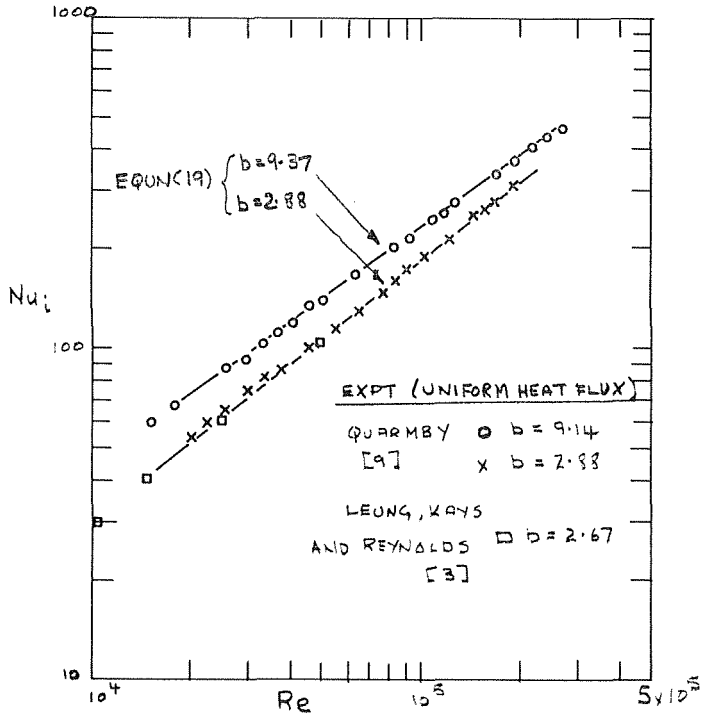

Fig. 7 Fully developed heat transfer with a linear rise of inner wall temperature, $b = 2.88$ and 9.37

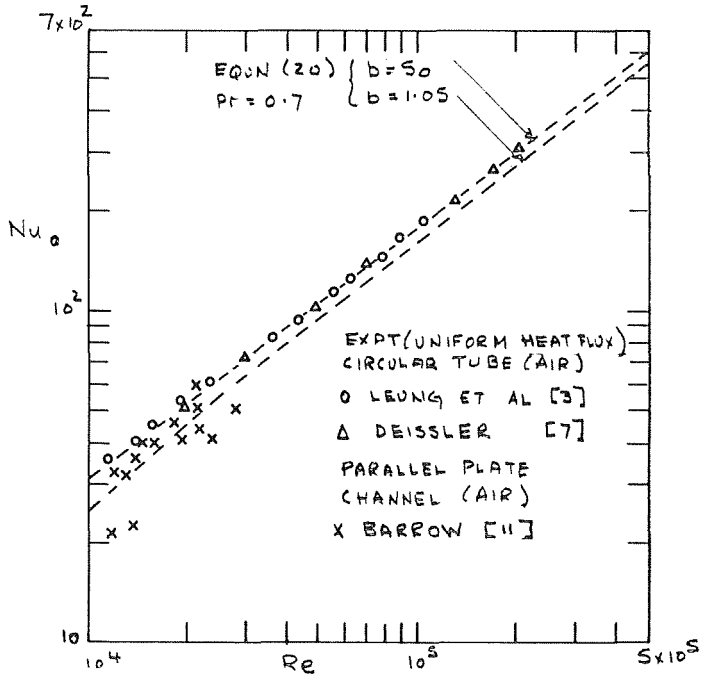

Fig. 8 Fully developed heat transfer with a linear rise of outer wall temperature, $b = 50$ and 1.05

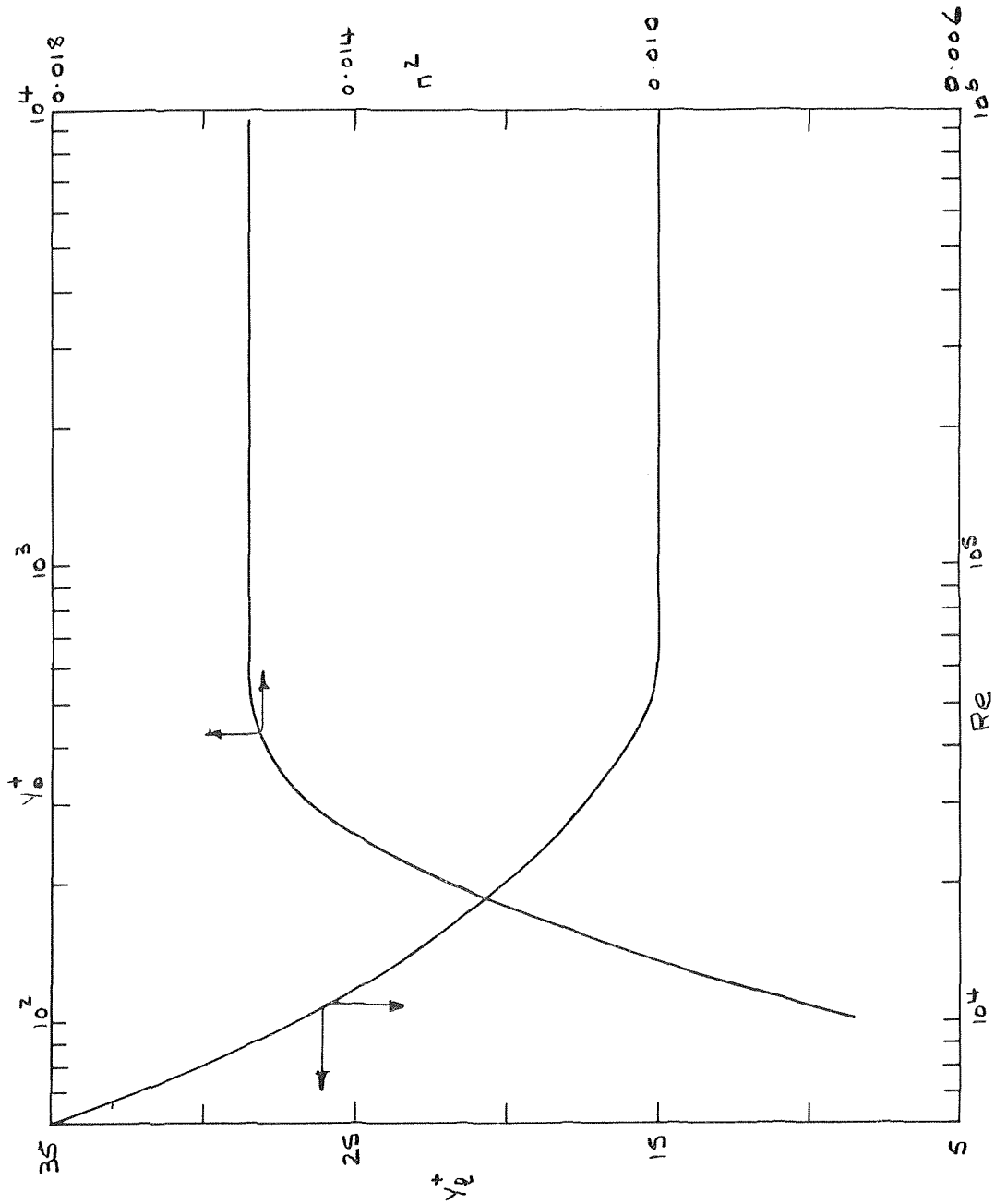

Fig. 9 Relation between the parameters of the turbulent velocity profile

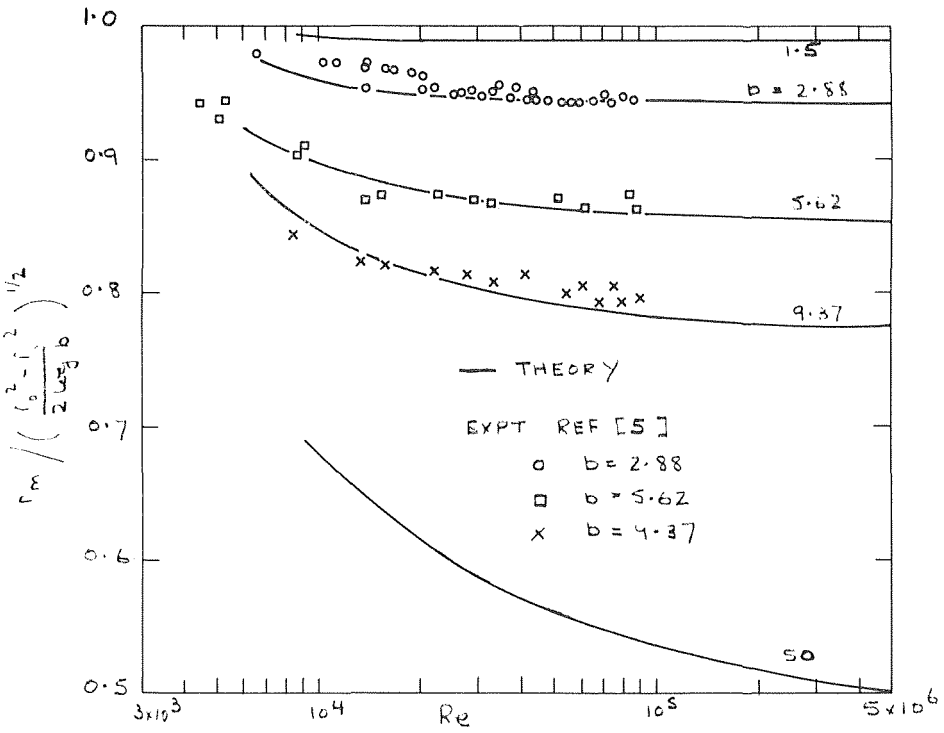

Fig. 10 Comparison between theory and experiment for the radius of maximum velocity

The boundary conditions on equations (23) and (24) are similar to those on equations (21) and (22).

The development of the foregoing equations is given in reference [6] where it is shown that the index n^2 and the sublayer thickness $y_1{}^+$ may be taken as functions of Re and $y_{mo}{}^+$. This is shown in Fig. 9. The von Karman constant K is taken as 0.36. As an example of the validity of equations (21)–(24), Fig. 10 compares the value for the radius of maximum velocity which they predict with the experimental measurements in reference [5].

If $r_o{}^+$ is chosen as the basic parameter, the other parameters $y_{mo}{}^+$, $y_{mi}{}^+$, and $r_i{}^+$ may be expressed in terms of $r_0{}^+$ by the following

$$y_{mo}{}^+ = \left(1 - \frac{a}{b}\right) r_o{}^+ \tag{25a}$$

$$y_{mi}{}^+ = \frac{a-1}{b} \frac{b(a^2-1)}{b^2-a^2} r_o{}^+ \tag{25b}$$

$$r_i{}^+ = \frac{1}{b} \frac{b(a^2-1)}{b^2-a^2} r_o{}^+ \tag{25c}$$

J. J. LORENZ
Graduate Student.

B. B. MIKIC
Associate Professor.

Massachusetts Institute of Technology, Cambridge, Mass.

The Effect of Thermocapillary Flow on Heat Transfer in Dropwise Condensation

The effect of fluid flow induced by surface tension forces on heat transfer through a drop was considered. The model is a hemispherical liquid drop growing on a flat isothermal surface. The solution was obtained by finite-difference techniques for different values of the Marangoni number (Nm) associated with surface tension forces and the Biot number (Bi) associated with heat transfer at the liquid-vapor interface. The ranges of parameters covered by this investigation include the regimes of most practical interest for water. The results show that the contribution of internal circulation in the drops to the increase of heat transfer in dropwise condensation is insignificant.

Introduction

When a saturated vapor is in contact with a surface whose temperature is below the saturation temperature then dropwise condensation will occur on the surface, i.e., liquid droplets will form, provided that the liquid does not wet the surface.

Within the past few years it has been shown that dropwise condensation is a nucleation phenomenon [1][1] and that all heat goes through growing droplets [2]. Further analysis, based on the model which neglects the effects of liquid circulation inside droplets, shows that only droplets of very small radius are active and that the relatively large drops contribute very little to the overall heat transfer.

Trefethen [3] suggested that larger drops could also be important for heat transfer if there was a significant internal circulation within the drops caused by surface tension forces resulting from nonuniform temperature gradients (thermocapillary flow). With a simple model he predicted an increase due to thermocapillary flow of approximately 170 times that predicted by the conduction solution alone. He observed circulation in larger drops but could not take any measurements.

The existence of flow induced by surface tension was first reported by Marangoni. Scriven and Sterling [4] reviewed the literature on "Marangoni Effects" up to 1960. Trefethen [5, 6] observed the motion of bubbles along a heated wire in acetone, and the motion of ice on a warm metal plate. Boys [7], Maxwell [8], Block [9], and others mentioned other surface tension-induced flow phenomena.

Even though thermocapillary flow has been known to occur in many physical processes, reported measurements of the dynamics of the flow are very rare. Furthermore, measurements of increases in heat transfer due to this type of flow have not been obtained. There were claims, however, that it may be important, as we mentioned earlier, in dropwise condensation [3] as well as in nucleate boiling [10]. No conclusive evidence substantiated the claims.

The purpose of this work is to determine the effects of thermocapillary flow on heat transfer in dropwise condensation by simultaneously solving the momentum and energy equations with an appropriate set of boundary conditions. A complete solution to the problem which goes as far as predicting actual heat tranfer rates through each drop is not attempted. Instead, the solution presented is primarily concerned with showing the percent increase in heat transfer over the conduction solution. In this respect the problem is modeled so that the effect of thermocapil-

[1] Numbers in brackets designate References at end of paper.

Contributed by the Heat Transfer Division of The American Society of Mechanical Engineers and presented at the ASME-AIChE Heat Transfer Conference, Minneapolis, Minn., August 3–6, 1969. Manuscript received by the Heat Transfer Division, November 12, 1968; revised manuscript received, February 24, 1969. Paper No. 69-HT-40.

Nomenclature

a = drop radius

$\mathrm{Bi} = \dfrac{h_e a}{k}$ (Biot number)

$\mathrm{Bi}' = \dfrac{ha}{k}$ (Biot number)

c = specific heat of the liquid

h = liquid-vapor interface heat transfer coefficient

$h_{\mathrm{avg}} = \dfrac{\int_0^a hr2\pi r dr}{\pi a^2}$, overall heat transfer coefficient

h_e = modified liquid-vapor interface heat transfer coefficient

h_r = local heat transfer coefficient along drop base, $\left[k \dfrac{\partial T}{\partial z}\Big/(T_s - T_0)\right]$

k = thermal conductivity of the liquid

$\mathrm{Nm} = -\dfrac{(T_s - T_0)a\beta}{\mu\alpha}$, the Marangoni number

$\mathrm{Nu}_r = \dfrac{h_r a}{k}$, local Nusselt number along drop base

$\mathrm{N}\mu_{\mathrm{avg}} = \dfrac{h_{\mathrm{avg}}\, a}{k}$, average Nusselt number

P = pressure

$\mathrm{Pr} = \dfrac{c\mu}{k}$, the Prandtl number

R, ϕ, θ = spherical coordinate system

r, z, θ = cylindrical coordinate system

r', z' = dimensionless coordinates

T = temperature

T_0 = temperature of drop base

T_s = temperature of vapor

V = velocity

$V' = \dfrac{Va}{\alpha}$, dimensionless velocity

α = thermal diffusivity of the liquid

$\beta = \dfrac{d\sigma}{dT}$, derivative of surface tension with respect to temperature

σ = surface tension

μ = absolute viscosity of the liquid

ω = vorticity

ρ = density of the liquid

τ = shear stress

$\theta = \dfrac{T - T_0}{T_s - T_0}$, dimensionless temperature

lary flow is somewhat overestimated and results regarding increases in heat transfer provide an upper bound.

Problem Statement

Model. A hemispherical liquid drop on a flat isothermal surface at T_0 is considered to be growing by condensation of saturated vapor at temperature T_s. The growth is considered to be quasi steady. There is a finite heat transfer coefficient, h, between vapor and liquid-vapor interface. Viscosity of vapor is negligible compared with viscosity of liquid. Viscosity, thermal conductivity, and density of liquid are constant. Viscous terms are negligible in the energy equation.

The solution domain is given in Fig. 1. The problem, as stated earlier, is specified by the following relations:

Continuity Equation

$$\nabla \cdot \mathbf{V} = 0 \tag{1}$$

Momentum Fquations

$$\rho \frac{D\mathbf{V}}{Dt} = -\nabla P + \mu \nabla^2 \mathbf{V} + \mathbf{F} \tag{2}$$

Energy Equation

$$\rho C \frac{DT}{Dt} = k \nabla^2 T \tag{3}$$

Referring to Fig. 1, the boundary conditions written in cylindrical coordinates are as follows:

At $z = 0$, $0 < r < a$,

$$V_r = 0,\ V_z = 0,\quad T = T_0, \tag{4}$$

At $r = 0$ $0 < z < a$,

$$V_r = 0,\quad \frac{\partial V_z}{\partial r} = 0,\quad \frac{\partial T}{\partial r} = 0 \tag{5}$$

At $z = \sqrt{a^2 - r^2}$, $0 < r < a$

$$V_r \cdot r + V_z \cdot z = 0$$

$$-k\left(\frac{\partial T}{\partial r}\frac{r}{a} + \frac{\partial T}{\partial z}\frac{z}{a}\right) = h(T - T_s)$$

$$\frac{\beta}{a}\left(\frac{\partial T}{\partial r}\cdot z - \frac{\partial T}{\partial z} r\right) = \mu\left[\frac{r}{a}\frac{\partial}{\partial r}\left(V_r \frac{z}{a} - V_z \frac{r}{a}\right) + \frac{z}{a}\frac{\partial}{\partial z}\left(V_r \frac{z}{a} - V_z \frac{r}{a}\right) - \frac{1}{a}\left(V_r \frac{z}{a} - V_z \frac{r}{a}\right)\right] \tag{6}$$

The symbols used in the foregoing relations are introduced in the Nomenclature. The boundary conditions at $z = 0$ and $r = 0$ are obvious. At the boundary, $z = \sqrt{a^2 - r^2}$ (relations (6)), the first equation states the condition of zero liquid velocity normal to the interface; the second relation, written in spherical coordinates, states that: $k\dfrac{\partial T}{\partial R} = -h(T - T_s)$. The last one states that the change in surface tension along the boundary must be balanced by shear force. In spherical coordinate this condition is:

At $R = a$

$$\tau_{R\phi} = \frac{\partial \sigma}{a \partial \phi} = \frac{1}{a}\frac{d\sigma}{dT}\frac{\partial T}{\partial \phi} \equiv \frac{\beta}{a}\frac{\partial T}{\partial \phi}$$

To put the problem in a form which is more manageable, the following dimensionless qualities are defined:

$$\theta \equiv \frac{T - T_0}{T_s - T_0};\ V_r' \equiv \frac{V_r a}{\alpha};\ V_z' \equiv \frac{V_z a}{\alpha};\ r' \equiv \frac{r}{a};\ z' \equiv \frac{z}{a}$$

Furthermore, we introduce a stream function ψ defined as follows:

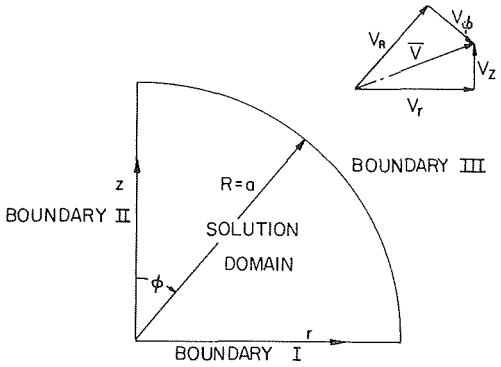

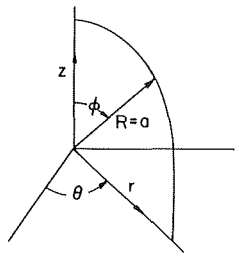

Fig. 1 Solution domain

$$V_r' = -\frac{1}{r'}\frac{\partial \psi}{\partial z'} \text{ and } V_z' = \frac{1}{r'}\frac{\partial \psi}{\partial r'}$$

By taking the curl of the momentum equation (2), and making use of some standard vector relations, the following was obtained:

$$\frac{\partial}{\partial z'}\left(\frac{\omega}{r'}\frac{\partial \psi}{\partial r'}\right) + \frac{\partial}{\partial r'}\left(-\frac{\omega}{r'}\frac{\partial \psi}{\partial z'}\right) = P_r\left\{\frac{\partial^2 \omega}{\partial z'^2} + \frac{\partial}{\partial r'}\left[\frac{1}{r'}\frac{\partial (r'\omega)}{\partial r'}\right]\right\} \tag{7}$$

where

$$-\omega = \frac{\partial}{\partial z'}\left(\frac{1}{r'}\frac{\partial \psi}{\partial z'}\right) + \frac{\partial}{\partial r'}\left(\frac{1}{r'}\frac{\partial \psi}{\partial r'}\right) \tag{8}$$

The dimensionless energy equation is

$$\frac{\partial \psi}{\partial r'}\frac{\partial \theta}{\partial z'} - \frac{\partial \psi}{\partial z'}\frac{\partial \theta}{\partial r'} = \frac{\partial}{\partial r'}\left(r'\frac{\partial \theta}{\partial r'}\right) + r'\frac{\partial^2 \theta}{\partial z'^2} \tag{9}$$

Boundary conditions corresponding to the new variables are:

At $z' = 0$, $0 < r' < 1$,

$$\psi = 0;\ \frac{\partial \psi}{\partial z'} = 0;\ \theta = 0 \tag{10}$$

At $r' = 0$, $0 < z' < 1$,

$$\psi = 0;\ \omega = 0;\ \frac{\partial \theta}{\partial r'} = 0 \tag{11}$$

At $z' = \sqrt{1 - (r')^2}$, $0 < r' < 1$,

$$\psi = 0;\ \frac{\partial \theta}{\partial r'} r' + \frac{\partial \theta}{\partial z'} z' = -\mathrm{Bi}'(\theta - 1)$$

$$\omega + \frac{2}{r'}\left(\frac{\partial \psi}{\partial r'} r' + \frac{\partial \psi}{\partial z'} z'\right) = -\mathrm{Nm}\left(\frac{\partial \theta}{\partial r'} z' - \frac{\partial \theta}{\partial z'} r'\right) \tag{12}$$

where

$$\mathrm{Nm} \equiv -\frac{(T_s - T_0)a\beta}{\mu\alpha} \text{ and } \mathrm{Bi}' \equiv \frac{ha}{k}$$

Equations (7)–(9) with boundary conditions (10)–(12) were

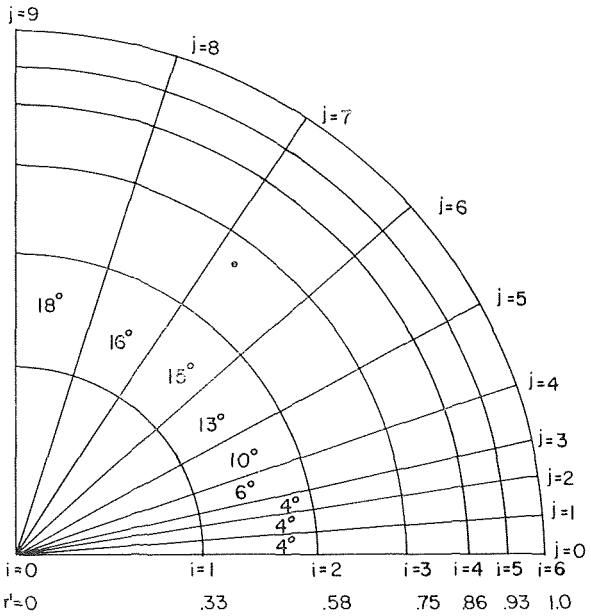

Fig. 2 Finite-difference grid network

solved numerically using a computer program called EPS [11] which solves equilibrium field problems in two-dimensional continua. An irregular 54-grid point network was employed as shown in Fig. 2. This grid was decided upon after several trial runs, compromising between grid refinement (accuracy) and available computer time.

The nonlinearity and coupling between velocity and temperature in the governing equations and boundary conditions was handled by iteratively solving linearized finite-difference equations. This iteration involved repeatedly solving a set of about 160 difference equations until maximum solution changes were about 1 percent of the value of the field variables. To get this convergence, a large amount of computer time was needed; therefore, only the solutions in the most important ranges were generated (Bi = 1 to 200 and Nm = 0 to 550). On the IBM 7094 computer it took about 20 min computer time to generate a solution for one given value of each dimensionless group.

In the process of generating solutions for various parameters of the system (Bi′, Nm, Pr) we found that inertia terms in the momentum equation could be neglected in the range of parameters of interest for this work. The flow then was considered as inertia-free; hence the left-hand side of equation (7) was set to be zero. In this way the only dimensionless groups left in the system are Bi′ and Nm.

An additional modification is introduced at the boundary $z' = \sqrt{1 - (r')^2}$. Since at the base the temperature was prescribed ($T = T_0$), for very large h, a discontinuity begins to develop near the drop base. This situation was difficult to handle with finite-difference equations even for a much more refined grid than the one used here. To insure that such a discontinuity would not disturb the solution for large values of h, we decided to define an h_e which decreases toward the surface of the cooling plate as shown in Table 1; (see Fig. 2).

Table 1

j	9	8	7	6	5	4	3	2	1	0
h_e/h	1	1	1	1	0.9	0.75	0.40	0.10	0.05	0.00

Consequently, instead of $\mathrm{Bi}' = \dfrac{ha}{k}$ in boundary condition (12), we have $\mathrm{Bi} = \dfrac{h_e a}{k}$. Therefore, if a run is taken at, say, Bi = 100 this will mean that Bi actually decreases from 100 to 0 as shown. The foregoing modification, as it will be shown, increases the relative significance of the thermocapillary flow.

Ranges of Parameters. As just pointed out, the range of parameters covered in this work is Bi = 1 to 200 and Nm = 0 to 550. In addition, the solution for Bi = 0 is a trivial solution of no heat flux ($h = 0$, $T = T_0$ everywhere inside the drop, no circulation is present). Also, for Bi = ∞, $h = \infty$, the liquid-vapor interface temperature is uniform (T_s) and therefore the thermocapillary driving force $\left(-\mathrm{Nm}\dfrac{d\theta}{d\phi}\right)$ is zero everywhere, implying no liquid motion.

For water, drops of small size are covered with low values of Bi and Nm. For example, a drop of 2 microns in radius, for $h = 10^5$ Btu/hr-ft² deg F will have Bi = 2, and for $T_s - T_0 = 1$ deg F, Nm = 4.5. The foregoing value for Nm corresponds to the atmospheric pressure; at lower pressures, Nm would be somewhat smaller (mainly due to the increased μ). Bi is a weak function of pressure, provided that h is specified. However, h itself is a very strong function of the system pressure. A detailed discussion of variations of h and its order of magnitude is beyond the scope of the present work. Nevertheless, we would like to mention that evaluation of the liquid-vapor interface heat transfer coefficient could be made from Shrage's relations in a simplified form (developed by several authors, see, for example, [12]), provided that one knows the evaporation or condensation coefficient. Reference [13] gives a survey of values for the condensation coefficient, experimentally obtained by different investigators. The condensation coefficient of unity will give, at atmospheric pressure, h of the order of 10^6 Btu/hr-ft² deg F. Indirect calculations of h from carefully conducted dropwise condensation experiments, in the absence of noncondensible gases in the system [14, 15], indicate that interfacial h is of the same order as one would calculate it from Shrage's relation with the condensation coefficient of unity.

The large drop size corresponds to the higher values of Bi and Nm. A water drop, for example, of radius 200 microns at, say, $h = 10^5$ Btu/hr-ft² deg F, will have Bi = 200 and at $T_s - T_0 = 1$ deg and atmospheric pressure, Nm = 480.

In the ranges of physical parameters covered in this work, the following may be concluded: for water, the range of Bi = 1 to 200 corresponds to $(a \cdot h) \approx 1 \times 10^5$ to 2×10^7 micron Btu/hr-ft² deg F, respectively; Nm = 0 to 550 corresponds to $[a \cdot (T_s - T_0)] = 0$ to 1000 microns deg F. The foregoing range of parameters covers all the cases of practical interest (drop size range) for which the conduction through drops is the limiting factor (i.e., for sufficiently high values of $a \cdot h$).

In reference [16] it has been shown that the ratio (interface resistance/conduction resistance) for any drop can be approximated (neglecting internal circulation) as $\dfrac{2k}{ha} = \dfrac{2}{\mathrm{Bi}}$. Therefore, the value of Bi ≥ 1 will cover all those drops for which conduction resistance is greater or equal to one third of the total resistance

The term conduction resistance in the foregoing refers to the thermal resistance from the surface of the drop at the liquid-vapor interface to the base of the drop (based on the average temperature difference between the interface and the base of the drop). For lower values of Bi, the interface resistance becomes a controlling factor and the presence or absence of a strong liquid motion inside a condensing drop will not significantly affect the overall resistance.

Results

For a typical choice of parameters (Bi = 100, Nm = 450), the stream function ψ is plotted in Fig. 3. The plot shows the flow pattern inside the drop. The variation in surface tension with temperature, together with temperature nonuniformity on the boundary $z' = \sqrt{1 - (r')^2}$, results in the dimensionless driving force $-\mathrm{Nm}\dfrac{d\theta}{d\phi}$, acting on the boundary, which pulls the liquid downward setting the pattern shown in the figure.

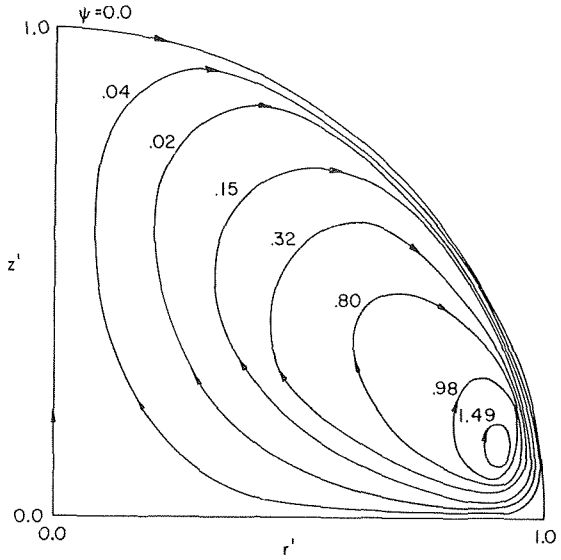

Fig. 3 Flow field inside liquid drop (Bi = 100, Nm = 450)

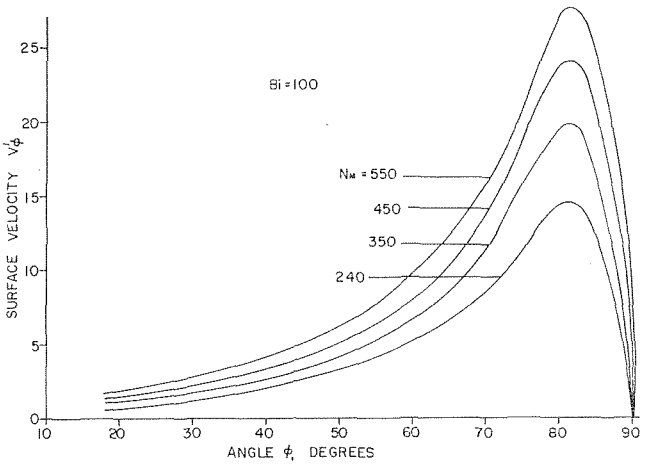

Fig. 4 Surface velocity distribution for several values of Nm

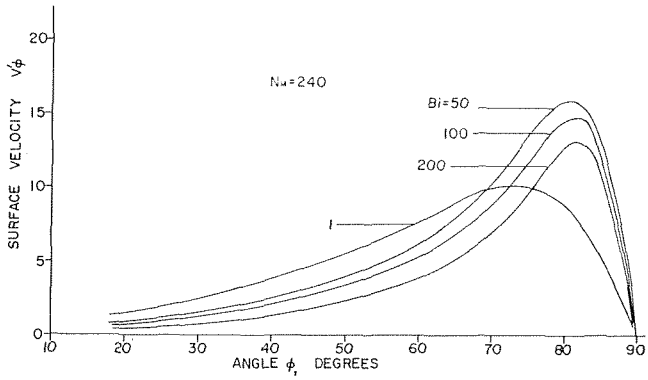

Fig. 5 Surface velocity distribution for several values of Bi

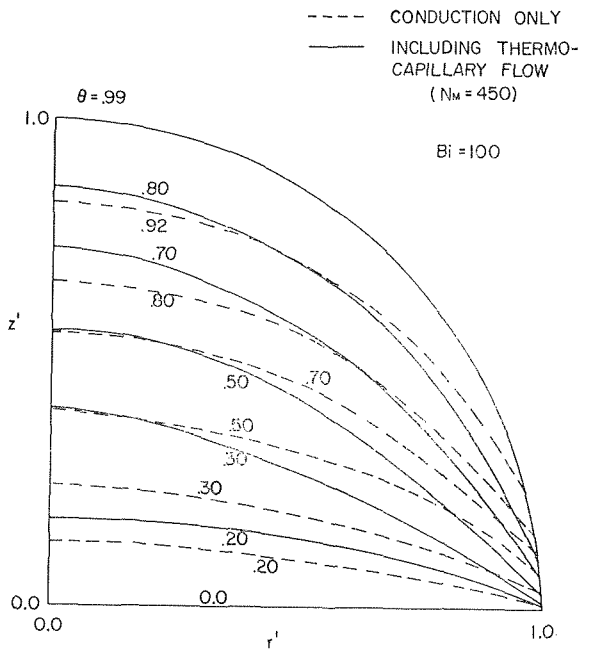

Fig. 6 Comparison of isotherms for conduction with isotherms including thermocapillary flow

Fig. 4 shows surface velocity as a function of ϕ at constant Bi for various values of Nm. The fluid velocity, as can be seen from the figure, increases to a maximum of about 82 deg (for this particular value of Bi number) and then decreases rapidly to zero at the base of the drop. Fig. 5 shows the effect of varying Bi at constant Nm. The maximum value of surface velocity increases with Bi, for Bi $<$ 50 and decreases for Bi $>$ 50. The position of the maximum moves to the higher values of ϕ with increasing Bi, indicating that most of the temperature variations at the surface are more and more concentrated near the corner for higher Bi.

The temperature field, for Bi = 100 and Nm = 450, is shown in Fig. 6. For comparison in the figure are also plotted isotherms for conduction only (Nm = 0). It can be seen from the plot that internal circulation increases the temperature gradient near the right-hand corner.

The surface temperature, as a function of ϕ is given in Fig. 7 for Bi = 100 at various Nm. The most interesting thing about the temperature profiles is the fact that temperature is almost uniform from 0 to 70 deg, which, of course, implies that over this range the thermocapillary driving force is almost zero. Only in the narrow range near the corner, where the temperature gradient is most pronounced, the driving force is significant.

In Fig. 8 the surface temperature distribution is shown for various values of Bi and Nm equal to zero. In each case the temperature gradients are largest at the wall, as can be seen from

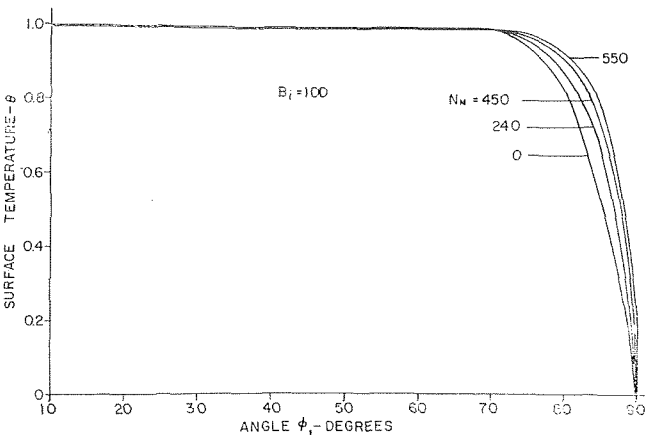

Fig. 7 Surface temperature distribution for several values of Nm

Fig. 9. For increasing Bi from 50 to 200 the local gradient at the base increases but the average gradient over the drop surface decreases. Furthermore, for Bi decreasing from 50 to 1, the temperature gradients decrease near the base and increase elsewhere.

The percentage increase of average Nusselt number (or overall

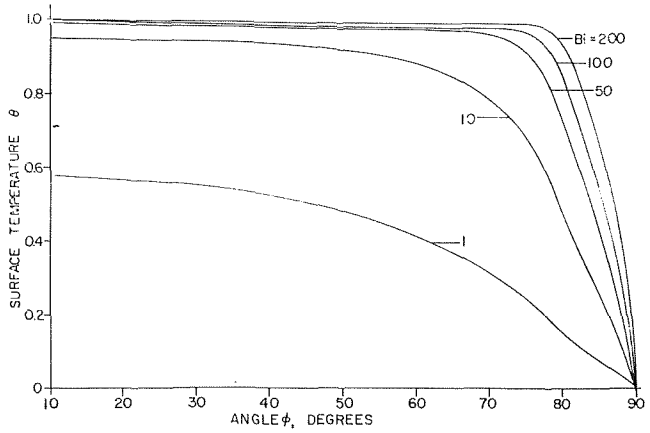

Fig. 8 Surface temperature distribution for several conduction solutions (Nm = 0)

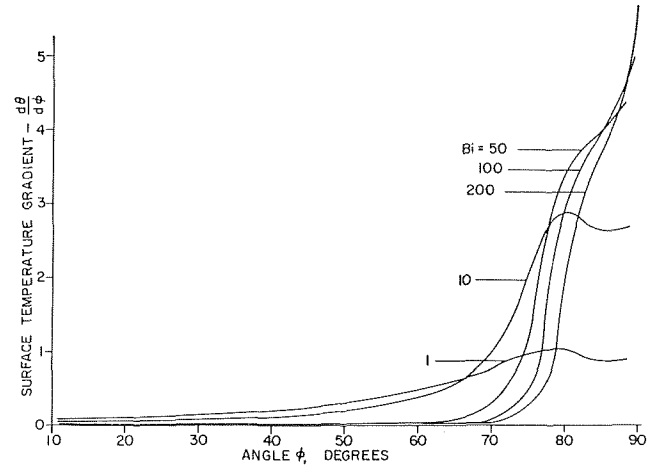

Fig. 9 Temperature gradient along drop surface

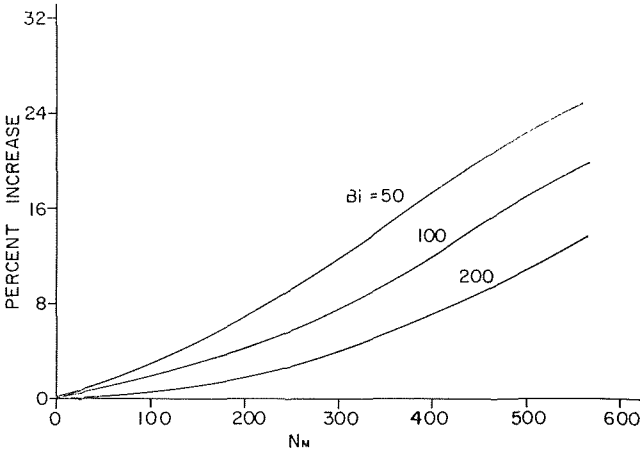

Fig. 10 Percent increase in average Nusselt number over conduction solution

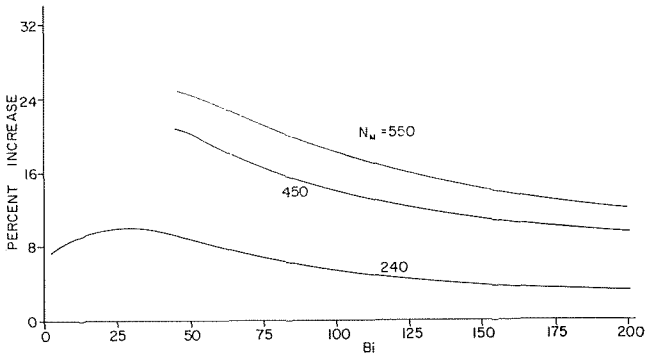

Fig. 11 Percent increase in average Nusselt number over conduction solution

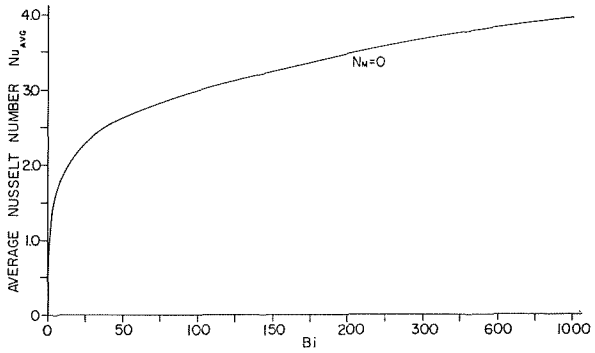

Fig. 12 Average Nusselt number over drop base for conduction only

heat transfer coefficient) as a function of Nm with Bi as a parameter is plotted in Fig. 10. The cross plot, percent increase as a function of Bi and Nm as a parameter, is shown in Fig. 11. As Nm increases at constant Bi the effect of thermocapillary convection increases. With increasing Bi (from 50 to 200) at constant Nm the percent increase in heat transfer decreases. This is due to the fact that increase in h (increase in Bi at constant Nm) in this range of Bi, makes surface temperature uniform over a larger portion of the surface reducing the average driving force $\left(-\mathrm{Nm}\,\frac{d\theta}{d\phi}\right)$ and consequently reducing the liquid circulation too. This can be easily seen and understood from Figs. 5, 8, and 9. The maximum increase in heat transfer for the range covered is only about 25 percent occurring at Bi = 50, Nm = 550. These parameters correspond to relatively large drops and very large $(T_s - T_0)$. Drops of this range do not contribute much to the heat transfer in dropwise condensation so that an increase of about 25 percent above the conduction solution is much less than required to make their contribution significant. The drop range of interest would have a radius of the order of a few microns and this could correspond to low values of Bi (approximately of the order of unity) and a value of Nm of around 5. Our calculation shows that in this range the increase in heat transfer is only a few percent. The average Nusselt number for the conduction solution is plotted against Bi in Fig. 12.

Discussion

The conclusions achieved in this work are based on the previously introduced model which somewhat deviates from the actual conditions in dropwise condensation. For this reason in the following we will discuss the effects of these deviations on the validity of our conclusions.

The drop growth is considered to be quasi steady. Since the heat capacity of the growing drop in the range of interest is small compared with heat fluxes through the drop, the transient effects are negligible on the temperature distribution. On the other hand, the quasi-steady approach neglects the inertia of condensing liquid, i.e., it is assumed that the condensate, as it condenses, will instantaneously achieve the velocity corresponding to the steady-state solution. Consequently, the velocity field as well as the overall effects of thermocapillary flow, calculated with the foregoing approach, will be somewhat overestimated.

In the momentum equations the inertial terms were neglected.

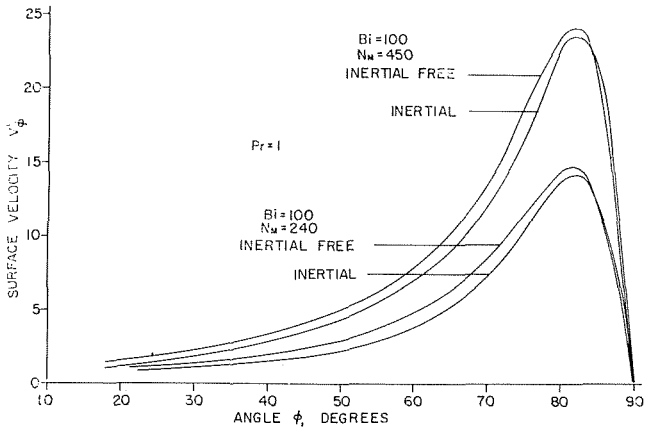

Fig. 13 Comparison of surface velocity for inertial and inertial free flow

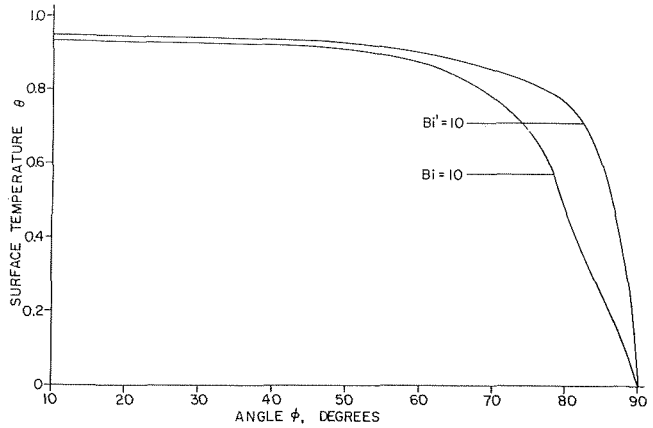

Fig. 15 Comparison of surface temperatures for constant and variable Biot number

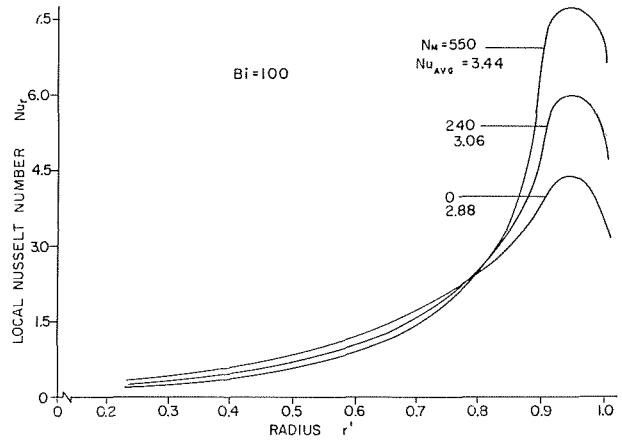

Fig. 14 Local Nusselt number along drop base

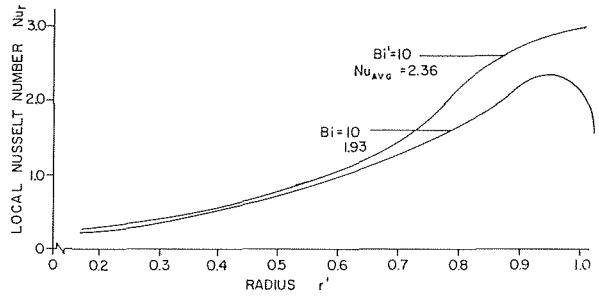

Fig. 16 Comparison of local Nusselt number along drop base for constant and variable Biot number

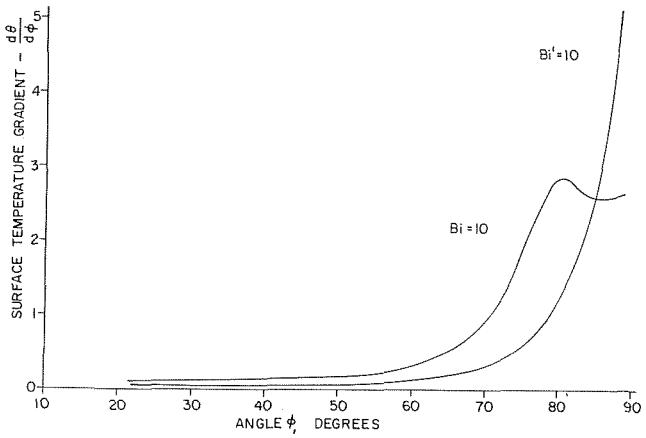

Fig. 17 Surface temperature gradient for constant and variable Biot number

In Fig. 13 the values for surface velocity calculated with and without inertial term, at Bi = 100, Pr = 1 and two values of Nm: 240 and 450, respectively, are plotted. These curves reveal that the presence of the inertial terms did not change the velocity distribution substantially. The change in the average Nusselt number was 2 percent (higher values for inertial free flow). This indicates that this part of our modeling increased the effect of thermocapillary flow (although only slightly).

Another critical part of the modeling was the modification of liquid-vapor heat transfer coefficient in the vicinity of the right-hand corner. This would obviously affect the total amount of heat transferred to the surface base considerably. Fig. 14 shows the values of local Nusselt number at the base of the drop (defined in the Nomenclature) as a function of dimensionless radius for three values of Nm (listed in the figure) and Bi = 100. Near the corner, as a consequence of the model, Nu_r decreases, although it would increase all the way toward the end if the interface heat transfer, h, were kept constant.

In Figs. 15–17 we compared the surface temperature profile, local Nusselt number, and the surface temperature gradient, respectively, for the two cases, namely, when the interface h was kept constant (Bi′ = 10) and when h was modified according to the scheme introduced previously. The surface temperature and the Nu_r were lowered with our model everywhere. However, the temperature gradient was on the average, increased, indicating that the internal circulation's effects are increased. Physically this is easy to see, the modified interface heat transfer coefficient (h_e) will increase the nonuniformity with the surface temperature, and this gives the higher value for the thermocapillary force at the surface.

It is safe then to conclude that our model increased the relative effect of thermocapillary flow by reducing the conduction contribution and increasing the circulation. Consequently, our conclusion, that the effects of internal circulation on the heat transfer in dropwise condensation is insignificant, is valid.

Conclusion

Thermocapillary flow does not contribute significantly in the dropwise condensation of water. The range covered by this investigation was $1 \leq Bi \leq 200$ and $Nm \leq 550$. This included, for water, the drop size range of practical interest for which the heat resistance through droplets is the predominant resistance. The results show that the increase in heat transfer is not higher than a few percent over the one which could be predicted neglecting internal circulation.

References

1 McCormick, J. L., and Westwater, J. W., "Nucleation Sites for Dropwise Condensation," *Chemical Engineering Science*, Vol. 20, 1965, p. 1021.

2 Umur, A., and Griffith, P., "Mechanism of Dropwise Condensation," JOURNAL OF HEAT TRANSFER, TRANS. ASME, Series C, Vol. 87, 1965, p. 275.

3 Trefethen, L., "Dropwise Condensation and the Possible Importance of Circulation Within Drops Caused by Surface Tension Variation," General Electric Co., Report No. 58GL47, Feb. 1958.

4 Scriven, L. E., and Sterling, C. V., "The Maragoni Effects," *Nature*, Vol. 187, 1960, p. 186.

5 Trefethen, L., "A Note on the Explanation of Dancing Ice," Tufts University Mechanical Engineering Report No. 9-23-58, 1958.

6 Trefethen, L., "On the Jet Propulsion of Bubbles in a Heated Liquid," Tufts University Mechanical Engineering Report No. 8-1-61, 1961.

7 Boys, C. V., "Soap-Bubbles and the Forces Which Mold Them," Society for Promoting Christian Knowledge, London, 1890. Reprinted Doubleday Anchor Books, Garden City, 1959.

8 Maxwell, M. J., "Capillary Action," *Encyclopedia Britannica*, 9th ed., 1891.

9 Block, M. J., "Surface Tension as the Cause of Benard Cell and Surface Deformation in a Liquid Film," *Nature*, Vol. 178, 1956, p. 650.

10 Brown, W. R., Jr., "Study of Flow Surface Boiling," PhD thesis, Mechanical Engineering Department, M.I.T., Cambridge, Mass., June 1967.

11 Tillman, C., "EPS" Memorandum, Project MAC-M-284, M.I.T., Cambridge, Mass., Nov. 1965.

12 Umur, A., and Griffith, P., "Mechanism of Dropwise Condensation," JOURNAL OF HEAT TRANSFER, TRANS. ASME, Series C, Vol. 87, 1965, p. 275.

13 Nabarian, K., and Bromley, L. A., "Condensation Coefficient of Water," *Chemical Engineering Science*, Vol. 18, 1963, pp. 651–660.

14 Citakoglu, E., and Rose, J. W., "Dropwise Condensation—Some Factors Influencing the Measurements," *International Journal of Heat and Mass Transfer*, Vol. 11, 1968, pp. 523–537.

15 Griffith, P., and Graham, C., M.I.T. Heat Transfer Laboratory, personal communication, 1968.

16 Mikic, B., "On Mechanism of Dropwise Condensation," paper submitted to the *International Journal of Heat and Mass Transfer*.

P. P. ZEMANICK
Supervisor,
Core Structural Analysis and Methods,
Westinghouse Astronuclear Laboratory,
Pittsburgh, Pa. Assoc. Mem. ASME

R. S. DOUGALL
Associate Professor,
Department of Mechanical Engineering,
University of Pittsburgh,
Pittsburgh, Pa. Mem. ASME

Local Heat Transfer Downstream of Abrupt Circular Channel Expansion

Experimental work was performed to determine local Nusselt numbers in the region beyond an abrupt expansion in a circular channel. Three expansion geometries, ratios of upstream-to-downstream diameter of 0.43, 0.54, and 0.82, were tested with air as the working fluid. Data are shown for Reynolds numbers from 4000 to 50,000–90,000 depending on geometry. Selected comparisons with previously published data for air and water are included.

Introduction

THE DETERMINATION of channel wall convective heat transfer characteristics has likely been the most important engineering aspect of heat transfer research. However, while data and analysis for heat transfer in channels of constant cross section are abundantly represented in the literature, relatively little research is reported for channels with abrupt changes in flow area, even though this latter geometry occurs frequently in heat-exchanger design. The lack of information can probably be attributed to the complexity of the flow field in this geometry as well as to the smaller interest in local heat transfer data in the era before such high-performance heat exchangers as modern-day nuclear reactors and gas-turbine engines.

The purpose of the research reported here was to make a contribution in this relatively lightly explored technical area by studying, in particular, local heat transfer behind an abrupt expansion in a circular channel for the turbulent, subsonic regime. A range of Reynolds numbers and geometries were tested with air as the working fluid.

Review of Literature

Recognition of the need for thermal research on the abrupt channel expansion problem is evidenced by the fact that two papers closely related to the present effort have been published on this subject since this research project began in Jan. 1966. The first, and more closely related, is the work of Krall and Sparrow [1][1] which was a heat transfer study for the region downstream of an orifice in a circular channel with water as the working fluid. The ratio of orifice to downstream diameters was varied from $^1/_4$ to $^2/_3$ and the downstream Reynolds number range was 10,000 to 130,000. The second recent paper is that of Filetti and Kays [2] in which work is reported with abrupt, symmetrically expanded flat ducts. Upstream to downstream channel height ratios of about $^1/_2$ and $^1/_3$ were studied for a Reynolds number range of 70,000 to 205,000. The flat duct data were not found to give really useful comparisons with the present work because the two-dimensional expansion always shows asymmetric reattachment. This is in contrast to the cylindrical case which appears to expand evenly until relatively high upstream velocities are reached.

The only other heat transfer data known to exist for the abrupt cylindrical expansion case are the results of a block of work performed at the National Engineering Laboratory, East Kilbride, Scotland. The most extensive work was with water as the working fluid. Testing reported by Ede, Hislop, and Morris [3] and by Ede, Morris, and Birch [4] covered diameter ratios of 0.3, 0.5, and 0.8, and a downstream Reynolds number range of 1000 to 50,000. Data with air flowing through the channel are reported by Ede [5], and by Emerson [6]. These data were restricted to practically the same diameter ratio, 0.50 for the former work and 0.58 for the latter. The corresponding Reynolds number ranges were 2000 to 43,000 and 14,500 to 105,000, respectively. Use of these data is somewhat complicated by the fact that only a fraction of the National Engineering Laboratory data is reported for the case of heating in the downstream channel only. The remainder is for channel wall heating both before and after the expansion. Measurable differences between the two heating schemes are noted. For the case of downstream pipe heating only, the reattachment point is shifted slightly downstream and the peak Nusselt number is increased.

Two sets of heat transfer data for the two-dimensional geometry of a single backward facing step are available. The two channel width ratios were 0.94, a relatively small change in flow area, and 0.81, a more interesting geometry. The data are reported by Seban, Emery, and Levy [7]. Reynolds numbers between 0.8 and 2.5×10^6 were represented. These experiments were with air.

Test Apparatus

More detailed material than that given next concerning the test apparatus and concerning the test procedures and data reduction methods (discussed briefly in the next section) can be found in reference [8].

[1] Numbers in brackets designate References at end of paper.

Contributed by the Heat Transfer Division of THE AMERICAN SOCIETY OF MECHANICAL ENGINEERS and presented at the ASME-AIChE Heat Transfer Conference, Minneapolis, Minn., August 3–6, 1969. Manuscript received by the Heat Transfer Division, January 13, 1969; final manuscript received, April 28, 1969. Paper No. 69-HT-35.

Nomenclature

d = upstream (smaller) tube diameter
D = downstream (larger) tube diameter
Nu = local Nusselt number, referred to downstream diameter
Nu_{fd} = Nusselt number associated with fully developed flow, referred to downstream diameter
Nu_{max} = maximum Nusselt number, referred to downstream diameter, assumed to occur at reattachment point
Pr = local Prandtl number
Re = local Reynolds number, referred to downstream diameter
Re_d = Reynolds number just before expansion, referred to upstream tube diameter and upstream tube fluid properties just before expansion

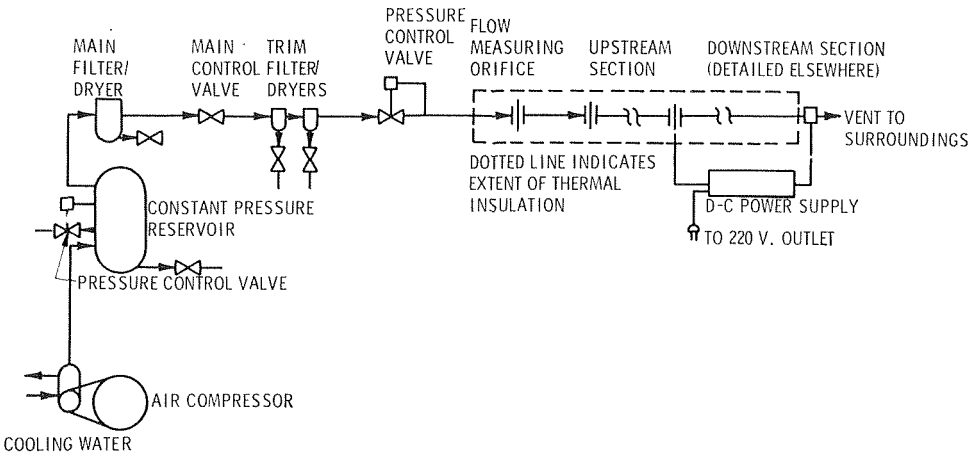

Fig. 1 Test apparatus flow schematic

The test apparatus flow schematic is shown in Fig. 1. Ambient air was pumped by a constant-speed, water-cooled, two-stage compressor into a constant pressure reservoir. Air for the experimental apparatus was drawn from the reservoir and passed through three filter/dryers in series. These air cleaners, utilizing centrifugal moisture separation followed by filtration through a porous stone or sintered metal cylinder, were intended to remove oil, water, and solid particles from the airstream. Frequent blowdown at the reservoir base, at each of the filters, and at other low spots in the piping insured a clean air supply to the test section.

A constant flow rate was maintained by metering the air through a pressure control valve located just downstream of the air filters. The flow rate was measured by one of the two water-calibrated sharp-edged orifices installed just upstream of the test section.

The test section itself was installed along the center line of a 2-ft by 2-ft-wide by 16-ft-long plywood insulating box filled with layers of glass wool. The intent was to reduce radial heat losses to a negligible level by surrounding the test section by approximately 1 ft of efficient insulation in all directions. The insulating box extended from upstream of the flow-measuring orifice to the point where the working fluid was exhausted to the environment.

A test section was constructed with three alternate upstream test sections, with inside diameters of 0.40, 0.50, and 0.76 in., respectively, and with lengths at least equal to 100 inside diameters. The downstream section consisted of a 102-in. length of tubing with a 1-in. OD and a 0.035-in. wall. Upstream and downstream sections were of type 304 stainless-steel seamless tubing. The two test sections were jointed at a transition flange designed to center the upstream section and provide a sharp, symmetric expansion, to insulate the two sections one from the other electrically and thermally, and to serve as the upstream electrical connection to the downstream test section. The essential material in the transition construction was Johns-Manville marinite, an acceptably machinable insulation material of asbestos fiber and diatomaceous silica with an inorganic binder. The details of the transition flange can be found in Fig. 2.

The only instrumentation upstream of the larger diameter pipe was pressure and temperature instruments related to flow measurement and two thermocouples 1-in. upstream of the expansion. One of these thermocouples was mounted on the surface of the upstream section to give at least a qualitative measure of the insulating effectiveness of the transition flange. The other was immersed in the fluid. The immersed thermocouple was threaded through a 0.050-in. hypodermic needle installed through the tube wall and cut to a length designed to place the thermocouple bead at the channel center line. The possibility of the probe affecting the expansion flow pattern was investigated by rotating the smallest upstream section through three different

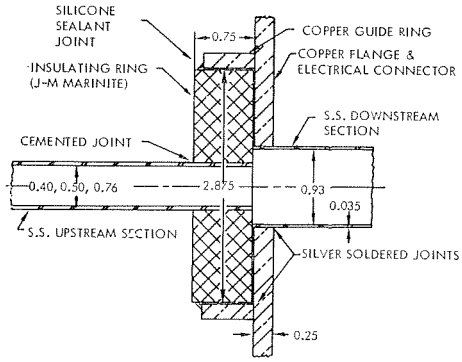

Fig. 2 Details of transition flange construction

probe orientations (90 and 180 deg from the usual position) and studying downstream temperature data for each case. No discernible difference in postexpansion wall temperatures was detected.

The vast majority of instrumentation, 53 surface thermocouples and one probe, was installed on the downstream test section. Near the expansion, thermocouples were installed every 0.25 in. to study in detail the phenomenon occurring in this region. Seven in. downstream of the expansion, the thermocouple spacing was increased. All surface thermocouples were installed over a sublayer of porcelainlike Sauereisen No. 8 cement (measured at 0.012 ± 0.001 in.) to provide electrical isolation from the resistance heated tube. A small quantity of the same cement was used to hold the thermocouple in place. Thermocouple output was measured with a manually balanced precision potentiometer. The downstream section was heated resistively by means of a 3.6-kva d-c power supply.

Test Procedure and Method of Data Reduction

A combination of test rig heat capacity and the heat capacity of the rather massive components of the air pumping and storage equipment required a minimum running time of 3 hr before steady-state conditions were approached. Even after this waiting period, constant heating up of the compressor proper made completely stable conditions impossible. Data were collected when main test section inlet temperature rose not more than 2 deg F per hr. At this time, data from all instrumentation were collected, a task requiring approximately 15 min, and then the same instruments were read in reverse order, the entire 30-min process yielding two sets of data which were simply averaged. Special data readings corroborated the approximate validity of this procedure. After the first data set was collected, steady

state (2 deg F/hr temperature rise) could be attained within 1 hr for a new power-flow combination.

There was real concern that the working fluid might reach the test section contaminated by oil from the piston-type compressor or by water during periods of high environmental specific humidity. In addition to the precaution of installing three air cleaners (each with a blowdown valve) in series, additional drain valves were installed at low points in the piping and cracked during frequent blowdowns. The effectiveness of these measures was indicated by the fact that little or no moisture collected in the downstream filter moisture bowl and that neither moisture nor oil traces were ever detected at the mouth of the main test section.

Regarding the relative settings of flow and power during the test series, it was felt that a more coherent mass of data could be collected if the flow-to-heat flux ratio were kept approximately constant, given a nearly constant axial temperature rise in the bulk fluid temperature. In an attempt to strike a compromise between having fairly constant fluid properties along the test section (small temperature rise) and having large enough bulk-to-surface temperature differences (large heat flux), an axial temperature rise of 60 deg F was chosen.

The data correlation was accomplished by a computer program written for this purpose. The first calculation was for flow rates, which were calculated by well-known orifice relationships, as described in Stearns, et al. [9], for instance.

The upstream temperature probe (installed 1 in. before the expansion) was not corrected for radiative losses or stem conduction because wall and fluid thermocouple temperatures were almost identical. However, the stream versus total temperature correction was not negligible for the higher flow rates. For this probe, subjected as it was to considerable wall influence through direct metallic contact over a short path between the wall and the thermocouple bead, a recovery factor of $Pr^{0.33}$ was applied. This recovery factor is associated with adiabatic circular channels and seemed appropriate. Furthermore, this choice of recovery factor was supported by heat-balance computations and by data like those displayed in Fig. 8. The stream temperature just beyond the expansion was the temperature deduced in this way from the upstream temperature probe followed by a correction for adiabatic expansion of the air from the upstream flow area to the downstream section flow area. The downstream (101 in. from the expansion) temperature probe reading was converted to local bulk temperature by applying corrections for radiation effects, fluid transverse temperature profile, and recovery factor. The downstream probe was constructed to make the thermocouple junction a nearly adiabatic sphere, so that, first, stem conduction could be ignored and, second, a recovery factor of 0.65 was applicable.

The two probe temperatures were used as just discussed to deduce fluid bulk temperaures just beyond expansion and at a point 101 in. downstream. The local fluid temperature was calculated from a straight-line bulk-temperature distribution assumed to exist between these two points. Parallel calculations were performed in which local bulk temperature was calculated iteratively and piecemeal along the channel based on the locally determined convective heat transfer coefficient and known wall temperatures. However, this scheme yielded only negligibly different results (Nusselt number) in the area of greatest interest, in the vicinity of the expansion, and, furthermore, sometimes gave entirely erroneous developed flow Nusselt numbers since even a relatively small accumulated error in local bulk temperature (from a heat-balance point of view) could give downstream local film temperature differences that were grossly in error. For example, at low flow rates, a 3 deg F accumulated discrepancy at 87 in. from the expansion would be approximately a 5 percent error in heat balance but a 15 percent error in local film temperature difference and Nusselt number. Consequently, the linear axial fluid temperature distribution was applied as a compromise which would affect upstream results little but serve as a consistent basis for upstream and fully developed results, which are widely compared next.

Moving from fluid bulk temperature determination to the surface temperatures, the only direct surface temperature correction was one to calculate inside wall temperature from measured outside wall temperature. The calculations were made on the assumptions that, first, the radial temperature gradient in the tube wall was zero at the outside surface and, second, that the second derivative of temperature with respect to axial location was constant throughout the radial dimension of the tube. This correction influenced the maximum Nusselt number up to 2 percent, the greatest influence being exerted for high flow/power conditions.

The convective heat transfer correlation proper was accomplished in such a way as to take into account both radial conduction losses through the insulating blanket as well as axial conduction effects. The radial conduction loss was based on a cylindrical model with inside radius of 1/2 in. and an outside radius of 12 in. In the region of most interest, up to about 14 step heights from the expansion, the radial heat loss was calculated to be always less than 2 percent of the heat generated in the test section. However, at 87 in., where wall temperatures were much higher, the percentage was almost 15 percent for the lowest flow/power case in each geometry, 10 percent for the second lowest case, then gradually reduced fractions as test section convection increased to compete more successfully with the radial conductive path. This heat loss was considered to be adequately taken into account.

A lower degree of confidence is held in the correction for axial conduction. However, the following attack on the problem was formulated to make the correction as precisely as possible under the circumstances. The conduction for an internally heat generating solid involves, of course, the second derivative of temperature with respect to axial location, assuming azimuthal symmetry and a separable radial temperature distribution. A straightforward finite-difference approach (first three terms of the Taylor expansion) based on as-measured temperatures 1/4 in. apart proved grossly inadequate. The final corrections were based on a central difference differentiation formula incorporating closely spaced values taken from smooth curves drawn through the measured temperatures versus axial location with an exaggerated temperature scale. While the 0.035-in. wall thickness obviously did not make axial conduction near the expansion negligible, the thickness was small enough for the conductive effect to decline rapidly with distance from the expansion. The first axial location chosen for the presentation of reduced data is 0.625 in. Axial conduction can affect Nusselt number by up to 50 percent at this point. However, for the upstream sections with 0.40 and 0.50-in. inside diameter, this point is relatively far from the Nusselt number peak. In the peak heat trasfer region, corrections of 0–6 percent are encountered. The correction is more critical for the 0.76-in. upstream section; for, in this case, the maximum Nusselt number appears to exist at 0.625 in. or earlier for all but the lowest flow. Consequently, the first displayed data point as well as maximum heat transfer point both have axial conduction corrections of 5 (highest flow/power) to 50 percent. This discussion of potential difficulties arising from the axial conduction correction must be closed with a reference to the reduced data shown in the following section. The internal consistency of all the data collected for a given geometry (except for the lowest flow-rate data which seems somewhat different in each case) as shown in Figs. 4–6, as well as the fair consistency of all the maximum Nusselt numbers for all the geometries as shown in Fig. 8 imply that the method chosen to make this correction was adequate.

Broad use is made in the data correlation of the ratio between local and fully developed Nusselt numbers. For the purposes of this paper, the data 87 in. from the expansion (about 94 dia) is considered fully developed.

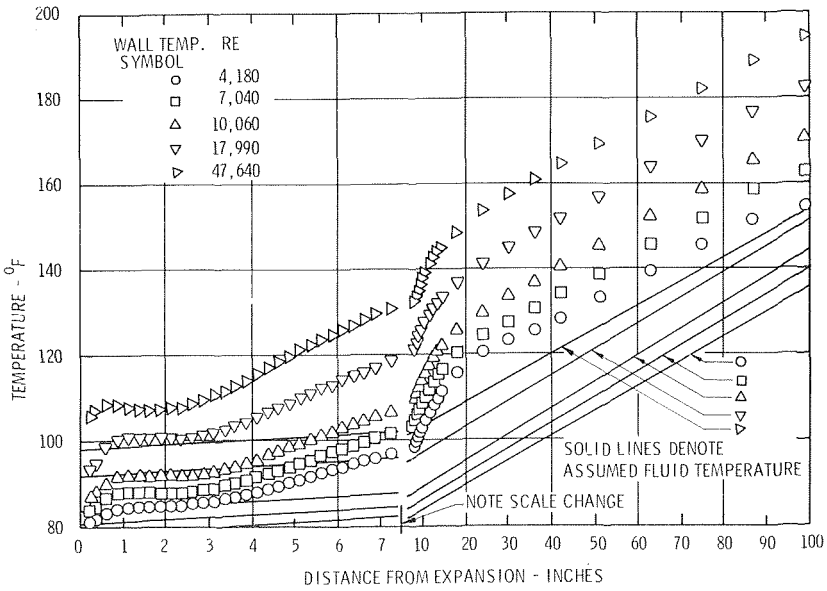

Fig. 3 Axial distribution of wall and bulk temperatures, $d/D = 0.43$

Raw and Reduced Data

The purpose of this section is to present the actual test data in terms of wall and fluid temperatures as well as in correlated form showing the relationships between geometry, Nusselt numbers, and Reynolds numbers.

A typical axial temperature distribution is presented graphically in Fig. 3 for the case of $d/D = 0.43$. The wall temperatures shown are those calculated for the inner surface. The bulk temperature lines are merely the linear distributions assumed to exist between the bulk temperatures calculated as described in the preceding section for the point just past the expansion and at 101 in. from the expansion. Therefore, the temperatures shown are exactly those used in the Nusselt number determination. Because of large and difficult to define axial conduction effects, correlations will not be presented for the first two temperature points seen in this figure, that is, at 0.25 in. and at 0.375 in. from the expansion.

The temperature distributions themselves give some qualitative suggestions concerning the phenomenon being studied, i.e., heat transfer effectiveness downstream of an abrupt expansion. Nusselt number is inversely proportional to the wall-to-bulk temperature difference for a fixed heat flux and constant properties. Fig. 3, associated with the smallest diameter ratio, shows that minimum temperature differences occur between about 1.5 and 2.5 in. from the expansion. Therefore, the maximum Nusselt numbers can be expected to be found in the same area. (The possibility is not overlooked of a second Nusselt number peak between the expansion and 0.625 in. However, a detailed study of this relatively short postexpansion region would be an adequate subject in itself for a separate experimental program. All the comments which follow include the implicit admission that a second peak might exist.)

In the following three figures, the local heat transfer effects of the expansion are displayed in terms of the ratio between local Nusselt number and the fully developed value. As was explained previously, fully developed Nusselt number means the value calculated from measurements taken at 87 in., about 94 dia downstream of the expansion. Furthermore, the ratio is actually referred to the quantity $(Nu/Re^{0.8}Pr^{0.4})$, an effort to relate local Nusselt number to the fully developed value at the same local fluid properties. Along the abscissa of the figures, the step height (i.e., $(D\text{-}d)/2$) is selected as the measure of axial distance. This choice was indicated as a logical one both by the analytic work on this problem [8] as well as by the present and previously reported abrupt expansion data. The data for the smallest diameter ratio, Fig. 4, show a peak Nusselt number between 6 and 9 step heights. Ignoring the maximum Reynolds number information, the remaining peaks are clustered close to 9 step heights. Although the problematic axial conduction correction may be biasing the correlation, the data for this largest expansion do suggest the existence of a second peak nearer the "corner" of the expansion. The data for the intermediate expansion, Fig. 5, are similar in general shape to the previous case. Peak Nusselt numbers fall between 5 and 8 step heights downstream of the expansion. However, ignoring the maximum Reynolds number case as before, the maxima favor a location near 7 step heights. The large diameter ratio data, Fig. 6, do not include clear maximum points. Excluding the somewhat anomalous low flow data, the maximum heat transfer is shown to occur at 0.625 in. or earlier. The manner in which the 0.625-in. Nusselt numbers compare with the peak values for the other two geometries, as seen in Fig. 8 and briefly discussed earlier, implies that the peaks are attained or nearly attained at 0.625 in., or at about 7 step heights.

Note that the distribution of the data in Fig. 6 follows a shape different from what was seen in Figs. 4 and 5. The same trend of broad-peaked axial Nusselt number distributions for small diameter ratios (d/D) and sharp-peaked distributions for large ratios is reported by Ede, Morris, and Birch [4], Ede, Hislop, and Morris [3], and Krall and Sparrow [1] for comparable data on water. It is also seen that the distribution for the run of lowest Reynolds number in each geometry is somewhat different from the rest of the data. It seems not unreasonable to surmise that these low flows, Reynolds number range between 4000 and 5000, are not turbulent or energetic enough to produce the same consistent hydraulic pattern generated by the higher flow rates, characterized by Reynolds numbers greater than 7000. Another credible possibility is that the various uncertainties in parameter measurement and data reduction, most of which are worst for the lowest flow and power, make the reduced data less valid. Another set of data which is not entirely consistent with other data for the same expansion geometry is the highest flow results for the 0.43-dia ratio. A second set of data collected under approximately the same conditions verified this maximum local to fully developed Nusselt number (within 10 percent) as well as the approximate distribution. Perhaps compressibility effects not felt by the other tests make these data, collected under conditions of the highest upstream section Mach number (about

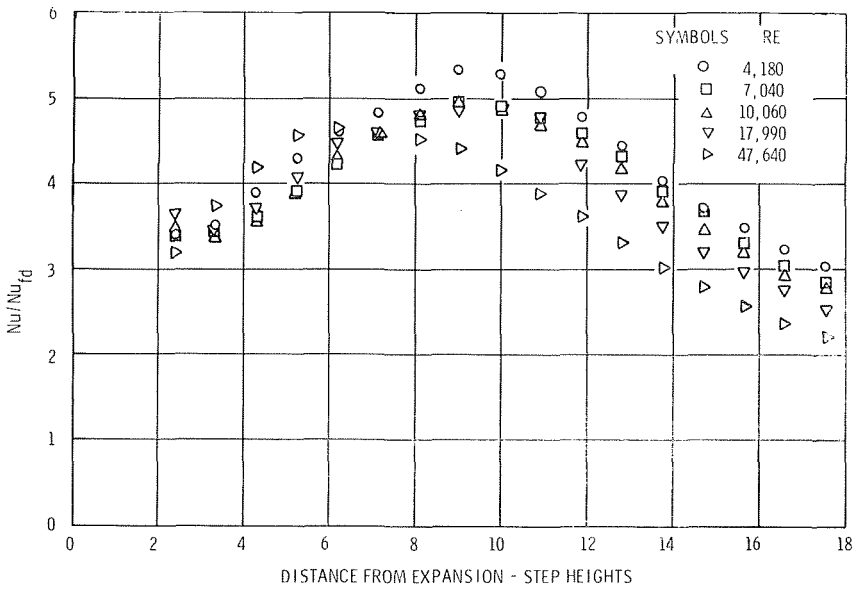

Fig. 4 Axial distribution of local to fully developed Nusselt number ratio, $d/D = 0.43$

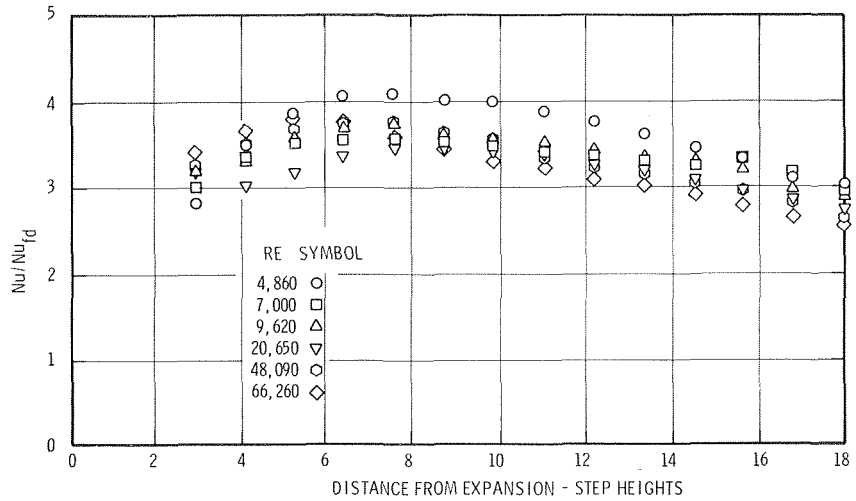

Fig. 5 Axial distribution of local to fully developed Nusselt number ratio, $d/D = 0.54$

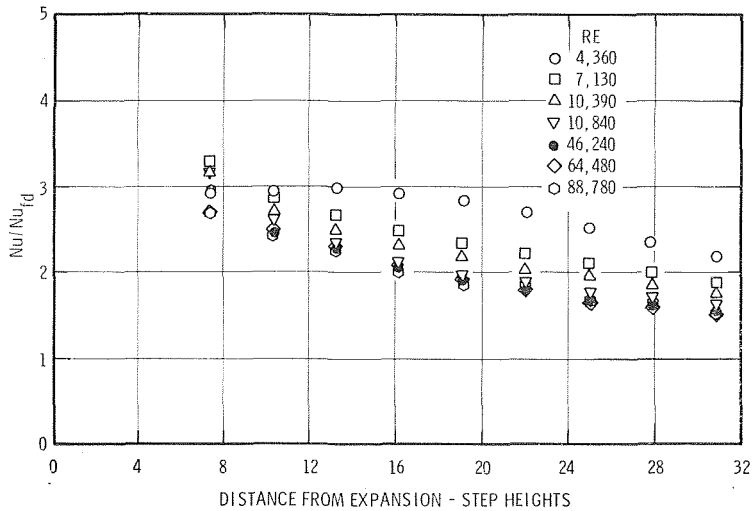

Fig. 6 Axial distribution of local to fully developed Nusselt number ratio, $d/D = 0.82$

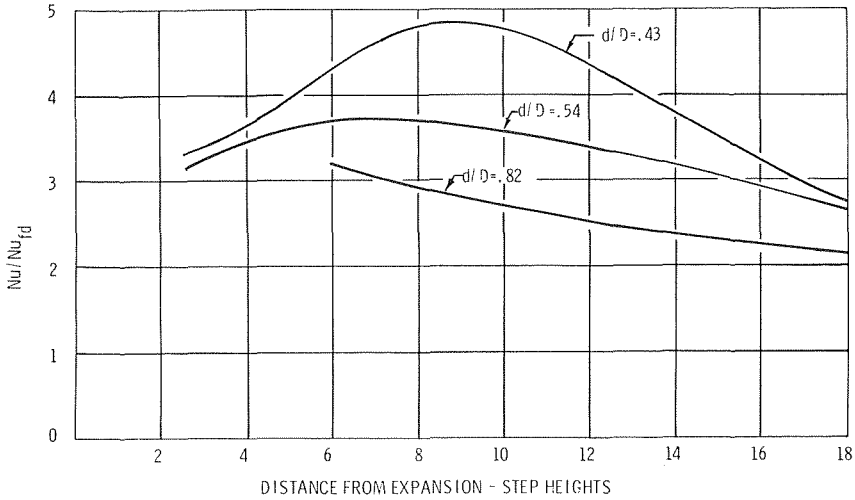

Fig. 7 Approximate axial distribution of Nusselt number ratio

0.54) of any data, point to somewhat different heat transfer characteristics. In any case, ignoring the low flow results in all three geometries and the highest flow case in the 0.43-dia ratio geometry, the results within a given geometry can be seen to fall within a rather narrow band. A fairly consistent but small Reynolds number dependence can be seen on the downstream side of each peak, the ratio of local to fully developed Nusselt number decreasing as the Reynolds number increases. However, the dependence is, by and large, quite minor. This is a surprising result, since Krall and Sparrow [1] show clear-cut important Reynolds number dependence of the Nusselt number ratio for water.

Fig. 7 shows approximate axial distributions of the local to fully developed Nusselt number ratio for the three geometries as derived from the preceding three figures. The curves show that the larger the ratio between upstream and downstream diameters, the larger are integrated and local increases in heat transfer beyond the change in diameter. Second, for a given downstream channel diameter, the location of peak heat transfer moves nearer the expansion the smaller the difference between diameters. This is true in the dimension of "step heights" and all the more true in the dimension of "downstream diameters." The correlating advantage of using step heights as the dimensionless axial distance parameter is demonstrated in Fig. 7. For, whereas the location of maximum Nusselt number is 7–9 step heights for all three geometries, the range in downstream diameters is approximately 0.5–2.5 dia.

Dependence of separated flow phenomena on Reynolds number to the $^2/_3$ exponent is not unusual. Fig. 8 shows maximum Nusselt numbers plotted against upstream Reynolds numbers. The straight-line fit, which is a fair representation of the data, has as its equation

$$\mathrm{Nu}_{\max} = 0.20\ \mathrm{Re}_d^{0.667}$$

Although the test program was not mounted to investigate fully developed heat transfer, it is interesting to compare the downstream results with published correlations for fully developed Nusselt numbers. The downstream results are especially interesting insofar as the 87-in. results are used in the $\mathrm{Nu}/\mathrm{Nu}_{fd}$ ratio in Figs. 4–6. These fully developed Nusselt numbers are plotted in Fig. 9 versus local Reynolds number. For the sake of comparison, a line is shown representing the classic Dittus-Boelter equation with an initial constant of 0.024.

Another matter related to the overall validity of the experimental results is the question of the heat balance. The original dissertation [8] can be consulted for detailed heat-balance results. The largest discrepancy encountered was 7.4 percent (calculated heat input less than measured). The next highest error in the

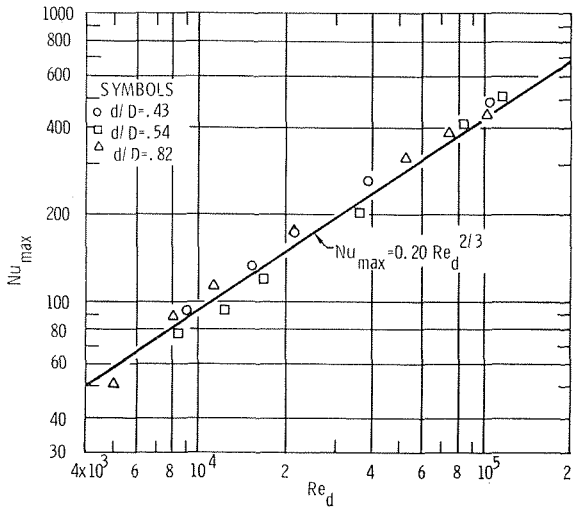

Fig. 8 Maximum Nusselt number versus upstream Reynolds number

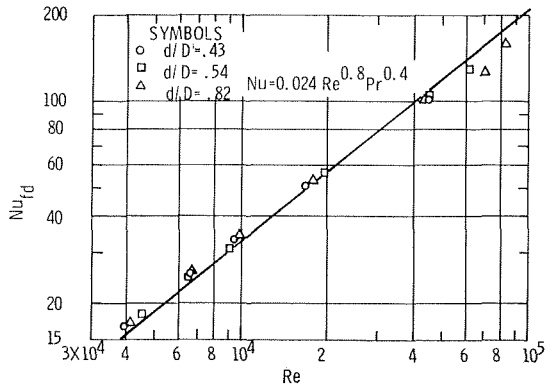

Fig. 9 Fully developed Nusselt number versus Reynolds number

heat-balance comparison was 4.3 percent. Although the axial distribution of actual test section resistance was not known, a set of precise overall voltage/current measurements showed the test section plus connections to have a resistance 3.8 percent higher than that calculated from the resistivity of type 304 stainless steel and the manufacturer's nominal dimensions. Factoring this kind of correction into the calculations would give a more even distribution of positive and negative heat-balance dif-

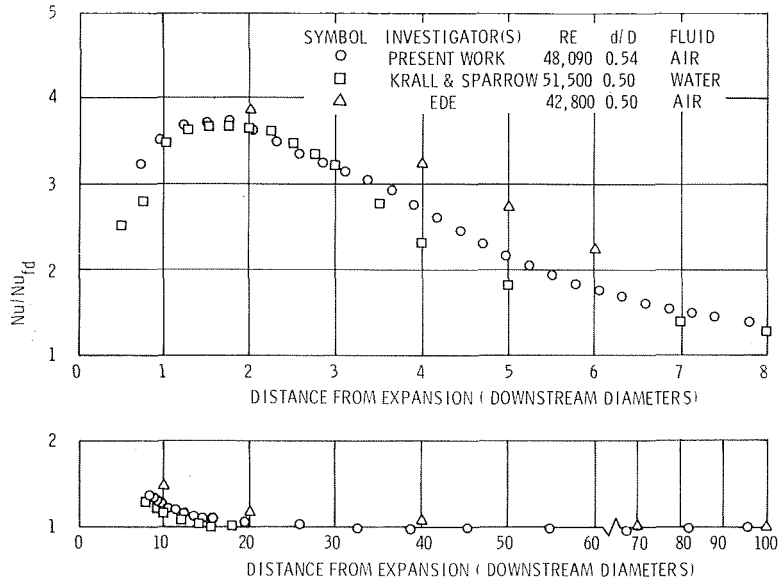

Fig. 10 Comparison of results for d/D = 0.54, Re = 48,090, with published data

ferences, reduce the maximum discrepancy to 4.4 percent, and reduce the average discrepancy from −2.3 to +1.5 percent.

A final item bearing on the general validity of the data is the axisymmetry of the expansion. In an effort to provide some check on the symmetry of conditions beyond the expansion, "monitoring" thermocouples were installed diametrically opposed to the main line of thermocouples along the top edge of the downstream test section. The thermocouples were mounted 1, 2, and 4 in. from the expansion. In the worst case, the highest flow rate for the greatest expansion, a case seen to be anomalous in other respects, the asymmetry difference was found to be able to affect Nusselt number calculations by about 7 percent. Potential errors of 4–6 percent were found in the case of the greatest expansion ratio for the other flows. The other geometries show potential local errors of up to 4 percent. In spite of the possible errors, however, it must be noted that the differences are small in absolute magnitude, small enough to be attributed wholly or partially to the various causes of experimental scatter. In fact of the 54 points of comparison only six were as large as 0.5 deg F, and three of the six points were associated with such large film temperature drops that errors of only 1–2 percent are involved. Nevertheless, although the absolute magnitude of the differences is small, asymmetries are detected and must be admitted to possibly cause correlation errors to the extent indicated.

Comparisons With Previously Published Results

Several direct comparisons with existing data are available.

It has been stated previously that there is only one known source of data for a cylindrical expansion with air as the test fluid and with only the downstream section heated; namely, the work of Ede [5]. In the same reference, data are shown which demonstrate that local to fully developed Nusselt number ratios decrease and the point of maximum Nusselt number shifts somewhat when both upstream and downstream sections are heated. Fortunately, the single geometry investigated by Ede, d/D = 0.50, is reasonably close to the 0.54 d/D configuration that was investigated in the present work. Furthermore, there is a near correspondence of downstream section Reynolds numbers as a basis for comparison (Ede—42,800; present work—48,900). For reasons to be discussed next, a third case is added to the comparison, the work of Krall and Sparrow [1] with water as the working fluid and downstream section only heated. The latter data are for d/D = 0.50 and a Reynolds number of 51,500. The data were all correlated on the basis of the ratio of local to

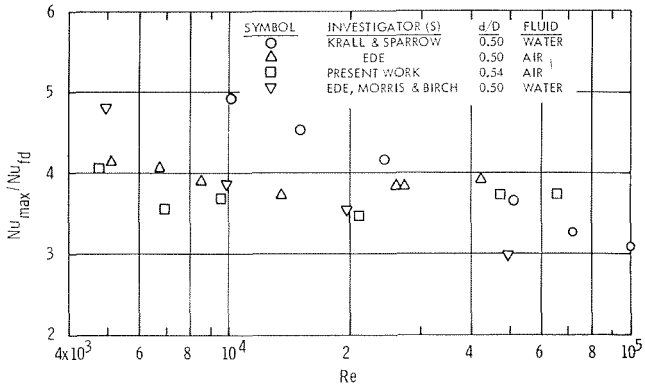

Fig. 11 Effect of Reynolds number on maximum Nusselt number ratio

fully developed Nusselt number versus axial location in downstream section diameters. The comparative data can be seen in Fig. 10. The maximum Nusselt number ratio differs little in magnitude among the three cases. It is surprising to see that the present data agrees better with the water data than with Ede's air data. The agreement in magnitude with the water data is coincidental since water data, as will be demonstrated shortly, typically shows a strong Reynolds number dependence in the Nusselt number ratio. However, there is striking agreement in the location of the maximum Nusselt number and in the Nusselt number distribution in the vicinity of this maximum point. Better agreement would be expected among the data downstream of reattachment as the flow becomes fully developed. However this is an example (actually a less striking example than will be shown in the following two figures) of the scatter among the small amount of test data related to the expansion phenomenon and indicative, perhaps, of the difficulty of collecting and correlating such data.

Fig. 11 demonstrates a point alluded to in the previous section. Water data show a clear, monotonic dependence on Reynolds number of the maximum to fully developed Nusselt ratio. See the water data of Krall and Sparrow [1] and of Ede, Morris, and Birch [4] as plotted on the figure. The air data of Ede [5] and the present investigation show no obvious Reynolds number effect, except perhaps that the lowest Reynolds number case (Reynolds number of about 5000) shows the highest ratio. An

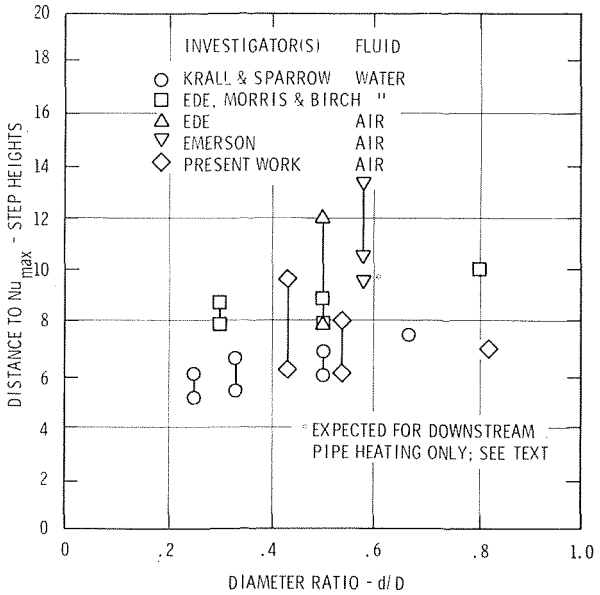

Fig. 12 Effect of expansion ratio on location of maximum Nusselt number

additional indication of the data in this figure is that the magnitude of the maximum Nusselt number ratio agrees reasonably well between Ede's work and the present effort. Ede's data point to an average value of Nu_{max}/Nu_{fd} of approximately 3.9, while the present work gives a value of about 3.6. The numbers are close together and are related qualitatively as expected; that is, the larger the ratio of small to large pipe diameters the smaller the maximum Nusselt number ratio.

The next comparison, Fig. 12, deals with the location of maximum Nusselt number. The data sources have all been discussed previously. The peak locations in the dimension of step heights are shown for various expansion ratios. In most cases, ranges are shown, indicating either data scatter among the various flow rates investigated or a dependence on a parameter like Reynolds number. The data of Ede, Morris, and Birch [4] and of Emerson [6] are for test rigs with upstream and downstream sections heated. Such an arrangement, which involves a fully developed thermal boundary layer upstream of the expansion, is expected to give a maximum Nusselt number downstream of the hydrodynamic reattachment point. A separate experiment by Emerson [6] to find hydraulic reattachment (by means of oil drop smears) would place his expected point of maximum Nusselt number at the point designated by an asterisk in the figure if the downstream section only were heated. The data scatter is too widespread to deduce a single number or narrow band for the peak location. A band of 5–10 step heights includes almost all the data. A more specific conclusion seems unwarranted. As was the case with Fig. 10, the present data agree better with the water data of Krall and Sparrow than with the air data. Furthermore, these water data appear to favor a maximum Nusselt number location of about 6 step heights, a location consistent with the analytic results developed by the authors elsewhere [8].

Conclusions Concerning the Test Data

For the range of Reynolds numbers and expansion ratios studied, the following conclusions are drawn from the test data.

1 The flow beyond an abrupt expansion in a circular channel shows a considerable enhancement (over the fully developed value) of the *average* convective heat transfer coefficient in the separated flow region. Furthermore, although the data do leave some question concerning the area immediately beyond the expansion, the *local* heat coefficients likewise appear always to be higher than the fully developed value.

2 The degree of heat transfer coefficient enhancement, both maximum and average, increases strongly as the ratio of downstream to upstream diameter increases.

3 The location of maximum heat transfer, presumably at the end of the separated flow region, moves downstream as the ratio of downstream to upstream diameter increases. This is a strong function if the distance from the expansion is measured in downstream diameters, but a relatively weak function in terms of step heights downstream from the expansion.

4 Correlation of the data in the form of local to fully developed Nusselt number ratio versus distance from the expansion gives a reasonably close clustering of the data for a given geometry and for downstream Reynolds numbers in excess of 7000.

5 The peak Nusselt number exhibits a clear dependence on upstream Reynolds number raised to approximately the $^2/_3$ exponent. The equation that reasonably represents the maximum Nusselt number data of all three geometries tested is

$$Nu_{max} = 0.20\ Re_d^{0.667}$$

6 At high velocities, the abrupt cylindrical expansion flow pattern is susceptible to asymmetric reattachment, with this susceptibility apparently increased as the ratio of downstream to upstream diameters is increased.

Acknowledgments

The first author gratefully acknowledges the support of the Westinghouse Astronuclear Laboratory, under whose Graduate Scholarship Program this work was undertaken. The authors also wish to thank the Department of Mechanical Engineering, University of Pittsburgh, for making the necessary experimental equipment available and the National Science Foundation for its support with regard to computer usage (NSF Grant G11309).

References

1 Krall, K. M., and Sparrow, E. M., "Turbulent Heat Transfer in the Separated, Reattached, and Redevelopment Regions of a Circular Tube," JOURNAL OF HEAT TRANSFER, TRANS. ASME, Vol. 88, No. 1, Series C, Feb. 1966, pp. 131–136.

2 Filetti, E. G., and Kays, W. M., "Heat Transfer in Separated, Reattached, and Redevelopment Regions Behind a Double Step at Entrance to a Flat Duct," JOURNAL OF HEAT TRANSFER, TRANS. ASME, Vol. 89, No. 2, Series C, May 1967, pp. 163–168.

3 Ede, A. J., Hislop, C. I., and Morris, R., "Effect on the Local Heat Transfer Coefficient in a Pipe of an Abrupt Disturbance of the Fluid Flow: Abrupt Convergence and Divergence of Diameter Ratio 2/1," *Proceedings of the Institution of Mechanical Engineers*, London, Vol. 170, No. 38, 1956, pp. 1113–1126.

4 Ede, A. J., Morris, R., and Birch, E. S., "The Effect of Abrupt Changes of Diameter on Heat Transfer in Pipes," NEL Report No. 73, National Engineering Laboratory, East Kilbride, Glasgow, Scotland, Dec. 1962.

5 Ede, A. J., "Effect of an Abrupt Disturbance of the Flow on the Local Heat Transfer Coefficient in a Pipe," HEAT 164, National Engineering Laboratory, East Kilbride, Glasgow, Scotland, Jan. 1959.

6 Emerson, W. H., "Heat Transfer in a Duct in Regions of Separated Flow," *Proceedings of the Third International Heat Transfer Conference*, Paper No. 26, Aug. 1966, pp. 267–275.

7 Seban, R. A., Emery, A., and Levy, A., "Heat Transfer to Separated and Reattached Subsonic Turbulent Flows Obtained Downstream of a Surface Step," *Journal of the Aero/Space Sciences*, Vol. 26, No. 12, Dec. 1959, pp. 809–814.

8 Zemanick, P. P., "Local Heat Transfer Downstream of Abrupt Expansion in Circular Channel With Subsonic Turbulent Air Flow," PhD thesis, Mechanical Engineering Department, University of Pittsburgh, 1968.

9 Stearns, R. F., et al., *Flow Measurements With Orifice Meters*, D. Van Nostrand Company, Inc., New York, 1951.

W. NAKAYAMA
G. J. HWANG
K. C. CHENG

Department of Mechanical Engineering,
University of Alberta,
Edmonton, Alberta, Canada

Thermal Instability in Plane Poiseuille Flow

The conditions marking the onset of longitudinal columnar vortices due to buoyant forces are studied for fully developed laminar flow between two infinite horizontal parallel plates with nonlinear basic temperature profile. The wall temperatures at the bottom and top plates, T_1 and T_2, respectively, are assumed to vary linearly in the main flow direction. The nonlinear basic temperature distribution and convective motion due to longitudinal disturbance component give rise to the influence on stability criteria: This influence may be expressed by a characteristic parameter representing the effect of longitudinal temperature gradient. Numerical values for critical Rayleigh numbers based on temperature difference, $T_1 - T_2$, are found for various Prandtl numbers and the parameter μ characterizing the effect of longitudinal wall temperature gradient. An increase in value for μ reduces the critical Ra further to a value less than 1708 when $T_1 > T_2$, and this tendency becomes pronounced as Pr increases. Results for the cases $T_1 \leqq T_2$ also show that the vortex rolls can be caused by the effect of longitudinal temperature gradient. Tentative discussion in terms of Richardson number is made to define the region where columnar vortices have priority of appearance over two-dimensional Tollmien-Schlichting waves. The computed secondary flow streamlines and perturbation temperatures show that the mode of convection motion is also affected by the parameter μ.

Introduction

In order to make an accurate heat transfer prediction for a flow with body forces, it is necessary to examine the possibility of secondary motion and determine which type of motion is most probable among various types of secondary flows. Body forces acting in a direction perpendicular to the main flow can cause steady secondary flow in ducts. A typical example can be found in a curved pipe, where a pair of vortices for the secondary flow is formed due to nonuniform distribution of the centrifugal forces in the flow field. In this case the secondary flow appears as soon as the fluid is brought into motion in the axial direction. However, when a fluid passage has an infinite extent in the direction perpendicular to both body force and main flow, the body force may leave the main flow unchanged in some regions with small body force parameters, and provides only a potential of instability. As the body force parameter increases beyond a critical value, specific type of secondary motion results, and the flow can no longer maintain its original pattern. A well-known example is the Taylor vortices developed between rotating concentric cylinders. When a stationary secondary flow is set up in a two-dimensional channel, it takes the form of columnar vortices whose axes are in the direction of the main flow.

The purpose of the present paper is to examine the possibility of onset of longitudinal vortex-type secondary flow between two

Contributed by the Heat Transfer Division of The American Society of Mechanical Engineers and presented at the ASME-AIChE Heat Transfer Conference, Minneapolis, Minn., August 3–6, 1969. Manuscript received by the Heat Transfer Division, December 6, 1968; revised manuscript received, April 28, 1969. Paper No. 69-HT-37.

Nomenclature

A_n = coefficients in series expansion defined in equation (19)
a = wave number
C_{ij} = elements of a matrix defined in equation (22)
c = complex wave speed
D = d/dz
F = body force
Gr = Grashof number, $g\beta\Delta Th^3/\nu^2$
g = gravitational acceleration
h = distance between two infinite horizontal flat plates
L = operator defined in equation (16)
p = pressure
Pr = Prandtl number, ν/κ
Ra = Rayleigh number, $g\beta\Delta Th^3/\nu\kappa$
Ra_τ = Rayleigh number, $g\beta\tau h^4/\nu\kappa$
Re = Reynolds number, $U_0h/2\nu$
Ri = Richardson number, $-g\beta\Delta Th/16U_0^2$
t = dimensionless time
T = temperature
T_0 = bottom plate temperature at $x' = 0$
T_1 = temperature at bottom plate
T_2 = temperature at upper plate
U = velocity in the x'-direction
U_0 = maximum velocity in the unperturbed flow
u, v, w = dimensionless velocity perturbations in the x, y, and z-directions (after equation (9), these denote z-functions)
x, y, z = dimensionless rectangular coordinates
$|\ |$ = determinant or absolute value
$[\ ]$ = matrix
β = coefficient of thermal expansion
ΔT = temperature difference between two plates, $T_1 - T_2$
θ = dimensionless temperature perturbation
κ = thermal diffusivity
λ = wavelength of vortex rolls
μ = parameter, $\mathrm{Re}\,\tau h/\Delta T$
ν = kinematic viscosity
ρ = density
τ = temperature gradient in x'-direction for two plates
ψ = secondary flow stream function
ψ_u = basic velocity profile function
ψ_θ = basic temperature profile function
∇_1^2 = Laplacian operator in $x'y'$-plane

Superscripts and Subscripts

$'$ = disturbance quantities, differentiation with respect to z or dimensional quantities
$*$ = critical value
b = basic quantities in unperturbed state
m, n = integers
x, y = in corresponding directions

horizontal parallel plates due to buoyancy. The bottom and top plates are assumed to be at different temperature levels and each changes linearly in the direction of main flow. This wall temperature condition appears to be realized on thin broad fins found in some types of heat exchangers.

The stability of horizontal parallel flow under effect of buoyancy has been studied theoretically and experimentally by many investigators. Gill and del Casal [1][1] made the analysis for the effect of variable viscosity and buoyancy on two-dimensional velocity profiles and gave a qualitative discussion for the stability of flow in view of the Tollmien-Schlichting theory. However, they did not consider the vortex-type secondary flow. In experiments longitudinal vortex rolls were observed by Terada, et al. [2] in liquid flow with free upper surface, by Terada and Tamano [3], Mori and Uchida [4] in Poiseuille flow, and by Chandra [5], Bénard and Avsec [6], and Brunt [7] in plane Couette flow. Those vortex rolls can be regarded as an infinitely elongated form of convection cells which are familiar in the Bénard problem. Basic temperature profile prior to the onset of convection induces a potential of instability in either a forced flow or a fluid layer. When the bottom and top plates are kept at different temperatures but uniform on each plate, the basic temperature profile becomes linear in the fully developed region of flow. This is the same form as was found in the classical Bénard problem. When we follow the linearized theory, we find that equations for thermal stability in a forced flow are essentially the same as those for the Bénard problem. Therefore, the critical value of Ra (based on the temperature difference and the distance between two plates) is given as 1708. Using this wall temperature condition, Kuo [8], Deardorff [9], Gallagher and Mercer [10], and Ingersoll [11], studied theoretically the effect of shear on thermal stability in plane Couette flow. They examined the stability against disturbances whose wave front is at any angle to the direction of flow, and showed that longitudinal vortex rolls occur at 1708 which is independent of the presence of shear, and is the lowest among the critical values of Ra. Very recently Gage and Reid [12] made an analysis for plane Poiseuille flow, and presented a Ra-Re diagram showing under what conditions longitudinal vortex rolls have priority over other secondary motions.

In the present problem the wall temperature gradient along the main flow yields a nonlinear basic temperature distribution. This nonlinearity is increased by the wall temperature gradient, the velocity of flow, and the Prandtl number. In a quiescent horizontal fluid layer, nonlinear basic temperature profile may result from internal heat sources. In this respect the stability problem considered in this paper is analogous to that for heat generating fluid layer. Sparrow, Goldstein, and Jonsson [13] applied the polynomial expansion method to the perturbation equation and obtained the stability criteria for heat-generating fluid layer between two rigid boundaries with fixed temperatures. The results by the linear theory show that the parabolic part of basic temperature profile decreases the stability. More recent theoretical and experimental developments for the heat-generating-layer problem can be found in the literature [14–18]. In view of these works, though some of them were done under different boundary conditions, one can expect in the present problem that stability criteria and mode of convection motion are influenced by the nonlinearity of basic temperature profile. It should be noted also that there is an effect of basic velocity profile on the stability which is not observed in a forced flow with linear basic temperature or heat-generating fluid layer. The present study provides new data on the stability criteria for plane Poiseuille flow which have been studied so far only under the isothermal condition or the condition of uniform but different temperatures at the top and bottom plates. As far as the authors are aware, no attempt has been made in the past to find the stability criteria for the present problem. In this study we follow the linear theory assuming that

[1] Numbers in brackets designate References at end of paper.

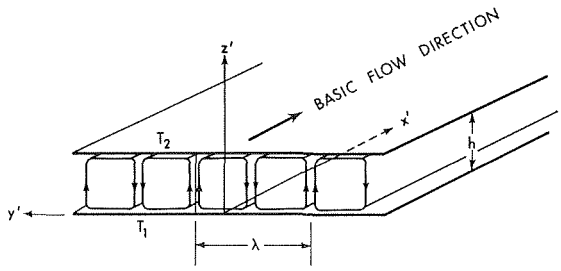

Fig. 1 System of coordinates

1 Velocity and temperature profiles are fully developed.
2 Boussinesq approximation can be applied.
3 Physical properties are constant.

Fundamental Equations

The system of coordinates is shown in Fig. 1 where two infinite horizontal flat plates are located at $z' = 0$ and h, respectively. The wall temperature on the bottom and top plates are given as

$$T_1 = T_0 + \tau x' \quad \text{and} \quad T_2 = T_0 - \Delta T + \tau x' \tag{1}$$

respectively, where T_0 is reference temperature, ΔT temperature difference between the upper and lower plates, and τ constant temperature gradient in the x'-direction. The fully developed velocity (U) and temperature (T) distributions in the unperturbed state are

$$U_b = 4U_0 \left(\frac{z'}{h}\right)\left[1 - \left(\frac{z'}{h}\right)\right] \tag{2}$$

$$T_b = T_1 - \frac{1}{3}\frac{U_0 \tau h^2}{\kappa}\left(\frac{z'}{h}\right)\left[1 - 2\left(\frac{z'}{h}\right)^2 + \left(\frac{z'}{h}\right)^3\right] - \Delta T\left(\frac{z'}{h}\right) \tag{3}$$

where U_0 is the maximum velocity.

Perturbations are now superimposed on the basic velocity and temperature fields, yielding $U = U_b + u'$, $V = v'$, $W = w'$, $T = T_b + \theta'$ and $p = p_b + p'$, where V and W are velocity components in the y' and z'-directions, respectively, and p_b is the pressure for the unperturbed state. Introducing the nondimensional quantities $(x, y, z) = (x', y', z')/h$, $(u, v, w) = (u', v', w')h/\nu$, $\theta = \theta'/\Delta T$, dimensionless time scale $t = t'\nu/h^2$, Grashof number $\mathrm{Gr} = g\beta\Delta T h^3/\nu^2$, and Reynolds number $\mathrm{Re} = U_0 h/2\nu$, the linearized equations for perturbation components are obtained in the following dimensionless form after eliminating pressure terms.

$$\left(\frac{\partial}{\partial t} + \mathrm{Re}\,\psi_u \frac{\partial}{\partial x} - \nabla^2\right)\nabla^2 w - \mathrm{Re}\,\psi_u'' \frac{\partial w}{\partial x} = \mathrm{Gr}\,\nabla_1^2 \theta \tag{4}$$

$$\left(\frac{\partial}{\partial t} + \mathrm{Re}\,\psi_u \frac{\partial}{\partial x} - \frac{1}{\mathrm{Pr}}\nabla^2\right)\theta = (1 + \mu\,\mathrm{Pr}\,\psi_\theta')w - (\mu/\mathrm{Re})u \tag{5}$$

where

$$\nabla_1^2 \equiv (\partial^2/\partial x^2 + \partial^2/\partial y^2), \qquad \psi_u = 8z(1 - z),$$

$\psi_\theta = (2z/3)(1 - 2z^2 + z^3)$ and prime denotes differentiation with respect to z. The characteristic parameter $\mu = \mathrm{Re}\,\tau h/\Delta T$ represents the effect of longitudinal temperature gradient, and $\mu\,\mathrm{Pr}$ the magnitude of departure of T_b from the linear distribution. The equation for u, though it is used in deriving equation (4), remains to be determined for equation (5). This will be given in a later discussion for longitudinal vortex rolls.

In order to show the region of interest in our study, we consider the following general form of disturbance

$$u = u(z) \exp [i(a_x x - \text{Re } ct) + ia_y y] \quad (6)$$

$$w = w(z) \exp [i(a_x x - \text{Re } ct) + ia_y y] \quad (7)$$

$$\theta = \theta(z) \exp [i(ax_x - \text{Re } ct) + ia_y y] \quad (8)$$

where a_x and a_y are wave numbers in the x and y-directions, respectively, and c is a complex quantity divided by Re where the imaginary part is related to the growth rate and the real part to the phase speed. Substituting equations (6)–(8) into equations (4) and (5), we find

$$[(D^2 - a^2) - i \text{ Re } (a_x\psi_u - c)](D^2 - a^2)w + ia_x \text{ Re } \psi_u''w = a^2 \text{ Gr } \theta \quad (9)$$

$$\left[\frac{1}{\text{Pr}} (D^2 - a^2) - i \text{ Re } (a_x\psi_u - c)\right]\theta = -(1 + \mu \text{ Pr } \psi_\theta')w + \frac{\mu}{\text{Re}} u \quad (10)$$

where $a = (a_x^2 + a_y^2)^{1/2}$, $D \equiv (d/dz)$, and (z) is now dropped from the expressions for u, w, and θ.

1 The equations for the longitudinal vortex rolls are obtained by setting $a_x = 0$. It is clear that the basic velocity profile function ψ_u has no direct influence on the hydrodynamic equation (9). However, the effect of ψ_u appears through u in the energy equation (10). The equation for u is now given as

$$[(D^2 - a^2) + i \text{ Re } c]u = \text{Re } \psi_u'w \quad (11)$$

where the pressure gradient in the x-direction is held constant at the value for the unperturbed state ($\partial p'/\partial x' = 0$). The interference of ψ_u with perturbed temperature field is inherent in the present problem since $\mu \neq 0$, but it diminishes as $\mu \to 0$.

The ratio of convection to conduction contribution in the basic temperature field is represented by μ Pr. When $\mu \to 0$, equations (9) and (10) reduce to the equations for the classical Bénard problem. Under the condition of uniform but different wall temperatures, the critical Rayleigh number Ra* (Ra $\equiv$ Gr Pr) is given as Ra* = 1708 regardless of the presence of forced flow.

2 For transverse roll-type disturbances, we set $a_y = 0$. It can then be seen that equation (9) reduces to the Orr-Sommerfeld equation when Re $\gg a_x$ Gr.

3 When $a_x \neq 0$, $a_y \neq 0$, the disturbances are three-dimensional. If a_x Re $\gg a^2$ Gr, the problem becomes purely hydrodynamical, and reduces to a two-dimensional problem [case (2)] under Squire's transformation. The analyses for the case a_x Re $\sim a^2$ Gr, $\mu = 0$ and Couette flow can be found in the literature [8–11]. The results for stability criteria show that the flow is more stable for three-dimensional disturbances than for the disturbance of type 1 in certain regions of Re. Gage and Reid [12] showed for the case of plane Poiseuille flow with $\mu = 0$ that Squire's theorem is still valid when $T_2 > T_1$ and Pr = 1. They also pointed out that longitudinal vortex rolls are the most probable in the region Ri $< -0.92 \times 10^{-6}$, where Ri is the Richardson number defined as $-g\beta\Delta Th/16U_0^2$. The limiting case Re $\to 0$, $\mu \to 0$ yields the classical Bénard problem where three-dimensional convection cells are a subject of interest.

In the present study it is desired to find out the criteria of marginal stability for longitudinal vortex rolls which are considered to be most important among various types of secondary motion in some regions of Re. From equations (9)–(11), setting $c = a_x = 0$, we obtain

$$(D^2 - a^2)^2 w = a^2 \text{ Gr } \theta \quad (12)$$

$$\frac{1}{\text{Pr}} (D^2 - a^2)\theta = -(1 + \mu \text{ Pr } \psi_\theta')w + \frac{\mu}{\text{Re}} u \quad (13)$$

$$(D^2 - a^2)u = \text{Re } \psi_u'w \quad (14)$$

or denoting Ra $\equiv$ Gr Pr (Rayleigh number),

$$(D^2 - a^2)^4 w = -a^2 \text{ Ra } [(D^2 - a^2) + \mu L]w \quad (15)$$

where

$$Lw \equiv \text{Pr } (D^2 - a^2)(\psi_\theta' w) - \psi_u' w = 2\left[4(1 + \text{Pr})(2z - 1) - 8 \text{ Pr } z(1 - z)D + \frac{1}{3} \text{ Pr } (1 - 6z^2 + 4z^3)(D^2 - a^2)\right] w \quad (16)$$

Boundary conditions are

$$w = Dw = \theta = u = 0 \quad \text{at} \quad z = 0 \text{ and } 1 \quad (17)$$

Correspondingly, for equation (15)

$$w = Dw = (D^2 - a^2)^2 w = (D^2 - a^2)^3 w = 0 \quad \text{at} \quad z = 0 \quad \text{and} \quad 1 \quad (18)$$

Method of Solution

In view of the considerable complexity of equations (12)–(14) or (15)–(16), the numerical technique employed by Sparrow, et al. [13], for the fluid layer problem seems to be most powerful for our purpose. The unknown function w in equation (15) is now expressed in the following power series

$$w = \sum_{n=0}^{\infty} \frac{A_n}{n!} z^n \quad (19)$$

where A's are constant coefficients. Applying the boundary conditions (18) at $z = 0$, we obtain

$$A_0 = A_1 = 0, \qquad A_4 = 2a^2 A_2, \qquad A_6 = 3a^4 A_2 \quad (20)$$

Substitution of equation (19) into equations (15) and (16) yields the following recursion formula for $A_n (n \geq 8)$ after equating the coefficients of z^n.

$$A_{m+8} = 4a^2 A_{m+6} - 6a^4 A_{m+4} + [4a^6 - a^2 \text{ Ra } (1 + 2 \text{ Pr } \mu/3)]A_{m+2} - [a^8 - a^4 \text{ Ra } + 8 \text{ Pr } \mu a^2 \text{ Ra } \{-(1 + 1/\text{Pr}) - 2m - a^2/12 - m(m - 1)/2\}]A_m - 16 \text{ Pr } \mu a^2 \text{ Ra } [(1 + 1/\text{Pr})m + m(m - 1) + m(m - 1)(m - 2)/6]A_{m-1} - 4m(m - 1) \text{ Pr } \mu a^4 \text{ Ra } A_{m-2} + (8m/3)(m - 1)(m - 2) \text{ Pr } \mu a^4 \text{ Ra } A_{m-3} \quad (21)$$

Now in equation (19), the four constants A_2, A_3, A_5, and A_7 still remain unknown. The boundary conditions (18) at $z = 1$ provide the following homogeneous algebraic equations for these coefficients.

$$\begin{bmatrix} C_{11} & C_{12} & C_{13} & C_{14} \\ C_{21} & C_{22} & C_{23} & C_{24} \\ C_{31} & C_{32} & C_{33} & C_{34} \\ C_{41} & C_{42} & C_{43} & C_{44} \end{bmatrix} \begin{bmatrix} A_2 \\ A_3 \\ A_5 \\ A_7 \end{bmatrix} = 0 \quad (22)$$

where C_{ij} $(i, j = 1, 2, 3, 4)$ are functions of Pr, μ, a, and Ra as cited in Appendix 1.

The determinant of the coefficient matrix $[c_{ij}]$ must be zero in order that a nontrivial solution exists; thus

$$|C_{ij}| = 0 \quad (23)$$

In order to obtain a set of parameters Pr, μ, a, and Ra satisfying the condition (23), the values for Pr and μ are preassigned, and the relation between a and Ra is sought. Final numerical results are obtained for the minimum value of Ra which gives a critical Rayleigh number with corresponding wave number a for the prescribed values of Pr and μ. All computations are performed by IBM 360 insuring accuracy for the first eigenvalues of Ra such that

$$\epsilon = \frac{|C_{ij}|^{n+5} - |C_{ij}|^n}{|C_{ij}|^{n+5}} < 10^{-5}$$

and for the second eigenvalues $\epsilon < 10^{-4}$.

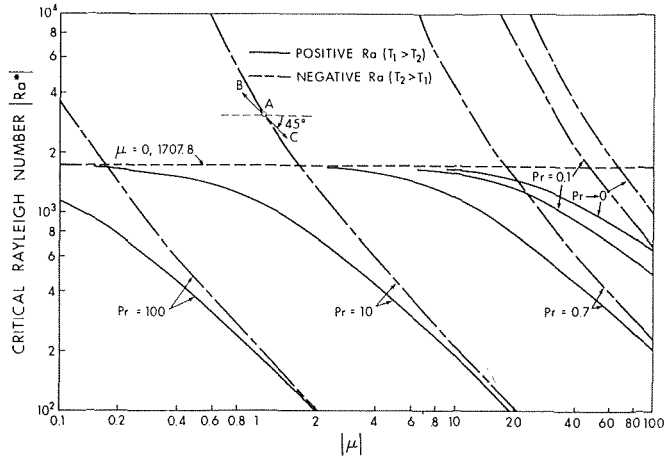

Fig. 2 Stability boundaries for longitudinal vortex rolls

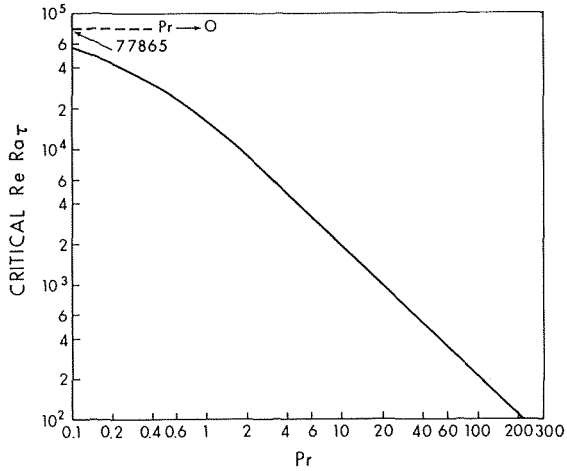

Fig. 3 Stability boundary for the case $\mu \to \infty$

In addition to obtaining numerical results for neutral stability curves, secondary flow streamlines, perturbations of the axial velocity and perturbation temperature are also computed. Secondary flow stream function ψ is defined by $v = \partial\psi/\partial z$, $w = -\partial\psi/\partial y$.

Results and Discussion

The results of stability calculations are shown in Fig. 2. Solid lines represent the case for $T_1 > T_2$ (positive Ra), and broken lines for $T_1 < T_2$ (negative Ra). Detailed numerical results for these curves are listed in Appendix 2. Each curve represents a boundary above which flow is unstable and below which flow is stable. One of the most interesting results is that, if $T_1 > T_2$, the temperature difference ΔT required for the onset of secondary flow decreases as the main flow velocity and the temperature gradient τ are increased. The cause of the decrease in stability comes partly from the nonlinear basic temperature profile and partly from the effect of disturbance component u which is brought into the present problem by the presence of temperature gradient τ and the main flow U. The effect of the nonlinear basic temperature profile is in qualitative agreement with that found in a heat-generating fluid layer discussed by Sparrow, et al. [13]. The effect of the parabolic part of basic temperature profile is more pronounced with increase in Pr; thus a flow with large Pr is more unstable than one with small Pr. All solid curves converge to the value 1708 as $\mu \to 0$. From observation of equations (12)–(16), it can be seen that the role of disturbance u becomes significant when Pr $\lesssim 1$. This effect of u will never be found in problems where there is no temperature gradient ($\tau = 0$) or no main flow.

The curves for the limiting case Pr $\to 0$ are also shown in Fig. 2. In this case the basic temperature profile is governed solely by the wall temperature condition so as to cause linear variations in both the z and x-directions. In case of $T_1 > T_2$, instability is due to both adverse temperature gradient in the z-direction and the presence of τU (in nondimensional form μ), whereas in case of $T_1 < T_2$ the only cause of instability is τU. These limiting cases are unrealistic, nevertheless they confirm that the effect of μ through the disturbance u does decrease stability. It should be noted that u is closely related to the basic velocity profile as shown in equation (14).

When we fix the product τU_0 and change ΔT, a point representing the flow condition moves along a straight line whose downward direction makes an angle of 45 deg with the positive direction of the abscissa. (See the line B-A-C in Fig. 2.) As $|\mu|$ increases, every curve approaches asymptotically to a 45-deg straight line. This means that the stability criteria now become independent of ΔT as $|\mu| \to \infty$, and are determined by the product of Re and Rayleigh number based on τ

$$\mathrm{Ra}_\tau = g\beta\tau h^4/\kappa\nu.$$

In Fig. 3, the critical numbers of the parameter Re Ra$_\tau$ are shown against Pr for the case $|\mu| \to \infty$. Infinite $|\mu|$ may be realized by zero temperature difference between the two plates ($\Delta T = 0$). In this case we have to change the definition of θ to that based on τh. At this point it is noted that the present configuration of fluid passage corresponds to a limiting case of a rectangular channel for which numerical computation was done by Cheng and Hwang [19] for various aspect ratios. According to their calculation under conditions of uniform wall temperature around a circumference and varying linearly in the main flow direction, secondary flow in the central region of the channel diminishes as the aspect ratio (width/height) approaches infinity. The present study reveals that there is a possibility of secondary flow even in the case of infinite aspect ratio.

In the analysis of Cheng and Hwang [19], secondary flow induced by the variation of body forces near the sidewall is actually considered. This type of secondary flow can be found in various ducts and pipes under the effect of body forces. In this case the gradient of the body force F in the y-direction, $\partial F/\partial y$, appears on the right-hand side of equation (12). Since F is a known function of basic velocity or temperature, all the fundamental equations do not yield an eigenvalue problem. Secondary flow is driven by the body force F whenever fluid is moving in a curved channel, or temperature distribution is present. In the present problem, $\partial F/\partial y = 0$, and the cause of secondary flow is the disturbance imparted to the flow. Disturbance may disappear if dissipation effect is predominant. It may develop into a form of vortex rolls due to body forces, or change the flow into a turbulent state, under certain circumstances. The condition for a discrete change of flow pattern can be determined as a solution of eigenvalue problem. The case of vanishing gradient, $\partial F/\partial y = 0$ where F is buoyancy, can also be produced by specific wall temperature condition in a duct such as a rectangular channel with finite aspect ratio. Stability problem for such a case was discussed by Sherman [20] recently.

As we reverse the wall temperature condition such that $T_2 > T_1$ and increase $|\Delta T|$, the critical point moves upward along a broken line as shown in Fig. 2. It can be easily seen that an increase in $|\Delta T|$ for a given τU_0 brings flow to the stable side ($A \to B$) whereas a decrease in $|\Delta T|$ brings flow to the unstable side ($A \to C$). This result is intuitively correct, since the increase in $|\Delta T|$ makes a positive contribution to the stable structure of flow when $T_2 > T_1$. At the values of μ which give completely stable structure (no adverse temperature gradient in the fluid), the broken lines approach infinity.

In Fig. 4 the relation between critical wave number a and μ is shown together with the values of a for a limiting case $|\mu| \to \infty$ with Pr as a parameter. As Pr $\to 0$, the trend of the curves for

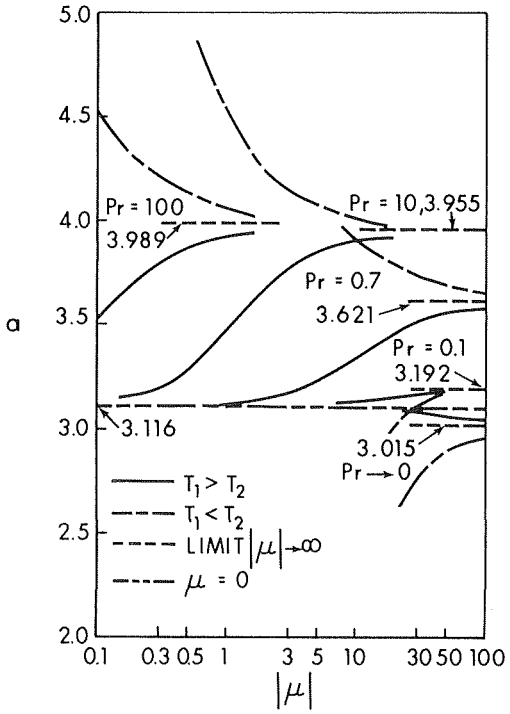

Fig. 4 Critical wave number versus μ

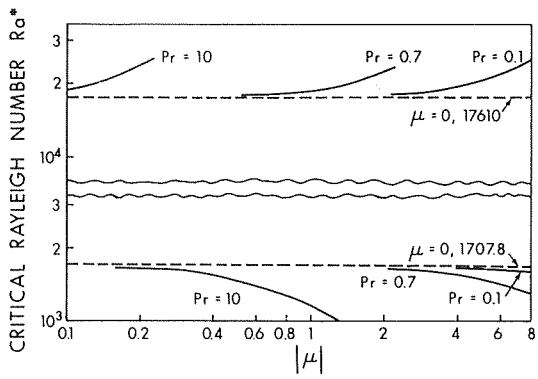

Fig. 5 Second critical eigenvalues of Ra

$T_1 \gtrless T_2$ becomes opposite to that for a high Pr. This is due to the effect of μ through disturbance component u. In the case of $a \lesssim 4.5$, vortex rolls are singly laid between the plates; whereas for $a \gtrsim 4.5$, secondary motion forms double vortex rolls as shown in Fig. 6(c). Similar double structure is known from Taylor's experiments [21] for rotating cylinders and also from the theoretical work by Debler [14] for a heat-generating fluid layer problem. Within the range of the present study this phenomenon is found only for the case $T_1 < T_2$.

From equation (23), the second critical eigenvalues of Ra for the case $T_1 > T_2$ are computed. These values are represented by the upper curves for three selected values of Pr in Fig. 5 to show that they are much larger than the first eigenvalues represented by the lower curves, and this tendency becomes more pronounced as μ increases. The second critical values may have no practical importance because they are derived on the assumption of Poiseuille flow. The basic flow and temperature fields differ considerably from the Poiseuille flow field at a high Ra due to secondary flow which might be set up at the first critical Ra. However, results indicate that we may expect a flow pattern, determined solely from the first eigenfunction, to exist in some regions of Ra near the first critical values, though nonlinear terms may play some role in the fundamental equations at high Ra.

Figs. 6(a–c) show secondary flow streamlines and isothermal lines of perturbation temperature for typical cases. The values of ψ and θ are those obtained by setting $-A_2/a = 1$. This normalization corresponds to setting the coefficient of a leading term in the series expansion of ψ unity. [Note: $\psi = -\sin ay\{(A_2/a)z^2/2! + (A_3/a)z^3/3! + \ldots\}$.] Isothermals have only one eye when there is no maximum basic temperature in the fluid, otherwise two eyes exist. The center of vortices moves downward as μ increases for the case $T_1 > T_2$; but very gradually. For the case $T_2 > T_1$, the movement of vortex center is opposite. Fig. 6(c) shows double vortex structure. In Fig. 7, the perturbations of the axial component of velocity on the line A-A (see a cross-sectional view in the figure) are shown for several combinations of Pr and μ.

Finally, for the completeness of the present study, it is necessary to show the region of parameters (Re, Ra_τ, Ra) where the longitudinal vortex rolls may exist. As a measure, the critical value of Re (= 5400) for two-dimensional Tollmien-Schlichting waves is compared with the stability criteria based on buoyancy effect in Fig. 8 for air (Pr of 0.7). When a point representing the hydrodynamic (Re) and thermal (Ra, Ra_τ) conditions of a flow is in the region below $\mathrm{Re}^* = 5400$ but above the slant straight line for a given value of μ, then the flow is considered to be unstable, predominantly for the vortex rolls. Gage and Reid [12]

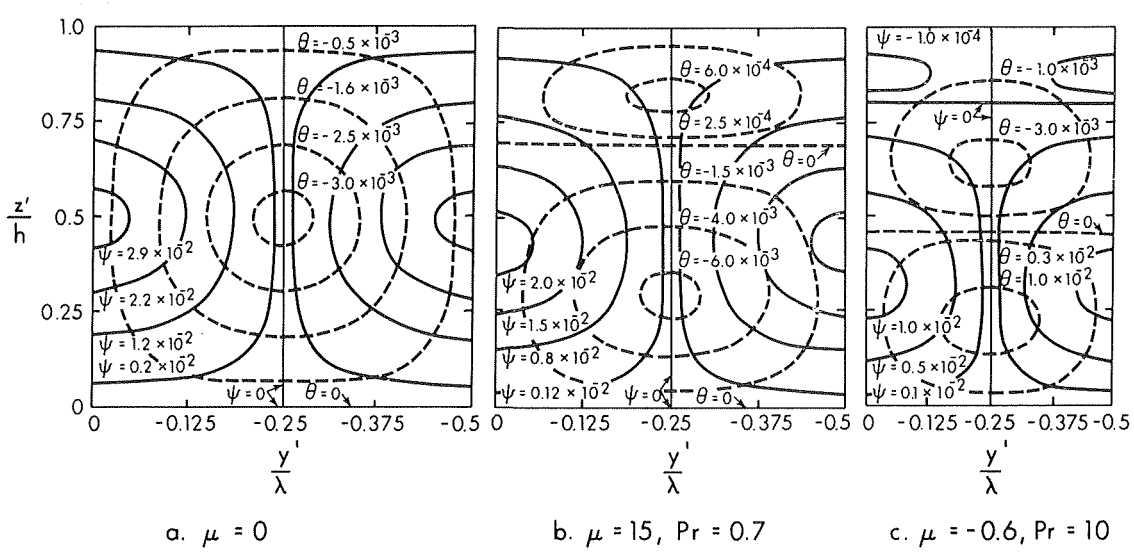

Fig. 6 Secondary flow streamlines and isothermals of perturbation temperature

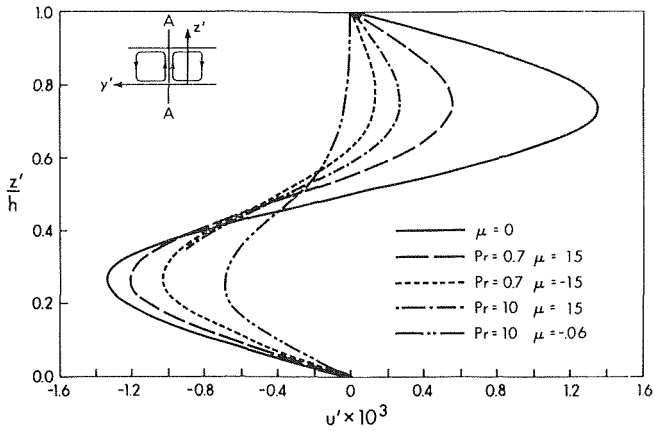

Fig. 7 Perturbations of axial velocity component

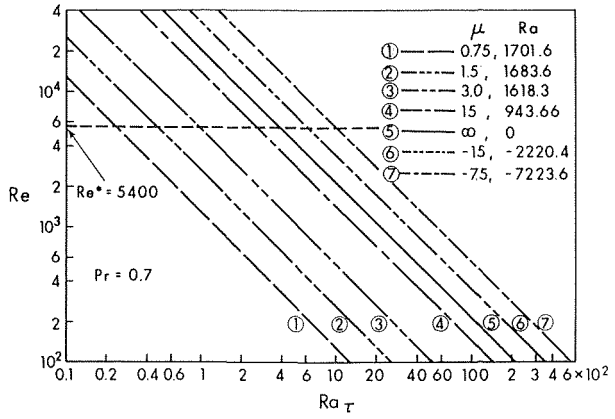

Fig. 8 Comparison of thermal instability with hydrodynamic instability

pointed out that the critical Reynolds number for the *T-S* waves is also influenced by thermal structure of flow. Their results show that the critical Re increases as stable structure ($T_2 > T_1$) is enhanced. Thus the comparison in Fig. 8 is only tentative. A more convenient comparison can be made by using Richardson number which is related to the other parameters by $\mathrm{Ri} = -\mathrm{Ra}/64\ \mathrm{Re}^2\ \mathrm{Pr}$. According to the analysis in reference [12] for the case $T_1 > T_2$, Pr = 1, and $\mu = 0$, in the region $\mathrm{Ri} < -0.92 \times 10^{-6}$ the longitudinal vortex rolls are more probable than *T-S* waves. This criterion is clearly influenced by the presence of μ as shown in Table 1 where Pr is taken as 0.7. It is also seen that at extremely low Re there is a possibility of transverse or three-dimensional vortex rolls as observed by Chandra [5] in a plane Couette flow.

The assumption of fully developed laminar flow should also be examined carefully, since instability in the entrance region might be significant under certain circumstances. It may be reasonable to assume that steep temperature gradient in the boundary layer near the entrance region may cause secondary motion. However, when the influence of this secondary motion on the fully developed basic velocity and temperature fields is negligibly small, and the growth or decay of the motion is dependent on the thermal structure of fully developed region, the present results are considered to be sufficiently valid. Therefore the validity of the present analysis depends on the growth rate of disturbance in the entrance region. At the present stage of theoretical investigation, further studies are required to determine under what conditions the instability of the entrance region may influence the stability of the whole region of flow.

Table 1 Critical values of Ri ($\Delta T > 0$) below which longitudinal vortex rolls have priority of appearance over the *T-S* waves (Pr = 0.7)

μ	0	10	100	∞
$\mathrm{Ri}^* \times 10^6$	−1.3	−0.91	−0.15	0

Acknowledgment

This work was partly supported by the National Research Council of Canada through Grant NRC A-1655. The first author (W. Nakayama) wishes to thank the Department of Mechanical Engineering, University of Alberta, for postdoctoral fellowship. The second author (G. J. Hwang) is indebted to the National Research Council of Canada for postgraduate scholarship. The authors also wish to thank Miss Helen Wozniuk for her excellent typing of the manuscript and Mrs. Evelyn Buchanan for her contribution to the editorial revision of the original manuscript.

References

1 Gill, W. N., and del Casal, E., "A Theoretical Investigation of Natural Convection Effects in Forced Horizontal Flows," *AIChE Journal*, Vol. 8, 1962, pp. 513–518.

2 Terada, T., and Second Year Students of Physics, "Some Experiments on Periodic Columnar Forms of Vortices Caused by Convection," report of the Aeronautical Research Institute, Tokyo University, Vol. III, 1, No. 1, Jan. 1928.

3 Terada, T., and Tamano, M., "Further Researches on Periodic Columnar Vortices Produced by Convection," report of the Aeronautical Research Institute, Tokyo University, Vol. IV, 12, No. 53, Dec. 1929.

4 Mori, Y., and Uchida, Y., "Forced Convective Heat Transfer Between Horizontal Flat Plates," *International Journal of Heat and Mass Transfer*, Vol. 9, 1966, pp. 803–817.

5 Chandra, K., "Instability of Fluids Heated From Below," *Proceedings, Royal Society*, London, Series A, Vol. 164, 1938, pp. 231–242.

6 Bénard, H., and Avsec, D., "Travau récents sur les tourbillons cellulaires et les tourbillons en bandes applications a lástrophysique et a la météorologie," *Journal de Physique*, No. 11, 1930, pp. 486–500.

7 Brunt, D., "Experimental Cloud Formation," *Compendium of Meteorology*, American Meteorological Society, 1951, pp. 1255–1262.

8 Kuo, H. L., "Perturbation of Plane Couette Flow in Stratified Fluid and Origin of Cloud Streets," *Physics of Fluids*, Vol. 6, 1963, pp. 195–211.

9 Deardorff, J. W., "Gravitational Instability Between Horizontal Plates With Shear," *Physics of Fluids*, Vol. 8, 1965, pp. 1027–1030.

10 Gallagher, A. P., and Mercer, A. M., "On the Behavior of Small Disturbances in Plane Couette Flow With a Temperature Gradient," *Proceedings, Royal Society*, London, Series A, Vol. 286, 1965, pp. 117–128.

11 Ingersoll, A. P., "Convective Instabilities in Plane Couette Flow," *Physics of Fluids*, Vol. 9, 1966, pp. 682–689.

12 Gage, K. S., and Reid, W. H., "The Stability of Thermally Stratified Plane Poiseuille Flow," *Journal of Fluid Mechanics*, Vol. 33, 1968, pp. 21–32.

13 Sparrow, E. M., Goldstein, R. J., and Jonsson, V. K., "Thermal Instability in a Horizontal Fluid Layer: Effect of Boundary Conditions and Nonlinear Temperature Profile," *Journal of Fluid Mechanics*, Vol. 18, 1964, pp. 513–528.

14 Debler, W. R., "On the Analogy Between Thermal and Rotational Hydrodynamic Stability," *Journal of Fluid Mechanics*, Vol. 24, 1966, pp. 165–176.

15 Roberts, P. H., "Convection in Horizontal Layers With Internal Heat Generation Theory," *Journal of Fluid Mechanics*, Vol. 30, 1967, pp. 33–49.

16 Tritton, D. J., and Zarraga, M. N., "Convection in Horizontal Layers With Internal Heat Generation. Experiments," *Journal of Fluid Mechanics*, Vol. 30, 1967, pp. 21–31.

17 Watson, P. M., "Classical Cellular Convection With a Spatial Heat Source," *Journal of Fluid Mechanics*, Vol. 32, 1968, pp. 399–411.

18 Joseph, D. D., and Shir, C. C., "Subcritical Convective Instability, Part 1. Fluid Layers," *Journal of Fluid Mechanics*, Vol. 26, 1966, pp. 753–768.

19 Cheng, K. C., and Hwang, G. J., "Numerical Solution for Combined Free and Forced Laminar Convection in Horizontal Rectangular Channels," to be published in JOURNAL OF HEAT TRANSFER, TRANS. ASME.

20 Sherman, M., "Convective Instabilities in Fully Developed Flows," JOURNAL OF HEAT TRANSFER, TRANS. ASME, Series C, Vol. 90, 1968, pp. 84–86.

21 Taylor, G. I., "Stability of a Viscous Liquid Contained Between Two Rotating Cylinders," *Philosophical Transactions*, Series A, Vol. 223, 1923, pp. 289–343.

APPENDIX 1

Elements of matrix $[C_{ij}]$

$$C_{11} = \frac{1}{2} + \frac{2a^2}{4!} + \frac{3a^4}{6!} + K_{1,2}$$

$$C_{12} = \frac{1}{3!} + K_{1,3}$$

$$C_{13} = \frac{1}{5!} + K_{1,5}$$

$$C_{14} = \frac{1}{7!} + K_{1,7}$$

$$C_{21} = 1 + \frac{2a^2}{3!} + \frac{3a^4}{5!} + K_{2,2}$$

$$C_{22} = \frac{1}{2} + K_{2,3}$$

$$C_{23} = \frac{1}{4!} + K_{2,5}$$

$$C_{24} = \frac{1}{6!} + K_{2,7}$$

$$C_{31} = -\frac{a^4}{2} - \frac{a^6}{4} + K_{3,2}$$

$$C_{32} = -2a^2 + K_{3,3}$$

$$C_{33} = 1 - \frac{a^2}{3} + K_{3,5}$$

$$C_{34} = \frac{1}{3!} - \frac{a^2}{60} + K_{3,7}$$

$$C_{41} = -\frac{3}{2}a^6 + \frac{3}{8}a^8 + K_{4,2}$$

$$C_{42} = 3a^4 + K_{4,3}$$

$$C_{43} = -3a^2 + \frac{a^4}{2} + K_{4,5}$$

$$C_{44} = 1 - \frac{a^2}{2} + \frac{a^4}{40} + K_{4,7}$$

where

$$K_{1,j} = \sum_{n=8}^{m} \frac{B_{n,j}}{n!}$$

$$K_{2,j} = \sum_{n=8}^{m} \frac{B_{n,j}}{(n-1)!}$$

$$K_{3,j} = \sum_{n=8}^{m} \left[\frac{1}{(n-4)!} - \frac{2a^2}{(n-2)!}\right] B_{n,j}$$

$$K_{4,j} = \sum_{n=8}^{m} \left[\frac{1}{(n-6)!} - \frac{3a^2}{(n-4)!} + \frac{3a^4}{(n-2)!}\right] B_{n,j}$$

$$j = 2, 3, 5, 7,$$

and B's are the coefficients in the following equation for $A_n (n \geq 8)$ [c.f. equation (21)].

$$A_n = B_{n,2}A_2 + B_{n,3}A_3 + B_{n,5}A_5 + B_{n,7}A_7$$

Infinite series for K's were terminated when the desired convergence was obtained.

APPENDIX 2

Numerical Results

Pr = 100

μ	a	Ra*
0	3.116	1707.8
0.075	3.399	1322.3
0.225	3.738	699.80
0.525	3.878	346.70
0.75	3.911	250.85
1.5	3.950	130.38
−1.875	4.021	−111.87
−1.125	4.043	−190.38
−0.75	4.069	−293.13
−0.525	4.104	−433.09
−0.225	4.256	−1174.8
−0.15	4.387	−2013.3
−0.075	4.761	−6094.9

Pr = 0.1

μ	a	Ra*
0	3.116	1707.8
3	3.118	1693.0
7.5	3.127	1623.0
15	3.145	1441.9
22.5	3.159	1256.5
30	3.169	1098.4
45	3.179	864.97
60	3.184	708.49
75	3.186	598.43
−75	3.184	−954.09
−52.5	3.173	−1514.8
−37.5	3.151	−2447.0
−26.25	3.098	−4355.3
−18.75	2.988	−8273.1

Pr → 0

μ	a	Ra*
0	3.116	1707.8
7.5	3.113	1661.2
15	3.105	1547.1
26.25	3.091	1341.0
45	3.073	1051.9
75	3.056	762.02
−75	2.947	−1445.9
−52.5	2.907	−2390.4
−37.5	2.844	−4077.9
−30	2.777	−6078.2
−22.5	2.645	−1096.50

Numerical Results

Pr = 10		
μ	a	Ra*
0	3.116	1707.8
0.375	3.221	1568.0
0.75	3.397	1309.3
1.5	3.616	913.62
3	3.775	548.47
4.5	3.830	389.25
7.5	3.881	245.65
11.25	3.906	167.97
15	3.918	127.59
−18.75	3.986	−109.36
−11.25	4.006	−186.05
−7.5	4.031	−286.34
−5.25	4.064	−422.83
−3.75	4.107	−618.79
−3	4.145	−804.18
−2.25	4.208	−1144.4
−1.5	4.331	−1957.7
−1.125	4.451	−2982.7
−0.75	4.683	−5894.1
−0.675	4.760	−7205.5
−0.6	4.858	−9164.4

Pr = 0.7		
μ	a	Ra*
0	3.116	1707.8
1.5	3.128	1683.6
3	3.160	1618.3
5.25	3.223	1478.6
7.5	3.284	1329.0
15	3.415	943.66
30	3.510	575.38
45	3.546	410.98
60	3.564	319.20
75	3.576	260.81
−75	3.667	−309.83
−52.5	3.687	−459.59
−37.5	3.712	−676.76
−30	3.735	−884.47
−22.5	3.770	−1271.0
−18.75	3.798	−1620.4
−15	3.836	−2220.4
−11.25	3.891	−3462.0
−7.5	3.962	−7223.6
−6.75	3.973	−9022.1

Critical Second Eigenvalues

Pr = 10		
μ	a	Ra_{II}*
0	5.365	17610
0.075	5.359	18444
0.1125	5.364	19519
0.1875	5.471	23050
0.225	5.597	25328

Pr = 0.7		
μ	a	Ra_{II}*
0	5.365	17610
0.15	5.366	17636
0.3	5.369	17712
0.45	5.374	17839
0.75	5.392	18252
1.125	5.432	19077
1.5	5.498	20267
2.25	5.741	23703

Pr = 0.1		
μ	a	Ra_{II}*
0	5.365	17610
0.75	5.374	17677
1.5	5.404	17877
3	5.521	18685
5.25	5.840	20941
7.5	6.279	24315

A. FEINGOLD
Professor and Chairman.

K. G. GUPTA
Research Assistant.

Department of Mechanical Engineering,
University of Ottawa,
Ottawa, Ontario, Canada

New Analytical Approach to the Evaluation of Configuration Factors in Radiation From Spheres and Infinitely Long Cylinders

It is shown in this paper that, in the case of radiation from spheres and infinitely long cylinders to a certain class of surfaces, the configuration factors are independent of the validity of Lambert's cosine law. A new technique has been developed to calculate the configuration factors in radiation from spheres and infinitely long cylinders and, with this technique, formulas have been obtained for several geometries for which no solutions have previously appeared in the literature.

Introduction

In the existing literature on radiant-interchange configuration factors, the underlying assumption is that the directional distribution of the emitted radiation follows Lambert's cosine law. It is shown in this paper that, in the case of radiation from spheres to a certain class of surfaces, the configuration factors are independent of the validity of Lambert's law. A new technique is developed to calculate the configuration factors in radiation from spheres, and formulas are obtained for several important geometries. All, except one, have never been solved in closed-form to the best of the knowledge of the present authors. Only the formula for the special case of the factor from sphere to a particularly positioned rectangle appears in the literature.

Extremely simple formulas resulted from the present investigation in certain cases in which the heretofore used methods led to multiple integrals of forbidding complexity which often could only be solved by numerical processes.

Reasoning, similar to the one applied to the spheres, is further extended to infinitely long cylinders. The results prove that two formulas widely reproduced in the literature are incorrect and that the scope of these formulas has, at any rate, not been fully appreciated heretofore. A new closed-form expression is developed for a factor from an infinitely long cylinder to a portion of a nonconcentric cylindrical enclosure.

Contributed by the Heat Transfer Division of The American Society of Mechanical Engineers for publication (without presentation) in the Journal of Heat Transfer. Manuscript received by the Heat Transfer Division, November 7, 1968; revised manuscript received April 21, 1969. Paper No. 69-HT-J.

Radiation From a Sphere to a Coaxial Disk

For the purpose of this paper we shall say that a disk is coaxial with a given sphere when it lies in a plane perpendicular to the line joining its center with the center of the sphere.

Fig. 1 represents a sphere and a projection of the coaxial disk AB.

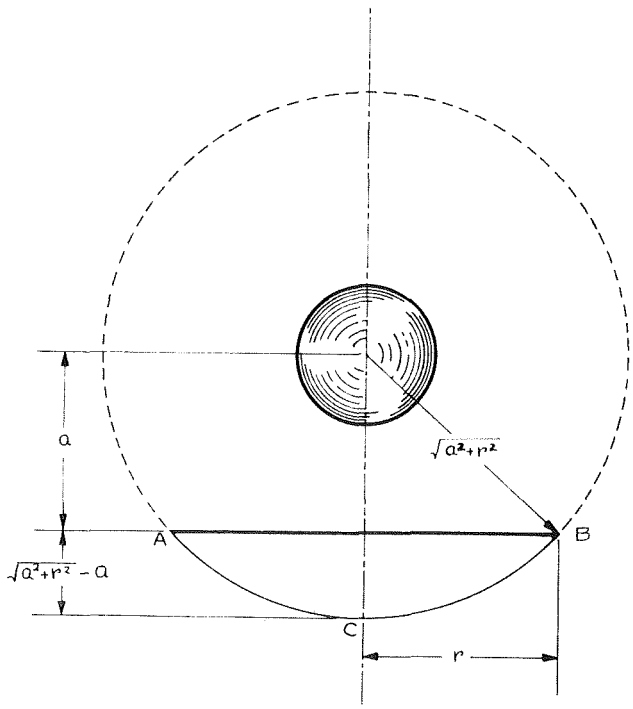

Fig. 1

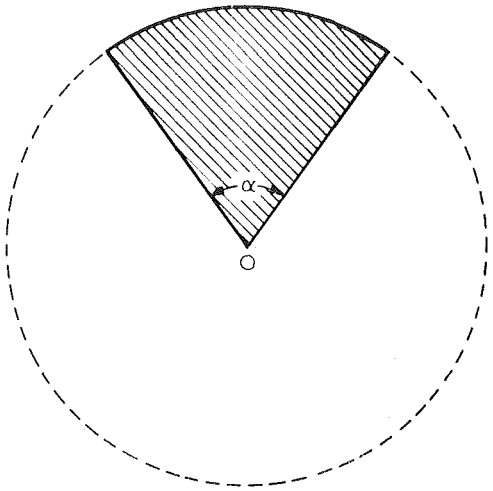

Fig. 2

The factor from the sphere to the disk AB is the same as from the sphere to the hollow spherical surface ACB, provided that AB does not intersect the sphere. This is so because any ray, emanating from any point on the radiating sphere and striking the disk, would necessarily also strike the surface ACB. The opposite is equally true—thus, any ray striking ACB could not come from the radiating sphere without passing through the circle AB. This observation is the keystone of the method developed below.

It must further be observed that the irradiation per unit area on the surface of the outer sphere is the same at every point quite irrespectively of the validity of Lambert's cosine law; provided only that, whatever is the angular distribution of emanating energy, this distribution does not vary throughout the radiating surface. This represents no real restriction, because in most practical cases the surfaces of radiating spheres can be considered homogeneous, while not necessarily behaving in accordance with Lambert's law.

The factor from the radiating sphere to the outer sphere is, obviously, unity. Thus, bearing in mind our previous remarks, we must conclude that the factor from the sphere to the area ACB (and with it the factor from the sphere to the coaxial disk) is equal to the ratio between the area of the spherical segment ACB and the total area of the outer sphere. Thus, the factor from the sphere to the disk is

$$F_{s\text{-}d} = \frac{2\pi\sqrt{a^2 + r^2}\,(\sqrt{a^2 + r^2} - a)}{4\pi(a^2 + r^2)} = \frac{1}{2} - \frac{a}{2\sqrt{a^2 + r^2}} \tag{1}$$

In order to obtain this factor as a function of a dimensionless quantity, let us introduce the ratio $R = r/a$ which may conveniently be called *the relative radius*. After simplification, we obtain

$$F_{s\text{-}d} = \frac{1}{2} - \frac{1}{2\sqrt{1 + R^2}} \tag{1'}$$

For a sector of the disk (see Fig. 2) the factor is

$$F_{s\text{-sector}} = \frac{\alpha}{2\pi}\left[\frac{1}{2} - \frac{a}{2\sqrt{a^2 + r^2}}\right] \tag{2}$$

or

$$F_{s\text{-sector}} = \frac{\alpha}{2\pi}\left[\frac{1}{2} - \frac{1}{2\sqrt{1 + R^2}}\right] \tag{2'}$$

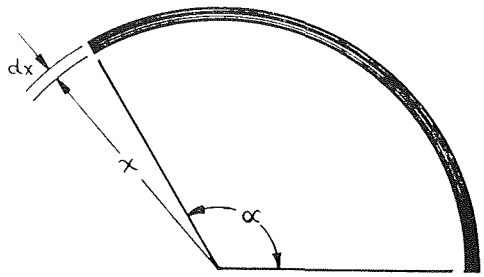

Fig. 3

Radiation From a Sphere to an Infinitesimal, Coaxial Ring

We shall now consider the differential increase in the factor $F_{s\text{-}d}$ as r grows from a value x to $x + dx$. This increase represents the factor from a sphere to an infinitesimal ring of radius x and width dx.

$$dF_{s\text{-inf. }r} = \frac{ax}{2}(a^2 + x^2)^{-3/2}dx \tag{3}$$

For a portion of such a ring subtending an angle α at the center (see Fig. 3), the factor is

$$dF_{s\text{-seg. inf. }r} = \frac{\alpha}{2\pi}\frac{ax}{2}(a^2 + x^2)^{-3/2}dx \tag{4}$$

The dimensionless form of these equations is obtained by defining the ratio $X = x/a$ and substituting aX for x and adX for dx. After simplification, we have

$$dF_{s\text{-inf. }r} = \frac{X}{2}(1 + X^2)^{-3/2}dX \tag{3'}$$

$$dF_{s\text{-seg. inf. }r} = \frac{\alpha}{2\pi}\frac{X}{2}(1 + X^2)^{-3/2}\,dX \tag{4'}$$

Radiation From a Sphere to an Infinitesimal Area Lying in a Plane Which Does Not Intersect the Sphere

It will be useful to consider at this point the factor from a sphere to a unit area on a coaxial ring. This *factor per unit area* is

$$dF_{s\text{-unit area}} = \frac{dF_{s\text{-inf. }r}}{2\pi x dx} = \frac{a}{4\pi}(a^2 + x^2)^{-3/2}$$

Therefore, the factor from sphere to a differential element of area lying in a plane which does not intersect the sphere is

$$dF_{s\text{-}dA_R} = \frac{a}{4\pi}(a^2 + x^2)^{-3/2}dA_R \tag{5}$$

where x is the distance between this element and the perpendicular drawn from the center of the sphere to the plane of this element.

Putting $X = x/a$ and $dA = dA_R/a^2$, we get

$$dF_{s\text{-}dA} = \frac{1}{4\pi}(1 + X^2)^{-3/2}dA \tag{5'}$$

It should now be noted that equation (5′) has been developed from equation (1) through a process which required no reference to Lambert's law and is, therefore, just as independent from this law as equation (1), itself. Further, this independence applies equally to any finite area lying in a plane which does not intersect the sphere.

A digression may be in order at this point in relation to the reciprocity law. It is well known that this law is in general not valid for non-Lambertian surfaces. Since the factors obtained here are valid also for Lambertian surfaces, the reciprocity law will apply, provided only that the surface paired with the sphere follows Lambert's law.

Radiation From a Sphere to a Segment of a Coaxial Disk

Fig. 4 represents the disk AB in Fig. 1, viewed from above. Point O is the projection of the center of the sphere. This projection coincides with the center of the disk.

The angle subtended at O by the shaded ring is $2 \cos^{-1} \frac{h}{x}$. Thus, utilizing equation (4), we obtain

$$F_{s\text{-seg.}} = \int_h^r \frac{2 \cos^{-1} \frac{h}{x}}{2\pi} \frac{ax}{2} (a^2 + x^2)^{-3/2} dx$$

$$= \frac{1}{8} - \frac{a \cos^{-1} \frac{h}{r}}{2\pi \sqrt{a^2 + r^2}} + \frac{1}{4\pi} \sin^{-1} \frac{(a^2 - h^2)r^2 - 2a^2h^2}{(a^2 + h^2)r^2} \quad (6)$$

Equation (6) is transformed to a dimensionless form by the substitutions $R = r/a$ and $H = h/a$.

$$F_{s\text{-seg.}} = \frac{1}{8} - \frac{\cos^{-1} \frac{H}{R}}{2\pi \sqrt{1 + R^2}} + \frac{1}{4\pi} \sin^{-1} \frac{(1 - H^2)R^2 - 2H^2}{(1 + H^2)R^2} \quad (6')$$

It may perhaps be useful to underline the method employed in this section which can be used to an advantage in calculating factors from spheres to other plane areas. The multiple integration, commonly resorted to in the existing literature, has here been replaced by a single integral.

The graphic representation of the dependence of $F_{s\text{-seg}}$ on R and on a ratio $Z = H/R$ is shown in Fig. 5.

Radiation From a Sphere to a Coaxial Rectangle

We shall say that a rectangle is coaxial with a given sphere when it lies in a plane perpendicular to the line joining its center with the center of the sphere.

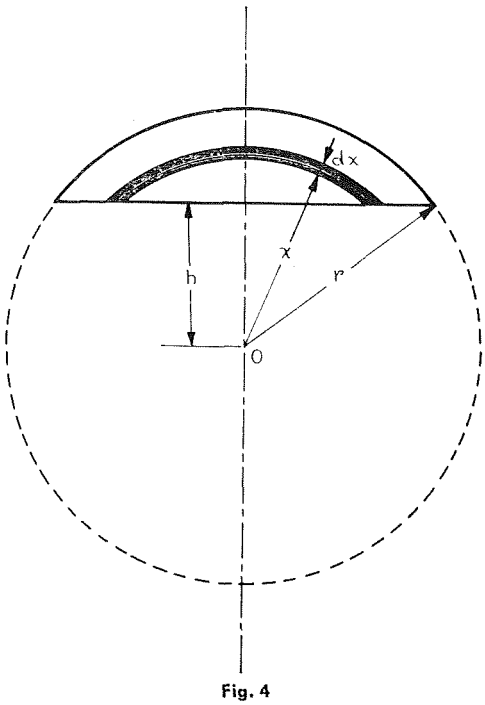

Fig. 4

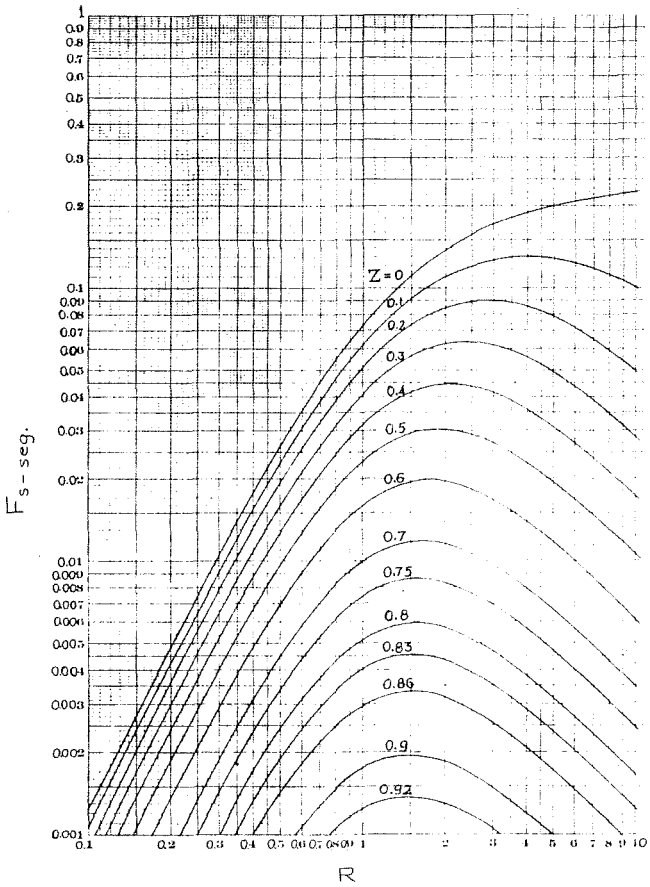

Fig. 5 Configuration factors from a sphere to a segment of a coaxial disk

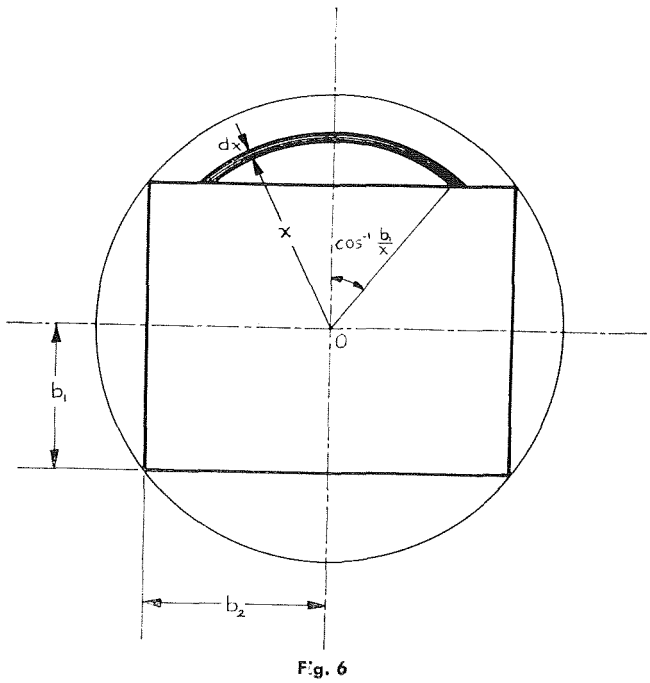

Fig. 6

Fig. 6 represents the view from above of a rectangle measuring $2b_1 \times 2b_2$, which is circumscribed by a circle of radius $\sqrt{b_1^2 + b_2^2}$. The center of the rectangle, O, coincides with the projection of the center of the sphere.

The factor from the sphere to this rectangle can be obtained by subtracting the sum of the factors from the sphere to the four segments from the factor from the sphere to the circle; it can, therefore, be easily calculated with the help of equations (1) and (6).

Thus,

$$F_{s\text{-rect.}} = F_{s\text{-}d} - 2\int_{b_1}^{\sqrt{b_1^2+b_2^2}} dF_{s\text{-seg. inf. }r} - 2\int_{b_2}^{\sqrt{b_1^2+b_2^2}} dF_{s\text{-seg. inf. }r} = \frac{1}{2} - \frac{a}{2\sqrt{a^2+b_1^2+b_2^2}} - 2\int_{b_1}^{\sqrt{b_1^2+b_2^2}} \frac{2\cos^{-1}\dfrac{b_1}{x}}{2\pi}\,\frac{ax}{2}\,(a^2+x^2)^{-3/2}dx - 2\int_{b_2}^{\sqrt{b_1^2+b_2^2}} \frac{2\cos^{-1}\dfrac{b_2}{x}}{2\pi}\,\frac{ax}{2}\,(a^2+x^2)^{-3/2}dx$$

$$= \frac{1}{2\pi}\left[\sin^{-1}\frac{2a^2b_1^2 - (a^2-b_1^2)(b_1^2+b_2^2)}{(a^2+b_1^2)(b_1^2+b_2^2)} + \sin^{-1}\frac{2a^2b_2^2 - (a^2-b_2^2)(b_1^2+b_2^2)}{(a^2+b_2^2)(b_1^2+b_2^2)}\right] \quad (7)$$

After introducing the ratios $B_1 = b_1/a$ and $B_2 = b_2/a$, the nondimensional form of equation (7) becomes

$$F_{s\text{-rect.}} = \frac{1}{2\pi}\left[\sin^{-1}\frac{2B_1^2 - (1-B_1^2)(B_1^2+B_2^2)}{(1+B_1^2)(B_1^2+B_2^2)} + \sin^{-1}\frac{2B_2^2 - (1-B_2^2)(B_1^2+B_2^2)}{(1+B_2^2)(B_1^2+B_2^2)}\right] \quad (7')$$

Equation (7) is equivalent to the expression obtained by Mackey, et al., (1943), for the factor from sphere to a coaxial rectangle. These authors assumed that the size of the sphere is very small as compared to the dimensions of the rectangles. The same factor has later been obtained independently by Wilson, Hwang, and Crank (1962) by means of the usual method of quadruple integration, involving in this case some rather complicated three-dimensional drawings. Their contribution lies in the fact that they have shown that the radius of the sphere does not influence the factor, provided that the plane of the rectangle does not cut the sphere. They have found, thus, that the restriction imposed by Mackey et al. (1943) was unnecessary. However, the conventional approach used by these authors precluded them from discovering that the assumption of validity of Lambert's law is also superfluous.

Radiation From a Sphere to a Coaxial Right Circular Cylinder

Surprisingly simple expression is obtained for the factor from a sphere to a right circular cylinder of length $2a$ and radius r, when the sphere is placed at the center of the cylinder (see Fig. 7).

Because the factor from the sphere to an enclosure containing this sphere is unity, the factor from the sphere to the cylinder can be obtained by subtracting from unity the factors from sphere to the two bases. Using equation (1), we have

$$F_{s\text{-cyl.}} = 1 - 2\left[\frac{1}{2} - \frac{a}{2\sqrt{a^2+r^2}}\right] = \frac{a}{\sqrt{a^2+r^2}} \quad (8)$$

After the transformation $R = r/a$, the factor becomes

$$F_{s\text{-cyl.}} = \frac{1}{\sqrt{1+R^2}} \quad (8')$$

If the sphere and the cylinder are coaxial but not concentric (see Fig. 8), the relevant self-explanatory equation is

$$F_{s\text{-cyl.}} = \frac{1}{2}\left[\frac{a_2}{\sqrt{a_2^2+r^2}} - \frac{a_1}{\sqrt{a_1^2+r^2}}\right] \quad (9)$$

Putting $R_1 = r/a_1$ and $R_2 = r/a_2$, we obtain

$$F_{s\text{-cyl.}} = \frac{1}{2}\left[\frac{1}{\sqrt{1+R_2^2}} - \frac{1}{\sqrt{1+R_1^2}}\right] \quad (9')$$

Radiation From a Sphere to a Polygon

Let us consider an arbitrary n-sided polygon lying in a plane which does not intersect the radiating sphere, e.g., the polygon $ABCDEA$ in Fig. 9. Let point O be projection of the center of the sphere on that plane. This projection can fall either within the polygon, or without. It will be sufficient to examine the latter case, because it is more comprehensive than the former, as will readily be understood from the following analysis.

By joining the corners of the polygon to the point O, we obtain n triangles with a common vertex at that point. The problem is now reduced to the evaluation of the factor from a sphere to an arbitrary triangle with a vertex at O. The factor from the sphere to the polygon will be a simple algebraic sum of n such sphere-to-triangle factors, provided that the factors for the triangles which lie completely outside the polygon are considered negative.

Let the triangle OCD in Fig. 10 be of the aforementioned triangles. We shall now draw two circles with the common center at O and with the respective radii OC and OD. The factor $F_{s\text{-}\Delta OCF}$ (from the sphere to the triangle OCF) can be obtained by subtracting a factor to segment (equation (6)) from a factor to a

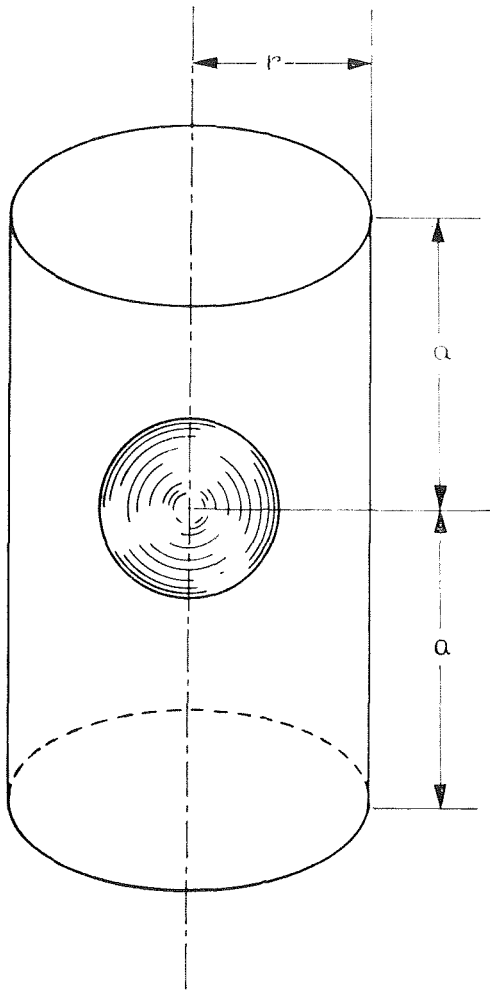

Fig. 7

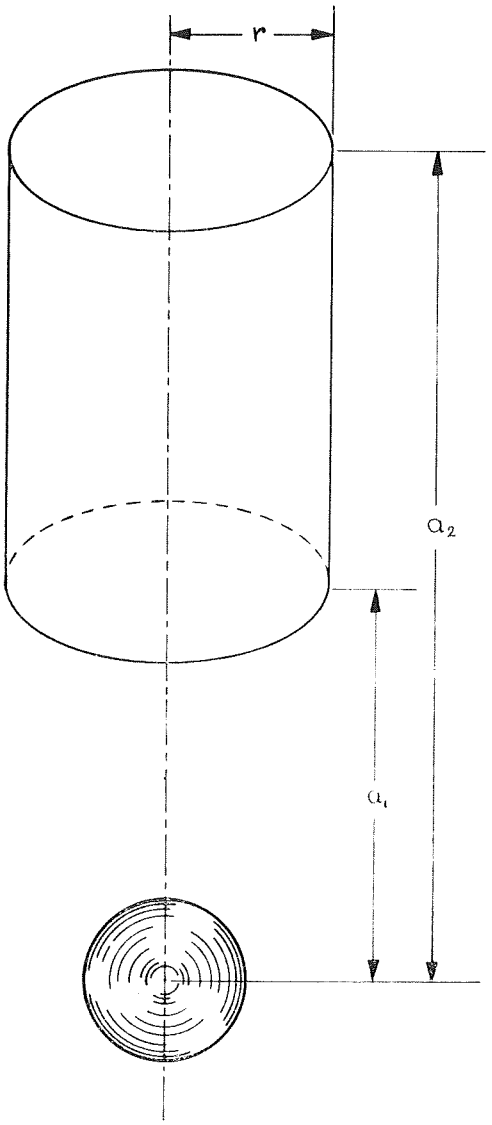

Fig. 8

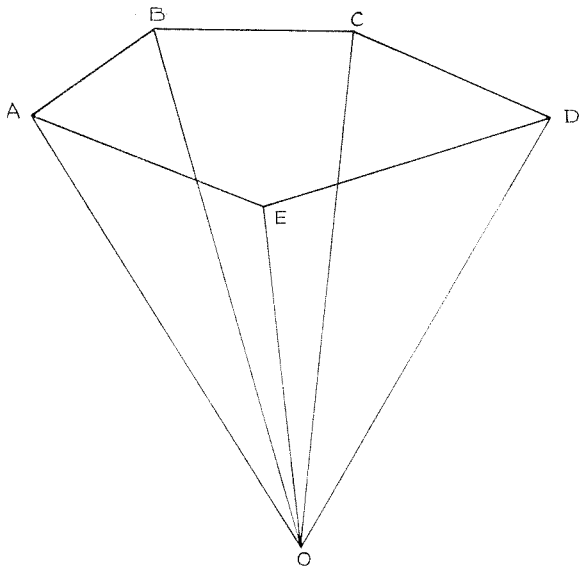

Fig. 9

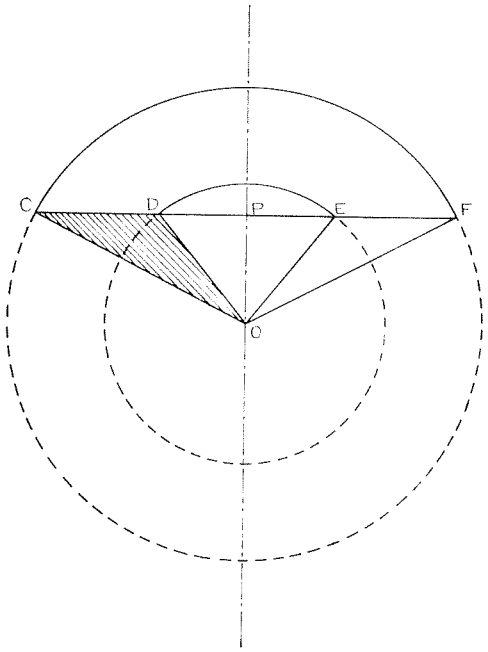

Fig. 10

sector (equation (2)). The same applies to the factor $F_{s\text{-}\Delta ODE}$ (from the sphere to the triangle ODE).

Clearly,

$$F_{s\text{-}\Delta OCD} = \frac{1}{2}\left[F_{s\text{-}\Delta OCF} - F_{s\text{-}\Delta ODE}\right]$$

where

$$F_{s\text{-}\Delta OCF} = \left[\frac{1}{2} - \frac{a}{2\sqrt{a^2 + \overline{OC}^2}}\right]\frac{\cos^{-1}\dfrac{\overline{OP}}{\overline{OC}}}{\pi}$$

$$-\left[\frac{1}{8} - \frac{a\cos^{-1}\dfrac{\overline{OP}}{\overline{OC}}}{2\pi\sqrt{a^2 + \overline{OC}^2}} + \frac{1}{4\pi}\sin^{-1}\frac{(a^2 - \overline{OP}^2)\overline{OC}^2 - 2a^2\overline{OP}^2}{(a^2 + \overline{OP}^2)\overline{OC}^2}\right]$$

$$= \frac{\cos^{-1}\dfrac{\overline{OP}}{\overline{OC}}}{2\pi} - \frac{1}{4\pi}\sin^{-1}\frac{(a^2 - \overline{OP}^2)\overline{OC}^2 - 2a^2\overline{OP}^2}{(a^2 + \overline{OP}^2)\overline{OC}^2} - \frac{1}{8}$$

and

$$F_{s\text{-}\Delta ODE} = \left[\frac{1}{2} - \frac{a}{2\sqrt{a^2 + \overline{OD}^2}}\right]\frac{\cos^{-1}\dfrac{\overline{OP}}{\overline{OD}}}{\pi}$$

$$-\left[\frac{1}{8} - \frac{a\cos^{-1}\dfrac{\overline{OP}}{\overline{OD}}}{2\pi\sqrt{a^2 + \overline{OD}^2}} + \frac{1}{4\pi}\sin^{-1}\frac{(a^2 - \overline{OP}^2)\overline{OD}^2 - 2a^2\overline{OP}^2}{(a^2 + \overline{OP}^2)\overline{OD}^2}\right]$$

$$= \frac{\cos^{-1}\dfrac{\overline{OP}}{\overline{OD}}}{2\pi} - \frac{1}{4\pi}\sin^{-1}\frac{(a^2 - \overline{OP}^2)\overline{OD}^2 - 2a^2\overline{OP}^2}{(a^2 + \overline{OP}^2)\overline{OD}^2} - \frac{1}{8}$$

Therefore,

$$F_{s\text{-}\Delta OCD} = \frac{1}{4\pi}\left[\cos^{-1}\frac{\overline{OP}}{\overline{OC}} - \cos^{-1}\frac{\overline{OP}}{\overline{OD}}\right]$$

$$- \frac{1}{8\pi}\left[\sin^{-1}\frac{(a^2 - \overline{OP}^2)\overline{OC}^2 - 2a^2\overline{OP}^2}{(a^2 + \overline{OP}^2)\overline{OC}^2}\right.$$

$$\left. - \sin^{-1}\frac{(a^2 - \overline{OP}^2)\overline{OD}^2 - 2a^2\overline{OP}^2}{(a^2 + \overline{OP}^2)\overline{OD}^2}\right]$$

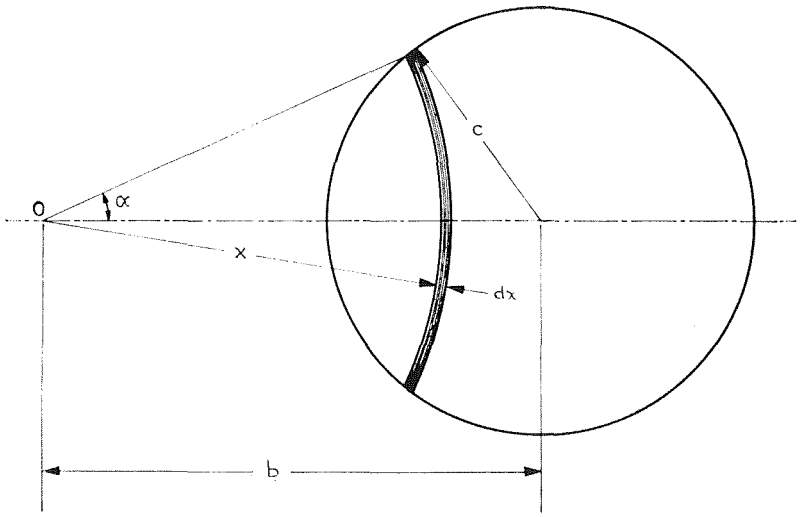

Fig. 11(*a*) $b \geq c$

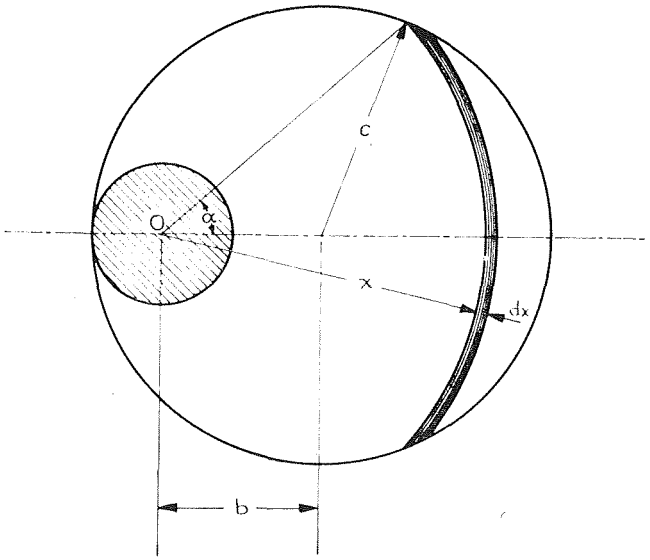

Fig. 11(*b*) $b < c$

Radiation From a Sphere to a Noncoaxial Disk

Point O in Figs. 11(a) and 11(b) is the projection of the center of the radiating sphere and the shaded arcs are drawn with O as their center. Evidently, the whole surface of the disk can be covered by such arcs in Fig. 11(a), but not so in Fig. 11(b). Therefore, the integral of equation (4) with appropriate limits will give us the factor from the sphere to the disk in the former case; while in the latter, another factor (from the sphere to the coaxial disk, shaded in the figure) will have to be added to the integral.

In both figures we have

$$\alpha = \cos^{-1} \frac{x^2 + b^2 - c^2}{2xb}$$

Thus, for $b \geq c$

$$F_{s\text{-noncoax. }d} = \int_{b-c}^{b+c} \frac{\cos^{-1} \dfrac{x^2 + b^2 - c^2}{2xb}}{\pi} \frac{ax}{2} (a^2 + x^2)^{-3/2} dx \tag{10}$$

and, for $b < c$

$$F_{s\text{-noncoax. }d} = \int_{c-b}^{b+c} \frac{\cos^{-1} \dfrac{x^2 + b^2 - c^2}{2xb}}{\pi} \frac{ax}{2} (a^2 + x^2)^{-3/2} dx + \frac{1}{2} - \frac{a}{2\sqrt{a^2 - (c-b)^2}} \tag{11}$$

It can be shown that the equations (10) and (11) lead to elliptic integrals and cannot, therefore, be integrated in terms of elementary functions. It was thought, however, that it may be useful to present in Fig. 12 the numerically computed values of the factor as a function of the dimensionless ratios $Z = b/c$ and $R = c/a$.

Some Special Cases

The radiation from a sphere to a surrounding concentric cube is equally divided among its six sides irrespectively of the validity of Lambert's law. Thus, the factor from a sphere to a coaxial square, the side of which is twice the distance between their centers, must be equal to 1/6. This is in agreement with the result obtained from equation (7′) by putting $B_1 = B_2 = 1$.

Similar things could be said in relation to any other regular polyhedron. An appropriate calculation may provide an interesting exercise.

Radiation From an Infinitely Long Cylinder to an Infinitely Long Parallel Rectangle

The same reasoning employed in the development of equation (1) can be applied to the radiation from an infinitely long cylinder to a parallel, symmetrically placed, infinite rectangle appearing in cross section in Fig. 13.

AB represents the width of the rectangle and ACB is an arc of a circumscribed circle concentric with the cylinder. Provided that AB does not intersect the cylinder, the factor from the radiating cylinder to the rectangle is the same as the factor from this cylinder to the portion ACB of the outer cylinder. Irrespectively of the validity of Lambert's law this factor equals α/π and does not depend on the radius of the radiating cylinder. Because $\alpha = \tan^{-1}(b/a)$, we have

$$F_{\text{cyl.-symm. rect.}} = \frac{1}{\pi} \tan^{-1} \frac{b}{a} \tag{12}$$

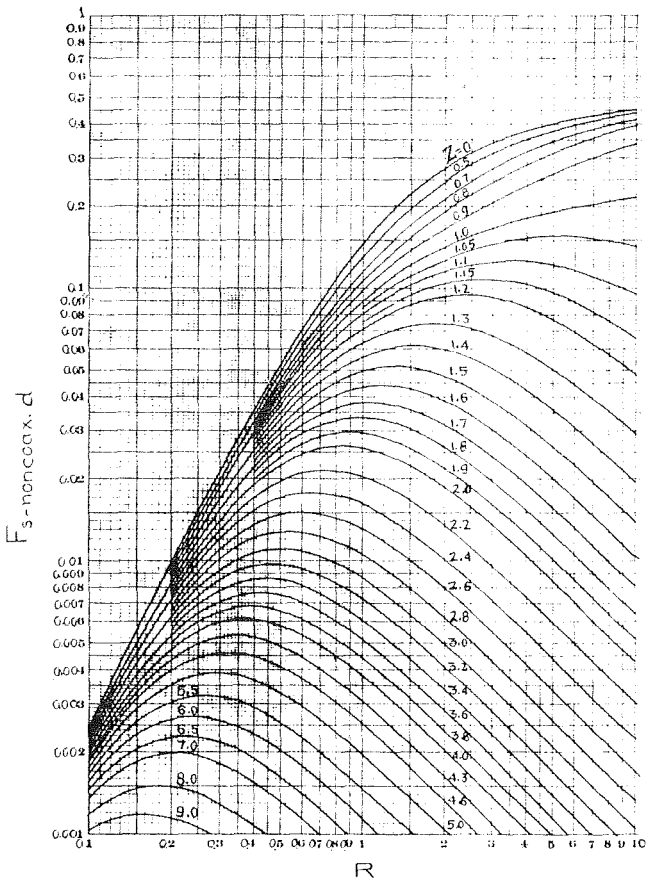

Fig. 12 Configuration factors from a sphere to a noncoaxial disk

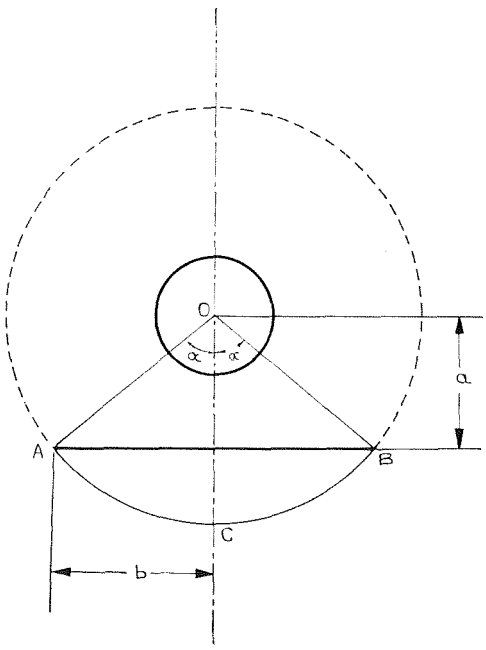

Fig. 13

Putting $B = b/a$

$$F_{\text{cyl.-symm. rect.}} = \frac{1}{\pi} \tan^{-1} B \qquad (12')$$

If the rectangle is not placed symmetrically (see Fig. 14), we obtain through simple subtraction

$$F_{\text{cyl.-nonsymm. rect.}} = \frac{1}{2\pi} \left(\tan^{-1} \frac{b_1}{a} - \tan^{-1} \frac{b_2}{a} \right) \qquad (13)$$

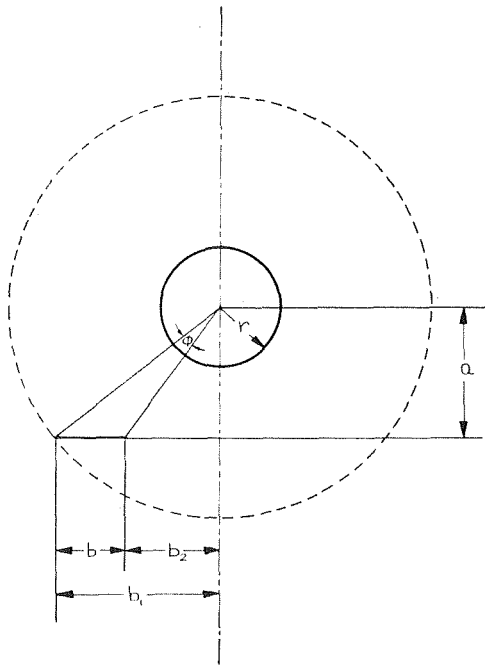

Fig. 14

$$F_{\text{cyl.-nonsymm. rect.}} = \frac{1}{2\pi} (\tan^{-1} B_1 - \tan^{-1} B_2) \qquad (13')$$

It can be seen from Fig. 14 that this factor is simply $\phi/2\pi$. This could have been guessed intuitively, but it is not easy to prove directly.

Assuming now that the rectangle radiates in accordance with Lambert's law, we can apply the reciprocity theorem, and obtain

$$F_{\text{rect.-cyl.}} = \frac{r}{b} \left(\tan^{-1} \frac{b_1}{a} - \tan^{-1} \frac{b_2}{a} \right) \qquad (14)$$

Putting $b = b_1 - b_2$, $R = r/a$, $B_1 = b_1/a$ and $B_2 = b_2/a$, we get

$$F_{\text{rect.-cyl.}} = \frac{R}{B_1 - B_2} (\tan^{-1} B_1 - \tan^{-1} B_2) \qquad (14')$$

The parentheses in this formula have been erroneously omitted by Hamilton and Morgan (1952) and that mistake has been subsequently reproduced in many books, among them the widely used text by Sparrow and Cess (1967). Apart from the error involved, it should be pointed out that in these references the reciprocal factor, from the cylinder to the rectangle, has not been evaluated. Thus, its independence from the radius of the radiating cylinder has not been noted.

In this connection it ought to be mentioned that another formula in Hamilton and Morgan (1952) is mistaken. Fig. 15 is a reproduction from this work. An infinitely long strip of infinitesimal width is denoted by P_2. The factor from this strip to the cylinder is given as

$$F_{P_2-A_1} = \frac{N^2}{N^2 - M^2}$$

This is manifestly wrong, as can be seen by putting $N = M$ which would lead to an infinitely large factor. The correct result can be obtained from equation (12).

Let the width of P_2 be dm.

$$F_{\text{cyl.-rect. of width } m} = \frac{1}{2\pi} \tan^{-1} \frac{m}{n}$$

$$\frac{dF_{\text{cyl.-rect. of width } m}}{dm} = \frac{1}{2\pi \left(1 + \frac{m^2}{n^2} \right) n}$$

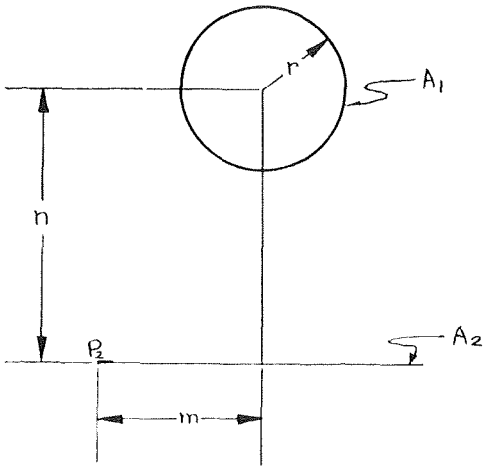

Fig. 15 $M = m/r$, $N = n/r$

But

$$dF_{\text{cyl.-rect. of width } m} = F_{A_1-P_2}$$

Thus

$$F_{A_1-P_2} = \frac{ndm}{2\pi(n^2 + m^2)} \tag{15}$$

Therefore

$$F_{P_2-A_1} = \frac{2\pi r}{dm} F_{A_1-P_2}$$

$$= \frac{rn}{n^2 + m^2}$$

$$= \frac{N}{N^2 + M^2} \tag{16}$$

Again the erroneous result received wide currency, being reproduced, among others, in a book by Wiebelt (1966).

The remarks regarding these errors are made in the interest of the users and should in no way be interpreted as a criticism of the authors involved.

Radiation From an Infinitely Long Cylinder to an Infinitely Long Nonconcentric Cylindrical Enclosure

We shall now use equation (15) as a starting point in our quest for an analytical expression for a factor from the infinitely long inner cylinder shown in Fig. 16 to the portion PQ of the outer cylinder.

Equation (15) represents the factor to an arbitrary infinitely long strip of width dm identified by the variables m and n shown in Fig. 16. But m, dm and n are functions of the angle α. Specifically:

$$m = e \sin \alpha$$

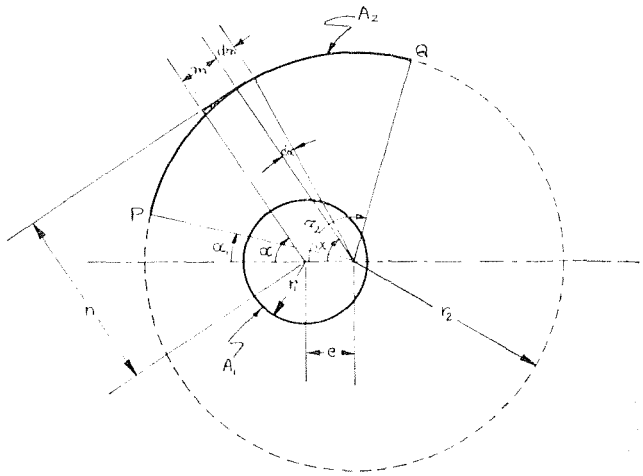

Fig. 16

$$dm = r_2 d\alpha$$

$$n = r_2 - e \cos \alpha$$

where e is the distance between the centers of the two cylinders.

Let dA_2 denote the area of the strip dm. Equation (15) becomes now

$$F_{A_1-dA_2} = \frac{ndm}{2\pi(n^2 + m^2)} = \frac{(r_2 - e \cos \alpha) r_2 d\alpha}{2\pi(r_2^2 - 2r_2 e \cos \alpha + e^2)}$$

Integrating from α_1 to α_2 we obtain the required factor $F_{A_1-A_2}$, from the inner cylinder to the portion PQ of the outer cylinder.

$$F_{A_1-A_2} = \frac{r_2}{2\pi} \int_{\alpha_1}^{\alpha_2} \frac{r_2 - e \cos \alpha}{(r_2^2 - 2r_2 e \cos \alpha + e^2)} d\alpha$$

$$= \frac{1}{2\pi} \left[\frac{\alpha_2 - \alpha_1}{2} + \tan^{-1}\left(\frac{r_2 + e}{r_2 - e} \tan \frac{\alpha_2}{2}\right) - \tan^{-1}\left(\frac{r_2 + e}{r_2 - e} \tan \frac{\alpha_1}{2}\right)\right] \tag{17}$$

As was the case with the factors given by equations (12) and (13), $F_{A_1-A_2}$ is independent of the radius of the inner cylinder and of the applicability of Lambert's law.

References

Hamilton, D. C., and Morgan, W. R., NACA Technical Note No. 2836, 27, and 34, 1952.

Mackey, C. O., et al., "Radiant Heating and Cooling Part I," Engineering Experimental Station Bulletin, Ithaca, N. Y., Vol. 32, Aug. 1943.

Sparrow, E. M., and Cess, R. E., *Radiation Heat Transfer*, Brooks/Cole, Belmont, Calif., 1967, pp. 301–304.

Wiebelt, J. A., *Engineering Radiation Heat Transfer*, Holt, Rinehart, & Winston, New York, Aug. 1966.

Wilson, T., Hwang, C. L., and Crank, R. E., Kansas State University Bulletin No. 4, Kansas Engineering Experiment Station, Manhattan, Kan., Vol. 46, Apr. 1962.

C. A. DEPEW
Associate Professor,
University of Washington,
Seattle, Wash. Mem. ASME

E. R. CRAMER[1]
Engineer,
General Electric Company,
San Jose, Calif. Assoc. Mem. ASME

Heat Transfer to Horizontal Gas-Solid Suspension Flows

Heat transfer and pressure-drop characteristics of a gas-solid suspension flow in a horizontal circular tube were investigated using glass spheres of two sizes, 30 and 200 micron. The airflow rate was held constant at three different values in a 0.71-in-ID tube such that Reynolds numbers of 10,000, 15,000, and 30,000 were produced. Solid loading ratios on a mass basis were as large as 7. The purpose of the investigation was to observe the effect of stratification on the heat transfer characteristics of the system. The pressure-drop results indicate that the solids were suspended in all cases, but the heat transfer data show significant difference between the temperature of the tube wall at the top and bottom with the small particles. Nusselt numbers were as much as $2^1/_2$ times larger on the bottom side than on the top side. No such effect was produced with the large particles. The pressure-drop data indicate significant wall interaction for the large size, but not for the small size.

Introduction

THE BROAD application and importance of the pneumatic conveyance of solids needs no recounting here. In such systems, the possibility of thermal-energy exchange with the boundary exists and, indeed, the influence of suspended particles on this exchange mechanism may be of critical importance in design. Several previous theoretical and experimental investigations have dealt with the problem of heat transfer to gas-solid suspensions in the vertical orientation where the gravity force is axial and the flow field is symmetrical [1–7].[2] These and other pertinent publications are summarized in an excellent book [8].

In comparison to the vertical orientation, the horizontal configuration is inherently asymmetric and it requires individual treatment. Two previous investigations [9, 10] using horizontal heat transfer systems did not report the quantitative effect of vertical concentration gradients and no results which are comparable to those presented herein are known by the authors. The effect of gravity on a suspension flowing in the horizontal orientation is to cause the denser phase to settle toward the bottom of the pipe. The ability of the continuous phase to support a denser solid phase is found to depend on the velocity and fluid properties. Always, however, the tendency is for the solids concentration to be higher along the bottom of the pipe. In the extreme, the solids form a more or less continuous bed and move along without appreciable mixing of the two phases. Under this extreme condition, the solid bed may form an insulating barrier to heat transfer, but in the normal circumstance, when a circumferentially uniform heat flux is imposed, the lower wall is expected to be cooler than the top wall due to the normally high thermal capacity of the solid phase and, hence, its greater cooling effectiveness.

Although some consideration of particle distribution, pressure drop, and minimum transport conditions [11–13] has been given for isothermal conditions in the literature, no information exists which quantitatively describes the variation of temperature or heat transfer coefficient when a heat flux is imposed at the boundary in horizontal systems. This investigation was carried out to obtain some initial answers to the following questions:

1 At what concentration does the temperature at the tube bottom become measurably less than at the top?
2 How large does the temperature difference become?
3 Does design for conveyance constitute adequate design for heat transfer?

The answers to these questions were obtained for a limited range of parameters, but much further work remains to be done to verify and to generalize the specific conclusions of this paper.

Experimental Apparatus and Techniques

Flow System. The experimental apparatus used in this investigation is shown schematically in Fig. 1. The basic flow loop was developed during the course of previous studies [14], and it was modified to produce the configuration for the current research. The primary element is the uniform-flux heat transfer section which is placed in the horizontal position for these experiments. The suspension is produced by adding glass spheres to the metered air which comes from the laboratory compressed air supply. Glass spheres are supplied by a batch hopper which is mounted on a platform scale. The weight of the feed hopper is continuously

[1] Formerly, Research Assistant, University of Washington, Seattle, Wash.

[2] Numbers in brackets designate References at end of paper.

Contributed by the Heat Transfer Division of THE AMERICAN SOCIETY OF MECHANICAL ENGINEERS and presented at the ASME-AIChE Heat Transfer Conference, Minneapolis, Minn., August 3–6, 1969. Manuscript received by the Heat Transfer Division, December 16, 1968; revised manuscript received, April 16, 1969. Paper No. 69-HT-62.

Nomenclature

c = specific heat
D = inside tube diameter
h = local heat transfer coefficient
Nu = Nusselt number
P' = average pressure gradient, psi/in.
q = local heat flux
T = temperature
u = particle terminal velocity
u_f = pipe "friction velocity"
W = mass flow rate

Subscripts

a = air
b = bottom tube wall
ma = air mean
mm = mixture mean
ms = solids mean
0 = inlet condition
s = solids
t = top tube wall
w = wall
x = local value at x in. from inlet
∞ = average if 7 values nearest tube outlet

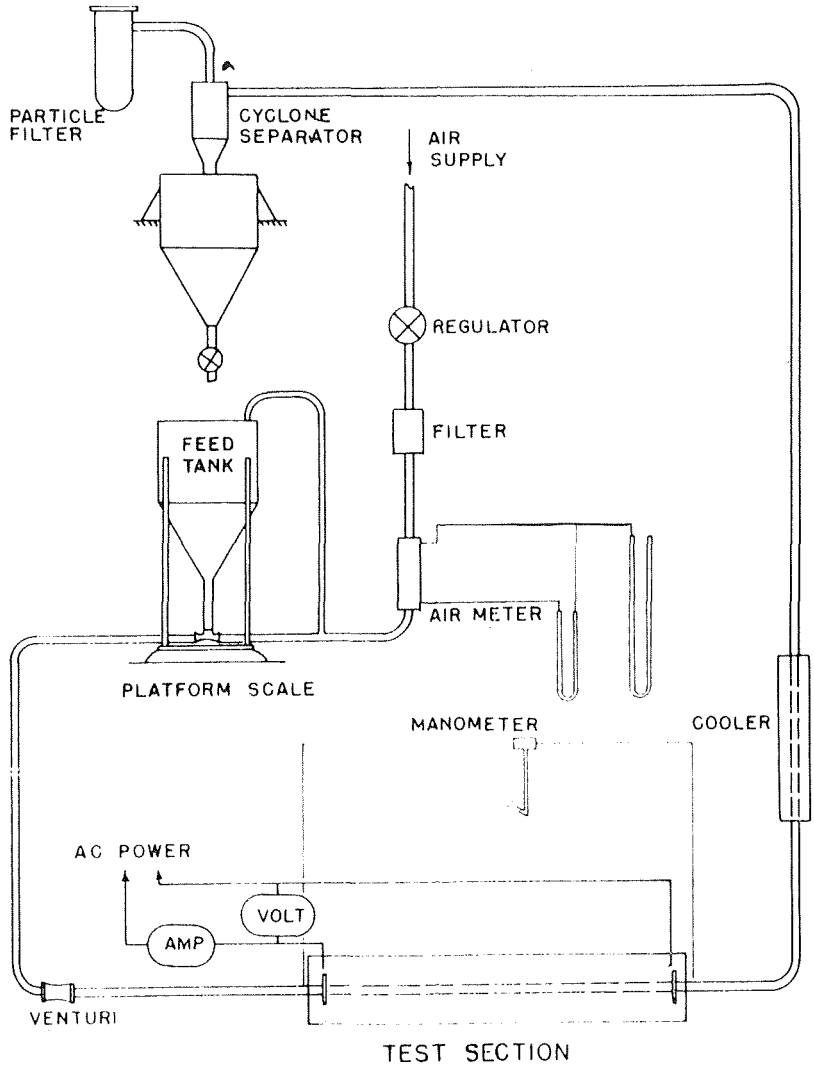

Fig. 1 Schematic diagram of experimental apparatus

monitored by a strip chart recorder reading the output of a strain-gage resistance bridge on a cantilever beam which restrains the scale arm. The flow of solids is adjusted at the feed nozzle which admits solids to the flow at the throat of a venturi nozzle.

The solid particles used in the investigation were glass spheres manufactured by the Minnesota Mining and Manufacturing Company. The diameter range of the large size used was 117–240μ. The average bead diameter of the small size was 28μ. They will be referred to as the 200μ size and the 30μ sizes, respectively. The mixture passes through a second venturi nozzle to make the distribution symmetrical at the entrance to the flow development section. This development section is 100 dia long and it provides a fully developed hydrodynamic flow condition at the onset of heating. The 0.75-in-dia $\times$ 80-in-long heat transfer section of type 304 stainless-steel tubing has copper electrode flanges for conduction of electric current through the 0.020 $\pm$ 0.003-in-thick tube wall. Two diametrically opposed Fe-Co thermocouples were spot-welded to the outside wall at each of 22 locations along the tube. The test section was thermally insulated with a minimum of 4 in. of powdered insulation over its entire length. Details of the thermocouple installation and locations are described in the previous publication [4]. The tube was oriented such that the thermocouples were at top and bottom. Calculation showed that longitudinal conduction, circumferential conduction, and the temperature difference between the outside and the inside tube wall are all negligible.

Following the test section, the flow is passed through a water-cooled heat exchanger to restore the solids to near room temperature for subsequent reuse. Flow continues through a double-effect cyclone separator where the bulk of the solids is removed to a storage hopper. The airflow exhausts to the room through a cloth filter bag. Operation of the system is quasi-steady, with the steady period of operation dependent on the solids rate due to the limited supply of solids in the feed tank. Run periods ranged from 15 min to several hr.

In addition to those on the heated section, thermocouples were mounted on the approach section to determine the mixture inlet. Thermocouple output was recorded by a strip chart recorder; airflow was measured with a calibrated Meriam laminar flow element to 2 percent accuracy; voltage and current were measured with calibrated Weston meters to $^1/_2$ per cent accuracy.

Experimental Procedure. An initial series of 19 runs with air only over a range of Re from 10,000 to 70,000 was made to check the overall and local system performance. These initial runs served a twofold purpose. By measuring the outlet mixed mean temperature and performing a heat balance, the heat loss from the heated section to the room was determined. The temperature of the tube wall at the last thermocouple on the heated section was maintained at 275 $\pm$ 5 F for all tests including the solids suspension runs, thus maintaining a nearly constant-heat-loss value. This heat loss value of 39 Btu/hr, which is roughly 5 percent of the heat input, was subtracted from the gross heat input to determine the net heat added to the suspension flows. The second purpose of the series with air alone was to verify the phenomenological performance of the system, as will be discussed in the following section.

Check runs were made periodically through the program to insure the continued satisfactory performance. About 2 hr were required for warm up. Constancy of all temperatures was noted for about 15 min prior to the introduction of solids, after which about 5 min were allowed for conditions to stabilize. The system had a 30-sec time constant for step inputs of power and step changes of airflow rate, and 5 min was more than adequate. The sequence of events for a test run was as follows:

1 Warm up with air flowing at a desired flow rate, maintain outlet tube wall temperature of 275 ± 5 F.

2 Establish solids flow at an estimated concentration.

3 Regulate heating power and air rate to restore original flow rate and outlet wall temperature.

4 Record data after observing a steady condition for all instruments.

The first series of suspension runs which were made produced results that were unreasonable. Axial tube wall temperature variations at distances beyond the thermal entry region contained maxima and minima which were 25-deg apart for some cases. This type of variation was found to depend on both tube straightness and approach section alignment. Adjustable supports were placed at 20-dia intervals and both sections were made colinear to within 0.01 in. with the aid of a surveyor's transit. Only those results which were produced after this alignment procedure are reported herein.

Analysis of Results. The local Nusselt number, hD/k, is based on the local heat transfer coefficient, which is defined by

$$h \equiv \frac{q}{(T_w - T_{mm})}$$

T_{mm} is the mean temperature that would exist if the phases were in thermal equilibrium and it is based upon an energy balance:

$$T_{mm} = T_0 + \frac{qDx}{W_a c_a + W_s c_s}$$

The heat flux is assumed to be uniform since the tube electrical resistivity is nearly constant, the heat loss is a small part of the total heat transferred, and tube wall conduction is estimated to be negligible. In the air-alone tests, $W_s = 0$, and the same formulas are used with T_w, the average of the top and bottom thermocouple readings.

During the tests with only air flowing, the top and bottom thermocouples at most of the axial locations indicated the same temperature. There were a few exceptions due to tube nonuniformity or inaccurate thermocouples, but the difference was always less than 3 F. When solids are flowing, heat transfer coefficients are calculated separately for the top and bottom tube walls based on their respective measured temperatures, but the same values of heat flux and mixture mean temperature are used.

The Reynolds number is always based on the mean flow rate and physical properties of the air. When air-only runs are made, the average mixing cup temperature is used; when solids are present, the inlet air conditions are used for evaluation of the physical properties.

Experimental Results and Discussion

Tests were conducted for the following conditions: airflow only; air Reynolds numbers of 10,000, 15,000, and 30,000 with 30μ particles; air Reynolds numbers of 15,000 and 30,000 with 200μ particles.

Heat Transfer With Air. Nineteen runs were made without solids present to assess the system performance and capability for accurate and repeatable results. The tests covered a range of Reynolds numbers from 10,000–70,000, and the resulting asymptotic Nusselt numbers are shown in Fig. 2. The solid line represents the previous data of Depew [15] and the analysis of Sparrow, Hallman, and Siegel [16]. The experimental data are within ±5 percent of the expression. Further confidence in the system is engendered by the fact that the 5 percent thermal-entry length for all tests was from 9–14 dia long. This is in agreement with Sparrow's value of 12 at Re = 50,000 and Depew's range of 11–13 dia. These results are considered to be substantial verification of the system and its instrumentation.

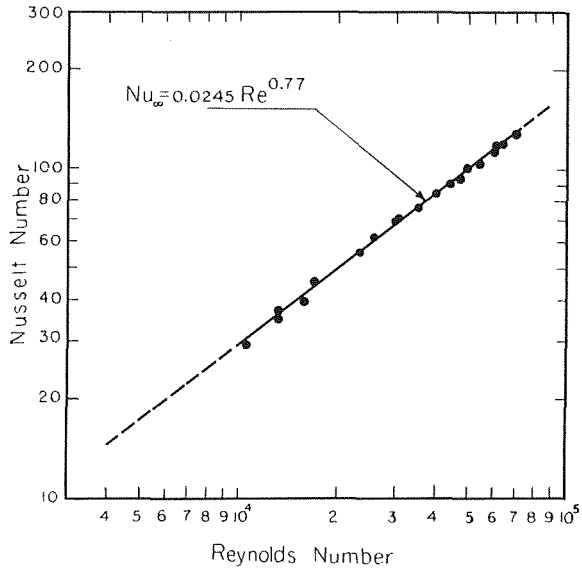

Fig. 2 Asymptotic Nusselt numbers versus Reynolds number for air-only flows

Heat Transfer With 30μ Particles. Local Nusselt numbers are presented in Fig. 3 as a function of axial distance for four different solids loading ratios with the air Reynolds number held constant at 15,000. These results are typical of the 12 runs made at this air rate and they show the essential characteristics of the system performance. Fig. 4 shows the high-loading ratio run plotted as the Nusselt number ratio (ratio of local value of Nu to Nu at $x/D = 101$) versus axial distance. Fig. 5 is a plot of the asymptotic Nusselt number as a function of solids loading ratio with the comparable results from [14] for the vertical orientation also shown. Fig. 5 also shows similar curves for Re = 10,000 and 30,000. Local Nusselt numbers are not presented for these air rates since the behavior is similar to the series when Re = 15,000.

Fig. 3 clearly shows that Nu_b increases everywhere in the tube with the addition of solids, but the Nu_t is somewhat reduced by particles. The results also show that there is no appreciable tendency to prolong the length of the thermal-entry region contrary to the pronounced effect which was found for the same conditions in the vertical orientation. Fig. 4 shows only a modest prolongation of thermal-entry length to about 40 dia for the top-side values, while the axial profile for air alone adequately represents the data for the bottom side. The curves for Nusselt number ratio for other loading ratios are similar to Fig. 4, with a decreasing effect on the top-side profile as the loading ratio is decreased. Also, it is apparent from Fig. 4 that Nu_b has considerably more variation than the values along the top side. This result is made more evident by considering the standard deviation σ of the seven values at x/D greater than 50. At $Ws/Wa = 1.61$, σ is 1.0 on the bottom compared to 0.53 on the top; at 3.65, σ is 2.83 on the bottom compared to 0.51 on the top; at 7.24, σ is 5.03 on the bottom compared to 0.27 on the top. The variation of Nu_t with x/D is reproducible and regular, i.e., it can be seen from Fig. 3 that Nu_t ($x/D = 76$) is the highest of the last seven values for all loading ratios. It appears that this effect is systemic in spite of the careful alignment of the tube, as described in the previous section. Careful visual observation of the tube interior revealed no variation which could be considered as a possible cause of the variation, and it appears that variations within the straightness tolerance (0.01 in.) are responsible for the irregularity of the behavior of Nu_t.

Solid particles had only a nominal effect on the heat transfer coefficient on the top side, as shown by plotting Nu_∞ versus solids

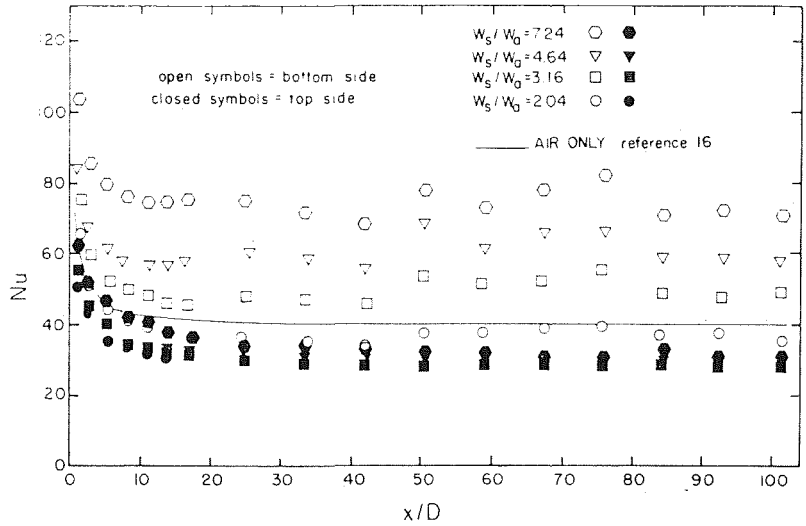

Fig. 3 Local Nusselt number for 30μ particles at Re = 15,000

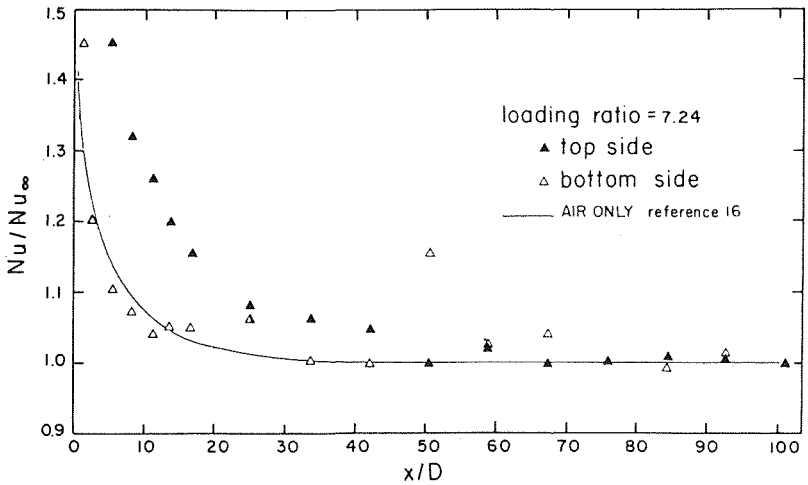

Fig. 4 Nusselt number ratio for 30μ particles at Re = 15,000

loading ratio, where Nu_∞ is the arithmetic average of the last 7 stations; i.e., for $x/D > 50$. Fig. 5 shows that, for Re = 15,000, along the top side Nu_∞ decreases by approximately 25 percent and remains nearly constant for loading ratios greater than 1 or 2. The effect of solid particles on the bottom-side tube wall temperature is significant, however, as shown by the increased value of Nu_∞ at high loading ratios. At lower values of loading ratio there is little evidence of stratification, and the temperatures at the top and bottom are virtually the same. As loading is increased, the higher concentration of solids at the tube bottom is effective in cooling the wall, such that at the intermediate Re and at the highest ratio shown in Fig. 5, 7.24, the difference in temperature of 90 F produces a Nusselt number at the bottom which is $2^1/_2$ times greater than at the top and almost twice as large as with no solids at all.

Also shown in Fig. 5 is the line representing the results of the vertical tube tests for Re = 15,000 and 30,000 from [14] for comparison. The variation at 15,000 is not unlike the curve for the bottom side of the tube, but it is closer to an average value for the top and bottom sides. Also, the minimum occurs at a lower loading ratio for the vertical tube and has a slightly lower value.

Turning attention to the results in Fig. 5 for the high and low flow-rate cases, notice that Nu_t is almost unaffected by solids loading ratio for the lower Reynolds number, but that Nu_t is reduced by about 34 percent at loading ratios greater than 2 for Re = 30,000. The most plausible explanation for this effect on Nu_t takes into account the residence time for particles to absorb heat from the air. That is, when Re = 10,000, the solids have roughly three times as much time for heat transfer as at the higher air velocity, and this additional residence time allows them to approach thermal equilibrium with the air. The closer that the solids are to the air temperature, the closer will be T_{mm} to the mean air temperature T_{ma}. If it is assumed that the particles are ineffective in altering the convective mechanism at the top of the tube, then the effect on Nu_∞ is entirely due to T_{mm}, and the condition where $T_{ma} = T_{mm}$ would result in invariant Nu_∞. For $T_{ma} > T_{mm} > T_{ms}$, $(T_w - T_{mm}) > (T_w - T_{ma})$ and Nu_∞ is less than for thermal equilibrium.

A rather unexpected result can be seen in Fig. 5 by noting that on the bottom wall Nu_∞ has the same value for all Re for a limited range of loadings. For the two lower air rates the range of agreement is from 1 to about 4, while the tests at Re = 30,000 produce coincident results only over loading ratios from 3–4. It is possible that the curves might continue to follow the results from the intermediate air rate, but the solids loading valve would not allow operation in this range. Further work is underway to investigate this region of loading ratio.

Heat Transfer With 200μ Particles. The Nusselt number ratio is increased by adding 200μ solids, also as shown in Fig. 6, for 4 loading ratios. The increased ratio results in a prolonged thermal-entry length to about 50 dia. Fig. 6 also shows that the difference between the ratio at the top and bottom is insignificant. This symmetry is also demonstrated in Fig. 7 where the asymptotic Nusselt numbers along the top and bottom are plotted as a

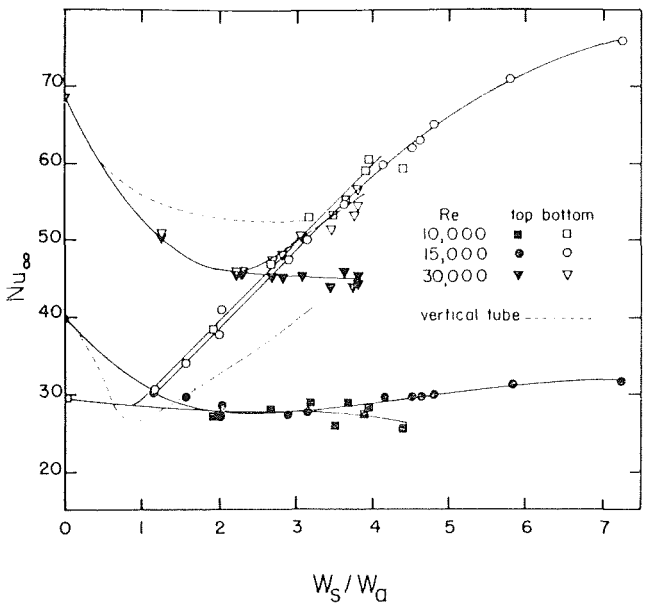

Fig. 5 Asymptotic Nusselt number for 30μ particle suspensions

conditions of this investigation, the ratio is always less than 0.1 when using 30μ particles and the ratio is greater than 1 when running with the 200μ size. This criterion suggests that the small size should flow in suspension, but that the 200μ particles should settle out. Thomas correlated his experimental results for minimum transport velocity for liquid-solid and gas-solid flows and he derived a relation among the terminal velocity, friction velocity, and the physical and fluid properties of the system. Using this correlation, which appears as equations (15) and (16) in [11], both sizes should flow in suspension. This conclusion is based on experimental data and is more reliable than the foregoing, which is suggested by letting $u/u_f = 0.2$.

Based on the foregoing discussion, it is reasonable to expect greater stratification effects with the large size, if any are present at all. Comparison of Figs. 5 and 7 shows the opposite; temperatures were symmetrical for the 200μ size and asymmetric for the other size. That the lower wall was much cooler without reaching Thomas' criterion is not, however, contradictory to the theory. A minimum transport velocity occurs when stationary or sliding particles occur at the bottom of the pipe and it is well below the condition of sizeable vertical concentration gradients.

The lack of any marked sign of stratification when running with 200μ particles is contradictory to the previous discussion, but a possible explanation may be found in the observations of bouncing flow made by Bagnold and by Adam, as reported by Wen [17].

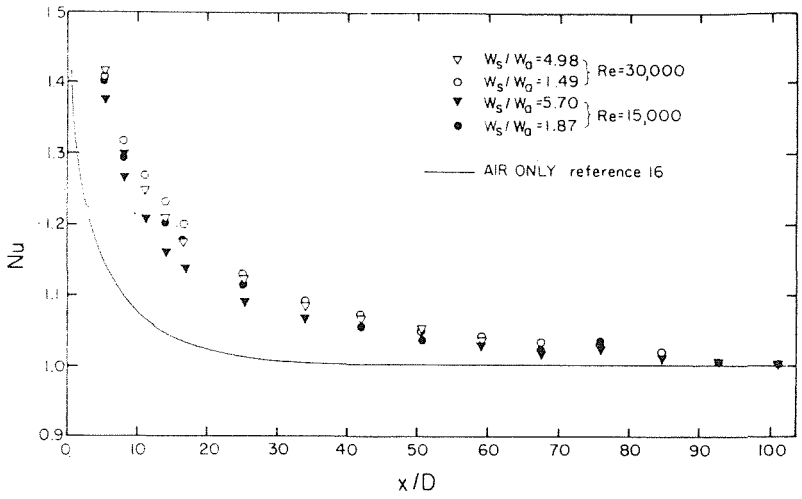

Fig. 6 Local Nusselt number for 200μ particle suspensions

function of solids loading ratio for both the high and low Reynolds numbers. The differences are minor and the results for the bottom side do not exhibit any of the behavior of the 30μ particles, Fig. 5. Additionally, the reduction of the asymptotic Nusselt number from the value for air alone on the top by about 19 percent is only about $^1/_2$ the reduction found with 30μ spheres.

Particle-Size Effects on Heat Transfer. Among the size characteristics of particles which are important in transfer of heat energy are surface area and particle terminal velocity. The smaller spheres used in this study have roughly 50 times more surface area per unit weight of solid than the larger ones have. For this reason alone, the small particles are expected to have a larger effect on heat transfer than the 200μ spheres, as was found in the previous studies [2, 3]. On the other hand, the larger particles have a higher terminal velocity, and according to Thomas' criterion [11] for minimum transport velocity, they should stratify to a greater extent than the smaller particles. Thomas cites the ratio of terminal velocity to pipe friction velocity as the major factor in determining the nature of the suspension flow, i.e., solids transported in suspension or a concentrated layer along the bottom of the pipe. If the ratio u/u_f is high, the phases would separate, but if the ratio is low, the turbulent eddies would support the solid phase for conveyance as a mixture. Thomas suggests a value of 0.2 as a convenient division between the two regimes. For the

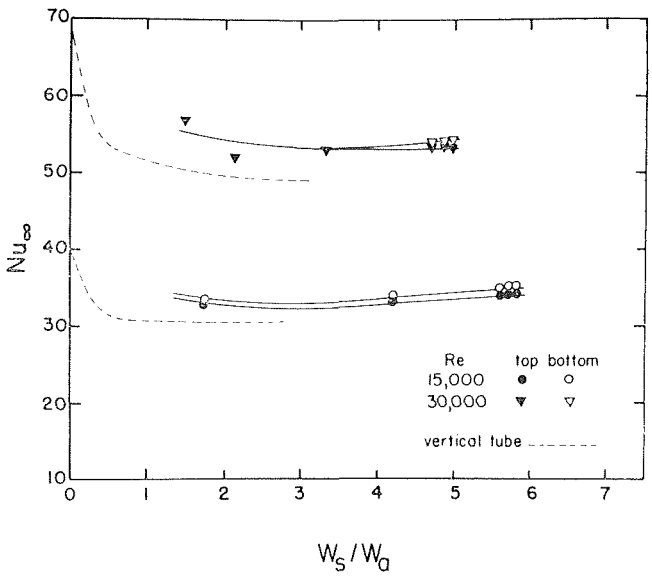

Fig. 7 Asymptotic Nusselt number for 200 μ suspensions

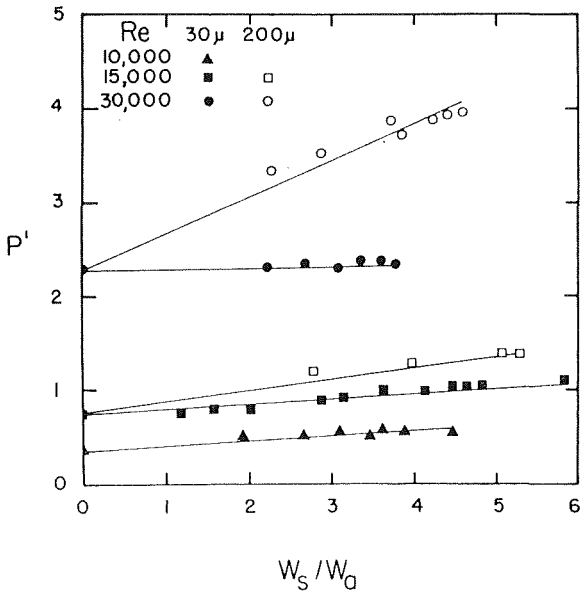

Fig. 8 Average pressure gradient versus solids loading ratio

In these studies, particles were observed to bounce from wall to wall as they were transported along the pipe. Mehta, et al. [13], postulate that the 97μ glass particles used in their pressure-drop studies moved primarily in bouncing flow, while the 36μ size followed suspension flow. The present results indicated a symmetry to the 200μ flow which could be the result of bouncing, and the pressure-drop data in Fig. 8 support these ideas. A larger pressure gradient would result with bouncing flow and its associated momentum transfer due to acceleration and deceleration. Note that the pressure drop increases linearly with loading ratio for the large spheres and that this increased pressure drop increases with the square of the air rate. These observations tend to verify the theory that there is substantial bouncing contact with the wall in the case of the large particles. On the other hand, the pressure gradient is only moderately affected by the 30μ size, indicating a much smaller momentum interaction with the wall. The concept that wall interaction, which is tantamount to bouncing, offers a plausible explanation for the observations in this work, but more direct measurements will be necessary for full confirmation of the phenomenon.

Summary and Conclusions

Although the amount of data and the range of parameters is limited, the results of this investigation pertaining to horizontal gas-solids suspension flows can be summarized in the following conclusions:

1 For solids loading ratios less than approximately unity, there is no asymmetry of wall temperature distribution.

2 For suspension with 30μ particles, the Nusselt number along the top wall of the horizontal tube is reduced to a value lower than with air alone.

3 For suspensions with 30μ particles, the Nusselt number along the bottom wall reaches a minimum value and then increases as the loading ratio is increased.

4 When 200μ particles are used, there is no asymmetry of wall temperature distribution for loading attained in this investigation.

5 Based on the heat transfer results, it appears that 30μ particles move in a stratified suspension flow, but that 200μ particles interact symmetrically with the tube wall. The pressure-drop results indicate significant wall interaction with the larger size, but no interaction was apparent with the smaller size within the accuracy of the pressure-drop measurements.

These conclusions should be considered to be tentative and subject to verification or modification with further research.

Acknowledgment

This work was supported by the National Science Foundation Grant No. GK-1134 and the College of Engineering, University of Washington.

References

1 Farbar, L., and Morley, M. J., "Heat Transfer to Flowing Gas-Solids Mixtures in a Circular Tube," *Industrial and Engineering Chemistry*, Vol. 49, No. 7, July 1957, pp. 1143–1150.

2 Farbar, L., and Depew, C. A., "Heat Transfer Effect to Gas-Solids Mixtures Using Solid Spherical Particles of Uniform Size," *Industrial and Engineering Chemistry Fundamentals*, Vol. 2, May 1963, pp. 134–135.

3 Tien, C. L., "Heat Transfer by a Turbulently Flowing Fluid-Solids Mixture in a Pipe," JOURNAL OF HEAT TRANSFER, TRANS. ASME, Series C, Vol. 83, 1961, pp. 183–188.

4 Depew, C. A., and Farbar, L., "Heat Transfer to Pneumatically Conveyed Glass Particles of Fixed Size," JOURNAL OF HEAT TRANSFER, TRANS. ASME, Series C, Vol. 85, May 1963, pp. 164–172.

5 Schluderberg, D. C., Whitelaw, R. L., and Carlson, R. W., "Gaseous Suspensions—A New Reactor Coolant," *Nucleonics*, Vol. 19, No. 8, 1961, p. 67.

6 Tien, C. L., and Quan, V., "Local Heat Transfer Characteristics of Air-Glass and Air-Lead Mixtures in Turbulent Flow," ASME Paper No. 62-HT-15.

7 Danziger, W. J., "Heat Transfer to Fluidized Gas-Solid Mixtures in Vertical Transport," *Industrial and Engineering Chemistry, Process Design and Development*, Vol. 2, 1963, p. 269.

8 Soo, S. L., *Fluid Dynamics of Multiphase Systems*, Blaisdell Publishing Co., 1967.

9 Briller, R., and Peskin, R. L., "Gas Solids Suspension Convective Heat Transfer at a Reynolds Number of 130,000," JOURNAL OF HEAT TRANSFER, TRANS. ASME, Series C, Vol. 90, Nov. 1968, pp. 464–468.

10 Sukomel, A. S., Tsvetkov, F. F., and Kerimov, R. V., "A Study of Local Heat Transfer From a Tube Wall to a Turbulent Flow of Gas Bearing Suspended Solid Particles," *Thermal Engineering—Soviet Power Industry Research and Technology*, Feb. 1967, pp. 116–122.

11 Thomas, D. G., "Transport Characteristics of Suspensions," *AIChE Journal*, Vol. 8, No. 1, July 1962, pp. 373–378.

12 Zenz, F. A., "Two-Phase Fluid-Solid Flow," *Industrial and Engineering Chemistry*, Vol. 41, 1949, p. 2801.

13 Mehta, N. C., Smith, J. M., and Comings, E. W., "Pressure Drop in Air-Solid Flow Systems," *Industrial and Engineering Chemistry*, Vol. 49, No. 6, June 1957, pp. 986–992.

14 Rajapaul, V. K., "Tube Size and Particle Size Effects on Heat Transfer to Flowing Gas-Solids Mixtures With Low Solid Loading Ratios," MS thesis in Mechanical Engineering, University of Washington, 1963.

15 Depew, C. A., "Heat Transfer to Air in a Circular Tube Having Uniform Heat Flux," JOURNAL OF HEAT TRANSFER, TRANS. ASME, Series C, Vol. 84, 1962, pp. 186–187.

16 Sparrow, E. M., Hallman, T. M., and Siegel, R. S., "Turbulent Heat Transfer in the Thermal Entrance Region of a Pipe With Uniform Heat Flux," *Applied Scientific Research*, Section A, Vol. 7, 1957, p. 37.

17 Wen, C. W., "Flow Characteristics in Solid-Gas Transportation System," *Pneumatic Transportation of Solids*, Spencer, J. D., Joyce, T. J., and Faber, J. H., eds., U. S. Department of Interior, Bureau of Mines, Information Circular 8314, 1966.

P. H. NEWELL, JR.
Associate Professor of Engineering, Assistant Professor of Physical Medicine and Rehabilitation, Director, Center for Bio-Engineering, University of Alabama in Birmingham, Birmingham, Ala. Mem. ASME

A. E. BERGLES
Associate Professor, Department of Mechanical Engineering, Massachusetts Institute of Technology, Cambridge, Mass. Mem. ASME

Analysis of Combined Free and Forced Convection for Fully Developed Laminar Flow in Horizontal Tubes

This paper summarizes an analytical investigation of the effects of free convection on fully developed laminar flow in horizontal circular tubes with uniform heat flux. Solutions for heat transfer and pressure drop, with both heating and cooling, were obtained for water with two limiting tube-wall conditions. The infinite-conductivity tube exhibits higher Nu and f than the glass tube, with Nu being over five times the Poiseuille value at Gr $\sim 10^6$. With the glass-tube boundary condition, significant circumferential wall temperature variations exist. A correlation for the difference between the wall temperatures at the top and bottom of the tube is presented. Design correlations for Nu and f are developed from the analytical solutions. The analytical predictions bracket recent experimental data for water.

Introduction

In spite of numerous analytical and experimental studies, it appears that no correlation has previously been developed which satisfactorily accounts for gravitational effects in laminar tube flow.

When a flowing fluid is heated in a horizontal tube, the fluid near the wall is warmer, and therefore lighter, than the fluid further removed from the wall; it therefore flows upward along the wall, and continuity requires a downflow of the heavier fluid near the center of the tube. As a result, there is a secondary fluid motion established which is symmetrical about a vertical plane passing through the axis of the tube, and combined with the axial flow, the three-dimensional streamlines exhibit a spiraling character. This secondary flow was demonstrated by means of a simple counterflow heat exchanger consisting of a $^1/_4$-in-ID pyrex tube centered in a plexiglas channel of square cross section [1, 2].[1] Photographs of the flow of water at Re = 150 in plan and elevation are depicted in Fig. 1, where the streamlines were marked with a very dilute solution of potassium permanganate maintained at the same temperature as the flowing fluid. A diagrammatic sketch of a cross-sectional view of the two-dimensional, secondary-flow streamlines is presented here since this could not be photographed.[2] Some of the details of this secondary flow have been examined via dye streamlines in water [4, 5], velocity profile measurements in oil [6], and velocity and temperature profile measurements in air [7].

A number of empirical correlations have been proposed for the heating or cooling of various fluids in horizontal laminar-tube-flow with approximately constant wall temperature [8–14]. In the majority of these investigations, the data correlations were attempted with a view toward obtaining average Nusselt numbers via various modifications of the Graetz solution which applies to the uniform wall temperature situation. When this boundary condition is imposed, the secondary flow develops to a maximum intensity, and diminishes to zero provided the tube is long enough.

Contributed by the Heat Transfer Division of The American Society of Mechanical Engineers and presented at the ASME-AIChE Heat Transfer Conference, August 3–6, 1969, Minneapolis, Minn. Manuscript received by the Heat Transfer Division, December 17, 1968; revised manuscript received, March 27, 1969. Paper No. 69-HT-39.

[1] Numbers in brackets designate References at end of paper.

[2] Mori and Futagami [3] recently presented axial photographs of airflow in a large diameter tube where smoke was used for visualization.

Nomenclature

B = dimensionless axial pressure gradient
c_p = specific heat at constant pressure
D = tube diameter
Fr = Froude number $\equiv gr_0/W_0^2$
f = Darcy-Weisbach friction factor
f_P = friction factor for Poiseuille flow = 64/Re
Gr = Grashof number $\equiv -\frac{gD^3}{\nu^2} \times (\hat{\rho}_w - 1) \simeq \frac{gD^3}{\nu^2}\beta\,(\bar{T}_w - T_b)$
g = gravitational acceleration
g_c = conversion factor, 32.174 ft-lb_m/lb_f-sec^2
h = heat-transfer coefficient
J = conversion factor, 778 ft-lb_f/Btu
k = thermal conductivity
L = axial length
Nu = Nusselt number $\equiv hD/k$
Nu_P = Nusselt number for Poiseuille flow, uniform heat flux Nu_P = 4.36
P = two-dimensional pressure distribution, $P(\hat{r}, \theta)$
P^* = dimensionless pressure = $P(r, \theta) + \hat{r}$ Fr
Pr = Prandtl number $\equiv c_p\mu/k$
p = pressure
$(q/A)_w$ = heat flux at solid boundary
Re = Reynolds number $\equiv \rho W_0 D/\mu$
r = radial distance
r_0 = tube radius
s = path length of two-dimensional streamline
T = temperature
ΔT = $T_w - T_b$
T_b = mixed-mean fluid temperature
t = time
u = velocity component in r-direction
v = velocity component in θ-direction
W_0 = average axial velocity
w = velocity component in z-direction

(Continued on next page)

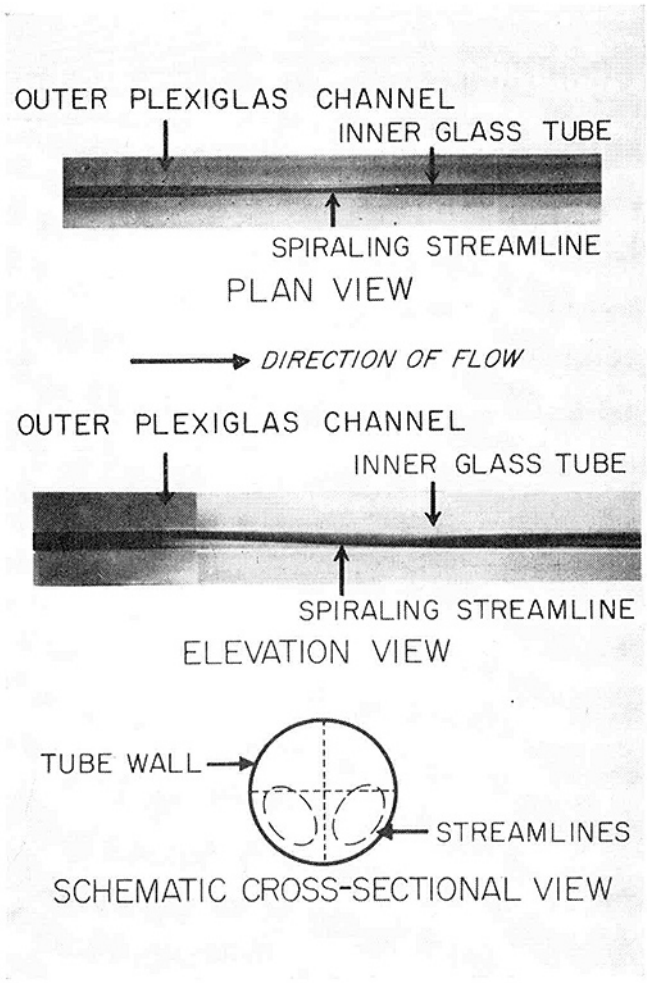

Fig. 1 Spiraling streamlines in plan and elevation

For a constant-heat-flux boundary condition, a wall-minus-fluid temperature difference obtains throughout the length of the heated tube; thus the free convection persists throughout the tube. Experimental data for the heating of air [7, 15] and water [16, 17] with approximately constant heat flux were recently reported. The secondary flow produces increases in the heat-transfer coefficient which can readily be of the order of 500 percent.

In general, the available empirical correlations of experimental data for either boundary condition apply only for limited ranges of variables, and are characterized by large uncertainties. This is not too surprising since the number of parameters is very large and difficulty would be expected in correlating data for significantly different fluids. In particular, the effects of temperature-dependent properties have not been isolated; for example, variable property effects have been correlated via the Grashof number, and buoyancy effects have been correlated via viscosity ratios.

The abundance of inhibiting factors associated with the experimental approach suggests that theoretical approaches should be considered. However, a solution of the complete problem, involving transient phenomena and entrance effects, is not currently possible. Accordingly, analytical work has centered on the more tractable problem of fully developed flow in uniformly heated tubes, with density as the only temperature-dependent property. Hanratty [4], Morton [18], del Casal and Gill [19], and Iqbal and Stachiewicz [20] considered series solutions using various quantities for a perturbation parameter. These results, which include both first and second-order perturbation analyses, are contrary to experience, for even moderate values of the expansion parameters. Mikesell [5] approached the problem in terms of a boundary-layer analysis; however, the analysis was unsuccessful since the formulation for the core flow could not be separated from that of the boundary layer. Mori and Futagami [3] recently reported a boundary-layer solution for Pr $\sim$ 1, utilizing the integral approach, which was in fair agreement with limited experimental results for air.

While these theoretical analyses have contributed to an understanding of the problem, they have not produced relationships which correlate the experimental observations to a reasonable degree of accuracy. Hence, it appeared appropriate to consider a more exact solution, via finite differences, for an appraisal of the effect of free convection in uniformly heated horizontal tubes, regarding the transport properties to be essentially constant.

The simplification of the problem to two dimensions brings it within the capability of currently available automatic computational equipment; however, it is necessary to comment on the practical utility of such a solution. Consider first the fully developed assumption.

If the heated section is preceded by an adequate [1] hydrodynamic calming length, the development of the secondary flow can be considered to occur in two stages. In the first stage, axial fluxes predominate [1], and the temperature profile develops almost as a symmetric flow. Then there exists a nonuniform radial density distribution and, in the second stage, the body forces come significantly into play. In this region the body forces are of the same order of magnitude as the inertial forces; this condition can be expressed with the following relationship [1]

$$\frac{L_2}{D} \sim \frac{\mathrm{Re}^2}{\mathrm{Gr}}. \tag{1}$$

The region, $L \sim L_1 + L_2$, in which the flow is being established can then be estimated by adding to equation (1) an estimate [1] for stage one; viz., $L_1/D = 0.05\ \mathrm{Re\ Pr}$. McComas and Eckert [15] reported data for air which appear to exhibit a fully developed

Nomenclature

z = axial coordinate
α = convergence-accelerating parameter in equation (27)
β = bulk modulus of expansion
ϵ = dimensionless radius to first intersection with specified streamline on ray which contains eye of two-dimensional streamlines
θ = azimuth angle measured from vertical center line
ζ = path length of three-dimensional streamline corresponding to axial pitch
λ = dimensionless axial pitch of three-dimensional streamline
μ = dynamic viscosity
ν = kinematic viscosity
ρ = density
τ = $-\partial\hat{T}/\partial\hat{z}$
ψ = stream function defined by equation (12)

Subscripts

avg = average property
b = property is evaluated at mixed-mean fluid temperature
max = maximum
min = minimum
w = property evaluated at average wall temperature

Superscripts

$\hat{}$ = dimensionless variable: $\hat{u} = u/W_0$, $\hat{v} = v/W_0$, $\hat{w} = w/W_0$, $\hat{z} = z/r_0$, $\hat{r} = r/r_0$, $\hat{\rho} = \rho/\rho_0$, $\hat{T} = T/T_b$, $\hat{p} = B\hat{z} + P(\hat{r}, \theta) = p/\rho_0 W_0^2$, $\hat{t} = tW_0/r_0$
$-$ = average property

All properties are evaluated at the mixed-mean fluid temperatures unless otherwise noted.

condition as predicted in this manner. Mori, et al. [7], reported developed flows of air with entrance lengths about 30 percent less than that predicted by this method, while the data of Shannon and Depew [16], for water at the ice point, indicate entrance lengths up to about 30 percent greater than predicted by the method just suggested. Thus the region in which the secondary flow is being established can be reckoned approximately.

Regarding the effect of variable transport properties on the radial velocity components, an exact analysis was made via the Frobeneous method to determine the effect of the variable viscosity of water on a fully developed laminar flow, neglecting gravity [1]. The results of this one-dimensional study, which corroborated the work of Poppendiek [25], indicated that deviations from the Poiseuille flow would be no larger than 15 percent. In fact, it was shown [1] that radial viscosity variations would result in deviations in the Nusselt number from the Poiseuille value of less than 5 percent provided

$$\frac{2r_0(q/A)_w}{k_bT_b} < 1.74. \tag{2}$$

Finally, it is necessary to consider the conditions under which a stable laminar flow will be expected. When all possible disturbances are eliminated, laminar flow may exist at Re $\sim 10^5$ [21]; however, it appears that when nominal care is exercised to prevent external disturbances, all disturbances will be attenuated only for Re $< 10^3$. From visualization studies under adiabatic conditions [1] it was found that for Re < 1000 the flow is stable, for $1000 <$ Re < 2000 a locally time-dependent, sinuous motion ensues, and at Re ~ 2000 the first disturbance eddy breaks away. This effect is corroborated by the work of Prengle and Rothfus [22]. Under diabatic conditions, there is some uncertainty as to whether the secondary flow retards or promotes the transition to turbulent flow. Altman and Staub [23] concluded that the free convection rendered the flow in rectangular ducts more stable, while Scott, et al. [24], contended that it was a destabilizing effect for tube flow. Mori, et al. [7], found that the transition Re (inferred by hot wire) at high inlet turbulence levels increased as the product Gr Nu was increased, but the opposite effect was observed at low turbulence levels. In no case, however, did the transition Re drop below 2000. Thus stable, laminar flows with heat transfer obtain in many practical situations for which analytical solutions will be applicable.

Analysis

Differential Formulation of the Secondary Flow Problem

The variation of the density in the presence of the earth's gravitational field provides, of course, the motive force for the secondary flow that is under consideration. However, when the density is primarily a function of temperature, as was first pointed out by Boussinesq [26], the variability of the density can often be ignored in all of the analytical expressions except the body-force term. This effects a considerable simplification in the mathematical formulation of the problem since part of the nonlinearities associated with the material derivatives are circumvented and since, with an iterative approach anticipated, the number of cycles of iteration required will be substantially reduced. Accordingly, the density will be treated as a constant in all of the terms in the governing equations except the expressions relating body forces.

In the treatment of problems involving free convection, it is customary to introduce the bulk modulus of expansion and express the results in terms of the Grashof number. However, the use of β assumes a linear relationship between ρ and T, and some error is introduced at higher ΔT where the free convection is very significant. In order to obtain a precise solution to the problem, the numerical calculations were performed for a specific fluid using an accurate formulation for $\rho(T)$. Since water is important in engineering practice and exhibits large secondary flow effects, it was chosen as the working fluid.

Employing cylindrical coordinates, and making the valid [1] assumption that, for water, the work associated with viscous dissipation is of no consequence, the differential equations of continuity, energy, and momentum are

$$\frac{\partial}{\partial \hat{r}}(\hat{r}\hat{u}) + \frac{\partial \hat{v}}{\partial \theta} = 0, \tag{3}$$

$$\hat{u}\frac{\partial \hat{T}'}{\partial \hat{r}} + \frac{\hat{v}}{\hat{r}}\frac{\partial \hat{T}'}{\partial \theta} - \tau\hat{w} = \frac{1}{\mathrm{Re\ Pr}}\left[\frac{1}{\hat{r}}\frac{\partial}{\partial \hat{r}}\left(\hat{r}\frac{\partial \hat{T}'}{\partial \hat{r}}\right) + \frac{1}{\hat{r}^2}\frac{\partial^2 \hat{T}'}{\partial \theta^2}\right], \tag{4}$$

$$\hat{u}\frac{\partial \hat{u}}{\partial \hat{r}} + \frac{\hat{v}}{\hat{r}}\frac{\partial \hat{u}}{\partial \theta} - \frac{\hat{v}^2}{\hat{r}} = -\frac{\partial \hat{p}}{\partial \hat{r}} - \mathrm{Fr}\,\hat{\rho}\cos\theta + \frac{1}{\mathrm{Re}}\left\{\frac{\partial}{\partial \hat{r}}\left[\frac{1}{\hat{r}}\frac{\partial}{\partial \hat{r}}(\hat{r}\hat{u})\right] + \frac{1}{\hat{r}^2}\frac{\partial^2 \hat{u}}{\partial \theta^2} - \frac{2}{\hat{r}^2}\frac{\partial \hat{v}}{\partial \theta}\right\}, \tag{5}$$

$$\hat{u}\frac{\partial \hat{v}}{\partial \hat{r}} + \frac{\hat{v}}{\hat{r}}\frac{\partial \hat{v}}{\partial \theta} + \frac{\hat{u}\hat{v}}{\hat{r}} = -\frac{1}{\hat{r}}\frac{\partial \hat{p}}{\partial \theta} + \mathrm{Fr}\,\hat{\rho}\sin\theta + \times\left\{\frac{\partial}{\partial \hat{r}}\left[\frac{1}{\hat{r}}\frac{\partial}{\partial \hat{r}}(\hat{r}\hat{v})\right] + \frac{1}{\hat{r}^2}\frac{\partial^2 \hat{v}}{\partial \theta^2} + \frac{2}{\hat{r}^2}\frac{\partial \hat{u}}{\partial \theta}\right\}, \tag{6}$$

and

$$\hat{u}\frac{\partial \hat{w}}{\partial \hat{r}} + \frac{\hat{v}}{\hat{r}}\frac{\partial \hat{w}}{\partial \theta} = -\frac{\partial \hat{p}}{\partial \hat{z}} + \frac{1}{\mathrm{Re}}\left[\frac{1}{\hat{r}}\frac{\partial}{\partial \hat{r}}\left(\hat{r}\frac{\partial \hat{w}}{\partial \hat{r}}\right) + \frac{1}{\hat{r}^2}\frac{\partial^2 \hat{w}}{\partial \theta^2}\right]. \tag{7}$$

The density data of reference [27] for the saturated liquid are related to the temperature with deviations of less than one percent over an interval from 40 to 350 deg F by

$$\rho = 62.4 - 7.83 \times 10^{-5}(T - 40)^2, \tag{8}$$

where ρ is in $\mathrm{lb_m/ft^3}$ and T is in deg F. Other property data were taken from references [28] and [29].

The boundary conditions for the analysis derive, from the assumption of a no-slip condition on the velocity at the bounding, solid surfaces, from the observation that symmetry about the vertical axis exists, and from the specification of thermal conditions at the tube wall. Consequently,

$$\text{At } \hat{r} = 1\text{: } \hat{u}(1, \theta) = \hat{v}(1, \theta) = \hat{w}(1, \theta) = 0;$$

$$\text{At } \theta = 0\text{: } \hat{v}(\hat{r}, 0) = 0, \frac{\partial \hat{T}}{\partial \theta}(\hat{r}, 0, \hat{z}) = 0, \text{ and } \frac{\partial w}{\partial \theta}(\hat{r}, 0) = 0;$$

$$\text{At } \theta = \pi\text{: } \hat{v}(\hat{r}, \pi) = 0, \frac{\partial \hat{T}}{\partial \theta}(\hat{r}, \pi, \hat{z}) = 0, \text{ and } \frac{\partial \hat{w}}{\partial \theta}(\hat{r}, \pi) = 0. \tag{9}$$

The most reliable boundary condition that can be physically imposed, with the joulean heating of cylindrical tubes, is that of insulating the outer tube surface. This problem, however, requires the simultaneous solution of the fluid and tube-material regions. This can be achieved, but the number of independent parameters that must be considered is almost prohibitively increased unless a specific experimental situation is alluded to. Therefore it was considered more useful, at least for these first exploratory calculations, to impose realistic, yet bracketing, conditions upon the thermal boundary conditions. This was accomplished by the utilization of two distinct sets of boundary conditions. The first, and most realistic boundary condition, involves the assertion that it is the fluid system that determines the circumferential temperature distribution at the tube wall; mathematically this is equivalent to asserting that the thermal conductance of the tube is equal to that of the stationary fluid. This is almost exactly true for glass tubes and is not very far from reality with metal tubes of moderate diameter due to their thin walls. Nevertheless, another extreme condition was con-

sidered in which it was assumed that the tube material exhibited an infinite thermal conductivity, and hence eliminated any circumferential temperature gradients at the tube wall, with the result that $\hat{T}(1, \theta)$ is constant. For both of these conditions relating to the temperature distribution around the girth of the tube, the radial heat flux at the wall was regarded as being uniform. Thus, since the thermal conductivity is being considered as constant, and

$$\left(\frac{\partial \hat{T}}{\partial \hat{r}}\right)_{r=1} = \frac{(q/A)_w r_0}{k_b T_b}, \tag{10}$$

the radial temperature gradient at the wall is also constant. So that the two thermal boundary conditions can be distinguished, they will be referred to as the "glass tube" and the "infinite conductivity tube" boundary conditions, respectively.

Now, if the momentum equations for the $\hat{r}$ and θ-directions are integrated with respect to $\hat{r}$ and θ, respectively, and the resulting expressions for $\hat{p}$ are differentiated with respect to $\hat{z}$, the results are equal only provided

$$\hat{p} = B\hat{z} + P(\hat{r}, \theta), \tag{11}$$

where B is an unknown constant. This permits, via the elimination of $\hat{p}$ from the equations of motion, a reduction in their number from three to two and reduces the number of equations in the system to be considered to four.

A stream function can also be defined such that

$$\hat{r}\hat{u} \equiv \frac{\partial \psi}{\partial \theta}, \text{ and } \hat{v} \equiv -\frac{\partial \psi}{\partial \hat{r}}, \tag{12}$$

thereby satisfying the continuity condition. Thus the system of differential equations to be considered has been reduced from five to three. They are

$$\frac{\partial^2 \hat{T}}{\partial \hat{r}^2} + \frac{1}{\hat{r}}\frac{\partial \hat{T}}{\partial \hat{r}} + \frac{1}{\hat{r}^2}\frac{\partial^2 \hat{T}}{\partial \theta^2} + \text{Re Pr}\left[\frac{1}{\hat{r}}\left(\frac{\partial \psi}{\partial \hat{r}}\frac{\partial \hat{T}}{\partial \theta} - \frac{\partial \psi}{\partial \theta}\frac{\partial \hat{T}}{\partial \hat{r}}\right)\right] + \text{Re Pr}\,\tau\hat{w} = 0, \tag{13}$$

$$\frac{\partial^2 \hat{w}}{\partial \hat{r}^2} + \frac{1}{\hat{r}}\frac{\partial \hat{w}}{\partial \hat{r}} + \frac{1}{\hat{r}^2}\frac{\partial^2 \hat{w}}{\partial \theta^2} + \frac{\text{Re}}{\hat{r}}\left[\frac{\partial \psi}{\partial \hat{r}}\frac{\partial \hat{w}}{\partial \theta} - \frac{\partial \psi}{\partial \theta}\frac{\partial \hat{w}}{\partial \hat{r}}\right] - B\,\text{Re} = 0, \tag{14}$$

and

$$\text{Fr}\left(\frac{\partial \hat{\rho}}{\partial \hat{r}}\hat{r}\sin\theta + \frac{\partial \hat{\rho}}{\partial \theta}\cos\theta\right) - \frac{\hat{r}}{\text{Re}}\left(\frac{\partial^4 \psi}{\partial \hat{r}^4} + \frac{2}{\hat{r}}\frac{\partial^3 \psi}{\partial \hat{r}^3} - \frac{1}{\hat{r}^2}\frac{\partial^2 \psi}{\partial \hat{r}^2} + \frac{1}{\hat{r}^3}\frac{\partial \psi}{\partial \hat{r}} + \frac{2}{\hat{r}^2}\frac{\partial^4 \psi}{\partial \hat{r}^2 \partial \theta^2} - \frac{2}{\hat{r}^3}\frac{\partial^3 \psi}{\partial \hat{r}\partial \theta^2} + \frac{4}{\hat{r}^4}\frac{\partial^2 \psi}{\partial \theta^2} + \frac{1}{\hat{r}^4}\frac{\partial^4 \psi}{\partial \theta^4}\right) + \frac{\partial \psi}{\partial \theta}\frac{\partial}{\partial \hat{r}}\left(\frac{\partial^2 \psi}{\partial \hat{r}^2} + \frac{1}{r}\frac{\partial \psi}{\partial \hat{r}} + \frac{1}{\hat{r}^2}\frac{\partial^2 \psi}{\partial \theta^2}\right) - \frac{\partial \psi}{\partial \hat{r}}\frac{\partial}{\partial \theta}\left(\frac{\partial^2 \psi}{\partial \hat{r}^2} + \frac{1}{\hat{r}}\frac{\partial \psi}{\partial \hat{r}} + \frac{1}{\hat{r}^2}\frac{\partial^2 \psi}{\partial \theta^2}\right) = 0. \tag{15}$$

In addition to these differential conservation equations, two integral conditions must be imposed to bound the system and to insure the uniqueness of the solution. These integral conditions are:

$$\int_0^{2\pi}\int_0^1 \hat{w}\hat{r}d\hat{r}d\theta = \pi, \tag{16}$$

and

$$\int_0^{2\pi}\int_0^1 \hat{T}\hat{w}\hat{r}d\hat{r}d\theta = \pi. \tag{17}$$

Physically, the constraints insure constancy of the mass flow and local bulk temperature, respectively.

The boundary conditions, in terms of the stream function, become

$$\frac{\partial \psi}{\partial r}(\hat{r}, 0) = 0, \quad \frac{\partial \psi}{\partial \hat{r}}(\hat{r}, \pi) = 0, \quad \frac{\partial \psi}{\partial \hat{r}}(1, \theta) = 0, \text{ and } \frac{\partial \psi}{\partial \theta}(1, \theta) = 0.$$

Moreover, since ψ, but for an additive constant (due to the definition of ψ being specified as a derivative), is the amount of fluid flowing through a section per unit of time, the constant of integration is conveniently chosen so that ψ is zero on the walls. Thus take $\psi(1, \theta) \equiv 0$. But, since for $\theta = 0$ and $\hat{r} = 1$, $\psi = 0$, and ψ = constant along $\theta = 0$, $\psi(\hat{r}, 0) \equiv 0$ also.

The pressure distribution $P(\hat{r}, \theta)$ is determined after the solutions for $\hat{T}$, $\hat{w}$, ψ, and B have been obtained. This is accomplished by solving the radial equation of motion (5) for an expression for $\partial\hat{p}/\partial\hat{r}$. This is equal to $\partial P/\partial\hat{r}$, however, since $\hat{p} = B\hat{z} + P(\hat{r}, \theta)$. The resulting expression is calculable, then since the solutions for $\hat{T}$, $\hat{w}$, and ψ are known, and integration along successive radii gives $P(\hat{r}, \theta)$ to within the arbitrary constant required to specify the pressure level.

The axial pitch of a streamline is an operational quantity if visualization of the flow is made possible and should, consequently, be calculated. The axial distance traversed in time, t, is given by

$$\hat{z} = \int_0^{\hat{t}} \hat{w}d\hat{t}, \tag{18}$$

and the time interval, $\hat{t}$, can be determined from the arc length of the *two-dimensional* streamlines. The time required to complete the two-dimensional streamline circuit is

$$\hat{t} = \int_s \frac{d\hat{s}}{\sqrt{\hat{u}^2 + \hat{v}^2}}, \tag{19}$$

or the differential time required to traverse an elemental length of the two-dimensional streamline is

$$d\hat{t} = \frac{d\hat{s}}{\sqrt{\hat{u}^2 + \hat{v}^2}}. \tag{20}$$

Thus, since

$$d\hat{s} = \sqrt{(\hat{r}d\theta)^2 + (d\hat{r})^2}, \tag{21}$$

$$d\hat{t} = \frac{\sqrt{(\hat{r}d\theta)^2 + (d\hat{r})^2}}{\sqrt{\hat{u}^2 + \hat{v}^2}}. \tag{22}$$

Hence, the pitch, λ, is given by

$$\lambda = \hat{z} = \int_s \hat{w}\frac{\sqrt{(\hat{r}d\theta)^2 + (d\hat{r})^2}}{\sqrt{\hat{u}^2 + \hat{v}^2}}. \tag{23}$$

The distance along a trajectory, ζ, is given by

$$\zeta = \int_s \hat{w}\frac{\sqrt{(\hat{r}d\theta)^2 + (d\hat{r})^2 + (dz)^2}}{\sqrt{\hat{u}^2 + \hat{v}^2}}. \tag{24}$$

The Darcy-Weisbach friction factor is given by

$$f = -4B, \tag{25}$$

and the Nusselt number is defined as

$$\text{Nu} \equiv \frac{hD}{k} = \frac{(q/A)_w D}{k_b(T_w - T_b)}. \tag{26}$$

Finite-Difference Formulation

The so-called central-difference operators, employed to transform equations (13)–(15) into algebraic, finite-difference equations, were obtained from manipulations with truncated Taylor's series. These operators had truncation errors of the order of the square of the grid spacing. The integral constraints and bound-

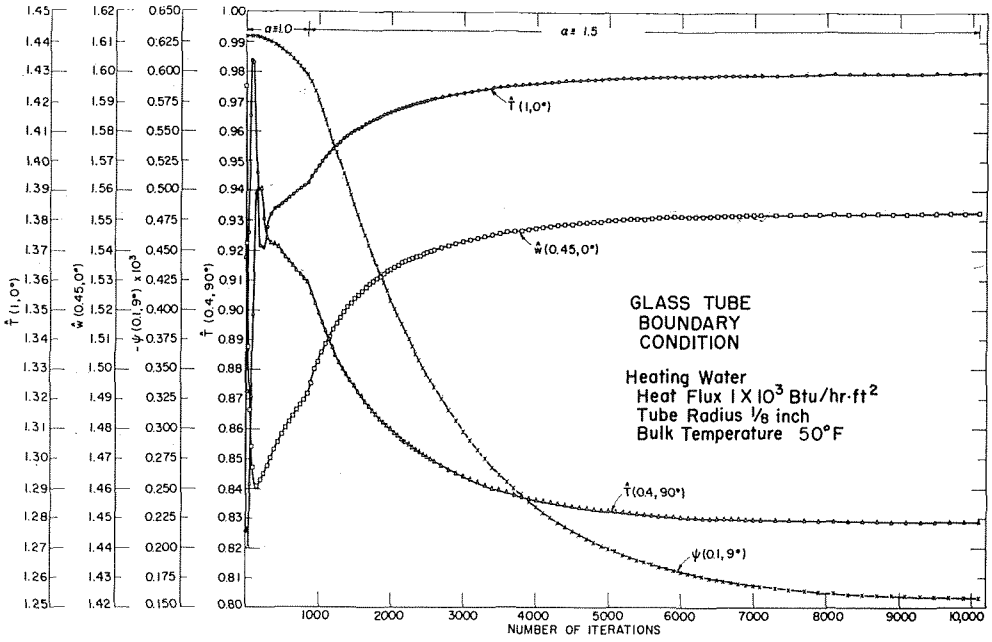

Fig. 2 Convergence behavior

ary conditions were also transformed by standard numerical techniques. Due to their excessive length, it is inappropriate to present the finite-difference formulation here; a detailed description is given in reference [1].

Solution Details

An iterative technique with successive over (or under) relaxation was utilized. This yielded the optimum convergence rates and provided for damping of oscillations in the event that poor initial guesses induced potentially divergent instabilities in the nonlinear system. The residuals, popularly used in relaxation calculations via desk computation, were not employed and stored, however, in this investigation since the core storage limits were already strained. Rather, after iteration at each grid point, the variables were modified in accordance with the formula

$$F = \alpha_F F_{\text{new}} + (1 - \alpha_F)F_{\text{old}} \tag{27}$$

where F represents any of the variables, $\hat{T}$, $\hat{w}$, ψ, or B; α the corresponding convergence-accelerating parameter; F_{new} the value of the pertinent variable from the current iteration; and F_{old} the value of the same variable from the previous iteration. Unfortunately, no theoretical basis exists for assigning values to the various α's, and one must resort to numerical experimentation. In the cases reported in this work, α's as low as 0.25 were required for stable behavior, and values as high as 1.5 were achieved with stable operation under differing circumstances.

As many as 50,000 cycles of iteration and as few as 1600 were acknowledged in the solution of the cases studied. It is significant that somewhat shorter computational times are required when the initial guesses are associated with employing the output of one case as the initial guess for the next, while maintaining a systematic alteration of the problem parameters.

Fig. 2 depicts the change in the temperature, the change in the axial velocity, and the change in the stream function with the number of cycles of iteration for representative grid points for a typical case. Oscillations are observed to occur at the beginning of the calculation. An account of the convergence rate was printed out by the program so that the plotting of the variables was not required. These results were estimated to be within about one percent of those that would be realized after an infinite number of iterations [1]. A nominal time for one converged case (using 20 × 20 grid, 10,000 iterations, and printing every 500 iterations) represents about 2½ hr on the IBM 7094 and about 11 hr on the IBM 7040 system.

The computational time increases drastically with grid refinement. Studies were made using finer grid networks, and it was found that the 20 × 20 grid formulation yields results which are within 5 percent of those using 40 × 40 grids, and that there is no significant difference between 40 × 40 and 80 × 80 grid formulations.

Regarding the initial guesses for $\hat{T}$, $\hat{w}$, ψ, and B required to initiate the iterative process, several schemes were utilized. These included: Poiseuille flow, Morton's [18] perturbation solution, the perturbation solution of del Casal and Gill [19], and various combinations and modifications of these. In general, most efficient computation was effected by using the solution to one case for the initial guess of another one, since the perturbation solutions were of limited use even as initial guesses.

Fortran program listings and instructions for use of these programs are given in [1].

Discussion of Results

Details of the Flow

Figs. 3–10 depict detailed results for a typical case: glass-tube boundary condition, $r_0 = 0.5$ in., $(q/A)_w = 10^3$ Btu/hr-ft², $W_0 = 0.1$ fps, and $T_b = 100$ deg F. The computed results are as follows: $\bar{T}_w = 120.5$ deg F, $\hat{T}(1, 0)/\hat{T}(1, \pi) = 2.25$, $\overline{\text{Gr}} = 1.241 \times 10^6$, Re = 1130, $\overline{\text{Nu}} = 11.23$, and $f = 0.071$. The rather modest average temperature difference produces significant stratification effects as well as substantial increases in $\overline{\text{Nu}}$ and f, which are 4.36 and 0.056, respectively, for the corresponding symmetric, or Poiseuille, flow.

Lines of constant temperature and lines representing constant values of the stream function are presented in Fig. 3. The maximum temperatures are observed to occur in the upper portion of the tube while the minimum temperatures are noted to occur in the lower region of the tube. Significant asymmetry of the stream function about the horizontal center line can be seen with this glass-tube case Increasing the tube radius and/or the heat flux results in the location of the eye of the spiraling streamlines being moved radially outward and farther into the lower portion of the tube. With the infinite-conductivity-tube boundary condition, much less asymmetry about the horizontal center line is observed; the principal effect of an increase in either tube radius or

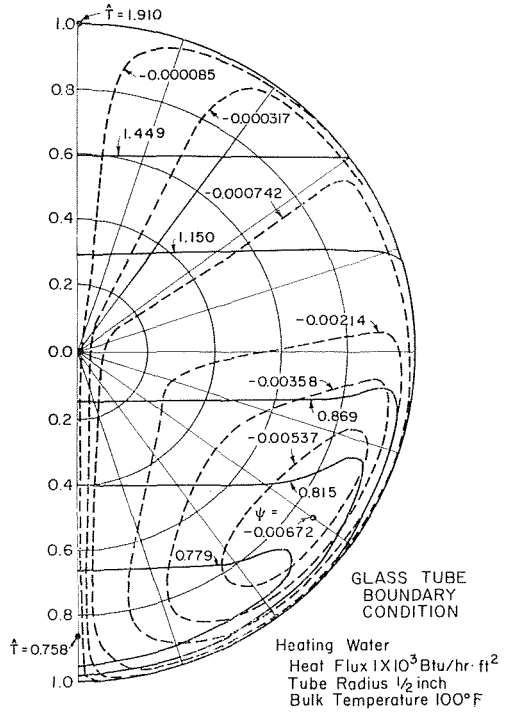

Fig. 3 Isotherms and two-dimensional streamlines

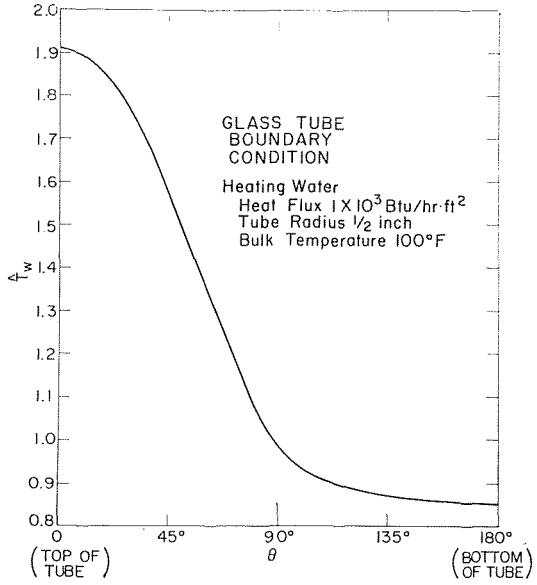

Fig. 6 Circumferential wall temperature variation

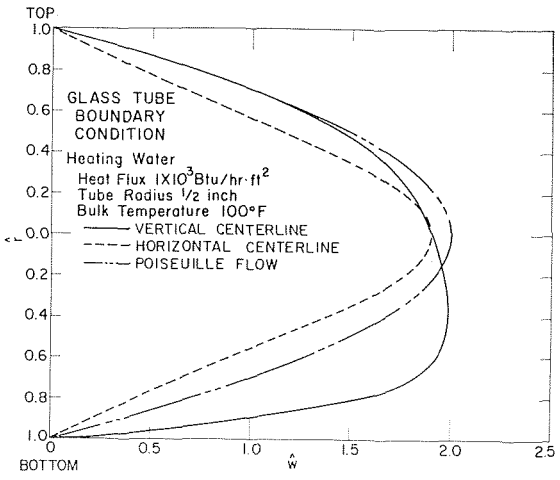

Fig. 4 Axial velocity distribution along vertical and horizontal center lines

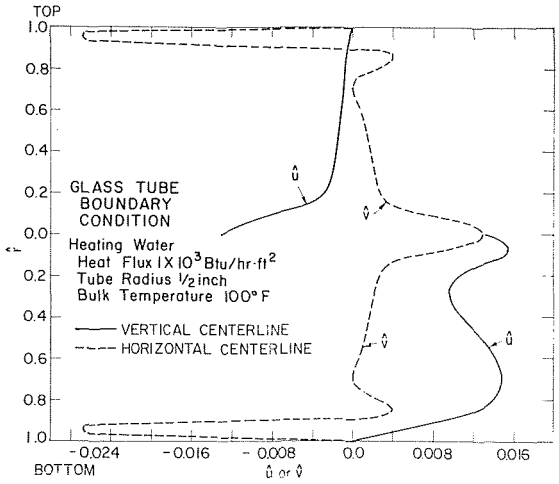

Fig. 7 Radial and azimuthal velocity distributions along vertical and horizontal center lines

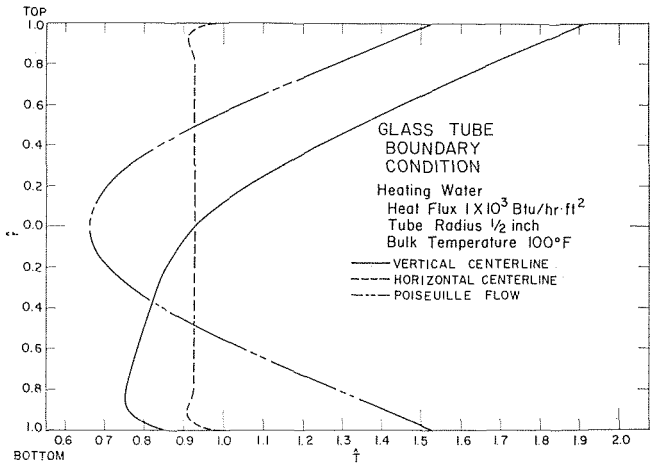

Fig. 5 Temperature distribution along vertical and horizontal center lines

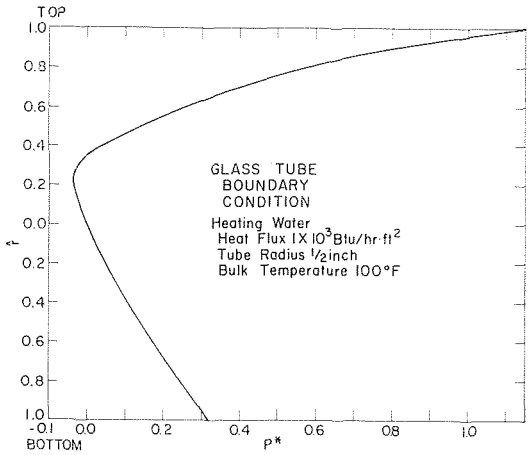

Fig. 8 Piezometric head distribution along vertical center line

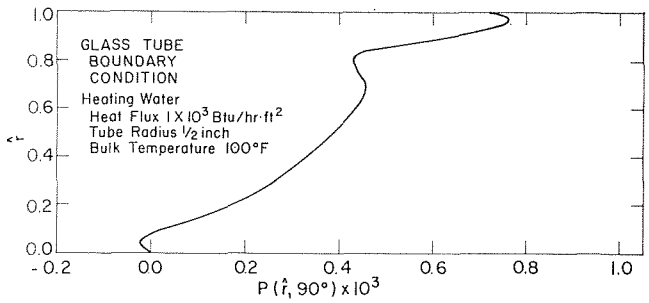

Fig. 9 Pressure distribution along horizontal center line

heat flux is to displace the eye radially outward. For both boundary conditions, the location of the eye of the streamlines is unaffected by alteration of the average axial velocity.

Figs. 4 and 5 depict the distribution along the vertical and horizontal center lines of the axial-velocity component and the temperature profiles, respectively. The corresponding Poiseuille profiles are presented for comparison. The effect of the secondary flow on the axial velocity profile is observed in Fig. 4 to shift the point of maximum velocity along the vertical center line toward the lower region of the tube. Fig. 5 emphasizes the marked asymmetry in the temperature distribution about the horizontal center line; the stratification effect is seen to be significant, with the minimum temperature occurring in the lower portion of the tube. The circumferential variation in the tube wall temperature is given in Fig. 6, where it is seen that a temperature difference of 106 deg F exists between the top and bottom of the tube. Furthermore, the wall temperature at the bottom is less than the bulk temperature. Experimental variations of this order have been reported for water in laminar flow [5] and turbulent flow [30, 31] at low Reynolds numbers. It is noted that this wide variation in fluid temperature precludes any analytical simplification via use of a constant bulk modulus of expansion. From a practical standpoint, this result suggests that numerous thermocouples are required to obtain average wall temperature measurements for tubes with small circumferential heat conduction. In addition, in order to maintain the constant-heat-flux boundary condition, it is necessary to choose tube materials with low temperature coefficients of electrical resistivity.

The radial and azimuthal velocity distributions along the vertical and horizontal center lines are shown in Fig. 7. It is significant that the asymmetric position of the eye of the streamlines induces reversals in the accelerations of the fluid particles along the vertical center line in the lower position of the tube. The secondary flow is portrayed quite vividly by the azimuthal velocity profiles along the horizontal center lines. It is significant also to note that, whereas in the symmetric developing flow situation the radial velocities attain large magnitudes [1], while apparently contributing in only a minor way to the heat transfer, the velocity components transverse to the principal direction of flow induced by free convection are quite small yet produce a very sizeable effect upon the heat transfer.

Although the pressure distribution throughout the cross section of the tube is very nearly hydrostatic, the effect of the secondary flow can be seen in the distribution of the pressure along the vertical center line and along the horizontal center line in Figs. 8 and 9, respectively.

Fig. 10 illustrates the axial pitch of streamlines, which is of interest in visualization studies. From this figure it is apparent that the pitch changes most drastically with the point of particle marking, measured along the ray containing the eye of the streamlines, near the axis of the tube. Consequently, considerable uncertainty is associated with methods for determining the pitch that involve the injection of marked particles at the center line of the tube. It appears that the most opportune particle-marking position occurs nearer the eye than nearer the tube axis.

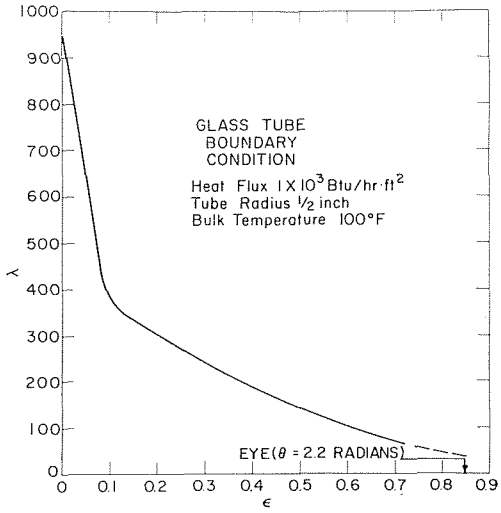

Fig. 10 Axial pitch of three-dimensional streamline as a function of radial-particle-marking position along the ray containing the eye

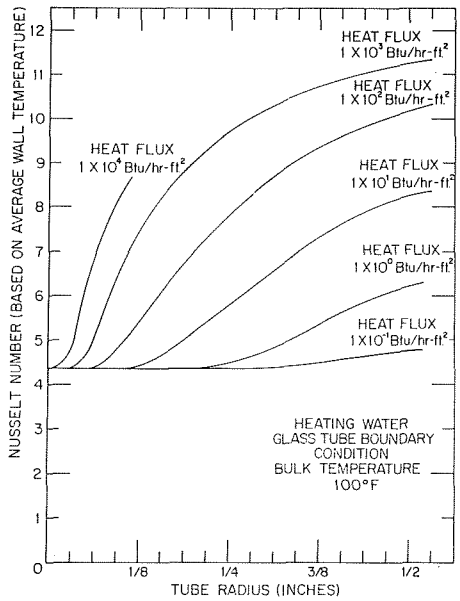

Fig. 11 Dependence of Nusselt number on tube radius and heat flux

However, the measurement of the pitch very near the eye will require a very precise technique. Hanratty's perturbation solution, recorded in Appendix 2 of reference [4], severely overestimates the axial distance required for a streamer, identified at the tube axis, to reach the bottom of the tube [1].

The detailed flow information obtained in this study was used to examine conditions under which the boundary-layer approximation might be considered a valid approach to the study of the secondary flow [1]. It was found that the predominantly inviscid region defining the core could be reasonably well defined. However, since the core flow depends strongly on the boundary-layer flow, there appears to be no profitable motive for pursuing such a calculation involving the boundary-layer approximation.

Parametric Effects and Design Correlations

An extensive computational effort was undertaken to develop sufficient solutions to define the parametric effects and develop design correlations for heat transfer and pressure drop.

The effects of the problem parameters (heat flux, tube radius, wall temperature, and tube-wall boundary condition) upon the average Nusselt number are presented in Figs. 11 through 13.

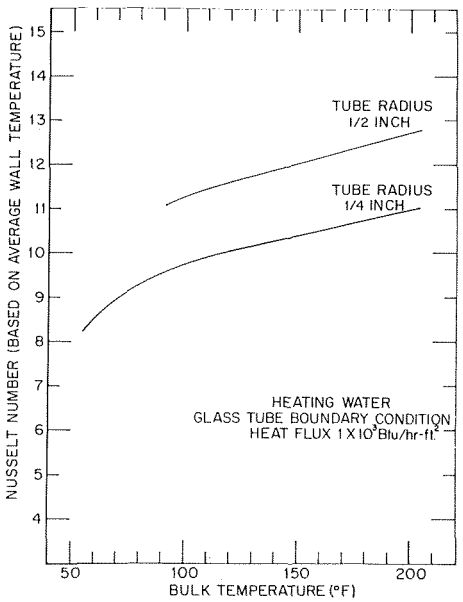

Fig. 12 Influence of bulk temperature and tube radius on Nusselt number

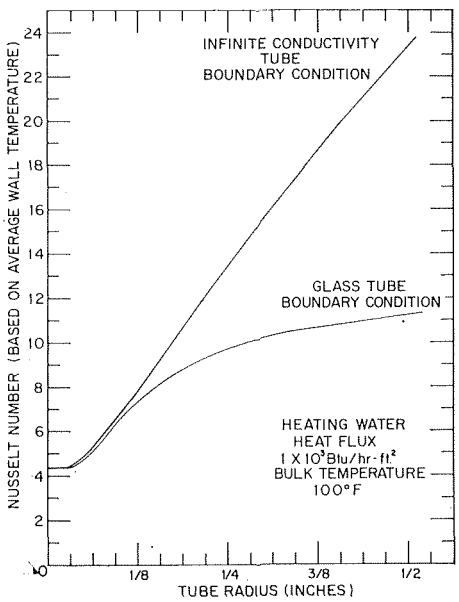

Fig. 13 Influence of tube-wall boundary condition on Nusselt number

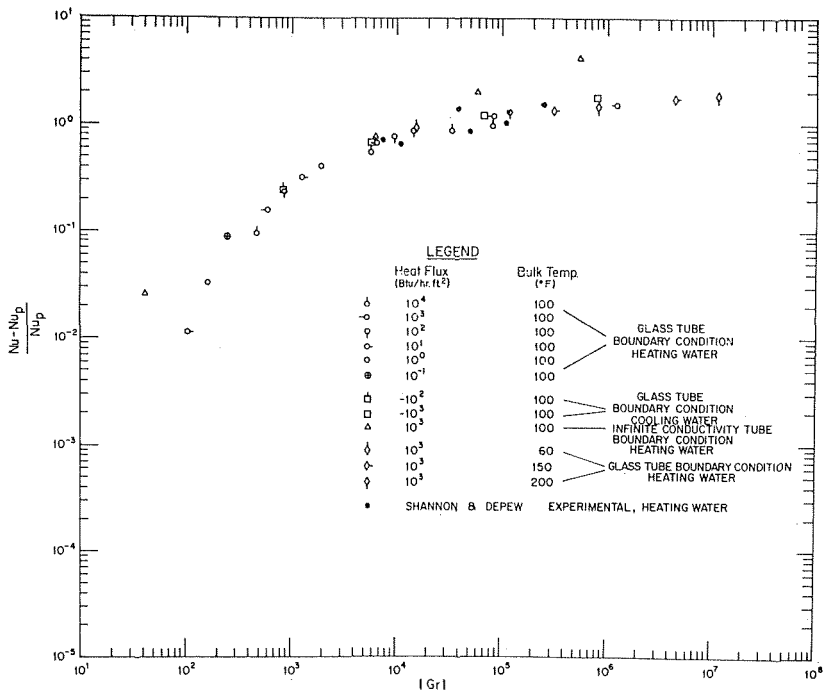

Fig. 14 Correlation of Nusselt number with Grashof number and comparison with experimental data

In Fig. 11, it is apparent that the Poiseuille flow model is valid only for capillary tubes and/or for minute heat fluxes. Fig. 12 indicates that as the bulk temperature is increased, the Nusselt number increases.

The glass-tube and infinite-conductivity-tube boundary conditions are compared in Fig. 13, where it is seen that the infinite-conductivity tube exhibits a much higher Nusselt number. A tube material which has a high conductance will not accommodate as large a circumferential temperature gradient as will those materials which have low thermal conductivities such as glass. Consequently, the stratification phenomenon is more pronounced with the glass-tube boundary condition, with the result that the driving potential for the secondary flow (the local ΔT) is lessened.

It was found that variations in the average axial velocity, which is physically an independent problem parameter, produced no changes in the average Nusselt number. This is, of course, a consequence of the fully developed assumption.

The traditional correlation parameter employed in problems involving free convection is the Grashof number. The improvement in average Nusselt number is plotted versus Grashof number in Fig. 14, where it is observed that calculated free-convection effects elevate the Nusselt number by over a factor of five at higher Grashof numbers. The analytical data point scatter is systematic, and smooth curves could be drawn through those data points representing the same tube-wall boundary condition, heat flux, and bulk fluid temperature. Shannon and Depew [16] recently reported data for the heating of water. Representative data from this study, corresponding to fully developed free convection, are shown to be bracketed by the present

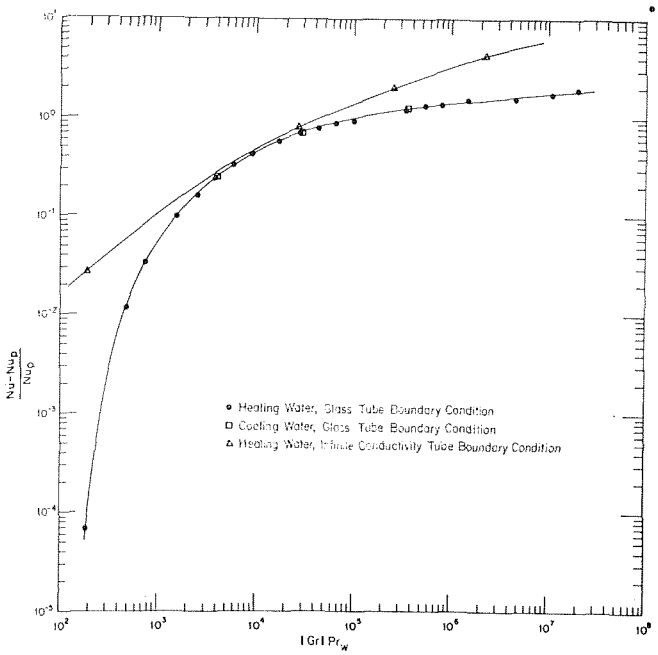

Fig. 15 Correlation of Nusselt number with Grashof-Prandtl number product

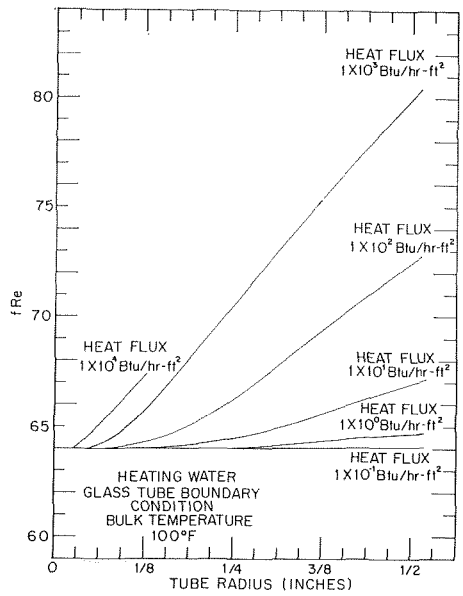

Fig. 16 Influence of tube radius and heat flux on pressure drop-parameter

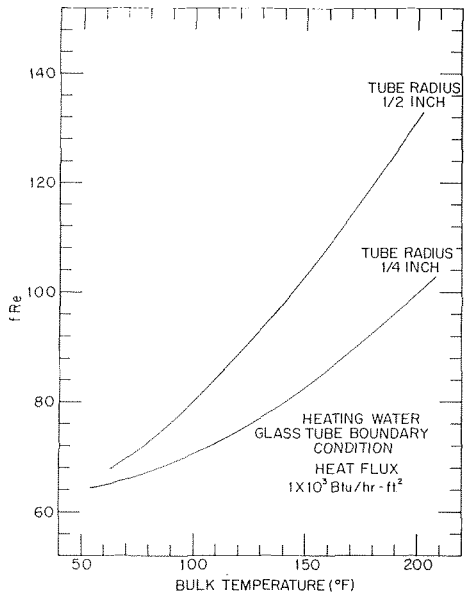

Fig. 17 Influence of bulk temperature and tube radius on pressure-drop parameter

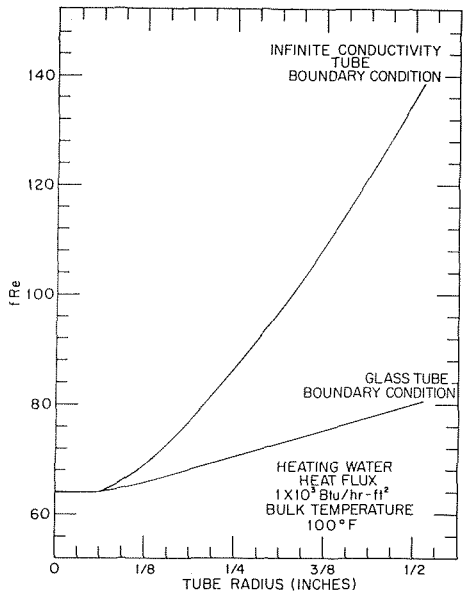

Fig. 18 Influence of tube-wall boundary condition on pressure-drop parameter

analytical predictions. The experimental data of Ede [17] are also bracketed by the analytical results of this study.

Final correlation curves were obtained by introducing the Prandtl number as shown in Fig. 15. In order to effect a successful correlation, it was necessary to evaluate the Prandtl number at the average wall temperature. Since the different tube-wall boundary conditions constitute systems which are not similar, the distinct correlations which are depicted should be expected. The water data of Shannon and Depew [16] or of Ede [17] could not be checked against the correlation since the Prandtl number could not be extracted from the published data. However, in view of the good agreement in Fig. 14, a reasonable correlation would be expected. An attempt was also made to include the limited air data of McComas and Eckert [15] and Mori and Futagami [3]. These air data were considerably above the present correlation curves. Several analytical solutions were also generated for a light oil, and significant deviations from the curves in Fig. 15 were noted. These results indicate that the present analytical correlation is valid only for water, and that additional calculations will be required to develop a general prediction. In view of the complex nature of the problem, it is certainly to be anticipated that additional dimensionless groups will be required to correlate data for more than one fluid.

The effects of the problem parameters upon the phenomenological, pressure-drop parameter are presented in Figs. 16 through 18. Again, the results are monotonic with respect to the average axial velocity. The limited extent of the applicability of the Poiseuille model in predicting pumping requirements is apparent in Fig. 16 and is similar to the heat-transfer parameter situation. The effects of bulk temperature changes are also in like directions as seen in Fig. 17. Associated with the infinite-conductivity-tube boundary condition are larger azimuthal velocities, tighter spirals (smaller values for the axial pitch of the streamlines), and consequently larger pressure drops compared to the glass-tube boundary condition as is shown in Fig. 18.

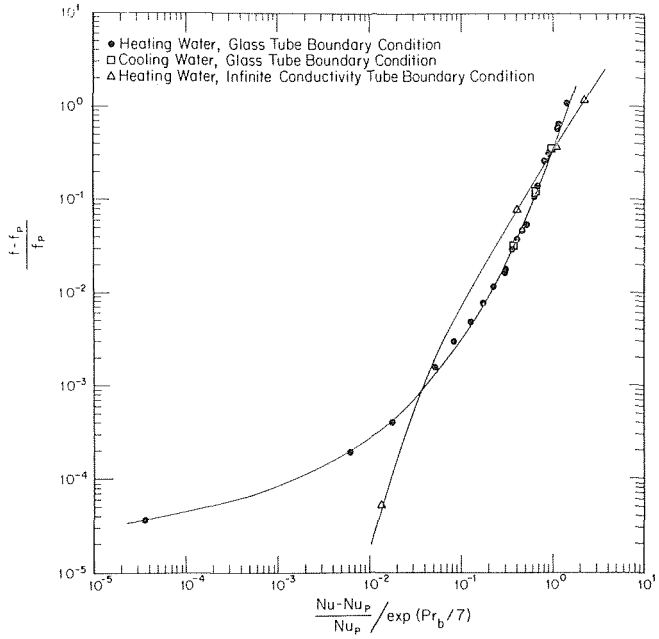

Fig. 19 Correlation of friction factor with Nusselt number

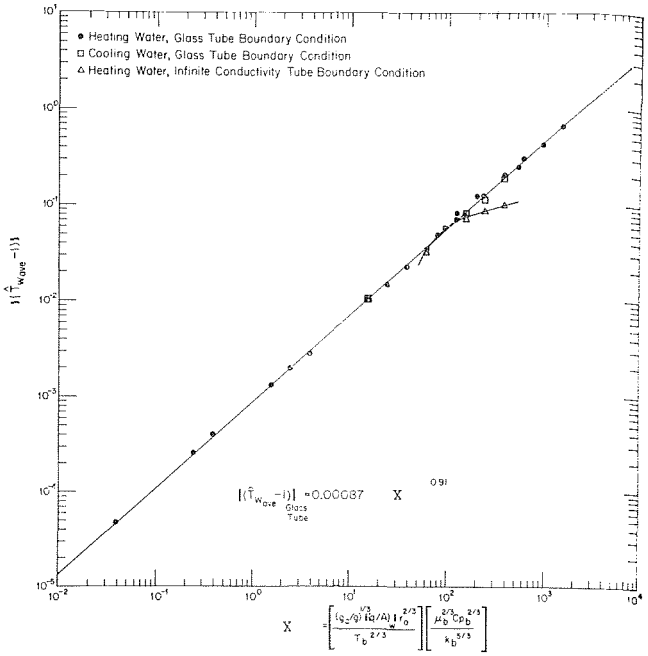

Fig. 21 Correlation for average wall temperature as an alternate to the intermediate Nusselt number calculation method

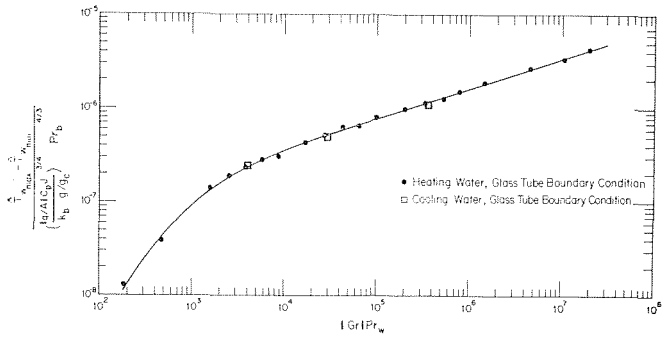

Fig. 20 Correlation of tube wall temperature stratification effect

Fig. 19 relates a correlation between the analytical results for the friction factor and the Nusselt and Prandtl numbers for both tube-wall boundary conditions considered. Unfortunately, no experimental results for the effect of heating on pressure drops were found in the literature for comparison.

With the glass-tube boundary condition, significant circumferential wall temperature variations exist. A correlation for the difference between the wall temperatures at the top and bottom of the tube is presented in Fig. 20.

Now, since the use of the Nusselt number really requires an extra calculation for the designer (generally either the heat flux or the wall temperatures is specified and the other is required), a correlation between the average wall temperature and a parameter involving the heat flux, bulk temperature, and fluid properties is presented in Fig. 21. A particularly simple correlation was obtained for the glass-tube case.

Conclusions

An analysis has been performed to determine the effects of free convection on fully developed laminar flow in horizontal circular tubes with uniform heat flux. A large-scale digital computer was used to solve an accurate finite-difference formulation of the governing equations. Solutions for heat transfer and pressure drop, with both heating and cooling, were obtained for water with two limiting tube-wall conditions: low thermal conductivity (glass tube) and infinite thermal conductivity.

A detailed presentation of data for velocity, temperature, and pressure distribution is given for a typical case with the glass-tube boundary condition. At a modest ΔT, extensive stratification of the flow is predicted, with the tube wall exhibiting a large circumferential temperature gradient. Due to the secondary flow, both Nusselt number and friction factor are higher than the values predicted for constant-property Poiseuille flow.

Numerous solutions were generated to examine the effects of system parameters on heat transfer and friction. The Nusselt number and friction factor increase as tube radius, heat flux, and bulk temperature are increased. As a consequence of the fully developed assumption, Nu and the increase of f Re above the Poiseuille value are unaffected by the average axial velocity. The infinite conductivity tube exhibits higher Nu and f than the glass tube, with Nu being over five times the Poiseuille value at Gr $\sim 10^6$. The analytical predictions bracket recent experimental data for water. A design correlation for Nu for both heating and cooling of water is developed from the analytical solutions (Fig. 15). Several other correlation curves were developed to facilitate computation of wall temperatures and friction factors.

The present data provide for an assessment of free-convection effects for water. Regarding extensions of this study, additional solutions for other fluids are required before a general correlation can be developed. However, the analytical formulation may have to be revised for other fluids to account for the effects of radial property variation and viscous dissipation. Specific applications may require solutions for the "any-tube" case where the tube and fluid regions are considered simultaneously. Eventually, the three-dimensional solution can be undertaken to study the development of the secondary flow.

Acknowledgments

This investigation was supported in part by the Francis Bitter National Magnet Laboratory which is sponsored by the Air Force office of Scientific Research and in part by NIH Grant No. FR 145. Computations were performed in part on the IBM 7094 system at the Massachusetts Institute of Technology Computation Center, and in part on the IBM 7040 system at the University of Alabama Medical Center Computer Research Laboratory. Profs. W. M. Rohsenow and W. H. Heiser gave generously of their time to the discussion of various aspects of this work.

References

1 Newell, P. H., Jr., "Laminar-Flow Heat Transfer in Horizontal Tubes," PhD thesis in Mechanical Engineering, M.I.T.-Cambridge, Mass., Mar. 1966.

2 Juvkam-Wold, H. C., "Visualization of Secondary Flow in Heated Tube," Course 2.55 Term Project, M.I.T., Cambridge, Mass. Jan. 1967.

3 Mori, Y., and Futagami, K., "Forced Convective Heat Transfer in Uniformly Heated Horizontal Tubes" (2nd Report, Theoretical Study), *International Journal of Heat and Mass Transfer*, Vol. 10, 1967, pp. 1801–1813.

4 Apostolakis, N., "Effect of Heat Transfer Upon Flow Field at Low Reynolds Numbers in Horizontal Tubes," MS thesis, University of Illinois, 1957.

5 Mikesell, R. D., "The Effect of Heat Transfer on the Flow in a Horizontal Pipe," PhD thesis, University of Illinois, 1963.

6 Gorton, C. W., Purdy, K. R., and Bell, C. J., "Nonisothermal Velocity Profiles," *AIChE Journal*, Vol. 9, No. 1, 1963.

7 Mori, Y., "Forced Convective Heat Transfer in Uniformly Heated Horizontal Tubes (1st Report) Experimental Study on the Effect of Buoyancy" *International Journal of Heat and Mass Transfer*, Vol. 9, 1966, pp. 453–463.

8 Colburn, A. P., "A Method of Correlating Forced Convection Heat Transfer Data and a Comparison With Fluid Friction," *American Institute of Chemical Engineers, Transactions*, Vol. 29, 1933, pp. 174–210.

9 Kern, D. Q., and Othmer, D. F., "Effect of Free Convection on Viscous Heat Transfer in Horizontal Tubes," *Transactions AIChE*, Vol. 39, 1943, pp. 517–555.

10 Eubank, O. C., and Proctor, W. S., "Effect of Natural Convection on Heat Transfer With Laminar Flow in Tubes," MS thesis, M.I.T., Cambridge, Mass., 1951.

11 Jackson, T. W., Spurlock, J. M., and Purdy, K. R., "Combined Free and Forced Convection in a Constant Temperature Horizontal Tube," *AIChE Journal*, Vol. 7, No. 1, 1961, p. 38.

12 Oliver, D. R., "The Effect of Natural Convection on Viscous-Flow Heat Transfer in Horizontal Tubes," *Chemical Engineering Sciences*, Vol. 17, 1962, p. 335.

13 Jackson, T. W., and Söhngen, E. E., "Bestimmung des Wärmeübergangs in Horizontalen Rohr bei Gleichzeitiger Freier und Erzwungener Strömung," *Chemie-Ingenieur Technik*, Vol. 33, 1961, p. 536.

14 Brown, A. R., and Thomas, M. A., "Combined Free and Forced Convection Heat Transfer for Laminar Flow in Horizontal Tubes," *Journal of Mechanical Engineering Science*, Vol. 7, 1965, pp. 440–448.

15 McComas, S. T., and Eckert, E. R. G., "Combined Free and Forced Convection in a Horizontal Circular Tube," JOURNAL OF HEAT TRANSFER, TRANS. ASME, Series C, Vol. 88, 1966, pp. 147–153.

16 Shannon, R. L., and Depew, C. H., "Combined Free and Forced Laminar Convection in a Horizontal Tube With Uniform Heat Flux," JOURNAL OF HEAT TRANSFER, TRANS. ASME, Series C, Vol. 90, 1968, pp. 353–357.

17 Ede, A. J., "The Heat Transfer Coefficient for Flow in a Pipe," *International Journal of Heat and Mass Transfer*, Vol. 4, 1961, pp. 105–110.

18 Morton, B. R., "Laminar Convection in Uniformly Heated Horizontal Pipes at Low Rayleigh Numbers," *Quarterly Journal of Mechanics and Applied Mathematics*, Vol. XII, Part 4, 1959, p. 410.

19 del Casal, E., and Gill, W. N., "A Note on Natural Convection Effects in Fully Developed Horizontal Tube Flow," *AIChE Journal*, Vol. 8, No. 4, 1962, p. 570.

20 Iqbal, M., and Stachiewicz, J. W., "Influence of Tube Orientation on Combined Free and Forced Laminar Convection Heat Transfer," JOURNAL OF HEAT TRANSFER, TRANS. ASME, Series C, Vol. 88, 1966, pp. 109–116.

21 Leite, R. J., "An Experimental Investigation of the Stability of Poiseuille Flow," *Journal of Fluid Mechanics*, Vol. 5, 1959, pp. 81–96.

22 Prengle, R. S., and Rothfus, R. R., "Transition Phenomena in Pipes and Annuar Cross Sections," *Industrial and Engineering Chemistry*, 1955, pp. 379–386.

23 Altman, M., and Staub, F. W., "The Effects of Superimposed Forced and Free Convection in Horizontal and Vertical Rectangular Ducts," presented at Second National Heat Transfer Conference AIChE-ASME, Chicago, Ill., 1958.

24 Scott, C., Eggleston, G. E., and Sibbitt, W. L., "Local and Average Coefficients of Heat Transfer for Horizontal Laminar Motion of Fluids in a Circular Tube," ASME Paper No. 55—SA-17, 1955.

25 Poppendiek, H. F., "Heating and Cooling Solutions for Viscous, Liquid Flow in Pipes," *Heat Transfer, Thermodynamics, and Education*, Boelter Anniversary Volume, McGraw-Hill, New York, 1964.

26 Boussinesq, J., "Hydrodynamique," *Comptes Rendus*, Vol. 110, 1890, pp. 1160–1238.

27 Keenan, J. H., and Keyes, F. G., *Thermodynamic Properties of Steam*, Wiley, New York, 1957.

28 McAdams, W. H., *Heat Transmission*, 3rd ed., McGraw-Hill, New York, 1954.

29 Kreith, F., *Principles of Heat Transfer*, 2nd ed., International Textbook, Scranton, Pa., 1965.

30 Newell, P. H., Jr., "On a Device Contrived for the Experimental Determination of the Variation of Local, Forced Convection, Heat Transfer Coefficients," MS thesis, University of Tennessee, 1961.

31 Allen, R. W., and Eckert, E. R. G., "Friction and Heat-Transfer Measurements to Turbulent Pipe Flow of Water (Pr = 7 and 8) at Uniform Wall Heat Flux," JOURNAL OF HEAT TRANSFER, TRANS. ASME, Series C, Vol. 86, 1964, pp. 301–310

C. J. MADAY[2]
Oak Ridge National Laboratory
and North Carolina State University

A Dynamic Programming Approach to Stabilize Forced-Convection Two-Phase Flow Systems With "Pressure-Drop" Oscillations[1]

Optimization theory is applied to a forced-convection two-phase flow system with heat addition described by a second-order system of differential equations. The mathematical model describes a physical system in which low-frequency pressure-drop oscillations occur, and these oscillations may either grow or decay with time depending on whether the system is stable. The dynamic programming approach is applied to obtain a suboptimal feedback control system which is very stable and exhibits no oscillatory behavior. A system is synthesized whereby pressure and temperature fluctuations are used to control heat-input fluctuations in order to provide stability.

Introduction

A NUMBER of analytical studies of two-phase flow systems have been made to develop spatially independent models so that spatially continuous processes could be characterized by lumped parameter representations. These studies describe the development of a system of governing equations based on the conservation of mass, momentum, and energy and their consequent solution to determine frequency response, stability, etc. In the equations which describe systems with fixed geometry, there are some quantities which are usually considered to be constant. These quantities, which include heat input, flow rates, and inlet and outlet pressures, are adjusted sometimes to obtain stability and/or to realize other performance parameters. In many other processes, stability is achieved by the application of a feedback controller. So too, in the case of two-phase flow systems, there is the possibility of using a feedback controller. This would mean that one or more of the aforementioned quantities would become a control variable which varies in time in some appropriate manner to attenuate temperature and pressure fluctuations generated by external disturbances. In the following development, the heat input is taken to be the control variable. Then optimal control theory is applied to the synthesis and design of a feedback controller to produce stability in a forced-convection two-phase flow system.

In a recent paper by Bankoff and Bandy [1],[3] optimization theory is applied to the design of a natural-circulation boiling water channel where the heat removal rate is to be maximized and the control variables are the flow area and the local heat input. The local heat flux is constrained to be less than some fraction of

[1] Research sponsored by the U. S. Atomic Energy Commission under contract with Oak Ridge Associated Universities, Inc., and Union Carbide Corp.

[2] Research Participant, Reactor Division, Oak Ridge National Laboratory, Summer 1968; Associate Professor, Department of Engineering Mechanics, North Carolina State University, Raleigh, N. C.

Contributed by the Heat Transfer Division of THE AMERICAN SOCIETY OF MECHANICAL ENGINEERS and presented at the ASME-AIChE Heat Transfer Conference, Minneapolis, Minn., August 3–6, 1969. Manuscript received by the Heat Transfer Division, October 15, 1968; revised manuscript received April 10, 1969. Paper No. 69-HT-43.

[3] Numbers in brackets designate References at end of paper.

Nomenclature

A_1 = flow area between supply tank and surge tank
A_2 = flow area between surge tank and heater
b_{ij} = defined in equations (57)–(60)
$c_{22} = \frac{1}{\tau_2}$
c_m = specific heat of heater material
D = differential operator
E = instantaneous minimum error function
e = error index
e_* = defined after equation (41)
H = power input to fluid
H_i = power input to heater
h = heat-transfer coefficient, error measure
$K_1 = [(P_1 - P_2)/Q_1^2]_0$
k, k_i, k_{ij} = k parameters, see equations (11)–(13)
L_1 = length of tubing between supply tank and surge tank
L_2 = length of tubing between surge tank and outlet
M = mass of heater
$\dot{m}$ = mass flow rate
m_1, m_2 = defined after equation (44)
n_1, n_2 = defined after equation (53)
P_1 = supply pressure
P_2 = surge tank pressure
P_{2a} = partial pressure of air in surge tank
P_{2v} = partial pressure of vapor in surge tank
P_3 = outlet pressure
Q_1 = volume flow rate into surge tank
Q_2 = volume flow rate out of surge tank
Q_{ev} = rate of loss of liquid due to evaporation
T = final time
T_w = heater wall temperature
T_f = saturation temperature of fluid in heater
t = present time
V_g = volume of gas in surge tank
V_l = volume of liquid in surge tank
μ = dummy time variable
ρ_l = liquid density
σ = future time
τ_1, τ_2 = defined after equations (47) and (49), respectively
ϕ_1, ϕ_2, ϕ_3 = weighting functions
δ = (preceding a quantity) perturbation of quantity away from its steady-state value
0 = steady-state value when used as subscript
$'$ = differentiation with respect to time. This does not apply to the Appendix.

the local burnout flux. It is also constrained to be nonnegative. They found that the optimum shape was flared at both ends and that, in the intermediate region, the diameter increased from inlet to outlet. The heat input, which was found to be at either the upper (some fraction of local burnout flux) or the lower (zero) constraint value, varied as a function of position along the channel. The work described next is concerned with forced-convection two-phase flow where the only control is the heat input.

According to Stenning and Veziroglu [2], there are two major types of instability associated with two-phase flow. The first occurs when the pressure drop decreases with increasing flow rate across a given test section and is associated with a low void fraction. This is often called pressure-drop instability. The second type of instability is caused by the interaction of pressure drop, flow rate, and mass storage and is sometimes called "density-wave" instability. In the following analysis, pressure-drop instability will be considered in order to illustrate the application of optimization theory to two-phase flow problems.

System Equations

The derivation of the system equations follows the work of Stenning and Veziroglu [2] very closely but with enough modifications to allow the use of dynamic programming to synthesize a control system. The frequency associated with the pressure-drop flow oscillations is rather low (1 to 5 rad/min) so that it is possible to assume quasi-steady conditions in the heater. For the same reason, it is also possible to neglect inertia effects.

The problem is one of one-dimensional unsteady flow for the system shown in Fig. 1. Two-phase flow representation is provided by the vapor volume in the surge tank and the liquid flow out of the tank. That is to say, liquid and vapor are present simultaneously in the model. Further, the surge tank provides for liquid storage so that the flow out of the tank may fluctuate as would occur with the onset of oscillations. Boiling effects are considered in an implicit manner through the variation of pressure drop with heat addition. It is interesting to note that in the experimental investigation [2] with this apparatus, instability was usually occasioned by boiling in the heater. The heat addition accelerated the flow with decreasing pressure drop and brought on the unstable oscillations. Stenning and Veziroglu [2] used water and Freon-11 in their work. Freon-11 is the working fluid in the examples considered in this paper.

The system under consideration is perhaps the simplest one which exhibits instability. This, in turn, allows insight to be gained in the synthesis of a feedback control system which renders stability to two-phase flows which may be unstable in the open-loop configuration.

The governing system equations are derived in the Appendix and are linearized on the assumption of small disturbances from the equilibrium conditions. The final form of these equations is [see equations (59) and (60)]

$$\frac{d}{dt}(\delta P_2) = b_{11}\delta P_2 + b_{12}\delta T_w \tag{1}$$

$$\frac{d}{dt}(\delta T_w) = b_{21}\delta P_2 + b_{22}\delta T_w + c_{22}\delta H_i \tag{2}$$

where δP_2, δT_w, and δH_i are perturbations of the surge tank pressure, the heater wall temperature, and the heat input, respectively, from the equilibrium values. The constants b_{ij} and c_{22} depend on system parameters. These equations are in a suitable form to facilitate the application of various methods of optimization theory to synthesize a control system. The calculus of variations approach and the dynamic programming approach are each considered. For either case an error measure is introduced

$$h[\delta P_2(\sigma), \delta T_w(\sigma), \delta H_i(\sigma), \sigma] = \phi_1(\delta P_2)^2 + \phi_2(\delta T_w)^2 + \phi_3(\delta H_i)^2 \tag{3}$$

with the associated error index

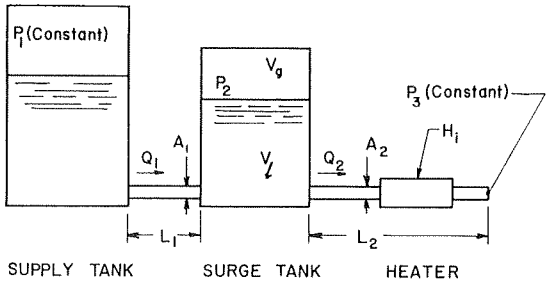

Fig. 1 Schematic of flow system

$$e(t) = \int_t^T h[\delta P_2(\sigma), \delta T_w(\sigma), \delta H_i(\sigma), \sigma]d\sigma. \tag{4}$$

Present or real time is t, future time is σ, and T is the final time at which the process is completed. The coefficients ϕ_1, ϕ_2, and ϕ_3 are weighting functions. They are somewhat arbitrary and are governed, to a certain extent, by system performance requirements.

The Calculus of Variations Approach

The minimization of the error index subject to the differential constraints of equations (1) and (2) is a typical problem of the calculus of variations. This approach does not lend itself readily to the treatment of linear problems since it results in a fourth-order system of linear differential equations which is computationally unstable. That is, terms with real and positive parts occur in the exponent. In an analytical solution, these terms are driven to zero by a judicious choice of initial conditions. Errors in numerical or analog solutions usually excite these terms, however, and they are a source of trouble. An interesting observation was that the auxiliary equation for this fourth-order system did not contain terms in odd powers. Another interesting observation and a useful result is that ϕ_3 can be set equal to unity without any loss of generality.

The Dynamic Programming Approach

The form of the system equations (1) and (2) and the form of the error measure are retained in this approach. The computational difficulties just mentioned do not occur in dynamic programming [3]. Instead, a set of nonlinear differential equations is introduced and this set is not solved in terms of elementary functions. Computer solution is required but it is noted that computers are usually employed in the solution of large linear systems.

When dynamic programming is used to obtain the optimal control equations for some system, it is convenient to put the process differential equations into vector form. For the present problem, equations (1) and (2) become

$$\mathbf{x}'(t) = B\mathbf{x}(t) + C\mathbf{m}(t) \tag{5}$$

where the elements of $\mathbf{x}(t)$ are the perturbations δP_2 and δT_w. The elements of $\mathbf{m}(t)$ are the control quantities and in this case the only nonzero term is $m_2 = \delta H_i$. B is a 2×2 matrix with constant elements b_{ij} and C is also a 2×2 matrix with constant elements, of which only c_{22} is not zero. In this notation, the error index is

$$e(t) = \sum_{n=1}^{2} \int_t^T \{\phi_n(\sigma)[x_n(\sigma)]^2 + \phi_3[m_2(\sigma)]^2\}d\sigma. \tag{6}$$

The instantaneous minimum-error function is defined as

$$E[\mathbf{x}(\mu), \mu] = \min_{\substack{m_2(\sigma) \\ [\mu, T]}} e(\mu). \tag{7}$$

The dummy time variable μ, defined on the interval $[t, T]$, is in-

troduced so that the actual time t can be treated as a constant during the optimization process.

The fundamental concept in the dynamic programming process is the principle of optimality. In the synthesis of control systems, the principle can be paraphrased from Bellman [4] as:

Principle of Optimality. An optimal control has the property that, whatever the initial conditions and control are, the subsequent control must be optimal with respect to the state resulting from the initial control.

This leads to the condition for minimum error,

$$\min_{m:(\mu)} \left(\sum_{n=1}^{2} \{\phi_n(\mu)[x_n(\mu)]^2 + \phi_3(\mu)[m_2(\mu)]^2\} + \sum_{n=1}^{2} x_n'(\mu) \frac{\partial E[\mathbf{x}(\mu), \mu]}{\partial x_n(\mu)} \right)_{\eta} = -\frac{\partial E[\mathbf{x}(\mu), \mu]}{\partial \mu}. \quad (8)$$

This equation is represented in a more convenient form as

$$\frac{\partial E[\mathbf{x}(\mu), \mu]}{\partial \mu} + \sum_{n=1}^{2} \{\phi_n(\mu)x_n(\mu)\} + \phi_3[m_2^*(\mu)]^2 + \sum_{n=1}^{2} x_n'^*(\mu) \frac{\partial E[\mathbf{x}(\mu), \mu]}{\partial x_n(\mu)} = 0 \quad (9)$$

and it is a partial differential equation for the instantaneous minimum-error function. The starred quantities are the minimizing values. Its solution is assumed to be of the form

$$E[\mathbf{x}(\mu), \mu] = k(\mu) - 2 \sum_{m=1}^{2} k_m(\mu)x_m(\mu) + \sum_{m=1}^{2} \sum_{j=1}^{2} k_{mj}(\mu)x_m(\mu)x_j(\mu) \quad (10)$$

where $k_{mj}(\mu) = k_{jm}(\mu)$. Substitution of E from this equation into equation (9) results in the following nonlinear ordinary differential equations for the k parameters:

$$-k'(\mu) = \sum_{n=1}^{2} [-c_{nn}^2 k_n^2] \quad (11)$$

$$-k_m'(\mu) = \sum_{n=1}^{2} (b_{nm}k_n - c_{nn}^2 k_n k_{nm}), \qquad m = 1, 2 \quad (12)$$

$$-k_{mj}'(\mu) = \sum_{n=1}^{2} (\phi_n a_{nm} a_{nj} + b_{nm}k_{nj} + b_{nj}k_{nm} - c_{nn}^2 k_{nm}k_{nj}), \qquad m, j = 1, 2 \quad (13)$$

where

$$c_{11} = 0 \text{ and } A = \begin{bmatrix} 1 & 0 \\ 0 & 1 \end{bmatrix}.$$

Since the desired output quantities coincide with the state variables x_n, A is the identity matrix as shown with the elements a_{ij}. Of the six k parameters, $k_1 = k_2 \equiv 0$ and $k_{12}(\mu) = k_{21}(\mu)$. It is noted that μ is a dummy time variable which disappears when the boundary conditions have been used with the solutions for the k parameters. The boundary conditions for the k parameters are found from the terminal value of the minimum-error function, i.e.,

$$E[\mathbf{x}(T), T] = 0. \quad (14)$$

In order to guarantee that this condition holds for all finite values of $\mathbf{x}(T)$, the k parameters must vanish at $\mu = T$, i.e.,

$$k(T) = k_m(T) = k_{mj}(T) = 0. \quad (15)$$

Solution requires the backward integration of equations (12) and (13) and the values of the k's are noted at some initial time t. The $k(t)$ are the initial conditions on the $k(\mu)$ and these are used in the complete system equations with all integrations proceeding in the forward direction.

The goal of this work is to determine the optimum feedback control system which will minimize the error index. For the process under consideration, the optimum control equation is

$$\delta H_i(t) = c_{22}[k_2(t) - k_{21}(t)\delta P_2(t) - k_{22}(t)\delta T_w(t)]. \quad (16)$$

Data are available for a marginally stable case and an unstable case and this information is used to determine the b_{ij} and c_{22} for equations (1) and (2).

Marginally Stable Case

This system is marginally stable with no feedback control and exhibits oscillations which are very lightly damped. The quantities of interest are

$\dot{m}$	= 2.35 lb/min	m_1	= −0.1480
e_*	= 1.705	m_2	= 0.800
τ_1	= 2.12 min	n_1	= 21.1
τ_2	= 0.0385 min	n_2	= 4.70
b_{11}	= −2.473	b_{12}	= 0.1045
b_{21}	= −56.25	b_{22}	= 1.064
c_{22}	= 25.97		

The auxiliary equation for this system without feedback is

$$D^2 + 1.409D + 3.247 = 0, \quad (17)$$

which shows damped oscillatory behavior.

The solutions for the k parameters are shown in Fig. 2. Since only k_{21} and k_{22} appear in the control equation ($k_2 \equiv 0$), these gains are of particular interest and it is seen that they are relatively uniform except for the last 5 sec or so. This suggests the possibility of a suboptimal feedback control system with constant k parameters which, for this case, are

$$k_{21} = -0.0158,$$

$$k_{22} = +0.0177.$$

It was assumed that $\phi_1 = \phi_2 = \phi_3 = 1.0$. The suboptimal control is obtained from equation (16)

$$\delta H_i(t) = 0.41\delta P_2(t) - 0.46\delta T_w(t). \quad (18)$$

When $\delta H_i(t)$ is substituted into equation (2), the system auxiliary equation is

$$D^2 + 13.36D + 31.69 = 0. \quad (19)$$

It can be verified that this system is nonoscillatory and also that disturbances will decay as $\exp(-3.08t)$ where t is given in minutes. By way of comparison, disturbances decayed as $\exp(-0.705t)$ in the open-loop system.

Unstable Case

In this situation, the physical parameters are chosen to make the open-loop system unstable. The parameters and the associated coefficients are

$\dot{m}$	= 2.30 lb/min	m_1	= −0.1580
e_*	= 1.700	m_2	= 0.916
τ_1	= 2.10 min	n_1	= 19.0
τ_2	= 0.0148 min	n_2	= 3.14
b_{11}	= −3.364	b_{12}	= 0.1605
b_{21}	= −152.67	b_{22}	= 3.927
c_{22}	= 67.57		

The auxiliary equation for the open-loop system is

$$D^2 - 0.563D + 24.5 = 0, \quad (20)$$

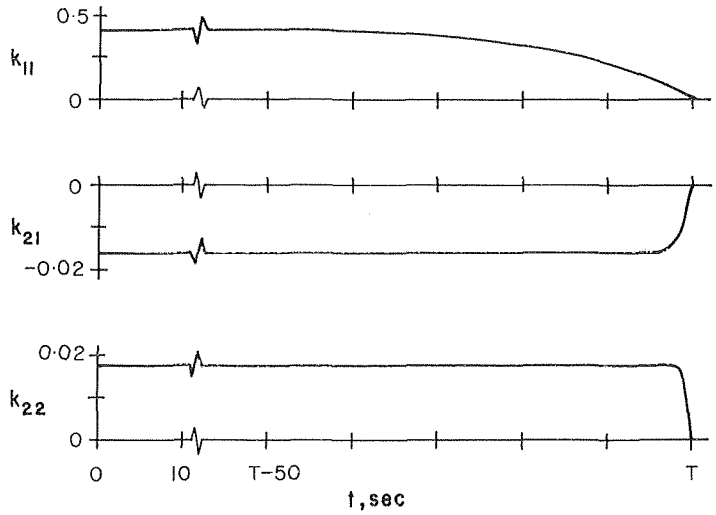

Fig. 2 *k*-parameters for open-loop marginally stable case

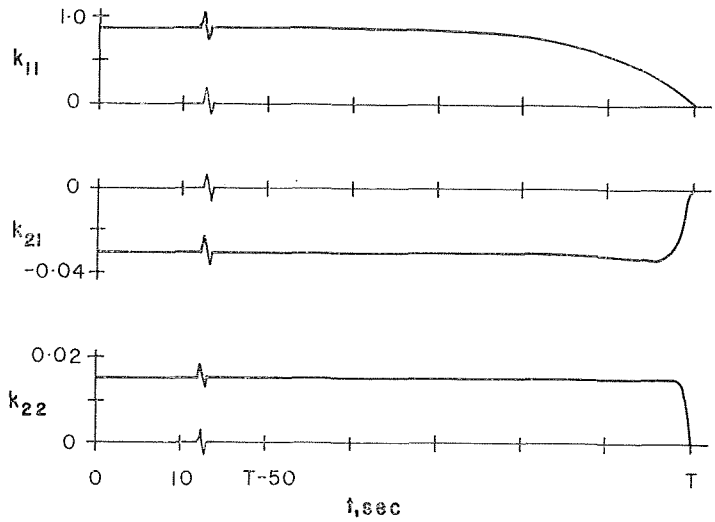

Fig. 3 *k*-parameters for open-loop unstable case

which shows instability because the roots contain a real and positive part.

The solutions for the k parameters are shown in Fig. 3 and, as in the previous case, the suboptimal control system with constant gains is suggested. The appropriate gains are

$$k_{21} = -0.0302,$$

$$k_{22} = +0.0153,$$

where it was assumed again that $\phi_1 = \phi_2 = \phi_3 = 1.0$. The suboptimal control equation is

$$\delta H_i(t) = 2.04\delta P_2(t) - 1.03\delta T_w(t), \tag{21}$$

and the associated auxiliary equation for the closed-loop system is

$$D^2 + 59.03D + 189.8 = 0. \tag{22}$$

It can be demonstrated that this closed-loop system is nonoscillatory and also that disturbances will decay as $\exp(-3.41t)$. It is interesting that the exponents in both cases are not significantly different from each other.

Discussion

Dynamic programming has been applied to a very simple forced-convection two-phase flow process to obtain a suboptimal feedback control system which is very stable. The system considered exhibits so-called pressure-drop oscillations which are occasioned by increasing flow rates with decreasing pressure drops. This is a low-frequency phenomenon with periods ranging from about 1 min to about 3 min.

The low-frequency character of the system oscillations permits considerable simplification of the governing equations and also permits linearization of these equations with some degree of confidence. The dynamic programming approach is particularly powerful in the treatment of linear systems since certain inherent difficulties associated with the method can be circumvented. This means that it is possible to obtain the feedback gains for a closed-loop system as functions of time with considerable ease on the computer.

Analog computer solutions showed that the feedback gains, associated with temperature and pressure fluctuations, were essentially uniform in time except for the 5 or 10 sec just before the final time. In processes which proceed for an indefinite time, it is suggested that the final time be arbitrarily large. Thus the gains can be considered constant and the feedback controller can be regarded as optimal. These constant feedback gains produced very stable systems with a high degree of damping. It is noted that the weighting functions ϕ_1 and ϕ_2 were taken to be unity in the development. The value of these functions could be adjusted, however, relative to some other op-

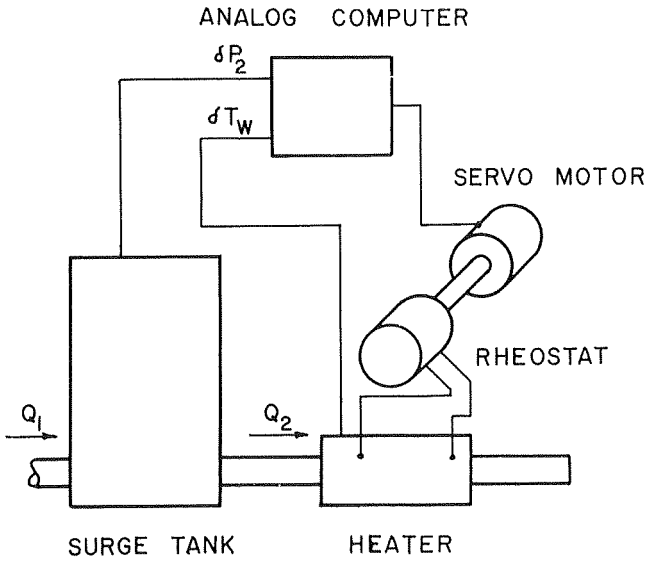

Fig. 4 Mechanization of control system

timization or performance criterion. This choice is open to the designer.

The use of a second-order system facilitated analytical examination of the system equations and the associated auxiliary equation. Thus it was possible to see the effects of the dynamic programming process without encountering the complications brought on by a large system. The process can be extended readily to larger systems, however, and to systems which describe density-wave oscillations and instability.

A possible mechanization of the feedback controller for pressure-drop oscillations is shown in Fig. 4.

References

1 Bankoff, S. G., and Bandy, D. B., "Optimal Shape of a Natural-Circulation Boiling Water Channel," *Proceedings of the JSME 1967 Semi-International Symposium on Heat Transfer*, Japan Society of Mechanical Engineers, Tokyo, Japan, Vol. II, pp. 55–64.

2 Stenning, A. H., and Veziroglu, T. N., "Flow Oscillations in Forced-Convection Boiling," Final Report, Vol. II, NASA CR-72122, NASA Grant NsG-424, Feb. 1967.

3 Merriam, C. W., III, *Optimization Theory and The Design of Feedback Control Systems*, McGraw-Hill, New York, 1964.

4 Bellman, R., *Dynamic Programming*, Princeton University Press, Princeton, N. J., 1957, p. 83.

5 Tong, L. S., *Boiling Heat Transfer and Two-Phase Flow*, Wiley, New York, 1965, Chapter 5.

APPENDIX

In this Appendix the detailed derivation of equations (1) and (2) is given. The system under consideration is shown in Fig. 1. The development is based upon the usual laws of conservation of mass, momentum, and energy.

The momentum equation between points 1 and 2 is

$$P_1 - P_2 = K_1 Q_1^2 + \rho_l \frac{L_1}{A_1} \frac{dQ_1}{dt}, \tag{23}$$

where Q_1 is the volume rate of flow into the surge tank. The momentum equation between 2 and 3 is

$$P_2 - P_3 = (P_2 - P_3)_s + \rho_l \frac{L_2}{A_2} \frac{dQ_2}{dt}, \tag{24}$$

where Q_2 is the volume flow rate out of the surge tank; $(P_2 - P_3)_s$ is the steady-flow pressure drop across the system and depends on Q_2 and the heat input. Since P_1 and P_3 each are constant,

$$P_1 - P_3 = \text{const.} \tag{25}$$

The continuity equation for the surge tank is

$$Q_1 - Q_2 - Q_{ev} = \frac{dV_l}{dt}, \tag{26}$$

where Q_{ev} is the rate of loss of liquid volume due to evaporation and V_l is the volume of liquid in the surge tank. If V_g is the volume of gas in the surge tank,

$$\frac{dV_l}{dt} = -\frac{dV_g}{dt} \tag{27}$$

and the conservation of mass implies

$$Q_{ev} = \frac{\rho_v}{\rho_l} \frac{dV_g}{dt}. \tag{28}$$

Therefore,

$$Q_1 - Q_2 = -\frac{dV_g}{dt} + \frac{\rho_v}{\rho_l} \frac{dV_g}{dt} = -\left(1 - \frac{\rho_v}{\rho_l}\right) \frac{dV_g}{dt}. \tag{29}$$

Since the gas in the surge tank is a mixture of air and saturated vapor,

$$P_2 = P_{2a} + P_{2v}, \tag{30}$$

where

P_{2a} = partial pressure of air,

P_{2v} = partial pressure of vapor.

The partial pressure P_{2v} is constant if the liquid temperature in the tank is constant and thermal equilibrium prevails, which in turn implies

$$P_{2a} V_g = P_{2a0} V_{g0} = \text{const.} \tag{31}$$

This is solved for V_g to give

$$V_g = \frac{P_{2a0} V_{g0}}{P_{2a}}, \tag{32}$$

and then V_g is differentiated with respect to time

$$\frac{dV_g}{dt} = -\frac{P_{2a0} V_{g0}}{P_{2a}^2} \frac{dP_{2a}}{dt}. \tag{33}$$

Up to this point, the analysis is identical to that in reference [2]. In the presentation of the thermal energy equation, the present development will take into account variations in heat input. Stenning and Veziroglu [2], by way of contrast, considered constant heat input in their work. Thus the thermal energy equation becomes

$$Mc_m \frac{dT_w}{dt} = H_i - H, \tag{34}$$

where H_i is the power input to the heater and H is the power input to the fluid. Under steady-state conditions with no losses,

$$H_{i0} = H_0. \tag{35}$$

The power input to the fluid is

$$H = hA(T_w - T_f), \tag{36}$$

where the heat transfer coefficient h is some appropriate function of Q_2 and other system parameters [5],

$$h = h(Q_2, \ldots). \tag{37}$$

The flow Q_2 is taken to be the governing argument while the other parameters are assumed to be essentially constant over the range considered.

Even this simplified model as given by the preceding equations consists of nonlinear differential equations. Since stability

analyses usually are concerned with attenuating perturbations as soon as they begin, a reasonable approach is to introduce small disturbances in the nonlinear equations and retain only the linear terms. Further, as long as the amplitude and the frequency are low, it is reasonable to neglect the inertia terms dQ/dt in equations (23) and (24).

Equation (23) then becomes

$$P_1 - P_2 = K_1 Q_1^2. \tag{38}$$

Perturbations are introduced through

$$\begin{aligned} P_1 &= P_{10}, \\ P_2 &= P_{20} + \delta P_2, \\ Q_1 &= Q_{10} + \delta Q_1 \end{aligned} \tag{39}$$

where it is noted that P_1 is constant. When P_1, P_2, and Q_1 from equations (39) are substituted into equation (38) and higher-order terms are neglected, there results

$$-\delta P_2 = 2K_1 Q_{10} \delta Q_1. \tag{40}$$

This equation is normalized by multiplying the left-hand side by P_{20}/P_{20} and the right-hand side by Q_{10}/Q_{10}, and then using the steady-state version of equation (38), to give

$$-\delta P_2' = 2e_* \delta Q_1', \tag{41}$$

where

$$\delta P_2' = \frac{\delta P_2}{P_{20}},$$

$$\delta Q_1' = \frac{\delta Q_1}{Q_{10}},$$

$$e_* = \frac{P_{10} - P_{20}}{P_{20}}.$$

When perturbations are introduced into equation (24), with the inertia term neglected,

$$\delta P_2 = \delta(P_2 - P_3)_s. \tag{42}$$

The right-hand side depends only on H and Q_2 so that

$$\delta P_2 = \left[\frac{\partial(P_2 - P_3)}{\partial H}\right]_0 \delta H + \left[\frac{\partial(P_2 - P_3)}{\partial Q_2}\right]_0 \delta Q_2. \tag{43}$$

In normalized form, this becomes

$$\delta P_2' = m_2 \delta H' + m_1 \delta Q_2', \tag{44}$$

with

$$m_1 = \frac{Q_{20}}{P_{20}}\left[\frac{\partial(P_2 - P_3)}{\partial Q_2}\right]_0,$$

$$m_2 = \frac{H_0}{P_{20}}\left[\frac{\partial(P_2 - P_3)}{\partial H}\right]_0.$$

The perturbed form of equation (29) is

$$\delta Q_1 - \delta Q_2 = -\left(1 - \frac{\rho_v}{\rho_l}\right)\frac{d(\delta V_g)}{dt}. \tag{45}$$

From equation (32), it is seen that

$$\delta V_g = -\frac{V_{g0}}{P_{2a0}} \delta P_2 \tag{46}$$

so that equation (45) becomes, in normalized form,

$$\delta Q_1' - \delta Q_2' = \tau_1 \frac{d(\delta P_2')}{dt} \tag{47}$$

with

$$\tau_1 = \left(1 - \frac{\rho_v}{\rho_l}\right)\frac{V_{g0}}{Q_0}\frac{P_{20}}{P_{2a0}}.$$

The perturbed form of equation (34) is

$$Mc_m \frac{d(\delta T_w)}{dt} = \delta H_i - \delta H, \tag{48}$$

while, in normalized form, it is

$$\tau_2 \frac{d(\delta T_w')}{dt} = \delta H_i' - \delta H', \tag{49}$$

where

$$\tau_2 = \frac{Mc_m}{H_0}(T_{w0} - T_{f0}).$$

When perturbations are introduced into equation (36), there results

$$\delta H = (T_{w0} - T_{f0})A\delta h + h_0 A(\delta T_w - \delta T_f). \tag{50}$$

Since the film coefficient h depends on Q_2 and since the saturation temperature T_f is a function of P_2,

$$\delta h = \frac{dh}{dQ_2}\delta Q_2, \tag{51}$$

$$\delta T_f = \frac{dT_f}{dP_2}\delta P_2. \tag{52}$$

In normalized form, equation (50) is, accounting for equations (51) and (52),

$$\delta H' = \delta T_w' - n_1 \delta P_2' + n_2 \delta Q_2', \tag{53}$$

where

$$n_1 = \frac{P_{20}}{T_{w0} - T_{f0}}\left(\frac{dT_f}{dP_2}\right)_0,$$

$$n_2 = \frac{Q_0}{h_0}\left(\frac{dh}{dQ_2}\right)_0.$$

In the remaining development, the primes will be omitted from the normalized perturbed quantities. Equations (41), (44), (47), (49), and (53) constitute the perturbed form of the governing equations. Some simplification is possible because some of the variables can be eliminated by means of substitution. The quantity δQ_1 can be eliminated from equations (41) and (47),

$$-\frac{\delta P_2}{2e_*} - \delta Q_2 = \tau_1 \frac{d(\delta P_2)}{dt}, \tag{54}$$

while δH can be eliminated from equations (44) and (53),

$$\delta P_2 = m_1 \delta Q_2 + m_2(\delta T_w - n_1 \delta P_2 + n_2 \delta Q_2), \tag{55}$$

and also from equations (44) and (49)

$$\tau_2 \frac{d(\delta T_w)}{dt} = \delta H_i - \delta T_w + n_1 \delta P_2 - n_2 \delta Q_2. \tag{56}$$

Finally, δQ_2 is eliminated from the three preceding equations to give the equations that will be used in the control system approach,

$$\frac{d}{dt}(\delta P_2) = \delta P_2\left[-\frac{1}{2e_*\tau_1} - \frac{1 + m_2 n_1}{\tau_1(m_1 + m_2 n_2)}\right] + \delta T_w \frac{m_2}{\tau_1(m_1 + m_2 n_2)} \tag{57}$$

$$\frac{d}{dt}(\delta T_w) = \delta P_2\left[\frac{n_1}{\tau_2} - \frac{n_2(1 + m_2 n_1)}{\tau_2(m_1 + m_2 n_2)}\right] + \delta T_w\left[-\frac{1}{\tau_2} + \frac{m_2 n_2}{\tau_2(m_1 + m_2 n_2)}\right] + \frac{1}{\tau_2}\delta H_i. \quad (58)$$

In the application of various aspects of optimization theory to control systems, it is convenient to put the foregoing equations into the following form

$$\frac{d}{dt}(\delta P_2) = b_{11}\delta P_2 + b_{12}\delta T_w \quad (59)$$

$$\frac{d}{dt}(\delta T_w) = b_{21}\delta P_2 + b_{22}\delta T_w + c_{22}\delta H_i. \quad (60)$$

P. D. McCORMACK
Professor.

H. WELKER

M. KELLEHER
The Thayer School of Engineering,
Dartmouth College,
Hanover, N. H.

Taylor-Goertler Vortices and Their Effect on Heat Transfer

An experimental measurement of the effect of Taylor-Goertler vortex formation on the heat transfer through the boundary layer on a concave wall has been made. A theoretical analysis based on independent mean and oscillatory flow components indicates that, although the heat transfer rate will fluctuate periodically in the spanwise direction, there should be no overall increase in heat transfer. The experimental results indicate that there is a significant increase in Nusselt number in the presence of the vortices. Interaction between the oscillatory and mean components must be accounted for, if the theoretical model is to be reliable.

Introduction

Taylor [1][1] was the first to attack the problem of instability in the flow contained between the concentric rotating cylinders. Taylor assumed a stable periodic vorticity contained in the boundary layer, which would trail in the direction of flow, Fig. 1. In appearance the vortices are similar to wing trailing vortices except they have alternate right and left-hand rotation. Taylor formulated the motion in mathematical terms, analyzed its stability, and verified the analysis with excellent correlation of theory and experimental results.

Fig. 1 sketches the streamlines of motion after the instability has set in. Colored fluid was injected into the annular volume such that it covered the inner cylinder. The relative velocity of the cylinders was increased until the boxlike disturbances appeared in rectangular zones periodic in the Z-direction. Taylor's vortices were steady, periodic and their size was a direct function of the spacing between the cylinders but independent of the rotational velocity.

A stability analysis by Goertler [2] in 1940 predicted that similar vortices should be formed in the boundary layer on a concave plate. Such an instability would be expected to arise when the centrifugal force becomes so large that the radial pressure gradient and viscous forces can no longer damp out small disturbances.

The vortices represent a steady type of flow. Fig. 2 demonstrates the phenomenon in the concave plate case.

It is obvious that these vortices grow with distance (in the direction of fluid flow). Goertler, however, analyzed a disturbance which grew with time. He postulated a small three-dimensional disturbance superimposed on a base flow of the form:

$$\begin{aligned} u_t &= u_0(y) + u_1(y) \cos(\alpha z) \exp(\beta t) \\ v_t &= v_1(y) \cos(\alpha z) \exp(\beta t) \\ w_t &= w_1(y) \sin(\alpha z) \exp(\beta t) \\ P_t &= P_0(y) + P_1(y) \cos(\alpha z) \exp(\beta t) \end{aligned} \tag{1}$$

The coordinate system used is a curvilinear system with x being the distance along the curved surface and z and y the distances perpendicular to the x-axis; see Fig. 3. u_t, v_t, w_t are components of the entire velocity. u_0 represents the undisturbed

[1] Numbers in brackets designate References at end of paper.

Contributed by the Heat Transfer Division of The American Society of Mechanical Engineers and presented at the ASME-AIChE Heat Transfer Conference, Minneapolis, Minn., August 3–6, 1969. Manuscript received by the Heat Transfer Division, May 13, 1968; final manuscript received, November 14, 1968. Paper No. 69-HT-3.

Nomenclature

C_p = specific heat at constant pressure; Btu/lb deg F
d = diameter of duct
e = emissivity
h = average heat transfer coefficient, q conv/area·ΔT(Btu/hr ft² deg F)
K_{ht} = thermal conductivity; Btu/hr ft deg F)
k = curvature $1/r$, (1/ft)
L = duct length
P_1 = amplitude of disturbance component of static pressure
P_0 = static pressure of base flow; lb/ft²
P_t = total static pressure, sum of base and disturbed static pressure; lb/ft²
q_t = total flux of energy from a heating element ($q_{cond} + q_{conv} + q_{rad}$), (Btu/hr ft²)
q_{cond} = flux of energy lost from a heating element by conduction through test surface, Btu/hr ft²
q_{conv} = flux of energy from a heating element by convection through boundary layer, $q_{conv} = h\Delta T$, Btu/hr ft²
q_{rad} = flux of energy from a heating element by radiation losses
r or R = radius of curvature
t = time; sec
T_1 = amplitude of disturbance temperature component
T_0 = undisturbed temperature of base flow; deg F
T_t = total temperature, sum of disturbed and base temperatures; deg F
T_∞ = temperature of full stream; deg F
T_w = temperature of wall of a flat plate or duct; deg F
$\overline{T_w}$ = average wall temperature for x 0→L; deg F
ΔT = temperature difference of wall and free stream, $T_w - T_\infty$; deg F
U_e = entrance velocity of flow entering a duct; fps
U_∞ = free-stream velocity for flow over a flat plate; fps
u_1 = amplitude of disturbance component of velocity in the x-direction, as defined by equation (1)

(*Continued on next page*)

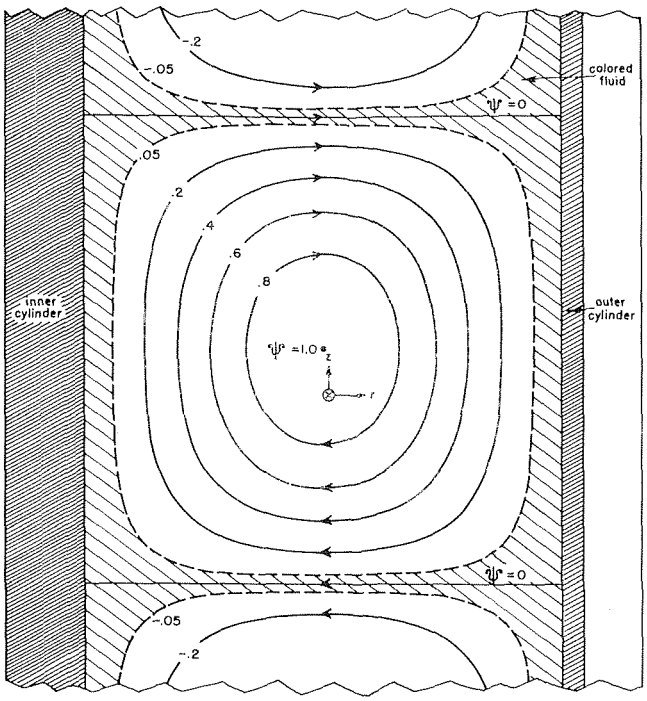

Fig. 1 Taylor vortices—streamlines of motion after instability has set in a fluid contained between two concentric cylinders rotating in the same direction. The space between the cylinders is small compared with the inside radius and ψ has been normalized.

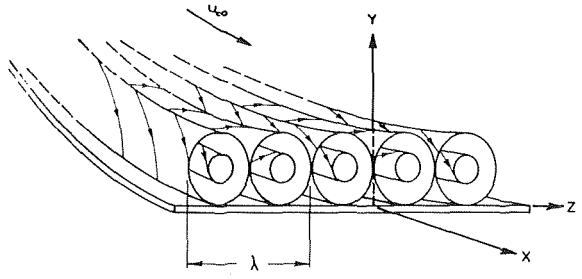

Fig. 2 Vortices caused by three-dimensional disturbances in the flow along a concave wall (Goertler)

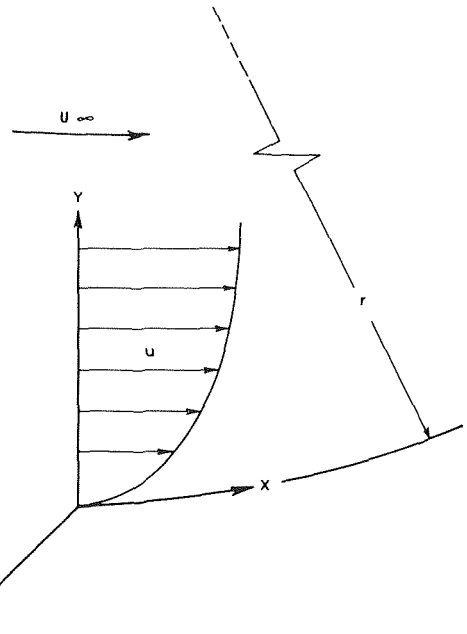

Fig. 3 Boundary-layer profile and the definition of axes for flow along a curved plate

velocity. Similarly P_0 represents the basic undisturbed pressure; u_1, v_1, w_1, and P_1 are the superimposed periodic disturbance functions. β is the measure of the time rate of growth.

As the neutral stability condition was his main object, Goertler's use of time variation was satisfactory. He derived a stability criterion which was enunciated in the form of the Goertler number:

Nomenclature

u_0 = base component of undisturbed velocity, in x-direction; fps

u_t = total velocity in x-direction, sum of base and disturbance components as defined in equation (1)

v_1 = amplitude of disturbance component of velocity in vertical (y) direction as defined in equation (1)

v_0 = base component of undisturbed velocity in vertical (y) direction; fps

v_t = total velocity in vertical (y) direction, sum of base and disturbance components as defined in equation (1)

w_1 = amplitude of disturbance component of velocity in spanwise (z) direction as defined in equation (1)

w_0 = base component of undisturbed velocity in spanwise direction (z); fps

w_t = total velocity in spanwise direction (z), sum of base and disturbance components as defined in equation (1)

W = width of test section

x = distance along curved or flat plate in direction of flow

y = distance perpendicular to surface

z = distance in spanwise direction perpendicular to x-y plane

α = measure of vortex width = $2\pi/\lambda$; ft^{-1}

β = growth factor defined by Goertler; sec^{-1}

δ = boundary-layer thickness or distance above surface at which point boundary-layer velocity equals 0.99 times the free-stream velocity; ft

λ = wavelength of disturbance

ν = Stefan-Boltzman constant = 0.1712×10^{-8} (Btu/hr ft^2 deg R^{-4})

γ = kinematic viscosity; ft^2/sec

θ_{tr} = momentum thickness at transition point for a curved or flat surface as defined by Liepman

ρ = density of fluid (slugs/ft^3)

$R_d^* \dfrac{d}{L}$ = Graetz number divided by Prandtl number

A = vortex size = $\alpha\delta$

B = growth factor = $\beta\delta^2/\gamma$

b = decay factor in equation (23)

C_0 = ratio of amplitude of disturbance component to base component = u/U

K = curvature = δ/r; dimensionless

η = distance from wall = y/δ

N = Goertler number $R_\delta\sqrt{K}$

(Continued on next page)

$$N = \frac{U_\infty \delta}{\gamma}\sqrt{\frac{\delta}{R}} \qquad (2)$$

In this work the Goertler numbers have been computed on the basis of the boundary-layer thickness δ, and not on the momentum thickness, δ^*. Recently, Smith repeated Goertler's work, but considered disturbances which grow with distance [3]. Smith retained many of the terms in the boundary-layer equations discarded in Goertler's analysis and thus had to resort to numerical techniques.

Fig. 4 shows the critical Goertler number versus the wave number ($A = \alpha\delta$) for constant amplification curves (β = const). The neutral stability curve ($\beta = 0$) defines the absolute minimum Goertler number for a given wave number. Below the neutral stability curve β is negative and the disturbances are damped, not amplified. The neutral stability curve found by Smith is compared with Goertler's in Fig. 4. Goertler's predicted vortex formation cannot occur for N less than 16 while Smith's lower limit was about 9. The curves above the neutral stability line show the lower bounds to the Goertler numbers for given growth factors (β).

It should be stressed that the presence of the vortices in the boundary layer does not produce turbulence until the entire range of wavelengths experience amplification.

Liepman investigated the laminar boundary-layer stability and transition to turbulence on curved surfaces [4, 5].

He found that the Reynolds number based on the free-stream velocity and distance from the leading edge, R_x, failed to predict the transition point for curved surfaces. He did find, however, the transition of laminar boundary layers on curved surfaces occurred at a critical Goertler number of about 240.

Fig. 5 shows the transition Reynolds number ($R_{x_{tr}}$) versus the parameter r/θ_{tr} where r is the radius of curvature and θ_{tr} is the momentum thickness at the point of transition.

The flat plate transition Reynolds number is shown in Fig. 5 by a horizontal line, while Liepman's criteria is shown by the sloping segmented line marked $N = 240$. Note that for smaller radii (i.e., smaller r/θ_{tr}) the data best fit Liepman's stability criteria; however, for larger r/θ_{tr} the data approach the flat plate transition criterion. Therefore, it can be concluded that the transition to turbulence of laminar boundary layers on highly concave surfaces is due to the buildup of Taylor-Goertler vorticity. As the surface becomes less concave, turbulence is promoted by the presence of both Taylor-Goertler vorticity and disturbances of the Tollmien-Schlichting type.

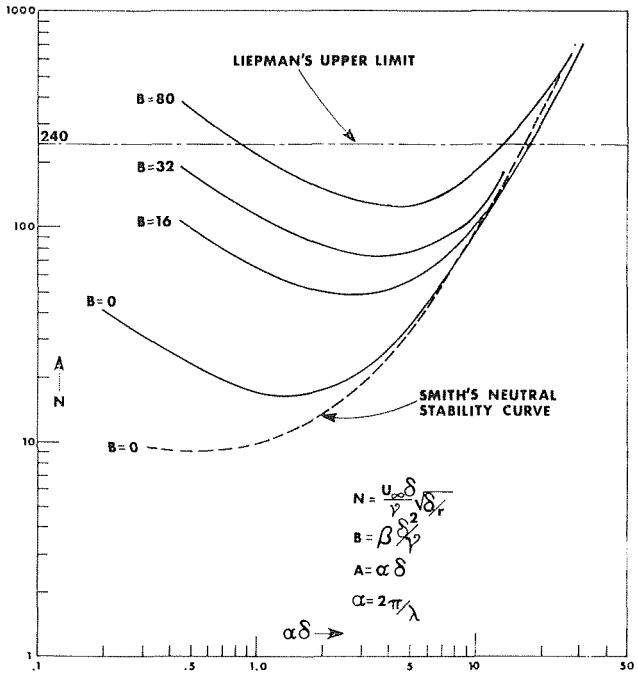

Fig. 4 Goertler number (N) versus wave number (A)

The lower and upper limits to the Goertler number are, respectively, 16 and 240. This range produces stable vortex development superimposed on a laminar base flow.

Neither Goertler or Smith set any upper limit on the growth of the vortices. However, Kirchgassner [6] has shown that there are absolute limits to the value of Goertler's disturbance component amplitudes u_1, v_1, and w_1. In the case of u_1 the absolute upper limit is the velocity of the free stream. The buildup to maximum size is very rapid.

Nomenclature

Nu_c = average Nusselt number for a curved duct = $h \cdot d/K_{ht}$

Nu_f = average Nusselt number for a flat duct = $h \cdot d/K_{ht}$

P = disturbed pressure coefficient = $2(P_1 - P_0)/\rho U_\infty^2$

P_r = Prandtl number $C_p\mu/K_{ht}$

R_d = Reynolds number based on entrance velocity and duct diameter = $U_e d/\gamma$

R_L = Reynolds number based on entrance velocity length of test section = $U_e \cdot L/\gamma$

R_x = Reynolds number based on free-stream velocity and distance from leading edge of a plate = $U_\infty \cdot X/\gamma$

R_{xtr} = transition to turbulence Reynolds number for a plate = $U_\infty \cdot X_{tr}/\gamma$

R_δ = Reynolds number for a plate based on free-stream velocity and boundary-layer thickness

S = amplitude factor defined in equation (23)

U = base velocity in x-direction = u_0/U_∞

u = amplitude of disturbance component of velocity in the x-direction = u_1/U_∞

v = amplitude of disturbance component of velocity in y-direction = v_1/U_∞

w = amplitude of disturbance component of velocity in z-direction = w_1/U_∞

X^+ = distance from leading edge of a surface = X/δ

ϕ = amplitude of disturbance temperature component = $T_1/(T_w - T_\infty)$

θ = undisturbed temperature of base flow = $(T_w - T_0)/(T_w - T_\infty)$

Subscripts

c = a curved surface

f = a flat surface

e = entrance conditions and properties of a duct

t = the subscripted quantity is the sum of the undisturbed base flow component and the disturbance component

0 = the subscripted quantity is a component of the base flow

1 = the subscripted quantity is an amplitude of a disturbance component

tr = the subscripted quantity is a property of the flow at the point of transition to turbulence

∞ = (infinity) and refers to properties of the free stream for flow over a flat plate

Superscripts

$'$ = differentiation with respect to η

$\bar{}$ = a bar over a quantity implies a mean value

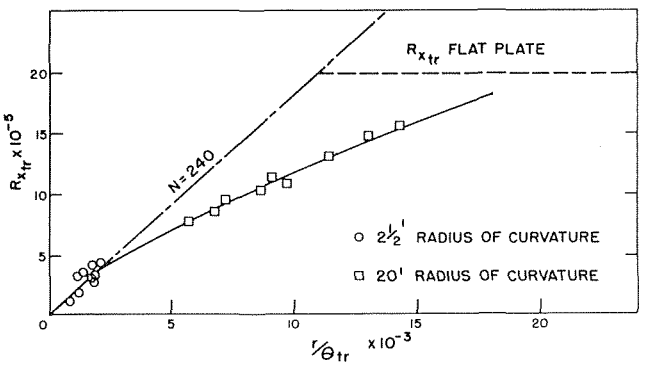

Fig. 5 Transition measurements on a concave plate (Liepman)

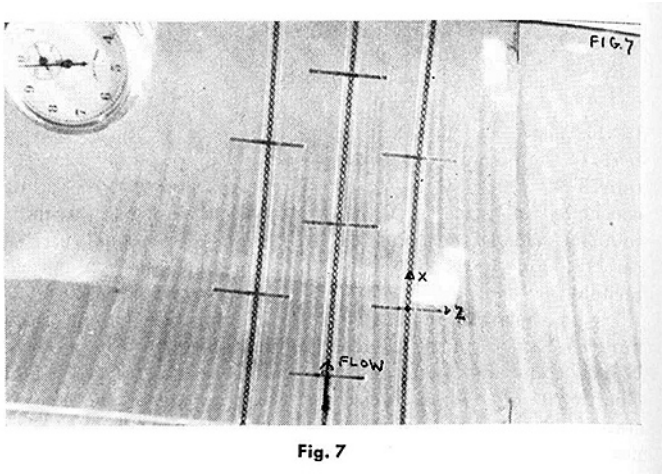

Fig. 7

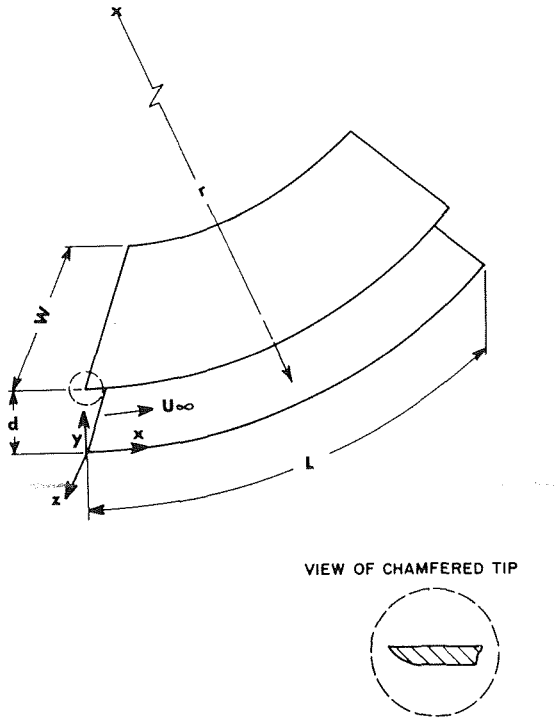

Fig. 6 Parallel plate dimensions

A very good discourse on this phenomenon is given in reference [11].

The objective of this work was to determine analytically and experimentally, the effect of Goertler's vortex formation on the heat transfer to the plate through the boundary layer.

Since the existence of the phenomenon to be studied had at best been shown indirectly by Liepman and McGahan it was first desired to demonstrate their existence with some visual technique. Once this had been accomplished the results of the visual technique could be compared with velocity measurements made with a hot wire anemometer.

The experimental work was therefore divided into two sections. The objectives of the first section were:

1 To design apparatus which would generate Taylor-Goertler vorticity.

2 To demonstrate the existence of said vorticity.

3 To gain sufficient understanding of the vortices in order that a meaningful heat transfer test could be run.

The objective of the second part was to investigate the effects of Taylor-Goertler vorticity on heat transfer. It was desired to verify the theoretical predictions that a heated curved surface should have areas of relatively high and low heat transfer in the presence of such periodic disturbances.

If this phenomenon causes a large increase in heat transfer, it would appear advantageous to attempt to incorporate it into a radically new heat exchanger design which would operate in the laminar flow regime.

Experimental Work on the Production and Characteristics of Taylor-Goertler Vorticity

The vortices were formed by blowing a laminar air stream over a concave plate, the combination of velocity and radius of curvature being such that the Goertler number was above 16 and less than 240. Because the flow from the wind tunnel decelerated as it flowed over the plate, a duct had to be formed by placing a second plate over the first. To avoid the conditions of pipe flow the test duct length had to be such that [7],

$$(L/d) < 0.12R_d$$

Fig. 6 shows a sketch of the test duct. It had the following dimensions,

$$r = 5 \text{ in.}$$
$$W = 13.7 \text{ in.}$$
$$L = 7.63 \text{ in.}$$
$$d = 20 \text{ in.}$$

The gas velocity could be varied from 5 to 125 fps. For example, at 20 fps with the foregoing radius of curvature, then

$$N \doteq 100.$$

For tunnel exit velocities from 0–30 fps (which covers the range of velocities used in this work), measurement showed that the intensity of turbulence at the exit was less than 1 percent. The velocity profile across the duct was very uniform over a length equal to the width of the duct (the wind tunnel width was 16.5 in. wide, compared to the 13.7 in. width of the duct).

The vortex formation was rendered visible (a transparent upper duct wall was used) by spraying the concave surface with a solution of methyl alcohol saturated with naphthalene, and then blowing the gas over it. Material is removed faster where the vortices are, so that distinct longitudinal streaks appear after some time. Fig. 7 is a photograph of the streaks after 2 min of running at a gas velocity of 22 fps. The average transverse wavelength was measured to be 0.2 in. As there were no side walls to the duct the streaks tended to diverge from the center line.

To investigate the fluid dynamic aspects of the problem further, a study of the mean boundary-layer velocity profile was undertaken using a hot-wire probe. The probe could be moved

through 5 cms laterally (the z-direction) and through 2.5 cms longitudinally (x-direction). The arrangement is shown in Fig. 8.

The probe measured the vector sum of the u_t and w_t components (total), but w_t is much smaller than u_t and so it can be considered that u_t alone is being measured.

Fig. 9 shows a plot of the mean boundary-layer velocity ($\bar{u}_t$) versus position on the z-axis. The time-varying component of the velocity was given by the peak-to-peak voltages as measured on an oscilloscope and these are entered as vertical bars through the points defining the mean velocity. During these measurements a naphthalene coating was applied and in Fig. 9 the cross-hatched sections mark the regions on the z-axis where the napthalene was rubbed off. It can be seen that the areas of high mass transport do indeed correspond with areas of high boundary-layer velocity.

The turbulence levels (proportional to the peak-to-peak oscillation magnitude) were a maximum in the low velocity regions (valleys) and at most about 3 percent of the free-stream velocity. So the flow remains quite laminar.

It was observed that the spanwise fluctuations recorded by the hot wire did not shift about in position, nor did they grow with time. So it is felt that in the analysis to be carried out it can be considered that the vortices, once formed, remain fixed in size and do not shift in the spanwise (z) direction.

Defining the strength of the disturbance as:

$$100\ (\bar{u}_{t\max} - \bar{u}_{t\min})/\bar{u}_{t\max}$$

and

$$\bar{u}_{t\max} - \bar{u}_{t\min} = (\bar{u}_0 + \bar{u}_1) - (\bar{u}_0 - \bar{u}_1) = 2\bar{u}_1$$

$$\therefore \text{strength} = 100\left(\frac{2\bar{u}_1}{\bar{u}_{t\max}}\right)$$

It was found that as the free-stream velocity was varied from 13–24 fps, the spanwise velocity pattern hardly changed, the wavelength (measured to be 0.2 in.) remains unchanged, and the disturbance strength remained in the region of 20–25 percent.

Observations also indicated that the spanwise wavelength did not alter with change in wall spacing or wall radius of curvature. Taylor found that the wavelength of the disturbances set up in the annular volume between rotating concentric cylinders *was* dependent on the spacing and curvature (that is, his phenomenon was geometry dependent).

The spanwise wavelength value of 0.2 in. would not be specifically predicted on the basis of any of the available stability analyses (Goertler's, etc.), although it lies in the feasible range. With a typical δ value, $\alpha\delta$ would be about 3. As $\alpha\delta$ remains fairly constant while the Goertler number is increased, one would expect merely an increase in the amplification factor, β, to occur. The apparent invariance of the spanwise wavelength is a feature which would well warrant further investigation.

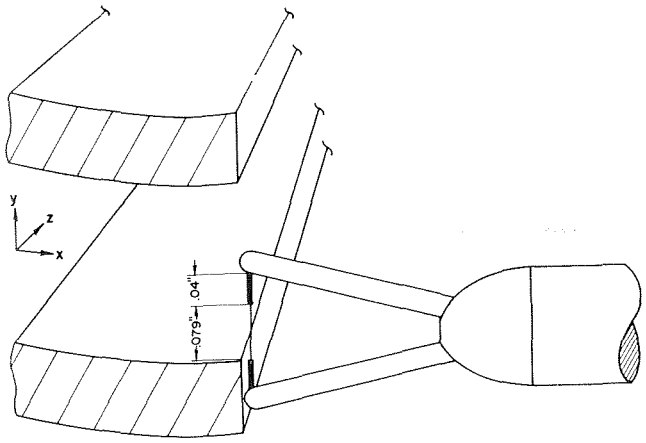

Fig. 8 Positioning of hot-wire anemometer at duct exit

Experimental Investigation of the Effects of Taylor-Goertler Vorticity on the Rate of Heat Transfer

As the theoretical model would predict areas of high and low heat transfer on the plate relative to the undisturbed flat plate case, it was desired to check this prediction. If true, then there should be no overall increase or decrease in heat transfer as a result of the spanwise fluctuations in velocity.

It was decided to measure the heat transfer on a cooling basis. The concave surface and a reference flat surface were heated by embedding heating elements in them (14 elements in each plate). The elements were laid parallel to the flow direction and were spaced 0.030 in. apart. They were each 0.1 in. wide, and the duct width (or span) was 13.7 in. The back and sides of the test section were well insulated to minimize conduction losses. The material on which the elements were laid had a very low conductivity also and so the conduction *between* elements was also minimized.

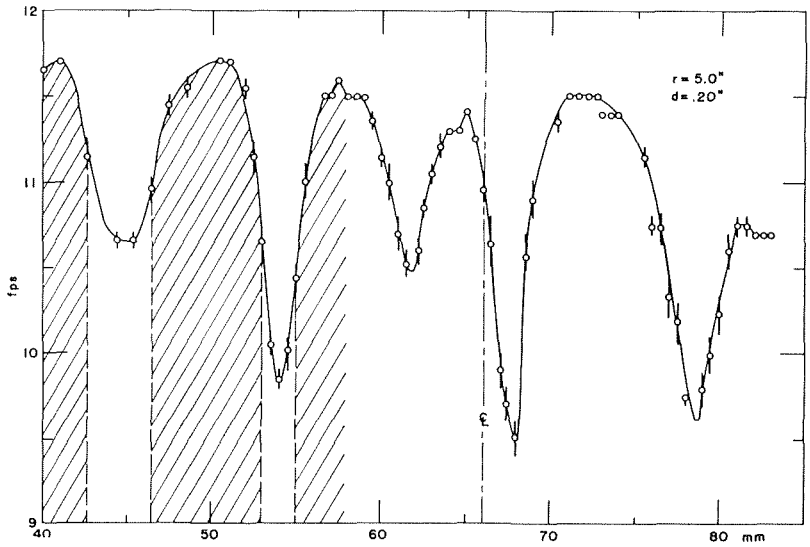

Fig. 9 Mean boundary-layer velocity versus transverse position (Z)

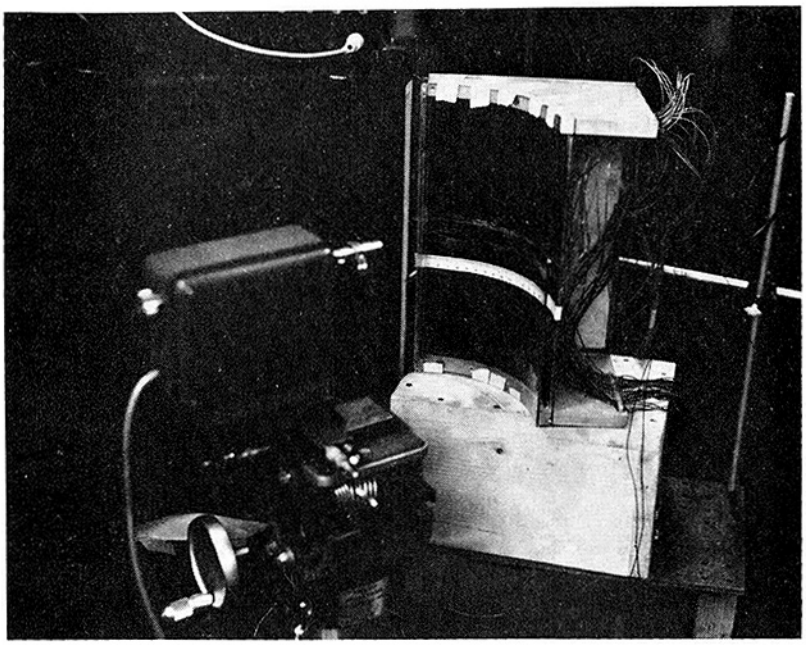

Fig. 10

The surface temperature was measured using an optical pyrometer (range 212–715 deg F) which can sense the temperature of 0.1-in-dia spot with an accuracy of ±2 percent. To allow thermal "viewing" of the heated surface, the upper walls of the ducts were made of 0.19-in. window glass. To get maximum emissivity the test surfaces were sprayed with krylon flat black paint.

Fig. 10 shows the optical pyrometer "looking" at the curved test section at the mouth of the wind tunnel.

A thermal balance on a given heating element gives

$$q_t = (\text{volts}) \cdot (\text{amps}) = q_{\text{conduction}} + q_{\text{radiation}} + q_{\text{convection}} \quad (3)$$

The heat transfer coefficient was defined as:

$$q_{\text{conv}} = h(\bar{T}_w - T_\infty) \quad (4)$$

and the Nusselt number was

$$\text{Nu} = \frac{hd}{K_{ht}} \quad (5)$$

where K_{ht} is the thermal conductivity of air. The losses due to conduction through the back of the test plate were estimated by heating the center heating element on the curved plate at various heating rates. Thermocouples embedded in the material measured the temperature at the back of the plate, and

$$q_{\text{cond}}(q_t, T_w) = K_{ht} \frac{(T_w - T_{\text{thermocouple}})}{\Delta y} \quad (6)$$

where

Δy = plate thickness

K_{ht} = thermal conductivity of wall material (fiberfax)

= 0.3 Btu in./ft² deg F

The ratio of q_{cond} to q_t was about 0.1 for all elements investigated in the heat transfer study performed on the curved duct. The loss for the flat plate, which operated at lower temperatures, was higher and

$$q_{\text{cond}} \simeq 0.2 q_t$$

In the experimental work, an average temperature of the heating elements was arrived at by scanning a set of 6 points along the length of the entire surface. The system, with air blowing from the tunnel and the heating on, was always allowed several minutes to come to thermal equilibrium, before measurements were taken. The entrance velocity varies from 5–30 fps and power input, entrance velocity (using the hot wire) and surface temperatures were recorded for each run.

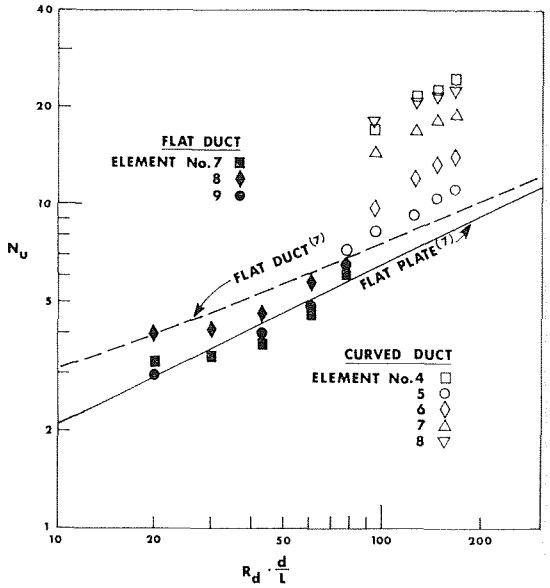

Fig. 11 Nusselt number versus $R_d \cdot d/L$

The following tables present some typical data taken and gives the computed heat transfer coefficients for the curved duct.

In Tables 1 and 2, column 1 gives the particular heating element, column 2 gives $(T_w - T_\infty)$, and column 3 shows the total heat flux from the element.

Column 4 gives the heat lost by radiation,

$$q_{\text{rad}} = e\nu(\bar{T}_w^4 - T_\infty^4) \quad (7)$$

and column 5 gives the heat transfer coefficient,

$$h = (q_t - q_{\text{cond}} - q_{\text{rad}})/(\bar{T}_w - T_\infty) \tag{8}$$

Column 6 gives the Nusselt number based on the duct diameter,

$$\text{Nu} = hd/K_{ht} \tag{9}$$

The Nusselt number one would observe on a heated flat plate of length L and a free-stream velocity equal to the duct entrance velocity, is

$$\text{Nu}_{fp} = 0.66\sqrt{R_d \frac{d}{L}} \tag{10}$$

This allowed the ratios Nu/Nu_{fp} to be computed and they are given in column 7.

Table 1 Curved duct—d = 0.325 in.; L = 7.5 in.

$$\text{R}_d \frac{d}{L} = 165$$

Element No.	$\bar{T}_w - T_\infty$	q_t	q_{rad}	h	Nu	Nu/Nu_{fp}
4	258	5740	521	18	24.3	2.9
5	253	2900	504	8.3	11.2	1.3
6	231	3180	436	10.5	14.2	1.7
7	213	3780	384	14.2	19.1	2.3
8	220	4550	404	16.8	22.6	2.7

Table 2 Flat duct—d = 0.25 in.; L = 7.8 in.

$$\text{R}_d \cdot \frac{d}{L} = 20$$

Element	$\bar{T}_u - T_\infty$	q_t	q_{rad}	h	N_u	$\frac{\text{N}_u}{\text{Nu}_{fp}}$
7	222	1380	410	3.1	3.3	1.1
8	288	2140	626	3.8	3.9	1.3
9	250	1520	495	2.9	3	1

The units of h are Btu/hr ft² deg F.

In Fig. 11 are plotted Nusselt numbers versus $R_d \cdot \frac{d}{L}$ for the flat duct and the curved duct. Also plotted is the *prediction* for heat transfer in the entrance region of a flat rectangular duct based on the analysis by Sparrow [7], who showed that

$$\text{N}_{u\text{duct}} = \text{Nu}_{fp}\left[1 + 3.65\left(\text{R}_d \cdot \frac{d}{L}\right)^{-1/2}\right]^{1/2} \tag{11}$$

The constant 3.65 is half the value of that used in Sparrow's work, because his Nusselt numbers were based on the length of the duct, while the Nusselt numbers in this work are all based on the duct diameter (d).

Fig. 12 shows $\frac{\text{Nu}_c}{\text{Nu}_{fp}}$ plotted versus the spanwise position, z, and also the average boundary velocity versus z. One recalls that in the naphthalene diffusion tests the areas of high mass transport corresponded to areas of high average boundary-layer velocity.

Not enough Nusselt number ratios at various z positions were available to say definitely whether or not areas of high heat transfer correspond to areas of high boundary-layer velocity. The dotted curve merely indicates what one would expect to get if there was a correspondence.

A more elaborate experimental arrangement would be called for to settle this and other questions concerning heat transfer on concave plates.

A sample of the surface temperatures recorded by the optical pyrometer for two adjacent heating elements, in the longitudinal directions, is given in Table 3.

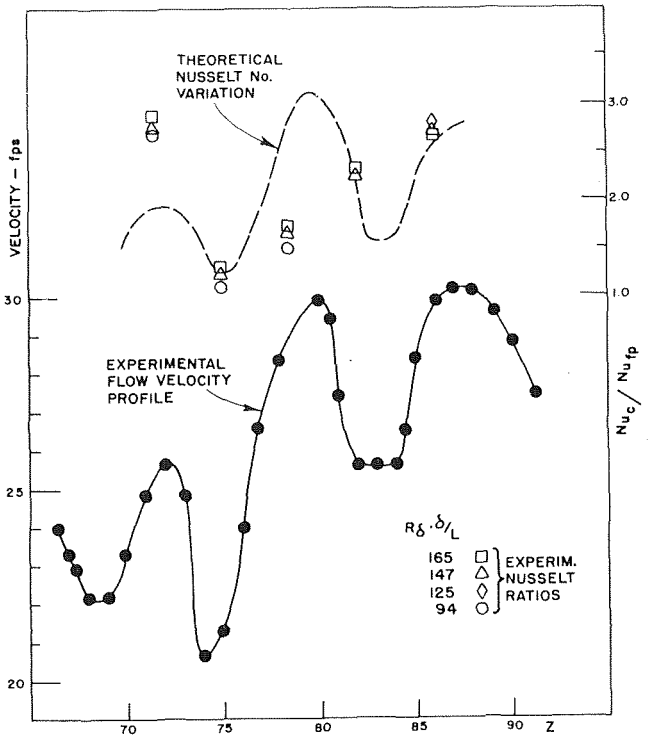

Fig. 12 Ratio $\text{Nu}_{\text{curved duct}}$ to $\text{Nu}_{\text{flat plate}}$ versus Z position

Table 3 Surface temperature distribution

Element number	Position x = 1.5	3	5	7	9	11 (cms)	Mean temperature (above 79 deg F)
1	301	321	341	384	372	303	258
2	292	350	319	373	355	319	253

At this point it is worth noting some significant aspects of these results.

It is evident from Fig. 11 that the flat duct experimental data follow the flat plate theory more closely than they follow Sparrow's predicted duct entrance region Nusselt numbers. It is reasonable that the Nusselt numbers for the entrance region of a duct should be greater than the corresponding Nusselt numbers for a flat plate. As the flow is accelerated in the duct entrance region and the average boundary layer is thinner, the velocity gradient through the boundary layer is greater. If the energy transport from the heated wall is carried by the same mechanism as the momentum transport (Reynold's analogy) one would expect Nu_{fd} to be greater than Nu_{fp}.

On the average, the recorded flat duct Nusselt numbers lie about 7 percent above the flat plate Nusselt numbers (theoretical). The theoretical curved duct Nusselt numbers lie about 20 percent above the flat plate numbers. However, Sparrow's theory had yet to be conclusively verified, and the conduction losses allowed for were upper limits.

The flat duct study was used to demonstrate the reliability of the apparatus. An estimate of an absolute upper limit to the experimental errors in the Nusselt numbers was made and turned out to be ±30 percent.

The curved duct Nusselt numbers are 30–190 percent greater than the flat plate Nusselt numbers, so that on the average the heat transfer from the curved surface is 110 percent greater than that from a flat surface. The effect is significantly above the ±30 percent experimental reliability.

This important result will be commented on again in the conclusions.

Theoretical Analysis

The curvilinear coordinate system used in the analysis is shown in Fig. 3. The base flow is in the x-direction (the arc length along the curved wall). The y-coordinate is perpendicular to the wall ($y = 0$ on the wall) and the z-coordinate is perpendicular to the x-y plane (spanwise direction).

An outline of the analysis is presented and for details the reader is referred to reference [8].

The flow model was set up under the following constraints:

1 The base flow is laminar and all fluid properties are invariant.

2 The velocity boundary-layer thickness δ is such that the $\delta/r \ll 1$. Following Goertler it was postulated that $u_0 = U_\infty =$ constant at $y = \delta$.

3 The minor effect of the wall curvature on the free flow was ignored.

4 The base flow is assumed parallel (i.e., $v_0 = 0$).

5 The radius of curvature is constant.

6 U_0 and P_0 were not functions of x.

7 The flow is incompressible and steady in the sense that the vortices build up to a maximum stable size and do not thereafter change with time (i.e., $\beta = 0$). Nor do they move in the spanwise direction.

8 There is no slip at the wall; i.e.,

$$u_t(0) = v_t(0) = w_1(0) \ldots \text{ etc.} = 0$$

9 u_0, p_0, T_0 represent the undisturbed flow components that would exist for the same flow conditions over a flat plate *without curvature*.

The full steady incompressible Navier-Stokes equation for the flow were found to be:

$$\frac{1}{1+ky}u_t\frac{\delta u_t}{\delta x} + u_t\frac{\delta u_t}{\delta y} + w_t\frac{\delta u_t}{\delta z} + \frac{ku_tv_t}{1+ky} = -\frac{1}{\rho(1+ky)} \cdot \frac{\delta p_t}{\delta x} + \gamma\frac{1}{(1+ky)^2}\frac{\delta^2 u_t}{\delta x^2} + \frac{\delta^2 u_t}{\delta y^2} + \frac{\delta^2 u_t}{\delta z^2} + \frac{k^2}{1+ky} \cdot \frac{\delta u_t}{\delta y} - \frac{k^2}{(1+ky)^2}u_t + \frac{2k}{1+ky}\frac{\delta u_t}{\delta x} \quad (12)$$

plus two similar equations in v_t and w_t.

The continuity and energy equations are, respectively,

$$\frac{1}{1+ky} \cdot \frac{\delta u_t}{\delta x} + \frac{\delta v_t}{\delta y} + \frac{\delta w_t}{\delta z} + \frac{kv_t}{1+ky} = 0 \quad (13)$$

the continuity equation, and

$$\frac{u_t}{1+ky} \cdot \frac{\delta T_t}{\delta x} + v_t\frac{\delta T_t}{\delta y} + w_t\frac{\delta T_t}{\delta z} = \frac{K_{ht}}{C_p}\frac{1}{(1+ky)^2}\left(\frac{\delta^2 T_t}{\delta x^2}\right) + \frac{\delta^2 T_t}{\delta y^2} + \frac{\delta^2 T_t}{\delta z^2} + \frac{k}{1+ky} \cdot \frac{\delta T_t}{\delta y} \quad (14)$$

the energy equation.

Boundary Conditons

1 At the edge of the velocity boundary layer defined by $y = \delta$.

(i) The base component of the boundary-layer velocity equals the free-stream velocity, $u_0(\delta) = U_\infty$

(ii) $\dfrac{du_0(\delta)}{dy} = 0$

(iii) The boundary-layer temperature equals the free-stream temperature $T_0(\delta) = T$

2 At the wall ($y = 0$)

(i) $u_0(0) = 0$

(ii) $T_0(0) = T_w =$ wall temperature

For the oscillatory component the boundary values are as follows:

3 At $y = \infty$

$$u_1(\infty) = v_1(\infty) = w_1(\infty) = p_1(\infty) = T_1(\infty) = 0$$

4 At $y = 0$

$$u_1(0) = v_1(0) = w_1(0) = p_1(0) = T_1(0) = 0$$

5 Equation (16) shows that

$$\frac{dv(0)}{dy} = \frac{dv(\infty)}{dy} = 0$$

Equations (12)–(14) were now linearized using equations (1) and following standard procedure. The steady flow (or base flow) equations were subtracted from the equations for the total flow.

This produced the following set of equations in the oscillatory components u_1, v_1, etc.

$$\gamma\frac{d^2u_1}{dy^2} + \frac{k\gamma}{1+ky} \cdot \frac{du_1}{dy} - \left[\alpha^2\gamma + \frac{k^2\gamma}{(1+ky)^2}\right]u_1 - \left[\frac{du_0}{dy} + \frac{ku_0}{1+ky}\right]v_1 = 0 \quad (15)$$

plus two similar equations in $-v_1$ and w_1.

$$\frac{dv_1}{dy} + \alpha w_1\frac{kv_1}{1+ky} = 0 \quad (16)$$

$$\frac{K_{ht}}{\rho C_p}T_1 - \frac{K_{ht}k}{\rho C_p(1+ky)} \cdot \frac{dT_1}{dy} - \frac{K_{ht}}{\rho C_p} \cdot \frac{d^2T_1}{dy^2} + v_1\frac{dT_0}{dy} + \frac{u_1}{1+ky} \cdot \frac{dT_0}{dx} = 0 \quad (17)$$

These equations were now nondimensionalized by using the following relations,

$$\eta\delta = U_\infty\delta/\nu,\ u_0 = UU_\infty,\ \frac{d^2u}{dy^2} = \frac{U_\infty}{\delta^2} \times \frac{d^2u}{d\eta^2},$$

$$A = \alpha\delta_1,\ u_1 = uU_\infty$$

$$w_1 = wU_\infty,\ y = \eta\delta,\ x = X^+\delta,\ \frac{du_1}{dy} = \frac{U_\infty}{\delta} \cdot \frac{du}{dy}$$

In this analysis the following ranges of variables were considered:

K—As $r = 5$ in. in the experimental work and δ varies from 0 to about 0.2, so K varies from 0–0.04 ($K = \delta/r$).

A—In the experimental work, λ was measured to be about 0.2 in. Thus A varies from 0–6 $\left(A = \dfrac{2\pi\delta}{\lambda}\right)$.

R—For flow velocities from 0–30 fps, R varies from 0–1000 ($R_\delta = U_\infty\delta/\gamma$).

As $(K\eta)^2$ was small compared to unity, so

$$(1+K\eta)^{-1} \doteqdot 1 - K\eta$$

$$(1+K\eta)^{-2} \doteqdot 1 - 2K\eta$$

The final nondimensional set of equations obtained was as follows:

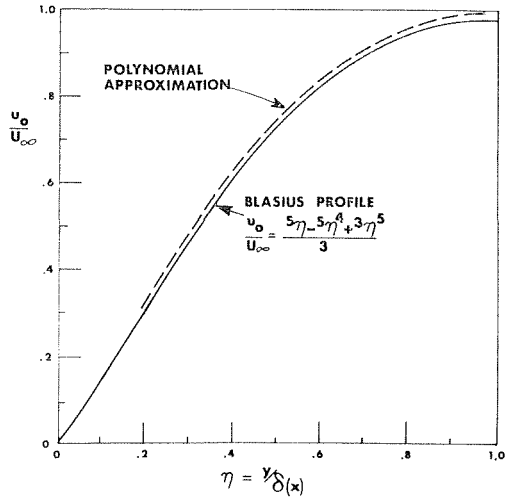

Fig. 13 Polynomial approximation versus Blasius profile

$$\frac{d^2u}{d\eta^2} + K\frac{du}{d\eta} - A^2u - \left(R_\delta \frac{dU}{d\eta} + R_\delta KU\right)v = 0 \quad (18)$$

$$\frac{d^2v}{d\eta^2} + K\frac{dv}{d\eta} - A^2v + 2KR_\delta Uu = \frac{R_\delta}{2}\cdot\frac{dP}{d\eta} \quad (19)$$

$$\frac{d^2w}{d\eta^2} + K\frac{dw}{d\eta} - A^2w = -\frac{AR_\delta p}{2} \quad (20)$$

$$\frac{dv}{d\eta} + Aw + Kv = 0 \quad (21)$$

$$\frac{d^2\phi}{d\eta^2} + K\frac{d\phi}{d\eta} - A^2\phi - \left(R_\delta P_r \frac{d\theta}{d\eta}\right)v = (R_\delta P_r)(1 - K\eta)u\frac{d\theta}{dX^+} \quad (22)$$

Solutions of the Equations

Due to the complexity of the foregoing equations, an approximate technique was resorted to, to obtain a useful solution.

It was assumed that the normal component of velocity (in the y-direction) takes the form,

$$V = S\eta^2 \exp(-b\eta) \quad (23)$$

where S is an amplitude factor and b is a decay factor.

A polynomial approximation to the Blasius profile was also adopted, agreeing with that profile to within 2 percent; see Fig. 13.

$$U = \frac{u_0}{U_\infty} = (5\eta - 5\eta^4 + 3\eta^5)/3 \text{ for } 0 \le \eta \le 1 \quad (24)$$

and

$$\frac{dU}{d\eta} = \frac{1}{3}(5 - 20\eta^3 + 15\eta^4) \text{ for } 1 \le \eta < \infty,\ U = 1, \frac{dU}{dy} = 0 \quad (25)$$

As U equals unity outside the boundary layer and matches the Blasius profile within it, one must solve equation (18) in both regions and match the solutions at $\eta = 1$.

The boundary conditions are as follows:

(a) $\eta = 0$; $u(0) = v(0) = w(0) = 0$

and from the equation of continuity

$$\frac{dv(0)}{d\eta} = 0$$

(b) at $\eta \to \infty$; $u(\infty) = w(\infty) = v(\infty) = 0$

$$\frac{dv(\infty)}{d\eta} = 0$$

(c) at $\eta = 1$, the solutions inside the boundary layer must match the solutions outside the boundary layer.

Solution for $\eta < 1$		Solution for $\eta > 1$
u	=	u
u^1	=	u^1
v	=	v

Note: the expression used for v (equation (23)) satisfies all the boundary conditions.

Substituting the expression for v into equation (21) gives the w component immediately:

$$w = -Kv - \frac{dv}{d\eta} \quad (26)$$

The equation to be solved for u, in both regions, is an inhomogeneous second-order linear differential equation of the form

$$\left(\frac{d^2}{dy^2} + K\frac{d}{d\eta} - A^2\right)u = f(\eta) \quad (27)$$

where

$$f(\eta) = \left(R_\delta \frac{dU}{d\eta} + R_\delta KU\right)v = R_\delta S \cdot \left(\frac{dU}{d\eta} + KU\right)\eta^2 \exp(-b\eta) \quad (28)$$

This equation was solved using the variation of parameters technique both inside and outside the boundary layer.

The general solutions obtained were:

$$u = [c_1 + c_1(\eta)]u_1(\eta) + [c_2 + c_2(\eta)]u_2(\eta) \quad (29)$$
$$0 \le \eta \le 1$$

$$u = [c_3 + c_3(\eta)]u_3(\eta) + [c_4 + c_4(\eta)]u_4(\eta) \quad (30)$$
$$1 \le \eta \le \infty$$

where,

$$u_1(\eta) = u_3(\eta) = e^{-(A + K/2)\eta}$$

$$u_2(\eta) = u_4(\eta) = e^{+(A + K/2)\eta}$$

The constant parameters c_1, c_2, c_3, and c_4 and the variable parameters $c_1(\eta)$, etc., were determined by applying the boundary conditions and matching the two solutions at $\eta = 1$ [8]. The analysis does not *predict* the final vortex size and so the parameter $A = \alpha d$, which measures the vortex size, was varied over a suitable range—in this case from 2–6.

The parameter S in equation (28), or the product $R_\delta S$ is also not predicted by the theory and has to be computed by comparison with experimental results. A value of $S = -2.81$ was determined.

Now R_L is the Reynolds number based on the entrance velocity and length of the test section,

$$R_L = U_e/\gamma$$

and R_δ is the Reynolds number for a plate based on the free-stream velocity and distance from the plate edge.

$$R_\delta = \frac{10}{3} \cdot \sqrt{R_L} \tag{31}$$

In the variation of parameters method used to evaluate the c_i and $c_i(\eta)$ an expansion in terms of η^P is involved. The value of P used in the computations was chosen so that the disturbance components reached their peak halfway through the boundary layer. Smith [3] has shown that this is a reasonable assumption. The value was $P = 4$.

The profiles $u(\eta)$, $v(\eta)$, and $w(\eta)$ are graphed in Fig. 14, for a typical set of parameter values.

The result predicts that the u component of velocity is significantly greater than either v or w and its gradient is also larger than that of v or w. So one would expect the u-component to be most effective in mass or energy transport from the curved wall.

It is also to be noted that v and u are out of phase. Thus, where the u-gradient is such that energy or mass is being transported *from* the boundary layer, the v-gradient is such that a flux *in* toward the wall is set up.

Fig. 14(b) shows that for $R_\delta K$ from 0–20, the change in curvature has little effect on the profiles. The peculiarity for $R_\delta K = -40$ is attributed to a breakdown in the validity of the linearization technique.

Temperature Profile

If one takes the Prandtl number as unity, K as small (say, 0.02), and $d\theta_t/dx$ as small, then the energy equation (22) has the same form as the equation for u, equation (18). Thus the nondimensional temperature and velocity profiles are the same,

$$\phi(\eta) = u(\eta)$$

Reynold's analogy takes the form:

$$\frac{\text{Stress on curved surface}}{\text{Stress on flat surface}} = \frac{\text{Forced convection on curved surface}}{\text{Forced convection on flat surface}}$$

or

$$\frac{\mathrm{Nu}_c}{\mathrm{Nu}_f} = \frac{(du_t/dy)_0}{(du_0/dy)_0} = \frac{\left(\dfrac{dU}{d\eta} + \dfrac{du}{d\eta}\cos(\alpha z)\right)_0}{\dfrac{dU}{d\eta_0}}$$

$$\doteq 1 + \left(\frac{du}{d\eta}\Big/\frac{dU}{d\eta}\right)\cos \alpha z$$

Now from (25),

$$\left(\frac{dU}{d\eta}\right)_0 = 5/3 \;\therefore\; \frac{\mathrm{Nu}_c}{\mathrm{Nu}_f} = 1 + 3/5\left(\frac{du}{d\eta}\right)_0 \cos(\alpha z) \tag{32}$$

From Fig. 14(a), the slope of u at the origin is about 1

$$\therefore \frac{\mathrm{Nu}_c}{\mathrm{Nu}_f} = 1 + 0.6\cos(\alpha z) \tag{33}$$

Thus the analysis predicts that the ratio of Nusselt numbers should fluctuate sinusoidally in the spanwise direction. *The increase or decrease in local heat transfer should be +60 percent with no overall increase for an integral number of waves.* One sees from equation (33) that the semiempirical relation for $\mathrm{Nu}_c/\mathrm{Nu}_f$ is independent of Nusselt number.

The dashed line in Fig. 12 shows the wave form one would expect from the theory, lifted upward to cover the region occupied by the experimental points. The lack of correlation is obvious. Skewing of the streamlines (so that they lay *across* the heating elements) *could* explain why the data didn't follow the sinusoidal curve. However, the theory, as it stands, does not explain the appreciable increase in the Nusselt number in the presence of the

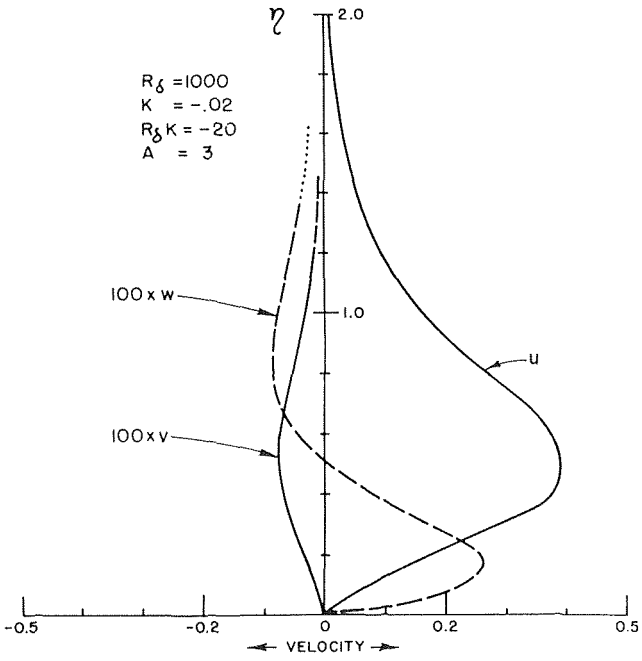

Fig. 14(a) Amplitude of disturbed velocity versus distance from a concave wall

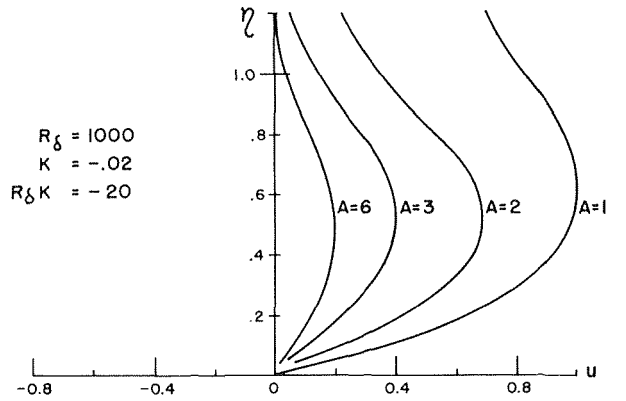

Fig. 14(b) Amplitude of disturbed velocity versus distance from a concave wall

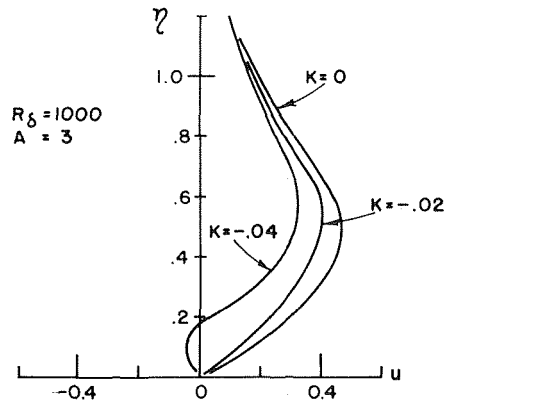

Fig. 14(c) Amplitude of disturbed velocity versus distance from a concave wall

Goertler vortices. For an integral number of wavelengths equation (33) predicts no overall increase in heat transfer over the flat plate case. Of course, an analysis based on linearized equations cannot predict a change in the overall rate of heat transfer. This increase could only be realized analytically, by the retention of the nonlinear terms in the fluid equations.

Recently, Sutera [9, 10] has obtained analog computer solutions to the full Navier-Stokes' equations for the case of finite vorticity addition to a boundary layer and the very appreciably changed heat transfer rates which result.

His model of vorticity amplification stretching would appear to be very relevant to the case of the buildup of Taylor-Goertler vortices on concave plates, and his analytical procedure could help to produce a more realistic analysis in this case.

Conclusions

The experimental work described in the section, "Experimental Work on the Production and Characteristics of Taylor-Goertler Vorticity," showed that the periodic disturbances known as Taylor-Goertler vortices did exist on the concave surface of the test ducts studied. The hot-wire data also showed that the disturbances did not change (within experimental error) with time and did not move about in the spanwise direction.

The prediction by the theory that the rate of naphthalene transport from the concave duct wall was due mainly to fluctuations in the u-component of velocity was consistent with the experimental studies.

The experimental results indicate that a 100–150 percent increase in Nusselt number occurs in the presence of Taylor-Goertler vortex formation on the concave wall of a duct. The theoretical analysis fails to predict such an overall increase in heat transfer. Being a linear analysis this isn't surprising. The basic assumption being that the total flow is the sum of the base and disturbed components, which are treated as independent of each other.

It is likely that the oscillatory components set up some sort of pressure gradient which changes the *mean* temperature and velocity profiles, producing an overall increase in heat transfer. Such an effect can only be catered for theoretically by retaining the nonlinear terms in the flow equations.

It is common practice to treat heat transfer in curved ducts as being closely approximated by heat transfer in a flat duct—at least for large radii of curvature. This work indicates clearly, however, that if the combination of Reynolds number, duct curvature, and fluid properties are such that the Goertler number lies between 16 and 300, this assumption is gravely in error.

The possibility also arises that by making use of curved ducts, the performance of heat exchangers can be significantly improved, at very little extra cost.

References

1 Taylor, G. J., "Distribution of Velocity and Temperature Between Rotating Cylinders," *Proceedings of the Royal Society*, London, Series A, Vol. 151, 1935, pp. 494–511.

2 Goertler, H., "On the Three-Dimensional Instability of Laminar Boundary Layers on Concave Walls," NACA TM 1375, 1942.

3 Smith, A. M. O., "On the Growth of Taylor-Goertler Vortices Along Highly Concave Walls," *Quarterly of Applied Mathematics*, Vol. 8, No. 3, 1955, pp. 233–262.

4 Liepman, H. W., "Investigation of Laminar Boundary-Layer Stability and Transition on Curved Boundaries," NACA Wartime Report, W-107, 1943.

5 Liepman, H. W., "Investigation on Concave Walls," NACA Wartime Report, W-87, 1945.

6 Kirchgassner, K., "Beitrag zu Einer Nichtlinearen Theorie der-Stabilitat von Schlichtenstromungen Langs Cylendrisch Gekrummter Wande Gegenuber Dreidimensionalen Stromungen," *Archive for Rational Mechanics and Analysis*, Vol. 6, 1960, p. 20.

7 Sparrow, E. M., "Analysis of Laminar Forced-Convection Heat Transfer in the Entrance Region of Flat Rectangular Ducts," NACA TN 3331, Jan. 1955.

8 Welker, H., "Heat Transfer Through the Laminar Boundary Layer on a Concave Wall," MS thesis, Dartmouth College, 1968.

9 Sutera, S. P., Malder, P. F., and Kestin, J., "On the Sensitivity of Heat Transfer in the Stagnation Point Boundary Layer to Free-Stream Vorticity," *Journal of Fluid Mechanics*, Vol. 16, 1963, Part 4, pp. 497–520.

10 Sutera, S. P., "Vorticity Amplification in Stagnation—Point Flow and Its Effect on Heat Transfer," *Journal of Fluid Mechanics*, Vol. 21, 1965, Part 3, pp. 513–537.

11 Hammerlin, G., *Journal of Rational Mechanics and Analysis*, Vol. 4, 1955, p. 279 (in German).

APPENDIX

Glossary

Base flow = undisturbed laminar flow over a flatplate.

Boundary-layer thickness = distance above the wall at which point the velocity profile reaches 0.99 the free-stream velocity.

Btu = abbreviation for British Thermal Unit.

Core = region in the center of a duct where the velocity profile is uniform and accelerating.

Disturbance = disturbance in this study was periodic vortices which were superimposed on the base flow. The disturbance was steady and periodic in the spanwise direction and should not be confused with oscillatory turbulence.

Center line of duct = half the distance between the walls, $d/2$.

Center line of test section = half the distance between the test section sides, $W/2$.

Element = thin strip of electrofilm laid on surface approximately 0.00900, 0.005 in. × 0.1 in. × 8 in.

Fiberfrax = a highly uniform structural insulating ceramic fabric which assumes equal thermal conductivity throughout $K_{hi} \approx 0.35$ Btu in/ft² deg F hr.

Entrance length to a duct = the distance from the entrance of a duct at which point the core velocity reaches 0.99 of its asymptotic value.

Fluctuation = periodic change in flow characteristics in the spanwise direction; should not be confused with time oscillations of flow characteristics.

Intensity of turbulence = (I_t) the rms value of oscillations as read on a rms voltmeter divided by the free-stream velocity. I_t = rms $U/U_\infty = 0.707\ (TL)/2$.

Leading edge = front edge of a surface upon which the flow first impinges, $x = 0$.

Lengthwise direction = distance along the surface in the direction of flow (x).

Oscillation = changes in fluid characteristics with time.

Spanwise direction = direction perpendicular to the x-y plane across the width of the test section (z).

Test section = three test sections were made and numbered I, II, III. Basically they were simply two parallel plates which formed a curved duct. The latter was specially prepared with a heated concave surface.

Turbulence level (TL) = ratio of peak-to-peak oscillation in velocity read by hot wire to free-stream velocity. $TL = (U_{Hi} - U_{Lo})/U_\infty$.

Vertical distance = distance above the wall (y).

Wavelength = distance in the z-direction required for one sinusoidal fluctuation of the disturbance.

Acknowledgment

This work was supported in part by a grant from the Air Force Office of Scientific Research, Propulsion Division (Dr. B. T. Wolfson).

Acknowledgment

This work was supported in part by a grant from the Air Force Office of Scientific Research, Propulsion Division (Dr. B. T. Wolfson).

DISCUSSION

A. M. O. Smith[2]

It is remarkable that the influence of concave curvature on heat transfer rates was not studied long ago. Professor McCormack and his co-workers are to be congratulated for their efforts in this area.

The paper brings forth several questions. The first one concerns the increased net heat transfer rate, which is contrary to linear theory. Why has it occurred? Are you sure you were measuring a true average for the entire plate? In the paper you say the heating elements were 0.1-in. wide, spaced 0.03-in. apart, and located parallel to the flow. Something is not clear. There appears to be interference. I presume you mean the elements are transverse to the flow, and if so, the 14 elements cover about one cycle. This extent may not be enough to obtain a good average. Another point arises; the flow is highly unstable. Perhaps, it is transitional, thus explaining the increased heat transfer rate, although your hot-wire measurements seem to deny this possibility.

I am curious how much the vortices have been amplified at your measurement station. Have you tried to make such calculations, as I did in your reference [3]?

The evaporation rate for naphthalene is proportional to the rate of heat transfer. This fact suggests a possible experiment with respect to the gross heat transfer rate. Under carefully controlled conditions, run the channel for a short period of time, learn the loss in weight w of naphthalene, and hence dw/dt either for the complete model or for an insert. For the same velocity, temperature and other conditions with naphthalene evaporate from a curved plate at the same rate as from a flat plate, or at a different average rate?

A statement is made in the paper as follows: "Since the existence of the phenomenon (Görtler vortices) to be studied had at best been shown indirectly by Liepman and McGahan, it was first desired to demonstrate their existence with some visual technique." Tani has demonstrated their existence (*Proceedings, International Council of the Aero Sciences*, Stockholm, 1962). Wortmann observed them visually and generally verified the theory by work in a water channel. His work was reported at the XI International Congress of Applied Mechanics, Munich, 1964. Neither of these experiments involved heat transfer.

Görtler-type instability can exist in either laminar or turbulent flows. What does it do to turbulent heat transfer? What does it do to separation? These are unanswered questions.

I would like to close by saying that interesting work has been reported but many questions still remain and it is hoped that Professor McCormack and his colleagues can continue their work on finding the answers.

[2] Chief Aerodynamics Engineer, Research, Douglas Aircraft Company, Long Beach, Calif.

Authors' Closure

As mentioned in the paper, the temperature of each heating element (on the curved duct) was taken as the average of 6 measurements taken along the element. A sample is given in Table 1— the average is 258 deg F and the spread is about ±9 percent. There are 14 such elements, each parallel to the flow. I do not understand Dr. Smith's objection to this arrangement. They do indeed cover just over 1 cycle of temperature (or velocity) variation in the spanwise (z) direction.

The flow was, in fact, very stable and the free stream turbulence fluctuations were always well under 3 percent of the free stream velocity—that is, less than 10 percent of the longitudinal velocity fluctuations associated with the Görtler vortices.

We did not measure the amplification factor of the vortices. However, our observations indicated that these reach a constant maximum strength at a certain distance along the curved plate (as expected from Kirchgassner's work) and our heat measurements were made in this region.

The suggestions for a further naphthalene experiment are appreciated.

We are now aware of the work of Tani and Wortman on demonstrating the formation and nature of Görtler vortices.

We agree that it is likely that Görtler vortices are present in the sublaminar layer in turbulent flow on concave plates and probably turbulent heat transfer. These and other unanswered problems associated with this interesting phenomena are worthy of continued attention.

H. H. KELLER

Senior Research Engineer,
Mobil Oil Corporation,
Dallas, Texas

E. S. HOLDREDGE

Professor,
Department of Mechanical Engineering,
Texas A & M University,
College Station, Texas

Radiation Heat Transfer for Annular Fins of Trapezoidal Profile[1]

A one-dimensional numerical solution is obtained for the steady-state thermal behavior of annular fins of trapezoidal profile which transfer heat by conduction and radiation. The results obtained are presented as charts relating fin efficiency to the dimensionless group $(r_T - r_B)\epsilon\sigma T_B^3/k \cos\alpha$, *for various values of the dimensionless groups* $r_B/(r_T - r_B)$, $Z_T/(r_T - r_B)$, *and arctan* $[(Z_B - Z_T)/(r_T - r_B)]$. *As presented the problem is the general formulation for the problem of radiating fins with flat surfaces.*

Extended surfaces transferring heat by radiation and conduction only are becoming increasingly important for space vehicles where these modes of heat transfer are the only means for disposing of waste heat. From the standpoint of mass reduction, it is generally preferable to utilize tapered fins for these applications.

The thermal behavior of straight radiating fins of rectangular profile has been studied by Lieblein [1],[2] Bartas and Sellers [2], and Tatum [3] using numerical techniques. Liu [4] has found an exact solution for a straight radiating fin of rectangular profile and Shouman [5] has found an exact solution for a radiating fin of constant area. Holstead [6], Mackay [7], and Reynolds [8] have analyzed a straight fin of trapezoidal profile by numerical methods. Chambers and Somers [9] studied annular fins of rectangular profile. The solutions for these geometries can be obtained as special cases of the geometry studied in this paper.

Treatment of Problem

A sketch of the fin to be studied is shown in Fig. 1. The following idealizations are made.

1 The conductive flow of heat is radial.
2 The heat flow and temperature distribution throughout the fin are independent of time.
3 There are no heat sources or sinks in the fin.
4 The temperature at the base of the fin is uniform.
5 The fin material is homogeneous, and the properties of the material are independent of the temperature.
6 There is no incident radiation on the surface of the fin.
7 There is no heat transfer from the tip of the fin.
8 The fin is a gray body.

These idealizations result in the following dimensionless differential equation and boundary conditions:

$$\frac{d^2U}{dR^2} + \left[\frac{1}{R+\rho} - \frac{\tan\alpha}{(1-R)\tan\alpha + \theta}\right]\frac{dU}{dR} - \frac{\beta U^4}{(1-R)\tan\alpha + \theta} = 0. \quad (1)$$

$$U(0) = 1.0 \quad (2)$$

$$\left(\frac{dU}{dR}\right)_{R=1} = 0. \quad (3)$$

The finite-difference equation describing the temperature distribution in this fin is given by

$$\psi_1 U_{I-1} + \psi_2 U_{I+1} - (\psi_1 + \psi_2)U_I - \frac{\left[\rho + \left(\frac{I-1}{N}\right)\right]U_I^4\beta}{N^2} = 0, \quad (4)$$

where

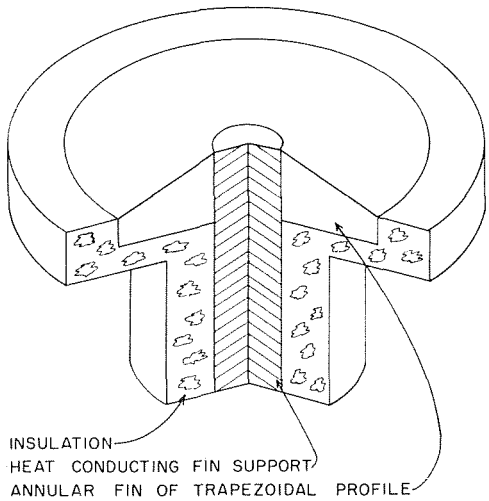

Fig. 1 Sketch of system

[1] This paper is based on a PhD dissertation submitted by H. H. Keller, to the Mechanical Engineering Department, Texas A & M University.

[2] Numbers in brackets designate References at end of paper.

Contributed by the Heat Transfer Division of The American Society of Mechanical Engineers and presented at the ASME-AIChE Heat Transfer Conference, Minneapolis, Minn., August 3–6, 1969. Manuscript received at ASME Headquarters, June 3, 1968. Paper No. 69-HT-6.

Nomenclature

I = subscript to denote nodal point
k = thermal conductivity
N = number of radial increments
r = radial position
r_B = radius of fin base
r_T = radius of fin tip
R = $(r - r_B)/(r_T - r_B)$
T = temperature
T_B = temperature at fin base
U = T/T_B
Z_B = fin thickness at base
Z_T = fin thickness at tip
α = angle of taper
β = $(r_T - r_B)\epsilon\sigma T_B^3/k \cos\alpha$
ϵ = emissivity
θ = $Z_T/(r_T - r_B)$
ρ = $r_B/(r_T - r_B)$
σ = Stefan-Boltzmann constant
ϕ = efficiency

$$\psi_1 = \left[\rho + \left(\frac{2I-3}{2N}\right)\right]\left\{\left[1 - \left(\frac{2I-3}{2N}\right)\right]\tan\alpha + \theta\right\} \quad (5)$$

$$\psi_2 = \left[\rho + \left(\frac{2I-1}{2N}\right)\right]\left\{\left[1 - \left(\frac{2I-1}{2N}\right)\right]\tan\alpha + \theta\right\}. \quad (6)$$

This equation is good for the limits $2 \leq I \leq N$, where I is 1 at the base of the fin and I is $N + 1$ at the tip of the fin.

The finite-difference equation written at the tip of the fin becomes

$$U_N - U_{N+1} = \frac{\beta U_{N+1}^4\left[\rho + \left(\frac{4N-1}{4N}\right)\right]}{2N^2\left[\rho + \left(\frac{2N-1}{2N}\right)\right]\left[\frac{\tan\alpha}{2N} + \theta\right]}. \quad (7)$$

Equations (4) and (7) together with the boundary condition

$$U_1 = 1.0 \quad (8)$$

constitute the complete finite-difference characterization of the dimensionless temperature distribution in an annular fin of trapezoidal profile.

Fin efficiency, used as the basis for determining a fin design, is defined as the ratio of the actual heat-flow rate to the heat-flow rate that would occur if the entire fin were at the temperature of its base. For this problem, the actual heat-flow rate was obtained by summing the radiant heat-flow rates from all of the finite elements. This results in the following equation for the efficiency:

$$\phi = \frac{\left(\rho + \frac{1}{4N}\right) + 2\sum_{I=2}^{N}\left[\rho + \left(\frac{I-1}{N}\right)\right]U_I^4 + \left[\rho + \left(\frac{4N-1}{4N}\right)\right]U_{N+1}^4}{N(2\rho+1)}. \quad (9)$$

Solution of Problem

The solution of the problem was accomplished by using the technique presented by Holstead [6]. The method first solves equation (7) for the temperature ratio U_N and notes that U_N is a function of only U_{N+1}. Hence, by assuming a value of U_{N+1}, U_N may be calculated directly. Likewise, equation (4) may be solved for U_{I-1}. This gives U_{I-1} as a function of U_I and U_{I+1}. Therefore U_{N-1} may be found since U_N and U_{N+1} are now known. This procedure is carried out until a value is obtained for U_1. This value is then compared to the required value of unity. If the calculated value of U_1 differs from unity by more than the desired tolerance, a new value of U_{N+1} is chosen and the calculations are repeated. A systematic procedure for selecting U_{N+1} is used so that the value of U_1 will approach unity rapidly.

The data obtained are presented here as charts relating fin efficiency to the dimensionless group β for three values of ρ (0.5, 1.0, 10.0), with α and θ held constant. The values of α and θ are successively fixed at all possible combinations of the three values of α, (0.0, 6.0, and 12.0 deg), and the three values of θ, (0.0, 0.05, 0.10), with the exception of both parameters equal to zero.

It should be noted that the number of parameters could be reduced to three by dividing both β and θ by $\tan\alpha$ and eliminating α as one of the parameters. This would reduce the number of charts needed to present the data. However, this removes some of the general nature of the problem since the case of α equals zero must be treated as a special case.

The efficiencies of annular fins of trapezoidal profile were compared to the efficiencies of straight fins with the same trapezoidal profile as determined by Holstead [6]. This comparison is presented in Table 1. The efficiencies of the annular fins are essentially the same as the efficiencies of the straight fins at a value of ρ equal to 10.

The results obtained here are valid for any one of six fin geometries. The three parameters which control the fin geometry are α, θ, and ρ. A value of zero for α denotes a rectangular profile. A value of zero for θ denotes a triangular profile. Nonzero values for both α and θ denote a trapezoidal profile. Straight fins with any of these three profiles may be represented by choosing ρ equal to or greater than 10. Thus the solution as presented here can be regarded as a general solution for fins having flat surfaces.

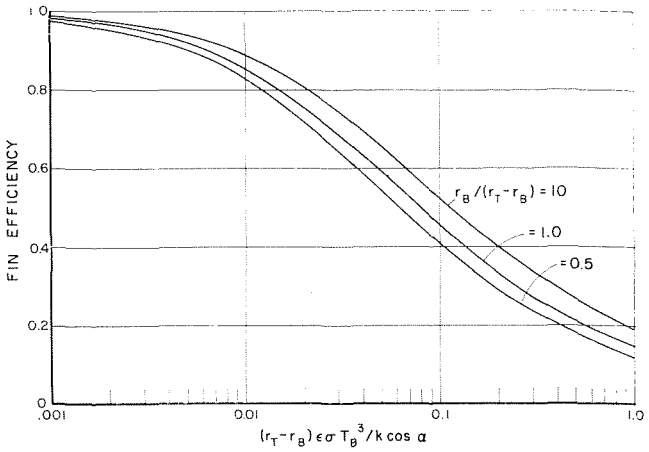

Fig. 3 Fin efficiency versus β for α = 0.00 and θ = 0.10

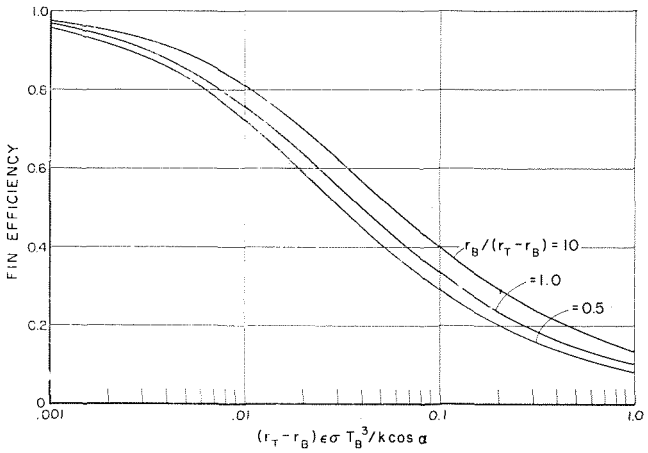

Fig. 2 Fin efficiency versus β for α = 0.00 and θ = 0.05

Table 1 Comparison of efficiencies for annular and straight fins of trapezoidal profile; α = 6.0 deg, θ = 0.05

	Straight	Annular fin		
β	fin	ρ = 0.5	ρ = 1.0	ρ = 10.0
0.010	0.91	0.856	0.878	0.905
0.020	0.84	0.761	0.793	0.835
0.040	0.74	0.638	0.678	0.736
0.060	0.67	0.558	0.602	0.666
0.100	0.58	0.459	0.505	0.573
0.200	0.455	0.337	0.381	0.448
0.400	0.345	0.239	0.277	0.338
0.600	0.29	0.194	0.228	0.283
1.000	0.23	0.148	0.177	0.225

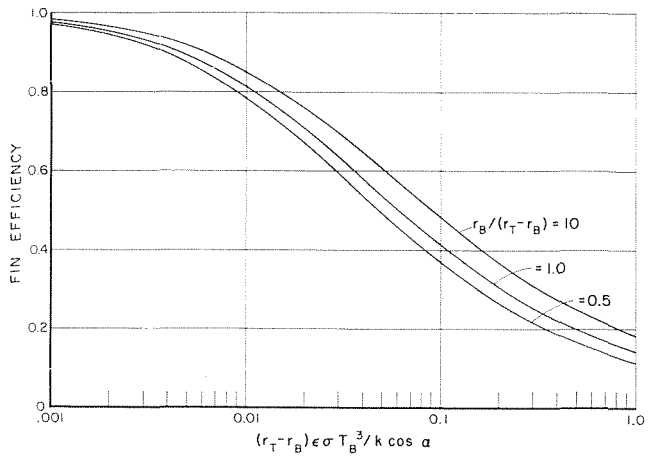

Fig. 4 Fin efficiency versus β for $\alpha = 6.00$ and $\theta = 0.0$

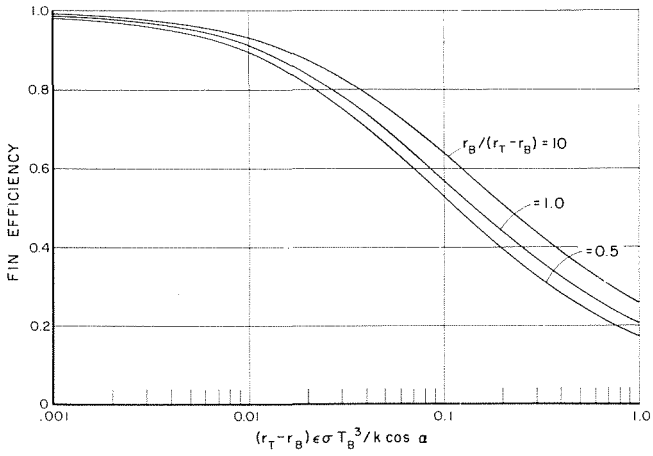

Fig. 7 Fin efficiency versus β for $\alpha = 12.00$ and $\theta = 0.0$

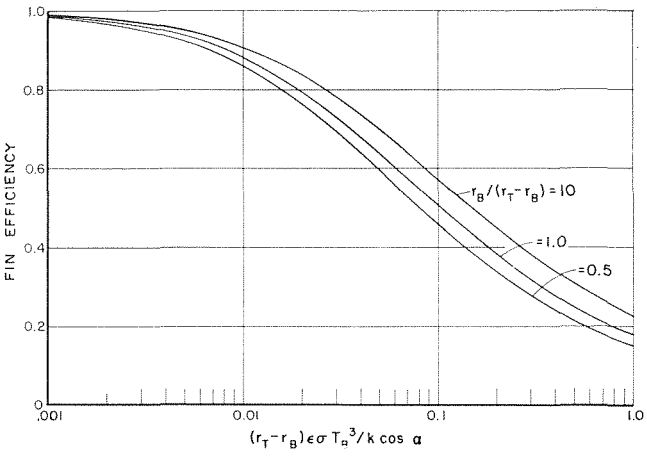

Fig. 5 Fin efficiency versus β for $\alpha = 6.00$ and $\theta = 0.05$

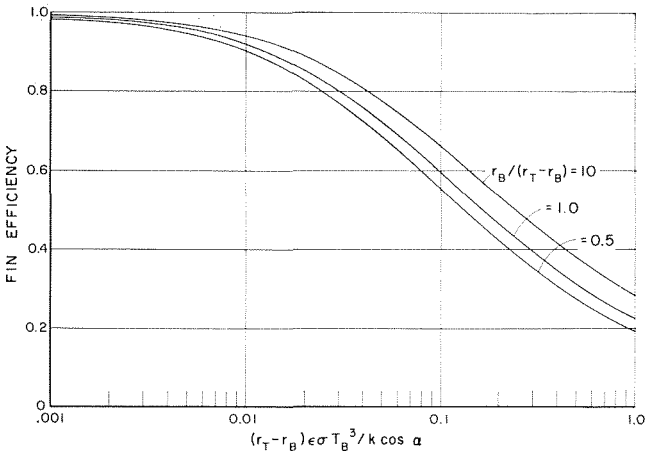

Fig. 8 Fin efficiency versus β for $\alpha = 12.00$ and $\theta = 0.05$

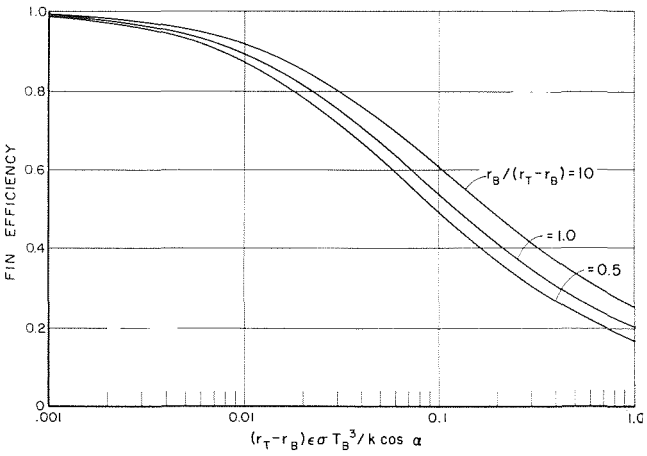

Fig. 6 Fin efficiency versus β for $\alpha = 6.00$ and $\theta = 0.10$

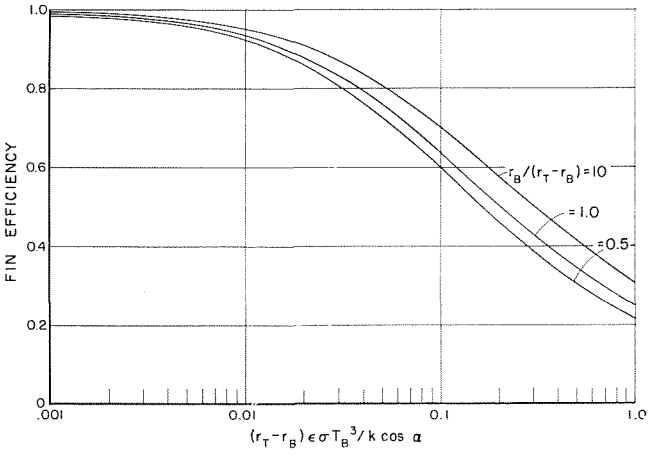

Fig. 9 Fin efficiency versus β for $\alpha = 12.00$ and $\theta = 0.10$

References

1 Lieblein, S., "Analysis of Temperature Distribution and Radiant Heat Transfer Along a Rectangular Fin of Constant Thickness," NASA Technical Note D-196, 1959.

2 Bartas, J., and Sellers, W. H., "Radiation Fin Effectiveness," JOURNAL OF HEAT TRANSFER, TRANS. ASME, Series C, Vol. 82, Feb. 1960, p. 73.

3 Tatum, J. W., "Steady-State Behavior of Extended Surfaces in Space," *American Rocket Society Journal*, Vol. 30, Jan. 1960, pp. 118–119.

4 Liu, C. Y., "On Minimum-Weight Rectangular Radiating Fins," *Journal of Aero/Space Sciences*, Vol. 27, Nov. 1960, pp. 871–872.

5 Shouman, A. R., "An Exact Solution for the Temperature Distribution and Heat Transfer Along a Constant Cross-Sectional Area Fin Transferring Heat by Radiation Only to Surroundings With Finite Equivalent Sink Temperature," unpublished paper, Department of Mechanical Engineering, New Mexico State University, 1965.

6 Holstead, R. D., "Radiation Heat Transfer for Straight Fins of Trapezoidal Profile," PhD dissertation, Texas A&M University, Jan. 1967.

7 Mackay, D. B., *Design of Space Powerplants*, Prentice-Hall, Englewood Cliffs, N. J., 1963.

8 Reynolds, W. C., "A Design-Oriented Optimization of Simple Tapered Radiating Fins," JOURNAL OF HEAT TRANSFER, TRANS. ASME, Series C, Vol. 85, Aug. 1963, pp. 193–201.

9 Chambers, R. L., and Somers, E. V., "Radiation Fin Efficiency for One-Dimensional Heat Flow in a Circular Fin," JOURNAL OF HEAT TRANSFER, TRANS. ASME, Series C, Vol. 81, Nov. 1959, pp. 327–329.

References

1 Lieblein, S., "Analysis of Temperature Distribution and Radiant Heat Transfer Along a Rectangular Fin of Constant Thickness," NASA Technical Note D-196, 1959.

2 Bartas, J., and Sellers, W. H., "Radiation Fin Effectiveness," JOURNAL OF HEAT TRANSFER, TRANS. ASME, Series C, Vol. 82, Feb. 1960, p. 73.

3 Tatum, J. W., "Steady-State Behavior of Extended Surfaces in Space," *American Rocket Society Journal*, Vol. 30, Jan. 1960, pp. 118–119.

4 Liu, C. Y., "On Minimum-Weight Rectangular Radiating Fins," *Journal of Aero/Space Sciences*, Vol. 27, Nov. 1960, pp. 871–872.

5 Shouman, A. R., "An Exact Solution for the Temperature Distribution and Heat Transfer Along a Constant Cross-Sectional Area Fin Transferring Heat by Radiation Only to Surroundings With Finite Equivalent Sink Temperature," unpublished paper, Department of Mechanical Engineering, New Mexico State University, 1965.

6 Holstead, R. D., "Radiation Heat Transfer for Straight Fins of Trapezoidal Profile," PhD dissertation, Texas A&M University, Jan. 1967.

7 Mackay, D. B., *Design of Space Powerplants*, Prentice-Hall, Englewood Cliffs, N. J., 1963.

8 Reynolds, W. C., "A Design-Oriented Optimization of Simple Tapered Radiating Fins," JOURNAL OF HEAT TRANSFER, TRANS. ASME, Series C, Vol. 85, Aug. 1963, pp. 193–201.

9 Chambers, R. L., and Somers, E. V., "Radiation Fin Efficiency for One-Dimensional Heat Flow in a Circular Fin," JOURNAL OF HEAT TRANSFER, TRANS. ASME, Series C, Vol. 81, Nov. 1959, pp. 327–329.

DISCUSSION

A. R. Shouman

The one-dimensional steady-state general heat transfer through radiating fins was studied.[3] The study covered the variable geometry fin, considered the radiating case, as well as the composite radiating convecting case with or without heat generation. The effect of dependency of thermal properties and heat generation on temperature was included. The conditions under which the governing differential equation can be solved exactly was pointed out. For the cases when an exact solution could not be obtained, a numerical evaluation technique was outlined. However, the graphs provided by the paper should be useful for the designer.

[3] Shouman, A. R., "Nonlinear Heat Transfer and Temperature Distribution Through Fins and Electric Filaments of Arbitrary Geometry With Temperature-Dependent Properties and Heat Generation," NASA Technical Memorandum NASA TM X-53621, June 14, 1967; superseded by NASA TN D-4257, Jan. 1968.

R. B. KINNEY[1]
Senior Research Engineer,
United Aircraft Research
Laboratories,
East Hartford, Conn. Assoc. Mem. ASME

E. M. SPARROW
Professor of Mechanical Engineering,
University of Minnesota,
Minneapolis, Minn. Mem. ASME

Turbulent Flow, Heat Transfer, and Mass Transfer in a Tube With Surface Suction

The problem of turbulent pipe flow with mass removal at the bounding surface is analyzed, and numerical results are presented for the friction factor, axial pressure gradient, heat and mass transfer coefficients, and velocity and temperature profiles. The results, which are relevant to forced-convection condensation in a tube (either with or without noncondensable gases) are shown to be substantially affected by even small amounts of wall suction. Therefore, the present findings do not support the current practice of using impermeable-boundary transfer coefficients in condensation calculations. The analysis is performed under the condition that the velocity field is locally self-similar. Corresponding conditions are used for the distributions of temperature and mass fraction. The cross-sectional distributions of the transverse velocity and the shear stress are not constrained in advance, but rather, are permitted to vary in accordance with the conservation laws. The turbulent transport is expressed in terms of the mixing-length model, modified in the neighborhood of the wall by a specially derived damping factor.

Introduction

Turbulent pipe flows in which there is withdrawal of mass (i.e., suction) at the boundaries of the flow are encountered in a variety of engineering applications. Such flows occur, for example, when components are separated from gas mixtures flowing in tubes whose walls are selectively porous. Another widely encountered application is forced-convection condensation in a tube. In this example, condensed liquid flows in an annular film adjacent to the cooled wall of the tube, and vapor flows through the core. There is a continuous transfer of mass across the interface between the vapor and the liquid phases. The vapor may thus be regarded as a turbulent pipe flow with mass removal at its boundary (i.e., at the interface).

With regard to the aforementioned condensation problem, it is interesting to observe that the effects of the interfacial mass transfer (i.e., the suction) on the predicted heat transfer, mass transfer, and friction coefficients of the vapor are generally ignored. Thus, for instance, when there are noncondensable gases in the vapor, the suggested mass transfer coefficient is that calculated for flow over an impermeable wall [1].[2] Similarly, the predicted interfacial shear is obtained using information for flow with an impermeable interface [2, 3].

Consideration of available results for other types of turbulent flows, in particular external flows, indicates that suction or blowing at the boundary can have a significant effect on all of the transfer coefficients. It is, therefore, to be expected that wall suction will have a distinct effect on the transport characteristics of turbulent tube-flows as well. An analytical investigation of the effect of wall suction on these flow characteristics, including friction, heat transfer, and mass transfer, is the subject of the present research.

In formulating the analytical model, every effort was made to

[1] Presently, Associate Professor of Aerospace and Mechanical Engineering, University of Arizona, Tucson, Ariz.

Contributed by the Heat Transfer Division of The American Society of Mechanical Engineers and presented at the ASME-AIChE Heat Transfer Conference, Minneapolis, Minn., August 3–6, 1969. Manuscript received at ASME Headquarters, May 9, 1968. Paper No. 69-HT-4.

[2] Numbers in brackets designate References at end of paper.

Nomenclature

c_f = friction factor, $2\tau_w/\rho\bar{u}^2$
c_p = specific heat at constant pressure
D = binary diffusion coefficient
D_t = eddy diffusion coefficient
DF = damping factor, equation (16)
g = temperature similarity variable, equation (27)
h = heat or mass transfer coefficient, equation (33) or (38)
j = diffusive mass flux, equation (37)
K = momentum flux factor, equation (19)
k = thermal conductivity
k_t = eddy conductivity
l = mixing length
l^+ = dimensionless mixing length, $l\sqrt{\tau_w/\rho}/\nu$
Nu = Nusselt number, equation (33) or (38)
Pr = Prandtl number, ν/α
p = static pressure
q = heat flux
Re = Reynolds number, $\bar{u}(2r_w)/\nu$
r = radial coordinate
r_w = tube radius
r^+ = dimensionless radial coordinate, $r\sqrt{\tau_w/\rho}/\nu$
r_w^+ = dimensionless tube radius, $r_w\sqrt{\tau_w/\rho}/\nu$
Sc = Schmidt number, ν/D
T = temperature
u = axial velocity
$\bar{u}$ = mean velocity
u^+ = dimensionless axial velocity, $u/\sqrt{\tau_w/\rho}$
v = transverse velocity
v_w = suction velocity at wall
v^+ = dimensionless transverse velocity, $v/\sqrt{\tau_w/\rho}$
W = mass fraction
x = axial coordinate
y = transverse coordinate normal to wall
y^+ = dimensionless transverse coordinate, $y\sqrt{\tau_w/\rho}/\nu$
α = thermal diffusivity
β = eigenvalue; β_1, first eigenvalue
γ = transport parameter, equation (26)
μ = viscosity
μ_t = eddy viscosity
ν = kinematic viscosity
ρ = density
τ = shear stress

Subscripts

b = bulk
0 = without surface mass transfer
w = at wall

preserve as much generality as possible. To this end, the local similarity concept is employed. This avoids the need to consider specific axial distributions of the suction velocity. Furthermore, radial distributions of shear stress and transverse velocity need not be specified in advance, but rather, follow from the conservation laws. The turbulent exchange model incorporated into the analysis is believed to be the best available representation consistent with surface mass transfer.

Numerical results are provided for application-oriented quantities such as the surface shear stress, the axial pressure gradient, and heat and mass transfer coefficients. Representative velocity and temperature profiles are also presented. The results depend upon the axial flow Reynolds number, the velocity ratio $v_w/\bar{u}$ (v_w = suction velocity at boundary, $\bar{u}$ = mean axial velocity), and, for heat and mass transfer, the Prandtl and Schmidt numbers.

Prior investigations of turbulent duct flows subject to surface mass transfer have been directed primarily toward fluid injection (i.e., blowing). This work is well summarized by Olson and Eckert [4]. Velocity-profile measurements for airflow in a porous tube with wall suction have been made by Weissberg and Berman [5]. These will be discussed in a later section of the present paper.

Velocity Problem

The analysis begins with the conservation equations for mass and momentum for turbulent flow in a circular tube. These may be written

$$\frac{\partial}{\partial r}(rv) + \frac{\partial}{\partial x}(ru) = 0 \tag{1}$$

$$\rho\left[r\frac{\partial u^2}{\partial x} + \frac{\partial}{\partial r}(ruv)\right] = -r\frac{\partial p}{\partial x} - \frac{\partial(r\tau)}{\partial r} \tag{2}$$

where the inertia terms (left-hand side of equation (2)) have been recast into a somewhat more convenient form by application of the continuity equation. The negative sign affixed to the viscous shear term anticipates a derivative, $\partial/\partial y$, in the definition of $\tau(y$ is normal to the wall). For the purposes of the present analysis, compressibility and variable properties are regarded as second-order influences and are omitted from the conservation equations.

Cross-Sectional Distribution of Shear. By application of the momentum equation, the distribution of the shear stress across the section can be derived, this distribution being one of the essential ingredients in the solution. First, equation (2) is formally integrated from an arbitrary radius r to r_w (r_w = tube radius). Then, the integration is specialized to the range $r = 0$ to $r = r_w$. In this way, the pressure gradient, $\partial p/\partial x$ (assumed independent of r), can be eliminated in favor of the wall shear stress and total integrated change in axial momentum flux. Following these steps, there results after rearrangement

$$\frac{\tau}{\tau_w} = \frac{r}{r_w} - \frac{\rho uv}{\tau_w} + \frac{\rho}{r\tau_w}\left\{\int_r^{r_w} r\frac{\partial u^2}{\partial x}dr - \left(1 - \frac{r^2}{r_w{}^2}\right)\int_0^{r_w} r\frac{\partial u^2}{\partial x}dr\right\} \tag{3}$$

The local similarity model will now be invoked. It is postulated that the velocity profiles are locally self-similar; that is,

$$\frac{u}{\bar{u}} = f\left(\frac{r}{r_w}\right) \tag{4}$$

where $\bar{u}$ is the local value of the mean velocity. Furthermore, from mass conservation

$$\frac{d\bar{u}}{dx} = -\frac{2v_w}{r_w} \tag{5}$$

so that, with equation (4)

$$\frac{\partial u}{\partial x} = -\frac{2v_w u}{r_w \bar{u}} \tag{6}$$

The integrals appearing in equation (3) can now be rephrased using equation (6). Following this step and the introduction of the well-known u^+, r^+ variables, there follows

$$\frac{\tau}{\tau_w} = \frac{r^+}{r_w{}^+} - u^+v^+ + 4\left(\frac{v_w}{\bar{u}}\right)\frac{r_w{}^+}{r^+}\left\{\left[1 - \left(\frac{r^+}{r_w{}^+}\right)^2\right] \times \int_0^{r_w{}^+} \frac{r^+u^{+2}}{r_w{}^{+2}}dr^+ - \int_{r^+}^{r_w{}^+} \frac{r^+u^{+2}}{r_w{}^{+2}}dr^+\right\} \tag{7}$$

Equation (7) represents the radial distribution of the shear stress consistent with the conservation-of-momentum principle and local similarity. Clearly, for the case in which surface mass transfer is absent ($v_w = 0$, $v = 0$), equation (7) reduces to the familiar linear variation of shear stress with pipe radius.

Inspection of equation (7) indicates that the evaluation of τ/τ_w depends upon a knowledge of the velocity distributions $v^+(r^+)$ and $u^+(r^+)$, as well as on the radial position r^+ and the prescribable constant parameters $r_w{}^+$ and $v_w/\bar{u}$. However, the transverse velocity v^+ can be eliminated as an independent entity by integrating mass conservation, equation (1), from $r = 0$ to $r = r$ and substituting equation (6) for $\partial u/\partial x$. These operations yield

$$v^+ = \frac{v_w{}^+}{r^+}\left[r_w{}^+ - \frac{2}{r_w{}^+\bar{u}^+}\int_{r^+}^{r_w{}^+} r^+u^+dr^+\right] \tag{8}$$

in which

$$v_w{}^+ = \left(\frac{v_w}{\bar{u}}\right)\frac{\mathrm{Re}}{2r_w{}^+} \tag{8a}$$

Re denotes the Reynolds number

$$\mathrm{Re} = \frac{\bar{u}(2r_w)}{\nu} \tag{9}$$

and use has been made of the fact that $\mathrm{Re} = 2r_w{}^+\bar{u}^+$. As a result of equation (8), it is seen that the distribution of the transverse velocity is explicitly related to the distribution of u^+.

Taken together, equations (7) and (8) provide a relationship between the radial distributions of τ and u^+. This relationship will serve as input to the shear stress-velocity gradient representation, the details of which will be discussed in the next section.

Turbulent Transport Model. For turbulent flows, it is customary to write the relationship between the shear stress and the velocity gradient in a form equivalent to the following

$$\tau = (\mu + \mu_t)\frac{du}{dy} \tag{10}$$

where μ_t denotes the eddy viscosity and y is the distance from the wall. There are a number of competing representations for μ_t, based on various models of the turbulent exchange process. After a careful consideration of the possibilities, it is the view of the authors that the mixing-length concept, suitably modified by a damping factor in the neighborhood of the wall, offers the best available representation.

In assessing the possible influence of wall mass transfer on the mixing length, it is to be noted that recent experience suggests that this quantity is insensitive to both mass transfer and compressibility effects. In particular, Townsend [6] has put forth strong arguments supporting the use of a universal mixing length ($l = 0.4y$) in the wall layer of turbulent flows with surface mass transfer. These arguments have been reinforced by Bradshaw [7]. In addition, Maise and McDonald [8] have demonstrated that the mixing length is sensibly independent of density variations over the entire thickness of compressible turbulent bound-

ary layers. Finally, Spalding [9], seeking a transport model that could be applied for all types of turbulent boundary layers, has recently advocated use of the mixing length, modified by a damping factor (after van Driest) near the wall. Consistent with the interpretations of these authorities, therefore, the mixing length in the fully turbulent portion of the flow may be viewed as a universal quantity which is, for all practical purposes, unaltered by surface mass transfer and compressibility effects.

Adopting this viewpoint, the turbulent viscosity μ_t is expressed in terms of the mixing length as follows

$$\mu_t = \rho l^2 |du/dy| \tag{11}$$

Upon introducing this representation for μ_t into equation (10) and rearranging, one obtains

$$\frac{\tau}{\tau_w} = \left(1 + l^{+2}\frac{du^+}{dy^+}\right)\frac{du^+}{dy^+} \tag{12}$$

An expression for the mixing length in pipe flow, purported to apply all the way from the wall to the center line, is the following [10, page 568]

$$\frac{l}{r_w} = 0.4\frac{y}{r_w} - 0.44\left(\frac{y}{r_w}\right)^2 + 0.24\left(\frac{y}{r_w}\right)^3 - 0.06\left(\frac{y}{r_w}\right)^4 \tag{13}$$

The first term of the foregoing, $l = 0.4y$, corresponds to Prandtl's hypothesis for small y/r_w.

It is widely held (e.g., [9, 11]) that the conventional mixing-length representation (e.g., equation (13)) overstates the effect of turbulence in the immediate neighborhood of the wall. One method of accounting for the damping effect of the wall has been proposed by van Driest [11]. Although van Driest's damping factor is, in itself, not directly applicable to turbulent flows with surface mass transfer, his model can be generalized to yield a damping factor for such flows.

The basis for the van Driest model can be stated as follows: An infinitely extended flat plate situated in an otherwise quiescent fluid environment oscillates harmonically in its own plane. Owing to viscosity, the amplitude of the oscillations experienced by the fluid diminish exponentially with increasing distance from the plate; that is, the damping factor is $\exp(-y^+/A^+)$, where A^+ is the damping constant. In the case in which the plate is stationary and the fluid is oscillating (turbulent eddies), the corresponding damping factor is $1 - \exp(-y^+/A^+)$.

To generalize the van Driest model for the case of surface mass transfer, suppose that there is a uniform suction v_w at the surface of the aforementioned oscillating plate. Correspondingly, the governing equation for the velocity field in the fluid above the plate is

$$\frac{\partial u}{\partial t} - v_w\frac{\partial u}{\partial y} = \nu\frac{\partial^2 u}{\partial y^2} \tag{14}$$

with the boundary condition $u = u_0 \cos \omega t$ at the plate surface. The steady periodic solution for u can be shown to be

$$u = u_0 \cos\left(\omega t - y\lambda^{1/2}\sin\frac{1}{2}\theta\right)\left\{\exp\left(-\frac{v_w y}{2\nu} - y\lambda^{1/2}\cos\frac{1}{2}\theta\right)\right\} \tag{15}$$

where

$$\lambda = \left(\frac{v_w^4}{16\nu^4} + \frac{\omega^2}{\nu^2}\right)^{1/2}, \quad \cos\theta = \frac{v_w^2}{4\lambda\nu^2} \tag{15a}$$

The exponential quantity within braces in equation (15) is the damping factor.

In accordance with the van Driest model, the damping factor for the case in which the plate is stationary and the fluid is oscillating (i.e., eddying) is obtained by subtracting the aforementioned exponential term from unity. After considerable rearrangement, this damping factor can be written as

$$DF = 1 - \exp\left\{-\chi - \frac{1}{\sqrt{2}}\left[\left(\chi^4 + 4\left(\frac{y^+}{A^+}\right)^4\right)^{1/2} + \chi^2\right]^{1/2}\right\} \tag{16}$$

in which

$$\chi = v_w{}^+ y^+/2 \tag{16a}$$

It may be verified that for flow in an impermeable tube ($\chi = 0$), equation (16) reduces to the damping factor proposed by van Driest. In the absence of evidence to the contrary, the damping constant A^+ will be assigned the same numerical value used by van Driest, that is, 26.

Continuing, the mixing-length representation, equation (13), can now be modified to take account of the damping of turbulent eddies in the immediate neighborhood of the wall. If, at the same time, dimensionless variables are introduced, there follows

$$\frac{l^+}{r_w{}^+} = 0.4(DF)\frac{y^+}{r_w{}^+} - 0.44\left(\frac{y^+}{r_w{}^+}\right)^2 + 0.24\left(\frac{y^+}{r_w{}^+}\right)^3 - 0.06\left(\frac{y^+}{r_w{}^+}\right)^4 \tag{17}$$

where DF is expressed by equation (16). The mixing-length representation of equation (17) is employed in conjunction with the τ/τ_w, du^+/dy^+ relation of equation (12).

Integrodifferential Equation for u^+. The shear-stress distribution expressed by equation (7) may now be substituted into equation (12), thereby yielding the governing equation for u^+. After replacing r^+ in favor of y^+ (i.e., $y^+ = r_w{}^+ - r^+$) and rearranging, one obtains

$$\begin{aligned}\frac{du^+}{dy^+} + l^{+2}\left(\frac{du^+}{dy^+}\right)^2 = {} & \frac{r^+}{r_w{}^+} - \left(\frac{v_w}{\bar{u}}\right) \\ & \times \left\{\frac{\mathrm{Re}}{2} - \frac{2}{r_w{}^+}\int_0^{y^+} u^+(r_w{}^+ - y^+)dy^+\right\}\frac{u^+}{r^+} \\ & + 4\left(\frac{v_w}{\bar{u}}\right)\frac{1}{r_w{}^+}\left\{\left[1 - \left(\frac{r^+}{r_w{}^+}\right)^2\right]\frac{\mathrm{Re}^2}{8}K \right. \\ & \left. - \int_0^{y^+} u^{+2}(r_w{}^+ - y^+)dy^+\right\}\frac{1}{r^+}\end{aligned} \tag{18}$$

with the boundary condition $u^+ = 0$ at $y^+ = 0$. The quantity K in the foregoing is an abbreviation for the momentum flux factor given by

$$K = \frac{1}{\pi r_w{}^2\bar{u}^2}\int_0^{r_w} 2\pi r u^2 dr = \frac{8}{\mathrm{Re}^2}\int_0^{r_w{}^+} u^{+2}(r_w{}^+ - y^+)dy^+ \tag{19}$$

It is seen that K is the ratio of the axial momentum transported by the actual flow to that transported by a slug flow moving at the mean velocity $\bar{u}$. In general, for turbulent flows, K is only slightly greater than unity. In addition, it is readily verified that $r_w{}^+$ and Re are related by

$$\mathrm{Re} = \frac{4}{r_w{}^+}\int_0^{r_w{}^+} u^+(r_w{}^+ - y^+)dy^+ \tag{20}$$

Equation (18) is a nonlinear integrodifferential equation for the velocity distribution $u^+(r^+)$. The equation contains a total of four parameters: $v_w/\bar{u}$, Re, $r_w{}^+$, and K. However, in light of equations (19) and (20), only two of these parameters are independent.

Solutions of equation (18) have been obtained numerically for specified parametric values of $v_w/\bar{u}$ and Re, respectively, spanning the range from 0–0.02 and from 10,000–150,000. In its broad outlines, the numerical scheme is as follows: Specific values are selected for $v_w/\bar{u}$ and Re. Then, trial values are assigned for $r_w{}^+$ and K. With these, equation (18) can be forward integrated from $y^+ = 0$ to $y^+ = r_w{}^+$. The thus-obtained velocity distribution $u^+(y^+)$ is then employed to evaluate K

and Re. If the numerical values of these quantities do not agree with those originally assigned, then new values of r_w^+ and K are selected and the process repeated until convergence is achieved.

Friction Factor, Pressure Drop. Once the velocity distribution has been determined, numerical results for the friction factor and pressure drop follow directly. The friction factor c_f is defined as

$$c_f = \tau_w/\tfrac{1}{2}\rho\bar{u}^2 \tag{21}$$

In terms of the variables of the analysis, c_f can be written

$$c_f = 2(2r_w^+/\mathrm{Re})^2 \tag{22}$$

In the presence of surface mass transfer, the axial pressure gradient dp/dx contains both wall shear and momentum flux contributions. From the integrated form of equation (2), the following expression for dp/dx can be derived

$$-\frac{dp/d(x/2r_w)}{\frac{1}{2}\rho\bar{u}^2} = 4c_f - 16\left(\frac{v_w}{\bar{u}}\right)K \tag{23}$$

Numerical results for these quantities will be presented in a later section of the paper.

Heat and Mass Transfer

The formulation and solution of the heat and mass transfer problems follow along identical lines. In the heat transfer problem, we are concerned with the temperature field and the wall heat flux for a fluid flowing in an isothermal tube. In the case of mass transfer, consideration is given to a binary gas mixture flowing in a tube at whose wall the mass fraction of one of the components is constant. Prior experience with turbulent flows suggests that the heat and mass transfer coefficients are not very sensitive to the specific nature of the thermal and mass-concentration boundary conditions at the wall [12].

The forthcoming development will be made primarily in terms of the heat transfer problem, specific comments on the mass transfer problem being deferred until the end of this section. The final results apply equally well to both transfer problems.

The starting point of the analysis is the energy equation for turbulent tube flow

$$\rho c_p\left(u\frac{\partial T}{\partial x} + v\frac{\partial T}{\partial r}\right) = -\frac{1}{r}\frac{\partial}{\partial r}(rq) \tag{24}$$

where

$$q = -(k + k_t)\frac{dT}{dy} \tag{25}$$

in which k_t denotes the eddy conductivity. Under the assumption that the turbulent Prandtl number is unity, that is, $k_t = c_p\,\mu_t$, and introducing the mixing length from equation (11), the expression for q becomes

$$q = -c_p\mu\gamma(y^+)\frac{dT}{dy} \qquad \gamma(y^+) = \frac{1}{\mathrm{Pr}} + l^{+2}\frac{du^+}{dy^+} \tag{26}$$

It will now be assumed that the temperature profiles are locally self-similar, so that [12]

$$\frac{T - T_w}{T_b - T_w} = g\left(\frac{r}{r_w}\right) \tag{27}$$

and, additionally, for consistency with the definition of the bulk temperature

$$\int_0^{r_w} rug dr \Big/ \int_0^{r_w} rudr = 1 \tag{28}$$

After application of the local similarity assumption, the energy equation becomes

$$u\left(\frac{dT_b/dx}{T_b - T_w}\right)g - v\frac{dg}{dy} = \frac{\nu}{(r_w - y)}\frac{d}{dy}\left[(r_w - y)\gamma\frac{dg}{dy}\right] \tag{29}$$

With respect to integration in y, the quantity $(dT_b/dx)/(T_b - T_w)$ is a constant. Thus one can write

$$\frac{dT_b/dx}{T_b - T_w} = -\frac{\beta^2}{r_w\,\mathrm{Re\,Pr}} \tag{30}$$

where the factor Re Pr is introduced for consistency with prior tube-flow analyses [12].

In light of the foregoing, the energy equation can now be recast in the form

$$\frac{d}{dy^+}\left[(r_w^+ - y^+)\gamma\frac{dg}{dy^+}\right] + (r_w^+ - y^+)v^+\frac{dg}{dy^+} + (r_w^+ - y^+)u^+g\frac{\beta^2}{r_w^+\,\mathrm{Re\,Pr}} = 0 \tag{31}$$

with the boundary conditions

$$g = 0 \text{ at } y^+ = 0, \qquad dg/dy^+ = 0 \text{ at } y^+ = r_w^+ \tag{32}$$

the last condition being an expression of symmetry. The distributions of u^+ and v^+ are known functions of y^+ from the already-discussed solutions of the velocity problem, while Re, $v_w/\bar{u}$, and Pr are prescribable parameters.

It is readily seen that equations (31) and (32) constitute a homogeneous mathematical system; therefore, β^2 plays the role of an eigenvalue. It is known that an infinite but discrete set of eigenvalues and associated eigenfunctions can be found to satisfy the foregoing mathematical system. However, it may be shown that the thermally fully developed temperature profile corresponds to the first eigenfunction. Thus it is sufficient for the purposes of the present investigation to obtain solutions to equation (31) corresponding to the first eigenvalue, β_1.

In determining values of β_1 for specified values of the parameters, the following numerical scheme was employed: First, it was recognized that the value of β_1 is unaffected by a change in the level of the eigenfunction g; that is, g multiplied by any constant is also a solution to equation (31) for a given β_1. Thus the wall derivative $(dg/dy^+)_w$ can be assigned any arbitrary value. With g and dg/dy^+ prescribed at $y^+ = 0$, a forward integration of equation (31) can be performed with $y^+ = 0$ as starting point. A trial value of β_1 is selected and the integration is carried out; note is then taken of the resulting value of (dg/dy^+) at $y^+ = r_w^+$. If this derivative is not zero (to within a specified tolerance), then a new trial value for β_1 is selected, and so on and so forth.

Once the first eigenvalue has been found, the corresponding eigenfunction g is scaled (i.e., multiplied by a constant) so that equation (28) is satisfied. In all subsequent developments, it will be assumed that we are dealing with properly scaled eigenfunctions, g.

After the eigenvalues β_1 and eigenfunctions g have been found, the heat transfer coefficient and Nusselt number can be evaluated. In the usual way, one defines

$$h = \frac{q_w}{T_w - T_b}, \qquad \mathrm{Nu} = \frac{h(2r_w)}{k} \tag{33}$$

so that, in terms of the variables of the analysis

$$\mathrm{Nu} = 2r_w^+(dg/dy^+)_w \tag{34}$$

By formally integrating equation (31) across the section from $y^+ = 0$ to $y^+ = r_w^+$ and making use of other pertinent relationships, the Nusselt number expression can be reduced to the form

$$\mathrm{Nu} = \frac{\beta_1^2}{2} + \mathrm{Re\,Pr}\left(\frac{v_w}{\bar{u}}\right) \tag{35}$$

Thus the Nusselt number is determined as soon as the eigenvalues β_1 are known.

The modifications of the just-concluded analysis that are relevant to the mass transfer problem will now be outlined. Let W_1 and W_2 represent the local mass fractions of the two components of a binary gas mixture. At every point in the cross section, $W_1 + W_2 = 1$. Mass conservation for component 1 yields the following diffusion equation

$$\rho\left(u\frac{\partial W_1}{\partial x} + v\frac{\partial W_1}{\partial r}\right) = -\frac{1}{r}\frac{\partial}{\partial r}(rj_1) \tag{36}$$

where the diffusive mass flux of component 1, j_1, is given by

$$j_1 = -\rho(D + D_t)\frac{dW_1}{dy} \tag{37}$$

Equations (36) and (37) are the counterparts of equations (24) and (25) of the heat transfer problem.

The solution of the diffusion equation follows along lines identical to those for the energy equation. If one defines a mass transfer coefficient and a corresponding Nusselt number as

$$h = \frac{j_{1w}}{W_{1w} - W_{1b}}, \qquad \mathrm{Nu} = \frac{h(2r_w)}{\rho D} \tag{38}$$

then the expression for Nu is

$$\mathrm{Nu} = \frac{\beta_1^2}{2} + \mathrm{Re\,Sc}\left(\frac{v_w}{\bar{u}}\right) \tag{39}$$

in which Sc is the Schmidt number.

The Nusselt numbers for heat and mass transfer, equations (35) and (39), respectively, are identical in form. In this connection, the mass transfer coefficient h, equation (38), must be defined in terms of the diffusive mass flux j_{1w} of component 1, rather than the total mass flux[3] of component 1. In some situations, the diffusive mass flux and the total mass flux are nearly equal, while in other situations the two mass fluxes are quite different. This important distinction does not seem to be widely recognized.

Results and Discussion

In the forthcoming presentation, first consideration will be given to quantities of direct engineering interest such as the friction factor, pressure gradient, and heat and mass transfer coefficients. Velocity and temperature profiles will be presented later.

Friction, Pressure Drop, Heat and Mass Transfer Coefficients. The variation of the friction factor with the relative suction velocity, $v_w/\bar{u}$, is shown in Fig. 1 for parametric values of the Reynolds number. The ordinate variable is the ratio c_{f0}/c_f, where c_{f0} is the friction factor for the case of zero suction, while c_f includes the effects of suction. The departure of the curves from unity is a direct measure of the effect of suction. The range of the abscissa parameter $v_w/\bar{u}$ includes operating conditions encountered in forced-convection condensation processes. For instance, in recent experiments involving condensing Freon-11, with and without air present as a noncondensable, the $v_w/\bar{u}$ values fell approximately in the range 0.002–0.005 [14].

The figure shows that the higher the suction velocity, the greater the friction factor; i.e., $c_{f0}/c_f < 1$. In other words, the fluid exerts a greater shear force on the bounding surface in the presence of suction than when suction is absent. If, as in the condensation problem, the flow is bounded by an annular fluid layer, then the drag force exerted on the layer is greater than that exerted by a flow without surface mass transfer. As a consequence, the resulting velocities in the annular fluid layer are

[3] The total mass flux includes both diffusive and convective contributions [13].

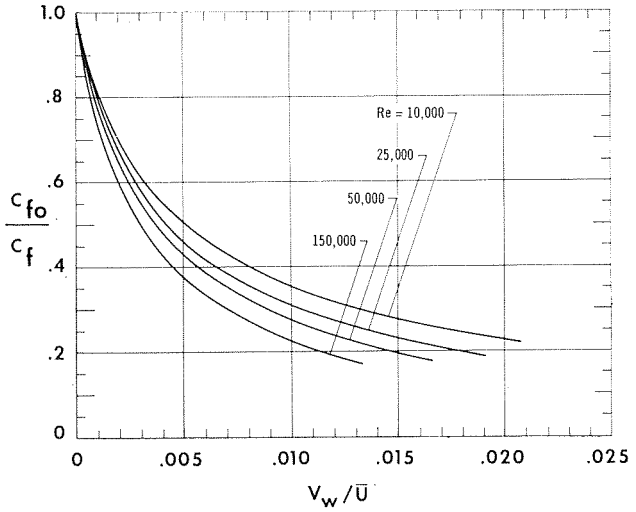

Fig. 1 Variation of local friction factor with relative suction velocity

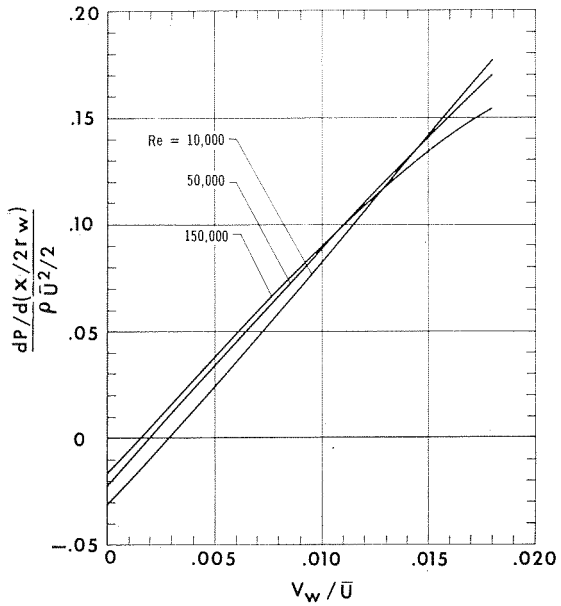

Fig. 2 Dependence of dimensionless axial pressure gradient on relative suction velocity

greater than those calculated by employing shear stress information for tube flows with impermeable boundaries.

A casual look at Fig. 1 suggests that a high Reynolds number flow is more sensitive to suction than is a low Reynolds number flow. In considering such a conclusion, cognizance must be taken of the fact that the abscissa variable contains $\bar{u}$ as well as v_w. For fixed r_w and ν, two flows with equal $v_w/\bar{u}$ and different Re will have different v_w. This follows from the fact that $v_w(2r_w)/\nu = (v_w/\bar{u})$ Re. In particular, the v_w for the higher Reynolds number flow will be higher. Thus the ordering of the curves in Fig. 1 reflects the fact that higher suction velocities are associated more with the high Reynolds number curves than with the low Reynolds number curves.

For fully developed tube flows without surface mass transfer, the friction factor and the axial pressure gradient, normalized by the dynamic pressure, are essentially equivalent quantities. On the other hand, in the presence of surface mass transfer, the pressure gradient is affected by changes in axial momentum flux as well as by the wall shear stress. In particular, when there is suction at the wall, the momentum change of the flow tends to cause an increase in pressure in the flow direction, while the wall shear tends to decrease the pressure.

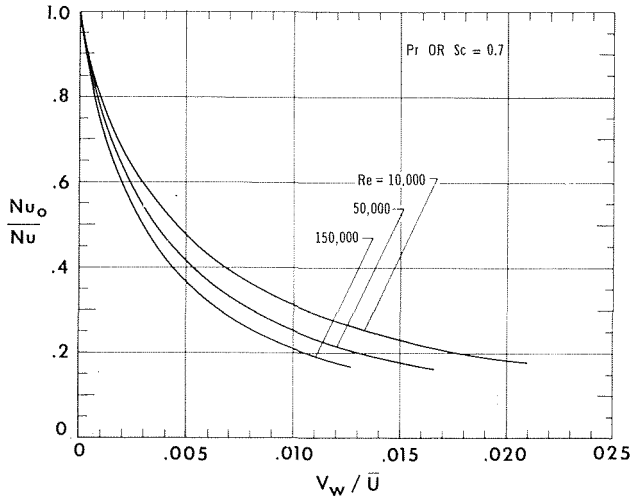

Fig. 3 Variation of local Nusselt number with relative suction velocity

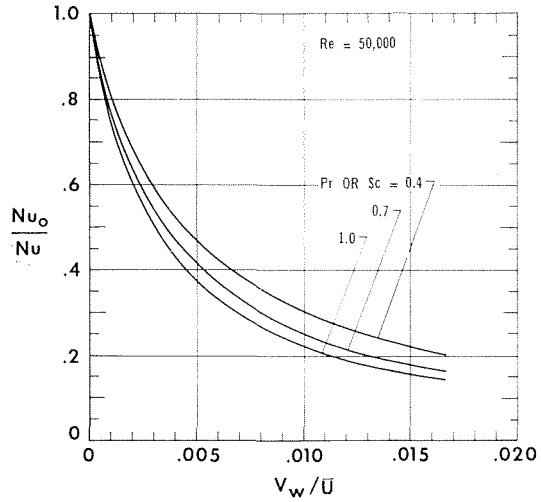

Fig. 4 Effect of Prandtl or Schmidt number on local Nusselt number for a fixed axial flow Reynolds number

Results for the axial pressure gradient are presented in Fig. 2 as a function of the relative suction velocity $v_w/\bar{u}$. The Reynolds number is the curve parameter. In the absence of suction, i.e., $v_w = 0$, the pressure gradient is negative. With increasing v_w, dp/dx changes sign and becomes positive. In accordance with the foregoing discussion, this behavior is indicative of the fact that the momentum change due to suction overrides the skin friction at the wall. It is known that flows characterized by positive pressure gradients are prone to separation. However, no amount of suction in fully developed turbulent pipe flow can reduce the velocity gradient at the wall to zero. Therefore, as long as the flow remains turbulent, separation cannot occur.

The effect of suction on the heat and mass transfer coefficients is illustrated in Fig. 3. On the ordinate, Nu is the Nusselt number in the presence of suction and Nu_0 is the Nusselt number for no suction. The results correspond to a Prandtl or Schmidt number of 0.7. The qualitative trends in evidence in Fig. 3 are the same as those already discussed in connection with the friction factors in Fig. 1. The results displayed in Fig. 3 emphasize the fact that even small amounts of suction cause a major increase in the Nusselt number. For instance, the Nusselt number for $v_w/\bar{u} = 0.004$ is approximately twice as large as that for $v_w/\bar{u} = 0$. Such a deviation is undoubtedly worthy of consideration in calculations of condensation involving noncondensable gases.

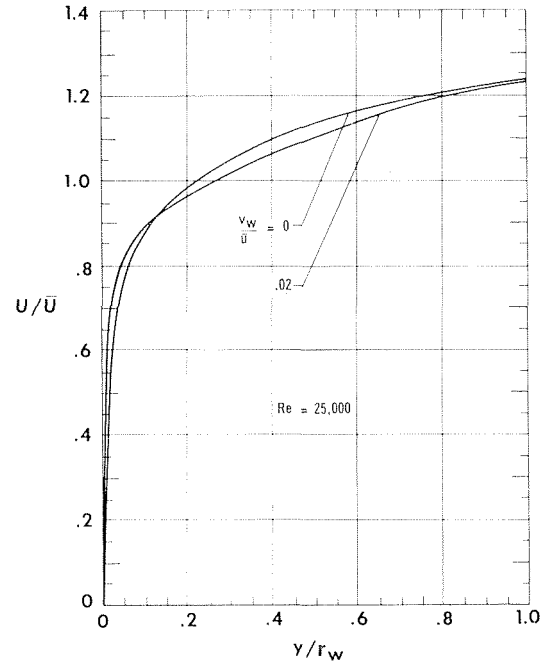

Fig. 5 Representative velocity profiles for two suction conditions

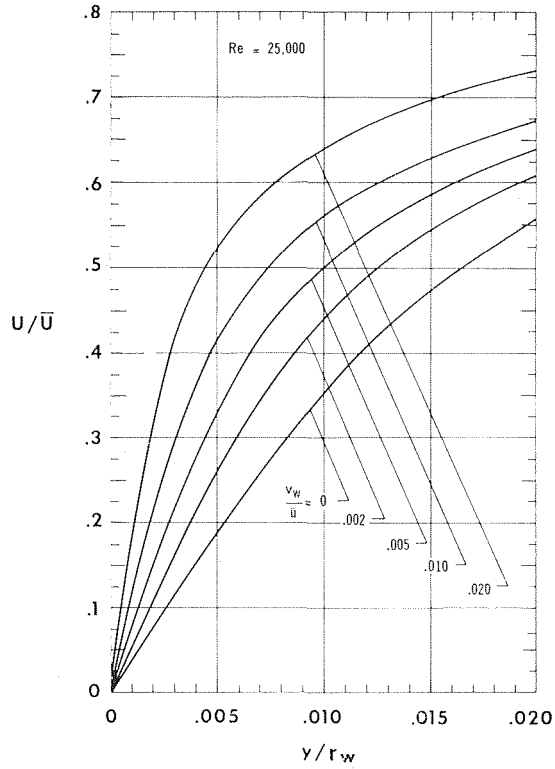

Fig. 6 Effect of suction on velocity profiles near tube wall

The influence of Prandtl or Schmidt number on the Nusselt number results is dealt with in Fig. 4. Curves are shown for Pr or Sc equal to 1.0, 0.7, and 0.4. Inspection of the figure shows that the higher the Prandtl or Schmidt number, the more sensitive is the Nusselt number to the effects of suction.

Velocity, Temperature, and Mass Fraction Profiles. Representative velocity profiles, plotted in terms of the variables $u/\bar{u}$ and y/r_w, are presented in Fig. 5. Curves are shown for the extreme values of $v_w/\bar{u} = 0$ and 0.02. From an overall viewpoint, the two pro-

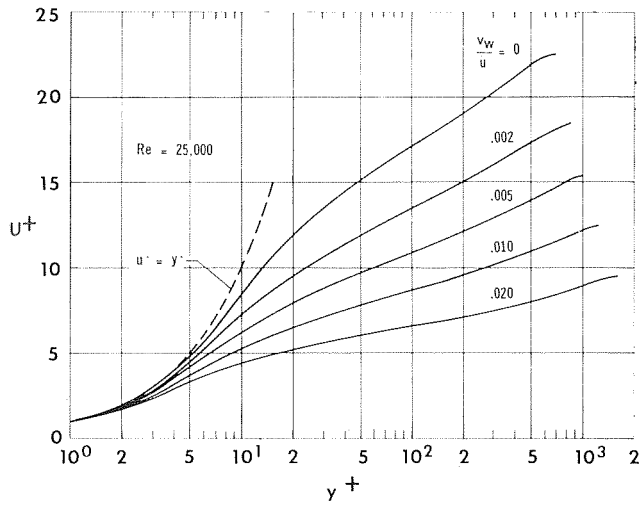

Fig. 7 Velocity profiles expressed in dimensionless friction coordinates

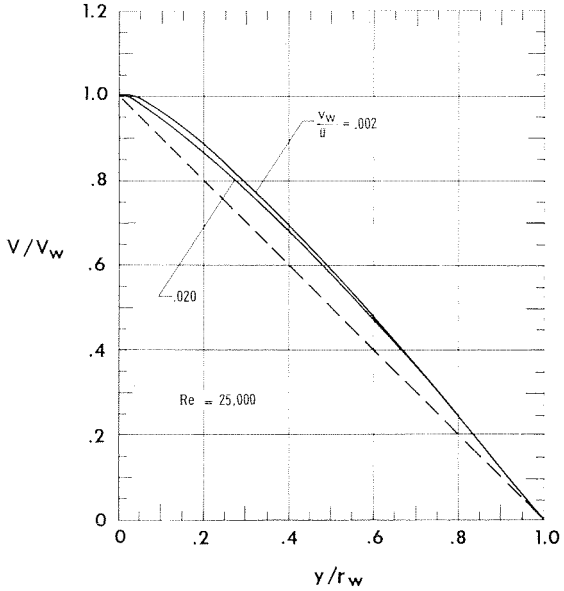

Fig. 8 Typical transverse velocity distributions

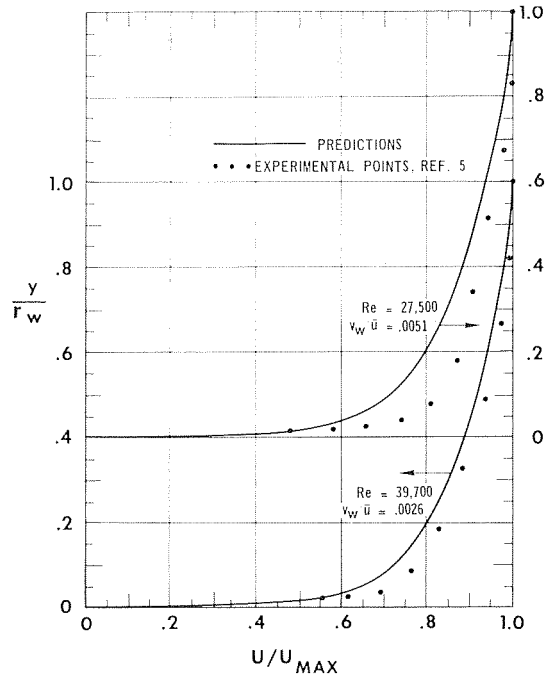

Fig. 9 Comparison of predicted and measured velocity profiles for two suction conditions

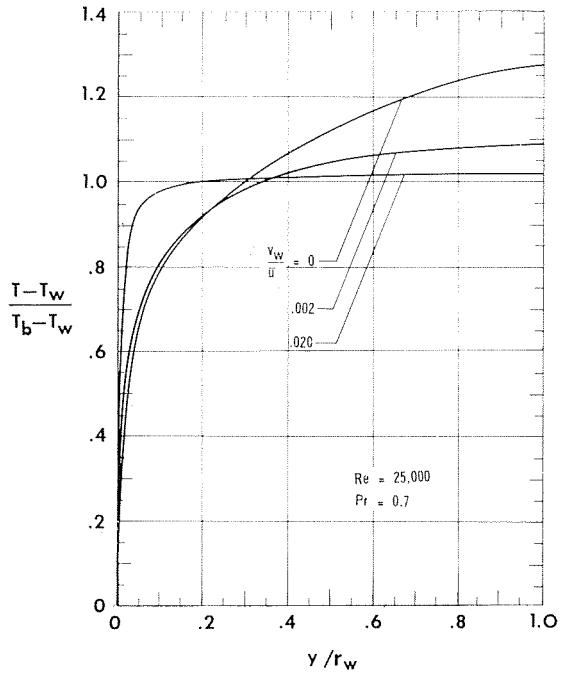

Fig. 10 Representative temperature profiles

files appear to differ very little from one another. However, a closer inspection shows that the profile corresponding to suction is very much steeper near the wall, as would be expected in view of the higher wall shear associated with a suction-modified flow. Furthermore, near the wall, the velocities are higher in the presence of suction. A more detailed display of the velocity profiles in the immediate neighborhood of the wall is provided by Fig. 6.

The occurrence of higher velocities near the wall helps explain the previous observation that higher Prandtl number (or Schmidt number) fluids are more affected by suction than are fluids with lower Prandtl numbers, Fig. 4. The higher the Prandtl number, the thinner is the thermal wall layer. Correspondingly, the region immediately adjacent to the wall plays an ever more dominant role in the thermal transport process as the Prandtl number increases. Thus higher velocities in the wall region are particularly effective in increasing the transfer coefficients.

Turbulent velocity profiles are often presented in terms of the dimensionless u^+, y^+ variables, and such a plot is given in Fig. 7. There is substantial spread among the curves for the various parametric values of $v_w/\bar{u}$. This is to be contrasted with the near congruence of the curves in Fig. 5. Evidently, in the presence of surface suction, the u^+, y^+ variables do not lead to a universal velocity representation as in the case of turbulent pipe flow without surface mass transfer.

Transverse velocities are induced by the surface suction. Representative profiles of transverse velocity are plotted in Fig. 8. A curve for $v_w/\bar{u} = 0$ does not appear in the figure because v is equal to zero in the absence of surface mass transfer. The transverse velocity profiles in Fig. 8 show only a weak dependence on $v_w/\bar{u}$. There is a moderate departure of the curves from a linear relationship between v and y (dashed line), such a linear relationship being a natural first guess concerning the radial variation of the transverse velocity.

It is of interest to compare the velocity profiles of the present analysis with the measurements of Weissberg and Berman [5]. Data points, taken from Figs. 5 and 6 of the just-cited paper, are compared with corresponding analytical curves in Fig. 9. The agreement may be viewed as satisfactory when it is realized that these measured and predicted results represent the first attempts at studying this problem in detail. However, more experimental work on the suction problem is evidently needed to help establish the analysis or to suggest modifications.

Representative temperature profiles are displayed in Fig. 10 for several values of $v_w/\bar{u}$. It is evident from the figure that the temperature distribution is markedly affected by suction, becoming flatter in the core and steeper near the wall as the suction velocity increases. By comparing Figs. 5 and 10, it is seen that any semblance of similarity between the velocity and temperature fields vanishes with strong suction. This trend is not unexpected, since the presence of suction introduces a momentum change into the velocity problem, such momentum change not having a counterpart in the heat transfer problem.

Concluding Remarks

The effect of surface suction on the frictional, heat-transfer, and mass-transfer characteristics of turbulent tube flows has been investigated analytically. In so doing, it has been necessary to postulate a model for the turbulent transport processes occurring within the flow. It is believed that the mixing-length model herein adopted is strongly supported by the presently available evidence. This evidence is understandably far from conclusive. Nevertheless, it is significant that the mixing-length model employed, when coupled with the local flow similarity hypothesis, yields predicted velocity profiles which are consistent with the only known experimental measurements made to date. Indeed, the level of agreement is well within the range shared by the results of early analytical and experimental studies of external boundary-layer flows with wall mass transfer.

Investigating a range of relative suction velocities and axial flow Reynolds numbers, it has been shown that even small amounts of suction can have an appreciable effect on the friction factor and Nusselt number results. Therefore, the present findings do not support the current practice of using impermeable-boundary transfer coefficients in condensation calculations.

References

1 McAdams, W. H., *Heat Transmission*, 3rd ed., McGraw-Hill, New York, 1954, Chapter 13.

2 Dukler, A. E., "Dynamics of Vertical Falling Film Systems," *Chemical Engineering Progress*, Vol. 55, No. 10, 1959, p. 62.

3 Soliman, M., Schuster, J. R., and Berenson, P. J., "A General Heat Transfer Correlation for Annular Flow Condensation," JOURNAL OF HEAT TRANSFER, TRANS. ASME, Vol. 90, Series C, 1968, p. 267.

4 Olson, R. M., and Eckert, E. R. G., "Experimental Studies of Turbulent Flow in a Porous Circular Tube With Uniform Fluid Injection Through the Tube Wall," *Journal of Applied Mechanics*, Vol. 33, TRANS. ASME, Vol. 88, Series E, 1966, p. 7.

5 Weissberg, H. L., and Berman, A. S., "Velocity and Pressure Distribution in Turbulent Pipe Flow With Uniform Suction," *Proceedings, Heat Transfer and Fluid Mechanics Institute*, 1955.

6 Townsend, A. A., "Equilibrium Layers and Wall Turbulence," *Journal of Fluid Mechanics*, Vol. 11, 1961, p. 97.

7 Bradshaw, P., "Mixing-Length Velocity Profile in Boundary Layers With Transpiration," *AIAA Journal*, Vol. 5, 1967, p. 1674.

8 Maise, G., and McDonald, H., "Mixing Length and Kinematic Eddy Viscosity in a Compressible Turbulent Boundary Layer," *AIAA Journal*, Vol. 6, 1968, p. 73.

9 Spalding, D. B., "Theories of the Turbulent Boundary Layer," *Applied Mechanics Reviews*, Vol. 20, 1967, p. 735.

10 Schlichting, H., *Boundary-Layer Theory*, McGraw-Hill, New York, 1968.

11 van Driest, E. R., "On Turbulent Flow Near a Wall," *Journal of the Aeronautical Sciences*, Vol. 23, 1956, p. 1007.

12 Kays, W. M., *Convective Heat and Mass Transfer*, McGraw-Hill, New York, 1966.

13 Hartnett, J. P., and Eckert, E. R. G., "Mass Transfer Cooling in a Laminar Boundary Layer With Constant Fluid Properties," TRANS. ASME, Vol. 79, 1957, p. 247.

14 Rudoy, W., "Local Heat Transfer Measurements for R-11 Condensing With and Without the Presence of a Noncondensing Gas," PhD thesis, Department of Mechanical Engineering, University of Minnesota, 1967.

It is of interest to compare the velocity profiles of the present analysis with the measurements of Weissberg and Berman [5]. Data points, taken from Figs. 5 and 6 of the just-cited paper, are compared with corresponding analytical curves in Fig. 9. The agreement may be viewed as satisfactory when it is realized that these measured and predicted results represent the first attempts at studying this problem in detail. However, more experimental work on the suction problem is evidently needed to help establish the analysis or to suggest modifications.

Representative temperature profiles are displayed in Fig. 10 for several values of $v_w/\bar{u}$. It is evident from the figure that the temperature distribution is markedly affected by suction, becoming flatter in the core and steeper near the wall as the suction velocity increases. By comparing Figs. 5 and 10, it is seen that any semblance of similarity between the velocity and temperature fields vanishes with strong suction. This trend is not unexpected, since the presence of suction introduces a momentum change into the velocity problem, such momentum change not having a counterpart in the heat transfer problem.

Concluding Remarks

The effect of surface suction on the frictional, heat-transfer, and mass-transfer characteristics of turbulent tube flows has been investigated analytically. In so doing, it has been necessary to postulate a model for the turbulent transport processes occurring within the flow. It is believed that the mixing-length model herein adopted is strongly supported by the presently available evidence. This evidence is understandably far from conclusive. Nevertheless, it is significant that the mixing-length model employed, when coupled with the local flow similarity hypothesis, yields predicted velocity profiles which are consistent with the only known experimental measurements made to date. Indeed, the level of agreement is well within the range shared by the results of early analytical and experimental studies of external boundary-layer flows with wall mass transfer.

Investigating a range of relative suction velocities and axial flow Reynolds numbers, it has been shown that even small amounts of suction can have an appreciable effect on the friction factor and Nusselt number results. Therefore, the present findings do not support the current practice of using impermeable-boundary transfer coefficients in condensation calculations.

References

1 McAdams, W. H., *Heat Transmission*, 3rd ed., McGraw-Hill, New York, 1954, Chapter 13.

2 Dukler, A. E., "Dynamics of Vertical Falling Film Systems," *Chemical Engineering Progress*, Vol. 55, No. 10, 1959, p. 62.

3 Soliman, M., Schuster, J. R., and Berenson, P. J., "A General Heat Transfer Correlation for Annular Flow Condensation," JOURNAL OF HEAT TRANSFER, TRANS. ASME, Vol. 90, Series C, 1968, p. 267.

4 Olson, R. M., and Eckert, E. R. G., "Experimental Studies of Turbulent Flow in a Porous Circular Tube With Uniform Fluid Injection Through the Tube Wall," *Journal of Applied Mechanics*, Vol. 33, TRANS. ASME, Vol. 88, Series E, 1966, p. 7.

5 Weissberg, H. L., and Berman, A. S., "Velocity and Pressure Distribution in Turbulent Pipe Flow With Uniform Suction," *Proceedings, Heat Transfer and Fluid Mechanics Institute*, 1955.

6 Townsend, A. A., "Equilibrium Layers and Wall Turbulence," *Journal of Fluid Mechanics*, Vol. 11, 1961, p. 97.

7 Bradshaw, P., "Mixing-Length Velocity Profile in Boundary Layers With Transpiration," *AIAA Journal*, Vol. 5, 1967, p. 1674.

8 Maise, G., and McDonald, H., "Mixing Length and Kinematic Eddy Viscosity in a Compressible Turbulent Boundary Layer," *AIAA Journal*, Vol. 6, 1968, p. 73.

9 Spalding, D. B., "Theories of the Turbulent Boundary Layer," *Applied Mechanics Reviews*, Vol. 20, 1967, p. 735.

10 Schlichting, H., *Boundary-Layer Theory*, McGraw-Hill, New York, 1968.

11 van Driest, E. R., "On Turbulent Flow Near a Wall," *Journal of the Aeronautical Sciences*, Vol. 23, 1956, p. 1007.

12 Kays, W. M., *Convective Heat and Mass Transfer*, McGraw-Hill, New York, 1966.

13 Hartnett, J. P., and Eckert, E. R. G., "Mass Transfer Cooling in a Laminar Boundary Layer With Constant Fluid Properties," TRANS. ASME, Vol. 79, 1957, p. 247.

14 Rudoy, W., "Local Heat Transfer Measurements for R-11 Condensing With and Without the Presence of a Noncondensing Gas," PhD thesis, Department of Mechanical Engineering, University of Minnesota, 1967.

DISCUSSION

Tuncer Cebeci[4]

The authors are to be commended on their analytical study concerning the problem of turbulent flow with mass transfer in tubes. The discusser would like to present some thoughts on which the authors may wish to comment.

First, I would like to comment on the way the authors have included the damping factor (DF) into the mixing-length expression given by equation (13). If we argue (as Van Driest did) that the presence of the wall changes the mixing length by

$$1 - \exp(-y/A)$$

where A is a constant defined as $26\nu(\tau_w/\rho_w)^{-1/2}$, then one should write equation (13) as

$$\frac{l^+}{r_w^+} = \left[0.4\,\frac{y^+}{r_w^+} - 0.44\left(\frac{y^+}{r_w^+}\right)^2 + 0.24\left(\frac{y^+}{r_w^+}\right)^3 - 0.06\left(\frac{y^+}{r_w^+}\right)^4\right] DF$$

rather than the way it is written; i.e., equation (17). Although for sucked boundary layers, the difference between the foregoing equation and the one given by equation (17) is negligible, the difference may be quite important for blown boundary layers where the sublayer thickness is not so small.

Second, I would like to comment on the generalization of Van Driest's model for flows with mass transfer. The expression that the authors obtain by solving the Stokes problem with mass transfer does not consider the pressure gradient effect. As it stands, the DF, as given by equation (16), in the absence of mass transfer, cannot be used for flows with pressure gradient since for such flows y^+ may approach zero (flow separation).

G. B. Wallis[5]

This paper contains a nice theoretical analysis of a significant practical problem. However, it would be more useful to engineers if some of the more important results could be expressed in a more compact form and could be related to simpler theoretical models. This is particularly true in the present case because the solution is not exact, but is based on some idealized model for turbulence, and it is not clear just what has been gained by the choice of a rather sophisticated calculation procedure which would be very time-consuming if it were used to solve all such problems in practice.

Now, there already exists a very simple model for interfacial shear in condensing flows, or flows with suction, based on the Reynolds flux concept.[6] According to this theory, the ratio C_{f0}/C_f, shown in the authors' Fig. 1, should depend on the ratio v_w/u_0, where u_0 is a characteristic transverse velocity characterizing the turbulence and is given by

$$u_0 = C_{f0}\bar{u} \tag{40}$$

[4] Senior Engineer/Scientist, Douglas Aircraft Company, Long Beach, Calif. Mem. ASME.

[5] Associate Professor of Engineering, Thayer School of Engineering, Dartmouth College, Hanover, N. H. Assoc. Mem. ASME.

[6] Silver, R. S., and Wallis, G. B., "A Simple Theory for Longitudinal Pressure Drop in the Presence of Lateral Condensation," *Proceedings, Institution of Mechanical Engineers*, Vol. 180, Part 1, 1965–1966, pp. 36–40.

Over the present range of Reynolds numbers the Blasius equation may be used to estimate C_{f0}; thus

$$C_{f0} = 0.079\ \mathrm{Re}^{-1/4} \tag{41}$$

A simple check as to the validity of the Reynolds flux theory is then to plot the authors' values of $v_w/\bar{u}$ versus Reynolds number at constant values of C_{f0}/C_f. The result is found to be a series of lines with a negative slope almost exactly equal to $1/4$. This indicates that plotting C_{f0}/C_f versus v_w/u_0 will indeed give one unique curve for the whole range of Reynolds numbers chosen by the authors.

Moreover, the simple theory of Silver and Wallis indicates that the equation of this unique curve should be

$$\frac{C_{f0}}{C_f} = \frac{1}{1 + \dfrac{v_w}{u_0}} \tag{42}$$

or, using equations (40) and (41) if a more direct equation is needed for practical computation,

$$\frac{C_{f0}}{C_f} = \frac{1}{1 + 12.7\ \mathrm{Re}^{1/4}\dfrac{v_w}{u}} \tag{43}$$

A crossplot of the authors' Fig. 1 reveals that all the results are very close to a slightly modified version of equations (42) and (43)

$$\frac{C_{f0}}{C_f} = \frac{1}{1 + 1.4\dfrac{v_w}{u_0}} = \frac{1}{1 + 17.5\ \mathrm{Re}^{1/4}\dfrac{v_w}{\bar{u}}} \tag{44}$$

In the absence of good experimental data we cannot determine which theory is the most accurate. However, that is not the point. The fact is that in most practical design situations utility and brevity are more important properties of a theory than elegance. It should not be left entirely up to the reader to manipulate the results into the most useful form. (For most purposes this means an algebraic equation in terms of simple functions, not a calculation procedure or a set of graphs.)

Even in academia, we are often left to explain an embarrassing gap between theories which are too simple to be accurate and those which are too complex to be useful.

Of course these criticisms do not apply to those parts of the paper which are concerned with velocity and temperature profiles. Clearly these cannot be predicted from one-dimensional or lumped-parameter theories.

Authors' Closure

The authors appreciate the interest shown in their work by Dr. Cebeci and Professor Wallis. The discussers have raised some interesting points, to which we would like to respond in order.

Dr. Cebeci is quite correct in asserting that some care must be exercised in applying the damping factor to the mixing length. It is noted, however, that for flow in an impermeable tube, as well as for the case of surface suction, the damping factor is essentially unity before the higher order terms in equation (17) become operative. Thus it is immaterial in this case whether one applies the damping factor to just the first linear term or to the entire expression. However, for the case of surface injection, one should follow the recommendation of Dr. Cebeci and apply the DF to the entire mixing length expression.

The second point raised by Dr. Cebeci is also well taken. For any flows in which the wall shear stress gets very small or goes to zero, it is a dangerous procedure to nondimensionalize variables with respect to $\sqrt{\tau_w/\rho}$. In this case, u^+ gets very large and y^+ gets very small; clearly this is a situation to be avoided in any calculation procedure.

It is apparent that Professor Wallis has taken considerable time to study the authors' results in light of his earlier simple model. However, it is not clear how Professor Wallis obtained his results (40) and (42). Having read his earlier paper, it appears to the authors that Professor Wallis still had to "manipulate the results" into a more useful form. Aside from this, the authors have compared more precise tabulations of their numerical results with the discusser's equation (44). Very satisfactory agreement is obtained over the entire range Re = 10,000 to 150,000.

By way of closing, the authors would like to caution Professor Wallis concerning his "check as to the validity of the Reynolds flux theory." It appears that all that has been demonstrated is some gross measure of consistency between the present calculations and those performed earlier by Wallis. Even then, an empirical adjustment had to be made to his result before approximate agreement could be achieved. The authors feel that more substantial evidence than this is required to validate the simple lumped-parameter theory proposed by Wallis.

R. G. BRESSLER
Associate Professor,
Department of Mechanical
and Aerospace Engineering.
Mem. ASME

P. W. WYATT[1]
Research Assistant,
Department of Nuclear Engineering.

The University of Tennessee,
Knoxville, Tenn.

Surface Wetting Through Capillary Grooves

The effects of capillary grooves on surface wetting and evaporation have been analyzed. An attempt has been made to obtain expressions which approximately describe the increase in heat transfer in order to select for given properties and temperature differences a groove of optimum design. For this purpose, it is assumed that the heat transfer mechanism is determined by thermal resistance of the liquid layers inside the grooves. From a numerical evaluation of linearized equations, heat transfer rates have been computed for grooves with triangular, semicircular, and square cross sections.

Introduction

The great importance which physical and chemical surface conditions have in boiling and evaporation has long been recognized [1],[2] and the effects of surface material, treatment, finish, past history, and liquid-surface combinations have been investigated in recent years. Phenomenological descriptions and experimental results, particularly with regard to nucleate boiling, can be found in various papers and texts [2, 3]. Of particular interest for most evaporation processes is the wettability of the heating surface, because nonwetting may lead, among other things, to reduced heat transfer and overheating of the surface. Moreover, the condition of surface wetting seems to be a most important criterion for high heat fluxes in all evaporation processes, and it represents a crucial property whenever the liquid phase forms a relatively thin layer on a heat-exchanger surface, e.g., in thin-film evaporators and spray or dry-type evaporators. In such applications, different methods are used to insure a uniform spreading of the liquid phase over most of the heating surface and to improve the surface wettability, if possible. The latter is mostly done by chemical treatment of the surface, by providing special finishes and roughnesses, or by adding surface-active substances to the liquid. The distribution of the liquid over the evaporator surface is often improved by utilizing advantageously the vapor shear at the liquid-vapor interface, e.g., in annular two-phase flow inside horizontal or vertical tubes. In addition, a variety of mechanical devices such as spiral fins, turbulators, moving scrapers, and wipers are used in different process heat exchangers, mostly for the same objective. Capillary wicking and surface deposits have been added more recently to this list.

Photographic studies of the evaporation of thin liquid films revealed that mechanical scrapers and wipers were unable to prevent completely a formation of dry spots, when any form of evaporation took place [4]. Irregularities of the heat fluxes which were observed at characteristic temperatures could be directly related to the partially dried-out areas. A modification of Nusselt's classical analysis of film condensation to interfacial evaporation, due to heat conduction through a falling liquid film, led to calculated heat transfer rates which explained qualitatively the relationship between surface wetting and overall performance. In the regime of nucleate boiling, the experimentally measured heat fluxes were up to 30 percent larger than those predicted from the laminar film model, but the differences decreased remarkably when the film thickness grew smaller, regardless of whether or not nucleation was observed. The results suggested that the heat transfer mechanism was governed by thermal conductance across the film. It was therefore postulated that the heat transfer rates in thin-film evaporators could be improved if the liquid phase might be spread more uniformly and thinly over the total heating surface. For this purpose, the author proposed to utilize capillary grooves as a means of distributing a liquid coolant in thin-film evaporators and later in dry-type evaporators, too [5].

The topic of surface wetting as a contact-angle and capillary-action phenomenon is discussed in several texts within the general framework of the physical chemistry of surfaces [6, 7]. The wetting process through capillary grooves is essentially a capillary-rise phenomenon and its dynamic behavior is of interest here. The governing differential equations for fluid motion induced by capillary forces under isothermal conditions have been derived for different conditions. Analytical solutions are available for several cases, e.g., for laminar flow of a wetting liquid inside capillary tubes of round or rectangular cross sections [8], between parallel plates [9], and within porous materials [10]. The fluid motion inside capillary grooves has been studied experimentally by Parker and Smoluchowski [11] who succeeded in enhancing the spreading of a liquid metal over a solid surface through etched grooves.

The present study[3] sought to investigate the effects which

[1] Presently, Engineer, Bettis Laboratories, Westinghouse Electric Corporation, Pittsburgh, Pa.

[2] Numbers in brackets designate References at end of paper.

Contributed by the Heat Transfer Division and presented at the ASME-AIChE Heat Transfer Conference, Minneapolis, Minn., August 3–6, 1969. Manuscript received by the Heat Transfer Division, April 3, 1969; revised manuscript received, July 16, 1969. Paper No. 69-HT-19.

[3] The research reported herein is part of an investigation supported by the Office of Naval Research under Contract NONR-4289 (02).

capillary grooves of different shape and size might have with respect to the wetting of a solid surface for the case of interfacial evaporation without bubble formation. In the following, it is assumed that a liquid coolant is lifted and distributed over a vertical heating surface by a system of capillary grooves. Through the thin liquid layers which are formed inside the grooves, heat is conducted from the wall to the liquid and evaporation takes place at the liquid-vapor interface. It is the purpose of this paper to examine the mentioned capillary effects in connection with interfacial evaporation.

Static Capillary Rise

When two immiscible fluids are in contact with each other, under conditions of mechanical equilibrium, their common interface can be determined from the fundamental equation of Young and LaPlace

$$\Delta p = \sigma(1/r_1 + 1/r_2) \tag{1}$$

where r_1 and r_2 are the principal radii of curvature; Δp represents the pressure difference across the interface, and σ is the interfacial, or surface, tension. The oldest method of measuring surface tensions is the observation of liquid rise in a vertical capillary. Here, the pressure difference across the meniscus in the capillary, Δp, must be equal to the hydrostatic pressure of the column of liquid of height, h, which is lifted inside the tube. If the liquid and vapor densities are denoted by ϱ_l and ρ_v, respectively, it follows that $\Delta p = g(\varrho_l - \rho_v)h$. For an approximate treatment of the capillary rise, when $r \ll h$, equation (1) can be reduced to a simpler relation with one radius of curvature, and the pressure difference becomes

$$\Delta p = 2\sigma/r = g(\varrho_l - \rho_v)h \tag{2}$$

In the case of a perfectly wetting liquid, the radius of curvature of the surface of the meniscus, r, equals the radius of the capillary, R. If the liquid does not wet the capillary surface completely, an angle of contact between the liquid and the solid surface, α, will be observed and the radius of curvature becomes $r = R(\cos \alpha)$. Thus the height, h, to which the liquid rises in a capillary tube can be ascertained by the relation

$$h = 2\sigma(\cos \alpha)/g(\varrho_l - \rho_v)R \tag{3}$$

The static contact angle, α, has been widely used as a criterion for surface wetting, which is usually considered as being limited to angles of 90 deg or less. Strictly speaking, however, a liquid that does not wet a solid would be characterized by an angle of 180 deg. The contact angle represents a mean value which averages local and microscopic effects of the combined properties of the liquid and the solid wall, which are affected by absorption of impurities and possible molecular reorientation of the solid surface in presence of the fluid. The apparent contact angle seems also to be influenced by the roughness of the surface. For the experimental part of this investigation, the required contact angles were measured; for the analytical study, a fixed contact angle was taken as a boundary condition.

Analytical Treatment

If a wetting liquid is in contact with a plane vertical wall, the liquid wets the solid surface due to capillary action up to a height, h_0, in mechanical equilibrium. The contour of the liquid interface as a function of y^*, the distance from the wall, is described by the differential equation

$$\frac{d^2z/dy^{*2}}{(1 + (dz/dy^*)^2)^{3/2}} = \frac{g(\varrho_l - \rho_v)z}{\sigma} \tag{4}$$

where z represents the local height or rise of the liquid interface. An analytical solution of equation (4) yields the expression [12]

$$y^* + (c^2 - z^2)^{1/2} - (c^2 - h_0^2)^{1/2} = (c/2)(\cosh^{-1}(c/z) - \cosh^{-1}(c/h_0)) \tag{5}$$

where

$$c = 2(\sigma/g(\varrho_l - \rho_v))^{1/2}$$

and the maximum height h_0 for the capillary rise at a plane wall is

$$h_0 = 2(\sigma/g(\varrho_l - \rho_v))^{1/2} \sin(\pi/4 - \alpha/2) \tag{6}$$

The liquid-vapor interface in a capillary groove with rectangular cross section under the action of gravity is shown schematically in Fig. 1. The contour of the liquid interface is represented by a surface $z(x, y)$ which is evaluated by solving the governing equation derived from a two-dimensional force balance. For this purpose, it is considered that, in mechanical equilibrium, the driving force which is acting on every fluid element $(dx\, dy\, z)$ is equal to the weight of the column of liquid $\rho g z(dxdy)$ which is lifted. Thus the driving force per unit area, due to surface tension, becomes

$$g(\varrho_l - \rho_v)z = \left\{ \frac{\partial^2 z}{\partial x^2}(1 + (\partial z/\partial x)^2)^{-2} + \frac{\partial^2 z}{\partial y^2}(1 + (\partial z/\partial y)^2)^{-2} \right\}$$

Nomenclature

A_S = free surface area
A_x = cross-sectional area
c = $2(\sigma/(\varrho_l - \rho_v)g)^{1/2}$
d = depth of groove
$\mathbf{d_0}$ = optimized groove depth, defined in equation (17)
g = magnitude of gravitational acceleration
h = height of meniscus above flat liquid surface
h_f, h_f' = fully wetted heights at static equilibrium or at steady-state evaporation
h_{fg} = latent heat of vaporization
h_0 = maximum rise of a liquid on a plane wall
k = thermal conductivity of liquid
Δp = pressure difference
Q = total heat transfer rate of groove
$\mathbf{Q_0}$ = maximum heat transfer rate of groove (with optimized depth)
r = radius of curvature
R = radius of tube
R_E = equivalent capillary radius defined in equation (10)
T_w, T_s = temperatures of solid-liquid and liquid-vapor boundaries
v = flow velocity in direction z
w = width of groove
x, y, y^* = coordinates
z, z' = heights of liquid-vapor interface inside a groove, at static equilibrium and at steady-state evaporation, respectively
α = angle of contact of liquid at solid surface
β = vertex angle of a triangular groove
δ = mean thickness of liquid layer in direction y
Λ = parameter defined in equation (14)
μ = dynamic liquid viscosity
ϱ_l, ρ_v = densities of liquid and vapor, respectively
σ = surface tension
ϕ = angle between x-axis and horizontal tangent to the groove surface
ψ = parameter defined in equation (19)
Ω = parameter defined in equation (15)
B, C, D, E = constants whose values are given when used in text

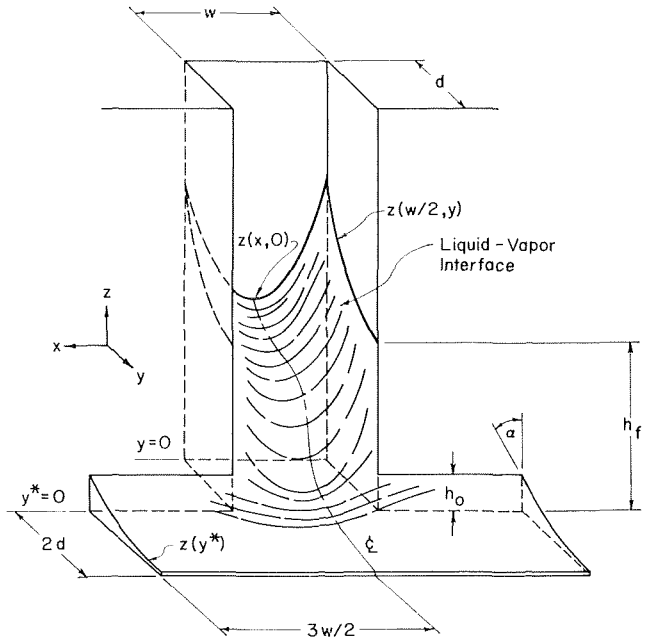

Fig. 1 Liquid-vapor interface in a capillary groove with square cross-sectional area

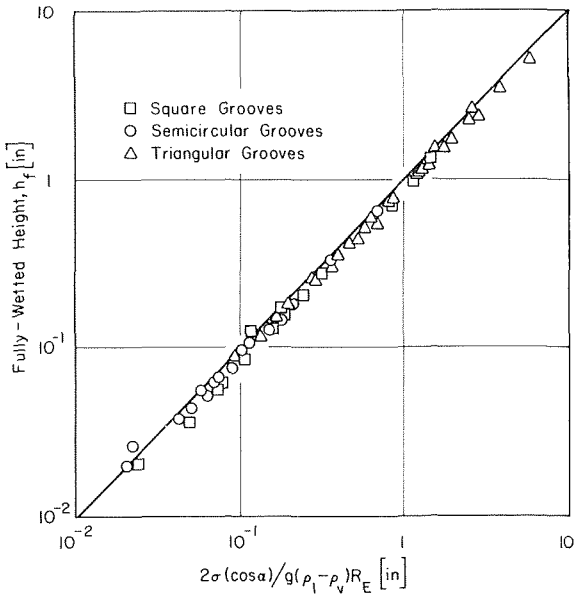

Fig. 2 Fully wetted static rise, h_f, calculated for capillary grooves

$$\times \sigma(1 + (\partial z/\partial x)^2 + (\partial z/\partial y)^2)^{1/2} \quad (7)$$

The differential equation (7) has been used to describe the liquid-vapor interface, subject to the following boundary conditions:

1 Along the liquid-vapor solid boundary, the contact angle, α, in a vertical plane normal to the groove surface remains constant. A Neumann boundary condition[4] is expressed by

$$\partial z/\partial x(\sin \phi) - \partial z/\partial y(\cos \phi) = \cot \alpha \quad (8)$$

where ϕ is the angle between the x-axis and a horizontal tangent to the groove surface.

2 The liquid-vapor interface along the lines $y = 3d$ and $x = 3w/2$ approaches the contour of the liquid interface given by equation (5). The distances for x and y were selected because experimental evidence indicated that these boundaries were acceptable for the purposes of this analysis.

3 Along the center line of the interface inside a groove, a symmetric condition yields $\partial z/\partial x = 0$. In addition, for triangular grooves, $\partial z/\partial y = -\cot \alpha$, at the apex ($x = 0$, $y = 0$).

Equation (7) has been solved numerically for grooves of triangular, semicircular, and square cross sections over a wide range of properties [13]. For the numerical treatment, each half groove (bilateral geometry) has been subdivided into 150–200 cells. All equations were written in finite-difference form and the interfacial surfaces $z(x, y)$ were calculated with an IBM 7040 computer.

Calculated Static Results

It was found that the height, h_f, up to which a groove is fully wetted can be approximated by a similar relation as given in equation (3), when $R \ll h_f$

$$h_f \approx 2\sigma(\cos \alpha)/g(\varrho_l - \rho_v)R_E \quad (9)$$

where R_E designates an equivalent capillary radius for grooves, which is defined by

$$R_E = 2\,\frac{\text{(cross-sectional area)}}{\text{(wetted perimeter)} - \text{(width)}} \quad (10)$$

Hence, R_E is given by $d/(\csc(\beta/2) - 1)$, $\pi d/(\pi - 2)$ or d for triangular, semicircular, or square grooves, respectively. It can be seen from Fig. 2 that most values of h_f, as determined from digital computation, are somewhat smaller (about 5 percent) than those calculated from equation (9). If grooves of the same depth are wetted by the same fluid, h_f reaches its largest values in triangular, and its smallest in semicircular grooves. The free surface area could not be predicted in a similarly simple way. For $h_f > 10w$, however, the interfacial area approached approximately a constant value $A_S \sim 0.96(h_f w)$.

Since the weight of the lifted liquid has to be balanced by the surface-tension forces in static equilibrium, the results of equation (9) can be interpreted as follows. If the cross-sectional area of a capillary groove could be filled completely, but only up to its fully wetted height h_f, the weight of the lifted liquid is $(h_f A_x(\varrho_l - \rho_v)g)$. This weight has to be equal to the difference between surface-tension components pulling in upward and downward directions, which gives

$$h_f A_x(\varrho_l - \rho_v)g = \sigma(\cos \alpha)((\text{wetted Perimeter}) - (\text{width})) \quad (11)$$

Since this force balance leads to equation (9), it might be expected that the volume of liquid which is rising inside a groove in excess of h_f should be approximately equal to the volume which is actually missing over the height h_f, since the liquid is not filling the cross-sectional area completely. The computed results have been compared with experimental observations of vapor-liquid interfaces.

Experimental Measurements

Test sections (2-in. OD; 3-in. long) were made of brass (ASTM B-18) and provided with capillary grooves of different sizes and shapes. All groove dimensions were measured with a microscope (50 and 100 × magnification). After being most carefully cleaned by a series of different solvents, the grooved test sections were set up inside a small desiccator where the test liquid was added. The general arrangement of the test procedure is illustrated in Fig. 3. The wetted grooves were illuminated by the monochromatic light of a sodium-vapor lamp (about 5889-5895 Angstrom) which allowed observation of the interfaces. The fully wetted height, h_f, the maximum rise, and other characteristic points were measured by means of a cathetometer. Benzene, methyl alcohol, and carbon tetrachloride were used as test fluids. The liquid surface tensions were determined by using the capillary-rise method and applying equation (3). With the same general test arrangement, the maximum rise, h_0, at a plane test surface (between grooves) was measured in each case; the results were used in combination with equation (6) to

[4] Specification of the normal component of the gradient of a variable at each point along the boundary.

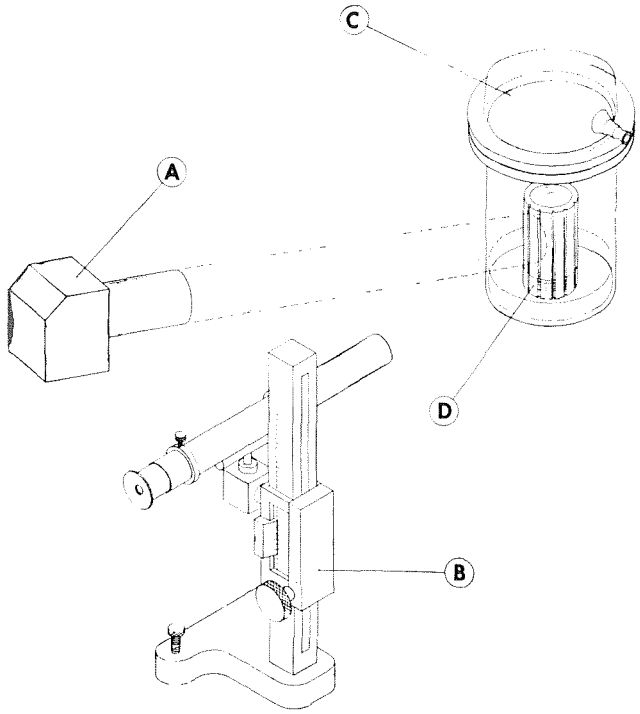

Fig. 3 Experimental measurement of capillary rise—A Light source; B Cathetometer; C Desiccator; D Grooved test surface

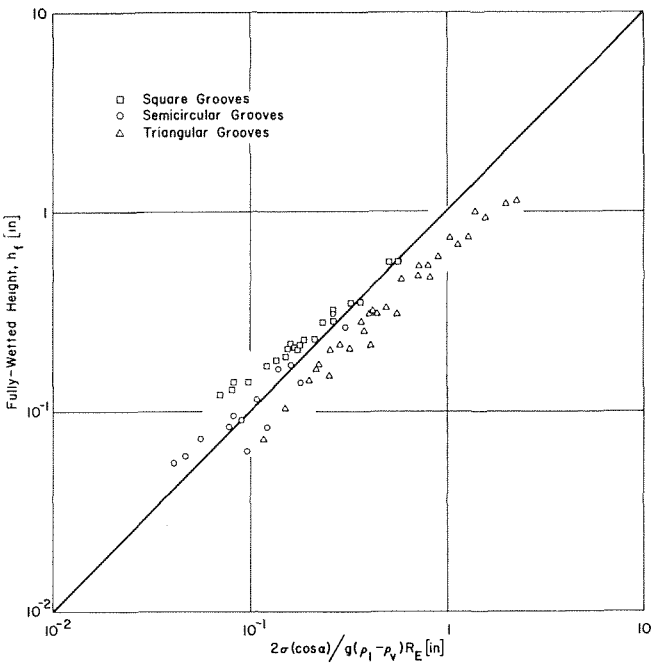

Fig. 4 Fully wetted static rise, h_f, measured in capillary grooves

determine the apparent contact angles, α. The results for fully wetted heights are presented in Fig. 4, which shows general agreement with the computed data.

Capillary Rise and Evaporation

As the temperature of the groove surface is increased, evaporation will eventually take place at the liquid-vapor interface. In the absence of vapor bubble formation or free convection, the heat liberated by this process is transferred by thermal conduction through the liquid which is rising in the capillary grooves. Considering heat flow in the y-direction only, the temperature distribution within the liquid layer is linear and the thermal resistance is proportional to a mean "film" thickness δ. Each liquid layer has zero film thickness at its upper edge and the

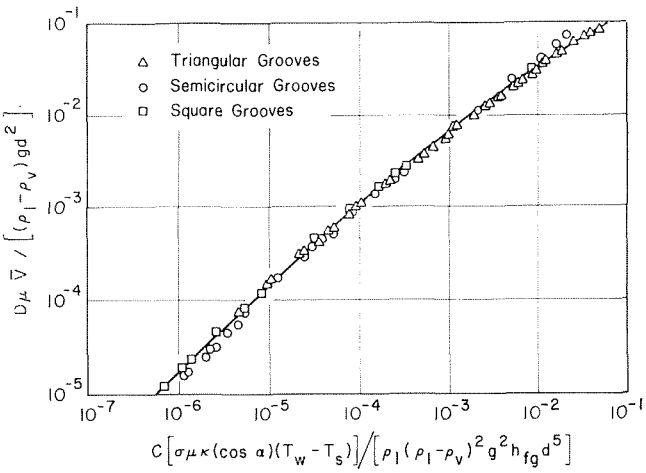

Fig. 5 Calculated mean velocities in terms of dimensionless parameters Λ and Ω defined in equations (14) and (15)

thickness increases in the downward direction. Under steady-state conditions, the rate at which the liquid is evaporated is equal to the rate at which the liquid is rising, due to capillary action. If the solid-liquid and liquid-vapor interfaces are isothermal at temperatures T_W and T_S, the average velocity v in direction z within a cross section element $(\Delta x \Delta y)$ can therefore be estimated to be

$$v = k(T_W - T_S)\Delta z'/\varrho_l h_{fg}\delta\Delta y \tag{12}$$

where k is the thermal conductivity and h_{fg} the latent heat of evaporation of the liquid.

When steady-state conditions are reached, the sum of the gravitational, viscous, and surface-tension forces acting on any liquid column $(dx\,dy\,z')$ is zero. z' denotes the dynamic height which is smaller than z, since the height of the liquid-vapor interface at any point (x, y) is decreased from $z(x, y)$ to $z'(x, y)$ because of the interfacial evaporation. It follows that the difference between the weight of the liquid column in static equilibrium $\varrho_l\, gz(dxdy)$ and the liquid column with evaporation $\varrho_l gz'$ $(dxdy)$ is equal to the viscous forces. Thus, for steady-state conditions and laminar flow, the governing equation can be written in a simplified form as

$$\partial^2 v/\partial x^2 + \partial^2 v/\partial y^2 = -(g(\varrho_l - \rho_v)/\mu)((z - z')/z') \tag{13}$$

where μ is the dynamic viscosity of the liquid phase. Based on the previously calculated static interfaces $z(x, y)$, the velocity distribution $v(x, y)$ has been evaluated by solving equation (13) together with equation (12) numerically.

Considering $z - z' \ll z$, the differential equations were replaced by finite-difference approximations [12] and the following boundary conditions were applied:

1 The velocity $v = 0$ along the liquid-solid boundary.

2 The normal velocity gradient at the liquid-vapor interface is zero.

3 The dynamic rise $z' = h_0$ at $y = d$; through this approximation, the calculated heat transfer rates account roughly for the additional heat transferred because of the groove.

4 The derivative $\partial v/\partial x = 0$ on the center line.

All numerical solutions are presented in Fig. 5 in terms of two dimensionless numbers Λ and Ω which are defined

$$\Lambda = C\sigma\mu k(\cos\alpha)(T'_w - T_s)/(\varrho_l(\varrho_l - \rho_v)^2 g^2 h_{fg} d^5) \tag{14}$$

$$\Omega = D\mu\bar{v}/(\varrho_l - \rho_v)gd^2 \tag{15}$$

In equations (14) and (15) are included two factors which vary for different groove geometries. The factor C is given for grooves with triangular, semicircular, and square cross sections by $(2\csc^3(\beta/2) - 2\csc^2(\beta/2))$, $(8(\pi - 2)/\pi^2)$ and (2); while D equals $(\csc^2(\beta/2))$, (2) and (2), respectively. An inspection of Fig. 5 reveals that the calculated results can be correlated reasonably well in terms of Λ and Ω. For a given groove geometry and

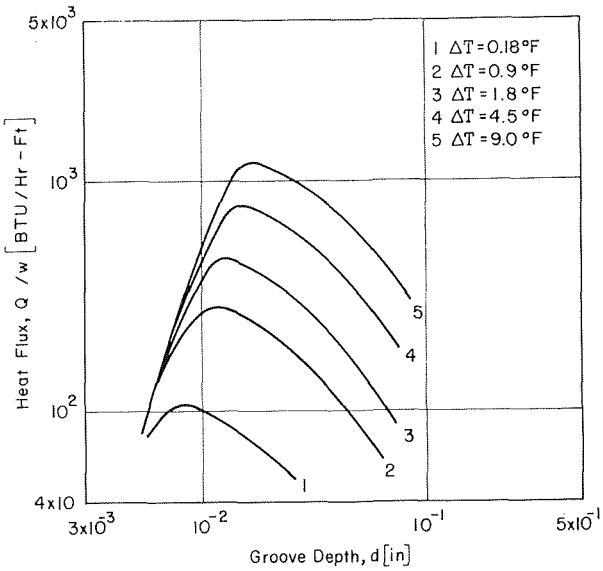

Fig. 6 Heat flux per unit groove width, Q/w, versus groove depth, d, for triangular grooves ($\beta = 30$ deg) and $(\sigma\mu k(\cos\alpha)/(\rho_l(\rho_l - \rho_v)^2 g^2 h_{fg}))$ $= 5.24 \times 10^{-14}$ (in.^{5}/deg F)

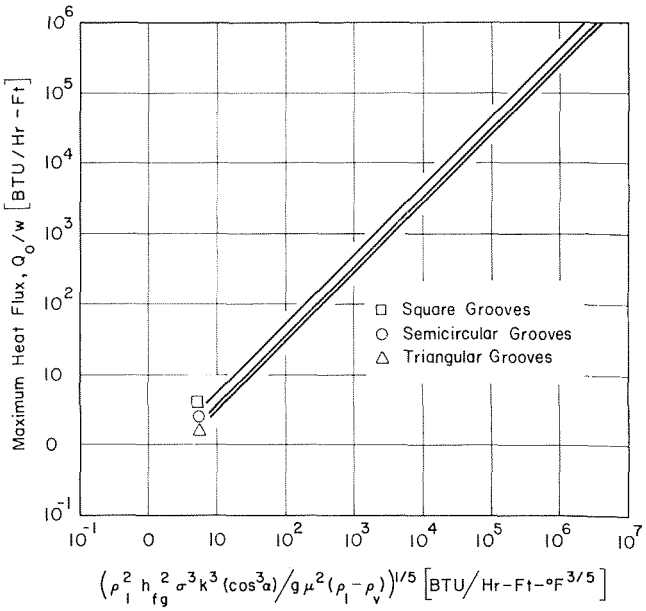

Fig. 7 Maximum heat flux per unit groove width, Q_0/w, for $(T_w - T_s)$ $= 1.8$ deg F versus parameter ψ defined in equation (19)

certain fluid properties, the average velocity $\bar{v}$ may be determined from the graph, if d and $(T_W - T_S)$ are known. The total heat flux Q can then be calculated from the relation

$$Q = \varrho_l \bar{v} A_x h_{fg} \tag{16}$$

Heat Transfer Rates

In this way, heat fluxes have been computed from the numerical solutions of the simplified velocity and conduction equations for three types of groove geometry: triangular, semicircular, and square. The results show that for a given set of properties and temperature difference between the solid-liquid and liquid-vapor boundaries $(T_w - T_s)$, the heat transfer rates are different for each individual groove design; they depend largely on the depth, and for triangular shapes on the vertex angle, too. A typical relationship between the heat flux per unit groove width, Q/w, and the depth, d, is illustrated in Fig. 6, with one example for a triangular groove. In a similar form, the heat transfer rates, Q/w, for all grooves exhibit maxima at some characteristic depths, $\mathbf{d}_0$. If for given properties and $(T_w - T_s)$, the depth of a triangular groove were kept constant but the vertex angle, β, were changed gradually, say, from 0–180 deg, the flow and hence heat transfer rates, Q/w, would vary gradually too. A smaller angle, for example, leads to increased capillary rise and improved wetting characteristics, but it also leads to larger dynamic velocity gradients and thus increased viscous forces. Consequently, the heat transfer rates would rise gradually as the angle changes from zero to a maximum value and return to zero again; it was found that they leveled out at a maximum around $\beta \approx 30$ deg. That is why only results for triangular grooves with a vertex angle of 30 deg are reported in this study.

From a curve fit of all computed data, the following expression was obtained for the depth, $\mathbf{d}_0$, at which the heat transfer rate per unit width reaches its maximum value, $\mathbf{Q}_0/w$, if all other parameters are kept unchanged. The relation may be written in the form

$$\mathbf{d}_0 = B\{\sigma\mu k(\cos\alpha)(T_w - T_s)/\varrho_l(\varrho_l - \rho_v)^2 g^2 h_{fg}\}^{1/5} \tag{17}$$

where the constant B is 5.11, 1.97, and 2.67 for 30-deg triangular, semicircular, and square grooves, respectively. Thus the optimum depths, $\mathbf{d}_0$, are different for each geometry, being largest for triangular and smallest for semicircular grooves. With the optimum depth, $\mathbf{d}_0$, as given by equation (17), the maximum heat transfer rate, $\mathbf{Q}_0/w$, is now

$$\mathbf{Q}_0/w = E\psi(T_w - T_s)^{3/5} \tag{18}$$

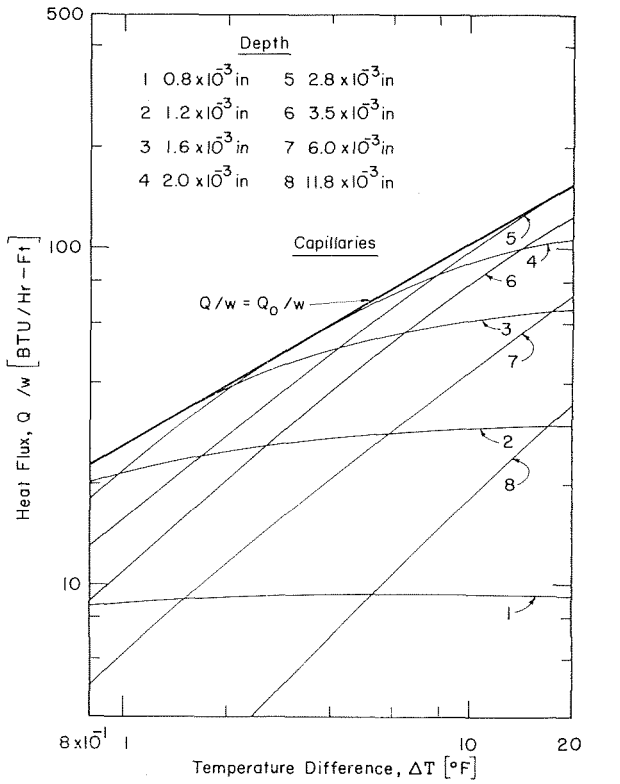

Fig. 8 Heat flux per unit groove width, Q/w, in semicircular grooves, calculated for freon -22 at $+40$ deg F

where E is a constant with a value of 0.269, 0.283, and 0.438 for 30-deg triangular, semicircular, and square cross sections. ψ denotes a function of all properties, which is defined as

$$\psi = \{\varrho_l^2 h_{fg}^2 \sigma^3 k^3 (\cos^3\alpha)/g\mu^2(\varrho_l - \rho_v)\}^{1/5} \tag{19}$$

Hence, the maximum heat transfer rates, $\mathbf{Q}_0/w$, in square grooves are larger than in other geometries.

A typical relationship is shown for one set of physical properties in Fig. 7. It should be noted that each of the three grooves which are compared in this graph is designed for its optimum depth, $\mathbf{d}_0$, which is different for each groove. Therefore, all three grooves in Fig. 7 have different depths and such a comparison might not be realistic. In addition, the optimum

depth, d_0, depends on the temperature difference $(T_w - T_s)$ too, which is shown for one case of semicircular grooves in Fig. 8. From these results it appears that the heat transfer rates per unit groove width, Q/w, depend in a complex way on the chosen geometry, depth, temperature difference, and physical properties. The performance of any capillary groove will vary largely according to the specific operating conditions. No particular groove type can give the highest heat flux, Q/w, neither for all temperature differences $(T_w - T_s)$, if the depth, d, and all properties remain unchanged; nor for all d's, if $(T_w - T_s)$ and the properties are constant. The optimum size, shape, and performance of a capillary-groove system must therefore be determined for each specific case. As a final illustration of this point, a plot of Q/w versus d for $(T_w - T_s) = 9$ (deg F) is presented in Fig. 9 for three selected fluid property groups. In a practical case, if the fluid properties and $(T_w - T_s)$ are known, a similar plot could be used to select the groove design with the highest performance per weight or volume. Estimated maximum heat fluxes per unit area Q/A are plotted versus $(T_w - T_s)$ in Fig. 10 for the analyzed capillary grooves together with predicted heat fluxes for interfacial evaporation with free convection [1] and pool boiling with evaporation [2]. The graph indicates the magnitude of the heat transfer rates which might be expected when using capillary grooves in the range of small temperature differences. The present results cannot be extrapolated to larger temperature differences because the assumed linearity in this analysis would be less valid and the onset of nucleate boiling in the grooves has not been considered here.

Summary and Conclusions

The effects of capillary grooves on surface wetting and evaporation have been examined for three groove types: square, semicircular, and triangular. The total capillary force has been determined in static equilibrium experimentally and theoretically. For the theoretical analysis, the governing differential equation has been solved numerically. It was found that all data for static capillary rise could be best represented in terms of a "fully wetted" height and an "equivalent" capillary radius, which led to a similar expression as that for capillary tubes.

For the heat transfer analysis, it was assumed that evaporation at the liquid-vapor interface takes place due to thermal conduction through the liquid layers inside the grooves. As a consequence of the surface evaporation, supplementary liquid is lifted by capillary action, and the system finally reaches steady state. Simplified and linearized equations for velocity and temperature distributions have been evaluated numerically in order to study the effects of the principal design parameters for capillary-grooved surfaces. Besides the relevant properties and the temperature difference $(T_w - T_s)$, the performance depends on geometrical factors such as the groove type, the depth (or width), and in triangular shapes, the vertex angle.

The computed heat transfer rates indicate that capillary grooves seem to offer definite advantages, which ultimately might lead to a reduction in size of process equipment where surface wetting is of importance. The selection of an optimum groove design, however, is a complex problem which requires knowledge of specific operating conditions. A vertex angle of approximately 30 deg led to the highest flow rates among triangular grooves. An expression was derived to determine maximum heat fluxes for each groove based on an optimized depth, d_0. Accordingly, square grooves are characterized by the highest heat transfer rates per unit groove width. The results change, however, if all grooves are compared at the same depth, d, and same temperature difference $(T_w - T_s)$.

The utilization of capillary forces in the design of heat exchangers to control surface wetting seems to offer additional advantages. Thus capillary systems in general do not require an additional power input, and capillary grooves may reduce problems which are commonly associated with the distribution and stabilization of two-phase mixtures in multiple-tube heat

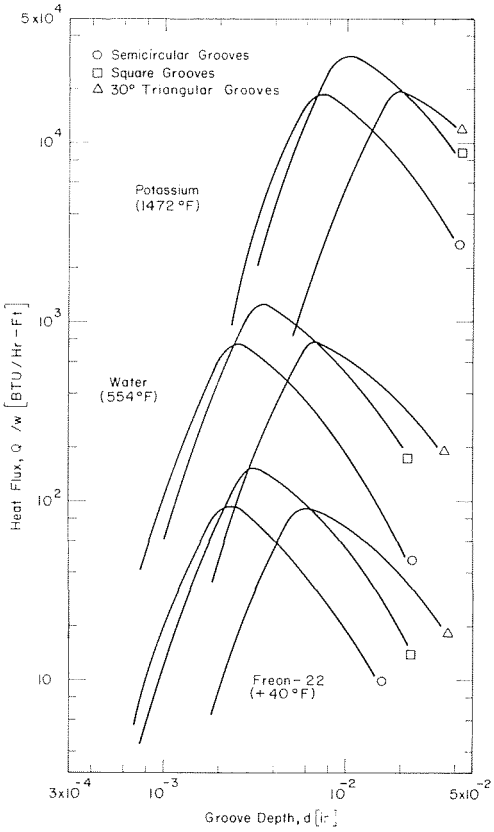

Fig. 9 Heat flux per unit groove width, Q/w calculated with $(T_w - T_s) = 9$ deg F for potassium, water, and freon −22

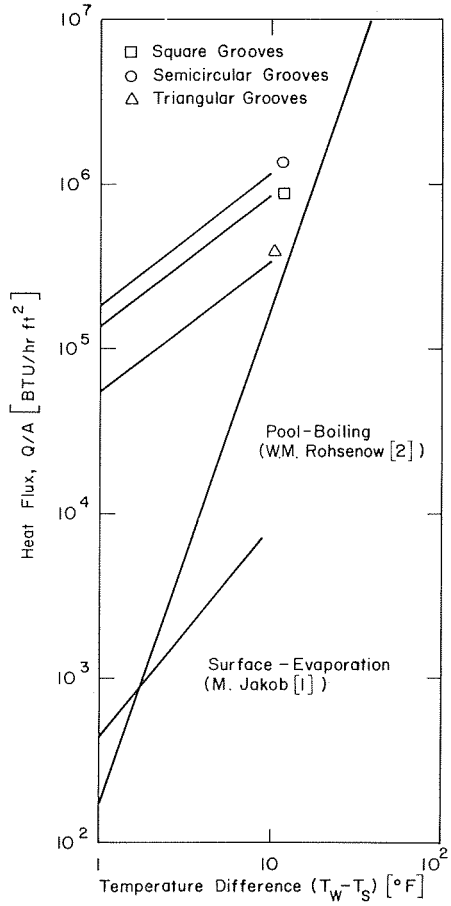

Fig. 10 Heat transfer rates per unit heating surface area, Q/A, as predicted for conduction through capillary grooves, for pool-boiling, and surface evaporation with free convection

exchangers. In addition, surfaces prepared in this way should be advantageous in situations where acceleration forces, such as might be found, e.g., on board an aircraft or ship during certain operations, would force the liquid away from the heating surface. When operating at low or zero gravity, grooved surfaces also seem to be able to distribute the liquid phase in a desired form. In all these cases, a proper application of capillary grooves might insure the required surface wetting to prevent disturbances in the heat transfer process or overheating of the surfaces. Besides the prerequisite of a capillary rise as such, the only practical limitation seems to be the tendency of a particular liquid to corrode a selected surface or to develop fouling and scaling-type deposits.

References

1 Jakob, M., *Heat Transfer*, Vol. 1, 1st ed., Wiley, New York, 1949.

2 Rohsenow, W. M., and Choi, H. V., *Heat Mass and Momentum Transfer*, Prentice-Hall, Englewood Cliff, N. J., 1961.

3 Tong, L. S., *Boiling Heat Transfer and Two-Phase Flow*, Wiley, New York, 1965.

4 Bressler, R., "Untersuchung des Waermeueberganges in einem Duennschichtverdampfer," *Forschungsberichte des Landes Nordrhein-Westfalen*, Nr. 770, Westdeutsch. Verl., Koeln, 1960.

5 Bressler, R. G., "Capillary Grooves in Refrigerant Evaporators," Carrier Corporation, Syracuse, Report Nr. 1006-12, 1962.

6 Adamson, A. W., *Physical Chemistry of Surfaces*, Wiley, New York, 1960.

7 Bikerman, J. J., *Surface Chemistry*, Academic Press, New York, 1958.

8 Schwartz, A. M., and Minor, F. W., "A Simplified Thermodynamic Approach to Capillarity," *Journal of Colloid Science*, Vol. 14, 1959, pp. 572–597.

9 Bikerman, J. J., *The Science of Adhesive Joints*, Academic Press, New York, 1961, pp. 45–51.

10 Cammerer, W. F., "Die Kapillare Fluessigkeits/bewegung in poroesen Koerpern," *VDI-Forschungsheft*, Nr. 500, VDI-Verl. Duesseldorf, 1963.

11 Parker, E. R., and Smoluchowski, R., "Capillarity of Metallic Surfaces," *Transactions of the American Society for Metals*, Vol. 35, 1944, pp. 362–371.

12 Reddick, H. W., and Miller, F. H., *Advanced Mathematics for Engineers*, 3rd ed., Wiley, New York, 1955, p. 110–113.

13 Wyatt, P. W., "The Effects of Capillary Grooves on Surface Wetting and Evaporation," MS thesis, The University of Tennessee, 1968.

T. CEBECI
Senior Engineer/Scientist.

A. M. O. SMITH
Assistant Chief of Aerodynamics.

G. MOSINSKIS
Engineer/Scientist.

Aerodynamics Research,
McDonnell Douglas Corp.,
Douglas Aircraft Co.,
Long Beach, Calif.

Solution of the Incompressible Turbulent Boundary-Layer Equations With Heat Transfer

The boundary-layer equations for laminar and turbulent incompressible flows about two-dimensional and axisymmetric flows are solved by an implicit finite-difference method. An eddy-viscosity concept is used to eliminate the Reynolds shear-stress term, and an eddy-conductivity concept is used to eliminate the time mean of the product of fluctuating velocity and temperature. Several flows have been computed by this method, and comparisons with experimental data and with the Bradshaw-Ferriss method are made. In general, the agreement is quite good.

Introduction

THE boundary-layer concept, first introduced in 1904 by Prandtl, divides the flow past a body into two regions: an inviscid region, governed by the Euler equations of motion, and a thin viscous region in the neighborhood of the body, governed by the boundary-layer equations. For laminar flow, the existence of a known relationship between the shear stress and the velocity gradient completes a set of partial differential equations, and exact solution of the boundary-layer equations is mathematically possible. With the advent of high-speed computers, quite satisfactory results have been obtained for skin fraction and heat transfer in incompressible and compressible flows. On the other hand, because of the limited understanding of the turbulent process, the problem of turbulent flow is phenomenological as well as mathematical, and exact solution of the boundary-layer equations is not possible. The usual boundary-layer equations for such flows contain a term involving the time mean of the product of two fluctuating velocities (the Reynolds shear stress) and a term involving the time mean of the product of a fluctuating velocity and a fluctuating temperature. At present, these terms have not been rigorously related to the mean velocity and mean temperature distributions. In order to proceed at all, the solutions must depend on some empiricism, which leads to various approaches and consequently to various methods[1] with varying degrees of accuracy in predicting boundary-layer parameters.

Contributed by the Heat Transfer Division of THE AMERICAN SOCIETY OF MECHANICAL ENGINEERS and presented at the ASME-AIChE Heat Transfer Conference, Minneapolis, Minn., August 3–6, 1969. Manuscript received at ASME Headquarters, January 3, 1969. Paper No. 69-HT-7.

[1] A summary of the latest prediction methods for incompressible, two-dimensional, turbulent boundary layers is given by Reynolds in reference [1].

Nomenclature

c_p = specific heat at constant pressure
C = viscosity-density parameter, $\rho\mu/\rho_e\mu_e$
f = dimensionless stream function; see equation (18)
g = dimensionless total enthalpy ratio
h = specific enthalpy, or heat transfer film coefficient wherever applicable
H = total enthalpy, $h + u^2/2$
k = flow index, = 0 (two-dimensional flow) and = 1 (axisymmetrical flow)
k_1, k_2 = constants in eddy-viscosity formulas
K = variable - grid parameter; see equation (30)
l = mixing length
L = reference body length
M = Mach number
Nu_x = Nusselt number hx/λ_t
p = pressure
Pr = Prandtl number, $\mu c_p/\lambda_t$
q = local heat-transfer rate per unit area
r = radial distance from axis of revolution
r_0 = body radius
R_x = Reynolds number, $U_e x/\nu_e$
R_θ = Reynolds number, $U_e\theta/\nu_e$
St = Stanton number, $-q_w/\rho_e U_e(H_e - H_w)$
t = transverse curvature term, $(y \cos\alpha)/r_0$
Δt = temperature difference between wall and free stream, $T_w - T_\infty$
T = absolute temperature
u = x-component of velocity
U_e = velocity at outer edge of boundary layer
v = y-component of velocity
x = distance along body surface measured from leading edge
y = distance normal to x
α = angle between y and r
β = velocity - gradient parameter, $2\xi/U_e(dU_e/d\xi)$
λ = intermittency factor
δ = boundary-layer thickness
δ^* = displacement thickness
ϵ = eddy viscosity
ϵ^+ = ratio of eddy viscosity to kinematic viscosity, ϵ/ν
η = transformed y-coordinate
θ = momentum thickness
λ = thermal conductivity
μ = dynamic viscosity
ν = kinematic viscosity
ξ = transformed x-coordinate
ρ = density
τ = shear stress
ψ = stream function

Subscripts

c = switching point between inner and outer eddy viscosity formulas
e = outer edge of boundary layer
l = laminar flow
t = turbulent flow
w = wall
∞ = free-stream conditions
$'$ = differentiation with respect to η

The present method uses an eddy-viscosity concept to eliminate the Reynolds shear-stress term and an eddy-conductivity concept to eliminate the time mean of fluctuating velocity and temperature. The eddy-viscosity formulation used here is the same as the one used for incompressible flow in several previous studies [2, 3]. The formulation worked well for incompressible flows, and hence it was extended to compressible flows. In the formulation, the boundary layer is regarded as a composite layer characterized by inner and outer regions. In the inner region, a constant eddy viscosity modified by an intermittency factor is used. The eddy-conductivity term is lumped into a "turbulent" Prandtl number that is assumed to be constant and equal to 0.9.

In principle, the present method is similar to the ones used by Herring and Mellor [4] and Patankar and Spalding [5]. The main difference between the three methods lies in the eddy-viscosity expression used for each region. In addition, the transformations used to stretch the coordinate normal to the flow direction as well as the numerical method used to solve the boundary-layer equations are considerably different.

Several incompressible turbulent flows with heat transfer are computed by the present method, and comparisons with experimental data and with the Bradshaw-Ferriss (BF) method [6] are made. The latter method differs from the present one in that it involves a solution of turbulence kinetic energy, mean momentum equation, continuity equation, and the instantaneous temperature equation by making certain assumptions to the turbulence terms appearing in these equations. In general, prediction of both methods is quite good.

Analysis

Boundary-Layer Equations. The boundary-layer equations for two-dimensional and axisymmetric compressible turbulent flow are [7]:

Continuity:

$$\frac{\partial}{\partial x}(r^k \rho u) + \frac{\partial}{\partial y}[r^k(\rho v + \overline{\rho' v'})] = 0 \tag{1}$$

Momentum:

$$\rho u \frac{\partial u}{\partial x} + (\rho v + \overline{\rho' v'}) \frac{\partial u}{\partial y} = \rho_e U_e \frac{dU_e}{dx} + \frac{1}{r^k}\frac{\partial}{\partial y}\left[r^k\left(\mu \frac{\partial u}{\partial y} - \overline{\rho u' v'}\right)\right] \tag{2}$$

Energy:

$$\rho u \frac{\partial H}{\partial x} + (\rho v + \overline{\rho' v'}) \frac{\partial H}{\partial y} = \frac{1}{r^k}\frac{\partial}{\partial y}\left[r^k \frac{\lambda_l}{c_p}\frac{\partial H}{\partial y} - \overline{\rho v' H'} + \mu\left(1 - \frac{1}{\Pr}\right) u \frac{\partial u}{\partial y}\right] \tag{3}$$

In these equations, the transverse curvature effect is retained because of its importance in predicting boundary-layer growth on slender bodies, such as certain missiles or at the tail of a streamlined body of revolution. In such cases the radius of the body may be the same order of magnitude as the thickness of the boundary layer, and neglect of this effect could be quite important.

The boundary conditions are

Momentum:

$$u(x,0) = 0,\ v(x,0) = 0 \text{ or } v(x,0) = v_w \text{ (mass transfer)}$$
$$\lim_{y \to \infty} u(x,y) = U_e(x) \tag{4}$$

Energy:

$$H(x,0) = H_w \text{ or or } \frac{\partial H}{\partial y}(x,0) = \left(\frac{\partial H}{\partial y}\right)_w,$$
$$\lim_{y \to \infty} H(x,y) = H_e(x) \tag{5}$$

Formulation of Eddy Viscosity and Turbulent Prandtl Number. In order to solve equations (1)–(3), it is necessary to relate $-\overline{u'v'}$, the Reynolds shear-stress term, and the $-\overline{v'H'}$ term to the dependent variables u (or v), and H, respectively. Here we use eddy viscosity (ϵ) and eddy-conductivity (λ_t) concepts, and set

$$-\overline{u'v'} = \epsilon \frac{\partial u}{\partial y} \tag{6}$$

and

$$-\overline{v'H'} = \lambda_t \frac{\partial H}{\partial y} \tag{7}$$

Equation (7) can also be written as

$$-\overline{v'H'} = \frac{c_p \epsilon}{\Pr_t}\frac{\partial H}{\partial y} \tag{8}$$

by defining the turbulent Prandtl number as $\Pr_t = c_p\epsilon/\lambda_t$.

The expression for ϵ in the inner region is based on Prandtl's mixing-length theory; that is,

$$\epsilon_i = l^2 \left|\frac{\partial u}{\partial y}\right| \tag{9}$$

where l, the mixing length, is given by $l = k_1 y$. A modified expression for l is used in equation (9) to account for the viscous sublayer close to the wall. This modification, suggested by Van Driest [8], is

$$l = k_1 y\left[1 - \exp\left(-\frac{y}{A}\right)\right] \tag{10}$$

where A is a constant for a given streamwise location in the boundary layer, and is defined as $26\nu(\tau_w/\rho)^{-1/2}$, with w denoting values at the wall. Equation (10) was developed for a flat plate. Here, we modify the constant A to account for pressure gradient. From the momentum equation it follows that the shear stress close to the wall may be written as

$$\tau = \tau_w + \frac{dp}{dx} y \tag{11}$$

If A is defined as $26\nu(\tau/\rho)^{-1/2}$, the constant becomes

$$26\nu\left(\frac{\tau_w}{\rho} + \frac{dp}{dx}\frac{y}{\rho}\right)^{-1/2} \tag{12}$$

Then the expression for inner eddy viscosity becomes

$$\epsilon_i = k_1^2 y^2 \left\{1 - \exp\left[-\frac{y}{26\nu}\left(\frac{\tau_w}{\rho} + \frac{dp}{dx}\frac{y}{\rho}\right)^{1/2}\right]\right\}^2 \left|\frac{\partial u}{\partial y}\right| \tag{13}$$

The expression for ϵ in the outer region is based on a constant eddy viscosity, ϵ_0,

$$\epsilon_0 = k_2 U_e \delta^* \tag{14}$$

modified by Klebanoff's [9] intermittency factor γ, approximated by the following formula

$$\gamma = \left[1 + 5.5\left(\frac{y}{\delta}\right)^6\right]^{-1} \tag{15}$$

which is a rough but very convenient approximation to the error function.

The choice of constants k_1 and k_2 in the eddy-viscosity formulas depends slightly on the definition of the boundary-layer thickness δ. As in several previous studies, for example, references [2, 3], the values of the constants k_1 and k_2 are taken to be 0.40 and 0.0168, respectively, and δ is defined as the y-distance for which $f' = 0.995$.

The constraint used to define the inner and outer regions is the continuity of the eddy viscosity; from the wall outward, the expression for inner eddy viscosity applies until $\epsilon_i = \epsilon_0$. The dividing point is y_c. Fig. 1 shows a typical eddy-viscosity variation across the boundary layer for a flat-plate flow.

Transformation of Boundary-Layer and Eddy-Viscosity Equations. Equations (1)–(3), which are expressed in the coordinates of the physical plane, require starting profiles, but these equations are singular at $x = 0$. For this reason, we first transform them as in the previous study [2], to a coordinate system that removes the singularity at $x = 0$, stretches the coordinate normal to the flow direction, and places the equations in an almost two-dimensional form. We use a combination of the Probstein-Elliot [10] and Levy-Lees [11] transformations.

$$d\xi = \rho_e \mu_e U_e \left(\frac{r_0}{L}\right)^{2k} dx. \qquad d\eta = \frac{\rho U_e}{(2\xi)^{1/2}} \left(\frac{r}{L}\right)^k dy \tag{16}$$

If a stream function ψ is introduced such that

$$\frac{\partial \psi}{\partial y} = \left(\frac{r}{L}\right)^k \rho u, \qquad \frac{\partial \psi}{\partial x} = -\left(\frac{r}{L}\right)^k (\rho v + \overline{\rho' v'}) \tag{17}$$

and if ψ is related to a dimensionless stream function f as

$$\psi(x,y) = (2\xi)^{1/2} f(\xi,\eta) \tag{18}$$

then the momentum equation, equation (2), and the energy equation, equation (3), become

Momentum:

$$[(1 + t)^{2k} C(1 + \epsilon^+) f'']' + f f'' + \beta \left[\frac{\rho_e}{\rho} - (f')^2\right] = 2\xi \left[f' \frac{\partial f'}{\partial \xi} - f'' \frac{\partial f}{\partial \xi}\right] \tag{19}$$

Energy:

$$\left\{(1 + t)^{2k} C \left[\left(1 + \epsilon^+ \frac{\mathrm{Pr}}{\mathrm{Pr}_t}\right) \frac{g'}{\mathrm{Pr}} + \frac{U_e^2}{H_e} \left(1 - \frac{1}{\mathrm{Pr}}\right) f' f''\right]\right\}' + f g' = 2\xi \left(f' \frac{\partial g}{\partial \xi} - g' \frac{\partial f}{\partial \xi}\right) \tag{20}$$

after the terms $-\overline{u'v'}$ and $-\overline{v'H'}$ are replaced by the relations given by equations (6) and (8). In equations (19) and (20), t is the transverse-curvature term, β is the pressure-gradient term, C is the viscosity-density term, and ϵ^+ is the ratio of eddy viscosity to kinematic viscosity. They are defined as follows

$$t = -1 + \left[1 + \frac{2L \cos \alpha}{r_0^2} \frac{(2\xi)^{1/2}}{\rho_e U_e} \int_0^\eta \frac{\rho_e}{\rho} d\eta\right]^{1/2}$$

$$\beta = \frac{2\xi}{U_e} \frac{dU_e}{d\xi}, \qquad C = \frac{\rho \mu}{\rho_e \mu_e}, \qquad \epsilon^+ = \frac{\epsilon}{\nu}$$

The dependent variables f' and g in equations (19) and (20) are dimensionless velocity and total-enthalpy ratios, respectively, defined as $f' = u/U_e$ and $g = H/H_e$. It can be seen from equations (19) and (20) that setting $k = 0$ reduces the boundary-layer equations to two-dimensional form. For axisymmetric flow with no transverse-curvature effect, $k = 1$ and $t = 0$, which indicates that the ratio of r to r_0 is unity, since

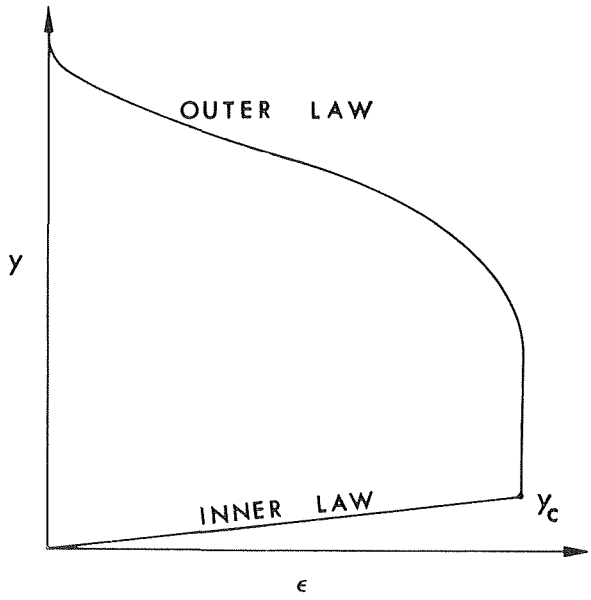

Fig. 1 Eddy-viscosity distribution across a boundary layer

$$r = r_0 + y \cos \alpha$$

and t in the physical plane is defined as $t = (y \cos \alpha)/r_0$. Furthermore, if ϵ^+ is zero, equations (19) and (20) reduce to a classical form of the compressible laminar boundary-layer equations.

The boundary conditions given by equations (4) and (5) become

Momentum:

$$f(\xi,0) = f_w = 0 \text{ or } f_w = -\frac{1}{(2\xi)^{1/2}} \int_0^\xi \left(\frac{L}{r_0}\right)^k \frac{\rho_w v_w}{\rho_e \mu_e U_e} d\xi \text{ (mass transfer)} \tag{21a}$$

$$f'(\xi,0) = 0 \qquad \lim_{\eta \to \infty} f'(\xi,\eta) = 1 \tag{21b}$$

Energy:

$$g(\xi,0) = \frac{H_w}{H_e} = g_w \text{ or } g_w'(\xi,0) = g_w' \tag{22a}$$

$$\lim_{y \to \infty} g(\xi,\eta) = 1 \tag{22b}$$

Similarly, we can transform the eddy-viscosity expressions by using the transformation given by equations (16) and (18). In dimensionless form, the expression for eddy viscosity for the inner region becomes

$$\epsilon_i^+ = k_1^2 \left(\frac{\rho}{\rho_e}\right)^2 \frac{(2\xi)^{1/2}}{\mu} \left(\frac{L}{r_0}\right)^k (1 + t)^k \, | f'' | \times \left[\int_0^\eta (1 + t)^{-k} \left(\frac{\rho_e}{\rho}\right) d\eta\right]^2 \times \left\{1 - \exp\left[-\frac{(2\xi)^{1/2}}{\mu} \frac{\rho}{\rho_e} \times \left(\frac{L}{r_0}\right)^{k/2} \frac{1}{26} \int_0^\eta (1 + t)^{-k} \frac{\rho_e}{\rho} d\eta \left(f_w'' \frac{\rho_w}{\rho} \frac{\mu_w}{(2\xi)^{1/2}} - \frac{\rho_e}{\rho} \frac{\mu_e}{(2\xi)^{1/2}} \beta \int_0^\eta (1 + t)^{-k} \frac{\rho_e}{\rho} d\eta\right)^{1/2}\right]\right\}^2 \tag{23}$$

For two-dimensional and axisymmetric flows, the definition of

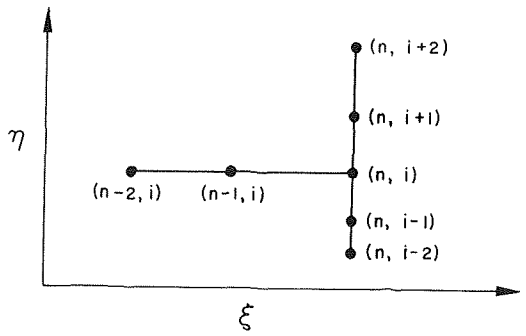

Fig. 2 Finite-difference molecule for the momentum equation at (n,i)

displacement thickness, δ^*, used in the outer eddy-viscosity expression is[2]

$$\delta^* = \int_0^\infty \left(1 - \frac{u}{U_e}\right) dy \tag{24}$$

which, in terms of the transformation defined by equations (16) and (18), becomes

$$\delta^* = \frac{(2\xi)^{1/2}}{\rho_e U_e}\left(\frac{L}{r_0}\right)^k \int_0^\infty (1 + t)^{-k} \frac{\rho_e}{\rho}(1 - f')d\eta \tag{25}$$

In dimensionless form, the expression for the outer eddy viscosity then becomes

$$\epsilon_0^+ = k_2\left(\frac{L}{r_0}\right)^k \frac{\rho}{\rho_e}\frac{(2\xi)^{1/2}}{\mu}\left[\int_0^{\eta_\infty} (1 + t)^{-k}\frac{\rho_e}{\rho}(1 - f')d\eta\right] \times \left\{1 + 5.5\left[\frac{\int_0^\eta (1 + t)^{-k}\,\rho_e/\rho\, d\eta}{\int_0^{\eta_\infty} (1 + t)^{-k}\,\rho_e/\rho\, d\eta}\right]^6\right\}^{-1} \tag{26}$$

Fluid Properties. Fluid properties that appear in the momentum and energy equations are density (ρ), viscosity (μ), specific heat at constant pressure (c_p), and thermal conductivity (λ). The latter appears in the energy equation through the laminar Prandtl number, Pr, defined as $\mathrm{Pr} = \mu c_p/\lambda_l$.

The present method is developed so that arbitrary fluid properties may be used. In other words, the fluid properties are inputs in the computer program in the form of formulas or tables as functions of temperature. In this study, air is treated as a perfect gas, and the fluid properties μ and ρ are assumed to be functions of specific enthalpy only; the specific heat of air at constant pressure, c_p, is assumed to be constant and equal to 6035 ft²/sec² deg R. The viscosity μ is obtained from Sutherland's law expressed as

$$\frac{\mu}{\mu_\infty} = \left(\frac{h}{h_\infty}\right)^{3/2}\frac{h_\infty + 1.19493 \times 10^6}{h + 1.19493 \times 10^6} \tag{27}$$

The density-enthalpy relation is obtained from the equation of state and from the assumption that static pressure remains constant within the boundary layer. Prandtl number is an input to the computer program.

Method of Solution

Solution of Momentum Equation. Before we solve equations (19) and (20) by an implicit finite-difference method, we first linearize equation (19). Introducing a translated stream function φ defined by $\varphi = f - \eta$ and replacing the streamwise derivatives by three-point finite-difference formulas at $\xi = \xi_n$, we get

$$[(1 + t)^{2k} C(1 + \epsilon^+)\varphi'']' + (\varphi + \eta)\varphi'' + \beta[(\rho_e/\rho) - (\varphi')^2 - 2\varphi' - 1] = 2\xi[(\varphi' + 1)(A_1\varphi' + A_2\varphi_{n-1}' + A_3\varphi_{n-2}') - \varphi''(A_1\varphi + A_2\varphi_{n-1} + A_3\varphi_{n-2})] \tag{28}$$

where for simplicity, the subscript n is dropped. At $\xi = \xi_n$, the quantities A_1, A_2, and A_3 are known, and the quantities hav-

[2] It is to be noted that the definition of δ^* for axisymmetric flows with transverse-curvature effect is not the same as the definition of δ^* for two-dimensional flows. In the former case, the displacement thickness is defined as

$$\delta^*\left(1 + \frac{\delta^*}{2r_0}\right) = \int_0^\infty \left(\frac{r}{r_0}\right)\left(1 - \frac{u}{U_e}\right) dy$$

which can be related to two-dimensional δ^* as follows:

$$\frac{\delta^*}{r_0} = -1 + \sqrt{1 + \frac{2\delta^*_{\text{two dimensional}}}{r_0}}$$

In the outer eddy-viscosity expression, however, the δ^* is used as a characteristic length, and its definition remains unchanged from that given by equation (24) for either incompressible, compressible, or axisymmetric flows with transverse-curvature effects.

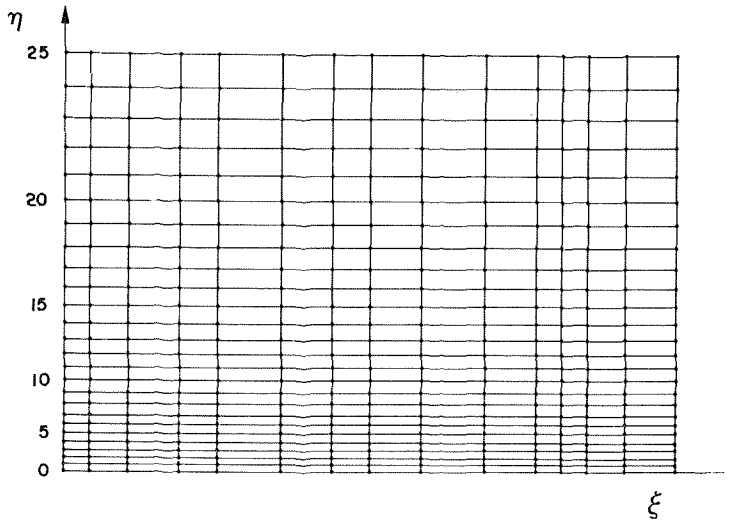

Fig. 3 Finite-difference variable-grid system in the η-direction

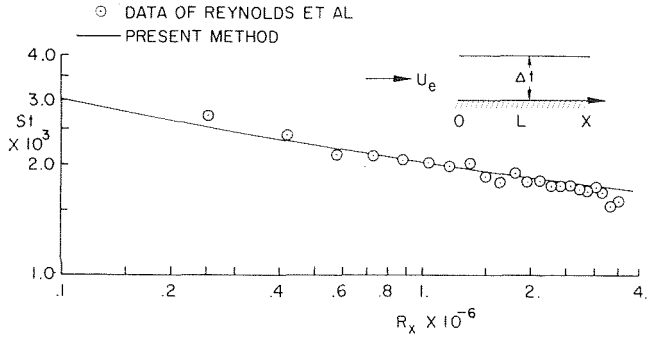

Fig. 4 Comparison of calculated and experimental Stanton numbers for the flat-plate boundary layer measured by Reynolds, Kays, and Kline [13]

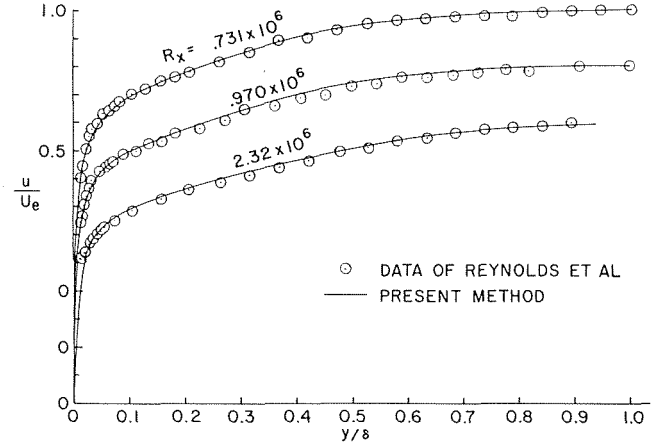

Fig. 5 Comparison of calculated and experimental velocity profiles for the flat-plate boundary layer measured by Reynolds, Kays, and Kline [13]

ing the subscripts n-1 and n-2 are known functions of η from solutions obtained at the two previous stations. Thus, at $\xi = \xi_n$, equation (28) is an ordinary differential equation in η. There is no problem of starting the solution, because the terms with streamwise derivatives disappear, since $\xi = 0$. At the next station, ξ_1, the three-point formulas are replaced by two-point formulas; at all stations farther downstream the three-point formulas are used.

To linearize equation (28), we assume that certain terms that make the equation nonlinear are known from the previous iteration; that is,

$$[(1 + t)^{2k} C_0 (1 + \epsilon^+)_0 \varphi''] + (\varphi_0 + \eta)\varphi'' + \beta[(\rho_e/\rho)_0 - \varphi_0'\varphi' - 2\varphi' - 1] = 2\xi[(\varphi_0' + 1)(A_1\varphi' + A_2\varphi_{n-1}' + A_3\varphi_{n-2}') - \varphi_0''(A_1\varphi + A_2\varphi_{n-1} + A_3\varphi_{n-2})] \quad (29)$$

The subscript 0 indicates that the function is obtained from a previous iteration.

The solution of equation (29) is obtained by an implicit finite-difference method after the dependent variable φ has been replaced by the perturbation terms $\overline{\Delta\varphi} = \varphi - \varphi_0$, $\overline{\Delta\varphi'} = \varphi' - \varphi_0'$, etc. The reason for choosing φ rather than f, and $\overline{\Delta\varphi}$ rather than φ, is that the round-off errors are reduced. Fig. 2 shows the finite-difference molecule used.

Solution of Energy Equation. The method of solution of the energy equation is similar to that of the momentum equation. Again the ξ-derivatives are replaced by finite-difference formulas that are identical to those in the momentum equation. As for the momentum equation, an implicit finite-difference method is used to solve the energy equation. However, this time the five-point finite-difference molecule is replaced by a three-point finite-difference molecule.

For details of solution of both momentum and energy equations, see reference [12].

Variable-Grid Spacing in η-Direction. The finite-difference formulas used both in momentum and energy equations contain a variable grid in the η-direction, which permits shorter steps close to the wall and longer steps away from the wall. The grid has the property that the ratio of lengths of any two adjacent intervals is a constant; that is, $\Delta\eta_i = K\,\Delta\eta_{i-1}$. The distance to the ith grid line is given by the following formula

$$\eta_i = h_1 \frac{K^i - 1}{K - 1} \qquad i = 0, 1, 2, 3, \ldots N \quad (30)$$

where h_1 is the length of the first step. Fig. 3 accurately represents the η-spacing for $\eta_\infty = 100$, $h_1 = 0.01$, and $K = 1.07$. In general, about 200 η-points are used in a typical turbulent flow calculation.

Starting the Solution. The calculations begin at the leading edge or at the stagnation point, where $\xi = 0$, and proceed downstream with arbitrary $\Delta\xi$-increments. At station $\xi = 0$, the flow is laminar, and it becomes turbulent at any specified station where $\xi > 0$. A calculation can be started at any ξ-location, provided that initial velocity and enthalpy profiles (flows with heat transfer) are specified. Of course, for flows without heat transfer, it is only necessary to specify the initial velocity profile.

Comparisons of Calculated and Experimental Results

The method discussed in previous sections has been used to compute several incompressible turbulent flows with heat transfer. These flows consist of flat-plate flows with heating and cooling as well as flows in both favorable and adverse pressure gradients with cooling.

Flat-Plate Flows. For constant-velocity flows with different distributions of wall temperatures, we have considered three separate sets of experimental data and have made comparisons of velocity profiles (when they were reported) and comparisons of local Stanton numbers.

The local Stanton number is defined as

$$\mathrm{St} = \frac{-q_w}{\rho_e U_e (H_e - H_w)} \quad (31)$$

which, in terms of transformed variables, can be written as

$$\mathrm{St} = \left(\frac{r_0}{L}\right)^k \left(\frac{C}{\mathrm{Pr}}\right)_w \frac{\mu_e}{(2\xi)^{1/2}} \left(\frac{g_w'}{1 - g_w}\right) \quad (32)$$

Figs. 4 and 5 show comparisons of local Stanton numbers and velocity profiles, respectively, on an isothermal, heated plate measured by Reynolds, Kays, and Kline [13]. In the calculations the laminar Prandtl number was assumed to be 0.70. Figs. 6 and 7 show the same types of comparisons for a flow measured by Seban and Doughty [14]. Here the calculations were performed for an isothermal heated plate for the same Prandtl number.

Seban and Doughty note that if their experimental results are expressed as

$$\mathrm{Nu}_x = C_1 \mathrm{R}_x^{4/5}$$

then the constant C_1 for their results is 0.0236. They further note that this constant is 0.024, according to Jakob's measurements, and is 0.023 according to Sugawara's measurements; it is 0.0255 according to Scesa's experiments, a value which is thought to be somewhat high. It is interesting to note that an average value for this constant obtained by the present method is 0.0235, a value that agrees quite well with these results.

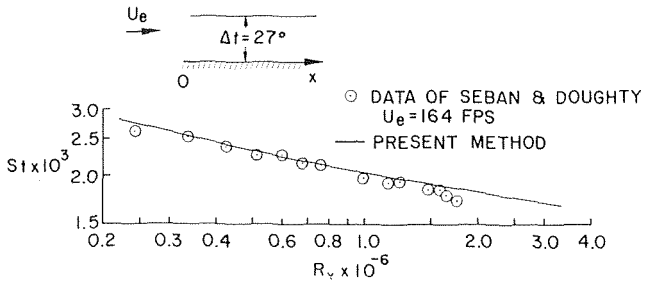

Fig. 6 Comparison of calculated and experimental Stanton numbers for the flat-plate boundary layer measured by Seban and Doughty [14]

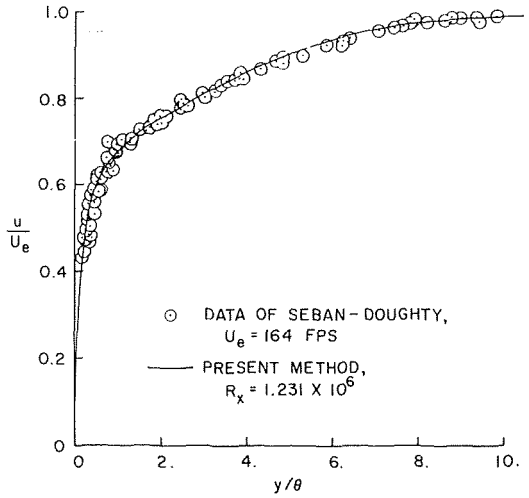

Fig. 7 Comparison of calculated and experimental velocity profiles for the flat-plate boundary layer measured by Seban and Doughty [14]

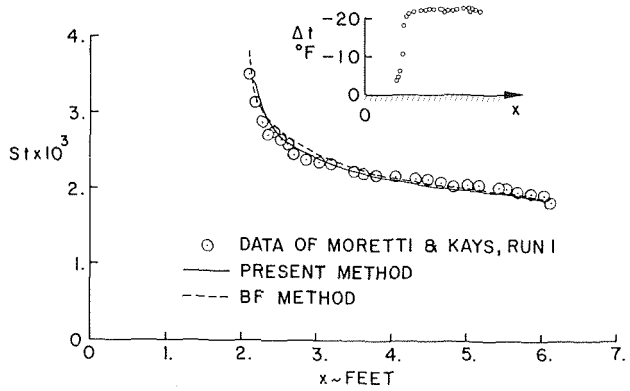

Fig. 8 Comparison of calculated and experimental Stanton numbers for the flat-plate boundary layer measured by Moretti and Kays [15]

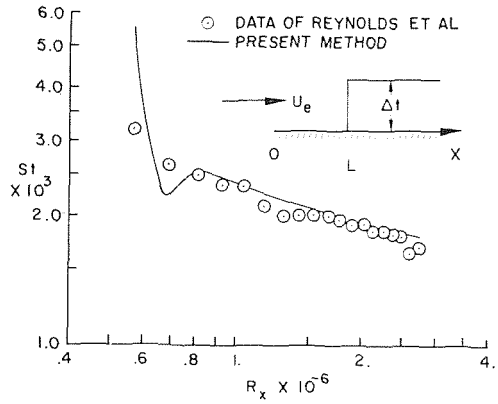

Fig. 9 Comparison of calculated and experimental Stanton numbers for the flat-plate boundary layer measured by Reynolds, Kays, and Kline [16]

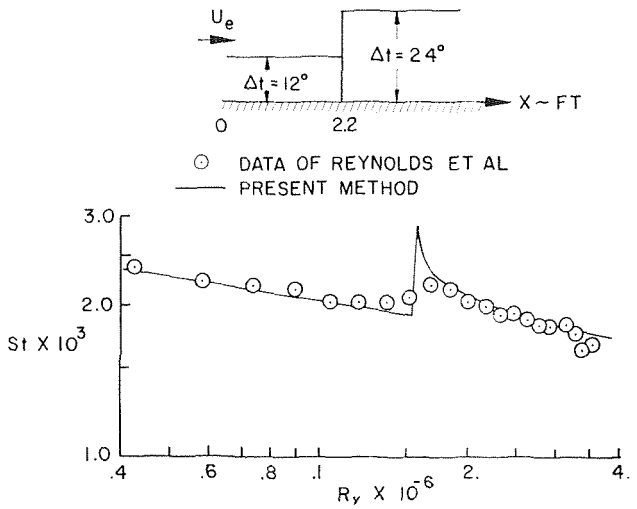

Fig. 10 Comparison of calculated and experimental Stanton numbers for the flat-plate boundary layer measured by Reynolds, Kays, and Kline [17]

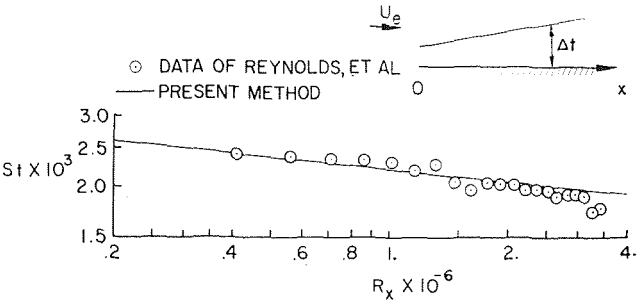

Fig. 11 Comparison of calculated and experimental Stanton numbers for the flat-plate boundary layer measured by Reynolds, Kays, and Kline [17]

Fig. 8 shows a comparison of calculated and experimental local Stanton numbers for an isothermal, cooled plate measured by Moretti and Kays [15]. The solid lines are those calculated by the present method and the dashed lines are those computed by the BF method [6]. Both methods predict the Stanton number very well, and the slight difference at the beginning of the flow can probably be attributed to different matching or starting conditions.

Fig. 9 shows the computed local Stanton numbers, together with the experimental values obtained by Reynolds, Kays, and Kline [16], for a step variation of wall temperature. Figs. 10 and 11 show comparisons of computed values with experimental values obtained by Reynolds, Kays, and Kline [17] for a double-step wall temperature and step-ramp temperature distribution, respectively. In all cases the agreement is quite good.

Accelerating Flows. Figs. 12–15 show the results obtained for four accelerating flows. The first three of these flows, labeled as Runs 12, 13, and 24, were measured by Moretti and Kays [15]. In the calculations, the experimental temperature difference between wall and free stream, $\Delta t(x)$, and velocity distribution, $U_e(x)$, were used as reported in reference [15]. This is the reason

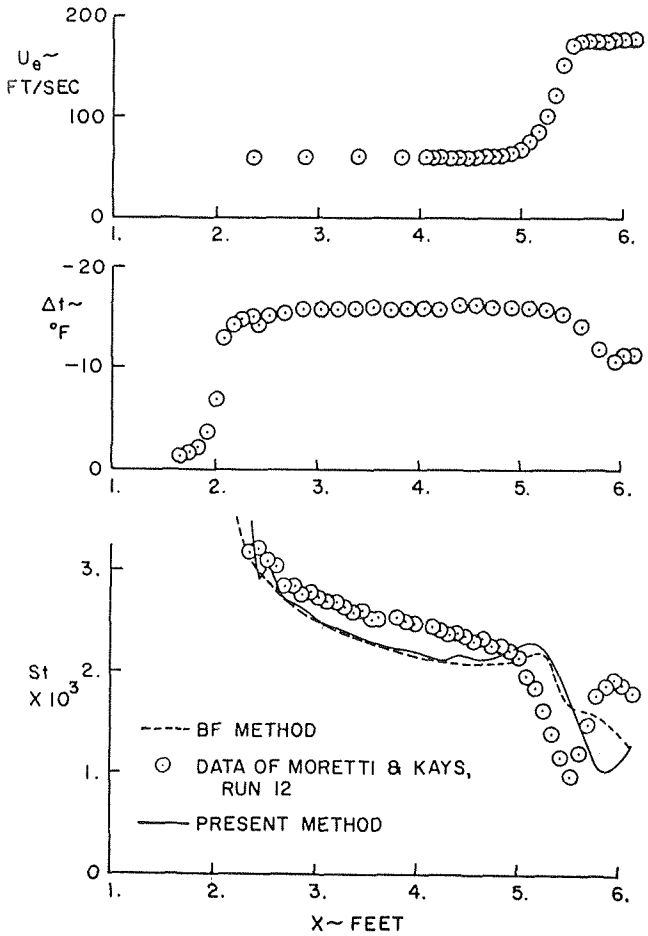

Fig. 12 Comparison of calculated and experimental Stanton numbers for the accelerating boundary layer measured by Moretti and Kays [15]

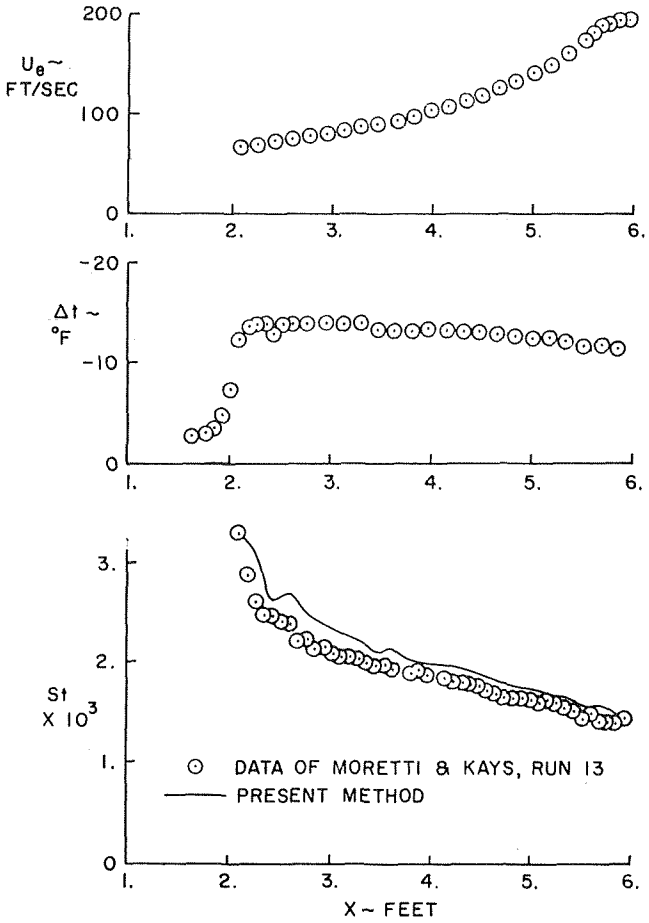

Fig. 13 Comparison of calculated and experimental Stanton numbers for the accelerating boundary layer measured by Moretti and Kays [15]

for the small oscillations that show up in the calculated values of Stanton number.

Fig. 12 also shows a comparison of the results obtained by the present method, together with those obtained by the BF method. In general, the results are in good agreement with each other. However, the present method shows the experimental trend in Stanton number better toward the end of the run.

Fig. 15 shows a comparison of calculated and experimental local Stanton numbers for the accelerating flow measured by Back and Seban [18], together with the experimental velocity distribution. The present results were obtained for a constant heat flux (data kindly supplied by Dr. Back) for a free-stream velocity of 110 fps. In this figure, the results obtained by the BF method are also included.

In general, both predictions have the same trend. Toward the end, both computed values agree well with each other. The disagreement between the results obtained by the present method and the BF method is probably due to the uncertainty in matching initial experimental conditions, since the BF method starts the computations with a lower Stanton number than the present method.

Decelerating Flows. Figs. 16 and 17 show comparisons of computed local Stanton numbers and experimental values for two decelerating flows measured by Moretti and Kays [15], together with the experimental streamwise $\Delta t(x)$ and $U_e(x)$ variations. In reference [6], Bradshaw and Ferriss also report their predictions for the flow shown in Fig. 17. For all practical purposes, their predictions agree quite well with the predictions of the present method and with experiment. It is interesting to note that Bradshaw and Ferriss report flow separation at $x \approx 8$ ft, on the basis of the linear extrapolation of the experimental velocity and temperature distributions. The same result was obtained by the present method.

Concluding Remarks

A numerical solution of the turbulent-boundary-layer equations based on a particular eddy-viscosity formulation and the assumption of a constant-turbulent Prandtl number is presented for incompressible flows with heat transfer. Several flows computed by this method show that the method is quite accurate, as it was in flows without heat transfer. It is remarkable that a simple eddy-viscosity formulation based on flat-plate data can give such satisfactory results.

The computation time of the present method is quite small. A typical flow consists of about 20 stations and can be calculated approximately in 1 min. on the IBM 360/65 digital computer.

References

1 Reynolds, W. C., "A Morphology of the Prediction Methods," *Proceedings of the 1968 Conference on Turbulent Boundary-Layer Prediction*, Stanford University, 1968.

2 Smith, A. M. O., and Cebeci, T., "Solution of the Boundary-Layer Equations for Incompressible Turbulent Flow," *Proceedings of the 1968 Heat Transfer and Fluid Mechanics Institute*, 1968, pp. 174–191.

3 Cebeci, T., and Smith, A. M. O., "A Finite-Difference Solution of the Incompressible Turbulent Boundary-Layer Equations by an Eddy-Viscosity Concept," *Proceedings of the 1968 Conference on Turbulent Boundary Layer Prediction*, Stanford University, 1968.

4 Herring, H. J., and Mellor, G. L., "A Method of Calculating Compressible Turbulent Boundary Layers," NASA CR-1144, Sept. 1968.

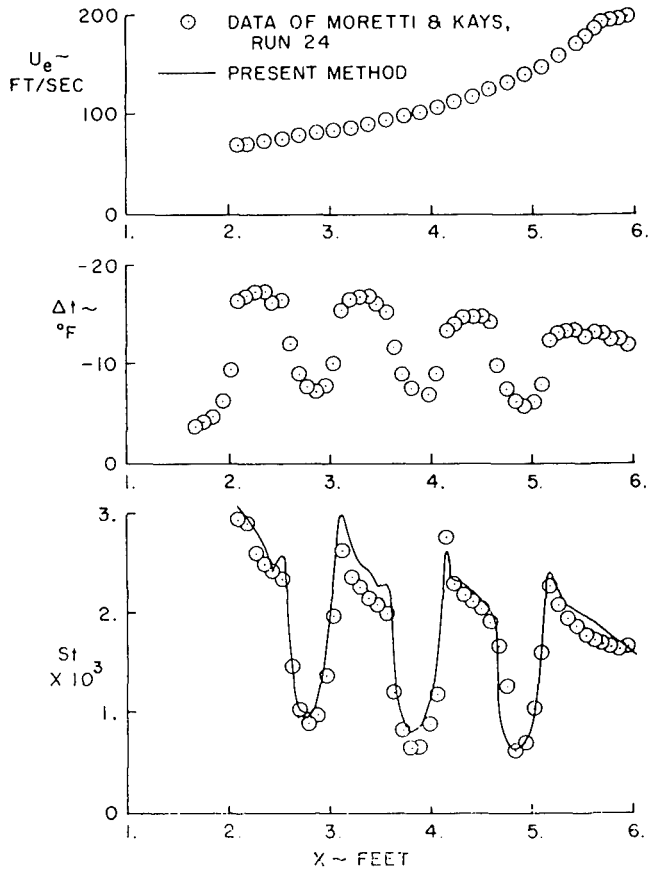

Fig. 14 Comparison of calculated and experimental Stanton numbers for the accelerating boundary layer measured by Moretti and Kays [15]

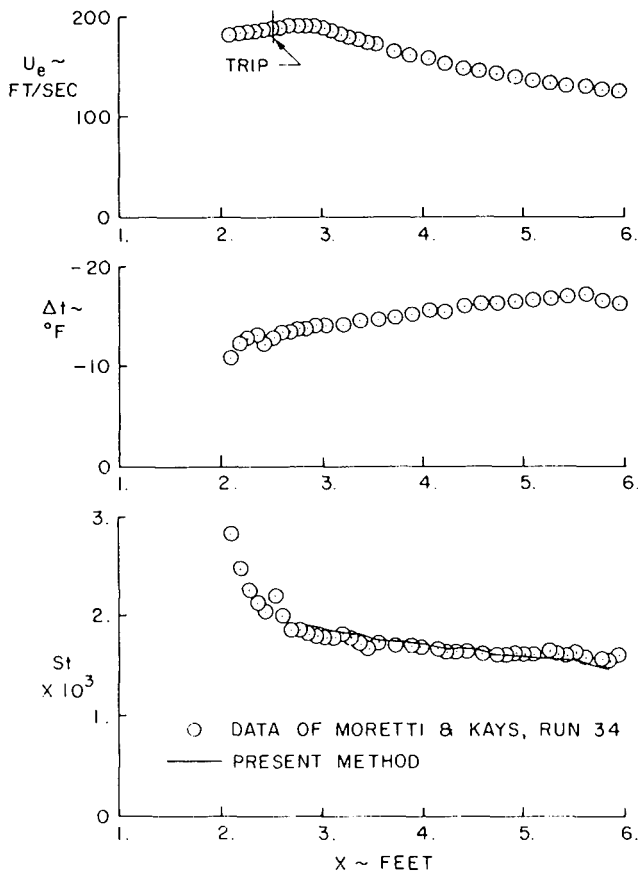

Fig. 16 Comparison of calculated and experimental Stanton numbers for the decelerating boundary layer measured by Moretti and Kays [15]

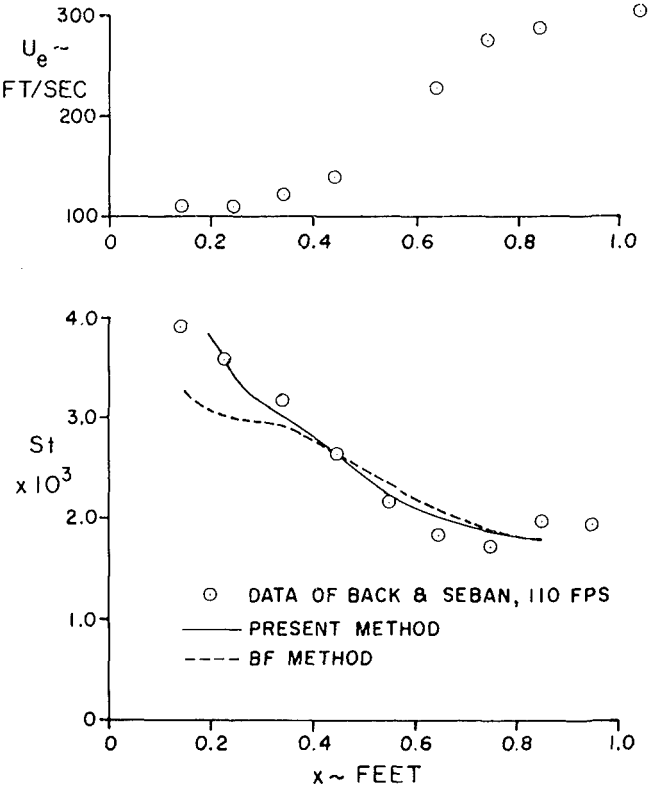

Fig. 15 Comparison of calculated and experimental Stanton numbers for the accelerating boundary layer measured by Back and Seban [18]

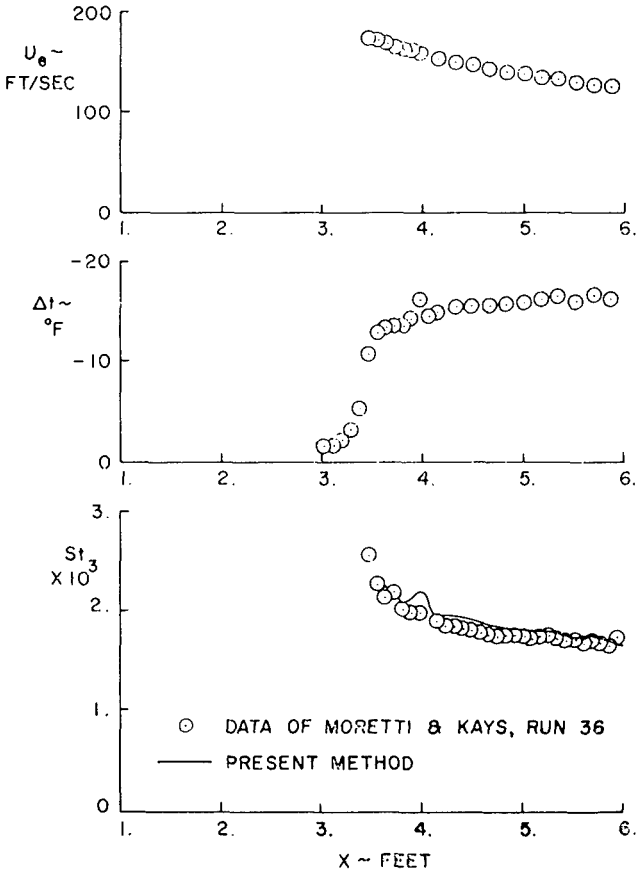

Fig. 17 Comparison of calculated and experimental Stanton numbers for the decelerating boundary layer measured by Moretti and Kays [15]

5 Patankar, S. V., and Spalding, D. B., *Heat and Mass Transfer in Boundary Layers*, C. R. C. Press, Cleveland, 1968.
6 Bradshaw, P., and Ferriss, D. H., "Calculation of Boundary-Layer Development Using the Turbulent Energy Equation—IV: Heat Transfer With Small Temperature Differences," NPL Aero Report 1271, May 1968.
7 Lin, C. C., *Turbulent Flows and Heat Transfer*, Vol. V, Princeton University Press, Princeton, N. J., 1959.
8 Van Driest, E. R., "On Turbulent Flow Near a Wall," *Journal of Aerospace Sciences*, Vol. 23, No. 11, Nov. 1956.
9 Klebanoff, P. S., "Characteristics of Turbulence in a Boundary Layer With Zero Pressure Gradient," NACA TN 3178, July 1954.
10 Probstein, R. F., and Elliott, D., "The Transverse Curvature Effect in Compressible Axially Symmetric Laminar Boundary-Layer Flow," *Journal of Aerospace Sciences*, Mar. 1956.
11 Hayes, W. D., and Probstein, R. F., *Hypersonic Flow Theory*, Academic Press, New York, and London, 1959, p. 290.
12 Cebeci, T., Smith, A. M. O., and Wang, L. C., "A Finite-Difference Method for Calculating Compressible Laminar and Turbulent Boundary Layers," Douglas Aircraft Company Report DAC 67131, 1969.
13 Reynolds, W. C., Kays, W. M., and Kline, S. J., "Heat Transfer in the Turbulent Incompressible Boundary Layer—I: Constant Wall Temperature," NASA MEMO 12-1-58W, Dec. 1958.
14 Seban, R. A., and Doughty, D. L., "Heat Transfer to Turbulent Boundary Layers With Variable Free-Stream Velocity," TRANS. ASME, Vol. 78, Jan. 1956, pp. 217–223.
15 Moretti, P. M., and Kays, W. M., "Heat Transfer Through an Incompressible Turbulent Boundary Layer With Varying Free-Stream Velocity and Varying Surface Temperature," Department of Mechanical Engineering, Stanford University, Report No. PG-1.
16 Reynolds, W. C., Kays, W. M., and Kline, S. J., "Heat Transfer in the Turbulent Incompressible Boundary Layer—II: Step Wall-Temperature Distribution," NASA MEMO 12-2-58W, Dec. 1958.
17 Reynolds, W. C., Kays, W. M., and Kline, S. J., "Heat Transfer in the Turbulent Incompressible Boundary Layer—III: Arbitrary Wall Temperature and Heat Flux," NASA MEMO 12-3-58W, Dec. 1958.
18 Back, L., and Seban, R. A., "Flow and Heat Transfer in a Turbulent Boundary Layer With Large Acceleration Parameter," *Proceedings, 1967 Heat Transfer and Fluid Mechanics Institute*, Stanford University, 1967.

5 Patankar, S. V., and Spalding, D. B., *Heat and Mass Transfer in Boundary Layers*, C. R. C. Press, Cleveland, 1968.
6 Bradshaw, P., and Ferriss, D. H., "Calculation of Boundary-Layer Development Using the Turbulent Energy Equation—IV: Heat Transfer With Small Temperature Differences," NPL Aero Report 1271, May 1968.
7 Lin, C. C., *Turbulent Flows and Heat Transfer*, Vol. V, Princeton University Press, Princeton, N. J., 1959.
8 Van Driest, E. R., "On Turbulent Flow Near a Wall," *Journal of Aerospace Sciences*, Vol. 23, No. 11, Nov. 1956.
9 Klebanoff, P. S., "Characteristics of Turbulence in a Boundary Layer With Zero Pressure Gradient," NACA TN 3178, July 1954.
10 Probstein, R. F., and Elliott, D., "The Transverse Curvature Effect in Compressible Axially Symmetric Laminar Boundary-Layer Flow," *Journal of Aerospace Sciences*, Mar. 1956.
11 Hayes, W. D., and Probstein, R. F., *Hypersonic Flow Theory*, Academic Press, New York, and London, 1959, p. 290.
12 Cebeci, T., Smith, A. M. O., and Wang, L. C., "A Finite-Difference Method for Calculating Compressible Laminar and Turbulent Boundary Layers," Douglas Aircraft Company Report DAC 67131, 1969.
13 Reynolds, W. C., Kays, W. M., and Kline, S. J., "Heat Transfer in the Turbulent Incompressible Boundary Layer—I: Constant Wall Temperature," NASA MEMO 12-1-58W, Dec. 1958.
14 Seban, R. A., and Doughty, D. L., "Heat Transfer to Turbulent Boundary Layers With Variable Free-Stream Velocity," TRANS. ASME, Vol. 78, Jan. 1956, pp. 217–223.
15 Moretti, P. M., and Kays, W. M., "Heat Transfer Through an Incompressible Turbulent Boundary Layer With Varying Free-Stream Velocity and Varying Surface Temperature," Department of Mechanical Engineering, Stanford University, Report No. PG-1.
16 Reynolds, W. C., Kays, W. M., and Kline, S. J., "Heat Transfer in the Turbulent Incompressible Boundary Layer—II: Step Wall-Temperature Distribution," NASA MEMO 12-2-58W, Dec. 1958.
17 Reynolds, W. C., Kays, W. M., and Kline, S. J., "Heat Transfer in the Turbulent Incompressible Boundary Layer—III: Arbitrary Wall Temperature and Heat Flux," NASA MEMO 12-3-58W, Dec. 1958.
18 Back, L., and Seban, R. A., "Flow and Heat Transfer in a Turbulent Boundary Layer With Large Acceleration Parameter," *Proceedings, 1967 Heat Transfer and Fluid Mechanics Institute*, Stanford University, 1967.

DISCUSSION

B. E. Launder[3]

The writer agrees with the authors that it is now computationally feasible and economically desirable to employ finite-difference procedures to predict heat transfer rates in boundary-layer flows.

Moreover, because the partial-differential equations can, with care, be solved to a high degree of accuracy, one can focus attention on the model of turbulence which is employed. It thus seems unfortunate that, by the use of equation (11), the authors have managed to get mathematical approximation entangled with physical hypothesis. The point is that, having chosen the Spalding-Patankar version of the van Driest function, i.e.:

$$A = 26\nu(\tau/\rho)^{-1/2}$$

they then approximate the shear stress appearing in the foregoing expression by

$$\tau = \tau_w + \frac{dp}{dx} \cdot y$$

(which is the authors' equation (11)). Equation (11) is correct only when convection is absent such as in fully developed flow between parallel planes. In many external boundary-layer flows the consequences of using equation (11) (rather than the exact value of τ) will not be important because the exponential term in equation (10) is negligible outside the sublayer—and across the sublayer itself equation (11) is often an adequate approximation. In strong accelerations, however, convective terms are known to be substantial even within the region where viscous stresses are important (e.g., Patel and Head [19][4]) and, consequently, the shear stress implied by equation (11) will be significantly too small. Indeed, it would seem likely that, for Moretti and Kays' run 12 (displayed in Fig. 12), the shear stress implied by equation (11) would fall to zero—or worse, become negative—within that region of the boundary layer where equation (10) was used.

The writer has made extensive boundary-layer calculations of strongly accelerated flows [20] with the same inner law as the authors except that the shear stress used in the calculation of A was that obtained from the finite-difference procedure itself. When this exact value of τ is used, the model does not give rise to the substantial drop in Stanton number shown by the authors in Fig. 12.

Superficially, the foregoing finding might suggest that it is preferable to use the authors' equation (11) rather than τ itself. However, to predict with confidence the complex structural changes which occur in strongly accelerated boundary layer is not an easy task. Some progress has been made (e.g., references [20–22]) but much remains to be done. To develop an adequate model of turbulence for such flows, it is imperative that any predictions should display the implications of the model alone and not those associated with mathematical approximation.

Additional References

19 Patel, V. C., and Head, M. R., "Reversion of Turbulent to Laminar Flow," *Journal of Fluid Mechanics*, Vol. 34, p. 371.
20 Jones, W. P., and Launder, B. E., "On the Prediction of Laminarescent Boundary Layers," ASME Paper No. 69-HT-13.
21 Launder, B. E., and Jones, W. P., "A Note on Bradshaw's Hypothesis for Laminarization," ASME Paper No. 69-HT-12.
22 Kays, W. M., Moffat, R. J., and Thielbahr, W. H., "Heat Transfer to the Highly Accelerated Turbulent Boundary Layer With and Without Mass Addition," ASME Paper No. 69-HT-53.

Chang-Keng Liu[5]

The authors are to be congratulated in providing still one more prediction method of the heat transfer in turbulent boundary layer. The usual boundary-layer approximations and assumptions were used and good agreement with experimental data was obtained with quite small computation time. These good results were obtained even in the pressure-gradient case in spite of the use of simple eddy-viscosity formulation based on flat-plate data.

One question from this discusser arises from the approximated formula of the intermittency factor given in equation (15). In Fig. 18, which is reproduced from Fig. 11 of reference [23],[6] equation (15) as plotted in the dotted line and added therein is seen to be much lower than the Gaussian distribution plotted in the solid line. Obviously, the modified value of the eddy viscosity in the outer region will be too low.

This brings up another question, i.e., the value of k_2 in equation (14). By dimensional arguments and based on test data of previous investigators, the value of k_2 was estimated by Clauser [24] to be 0.018 but by Rotta [25] to be 0.022. Recent investigation [26] showed that k_2 in the smooth wall case is approximately 0.024 ± 0.002. The value of 0.0168 used by the authors made the value of eddy viscosity in the outer layer much lower, after being modified by the already lower distribution of the intermittency factor.

However, the agreement between the proposed prediction method and most of the experimental data is surprisingly good in turbulent boundary-layer flows with and without longitudinal

[3] Department of Mechanical Engineering, City and Guilds College, Imperial College of Science and Technology, London, England. Mem. ASME.

[4] Numbers in brackets designate Additional References at end of Discussion.

[5] Member, Aerospace Sciences Laboratory, Lockheed Palo Alto Research Laboratory, Palo Alto, Calif.

[6] Numbers in brackets designate Additional References at end of Discussion.

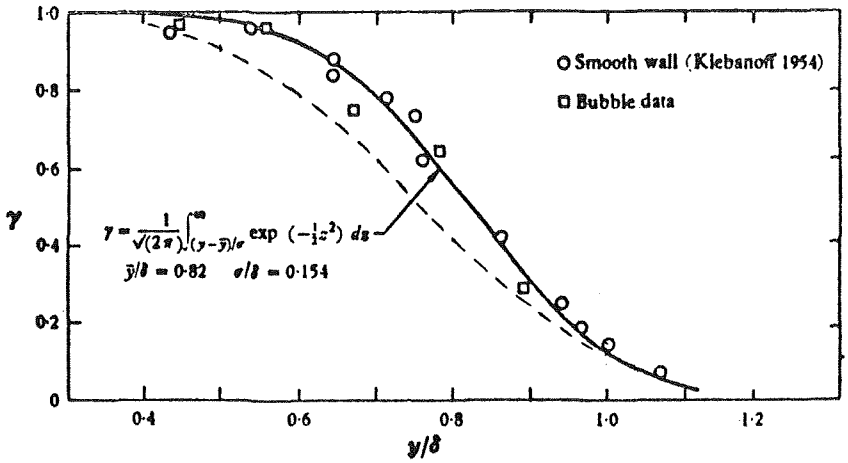

Fig. 18 Intermittency distribution by the bubble technique

pressure gradient. It will be interesting to know what effect some higher values of eddy viscosity and the intermittency factor distribution in the outer region of the boundary layer will have on the results of the present prediction method, particularly on the disagreement shown in Figs. 12 and 13.

Additional References

23 Kline, S. J., et al., "The Structure of Turbulent Boundary Layers," *Journal of Fluid Mechanics*, Vol. 30, Part 4, 1967, pp. 741–773, Fig. 11.

24 Clauser, F. H., "The Turbulent Boundary Layer," *Advances in Applied Mechanics*, Vol. LV, Academic Press, N. Y., 1956.

25 Rotta, J. C., "Turbulent Boundary Layers in Incompressible Flow," *Part I of Progress in Aeronautical Science*, Vol. 2, ed., Ferri, A., Pergamon Press, 1962.

26 Liu, C. K., "An Experimental Study of Turbulent Boundary Layer on Rough Walls," 1966, PhD dissertation, Mechanical Engineering Department, Stanford University.

Authors' Closure

Comments to Dr. B. E. Launder's Discussion

With respect to entangling mathematical approximation and physical hypothesis, we are not sure what Dr. Launder means. In the obscure field of turbulent boundary layers it seems to us that mathematical approximation and physical hypothesis should work hand in hand. One is desperately trying to penetrate the problem and any lead not obviously in violation of physical knowledge should receive serious consideration. No theory is much weaker than Prandtl's original derivation of the log law, but it works. That is our main defense. Our proof lies not in a few test cases but in many, as reported in this paper as well as in reference [3].

In interpreting the constant A appearing in Van Driest's expression

$$A = 26\nu \left(\frac{\tau_w}{\rho}\right)^{-1/2} \tag{33}$$

for flows with pressure gradient, we have several possibilities. One possibility is to use the local value of τ rather than its wall value (as it was first suggested by Spalding and Patankar and later adopted by several investigators) and write equation (33) as

$$A = 26\nu \left(\frac{\tau}{\rho}\right)^{-1/2} \tag{34}$$

Another possibility is to replace the value of τ appearing in equation (34) by the expression given by equation (12) which is obtained from the momentum equation applied very close to the wall, namely,

$$A = 26\nu \left(\frac{\tau_w}{\rho} + \frac{dp}{dx}\frac{y}{\rho}\right)^{-1/2} \tag{35}$$

Obviously, equations (34) and (35) are not the same. Equation (34) is written in a form that removes the singularity at separation that equation (33) has. If it does not give good agreement, as our expression does, this is not because equation (34) has "physical" hypothesis but bad assumptions! In writing the expression given by equation (35), we have assumed that the characteristic velocity which Van Driest assumed to be the friction velocity is affected by a "pressure" velocity which is given by $\sqrt{(dp/dx)(y/\rho)}$. Calculations, including the pressure gradient term in the exponential term of Van Driest's formula, so far give good agreement for a large number of flows. As an example we have calculated the accelerating flow measured by Back and Seban [18] with and without the pressure-gradient term in the damping constant. Results shown in Fig. 19 indicate the marked effect of the pressure-gradient term.

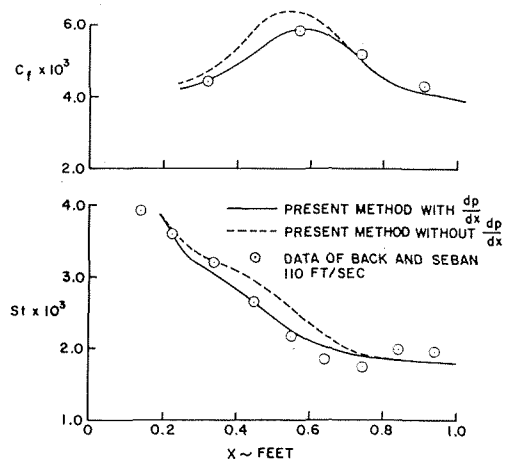

Fig. 19 Comparison of calculated and experimental results for Back and Seban's data [18]. Calculations were made with and without the pressure-gradient term in the damping constant

We also would like to point out that the approach used to modify the damping constant by using the momentum equation has also worked very well for turbulent flows with mass transfer. See references [27 and 28]. In this case the momentum equation was again written very close to the wall as

$$\frac{d\tau}{dy} - \frac{v_w}{\nu}\tau = \frac{dp}{dx} \tag{36}$$

which led to a damping constant given by

$$A^+ = 26\left\{-\frac{p^+}{v_w{}^+}\left[\exp(11.8\,v_w{}^+) - 1\right] + \exp(11.8\,v_w{}^+)\right\}^{-1/2} \tag{37}$$

where

$$p^+ = -\frac{dp}{dx}\frac{\nu}{\rho(u^*)^3}, \qquad v_w{}^+ = \frac{v_w}{u^*} \tag{38}$$

Fig. 20 shows our derived deviation of damping constant A^+ with blowing parameter $\sqrt{2/c_f}v_w{}^+$. The experimental values of A^+ were obtained from the data of Simpson, et al. [29], and Kendall [30], and were reported in reference [31] by Bushnell and Beckwith. The figure also shows the curve faired to the experimental data used by Bushnell and Beckwith, together with the results obtained from equation (37) for zero pressure gradient. The skin-friction values for equation (37) were obtained from Simpson's data [29] for blowing and from Tennekes' data [32] for suction. The agreement between equation (37), the experimental data, and the faired curve is very good for blowing parameter up to 14. For larger blowing parameters, the calculated A^+ values deviate from the faired curve used by Bushnell and Beckwith, but seem to agree reasonably well with experimental data except for one value.

Finally, should one include the convective terms in the damping constant? This is a good question and may be worth studying. On the other hand, according to the data of Back [33], the convective terms are quite small in comparison with the pressure-gradient term. If we write the incompressible momentum equation for two-dimensional flows in the form

$$u\frac{\partial u}{\partial x} + v\frac{\partial u}{\partial y} = -\frac{1}{\rho}\frac{dp}{dx} + \frac{\partial}{\partial y}(\tau/\rho) \tag{39}$$

it can be shown by direct integration that equation (39) can be written as

$$\frac{\tau}{\tau_0} = 1 - \frac{u_e(du_e/dx)}{(u^*)^2}y_1 + \frac{1}{2(u^*)^2}\frac{d}{dx}\int_0^{y_1} u^2dy - \frac{u}{(u^*)^2}\frac{d}{dx}\int_0^{y_1} udy + \frac{1}{2}\left(\frac{u}{u^*}\right)^2\frac{dy_1}{dx} \tag{40}$$

Taking y_1 as the distance from the wall where $y^+ = 30$ and using the experimental velocity profile to evaluate the integrals, Back found the result corresponding to the terms in equation (40) that

$$\frac{\tau_y{}^+ = 30}{\tau_0} = 1 - 0.17 - 0.004 + 0.025 - 0.034 = 0.82 \tag{41}$$

which indicates that the last three terms on the right side of equation (40) are negligibly small, with the only significant term being the one involving the pressure gradient.

Comments to Dr. Chang-Keng Liu's Discussion

The intermittency factor we use in the outer eddy viscosity formula has very little effect on the calculated results. For this reason, if the outer eddy viscosity becomes a little low, this will barely affect the results. As a matter of fact, calculations with and without equation (15) give almost identical results.

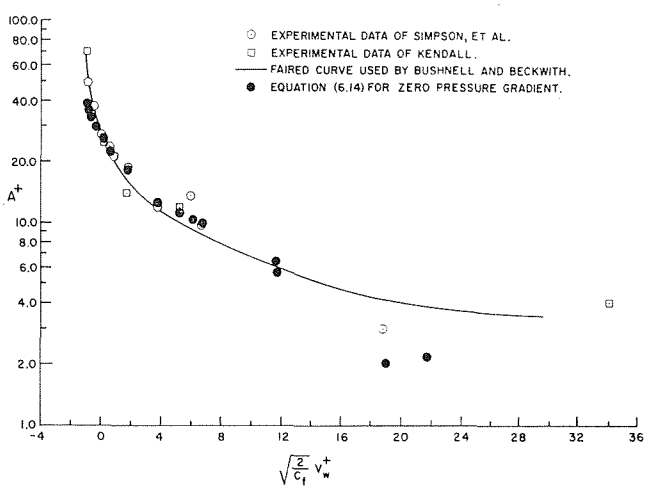

Fig. 20 Comparison of calculated and experimental damping constants for a flat-plate flow with mass transfer

The value of k_2 in the outer eddy viscosity expression varies with pressure gradient, although we assume it to be constant and equal to 0.0168. A better expression for the outer eddy viscosity should be

$$\epsilon_0 = \alpha u_e(x)\delta^*(x) \tag{42a}$$

where

$$\alpha = \alpha(x, dp/dx) \tag{42b}$$

This is not surprising because, as the flow approaches separation conditions, the outer region becomes larger, which means that the switching point between the eddy viscosity formulas, which occurs about 20 percent of the boundary layer for flat-plate flows, should become smaller. This would mean a higher α, or a variable α. The facts of the matter are that the subject constants were selected in 1963 and results agree so well with experiment that there has been no inclination to change them.

References

27 Cebeci, T., "The Behavior of Turbulent Flow Near a Wall," Douglas Report No. DAC 70014, 1969.

28 Cebeci, T., and Mosinskis, G., "Calculation of Heat and Mass Transfer in Turbulent Flows at Low Mach Numbers," Douglas Report No. DAC 70015, 1969.

29 Simpson, R. L., Kays, W. M., and Moffat, R. J., "The Turbulent Boundary Layer on a Porous Plate: An Experimental Study of the Fluid Dynamics With Injection and Suction," Report No. HMT-2, Stanford University, 1967.

30 Kendall, R. M., Rubesin, M. W., Dahm, T. J., and Mendenhall, M. R., "Mass, Momentum, and Heat Transfer Within a Turbulent Boundary Layer With Foreign Gas Mass Transfer at the Surface. Part 1—Constant Fluid Properties," Report No. 111, Vidya, Division of Itek Corp., Feb. 1964.

31 Bushnell, D. M., and Beckwith, I. E., "Calculation of Nonequilibrium Hypersonic Turbulent Boundary Layers and Comparisons With Experimental Data," AIAA Preprint No. 69-684.

32 Tennekes, H., "Similarity Laws for Turbulent Boundary Layers With Suction or Injection," Report VTH-119, Technological University, Delft, Dec. 1964.

33 Back, L. H., "Heat Transfer to Turbulent Boundary Layers With a Variable Free-Stream Variable," PhD thesis, Mechanical Engineering Department, University of California at Berkeley, 1962.

A. A. NICOL
Department of Mechanical Engineering,
University of Strathclyde,
Glasgow, Scotland;
Formerly,
Department of Mechanical Engineering,
University of Windsor,
Ontario, Canada

M. GACESA
Development Engineer,
Canadian Westinghouse Co., Ltd.,
Hamilton, Ontario, Canada.
Assoc. Mem. ASME

Condensation of Steam on a Rotating Vertical Cylinder

Heat transfer coefficients have been determined for steam condensing on a 1-in-dia vertical tube, rotating on its axis. The condensing heat transfer coefficients increased with speed of rotation and for the maximum rotational speed of 2700 rpm investigated, were found to be four or five times the stationary value. When the results were plotted in terms of the pertinent parameters of Nusselt number and Weber number, the Nusselt number was found to be constant for Weber numbers below 500, and above this the correlating equation was $N_{Nu_A} = 6.13\, N_{We}^{0.496}$.

Introduction

With the advent of space-age technology considerable interest has been shown in the effect of accelerations other than that of gravity on heat transfer systems. In this paper high heat transfer coefficients have been obtained by condensing steam on a vertical cylinder rotating on its axis, and the increase in heat transfer is attributed to the film being thrown off due to the centrifugal force acting on it.

Birt, et al. [1],[1] obtained heat transfer coefficients for steam condensing on the outside of a vertical 8.48-in-dia rotor. Their main interest, however, was in the overall heat transfer from steam to cooling water, and the steam side heat transfer coefficients were obtained from one thermocouple embedded at an unspecified location in the wall. They reported high condensation heat transfer coefficients ranging from 3000–9000 Btu/hr ft deg F, for centrifugal accelerations up to 70 g's. Yeh [2] carried out work on a horizontally rotating cylinder cooled on the inside by water and enclosed in a steam chamber. He discovered that the flow and heat transfer characteristics of the system went through three phases. At low rotational speeds the centrifugal force and the friction force between the shaft and the condensate film tended to counteract the force of gravity, causing in some instances carryover of the condensate and a reduction in heat transfer. The second phase occurred at higher rotational speeds when the liquid was sprayed off the cylinder making the liquid film thinner and giving an increase in the heat transfer rate. At high rotational speeds the film became very thin and droplets appeared which elongated and eventually became streaks. During this last phase the heat transfer rate became progressively smaller.

Singer and Preckshot [3] carried out heat transfer measurements on an apparatus similar to Yeh's but with some modifications. An interesting point in their technique was the fact that they did not measure the temperature on the rotating shaft, thereby obviating any problems which might have been encountered using slip rings. They measured the overall temperature drop between the cooling water and the steam atmosphere by means of stationary probes and knowing the heat flux from the water flow and temperature rise measurement, they calculated the overall heat transfer coefficient. By determining the water side heat transfer coefficient using the results of Kuo, et al. [4], they were then able to estimate the steam side coefficient. They also reported the presence of the three regimes described by Yeh and gave physical models and theoretical estimates of the heat transfer for two of the regions. At high rotational speeds they predicted that $N_{Nu} = f\, N_{We}^{0.5}$, a result of interest to this paper which will be referred to in the discussion section.

Recently, Hoyle and Matthews [5, 6] investigated the effect of diameter size as well as the speed of rotation on the transfer of heat from steam to horizontally mounted, water-cooled cylinders. The cylinders used in their study were 4, 8, and 10-in. outside diameters and provision was made for measuring the cylinder surface temperatures. Based on photographic studies they contended that the condensate layer was in laminar flow throughout. When their results were compared with those of Yeh, and Singer and Preckshot they differed in the respect that no decrease in heat transfer over the high range of Weber number was obtained.

In the present paper steam was condensed on the outside of a 1-in-dia tube and provision was made for measuring wall temperatures at a number of locations on the tube surface. The vertical geometry was chosen to make the problem more symmetrical in the lower regions of Weber number than is the case with the horizontal tube, and rotational speeds of up to 2700 rpm, corresponding to a Weber number of 5000, were investigated.

[1] Numbers in brackets designate References at end of paper.

Contributed by the Heat Transfer Division of The American Society of Mechanical Engineers and presented at the ASME-AIChE Heat Transfer Conference, Minneapolis, Minn., August 3–6, 1969. Manuscript received by the Heat Transfer Division, May 13, 1968; revised manuscript received, April 8, 1969. Paper No. 69-HT-36.

Nomenclature

d = distance from root of test section, ft

D = external diameter of condenser tube, ft

g = gravitational constant, ft/hr²

h_m = mean heat transfer coefficient, Btu/hr ft² deg F

k_A = thermal conductivity of water at atmospheric pressure, Btu/hr ft deg F

k_f = thermal conductivity of condensate, Btu/hr ft deg F

L = length of test section, ft

$N_{Nu} = \dfrac{h_m D_0}{k_f}$ = Nusselt number

$N_{Nua} = \dfrac{h_m D_0}{2k_A}$ = Nusselt number

$N_{We} = \dfrac{\rho_f \omega^2 D_0^3}{4\sigma g}$ = Weber number

ΔT = temperature difference across condensate film, deg F

T_0 = condenser surface temperature deg F

ρ_f = specific weight of condensate, lb/ft³

σ = surface tension, lb/ft

ω = angular velocity, 1/hr

λ = latent heat of vaporization, Btu/lb

ν = kinematic viscosity, ft²/hr

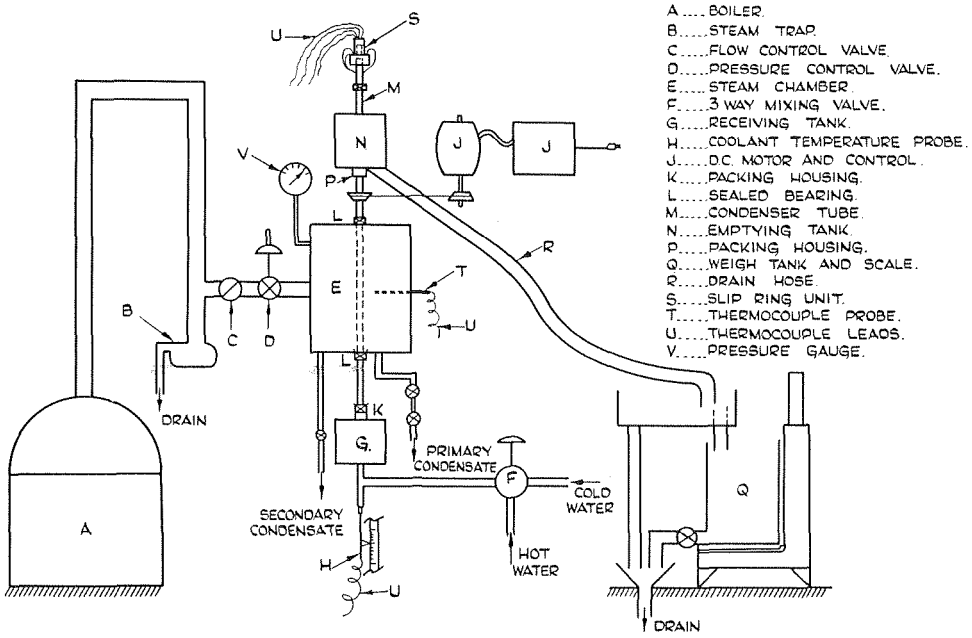

Fig. 1 Schematic layout of experimental rig

Apparatus and Instrumentation

Since the investigation was primarily experimental in nature the important aspects of the apparatus, namely, the steam chamber and the condenser tube will be described in some detail. The ancillary equipment such as the steam supply, cooling water mixer, etc., will be described more briefly with reference to Fig. 1.

The steam was supplied by an automatic boiler (A) which had a pressure range of 0–125 psig and was led to the steam chamber (E), through a flow control valve (C) and a pressure regulating valve (D). A condensate trap (B) was installed at the low point in the pipework to drain off any condensate in the system.

The cooling water leaving the three-way mixing valve (F) was mixed further by means of baffles in the receiving tank (G). The receiving tank also served as the anchoring base for the packing housing (K), a bearing (L), and the housing for the cold water temperature probe (P). From the receiving tank the cooling water entered the condenser tube from which it was ejected through three radial holes into the emptying tank (N). The temperature of the cooling water at any position inside the condenser tube could be measured with the probe (H) which contained a copper constantan thermocouple.

The position of the steam chamber with respect to the other equipment is shown in Fig. 1, and the details of it are shown in Fig. 2. The chamber consisted of two concentric boxes; each box was made in two halves and put together by means of vertical flanges with the inner box secured to the outer. Steam entered the outer box through the opening in one side and was deflected by a baffle so that it diffused evenly through all four sides of the inner box. Louvres covering the slots were installed to prevent droplets of condensate from being thrown from the tube and out through the slots. Steam that condensed on the walls of the outer box was drained through the secondary condensate outlet and discarded, and the condensate which formed on the condenser tube was collected and weighed at the primary condensate outlet.

A section of the condenser tube is shown in detail in Fig. 3. The aluminium tube was 1-in. OD $\times$ $^1/_4$-in. wall $\times$ 4 ft. long, and three grooves $^1/_8$ in. $\times$ $^1/_8$ in. were milled on the outside at 120-deg intervals. At the test section part of the tube, 10 circumferential slots were ground, perpendicular to each groove, approximately $^1/_{16}$ in. wide and such that the bottom of the slot was the same depth as the groove at the point of intersection. Holes 0.40-in. dia were drilled at the end of the slots and emerged from the surface $^3/_{32}$ in. beyond the slot. Copper-constantan thermocouples were then placed in the slots and holes, with the junction as close to the surface as possible. The grooves were then filled with an aluminium filler and the surface was rubbed smooth. When this had hardened, two aluminium disks were then fitted to the tube, one at either end of the test section and 10-in. apart. These disks effectively defined the test section and also prevented leakage of condensate into or out of the inner box. The disks were insulated from the tube by means of Teflon sleeves to minimize errors due to condensation on the disks themselves and the tube was then installed in the steam chamber.

Since the slip ring unit available had only 10 rings, the leads from 9 representative thermocouples were attached to it. All the copper leads were soldered together and attached to a single lead on the ring side of the slip ring unit. The nine constantan leads were attached singly to the remaining 9 positions on the unit. The outputs from the slip ring assembly and from the other stationary thermocouples were measured to an accuracy of $1\mu V$ using a potentiometer.

Experimental Procedure

During assembly of the apparatus, the outside surface of the condenser tube was thoroughly cleaned using steel wool, then polished using abrasive powder and finally washed with alcohol. At the beginning of each experiment the equipment was operated under test conditions for some time before readings were taken to insure that a steady state existed. The steam pressure at the boiler was adjusted so that when the steam was throttled to the test conditions of 6.3 $lb_f/in.^2$ g it was superheated by 2 deg F.

The cooling water temperature was measured at a number of points along the test section by means of a copper-constantan thermocouple inserted in a 0.0625-in-OD $\times$ 0.048-in-ID stainless-steel tube. This traveling thermocouple arrangement was installed in the condenser tube as shown in Fig. 1.

A small propeller, 1 in. from the thermocouple junction, was attached to the stainless-steel tube to insure thorough mixing of the cooling water as it passed over the thermocouple. A number of vane devices were tried before satisfactory results were obtained with the propeller.

The cooling water and condensate flow rates were measured by collecting the quantities involved. Seventy-six experiments

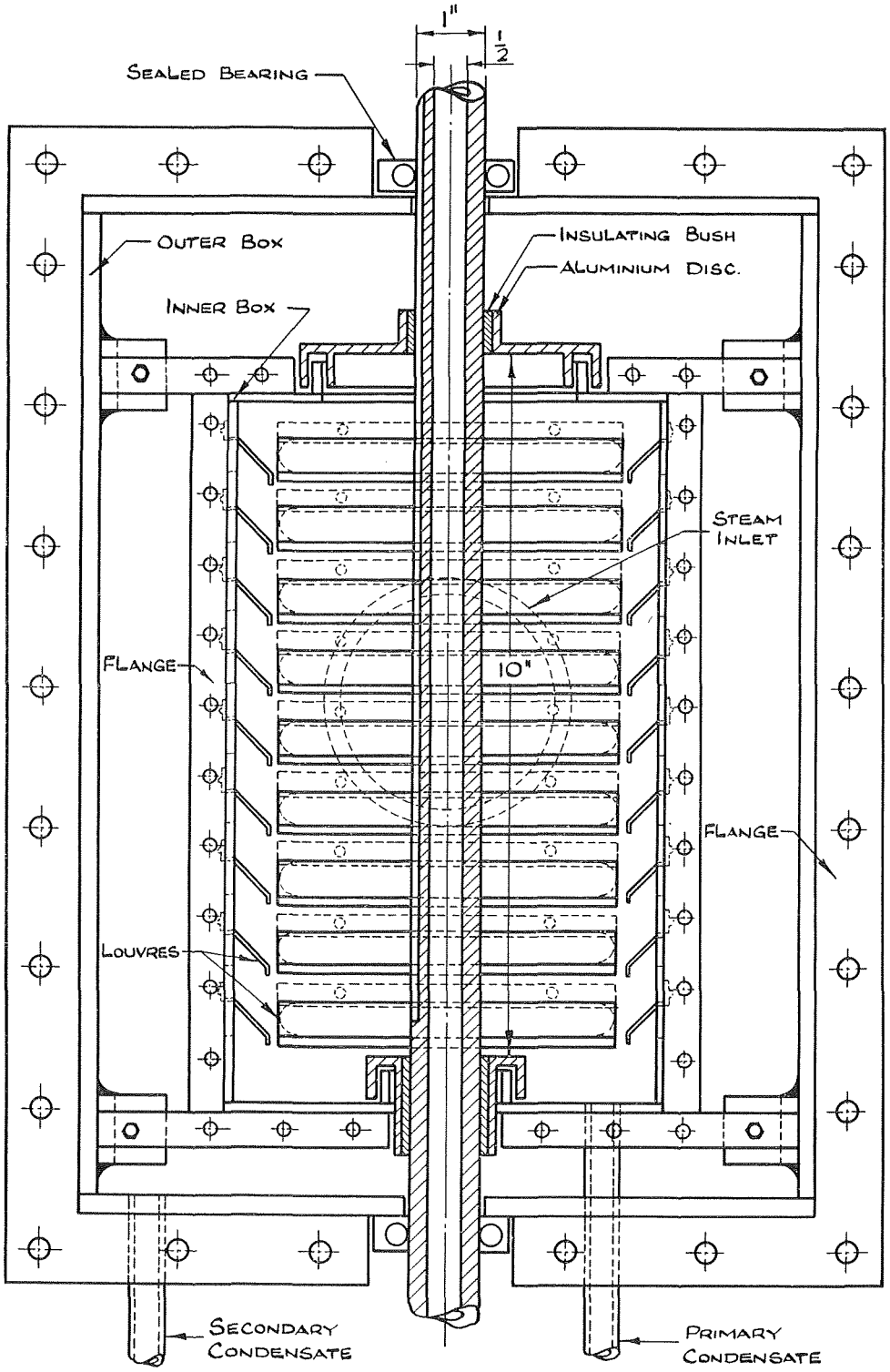

Fig. 2 Detail of steam chamber

were performed, varying the rotational speed from 0–2700 rpm and the cooling water temperature and flow from 45 deg F to 120 deg F and 3600 lb/hr to 7200 lb/hr, respectively.

Results and Discussion

Condenser surface temperatures for three rotational speeds are shown in Fig. 4. In these runs the coolant flow rate and inlet temperature were maintained at approximately 3600 lb/hr and 43 deg F, respectively. As the speed of rotation increases a definite increase in surface temperature occurs which can be taken as a good qualitative measure of the change in the condensing heat transfer coefficient since the heat load increases only slightly over this speed range.

Originally, it was intended to obtain local as well as overall heat transfer coefficients from the apparatus. But although Fig. 4 shows a marked increase in the surface temperature with speed, the end effects, shown by the falling end temperatures in the static case, were thought to be too severe to permit the cal-

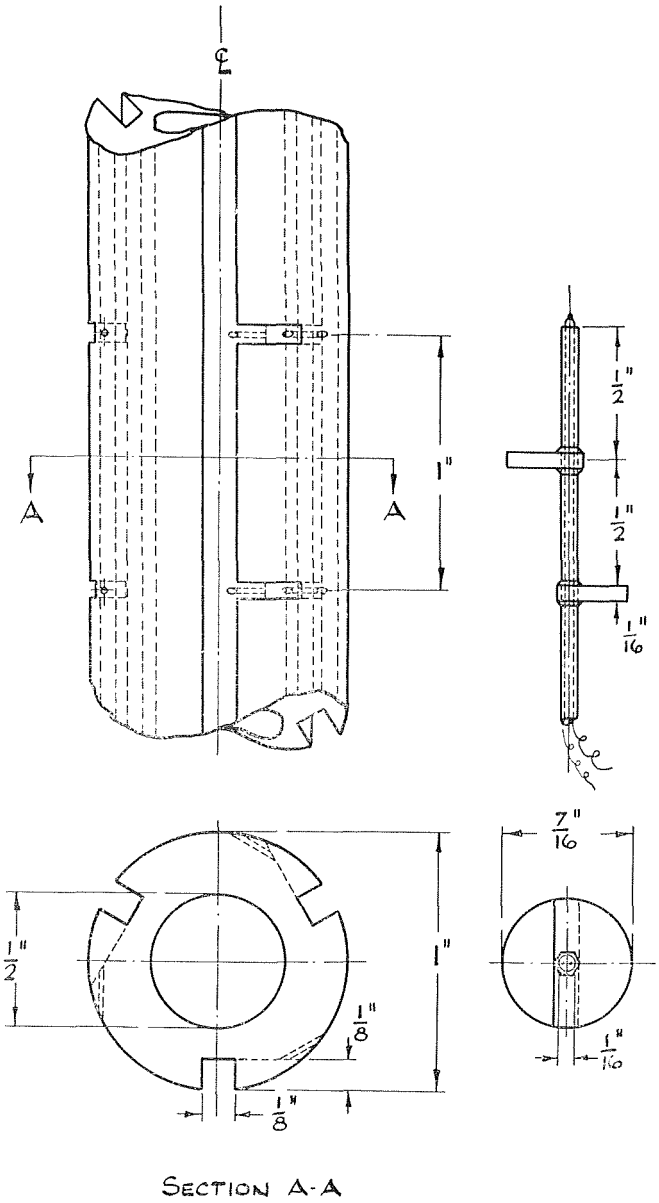

Fig. 3 Details of wall thermocouples and cooling water temperature probe

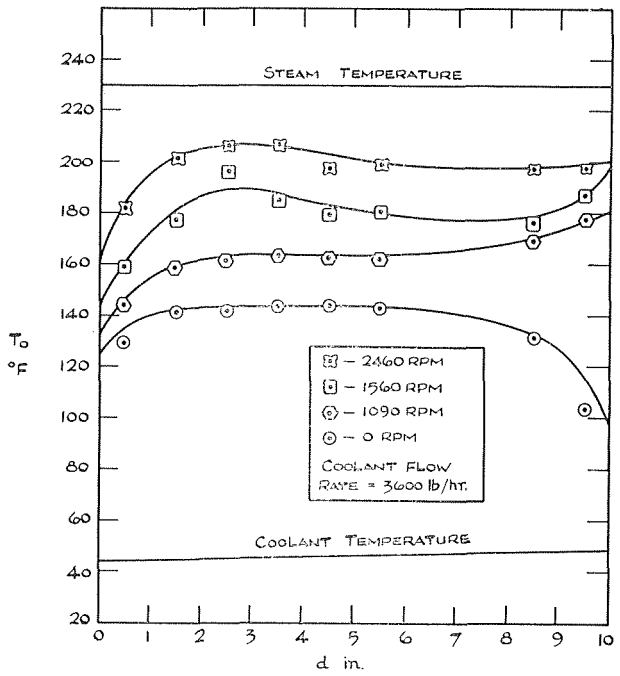

Fig. 4 Variation of condenser surface temperature with distance from bottom of test section

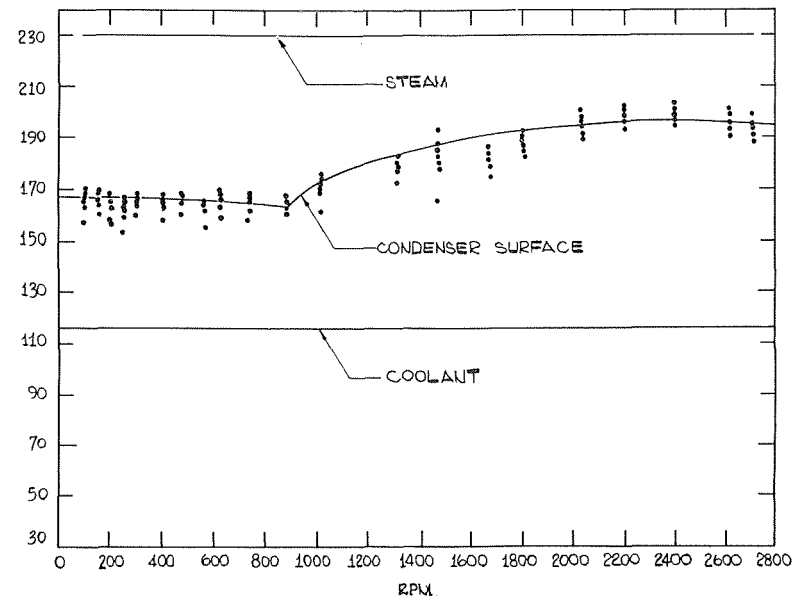

Fig. 5 Variation of condenser surface temperature with rotational speed for a coolant flow rate of 4800 lb/hr

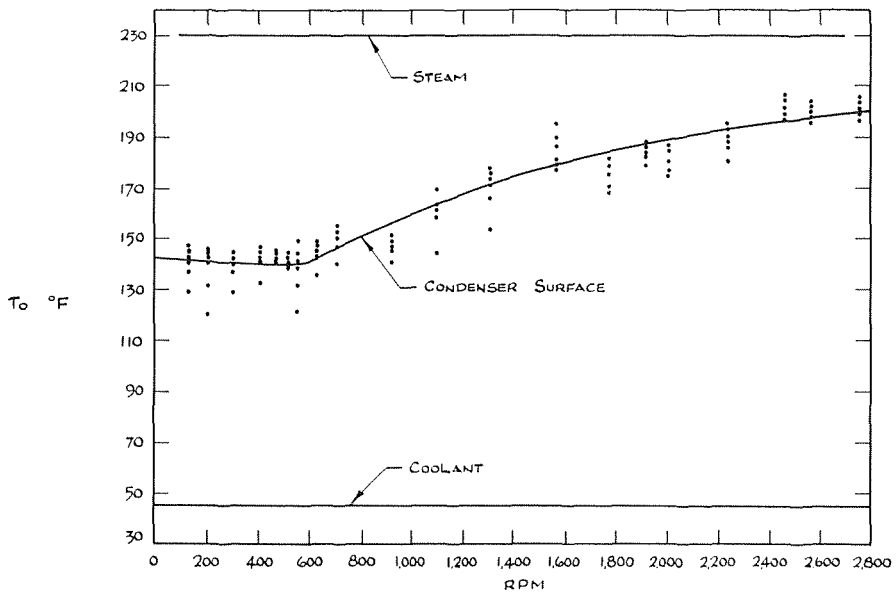

Fig. 6 Variation of condenser surface temperature with rotational speed for a coolant-flow rate of 3600 lb/hr

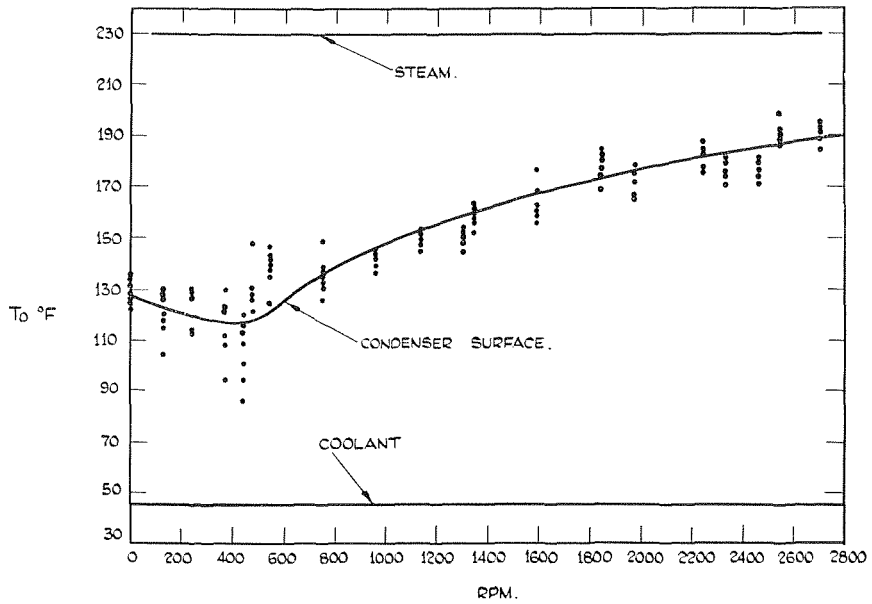

Fig. 7 Variation of condenser surface temperature with rotational speed for a coolant flow rate of 7200 lb/hr

culation of meaningful local coefficients. However, over the major part of the condenser surface, the surface temperature was consistent and the heat transfer coefficient and Nusselt number were based on the average surface temperature.

All the data are shown in Figs. 5–7, where each diagram represents one series of tests in which the cooling water inlet conditions were maintained essentially constant. The steam and coolant inlet temperatures are also shown. The exact flow rates, surface, and cooling water temperatures were reported in the work by Gacesa [7].

As in the discussion of the previous figure the increase in surface temperature with increasing rotational speed can only be used as a qualitative indication of the condensing heat transfer coefficient, since the cooling water outlet temperature changes slightly with increasing rotational speed. The shape of the curve drawn through the average temperature of the groups of points is seen to be essentially the same in all cases. Initially the temperature falls very slightly until some critical speed is reached where the temperature rises quite markedly, especially in Fig. 7, where the cooling water inlet temperature is lowest. This critical speed is dependent on the surface tension forces holding the film to the wall and the centrifugal forces which cause its detachment from the wall.

The basic data in the form of mean heat transfer coefficients against speed of rotation are shown in Figs. 8–10. Here the true magnitude of the increase in heat transfer with speed is shown and all three figures show significant increases in heat transfer coefficient, after an initial region at low speeds where h_m is affected only slightly.

Finally, the results were plotted as in Figs. 11 and 12 where in each case a Nusselt number has been plotted against the Weber number, which characterizes the effects of the surface tension and

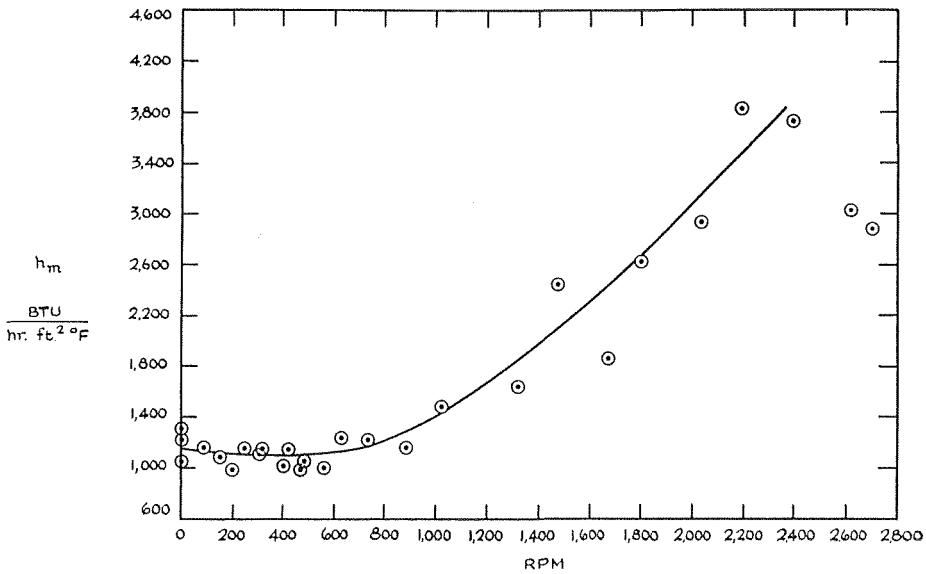

Fig. 8 Variation of heat transfer coefficient with rotational speed for a coolant flow of 4800 lb/hr

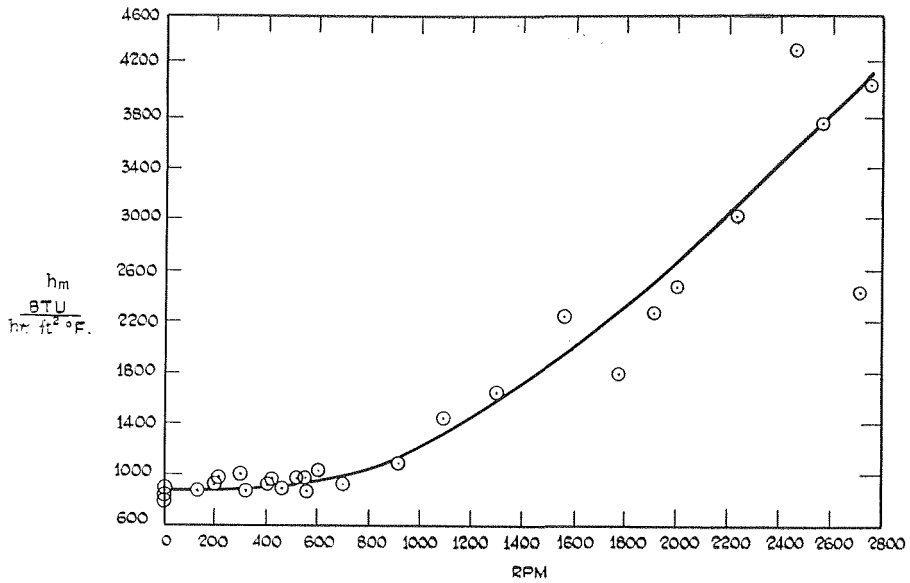

Fig. 9 Variation of heat transfer coefficient with speed of rotation for a coolant flow of 3600 lb/hr

centrifugal forces on the film. In Fig. 11, the influence of ΔT has been allowed for by dividing the Nusselt number by $\left(\frac{gL^3\rho\lambda}{\nu k\Delta T}\right)^{1/4}$. This enables the stationary and low Weber number results to be compared with the theoretical value for condensation on a vertical cylinder. The Nusselt number is based on the diameter, this being the important dimension for condensation at high rotational speeds and the stationary value of $\mathrm{Nu}\left(\frac{gL^3\rho\lambda}{\nu k\Delta T}\right)^{-1/4}$ calculated from Nusselt's theory is 0.0943. It can be seen that the best line through the low Weber number points lies slightly below 0.0943 and this can be attributed to the heat loss along the tube at the ends of the test section, which can be calculated as 4–5 percent of the total heat transferred in the section. Above a Weber number of about 250 the relationship is

$$\mathrm{N_{Nu}}\left(\frac{gL^3\lambda\rho}{\nu k\Delta T}\right)^{-1/4} = 0.00923\ \mathrm{N_{We}}^{0.39}$$

The correlation coefficient for this set of results is 0.886.

For the high-speed runs the inclusion of the $\left(\frac{gL^3\lambda\rho}{\nu k\Delta T}\right)^{-1/4}$ term did not affect the correlation to any significant extent and the results were recalculated with the Nusselt number based on $D/2$ so that they could be compared with those of other workers. The relationship for high Weber numbers in Fig. 12 is

$$\mathrm{N_{Nua}} = 6.13\ \mathrm{N_{We}}^{0.496}$$

with a correlation coefficient of 0.87. Comparison of these results with those of other workers is shown in Fig. 13. The curves of Yeh, and Singer and Preckshot represent data for 1-in.

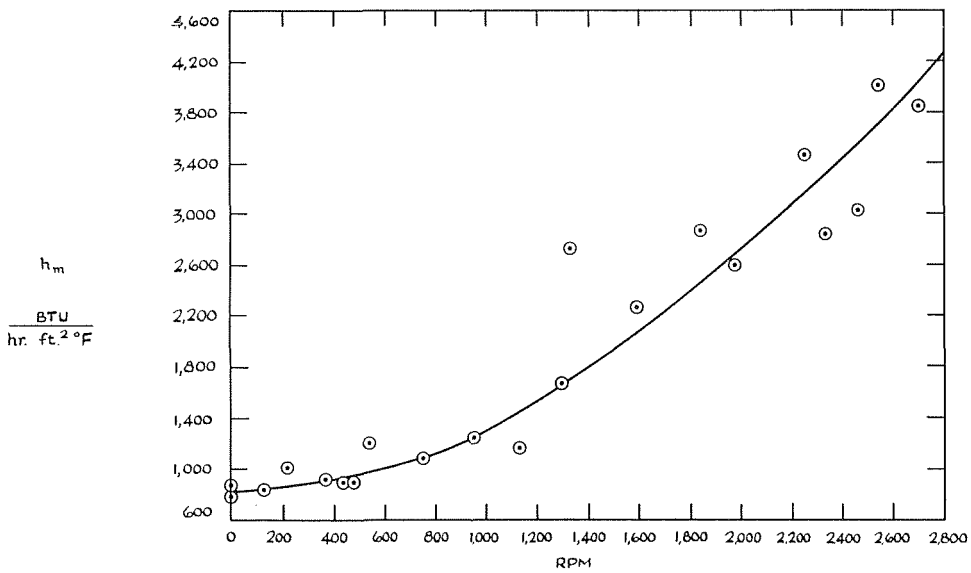

Fig. 10 Variation of heat transfer coefficient with rotational speed for a coolant flow rate of 7200 lb/hr

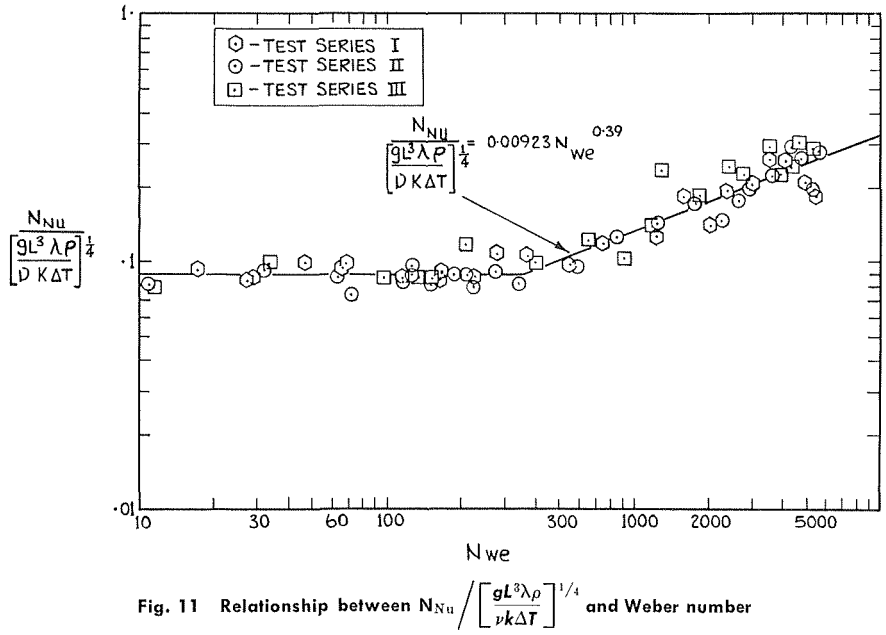

Fig. 11 Relationship between $N_{Nu} \Big/ \left[\frac{gL^3\lambda\rho}{\nu k\Delta T}\right]^{1/4}$ and Weber number

cylinders, and that of Hoyle and Matthews for a 4-in. cylinder. Initially, at low values of Weber number the present results predict lower Nusselt numbers than the others, as might be expected from a comparison of condensation on stationary horizontal and vertical cylinders: Garrett and Wighton [8] and Hassan and Jakob [9] report values of h_m to be almost twice as high for horizontal tubes as for vertical tubes. For high Weber numbers the trend is seen to be in agreement with the results of Hoyle and Matthews and the correlation equation for Weber numbers greater than 500 is

$$N_{Nua} = 6.13\ N_{We}^{0.496}$$

The converging curves for the horizontal and vertical geometries at high Weber numbers would seem reasonable since the centrifugal forces would dominate in this range and the effect of gravity on the film would become of decreasing importance.

It is also interesting to note that the power of the Weber number is almost the value of 0.5 predicted by Singer and Preckshot for this region. For high rotational speeds they proposed a model in which the surface was covered with hemispherical drops, which formed the controlling heat transfer resistance, and showed that the $N_{Nu} \propto N_{We}^{0.5}$. That they were unable to demonstrate this behavior at high speeds with their own apparatus, might possibly be due, as they suggested, to starving the surface of fresh vapor or to some inherent difficulty in their experimental technique. In this respect it is noticeable that the results based on actual temperature measurements (Hoyle and Matthews, and the author's) show the expected trend, while those of Singer and Preckshot, dependent on the results of Kuo, et al., for the calculation of the heat transfer coefficients, show a decreasing characteristic.

Acknowledgments

The authors would like to acknowledge the financial assistance given by the National Research Council for this project.

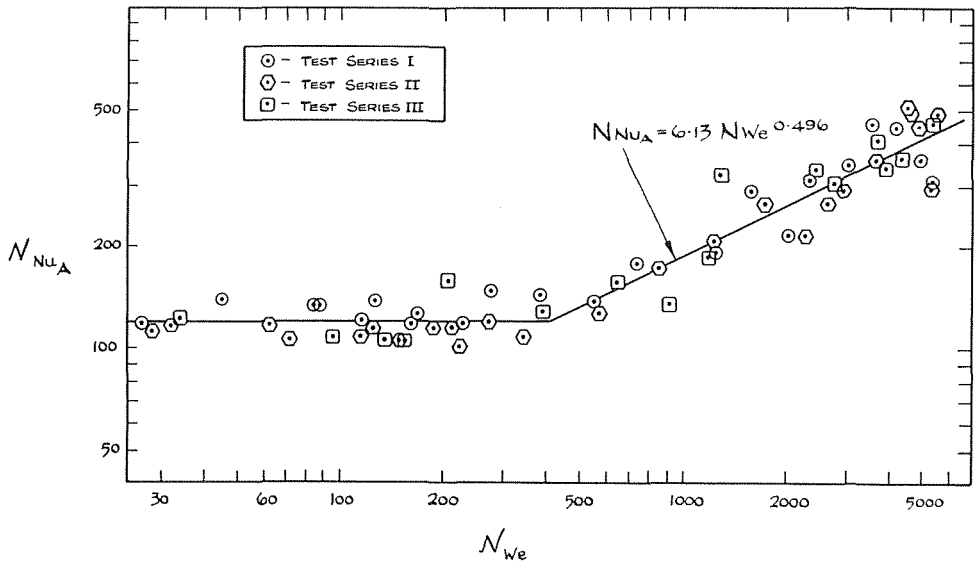

Fig. 12 Graph showing relationship between Nusselt number and Weber number

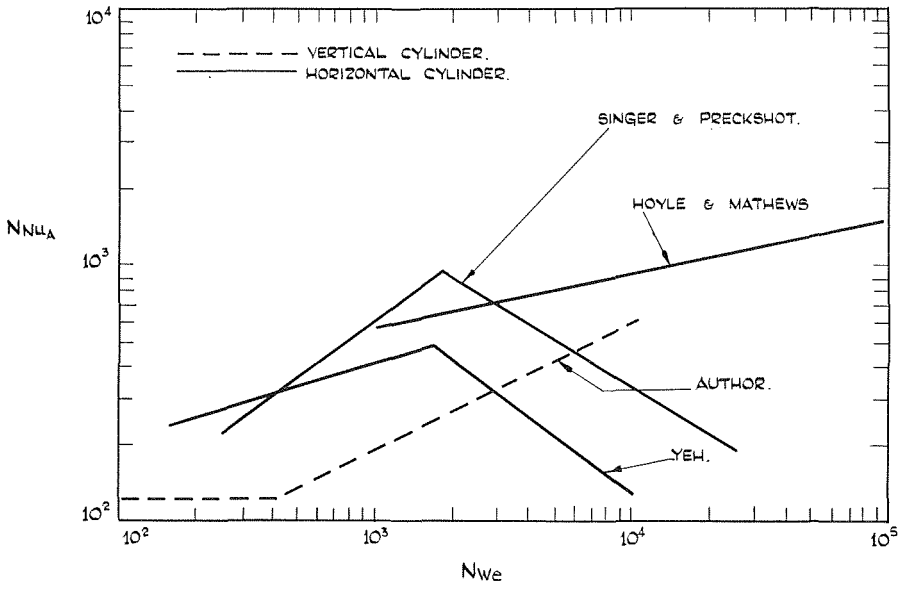

Fig. 13 Comparison of results for horizontal and vertical cylinders

References

1 Birt, D. C. P., et al., "Methods of Improving Heat Transfer From Condensing Steam and Their Application to Condensers and Evaporators," *Transactions of the Institution of Chemical Engineers*, Vol. 37, 1959, pp. 289–296.

2 Yeh, L., "The Effect of Surface Speed and Steam Pressure Upon the Transfer of Heat to a Rotating Cylinder," PhD thesis, Department of Mechanical Engineering, Imperial College of Science and Technology, London, England, 1953.

3 Singer, R. M., and Preckshot, G. W., "The Condensation of Vapor on a Horizontal Rotating Cylinder," *Proceedings of the Heat Transfer and Fluid Mechanics Institute*, No. 14, 1963, p. 205.

4 Kuo, C. T., et al., "Heat Transfer in Flow Through Rotating Ducts," JOURNAL OF HEAT TRANSFER, TRANS. ASME, Series C, Vol. 82, No. 2, 1960, pp. 139–151.

5 Hoyle, R., and Matthews, D. H., "The Effect of Speed on the Condensate Layer on a Cold Cylinder Rotating in a Steam Atmosphere," *Journal of Fluid Mechanics*, Vol. 22, 1965, p. 105.

6 Hoyle, R., and Matthews, D. H., "The Effect of Diameter Size and Speed of Rotation on the Heat Transfer From Steam to Cooled Cylinders," *International Journal of Heat and Mass Transfer*, Vol. 7, 1964, p. 1223.

7 Gacesa, M., "Condensation of Steam on a Vertically Rotating Cylinder," MASc thesis, University of Windsor, Ontario, Canada, 1965.

8 Garrett, T. W., and Wighton, J. L., "The Effect of Inclination on the Heat Transfer Coefficients for Film Condensation of Steam on an Inclined Cylinder," *International Journal of Heat and Mass Transfer*, Vol. 7, 1964, p. 1235.

9 Hassan, K. E., and Jakob, M., "Laminar Film Condensation of Pure Saturated Vapors on Inclined Circular Cylinders," ASME Paper No. 57-A-35.

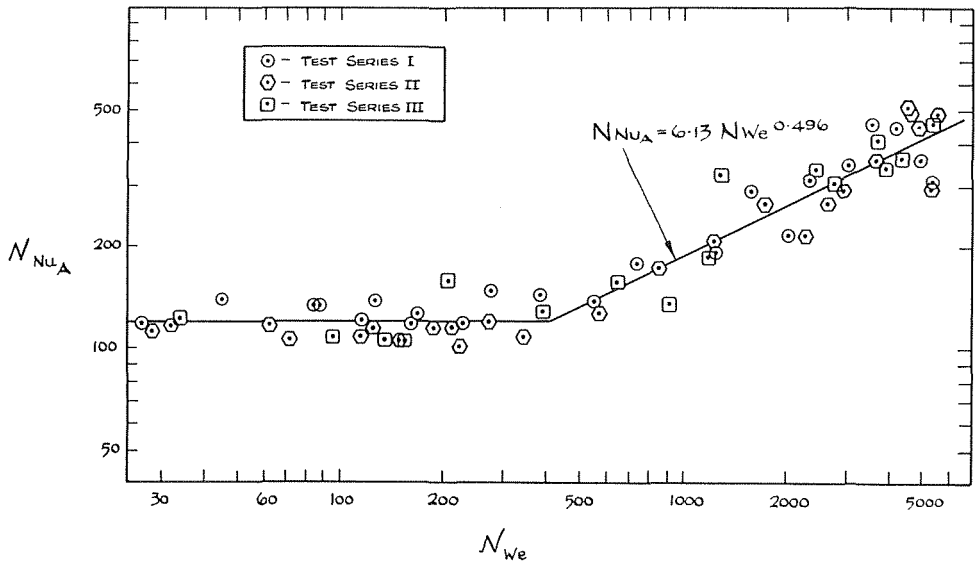

Fig. 12 Graph showing relationship between Nusselt number and Weber number

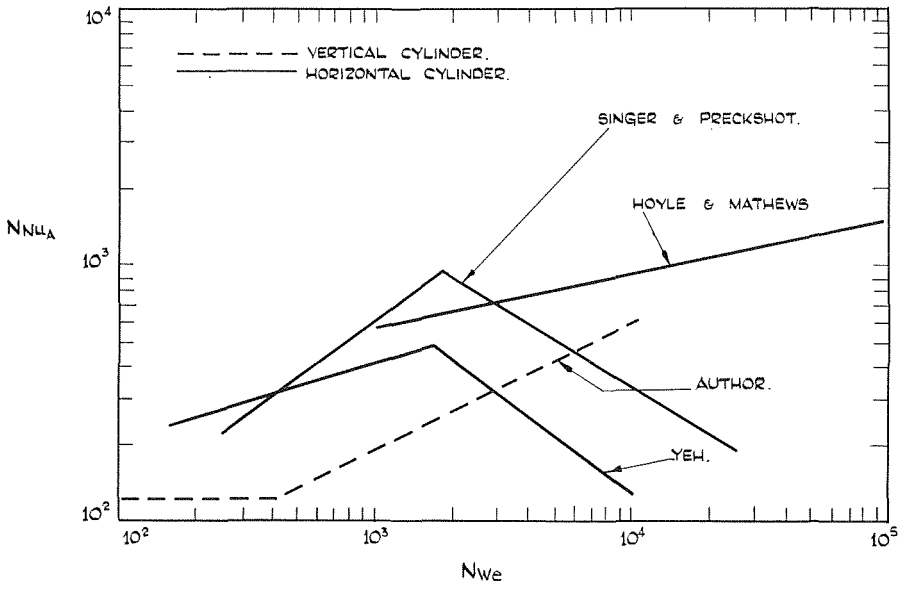

Fig. 13 Comparison of results for horizontal and vertical cylinders

References

1 Birt, D. C. P., et al., "Methods of Improving Heat Transfer From Condensing Steam and Their Application to Condensers and Evaporators," *Transactions of the Institution of Chemical Engineers*, Vol. 37, 1959, pp. 289–296.

2 Yeh, L., "The Effect of Surface Speed and Steam Pressure Upon the Transfer of Heat to a Rotating Cylinder," PhD thesis, Department of Mechanical Engineering, Imperial College of Science and Technology, London, England, 1953.

3 Singer, R. M., and Preckshot, G. W., "The Condensation of Vapor on a Horizontal Rotating Cylinder," *Proceedings of the Heat Transfer and Fluid Mechanics Institute*, No. 14, 1963, p. 205.

4 Kuo, C. T., et al., "Heat Transfer in Flow Through Rotating Ducts," JOURNAL OF HEAT TRANSFER, TRANS. ASME, Series C, Vol. 82, No. 2, 1960, pp. 139–151.

5 Hoyle, R., and Matthews, D. H., "The Effect of Speed on the Condensate Layer on a Cold Cylinder Rotating in a Steam Atmosphere," *Journal of Fluid Mechanics*, Vol. 22, 1965, p. 105.

6 Hoyle, R., and Matthews, D. H., "The Effect of Diameter Size and Speed of Rotation on the Heat Transfer From Steam to Cooled Cylinders," *International Journal of Heat and Mass Transfer*, Vol. 7, 1964, p. 1223.

7 Gacesa, M., "Condensation of Steam on a Vertically Rotating Cylinder," MASc thesis, University of Windsor, Ontario, Canada, 1965.

8 Garrett, T. W., and Wighton, J. L., "The Effect of Inclination on the Heat Transfer Coefficients for Film Condensation of Steam on an Inclined Cylinder," *International Journal of Heat and Mass Transfer*, Vol. 7, 1964, p. 1235.

9 Hassan, K. E., and Jakob, M., "Laminar Film Condensation of Pure Saturated Vapors on Inclined Circular Cylinders," ASME Paper No. 57-A-35.

DISCUSSION

B. T. Nijaguna[2]

I would like to comment on the surface temperature and on the use and validity of h_m (generally used in steady-state processes) in the case of an unsteady convection process at a solid surface—condensation of steam on a rotating vertical cylinder.

The boundary condition at the solid boundary of the cylinder could be written as (approximating to one-dimensional case)

[2] Department of Mechanical Engineering, University of Toronto, Toronto, Ontario, Canada.

$$h_m \Delta T = k \frac{\partial T_0}{\partial x} = Q \text{ (heat transferred) at any instant.}$$

If Q is negligibly different from one speed to another, as is mentioned in the body of the paper, then the temperature gradient in the solid

$$\frac{\partial T_0}{\partial x} = \frac{T_0 - T_{\text{coolant}}}{\partial x}$$

should be nearly the same for different speeds. T_{coolant} and wall thickness being constant, T_0, the surface temperature would be the same for all speeds. How could this discrepancy be accounted?

Fig. 1 is a combined graph, obtained by the superposition of Figs. 6, 7, 9, and 10 of the paper. ΔT, the difference between steam temperature and surface temperature, is indicated by AB for a coolant flow rate of 3600 lb/hr, while it is AC for a coolant flow rate of 7200 lb/hr. It is seen that the values of h_m are almost the same for the two coolant flow rates at all speeds. At any speed, the heat flux Q is given by $DE \times AB$ in the case of 3600 lb/hr case and $DE \times AC$ in the case of 7200 lb/hr case. In other words, the ratio of heat fluxes would be in the ratio of ΔT, i.e.,

$$\frac{AC}{AB} = \frac{\text{(heat flux at 7200 lb/hr)}}{\text{(heat flux at 3600 lb/hr)}}$$

This shows that heat flux in the case of 7200 lb/hr is about 30 to 35 percent more than the value of heat flux in the case of 3600 lb/hr, and is significantly different. If the heat fluxes were not significantly different, then the surface temperature would be the same. A heat flux versus speed plot would give a better picture.

As the condensate film forms and is torn off at a certain thickness, the process becomes an unsteady and a nearly cyclic process, and as such the accurate measurement of T_0 would be difficult. The main question would be, can one use the steady-state concept of h_m in an unsteady case such as this?

G. B. Wallis[3]

Condensation on a cylinder rotating at high speed, so that the centrifugal effects dominate gravity, should be dynamically similar to both condensation on a flat surface facing downward and film boiling on a flat surface facing upward. For the latter problem, Berenson[4] found that

$$h = 0.425 \left[\frac{k_g^3 \lambda g(\rho_f - \rho_g)}{\mu_g \Delta T \sqrt{\frac{\sigma}{g(\rho_f - \rho_g)}}} \right]^{1/4} \quad (1)$$

If we replace the vapor transport properties by those of the liquid, replace g by the centrifugal acceleration $\omega^2 D/2$, and neglect the vapor density compared with the liquid density, some rearrangement allows equation (1) to be written as

$$\text{Nu} = \frac{hD}{k_f} = 0.425 \left[\frac{\lambda L^3 g \rho}{k_f \mu \Delta T} \right]^{1/4} \left(\frac{D}{L} \right)^{3/4} (2\text{N}_{\text{We}})^{3/8} \times \left(\frac{g\rho D^2}{\sigma} \right)^{-1/4} \quad (2)$$

[3] Associate Professor of Engineering, Thayer School of Engineering, Dartmouth College, Hanover, N. H. Assoc. Mem. ASME.

[4] Berenson, P. J., "Film-Boiling Heat Transfer From a Horizontal Surface," JOURNAL OF HEAT TRANSFER, TRANS. ASME, Vol. 83, Series C, No. 3, Aug. 1961, pp. 351–358.

where

$$\text{N}_{\text{We}} = \frac{\rho g' D^2}{2\sigma} \quad (3)$$

is the Weber number used by the authors. (The symbol g in their expression is really a unit conversion constant g_0.)

For the authors' experiments we have $L/D = 48$, $g\rho D^2/\sigma = 106$ and equation (2) becomes

$$\frac{\text{Nu}}{\left(\frac{\lambda L^3 g \rho}{k \mu \Delta T} \right)^{1/4}} = 0.0094 \, \text{N}_{\text{We}}^{0.375} \quad (4)$$

This is almost indistinguishable from the authors' correlation in Fig. 11. Since equations (1) and (2) are theoretical, being based on analysis of the flow dynamics, we can use them with confidence under conditions which differ from those in the authors' experiments. Equation (4) merely confirms the general equation for a particular set of conditions and should not be used for other fluids or for water at other pressures. I suspect that the same applies to the correlation shown in Fig. 12.

Authors' Closure

The criticism of B. T. Nijaguna is based primarily on his statement that "*Q is negligibly different from one speed to another*, as is mentioned somewhere in the body of the paper." What is actually written at the beginning of the Results and Discussion Section is; "the heat load increases only slightly over this speed range." Three paragraphs later it is mentioned that the cooling water outlet temperature varies slightly with rotational speed. The anomaly posed by the critic is therefore self made, since Q does and must vary, and in the case of Fig. 4 the variation is about 30 percent. Furthermore, the reason for choosing the ΔT values to illustrate the results is evident when it is realized that in Fig. 4 ΔT varies by 300 percent while, as already mentioned, Q varies by 30 percent. The heat transfer coefficient h will be affected to a much greater extent by the ΔT variation and so the plots of T versus rpm are more representative of the trend of h than plots of Q versus rpm.

The use of the accepted heat transfer coefficients for this system seems reasonable since a dynamic equilibrium would exist and time average surface temperatures would be recorded. Perhaps on a microscopic scale some variation in surface temperature might be noticed, but in this case the thermal capacity of the tube wall prevented the observation of any such variation.

The comments of G. B. Wallis on the dynamic similarity between the rotating system and film boiling are valid and one would expect that such an analysis would produce similar dimensionless groups. However, the L/D ratio for the experiments was not 48 but 10, and so the constant in the new expression would be considerably different from 0.0094, thus casting doubt on whether Berenson's correlation can be used in its entirety in this case. Considering the different mechanisms involved in the boiling and condensing processes, it is not surprising that the constant is different even though the remainder of the correlation gives similar dimensionless groups on rearrangement.

Moreover, the correlation given in the paper is for the higher values of N_{we} only and the term $\left(\frac{g\rho D}{\sigma} \right)^{-1/4}$ in equation (2) would seem to be of doubtful physical significance under these circumstances.

W. J. FREA
Associate Professor,
Mechanical Engineering Department,
Michigan Technological University,
Houghton, Mich.

J. H. HAMELINK
Assistant Professor,
Western Michigan University,
Kalamazoo, Mich.

Heat Transfer From the Wall of a Porous Solid Involving Gas Injection and Vaporization

An experimental study was made of heat transfer with gas injection through a porous wall into a pool of liquid, including vaporization effects. Air bubbling from the surface of a graphite cylinder into water at atmospheric pressure was used. It was possible to determine limits on energy transfer due to convection and to latent heat transport. It was found that under some conditions it was possible to operate the system with the surface rejecting heat while at temperatures less than that of the bulk pool liquid.

Introduction

Previous heat transfer investigations of the effects of gas bubbling from a surface into a liquid have focused largely on conditions where vaporization of the liquid was minimal. The object in some cases was to study convective mixing produced by the bubbles in the absence of vaporization effects and relate the results to nucleate boiling. However, in boiling, heat transfer is influenced both by bubble-induced convection and by latent heat transport. In the work reported on in this paper, gas-injection rates, liquid temperatures, and heat fluxes were varied such that liquid vaporization was a significant factor in the heat transfer process. The tests were conducted primarily to obtain more information on the capability of vaporization with bubbling to promote heat transfer.

Background

Studies with gas injection producing evaporative cooling have been made by Larsen, et al. [1],[1] and Schmidt [2]. The cooling effect on the bulk liquid for cryogenic liquids, produced by the injection of a noncondensible gas, was investigated analytically and experimentally. Heat transfer rates considered were much lower than those of the present study.

Sims, Akturk, and Evans-Lutterodt [3] correlated earlier air bubbling results of Gose, et al. [13], as did Kudirka, Grosh, and McFadden [4] for their own data, considering convection only and using Kutateladze's [5] pool-boiling relationship. Good agreement was found for some test conditions, but not at the high and low ends of the Reynolds number ranges considered. Based on visual comparison of bubble geometries, gas injection appeared to closely simulate boiling.

In a recent investigation, Bard and Leonard [6] studied variations in the convective heat transfer coefficient produced by air bubbling through an orifice into a pool of hexane. It was proposed that during the bubble detachment phase the convective heat transfer coefficient reaches a very high value due to the liquid being drawn suddenly toward the orifice. Relating this mechanism to boiling, they concluded that correlations based on only bubble growth or rising phases alone might not be reliable.

Mixon, Chon, and Beatty [7] produced bubbles electrolytically and found that electrolytic bubbles, although much smaller than the usual boiling bubbles, are more effective for the enhancement of heat transfer than are surface boiling bubbles on a per unit bubble volume basis. In their work and in the later work of Bhand, Patgaonkar, and Gogate [8], effects on the heat transfer coefficient, on bubble size, and on number of bubbles, attributable to vaporization into the bubbles were noted.

In pool boiling from a nickel wire, Rallis and Jawurek [9] obtained measurements from which it was indicated that at high heat fluxes latent heat transport by vapor formation near the heating surface may represent the major portion of the total heat flux. Graham and Hendricks [10] concluded that for nucleate pool-boiling heat fluxes greater than 20 percent of the critical, vaporization becomes the chief contributor. The ability of an evaporating microlayer of liquid to produce high local heat fluxes and at the same time reduce the heat transfer surface temperature has been investigated analytically by Dzakowic and Frost [11].

Experimental Apparatus and Instrumentation

Arrangement of the apparatus used in these experiments is

[1] Numbers in brackets designate References at end of paper.

Contributed by the Heat Transfer Division of The American Society of Mechanical Engineers and presented at the 10th National Heat Transfer Conference, Philadelphia, Pa., August 11–14, 1968. Manuscript received by the Heat Transfer Division, February 29, 1968; revised manuscript received, February 19, 1969; final revised manuscript received, June 23, 1969. Paper No. 68-HT-46.

Nomenclature

c_p = average specific heat at constant pressure, Btu/lb$_m$ deg F
g = acceleration due to gravity, ft/hr^2
g_0 = conversion factor, 4.17 × 10^8 ft lb$_m$/lb$_f$hr^2
h = heat transfer coefficient, Btu/hr ft^2 deg F
i = enthalpy, Btu/lb$_m$
k = thermal conductivity, Btu/hr ft deg F
K_G = mass transfer coefficient lb$_m$-mole/hr lb$_f$
m = mass flux referred to heater surface area, lb$_m$/hr ft^2
M = molecular weight, lb$_m$/lb$_m$-mole
P = partial pressure, lb$_f$/ft^2
P_T = total pressure, lb$_f$/ft^2
q = heat flux referred to heater surface area, Btu/hr ft^2
q_j = heat flux due to joulian heating, Btu/hr ft^2
R = gas constant, ft lb$_f$/lb$_m$ deg R
T = temperature, deg R
V = volume flux referred to heater surface area, ft^3/hr ft^2
μ = viscosity, lb$_m$/ft hr
ρ = density, lb$_m$/ft^3
σ = surface tension for gas-liquid interface, lb$_f$/ft

Subscripts

c = convection
g = injected gas
H = heater surface
i = into control volume
I = interface between liquid and mixture
L = liquid
M = mixture of gas and vapor
0 = out of control volume
P = pool
S = refers to saturation temperature at vapor partial pressure
vb = refers to upperbound vaporization heat flux
V = vapor, or vaporization

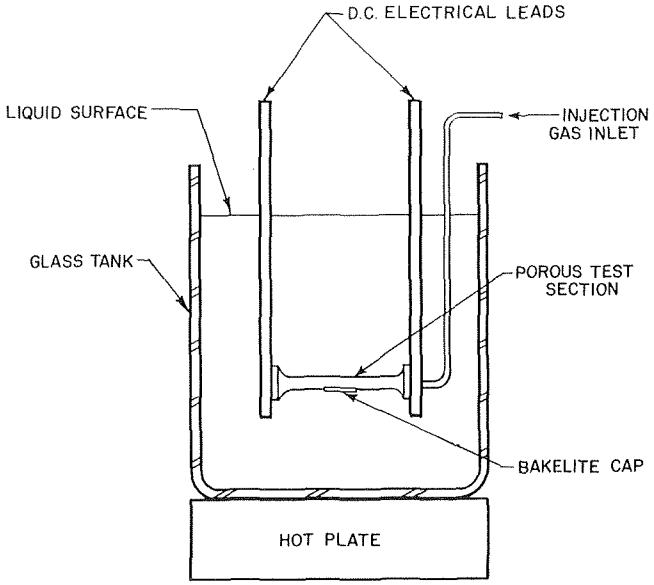

Fig. 1 Apparatus used in the experiments

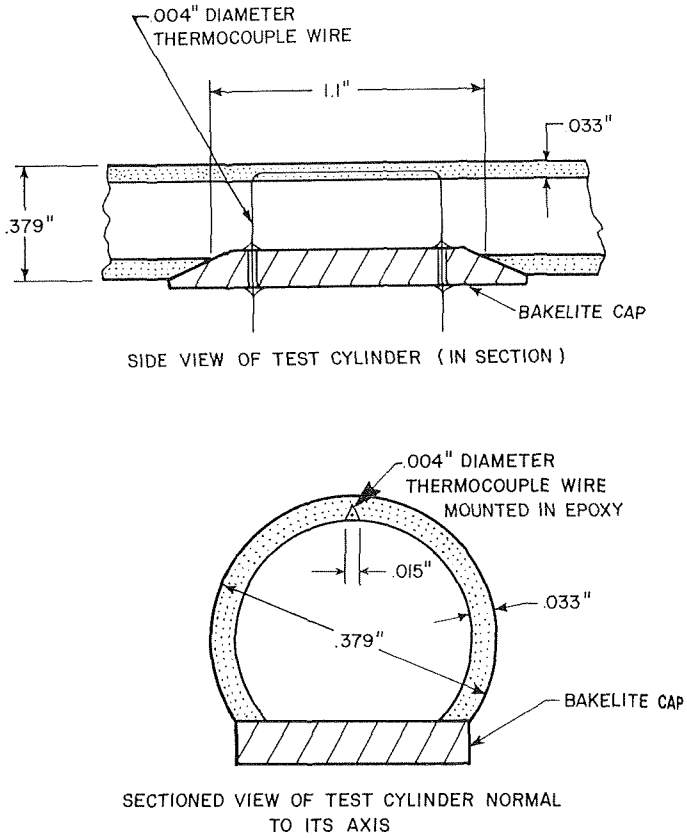

Fig. 2 Thermocouple arrangement for measuring wall temperature

shown in Fig. 1. The porous test section was a hollow cylinder with its axis horizontal and it was heated by passing electric current through it. A glass tank 8 in. × 8 in. × 14 in. deep, heated by an electric hot plate and open to the atmosphere was used to contain the pool liquid.

The test section was a 0.379-in. OD normally porous graphite cylinder, having a wall thickness of 0.033 in. Pore diameter ranges from 0.001–0.008 in. and porosity is about 50 percent with this material. The active length of the graphite test section was 1.1 in., and the overall length of the 0.379-in-dia portion was 2 in. Air was supplied to the inside of the test cylinder; flow rate of the air was found from the pressure drop across a calibrated restriction in the air supply line. Measurement accuracy of the air mass flow rate here is estimated as ±5 percent.

Test section temperature was measured by mounting a chromel-alumel thermocouple in the graphite cylinder wall as shown in Fig. 2. The thermocouple being mounted in this way produced a small region of the cylinder wall where no heat was generated. Analysis of the thermocouple region of the cylinder wall was made by numerical solution to the conduction heat transfer equation. It was concluded that the thermocouple should read the wall temperature correctly within less than ±2 deg F under the conditions of these tests. At low values of $T_H - T_P$ the possible error is reduced to an estimated ±0.4 deg F, dictated by the precision of the strip chart recorder that was used.

Using the bakelite cap shown in Figs. 1 and 2 produced approximately 30 percent reduction in cross-sectional area for electric-current flow and hence a greater heat-generation rate existed over the active length compared to the rest of the 0.379-in-dia portion. Therefore some heat conduction in directions along the test section axis was present. Calculation of a conservative estimate for the temperature decrease at the center of the active length (the thermocouple junction location) due to axial heat conduction showed it to be always less than 1 deg F for the tests reported on here.

An upper limit on the temperature drop through the graphite cylinder wall was computed and it was found that the maximum possible temperature drop from inner to outer wall was less than 2 deg F over the range of heat generation and air-injection rates studied. Therefore, the graphite cylinder was treated as having a uniform temperature through its wall.

Pool temperature was measured by a thermocouple located in the liquid, 1.5 in. from the test section surface and at the same elevation as the test section.

Measurement of the d-c heating voltage drop along the active length of the test section was obtained by two voltage taps, and current was measured by the voltage drop across a calibrated shunt. Calibrated voltmeters were used; the overall measurement accuracy of the heat-generation rate is estimated as ±5 percent.

Experimental Procedure

A test was begun with the pool liquid at room temperature. The external pool heater was then turned on and readings of pool temperature and temperature difference between test section and pool were recorded as the pool slowly increased in temperature. Data at various heat generation and airflow rate settings were taken until the pool reached its maximum attainable temperature, several degrees below saturation. The time interval at each heat generation and airflow rate setting was minimum of 5 min. Over a typical 5-min interval the pool temperature rose about 4 deg F.

It would be anticipated, due to the high degree of agitation produced by bubbling, that the pool temperature would be relatively uniform throughout at any instant (Mixon, Chon, and Beatty [5] found that when bubbles were being rapidly generated on the heating surface, no significant effects were produced by supplemental stirring of the pool liquid), and this factor would reduce the transient aspect of the tests conducted with varying pool temperature. To ascertain the presence of any transient effects, individual tests were conducted at steady pool temperature. Comparison with the results obtained under varying pool temperature showed no appreciable difference. Thus the results given here should closely represent values that would be obtained under steady pool temperature tests.

Experimental Results

In Fig. 3 is shown a plot of the $(T_H - T_P)$ versus T_P at several heat generation and airflow rates. The points are specific values taken from continuous strip chart recordings. Some of the

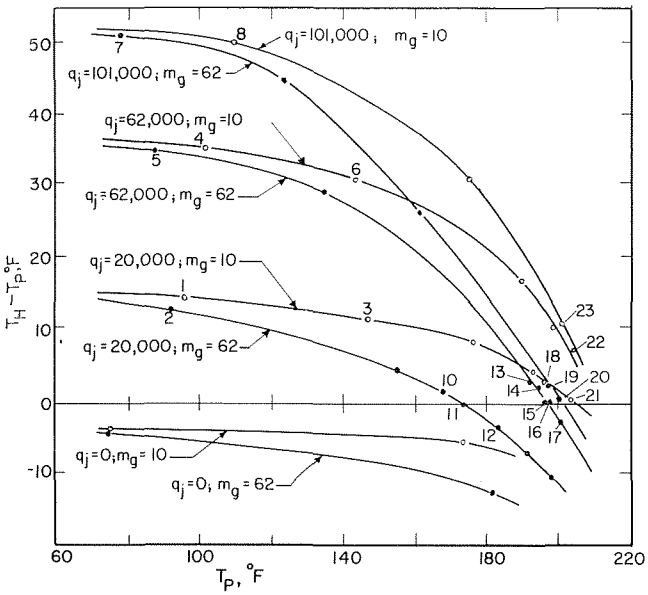

Fig. 3 Effect of pool temperature on heat transfer surface temperature difference with gas injection

points have been numbered so that their location on succeeding plots may be easily determined.

It is seen that the test section temperature is less than the pool temperature in some instances. Under conditions where $(T_H - T_P)$ is negative, the effect of convective heat transfer must be to add heat from the pool liquid to the test section. As calculations in later sections of this paper will show, under these negative temperature difference conditions the heat generated in the test section and the heat added from the pool by convection are able to be transferred away from the test section essentially only by vaporization of liquid.

Analysis of Results

A control volume is shown in Fig. 4 for which conservation of mass and of energy on a time average basis gives

$$q_j = m_{Li}(i_{L0} - i_{Li}) + m_{V0}(i_{V0} - i_{L0}) + m_g(i_{g0} - i_{gi}) \quad (1)$$

Kinetic and potential energies are neglected and none of the vapor produced by evaporation is considered to reenter the control volume. Equation (1) will be rewritten as

$$q_j = q_c + q_V + q_g \quad (2)$$

Measurements of the inlet gas temperature within the test section showed that it is approximately equal to the pool temperature. It will be assumed here that the injected gas is ideal and that it enters the control volume at the pool temperature and leaves at the vapor outlet temperature so

$$q_g = m_g c_P (T_M - T_P) \quad (3)$$

The injected gas initially contained negligible vapor, however, any initial vapor present can be treated as an integral component of the injected gas by using an appropriate value for specific heat.

By treating the injected gas as ideal, q_v and T_V can be related as follows. For the gas vapor mixture leaving the heating surface

$$V_V = V_g \quad \text{and} \quad T_V = T_g \quad (4)$$

The vaporization heat flux is

$$q_V = \rho_V V_V (i_{V0} - i_{L0}) \quad (5)$$

Making use of the relations

$$P_T = P_V + P_g \quad \text{and} \quad V_g = \left[\frac{mRT}{P}\right]_g \quad (6)$$

along with (4) and (5) gives

$$\frac{q_V}{(i_{V0} - i_{L0})} = \frac{m_g R_g T_V \rho_V}{(P_T - P_V)} \quad (7)$$

The resistance to heat transfer by vaporization $(1/h_V)$ is visualized as that due to heat conduction across a vaporizing liquid layer attached to the heating surface and having some time average thickness and heater surface area fraction. Temperature at the surface of this hypothetical layer should not be much higher than the saturation temperature corresponding to P_V in the mixture, as will be discussed in what follows. The definition of the relationship for vaporization heat flux that will be used here is

$$q_V = h_V(T_H - T_S) \quad (8)$$

There will be a resistance to vaporization of liquid into the gas vapor mixture; this resistance to mass transfer will lie only in the mixture, the liquid being a pure phase. The mass transfer rate in turbulent flow for constant temperature through a stationary gas can be written as

$$m_V = K_G M_V (P_I - P_V) \quad (9)$$

The temperature at an interface between the liquid and the mixture will be nearly equal to the saturation temperature of the liquid at P_I if thermodynamic equilibrium is nearly satisfied there. However, the value of P_I is unknown; assuming P_I equals P_V is the same as assuming an infinite K_G. Intensive convective mixing must occur between the injected gas and the vapor and K_G would be expected to be relatively large. If K_G is assumed infinite, the temperature at a liquid-mixture interface will nearly equal the saturation temperature at P_V.

It is seen that K_G could affect h_V, since K_G being less than infinity will tend to increase T_I, thus decreasing conduction through the liquid layer and giving a lower h_V at a particular $(T_H - T_S)$.

An upperbound on the vaporization heat flux at any test condition (other than $m_g = 0$) can be computed with equation (7) for given T_H, m_g, and P_T by assuming saturated vapor in the mixture and that $(T_H - T_S) = 0$. Saturation values for i_{V0}, i_{L0}, ρ_V, and P_V in (7) can be employed. The use of these assumptions implies that h_V and K_G are infinite.

At given q_j and m_g, the terms in equation (2) will all have particular time average values for a particular T_P. If T_P is increased, T_H will increase in order to satisfy the requirement of constant q_j. However, with P_T constant the upperbound vaporization heat flux increases with increased T_H (because $P_T - P_V$ in equation (7) decreases) and thus the convection flux needed to satisfy equation (2) is reduced. Hence less temperature difference between heater and pool is required as pool temperature increases. Even negative temperature differences can occur as shown in Fig. 3, indicating that the vaporization heat flux is greater than q_j and that the convective flux must be directed toward the test section.

It should be emphasized that the true vaporization heat flux is always less than the upperbound vaporization heat flux, since h_V and K_G are not infinite.

Convection Coefficient

Under test conditions where q_V and q_g are relatively small, the convective heat flux can be accurately computed using equations (2), (3), and (7). With a definition of the convection coefficient taken as

$$q_c = h_c(T_H - T_P), \quad (10)$$

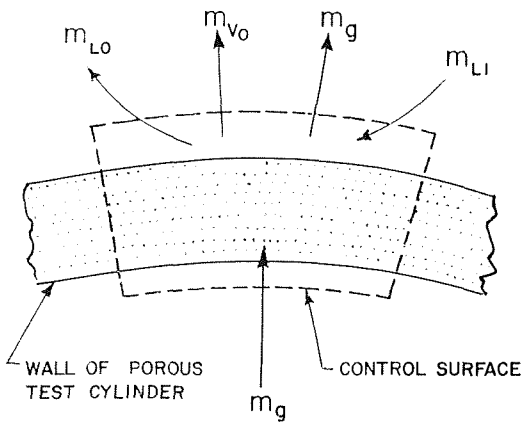

Fig. 4 Control volume geometry in a plane perpendicular to test cylinder axis

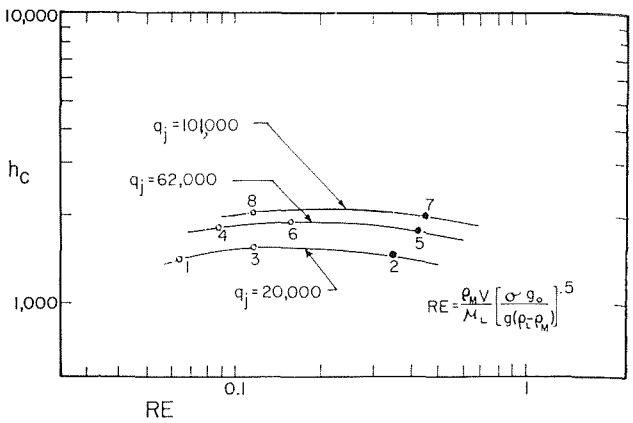

Fig. 5 Variation of convection coefficient with Reynolds number

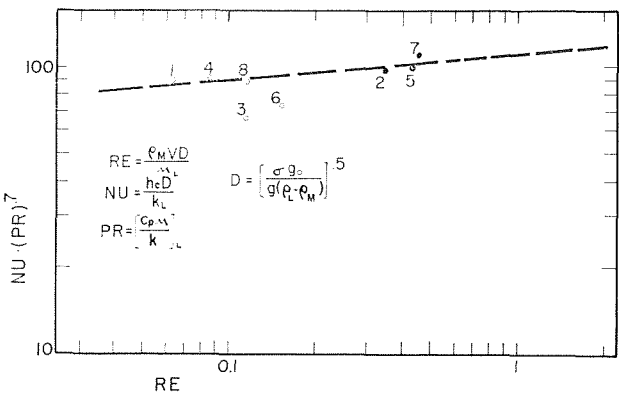

Fig. 6 Convection coefficient variation with parameters used in Rohsenow's method

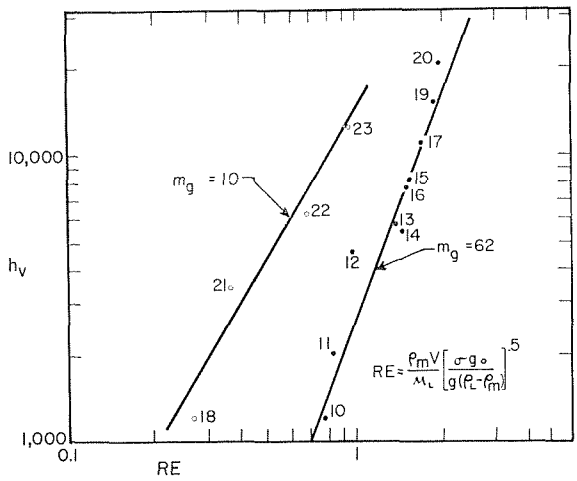

Fig. 7 Effect of Reynolds number on vaporization coefficient

the convection coefficient is plotted versus the Reynolds[2] number of the mixture volume flow rate in Fig. 5. Here it was assumed $(T_H - T_S) = 0$, so only data points from Fig. 3 were used for which the upperbound on q_V by equation (7) was less than 15 percent q_j and therefore error in computing q_V would not seriously effect the value obtained for h_c. The calculation of g_g with equation (3) for these same points showed it to be always less than 1 percent q_j so that energy absorbed by the change in enthalpy of the injected gas is very small.

The points plotted in Fig. 5 are also plotted in terms of the dimensionless parameters and exponents of Rohsenow's [12] correlation in Fig. 6. Fluid properties were evaluated at the heater surface temperature.

Similar to what has been found previously with electrolytically produced gas bubbles (7, 8), h_c at a given Re is seen in Fig. 5 to be greater at higher heat fluxes or more fundamentally, with the higher $(T_H - T_P)$ values that accompany the higher heat fluxes. Effect of $(T_H - T_P)$ is not evident in Fig. 6. However, an effect due to T_P with this correlation may be indicated since the two points in Fig. 6 having the lowest ordinates have the highest pool temperatures, approximately 145 deg F; the rest of the points are at pool temperatures ranging from 110 deg F down to 72 deg F.

[2] Reynolds number $= \frac{\rho_M V}{\mu_L}\left[\frac{g_0\sigma}{g(\rho_L - \rho_M)}\right]^{0.5}$

Vaporization Coefficient and Vaporization Heat Flux

Determination of the vaporization coefficient and the vaporization heat flux can be made accurately from data where heater and pool temperatures are equal, because convective heat flux should be nearly zero then. The values of h_V and q_V can also be found for data where the convective heat flux is not too large, by using an estimated value for h_c obtained based on the results shown in Figs. 5 and 6.

Results obtained for h_V taking the mixture as being saturated and using equations (2), (3), (7), (8), and (10), are plotted in Fig. 7. In calculating h_V, an estimation for h_c was used as obtained from the dashed line in Fig. 6. In order to restrict the effect of h_c estimation accuracy on h_V results, only data points from Fig. 4 were used for which q_c was less than 50 percent q_j. All of the points in Fig. 7 had q_g less than 1 percent q_j.

It should be pointed out that with respect to calculation of q_V, inaccuracy in the estimation of h_c is more likely to be significant than are the uncertainties in any of the experimental measurements. However, the value obtained for h_V is sensitive to the measurements of temperatures and of the air mass flow rate and is therefore more uncertain than q_V.

Two prominent effects shown in Fig. 7 are, first, that h_V reaches values several times higher than h_c, and, second, that h_V is found to be greater at a given Reynolds number with decreased m_g. An increased rate of vapor generated is required in order to produce a given Reynolds number as m_g is decreased. The increased vapor generation may cause increased h_V by producing a thinner time average liquid layer thickness or increased heater surface area fraction, or the increase in h_V may come about due to an in-

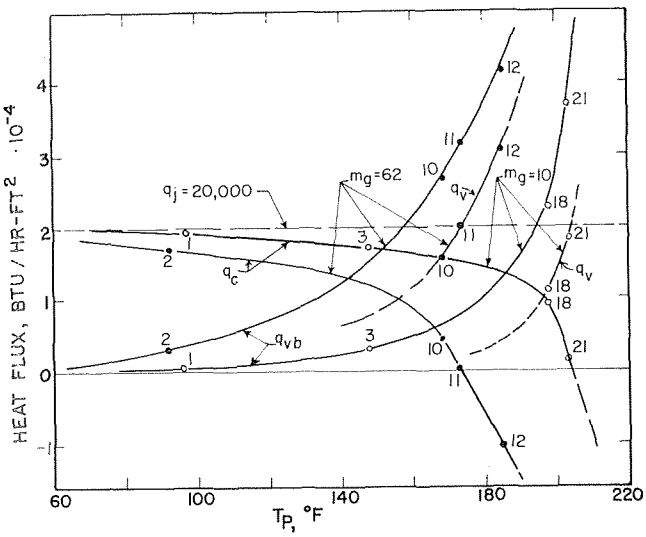

Fig. 8 Comparative effects of vaporization and convection when injection occurs

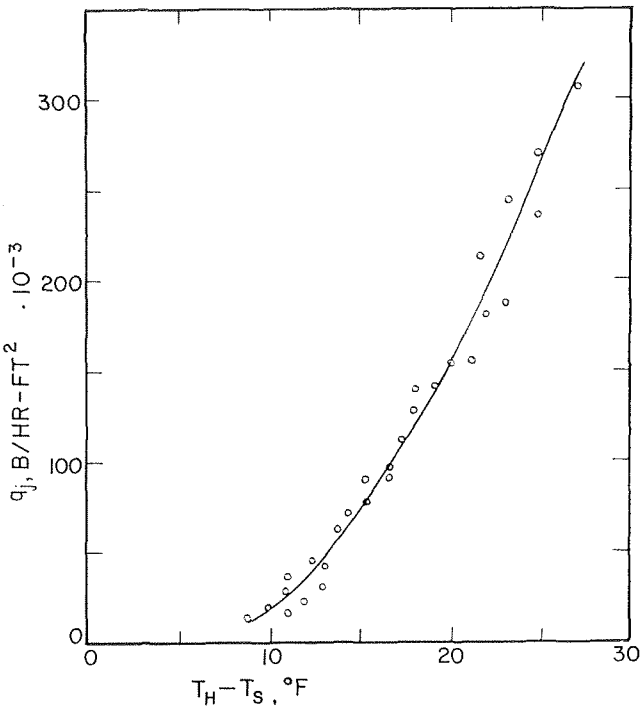

Fig. 9 Saturated nucleate pool boiling of water from a graphite surface

creased mass transfer coefficient accompanying a larger vapor generation rate.

Magnitude and Influence of Vaporization Effect

In Fig. 8 are plotted curves which show the relative magnitudes of q_V and q_c over the pool temperature range studied. The selection of q_j equal to 20,000 Btu/hr ft² as the value to be plotted was made because data at $(T_H - T_P)$ equal or nearly equal to zero at both gas-injection rates tested was available. Values for q_g were small, so q_g was not plotted.

Also shown are curves for the upper-bound vaporization heat flux q_{vb} at the two gas-injection rates, as computed from equation (7) with the observed values of T_H.

It is evident that q_V is substantially lower than q_{vb}, at least in the range where q_V was able to be accurately calculated. This was to be expected, since as shown previously h_V was never infinite.

Comparison With Boiling

An attempt to relate the results found here involving vaporization to the case of heat transfer in boiling with no gas injection will be made in what follows.

Saturated pool boiling of water at atmospheric pressure will be considered. Heat flux versus temperature difference for a cylindrical electrically heated graphite test section, 0.375-in. dia, mounted horizontally, is shown in Fig. 9. These results are similar to what is exhibited with a "clean" stainless-steel surface under the same test conditions.

Only one point on the nucleate-boiling curve will be considered since the conclusion reached would be the same for any of the points in the high heat-flux region. At q_j = 300,000 Btu/hr ft², the temperature difference is seen in Fig. 9 to be approximately 26 deg F. This heat flux and temperature difference will be compared with the results of the air-injection tests by imagining two extreme cases. First, if no convection were present, then q_V = 300,000 Btu/hr ft². The Reynolds number for this heat flux at a wall temperature 26 deg F above saturation is 4.3. Fig. 7 gives h_V for this Reynolds number of at least 20,000 Btu/hr ft² deg F, which is too high since q_V = 520,000 Btu/hr ft² would be predicted at $(T_H - T_S)$ = 26 deg F.

As the second case, a lower bound for q_V will be calculated. From Fig. 8, using an upper-bound Reynolds number of 4.3 and wall temperature 26 deg above saturation, h_c is 4600 Btu/hr ft² deg F. This gives an upper bound for q_c of 120,000 Btu/hr ft², and a lower bound for q_V would then be 180,000 Btu/hr ft² for which the Reynolds number is 2.6. Again, h_V from Fig. 7 is at least 20,000 Btu/hr ft² deg F and too high.

At a heat flux q_j of 300,000 Btu/hr ft² in saturated nucleate pool boiling of water at atmospheric pressure, a value for q_V equal to 260,000 Btu/hr ft² has been assigned (9) with an error bound of approximately ±13 percent. To within the error bound, the same value for q_V is indicated by the results of a later study [10]. This leaves q_c equal to 40,000 ± 34,000 Btu/hr ft², which does not conflict with the upper bound on q_c of 120,000 Btu/hr ft² found in the present investigation.

From the aforementioned, it is shown that the results in Fig. 7 cannot be directly extrapolated to the prediction of h_V in boiling. However, all of the results shown in Fig. 7 were at $(T_H - T_P)$ equal to 3 deg F or less, except point 23 which had $(T_H - T_P)$ equal to 11 deg F. The pool boiling result used for comparison was at $(T_H - T_P)$ = 26 deg F. Hence, an effect may be indicated that increased $(T_H - T_P)$ decreases h_V at a given Reynolds number to below what is shown in Fig. 9. This is opposite to the effect $(T_H - T_P)$ has on h_c, as was found for the data shown in Fig. 5.

Summary and Conclusions

For gas injection through the wall of a porous heater into water, *at moderate to high heat fluxes and gas-injection rates*, the following statements can be made based on the experimental evidence found here:

1 Gas injection can promote heat transfer from the surface to an extent such that, in some cases, the heating surface operates at a lower temperature than that of the bulk liquid

2 Heat transfer from the surface of the heater takes place through the action of two primary mechanisms, bubble-induced convection, and vaporization into the bubbles. Under conditions of low or negative temperature differences between heater and pool, the vaporization mechanism produces the major component of heat flux directed away from the heater.

3 Coefficients for the bubble-induced convection component

of the heat flux obtained when the vaporization component was low were found to increase with increased wall temperature difference at a given Reynolds number.

4 At low wall temperature differences where the convection component was small, the vaporization coefficient was found to be a strong function of Reynolds number, increasing with increasing Reynolds number. Decreased air-injection rate at a given Reynolds number increased the vaporization coefficient.

5 Vaporization coefficients with air injection at wall temperature differences in the range of 3 deg F were found to be higher than those in nucleate pool boiling at a wall temperature difference of 26 deg F when the nucleate-boiling heat flux is 300,000 Btu/hr ft^2. It is conjectured that increased wall temperature difference suppresses the vaporization coefficient at a given Reynolds number.

References

1 Larsen, P. S., Clark, J. A., Randolph, W. O., and Vaniman, J. L., "Cooling of Cryogenic Liquids by Gas Injection," *Advances in Cryogenic Engineering*, Vol. 8, ed., Timmerhaus, K. D., Plenum Press, New York, 1963.

2 Schmidt, A. F., "Experimental Investigation of Liquid-Hydrogen Cooling by Helium Gas Injection," *Advances in Cryogenic Engineering*, Vol. 8, ed., Timmerhaus, K. D., Plenum Press, New York, 1963.

3 Sims, G. E., Akturk, U., and Evans-Lutterodt, K. O., "Simulation of Pool Boiling Heat Transfer by Gas Injection at the Interface," *International Journal of Heat and Mass Transfer*, Vol. 6, 1963, pp. 531–535.

4 Kudirka, A. A., Grosh, R. J., and McFadden, P. W., "Two Phase Heat Transfer in a Tube With Gas Injection From the Walls," presented at the ASME-AIChE Heat Transfer Conference, Los Angeles, Calif., Aug. 1965, Paper No. 65-HT-47.

5 Kutateladze, S. S., "Heat Transfer in Condensation and Boiling," AEC Translation, AEC-tr-3770, 1952.

6 Bard, Y., and Leonard, E. F., "Heat Transfer in Simulated Boiling," *International Journal of Heat and Mass Transfer*, Vol. 10, No. 12, 1967, pp. 1727–1734.

7 Mixon, F. O., Chon, W. Y., and Beatty, K. C., Jr., "The Effect of Electrolytic Gas Evolution on Heat Transfer," *Chemical Engineering Progress*, Vol. 55, 1959, pp. 49–53.

8 Bhand, S. C., Patgaonkar, G. V., and Gogate, D. V., "Convective Heat Transfer in Weak Electrolytes Under the Action of Electrolytic Currents," *International Journal of Heat and Mass Transfer*, Vol. 8, No. 1, 1965, pp. 111–117.

9 Rallis, C. J., and Jawurek, H. H., "Latent Heat Transport in Saturated Nucleate Boiling," *International Journal of Heat and Mass Transfer*, Vol. 7, No. 10, 1964, pp. 1051–1068.

10 Graham, R. W., and Hendricks, R. C., "Assessment of Convection, Conduction, and Evaporation in Nucleate Boiling," NASA TN D-3943, 1967.

11 Dzakowic, G. S., and Frost, W., "An Analytical Solution for the Transient Temperature of a Heated Surface During Microlayer Evaporation," presented at the ASME Winter Annual Meeting, Pittsburgh, Pa., Nov. 1967, Paper No. 67-WA/HT-21.

12 Rohsenow, W. M., "A Method of Correlating Heat-Transfer Data for Surface Boiling of Liquids," TRANS. ASME, Vol. 74, July 1952.

13 Gose, E. E., Acrivos, A., and Peterson, E. E., "Heat Transfer to Liquids With Gas Evolution at the Interface," presented at the Mexico City meeting of the AIChE, 1960.

M. E. NEWELL

F. W. SCHMIDT

Mechanical Engineering Department,
The Pennsylvania State University,
University Park, Pa.

Heat Transfer by Laminar Natural Convection Within Rectangular Enclosures

Two-dimensional laminar natural convection in air contained in a long horizontal rectangular enclosure with isothermal walls at different temperatures has been investigated using numerical techniques. The time-dependent governing differential equations were solved using a method based on that of Crank and Nicholson. Steady-state solutions were obtained for height to width ratios of 1, 2.5, 10, and 20, and for values of the Grashof number, Gr_L', covering the range 4×10^3 to 1.4×10^5. The bounds on the Grashof number for $H/L = 20$ is $8 \times 10^3 \leq Gr_L' \leq 4 \times 10^4$. The results were correlated with a three-dimensional power law which yielded

$$H/L = 1 \qquad \bar{N}u_L' = 0.0547\ (Gr_L')^{0.397}$$

$$2.5 \leq H/L \leq 20 \qquad \bar{N}u_L' = 0.155\ (Gr_L')^{0.315}(H/L)^{-0.265}$$

The results compare favorably with available experimental results.

Introduction

THE STEADY convective motion of a fluid contained within a long horizontal rectangular enclosure is investigated using numerical techniques. The two vertical walls of the enclosure are held at different temperatures, and the top and bottom are considered perfect insulators. The objective of this investigation is to obtain relationships between the convective heat transfer coefficients and the imposed conditions. Heat transfer by radiation is not included since, for most fluids of practical interest, its effect may be considered to be independent of the convective effect. It is considered that the length of the enclosure is sufficiently large for two-dimensional motion to be assumed in the section considered.

A number of experimental investigations of convective flow within enclosed fluids have been carried out since the turn of the century. An excellent review of these is given by Carlson [5][1] and Elder [7]. In 1946, Jakob [11] analyzed the experimental results of Mull and Reiher [13] and proposed the following correlations:

$$2 \times 10^4 \leq \mathrm{Gr}_L' \leq 2 \times 10^5 \qquad \bar{\mathrm{N}}\mathrm{u}_L' = 0.18(\mathrm{Gr}_L')^{1/4}(\mathrm{H}/L)^{-1/9} \tag{1}$$

Contributed by the Heat Transfer Division of THE AMERICAN SOCIETY OF MECHANICAL ENGINEERS and presented at the ASME-AIChE Heat TransferConference, Minneapolis, Minn., August 3–6, 1969. Manuscript received by the Heat Transfer Division, July 9, 1968; revised manuscript received, February 25, 1969. Paper No. 69-HT-42.

[1] Numbers in brackets designate References at end of paper.

Nomenclature

A = coefficient in least-squares fit, equation (40)
B = coefficient in least-squares fit, equation (40)
C = coefficient of least-squares fit, equation (40)
c = coefficient in general form, equation (25)
f = dependent variable in general form, equation (25)
Gr_H = Grashof number, $g\beta\ H^3(T_H - T_c)/\nu^2$
Gr_L = Grashof number, $g\beta L^3(T_H - T_m)/\nu^2$
Gr_L' = Grashof number, $g\beta L^3(T_H - T_c)/\nu^2$
g = gravitational acceleration
H = height of enclosure
h = grid spacing in X-direction
K = thermal conductivity of fluid
k = grid spacing in Y-direction
L = width of enclosure
l = coefficient in general form, equation (25)
M = coordinate tangential to wall being considered
N = coordinate normal to wall being considered
$\bar{\mathrm{N}}\mathrm{u}_H'$ = mean Nusselt number, equation (35)
Nu_L = local Nusselt number, equation (32)
$\bar{\mathrm{N}}\mathrm{u}_L$ = mean Nusselt number, equation (33)
$\bar{\mathrm{N}}\mathrm{u}_L'$ = mean Nusselt number, equation (34)
Pr = Prandtl number
p' = fluid pressure above hydrostatic
q = coefficient in general form, equation (25)
q_x'' = local heat transfer rate
q'' = mean heat transfer rate
R = ratio of grid spacings, h/k
Ra = Rayleigh number, $\mathrm{Gr}_L\mathrm{Pr}$
Ra′ = Rayleigh number, $\mathrm{Gr}_L'\mathrm{Pr}$
r = coefficient in general form, equation (25)
s = coefficient in general form, equation (25)
T = temperature
T_c = temperature at cold wall
T_H = temperature at hot wall
T_m = mean temperature of fluid. In all cases here $T_m = (T_H + T_c)/2$
t = time relative to beginning of solution
U = nondimensional velocity in x-direction, uL/ν
u = velocity in x-direction
V = nondimensional velocity in y-direction, vL/ν
v = velocity in y-direction
X = transformed coordinate in x-direction
x = independent coordinate in vertical direction
Y = transformed coordinate in y-direction
y = independent coordinate in horizontal direction
z = coefficient in general form, equation (25)
α = thermal diffusivity of fluid
β = coefficient of thermal expansion
θ = nondimensional temperature, $(T - T_m)/(T_H - T_m)$
ν = kinematic viscosity of fluid
ρ = density of fluid
τ = nondimensional time, $t\ \nu/L^2$
ψ = stream function, equation (15)
Ψ = nondimensional stream function, ψ/ν
ω = vorticity, equation (16)
Ω = nondimensional vorticity, $L^2\omega/\nu$

$$2 \times 10^5 \leq \mathrm{Gr}_L' \leq 10^8 \qquad \overline{\mathrm{Nu}}_L' = 0.065(\mathrm{Gr}_L')^{1/3}(H/L)^{-1/9}. \tag{2}$$

Equation (2) is intended to describe turbulent flow conditions. Jakob proposed that equations (1) and (2) would be valid for values of H/L as small as 3, although this conclusion appears to be the subject of some question.

In 1961 Eckert and Carlson [5] published the results of their experimental work on this subject. They used a Mach-Zehnder interferometer to determine the temperature distribution in enclosures with several aspect ratios. The empirical equations they derived were as follows:

$$\overline{\mathrm{Nu}}_H' = 0.119(\mathrm{Gr}_H')^{0.3} \tag{3}$$

from which the following relationship is obtained

$$\overline{\mathrm{Nu}}_L' = 0.119(\mathrm{Gr}_L')^{0.3}(H/L)^{-0.1}. \tag{4}$$

Equation (3) implies that $\overline{\mathrm{Nu}}_H'$ is independent of L. The reason for this is that the relationship given is only intended to apply in cases where the flow may be considered to consist of two independent boundary layers, one on each wall.

An experimental study of natural convection in a rectangular enclosure using particle suspension techniques was reported by Elder [7]. High Prandtl number fluids were used and the Rayleigh number was varied up to 10^8. An excellent discussion of the flow patterns and temperature profiles was presented although no relationships for the Nusselt number were given.

Only a few analytical investigations of the current problem have been published, and those which have did not come to any conclusive agreement, or otherwise, with experimental results. In 1954, Batchelor [3] published the results of his analytical approach to the problem. He was unable to obtain any generalized solution to the governing differential equations, although certain limiting cases were solved. For small values of the Rayleigh number, Ra′, he obtained the solution in the form of a power series in Ra′. For cases where conditions near the center of the enclosure may be approximated by the solution for infinite H/L, Batchelor obtained the approximation

$$\overline{\mathrm{Nu}}_H' = H/L + (2\gamma - 1)\mathrm{Ra}'/720 \tag{5}$$

where $\frac{1}{2} < \gamma < 1$ and $\gamma \to 1$ as $\mathrm{Ra}' \to \infty$. For high values of Ra′, when the flow may be approximated by a continuous boundary layer surrounding a core of uniform temperature and vorticity, he derived the expression

$$\overline{\mathrm{Nu}}_H' = \gamma_1(\mathrm{Ra}')^{1/4}(H/L)^{-3/4} \tag{6}$$

which gives fairly good agreement with the results of Mull and Reiher when $\gamma_1 = 0.3$. Notice the high value of exponent on H/L compared with that of Jakob's correlation.

An analytical solution to this problem was presented by Poots [14] in 1958. He derived solutions in the form of doubly infinite series. No convergence analysis was given, and it was found to be very difficult to evaluate the solution to a reliable degree of accuracy. Apart from this, the main objection to the analytical solution is that it is restricted to idealized boundary condition and simple geometry, whereas a solution by finite differences can be easily modified to handle arbitrary temperature boundary conditions and irregular geometries.

An analysis of natural convection in an enclosure using integral techniques was reported by Emery and Chu [9]. The velocity and temperature profiles were considered to correspond to those for natural convection from a vertical plate in an infinite medium.

In 1966, Wilkes and Churchill [15] published one of the first successful attempts at solving the full two-dimensional, time-dependent differential equations describing the flow. They used an implicit alternating-direction finite-difference method and were able to obtain steady-state solutions for values of H/L of 1, 2, and 3, although solutions for only one value of Gr_L' were reported for H/L of 2 and 3. Values of $\overline{\mathrm{Nu}}_L'$ reported were up to 70 percent in excess of those given by Jakob's empirical equation. This was partly due to the low values of H/L used, compared with those for which Jakob's correlation is considered valid. Insufficient results prevented a correlation in the form of a power law from being made.

An analytical and experimental study of transient laminar natural convection in partially filled liquid containers was presented by Barakat and Clark [2]. An explicit finite-difference method was used to obtain the solutions and no results comparable with this study were presented.

Two papers were published on the numerical solution of steady natural convection in a square duct. Elder [8] replaced the differential equations at each mesh point by finite-difference expressions and then employed a Liebmann-type extrapolation method with alternate row and column scanning for the solution of the resulting set of difference equations. His results were compared with those obtained in his previous experimental investigation. The following expression was given for the Nusselt number:

$$\overline{\mathrm{Nu}}_L' = 0.25(\mathrm{Pr}\,\mathrm{Gr}_L')^{0.25} \text{ for } H/L = 1 \text{ and } \mathrm{Gr}_L'\,\mathrm{Pr} > 4000. \tag{7}$$

For a Prandtl number of 0.733 this reduces to

$$\overline{\mathrm{Nu}}_L = 0.231\ (\mathrm{Gr}_L')^{0.25}. \tag{8}$$

A similar study was conducted by Han [10]. His correlations indicated a relationship of the form

$$\overline{\mathrm{Nu}}_L' = 0.0782(\mathrm{Gr}_L')^{0.3594}.$$

Aziz and Hellums [1] presented a finite-difference technique for the numerical solution of three-dimensional natural convection in an enclosure. An alternating-direction method was used for the solution of the transient parabolic equations, energy and vorticity transport, while a successive overrelaxation method was used for the determination of the vorticity. Although some results are given, this paper principally presents a discussion of the various methods available.

An experimental and analytical study of moderate and high Prandtl number fluids was presented by MacGregor and Emery [12]. An explicit finite-difference technique was used in conjunction with a Gauss-Seidel iterative method for the solution of the time-dependent equations. Comparisons were presented of their computed and experimental results.

The objective of the present study is to investigate, using finite-difference techniques, the effect on the Nusselt number of the Grashof number, and the height to width ratio of the enclosure over sufficient ranges to enable correlations to be made and to compare these with existing experimental results. Although the only results reported here are for constant wall temperatures, the computer program used was set up to handle arbitrary temperature profiles and, through the use of transformations of the independent variables, any height to width ratio can be studied. One of the more unusual features of the method of solution is the use of a direct method to solve the sets of linearized difference equations, rather than an iterative method as is usually employed.

Theory

Governing Differential Equations

The physical model is shown in Fig. 1. In formulating the governing differential equations, the following assumptions were made:

1 Constant properties except in the formulation of the buoyancy term.
2 Compressibility effects and viscous dissipation can be neglected.
3 The fluid is Newtonian.
4 The flow is laminar and two-dimensional.

Under these conditions the differential equations describing the flow are given by Batchelor [3].

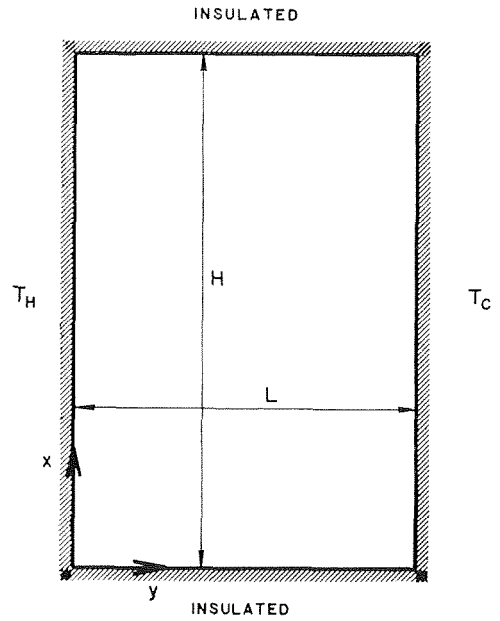

Fig. 1 Physical model

Continuity Equation:

$$\frac{\partial u}{\partial x} + \frac{\partial v}{\partial y} = 0, \tag{9}$$

Conservation of Momentum Equations:

$$\frac{\partial u}{\partial t} + u\frac{\partial u}{\partial x} + v\frac{\partial u}{\partial y} = \nu\left(\frac{\partial^2 u}{\partial x^2} + \frac{\partial^2 u}{\partial y^2}\right) - \frac{1}{\rho}\frac{\partial P}{\partial x} + gB(T - T_m) \tag{10}$$

$$\frac{\partial v}{\partial t} + u\frac{\partial v}{\partial x} + v\frac{\partial v}{\partial y} = \nu\left(\frac{\partial^2 v}{\partial x^2} + \frac{\partial^2 v}{\partial y^2}\right) - \frac{1}{\rho}\frac{\partial P}{\partial y} \tag{11}$$

Conservation of Energy Equation

$$\frac{\partial T}{\partial t} + u\frac{\partial T}{\partial x} + v\frac{\partial T}{\partial y} = \alpha\left(\frac{\partial^2 T}{\partial x^2} + \frac{\partial^2 T}{\partial y^2}\right). \tag{12}$$

The solution to the foregoing set of equations must satisfy the following conditions: on the walls,

$$u_0 = v_0 = 0$$

$$T = T_0 \quad \text{(given)}$$

or on an adiabatic wall

$$\left.\frac{\partial T}{\partial N}\right|_0 = 0.$$

Since the primary interest was in the steady-state solutions, the initial conditions used were chosen to be self-consistent and as near as possible to the expected steady-state solution.

The pressure term, P, may be eliminated from the system of equations by differentiating equations (10) and (11) with respect to y and x, respectively, and subtracting one from the other. After simplification, which involves the use of equation (9), the following is obtained:

$$\frac{\partial \omega}{\partial t} + u\frac{\partial \omega}{\partial x} + v\frac{\partial \omega}{\partial y} = \nu\left(\frac{\partial^2 \omega}{\partial x^2} + \frac{\partial^2 \omega}{\partial y^2}\right) - g\beta\frac{\partial T}{\partial y} \tag{13}$$

where the vorticity, ω, is defined as

$$\omega = \frac{\partial v}{\partial x} - \frac{\partial u}{\partial y}. \tag{14}$$

It is convenient to introduce the stream function, ψ, defined by

$$u \equiv \frac{\partial \psi}{\partial y}$$

$$v \equiv -\frac{\partial \psi}{\partial x} \tag{15}$$

The continuity equation (9) is thus satisfied. Equation (14) may now be written:

$$\omega = -\left(\frac{\partial^2 \psi}{\partial x^2} + \frac{\partial^2 \psi}{\partial y^2}\right) \tag{16}$$

The system to be solved now consists of equations (12), (13), (15), and (16).

Nondimensional Variables

In order that changes in the duct geometry could be conveniently investigated, the independent variables were transformed such that in the transformed system of coordinates, the duct geometry was always square. In some cases it was found desirable to compress certain areas of the duct more than others. In view of this, the equations were set up to accommodate nonlinear transformations.

Let the transformations be of the form

$$X = X(x/L)$$

$$Y = Y(y/L)$$

where X and Y, the coordinates in the transformed system, are single-valued functions with continuous derivatives up to the second in the region of interest. The remaining variables are arranged in nondimensional groups θ, Ψ, U, V, τ, and Ω as defined in the Nomenclature. The following nondimensional equations are thus obtained:

$$0 = (X')^2\frac{\partial^2\theta}{\partial X^2} + (Y')^2\frac{\partial^2\theta}{\partial Y^2} + (X'' - \mathrm{Pr}\,X'U)\frac{\partial\theta}{\partial X} + (Y'' - \mathrm{Pr}\,Y'V)\frac{\partial\theta}{\partial Y} - \mathrm{Pr}\frac{\partial\theta}{\partial\tau} \tag{17}$$

$$\mathrm{Gr}_L Y'\frac{\partial\theta}{\partial Y} = (X')^2\frac{\partial^2\Omega}{\partial X^2} + (Y')^2\frac{\partial^2\Omega}{\partial Y^2} + (X'' - X'U)\frac{\partial\Omega}{\partial X} + (Y'' - Y'V)\frac{\partial\Omega}{\partial Y} - \frac{\partial\Omega}{\partial\tau} \tag{18}$$

$$-\Omega = (X')^2\frac{\partial^2\Psi}{\partial X^2} + (Y')^2\frac{\partial^2\Psi}{\partial Y^2} + X''\frac{\partial\Psi}{\partial X} + Y''\frac{\partial\Psi}{\partial Y} \tag{19}$$

$$U = Y'\frac{\partial\Psi}{\partial Y}$$

$$V = X'\frac{\partial\Psi}{\partial X} \tag{20}$$

where

$$X' = \frac{dX}{d(x/L)} \text{ and } X'' = \frac{d^2X}{d(x/L)^2}$$

with similar expressions for Y' and Y''.

Equations (17) to (20) are in a form suitable for solution using finite-difference techniques. The solution must satisfy the following boundary conditions:

$$U_0 = V_0 = 0. \tag{21}$$

Using equations (20), equation (21) may be written as

$$\left.\frac{\partial\Psi}{\partial M}\right|_0 = \left.\frac{\partial\Psi}{\partial N}\right|_0 = 0 \tag{22}$$

provided

$$Y' \neq 0$$

and

$$X' \neq 0$$

where M and N are in the directions of the tangent and normal to the wall being considered. Thus Ψ_0 must be a constant on all walls. For convenience, $\Psi_0 = 0$ was chosen.

The boundary conditions for θ are as follows when T_0 is specified,

$$\theta = \frac{(T_0 - T_m)}{(T_H - T_m)} \tag{23}$$

and on an adiabatic wall,

$$\left.\frac{\partial\theta}{\partial N}\right|_0 = 0. \tag{24}$$

No explicit boundary conditions can be written for Ω, since the distribution of Ω must be such that both of the conditions on Ψ, namely, $\Psi_0 = 0$ and $\left.\frac{\partial\Psi}{\partial N}\right|_0 = 0$, are satisfied and only one of these conditions can be directly imposed on the solution.

Various initial conditions were used. In some cases they had to be chosen carefully in order to obtain stable solutions. However, for most cases uniform temperature and zero velocity were used. In cases where steady-state solutions were being sought for various values of Grashof number, Gr_L, with a fixed geometry, the initial condition for a new Grashof number were taken as the steady-state solutions obtained with the previous Grashof number.

Finite-Difference Representations of the Differential Equations

It is desired to write finite-difference approximations to equations (17) to (20) at selected points in the field, and then to solve the resulting sets of equations for the unknowns at these points. For the time-dependent relationships, equations (17) and (18), a scheme based on the method of Crank and Nicholson was used. Equations (19) and (20) were approximated using central differences.

Equations (17), (18), and (19) are of the general form

$$l\frac{\partial^2 f}{\partial X^2} + q\frac{\partial^2 f}{\partial Y^2} + r\frac{\partial f}{\partial X} + s\frac{\partial f}{\partial Y} + z\frac{\partial f}{\partial \tau} = c \tag{25}$$

where f represents either θ, Ω, or Ψ depending upon which equation is being considered, and l, q, r, s, z, and c represent the corresponding coefficients. For the purpose of establishing the difference equations the nodes were numbered as in Fig. 2. For interior nodes equations (17) and (18) were approximated using central differences by

$$\frac{1}{2}\left[\frac{l_3}{h^2}(f_1 - 2f_3 + f_5) + \frac{q_3}{k^2}(f_2 - 2f_3 + f_4) + \frac{r_3}{2h}(f_1 - f_5) + \frac{s_3}{2k}(f_4 - f_2) + \frac{l_8}{h^2}(f_6 - 2f_8 + f_{10}) + \frac{q_8}{k^2}(f_7 - 2f_8 + f_9) + \frac{r_8}{2h}(f_6 - f_{10}) + \frac{s_8}{2k}(f_9 - f_7)\right] + \frac{z}{d}(f_8 - f_3) = \frac{1}{2}(c_8 + c_3) \tag{26}$$

where f represents θ or Ω, respectively. The representation of equation (19) was obtained using central differences, and is

$$\frac{l_8}{h^2}(\Psi_6 - 2\Psi_8 + \Psi_{10}) + \frac{q_8}{k^2}(\Psi_7 - 2\Psi_8 + \Psi_9) + \frac{r_8}{2h}(\Psi_6 - \Psi_{10}) + \frac{s_8}{2k}(\Psi_9 - \Psi_7) = c_8. \tag{27}$$

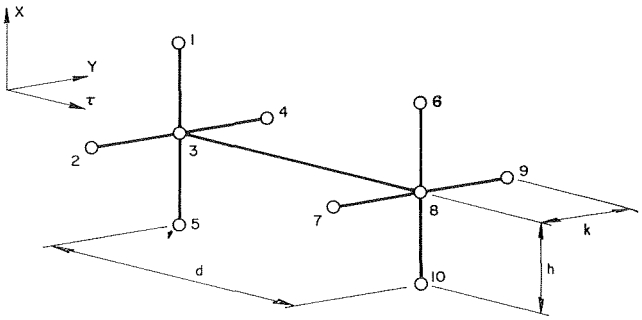

Fig. 2 Numbering system for interior nodes

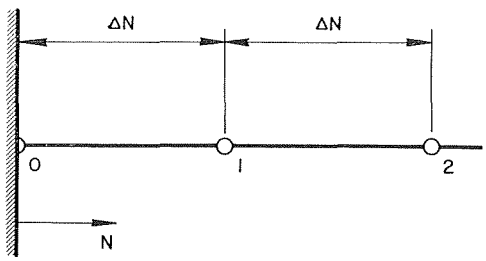

Fig. 3 Numbering system for nodes adjacent to walls

Equation (20) may be approximated using central differences by

$$U_8 = Y_8'(\Psi_9 - \Psi_7)/2k$$
$$V_8 = -X_8'(\Psi_6 - \Psi_{10})/2h. \tag{28}$$

The representations for nodes adjacent to walls where the conditions $\left.\frac{\partial\Psi}{\partial N}\right|_0$ and $\left.\frac{\partial\theta}{\partial N}\right|_0 = 0$ hold will now be considered. Using the numbering indicated in Fig. 3, three-point representations of $\left.\frac{\partial f}{\partial N}\right|_1$ and $\left.\frac{\partial^2 f}{\partial N^2}\right|_1$ were obtained by fitting a cubic polynomial through the values of f at points 0, 1, and 2, and satisfying the condition $\left.\frac{\partial f}{\partial N}\right|_0 = 0$. This yields the following approximations at node 1:

$$\left.\frac{\partial f}{\partial N}\right|_1 \simeq \frac{1}{4(\Delta N)}(-5f_0 + 4f_1 + f_2) \tag{29}$$

$$\left.\frac{\partial^2 f}{\partial N^2}\right|_1 \simeq \frac{1}{(\Delta N)^2}(f_0 - 2f_1 + f_2) \tag{30}$$

which were used when appropriate in place of the central difference representations in equation (26).

The only remaining nodes requiring special attention are those on the adiabatic walls. Using the numbering indicated in Fig. 3, a two-point representation may be obtained by fitting a parabolic polynomial through the values of f at points 0 and 1, and satisfying the condition $\left.\frac{\partial f}{\partial N}\right|_0 = 0$. The following representation of the second derivative is obtained:

$$\left.\frac{\partial^2 f}{\partial N^2}\right|_0 = \frac{2}{(\Delta N)^2}(f_1 - f_0). \tag{31}$$

This completes the finite-difference representations of the governing differential equations (17) to (20) for cases where the complete duct was considered. However, in cases where the temperature boundary conditions exhibit certain symmetries, the complete duct need not be considered, thus reducing the number of nodes needed for a given grid spacing.

By writing the appropriate difference representations of equa-

tions (17), (18), and (19) for all the nodes in the field, three sets of implicit nonlinear simultaneous difference equations were obtained. Also, by writing the appropriate difference representations of equations (20), two sets of explicit equations resulted. The solution sought had to satisfy, simultaneously, these five sets of equations.

Computation of Nusselt Numbers

In the analysis and presentation of the results by previous investigators, four types of Nusselt numbers have been utilized:

$$\mathrm{Nu}_L = -\frac{L}{(T_H - T_m)}\left.\frac{\partial T}{\partial y}\right|_{y=0} = -Y_0'\left(\frac{\partial\theta}{\partial Y}\right)_0 \tag{32}$$

$$\overline{\mathrm{Nu}}_L = -\frac{L}{(T_H - T_m)H}\int_0^H \left.\frac{\partial T}{\partial y}\right|_{y=0} dx = \frac{L}{H}\int_0^1 \frac{\mathrm{Nu}_L}{X'}\,dX \tag{33}$$

$$\overline{\mathrm{Nu}}_L' = -\frac{L}{(T_H - T_c)H}\int_0^H \left.\frac{\partial T}{\partial y}\right|_{y=0} dx = \overline{\mathrm{Nu}}_L/2 \tag{34}$$

$$\overline{\mathrm{Nu}}_H' = -\frac{1}{(T_H - T_c)}\int_0^H \left.\frac{\partial T}{\partial y}\right|_{y=0} dx = \frac{1}{2}\int_0^1 \frac{\mathrm{Nu}_L}{X'}\,dX. \tag{35}$$

In order to evaluate these, a representation of $\left.\frac{\partial\theta}{\partial Y}\right|_0$ was needed. For constant wall temperature and steady-state solution,

$$\left.\frac{\partial^2\theta}{\partial X^2}\right|_{Y=0} = \left.\frac{\partial\theta}{\partial X}\right|_{Y=0} = V_0 = \frac{\partial\theta}{\partial\tau} = 0$$

and for a linear transformation in the Y-direction, $Y' = 0$. Thus from equation (17)

$$\left.\frac{\partial^2\theta}{\partial Y^2}\right|_0 = 0. \tag{36}$$

Using the numbering indicated in Fig. 3, where N represents Y, a three-point representation of $\left.\frac{\partial\theta}{\partial Y}\right|_0$ may be obtained by fitting a cubic polynomial through the values of θ at points 0, 1, and 2 and satisfying equation (36). We obtain

$$\left.\frac{\partial\theta}{\partial Y}\right|_0 = \frac{-7\theta_0 + 8\theta_1 - \theta_2}{6k}. \tag{37}$$

The integrations required to evaluate the mean Nusselt numbers were carried out using Simpson's rule.

Method of Solution of the Difference Equations

It was assumed that the distributions of the five variables θ, Ω, Ψ, U, and V were known at time τ. In order to advance the solution through a step in time, an iterative solution was used. In this procedure, the representations of each of equations (17), (18), (19), and (20) were considered, in turn, to be linear in these variables and, while the representation of any one of these equations was being solved, the other variables appearing were treated as known functions.

First, the representation of equation (17) was solved for θ, treating U and V as known functions. For the first iteration, therefore, approximations to U and V at the new time step had to be made. Some past workers have used the distributions from the previous time step. Here, however, since the accuracy of the solution obtained at the first iteration depends solely on the accuracy of U and V, apart from rounding and truncation errors, an attempt was made to obtain a better initial estimate of the functions U and V at the new time step. This was done by linearly extrapolating from the previous two time steps.

Next, the representation for equation (18) was solved for Ω, treating U, V, and θ as known functions. Here, however, no boundary conditions for Ω were known. One way to get around this problem, which has proved successful, is to compute estimates of Ω on the boundaries from the most recent estimates of either Ψ using equation (19), or from U and V, using equation (20). The method used here will be described in the next section. Having established estimates of Ω on the boundaries, the solution of the representation of equation (18) was carried out in a manner similar to that used for equation (17).

The third step of the iteration involved solving the representation of equation (19) for Ψ treating Ω as a known function. The boundary condition $\Psi = 0$ was used.

Finally, the explicit representations of equation (20) were solved, using the most recently obtained distribution of Ψ.

The preceding four steps were repeated until the required accuracy was obtained. However, since the transient solutions were of secondary interest, the main objective being the steady-state solutions, the accuracy obtained at each time step did not need to be as good as that required for the steady-state solutions.

Estimation of Ω on the Boundaries

As was mentioned in the previous section, two methods are available for the determination of the distribution of Ω on the boundaries at any step in the iteration. The first method, where Ω was found using the most recent estimates of Ψ using equation (19), was utilized by both Wilkes and Churchill and Barakat and Clark, while Aziz and Hellums use the second where the values of U and V and equation (20) allowed Ω to be determined. From our experiences it was determined that the latter method yielded more stable results. Any instabilities which did occur could, in nearly all cases, be eliminated by using the mean of the distribution of Ω at the wall determined by this method and the distribution from the previous iteration. In terms of nondimensional variables, equation (14) becomes

$$\Omega = X'\frac{\partial V}{\partial X} - Y'\frac{\partial U}{\partial Y}. \tag{38}$$

On the walls the tangential derivatives of velocity are zero, so one or the other of the two terms on the right-hand side of equation (38) drops out. In either case, the representation of a normal derivative is required. Using the numbering indicated in Fig. 3, a three-point representation was obtained by fitting a parabolic polynomial through the values of independent variable at points 0, 1, and 2, which yields

$$\left.\frac{\partial f}{\partial N}\right|_0 = \frac{1}{2(\Delta N)}(4f_1 - f_2). \tag{39}$$

The truncation error in equation (39) is of one order less than that which is obtained by estimating Ω_0 from Ψ. However, the improved stability was considered to be of more importance.

Method of Solution of Each Set of Linearized Difference Equations

In cases where the whole duct was considered, each difference equation includes, at most, unknowns at the node and the four surrounding nodes. The nodes were numbered using an ordered system, and so the coefficient matrices of the resulting sets of simultaneous equations have all their nonzero elements contained in five diagonals grouped around the main diagonal. The use of conventional techniques for the solution of each set of equations is prohibitively wasteful because of the predominance of zero elements in the coefficient matrices. An iterative solution was not considered desirable since central difference representations of the first derivatives were used and the main diagonals of the coefficient matrices could become very weak. This can create formidable problems in devising an iterative scheme to give reliable results—indeed, to give results at all. The success of the iterative scheme appears to be greatly dependent upon the scanning procedure employed. Second, although iterative methods

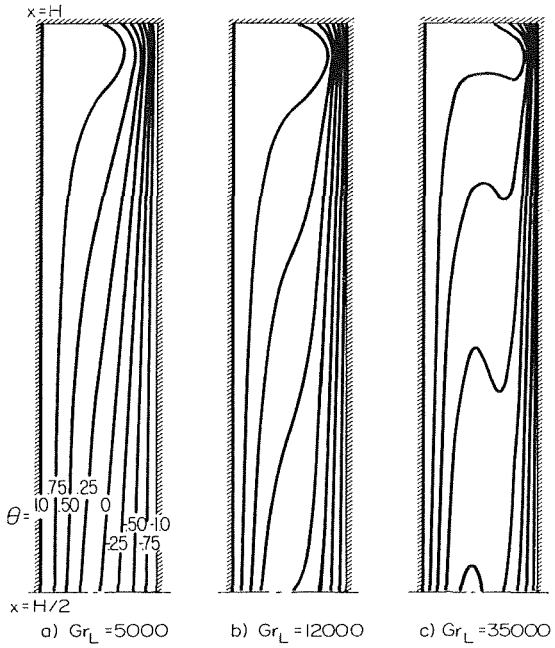

Fig. 4 Isotherms for $H/L = 10$

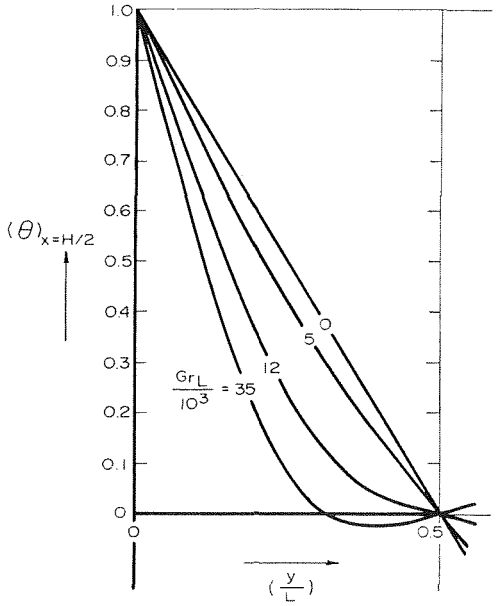

Fig. 5 Temperature profiles at $X = H/2$ for $H/L = 10$

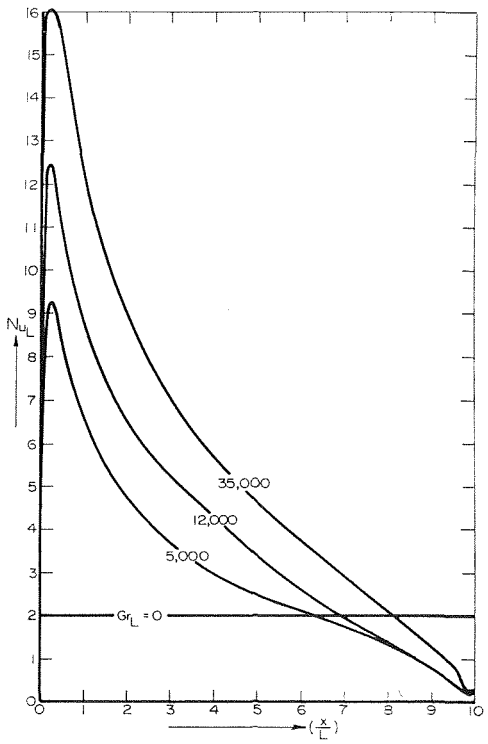

Fig. 6 Local Nusselt number versus $\left(\frac{x}{L}\right)$ for $H/L = 10$

virtually eliminate storage problems, computation time considerations limit the number of nodes which may be considered to about the same as can be used when direct solution is employed, provided economic storage techniques are used which do not store all the zero elements in the coefficient matrix.

For the foregoing reasons, a direct solution method was used, which gives reliable, accurate solutions, and only requires the storage of those elements contained between the two outermost nonzero diagonals of the coefficient matrix. The method used involves the triangular decomposition of the coefficient matrix followed by the solution of two triangular systems. Rounding errors present in the first solution are then reduced to negligible porportions by an iterative method. The theory is based on the method described by Bowdler, et al. [4], and is discussed in more detail in the Appendix.

Discussion of Results

Results are presented for values of Gr_L covering the range 2×10^3 to 7×10^4 for values of H/L of 1, 2.5, 10, and 20. All the results presented are for Pr = 0.733. In all cases, 13 nodes were used in the Y-direction, and 25 nodes in the X-direction except for the case $H/L = 20$ where 49 nodes were used in the X-direction. These grid systems were determined to be the most practical after running test cases with various numbers of nodes. The reasons for using more nodes when $H/L = 20$ were partly because of the relatively large distance to be covered in the X-direction, and partly because it was found that the various functions depended very little on X over most of the height but changed quite rapidly near the top and bottom, thus warranting a finer mesh size. In view of this finding a nonlinear coordinate transformation in the X-direction was used in the cases $H/L = 10$ and 20. The nonlinear transformations chosen were cubic, with symmetry about $X = H/2$ and were arranged to compress nodes into the regions near the top and bottom of the enclosure. For the cases $H/L = 1$ and 2.5, linear transformations were used in the X-direction, and for all cases linear transformations were used in the Y-direction.

An example of the effect of the Grashof number, Gr_L, on the steady-state nondimensional temperature distribution, θ, is shown in Fig. 4. Isotherms in the upper half of a duct for which $H/L = 10$ are shown for three values of Grashof number, Gr_L. For the relatively low Grashof number of 5000, the isotherms are not greatly affected by convection and are roughly parallel and equispaced over most of the enclosure. This is similar to the results in a case of pure conduction. The effect of the top and bottom walls only extends a short distance into the enclosure. When the Grashof number is raised to the intermediate value of 12,000, the effect of the top and bottom walls spreads further into the enclosure, and the isotherms in the central region tend toward the horizontal. For the relatively high Grashof number of 35,000, the effect of the top and bottom walls is apparent throughout the entire enclosure, and the structure of the temperature field resembles that of two boundary layers, one growing up the hot wall and the other growing down the cold wall. However, in the central region, the isotherms have gone past the

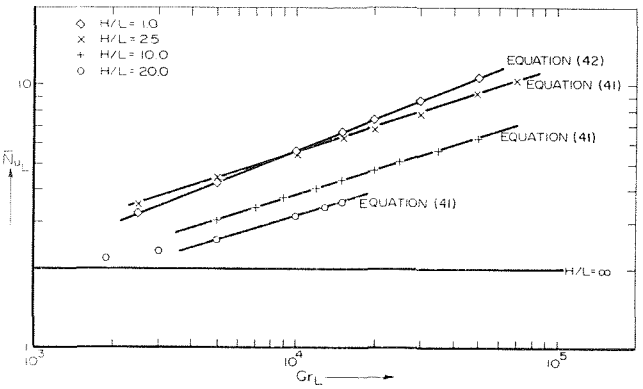

Fig. 7 Mean Nusselt number versus Grashof number

horizontal, indicating that the transport of energy there must be purely by convection. Also, this indicates that the two boundary layers do not become independent of each other as the Grashof number is increased, and so analyses based upon this assumption, as have sometimes been carried out, are open to some questions. A further increase in the Grashof number caused the distortion of the isothermals in the central region to become more severe. A transition to the secondary flow patterns similar to those reported by Elder [7] appears to be occurring although computational instabilities were encountered before these patterns could be established. Fig. 5 shows the nondimensional temperature profiles at $X = H/2$ for the same three cases as in Fig. 4.

An example of the variation of the local Nusselt number on the hot wall, Nu_L, with X/L is shown in Fig. 6. The value of Nu_L for pure conduction, $Gr_L = 0$, is 2. For nonzero Gr_L, convection increases Nu_L over most of the height of the enclosure; the maximum occurring very near the bottom of the wall. This is to be expected since the fluid there has just passed over the cold wall, so the temperature gradients are greatest. As the fluid rises up the hot wall, its temperature rises and the heat transfer rate decreases. As Gr_L is increased, the convective effect promotes greater heat transfer rates over the entire height of the enclosure wall.

The variation of the mean Nusselt number $\bar{N}u_L$, with Gr_L and H/L is shown in Figs. 7 and 8. The temperature difference associated with this Nusselt number is $(T_H - T_m)$. The solid lines shown are the results of least-squares fits through the data points. Referring to Fig. 7, it can be seen that $\bar{N}u_L$ increases with Gr_L for all values of H/L. This is due to the increasing contribution to the heat transfer made by convection. This means that for a given set of conditions, an increase in temperature difference will bring about more than a proportional increase in heat transfer. For small values of Gr_L, $\bar{N}u_L$ approaches the value 2 for all values of H/L, although this effect can only be seen here for $H/L = 20$. When this transition occurs, the flow has been classified by Carlson and Eckert as asymptotic flow. This effect occurs because for small Gr_L, the heat transfer is predominantly by conduction for which $\bar{N}u_L = 2$. Solution instabilities were encountered at high values of Gr_L. For $H/L = 20$, the limits were $4 \times 10^3 \leq Gr_L \leq 2 \times 10^4$ while for $H/L = 1$, 2.5, and 10 the limits were $2 \times 10^3 \leq Gr_L \leq 7 \times 10^4$.

An inspection of the data points in Fig. 7 shows that for nearly all the points plotted, the logarithm of $\bar{N}u_L$ bears a relation to the logarithm of Gr_L, which is very close to linear. The results for $H/L = 2.5$, 10, and 20 lie close to straight lines which are very nearly parallel, whereas the slope of the line through the points for $H/L = 1$ is noticeably steeper. As a result of having these two distinct trends, two different least-squares fits were employed, one for $H/L = 1$ and the other for $H/L = 2.5$, 10, and 20.

Referring to Fig. 8, it can be seen that two different regions exist and that for H/L greater than about 2, Nu_L decreases as H/L is increased. This is because most of the heat transfer into the fluid occurs near the bottom of the hot wall, and so adding more height to the enclosure does little to increase the total heat transfer and so the mean Nusselt number decreases. When H/L is less than 2, an increase in the height of the chamber will result in a more effective flow pattern for heat transfer. As a result, the mean Nusselt number will be increased. The results of Wilkes and Churchill also indicate this trend. It appears that the logarithms of $\bar{N}u_L$ and H/L bear a linear relation to each other for $H/L = 2.5$, 10, and 20, and so an expression of the form

$$\bar{N}u_L = A(Gr_L)^B(H/L)^C \tag{40}$$

was fitted through the data points for these cases, using a three-dimensional least-squares technique. The resulting expression is

$$\bar{N}u_L = 0.386(Gr_L)^{0.315}(H/L)^{-0.265}. \tag{41}$$

For the case $H/L = 1$, a two-dimensional least-squares fit was used, the resulting expression being

$$\bar{N}u_L = 0.145(Gr_L)^{0.397}. \tag{42}$$

Equations (41) and (42) are indicated by the solid lines in Figs. 7 and 8.

For the purpose of comparing these results with those of previous workers, mean Nusselt numbers, $\bar{N}u_L'$, and Grashof numbers, Gr_L', based on the total temperature difference across the enclosure were computed. In terms of $\bar{N}u_L'$ and Gr_L', equations (41) and (42) become

$$\bar{N}u_L' = 0.155(Gr_L')^{0.315}(H/L)^{-0.265} \tag{43}$$

and

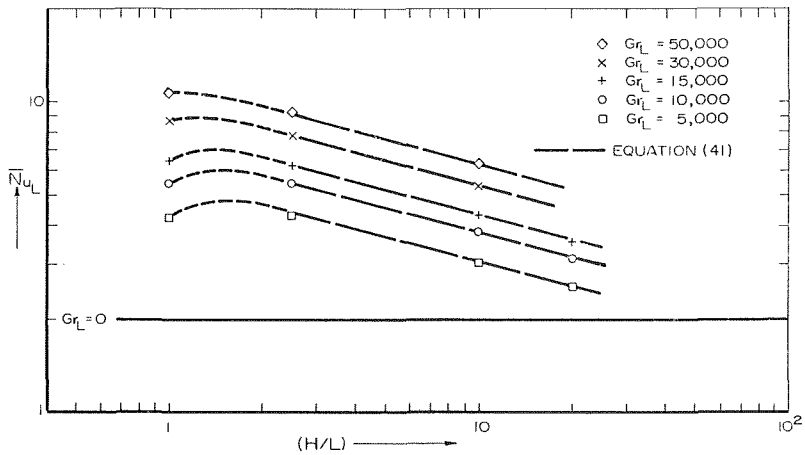

Fig. 8 Mean Nusselt number versus H/L

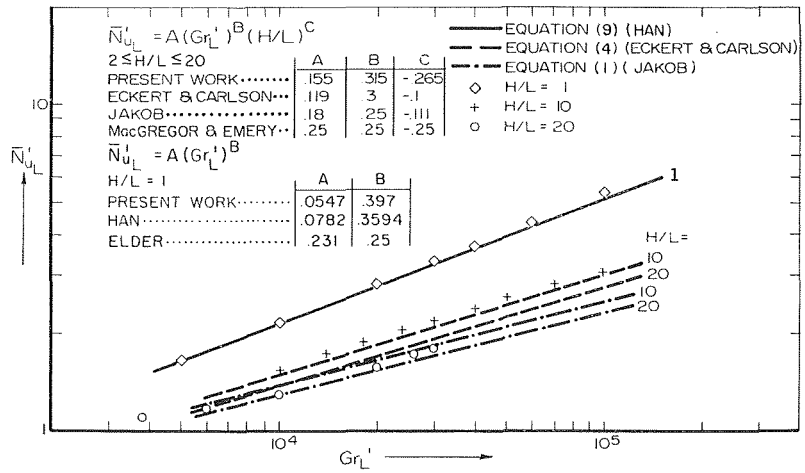

Fig. 9 Mean Nusselt number versus Grashof number

$$\bar{N}u_{L'} = 0.0547(Gr_{L'})^{0.397} \quad (44)$$

respectively.

A listing of the various expressions for $Nu_{L'}$ which have been previously reported is presented in Fig. 9. The exponent on $Gr_{L'}$ for the present study is higher than those given by all previous investigators but follows the trend indicated by Landis in his discussion of the work of Emery and Chu. This higher exponent may be due in part to the inclusion in the least-squares fit of the results for $H/L = 2.5$, since a least-squares fit through these points alone indicates a slightly higher exponent than that obtained for $H/L = 10$.

The exponent on H/L derived here is -0.265 which is considerably higher than the values obtained by either Jakob or Eckert and Carlson (-0.111 and -0.1, respectively) and of the same order as that of MacGregor, et al. One reason for this difference may possibly be explained by the way in which Eckert and Carlson derived their value for the exponent. As was pointed out in the Introduction, they stated that their result was derived only for cases where the flow may be considered to consist of two independent boundary layers, one on each wall, the structures of which would not be influenced by the spacing L. They then carried out a two-dimensional fit to correlate $\bar{N}u_{H'}$ with $Gr_{H'}$, and by converting the resulting expression to a relation between $\bar{N}u_{L'}$ and Gr_L, they derived the exponent on H/L. Thus the exponent, C, on H/L was calculated from the expression

$$C = 3B - 1$$

where B is the exponent on $Gr_{H'}$. The value of C computed by this method is critically dependent on the value used for B. For example, had Jakob used this method, he would have obtained a value of -0.25 and, if it had been used here, a value of -0.055 would have resulted.

A comparison of equation (44) with those of Han and Elder indicates similar trends for the Grashof number. MacGregor and Emery have used their expression setting $H/L = 1$ for purposes of comparing experimental and analytical results (Fig. 10 in reference [12]). The experimental values are all at a $Gr_{L'}$ greater than 1.4×10^5 but a superposition of equation (42) upon this figure indicates good agreement within the Grashof number limitation of the equation. The validity of MacGregor and Emery's expression for $H/L = 1$ is seriously questioned.

In order to more easily compare the results, the data points are plotted in terms of $Gr_{L'}$ and $\bar{N}u_{L'}$ for $H/L = 1$, 10, and 20 in Fig. 9. The lines shown represent the results of Eckert and Carlson, Jakob, and Han. It can be seen that the agreement between the present results and those of Han is quite good. The results of Eckert and Carlson lie below the present results for $H/L = 10$, and above them for $H/L = 20$. Thus it is to be expected that good agreement would be obtained for a value of H/L about midway between 10 and 20, which is roughly the middle of the range over which the results of Eckert and Carlson are intended to apply. The lesser influence attributed to the parameter H/L has already been discussed. The results of Jakob are lower than both the present results and those of Eckert and Carlson. No explanation to account for this has been found.

Conclusions

Results have been presented from which heat transfer rates through air enclosed in a rectangular enclosure can be calculated for various temperature differences and enclosure shapes. The results are in a close agreement with those of previous analytical studies and are in tolerable agreement with available experimental results.

References

1 Aziz, K., and Hellums, J. D., "Numerical Solution of the Three-Dimensional Equations of Motion for Laminar Natural Convection," *Physics of Fluids*, Vol. 10, 1967, p. 314.

2 Barakat, H. Z., and Clark, J. A., "Analytical and Experimental Study of the Transient Laminar Natural Convection Flows in Partially Filled Liquid Containers," *Proceedings of 3rd International Heat Transfer Conference*, Vol. II, 1966, p. 152.

3 Batchelor, G. K., "Heat Transfer by Free Convection Across a Closed Cavity Between Vertical Boundaries at Different Temperatures," *Quarterly of Applied Mathematics*, Vol. 12, 1954, p. 209.

4 Bowdler, H. J., et al., "Solution of Real and Complex Systems of Linear Equations," *Numerische Mathematik*, Vol. 8, 1966, p. 217.

5 Carlson, W. O., "Interferometric Studies of Convective Flow Phenomena in Vertical Plane Enclosed Air Layer," PhD thesis, Graduate School, University of Minnesota, 1956.

6 Eckert, E. R. G., and Carlson, W. O., "Natural Convection in an Air Layer Enclosed Between Two Vertical Plates With Different Temperatures," *International Journal of Heat and Mass Transfer*, Vol. 2, 1961, p. 106.

7 Elder, J. W., "Laminar Free Convection in a Vertical Slot," *Journal of Fluid Mechanics*, Vol. 23, 1965, p. 77.

8 Elder, J. W., "Numerical Experiments With Free Convection in a Vertical Slot," *Journal of Fluid Mechanics*, Vol. 24, 1966, p. 823.

9 Emery, A., and Chu, N. C., "Heat Transfer Across Vertical Layers," JOURNAL OF HEAT TRANSFER, TRANS. ASME, Series C, Vol. 87, 1965, p. 110.

10 Han, J. T., "Numerical Solutions for an Isolated Vortex in a Slot and Free Convection Across a Square Cavity," MASc thesis, Department of Mechanical Engineering, University of Toronto, 1967.

11 Jakob, M., *Heat Transfer*, Vol. 1, Wiley, New York, 1949.

12 MacGregor, R. K., and Emery, A. F., "Free Convection Through Vertical Plane Layers—Moderate and High Prandtl Number Fluids," ASME Paper 68-WA/HT-4, 1968.

13 Mull, W., and Reiher, H., "Der Wärmeschutz von Luftschichten," *Beihefte zum Gesundh-Ingenieur*, Reihe 1, Heft 28, 1930.

14 Poots, G., "Heat Transfer by Laminar Free Convection in Enclosed Plane Gas Layers," *Quarterly Journal of Mechanics and Applied Mathematics*, Vol. II, Part 3, 1958, p. 257.

15 Wilkes, J. O., and Churchill, S. O., "The Finite Difference

Computation of Natural Convection in a Rectangular Enclosure," *AIChE Journal*, Vol. 12, No. 1, 1966, p. 161.

APPENDIX

A direct solution method was used, for the solution of the set of difference equations, requiring only the storage of those elements contained between the two outermost nonzero diagonals of the coefficient matrix. The method used involves the triangular decomposition of the coefficient matrix followed by the solution of two triangular systems. Rounding errors present in the first solution are then reduced to negligible proportions by an iterative method. The theory is as follows.

Each set of equations may be written in the form

$$\hat{A}\bar{X} = \bar{B} \tag{45}$$

where

$\hat{A}$ = coefficient matrix
$\bar{B}$ = constant vector
$\bar{X}$ = solution vector

Provided $\hat{A}$ is nonsingular, it may be factorized in the form

$$\hat{A} = \hat{L}\hat{U} \tag{46}$$

where

$\hat{L}$ = lower triangular matrix
$\hat{U}$ = upper triangular matrix with unity elements on main diagonal

In the case where the nonzero elements of $\hat{A}$ are all contained within a band around the main diagonal, it may be shown that the nonzero elements of $\hat{L}$ and $\hat{U}$ all lie within corresponding bands.

Substituting equation (45) into (46), we obtains

$$\hat{L}\hat{U}\bar{X} = \bar{B}$$

which may be written as the two equations

$$\hat{L}\bar{Y} = \bar{B} \tag{47}$$

and

$$\hat{U}\bar{X} = \bar{Y} \tag{48}$$

where

$\bar{Y}$ = auxiliary vector.

These two triangular systems may be solved very simply by a back substitution type of approach, first solving equation (47) for $\bar{Y}$, then equation (48) for $\bar{X}$. In general, the solution thus obtained will contain rounding errors, but in most cases these may be reduced to negligible size by the following iterative method.

Let the first-obtained solution be $\bar{X}^{(0)}$, and let the difference between this and the true solution, $\bar{X}$, be the vector $\bar{E}^{(0)}$ such that

$$\bar{E}^{(0)} = \bar{X} - \bar{X}^{(0)}.$$

Form the vector $\bar{D}^{(0)}$ such that

$$\bar{D}^{(0)} = \bar{B} - \hat{A}\bar{X}^{(0)}$$

which, by the definition of $\bar{E}^{(0)}$, may be written

$$\begin{aligned}\bar{D}^{(0)} &= \bar{B} - A\bar{X} + \bar{E}\hat{A}^{(0)} \\ &= \hat{A}\bar{E}^{(0)}.\end{aligned}$$

Thus

$$\hat{A}\bar{E}^{(0)} = \bar{D}^{(0)}$$

which must be solved for $\bar{E}^{(0)}$. However, since the coefficient matrix, $\hat{A}$, is unchanged, the factors $\hat{L}$ and $\hat{U}$ are unchanged, and so only the solution of the two triangular systems is needed. Let the solution obtained from this system be $\bar{E}_1^{(0)}$, which will differ in general from $\bar{E}^{(0)}$ due to rounding errors. Then a second approximation to $\bar{X}$ is obtained from

$$\bar{X}^{(1)} = \bar{X}^{(0)} + \bar{E}_1^{(0)},$$

where $\bar{X}^{(1)}$ is the new approximation to the solution. The preceding procedure may be repeated until the required accuracy is obtained.

This method fails if the matrix, $\hat{A}$, is so ill-conditioned that the rounding errors in $\hat{L}$ and $\hat{U}$ are prohibitive. However, even in systems of several hundred equations, and where $\hat{A}$ has a relatively weak main diagonal, it has been found that only rarely have more than three iterations been needed for full-work (seven-place) accuracy in the largest element of the solution vector. It may be noted that higher than single-precision accuracy is not possible, since the computation of the vector $\bar{D}$ must be carried out in a higher precision arithmetic than the storage precision being used, although double-precision accumulation of inner products of the single-precision components should be used throughout.

As was pointed out, in cases where symmetry is present, which means that only half the duct need be considered, the difference equations for nodes on the line of symmetry involve not only the unknowns at a node and its immediate neighbors, but also the unknown at the node symmetrically opposite. This gives rise to an extra diagonal in the coefficient matrix. However, by suitable numbering of the nodes, this can be made into two extra diagonals which are totally contained within the original five diagonals, and so no extra storage is needed.

Computation of Natural Convection in a Rectangular Enclosure," *AIChE Journal*, Vol. 12, No. 1, 1966, p. 161.

APPENDIX

A direct solution method was used, for the solution of the set of difference equations, requiring only the storage of those elements contained between the two outermost nonzero diagonals of the coefficient matrix. The method used involves the triangular decomposition of the coefficient matrix followed by the solution of two triangular systems. Rounding errors present in the first solution are then reduced to negligible proportions by an iterative method. The theory is as follows.

Each set of equations may be written in the form

$$\hat{A}\bar{X} = \bar{B} \tag{45}$$

where

$\hat{A}$ = coefficient matrix
$\bar{B}$ = constant vector
$\bar{X}$ = solution vector

Provided $\hat{A}$ is nonsingular, it may be factorized in the form

$$\hat{A} = \hat{L}\hat{U} \tag{46}$$

where

$\hat{L}$ = lower triangular matrix
$\hat{U}$ = upper triangular matrix with unity elements on main diagonal

In the case where the nonzero elements of $\hat{A}$ are all contained within a band around the main diagonal, it may be shown that the nonzero elements of $\hat{L}$ and $\hat{U}$ all lie within corresponding bands.

Substituting equation (45) into (46), we obtains

$$\hat{L}\hat{U}\bar{X} = \bar{B}$$

which may be written as the two equations

$$\hat{L}\bar{Y} = \bar{B} \tag{47}$$

and

$$\hat{U}\bar{X} = \bar{Y} \tag{48}$$

where

$\bar{Y}$ = auxiliary vector.

These two triangular systems may be solved very simply by a back substitution type of approach, first solving equation (47) for $\bar{Y}$, then equation (48) for $\bar{X}$. In general, the solution thus obtained will contain rounding errors, but in most cases these may be reduced to negligible size by the following iterative method.

Let the first-obtained solution be $\bar{X}^{(0)}$, and let the difference between this and the true solution, $\bar{X}$, be the vector $\bar{E}^{(0)}$ such that

$$\bar{E}^{(0)} = \bar{X} - \bar{X}^{(0)}.$$

Form the vector $\bar{D}^{(0)}$ such that

$$\bar{D}^{(0)} = \bar{B} - \hat{A}\bar{X}^{(0)}$$

which, by the definition of $\bar{E}^{(0)}$, may be written

$$\bar{D}^{(0)} = \bar{B} - A\bar{X} + \bar{E}\hat{A}^{(0)}$$
$$= \hat{A}\bar{E}^{(0)}.$$

Thus

$$\hat{A}\bar{E}^{(0)} = \bar{D}^{(0)}$$

which must be solved for $\bar{E}^{(0)}$. However, since the coefficient matrix, $\hat{A}$, is unchanged, the factors $\hat{L}$ and $\hat{U}$ are unchanged, and so only the solution of the two triangular systems is needed. Let the solution obtained from this system be $\bar{E}_1^{(0)}$, which will differ in general from $\bar{E}^{(0)}$ due to rounding errors. Then a second approximation to $\bar{X}$ is obtained from

$$\bar{X}^{(1)} = \bar{X}^{(0)} + \bar{E}_1^{(0)},$$

where $\bar{X}^{(1)}$ is the new approximation to the solution. The preceding procedure may be repeated until the required accuracy is obtained.

This method fails if the matrix, $\hat{A}$, is so ill-conditioned that the rounding errors in $\hat{L}$ and $\hat{U}$ are prohibitive. However, even in systems of several hundred equations, and where $\hat{A}$ has a relatively weak main diagonal, it has been found that only rarely have more than three iterations been needed for full-work (seven-place) accuracy in the largest element of the solution vector. It may be noted that higher than single-precision accuracy is not possible, since the computation of the vector $\bar{D}$ must be carried out in a higher precision arithmetic than the storage precision being used, although double-precision accumulation of inner products of the single-precision components should be used throughout.

As was pointed out, in cases where symmetry is present, which means that only half the duct need be considered, the difference equations for nodes on the line of symmetry involve not only the unknowns at a node and its immediate neighbors, but also the unknown at the node symmetrically opposite. This gives rise to an extra diagonal in the coefficient matrix. However, by suitable numbering of the nodes, this can be made into two extra diagonals which are totally contained within the original five diagonals, and so no extra storage is needed.

DISCUSSION

F. Landis[2] and A. Rubel[3]

The authors have added to the growing literature on the computational analysis of natural convection flows in rectangular enclosures by presenting an additional computational scheme and by illustrating it over a large range of Grashof numbers and H/L ratios, although unfortunately only for one Prandtl number.

Although the paper discussed much of the previous literature, especially the work of MacGregor and Emery [12], which covers the same range of calculations, several recent investigations into numerical schemes and into the structure of natural convection have been omitted. This becomes especially important as Grashof numbers and aspect ratios are increased to the point where either stability problems may become severe or where cellular motions will arise.

An extensive study of numerical techniques for the solution of the transient equation system has been performed by Torrance [16][4] which fully discusses the errors inherent in various techniques.

Reference should also have been made to the work of deVahl Davis and his co-workers [17–19] who have analyzed both the transient and the steady flow behavior in vertical concentric cylinders and rectangular cavities.

In discussing the flow structure, deVahl Davis and Thomas as well as Rubel and Landis [20] and Polezhaev [21] have found secondary flows not unlike those observed by Elder [7]. It should be noted, however, that a mesh width which is too coarse can lead to spurious secondary flows even in a regime where computational stability is not a problem [22]. With a coarse mesh in either direction it is also difficult to gain an accurate representation of the flow near the hot and cold corners where the stream

[2] Department of Mechanical Engineering, New York University, Bronx, N. Y. Mem. ASME.
[3] Advanced Technology Laboratories, Inc., Jericho, N. Y.
[4] Numbers in brackets designate Additional References at end of Discussion.

function gradients show the sharpest change. As a result the difference equations tend to fail in representing the differential equations accurately unless the mesh size is very small. For the type of problem selected this frequently results in a local minimum temperature near the $x = 0$, $y = 0$ corner (especially at high Grashof numbers) which is likely to lead to instabilities. By using a finer mesh deVahl Davis and Thomas as well as Rubel and Landis were able to go to higher Grashof numbers than the authors without running into stability problems.

Too coarse a mesh can also lead to erroneous predictions of the Nusselt number. In reference [22] it is demonstrated that at $Gr_L' = 100{,}000$, $H/L = 1.0$, the Nusselt number decreases by about 15 percent in going from an 11×11 to a 21×21 grid. This mesh effect appears to be most severe at the lower aspect ratios and an evaluation of the authors' results suggests that their Nusselt number predictions for $H/L = 1.0$ and 2.5 may be slightly too high.

Work by deVahl Davis over a large range of the Rayleigh numbers and aspect ratios for both concentric cylinders and rectangular enclosures [23] led to a suggested correlation of the form

$$Nu_L' = 0.149\ (Ra_L')^{0.315}\ Pr^{0.027}(H/L)^{-0.204}(R_0/R_i)^{0.459} \quad (49)$$

where (R_0/R_i) is the radius ratio for concentric cylinders.

For the case discussed by the authors, this reduces to

$$Nu_L' = 0.135(Gr_L')^{0.315}(H/L)^{-0.204} \quad (50)$$

and is valid for a range of about $2.5 \leqslant H/L \leqslant 35$ and $10^4 \leqslant Gr_L' \leqslant 3 \times 10^5$. Although over the range given by Newell and Schmidt's equation (43) the results agree to within 10 percent, the discussers prefer to use the deVahl Davis correlation because of its wider applicability and because it appears to represent the aspect ratio trends slightly more accurately.

Based on a 21×21 grid for $H/L = 1.0$, the discussers obtained an approximate correlation of the form

$$Nu_L' = 0.082\ (Gr_L')^{0.344},\ 2 \times 10^4 \leqslant Gr_L' \leqslant 1 \times 10^5 \quad (51)$$

which is closest to the results of Han [10]. The higher Grashof number exponent proposed by the authors may have been influenced by their coarse mesh. The apparent inconsistency in the MacGregor and Emery data for $H/L = 1.0$ results was also confirmed by the discussers.

Additional References

16 Torrance, K. E., "Comparison of Finite-Difference Computation of Natural Convection," *Journal of Research, National Bureau of Standards*, Series B, Vol. 72B, No. 4, 1968.

17 deVahl Davis, G., and Kettleborough, C. F., "Natural Convection in an Enclosed Rectangular Cavity," *Transactions of the Institution of Engineers*, Australia, MCE, Vol. 1, 1965, p. 43.

18 deVahl Davis, G., "Laminar Natural Convection in an Enclosed Rectangular Cavity," *International Journal of Heat and Mass Transfer*, Vol. 11, 1968, p. 1675.

19 deVahl Davis, G., and Thomas, R. W., "Natural Convection Between Concentric Vertical Cylinders," International Symposium on High-Speed Computing in Fluid Dynamics (1968), to be published as *Supplement to Physics of Fluids*, Nov. 1969.

20 Rubel, A., and Landis, F., "A Numerical Study of Natural Convection in a Vertical Rectangular Enclosure," International Symposium on High-Speed Computing in Fluid Dynamics (1968), to be published as *Supplement to Physics of Fluids*, Nov. 1969.

21 Polezhaev, V. I., "Numerical Solution of a System of Two-Dimensional Unsteady Navier-Stokes Equations for a Compressible Gas in a Closed Region," *Izvestiia*, MZG, No. 2, 1967, p. 103.

22 Rubel, A., "A Numerical Study of Steady Laminar Natural Convection in a Vertical Rectangular Enclosure," PhD thesis, New York University, 1969.

23 deVahl Davis, G., Private Communication.

Authors' Closure

The authors wish to thank Dr. Landis and Dr. Rubel for their comments. The increase in the list of references to include those which have been recently published or will be published shortly is appreciated and will be most helpful to persons interested in this area.

The effect of grid size on the stability and accuracy of the solution was of great concern to the authors. Aris and Hellums [1] reported that for a particular set of conditions, a refinement of the grid size from 11×11 to 41×41 caused a change in the Nusselt number of 40 percent. Preliminary calculations by us and, as noted in the discussion, Rubel [22] have confirmed these facts, although de Vahl Davis [18] noted that his calculations were performed with an 11×11 grid since previous investigators had indicated that finer mesh points made relatively little significant difference in the final results. The calculation of the Nusselt number requires that the first derivative of the temperature normal to the walls be evaluated. The mesh size and the order of the finite difference approximation of the derivative thus significantly influences the accuracy of the calculation of the Nusselt numbers.

As noted in the paper, a nonlinear coordinate transformation was used in the X-direction for $H/L = 10$ and 20. The nonlinear transformations used were

$$H/L = 10 \quad X = \frac{3}{2000}\left(\frac{x}{L}\right)^3 - \frac{9}{400}\left(\frac{x}{L}\right)^2 + \frac{7}{40}\left(\frac{x}{L}\right) \quad (52)$$

$$H/L = 20 \quad X = \frac{3}{16{,}000}\left(\frac{x}{L}\right)^3 - \frac{9}{1600}\left(\frac{x}{L}\right)^2 + \frac{7}{80}\left(\frac{x}{L}\right). \quad (53)$$

An analysis of this transformation indicates that nodes are compressed near the top and the bottom of the enclosures where the gradients are most severe and where the largest truncation errors will occur. In fact, the mesh in the immediate vicinity of the corners is of the order of one half that for a 21×21 grid with $H/L = 10$ and of the order of one fourth that for a 21×21 grid with $H/L = 20$. It is felt that the coarse grid in the center position of the enclosure does not introduce significant errors. A discussion of the effect of grid size on the calculated Nusselt number has been presented by Newell.[5]

In conclusion the authors have not been able to precisely define the cause of the computational instabilities which were encountered at high Grashof number. It is felt that the solutions present are as accurate as possible within the limits of the computational equipment available.

[5] Newell, M. E., "Heat Transfer by Laminar Natural Convection Within Rectangular Enclosures," MS Thesis, Pennsylvania State University, 1968.

P. O. ROUHIAINEN
Stone & Webster Engineering Corporation,
Boston, Mass.

J. W. STACHIEWICZ
Professor,
Department of Mechanical Engineering,
McGill University,
Montreal, Canada.
Mem. ASME

On the Deposition of Small Particles From Turbulent Streams

It is shown in the paper that the two fundamental assumptions (that of equality of particle and fluid diffusivity and that of purely inertial coasting within the viscous sublayer) on which existing deposition models are based, are untenable under most actual conditions. The concept of Stokes stopping distance, in particular, is shown to be invalid, since the effect of shear-flow-induced transverse lift force, which heretofore has been disregarded, is not negligible when considering the passage of a dense particle through the viscous sublayer. Due to the action of this lift force much lower radial velocities are required at the edge of the sublayer to insure particle deposition on the wall than would be the case if Stokes drag were the only force present. This explains why deposition models based on Stokes stopping distance concept must resort to the use of unrealistically high radial velocities within the sublayer to insure agreement with experimental data.

Existing Deposition Models

THE transfer of solid particles or liquid droplets from turbulent streams to channel walls has been studied by a number of investigators both theoretically and experimentally. The theoretical treatment has generally been based on the diffusion model, in which particle flux is expressed in terms of particle diffusivity and concentration gradient.

Thus

$$N = (D + \epsilon_p) \frac{dc}{dy} \tag{1}$$

For very small particle sizes (in the submicron range) both the molecular diffusivity D and the turbulent eddy diffusivity ϵ_p must be considered, such as in the work of Lin, Moulton, and Putnam [1][1] and Beal [2]. For larger particle sizes, D is much smaller than ϵ_p and can be neglected. This is the model employed by Friedlander and Johnstone [3, 4] and Davies [5].

The first difficulty that must be overcome in order to solve this equation is the determination of the turbulent diffusivity of particles. Here all the authors use the same basic assumption that the diffusivities of the particles and of the fluid are identical. This assumption is reasonable for submicron particles (as in reference [1]) but becomes questionable for particle sizes of about 1μ and is shown to be completely untenable for 30μ particles (such as those used in reference [3]) as will be demonstrated in detail in the present paper.

Once particle diffusivities (ϵ_p) are equated to fluid diffusivities (ϵ_f), expressions for the latter must be found before equation (1) can be integrated.

If the classical approach of subdividing the boundary layer into three zones (laminar, buffer, and turbulent) is followed, ϵ_f in the laminar sublayer should be set to zero.

Lin, et al., found, however, that when this was done, and equation (1) was integrated to obtain the deposition velocity coefficient K, the theoretical results fell considerably below the experimental ones.

In order to overcome this discrepancy they proposed the following variation of ϵ_f in the laminar sublayer

$$\frac{\epsilon_f}{\nu} = \left[\frac{y^+}{14.5}\right]^3 \tag{2}$$

This is a purely empirical relation used for the very pragmatic reason that "it produces the best correlation" between their model and the experimental results.

Davies [5], who did not assume a laminated structure for the boundary layer, also derived an empirical equation for ϵ_f based on his experimental results. This equation holds for values of y^+ up to 500 (at pipe Re $= 10^4$) and gives the same order of magnitude of ϵ_p/ν in the laminar sublayer as equation (2). (At $y^+ = 5$ equation (2) gives 0.041 while Davies' equation gives 0.08.)

The model of Friedlander and Johnstone [4] is similar to Lin, et al., except that the molecular diffusivity D was assumed zero not only in the turbulent core but also in the laminar and buffer layers, which is reasonable for particles of more than 1μ dia.

[1] Numbers in brackets designate References at end of paper.

Contributed by the Heat Transfer Division of THE AMERICAN SOCIETY OF MECHANICAL ENGINEERS and presented at the AIChE-ASME Heat Transfer Conference, Minneapolis, Minn., August 3–5, 1969. Manuscript received at ASME Headquarters, January 27, 1969; revised manuscript received, April 21, 1969, Paper No. 69-HT-41.

According to Friedlander's model, eddies carrying the particles diffuse from the turbulent core to within the stopping distance of the wall, from where the particles coast to the wall by virtue of their inertia. This stopping distance depends of course on the initial velocity of the particle and is calculated by assuming Stokes drag relation for a sphere moving in a stagnant fluid.

The initial velocity is imparted to the particle by the transverse velocity fluctuations of the gas which carries it. The higher this fluctuating velocity, the larger the stopping distance. Unfortunately, unreasonably high initial velocities are required for the stopping distance to exceed the thickness of the laminar sublayer. Friedlander used a figure of $0.9u^*$ which, according to Laufer, exists at a distance of $y^+ = 80$ from the wall, or well into the turbulent core of the boundary layer. Even then the stopping distance was in most cases smaller than the thickness of the laminar layer.

If there were no eddies in the laminar layer no deposition should thus occur since no particles could diffuse to within one stopping distance of the wall. This conclusion leads Friedlander to employ in his analysis Liu's, et al., expression for ϵ_f in the sublayer [equation (2)].

Thus, according to this model, eddies from the turbulent core ($y^+ = 80$) penetrate the boundary layer and *retain their momentum* until they reach to within the Stokes stopping distance (S^+) of the wall (which could be as low as $y^+ = 1$ for 2μ particles.) In addition, a finite eddy diffusivity within the laminar layer must be assumed. If S^+ is calculated by using the actual value of v' at $y^+ = S^+$, transport coefficients are obtained which are some four orders of magnitude lower than those found experimentally by Friedlander and Johnstone.

In a more recent analysis Beal [2] discusses in detail the stopping distance assumption and notes that "while containing certain inconsistencies, (it) is the only one of several investigated whose results agree reasonably with the experimental data." He uses the same assumption himself. In addition, in order to calculate the deposition flux, he assumes that the radial velocity of the particles within the laminar and buffer layer is equal to *half* the axial velocity of the fluid at a given point y^+ from the wall. He admits this to be a somewhat unrealistic assumption and agrees that the radial velocity is probably much lower than the axial but, unless such an assumption is made, analytical results again fall short of experimental data.

We are thus faced with the situation that, in the best deposition models available today, assumptions, which cannot be defended on theoretical grounds and with which the authors themselves are somewhat unhappy, must be made in order to make the models agree with experimental data.

These assumptions will now be discussed in more detail and it will be demonstrated that the concept of Stokes stopping distance loses much of its significance when all the forces acting on a particle traversing a laminar boundary layer are taken into account.

Relationship Between Eddy Diffusivity of Particle and Fluid

The subject has received considerable attention in the past and Soo [6] presents an extensive discussion of it in Chapter 2 of his text, where an equation for ϵ_p/ϵ_f in terms of Lagrangian and Eulerian microscales of turbulence and of particle Reynolds number is given.

In trying to obtain a quantitative evaluation of ϵ_i/ϵ_f we found it more convenient to use the concept of frequency response developed by Hjelmfelt and Mockros [7].

The Basset, Boussinesq, Oseen equation for motion of a particle in a turbulent fluid as extended by Tchen [8] to the case of a moving fluid is

$$\frac{\pi}{6} d_p^3 \rho_p \frac{du_p}{dt} = 3\pi\mu d_p(u_f - u_p) - \frac{\pi}{6} d_p^3 \rho_f \frac{du_f}{dt} + \frac{1}{2}\frac{\pi}{6} d_p^3 \rho_f \left(\frac{du_f}{dt} - \frac{du_p}{dt}\right) + \frac{3}{2} d_p^2 \sqrt{\pi\rho_f\mu} \int_{t_0}^{t} \frac{(du_f/dt' - du_p/dt')}{\sqrt{t - t'}} dt' + F_e \quad (3)$$

This equation is not exact but is valid when the following relations hold [9]

$$\frac{d_p^2}{\nu}\frac{\partial u}{\partial x} \ll 1, \qquad \frac{u_p}{d_p^2\left(\dfrac{\partial^3 u}{\partial x^2}\right)} >> 1 \quad (3a)$$

Following Hinze's approach [10], we write the equation in a simplified form, neglecting the external force F_e

$$\frac{du_p}{dt} + a'u_p = a'u_f + b'\frac{du_f}{dt} + c'\int_0^t \frac{(du_f/dt' - du_p/dt')}{\sqrt{t - t'}} dt' \quad (4)$$

Expressing u_p and u_f by their Fourier integrals, we have

$$u_f = \int_0^\infty (\xi \cos \omega t + \lambda \sin \omega t) d\omega$$
$$u_p = \int_0^\infty (\sigma \cos \omega t + \varphi \sin \omega t) d\omega \quad (5)$$

Substituting equations (5) into (4) yields

$$\sigma = [1 - f_1]\xi + f_2\lambda$$
$$\varphi = -f_2\xi + [1 + f_1]\lambda \quad (6)$$

where

Nomenclature

a = particle radius, ft
D_{eq} = equivalent diameter = 4 flow area/wetted perimeter, ft
d_p = particle diameter, ft
$E_{(n)}$ = Lagrangian energy spectrum of velocity fluctuations
F_e = external force, lb
f = friction factor ($0.079\ \mathrm{Re}^{-0.25}$ in turbulent flow)
n = wave number, or frequency in cps
Re = Reynolds number = $U_{ave}D_{eq}/\nu$
S = Stokes stopping distance = $\rho_p d^2 v/18\mu$, ft
S^+ = Stokes stopping distance = Su^*/ν, dimensionless
U_{ave} = average stream velocity, fps
u^* = friction velocity = $U_{ave}\sqrt{f/2}$
u^+ = dimensionless velocity u/u^*
v = velocity in transverse direction, fps
v' = rms turbulent fluctuating velocity in y-direction, fps
y = distance from wall, ft
y^+ = dimensionless distance = yu^*/ν
ϵ = turbulent diffusivity, ft²/hr
η = ratio between amplitudes of oscillation of particle and fluid
κ = magnitude of velocity gradient du/dy, sec^{-1}
μ = absolute viscosity, lb/ft-hr
ν = kinematic viscosity, ft²/hr
ρ = density, lb/ft³
ω = angular frequency, rad/sec

Subscripts

f = fluid
p = particle

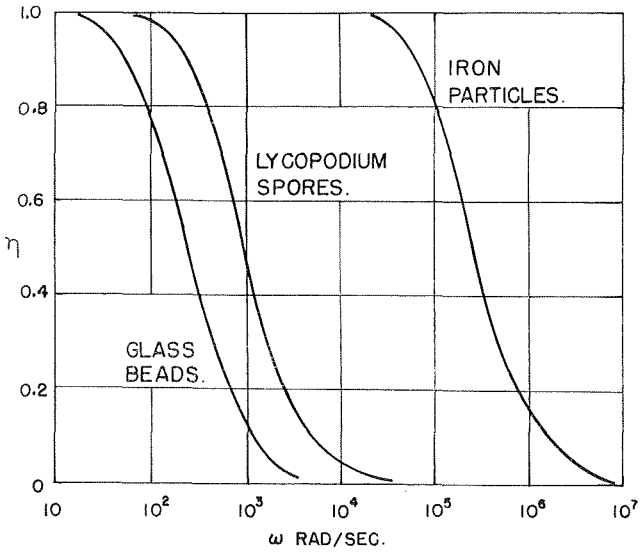

Fig. 1 Variation of amplitude ratio with frequency

$$f_1 = \frac{\omega(\omega + c'\sqrt{\pi\omega/2})(b' - 1)}{(a' + c'\sqrt{\pi\omega/2})^2 + (\omega + c'\sqrt{\pi\omega/2})^2}$$

$$f_2 = \frac{\omega(a' + c'\sqrt{\pi\omega/2})(b' - 1)}{(a' + c'\sqrt{\pi\omega/2})^2 + (\omega + c'\sqrt{\pi\omega/2})^2} \tag{7}$$

$$a' = \frac{36\mu}{(2\rho_p + \rho_f)d^2} \qquad b' = \frac{3\rho_f}{2\rho_p + \rho_f}$$

$$c' = \frac{18}{(2\rho_p + \rho_f)d}\sqrt{\frac{\rho_f\mu}{\pi}}$$

At this point, following Hjelmfelt and Mockros [7] we introduce the concept of amplitude ratio and phase angle between particle and fluid motion and express the velocity as follows:

$$u_p = \int_0^\infty \{\eta[\xi \cos(\omega t + \beta) + \lambda \sin(\omega t + \beta)]\} d\omega \tag{8}$$

where the amplitude ratio

$$\eta = \sqrt{(1 + f_1)^2 + f_2^2}$$

and the phase angle

$$\beta = \tan^{-1}\left[\frac{f_2}{1 + f_1}\right] \tag{9}$$

The amplitude ratio between particle and fluid fluctuations is thus seen to be primarily a function of the angular frequency ω of fluid fluctuations, as well as being a function of fluid and particle properties. Fig. 1 shows a plot of the amplitude ratio η against ω for the three types of particles investigated in this work.[2] It is evident that particle frequency response decreases from unity to zero within about two decades of ω.

To determine actual particle eddy diffusivity as a function of Reynolds number we must obtain relations between eddy diffusivity and amplitude ratio and between angular frequency and Reynolds number.

In terms of the Lagrangian energy spectra ($E_f(n)$ for fluid and $E_p(n)$ for particles), the ratio of eddy diffusivities is [10, p. 359]

[2] These particular types were chosen because they were readily available for experimental work, and were in the right size range. Information on them is given in Appendix A.

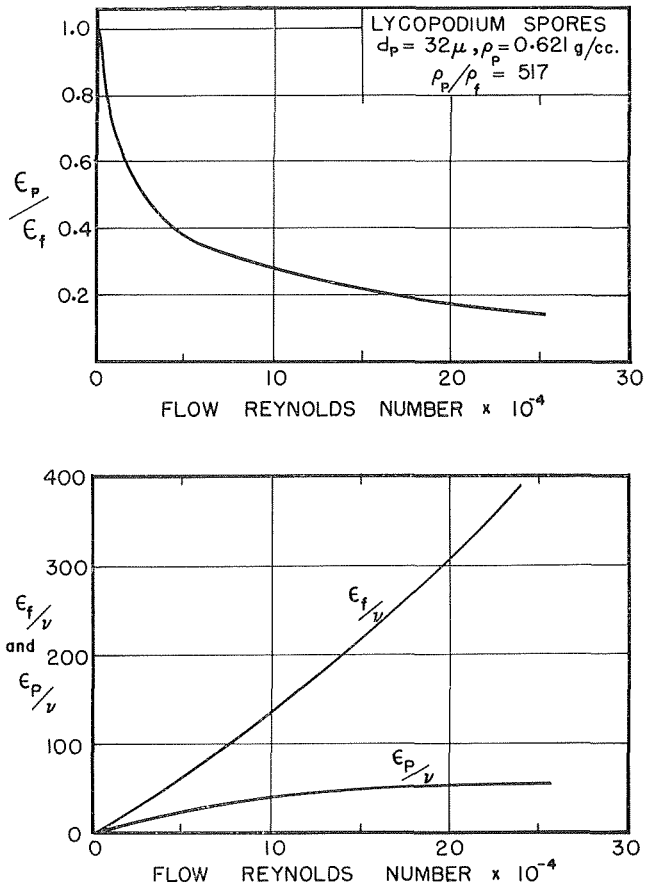

Fig. 2 Variation of particle and fluid diffusivities with Reynolds number

$$\frac{\epsilon_p}{\epsilon_f} = \frac{\int_0^\infty E_p(n)dn}{\int_0^\infty E_f(n)dn} \tag{10}$$

where n is the wave number, or frequency in cps.

Using the result obtained by Tchen [8]

$$\frac{E_p(n)}{E_f(n)} = (1 + f_1)^2 + f_2^2 \tag{11}$$

it follows from equation (9) that

$$E_p(n) = \eta^2 E_f(n) \tag{12}$$

from which we obtain

$$\frac{\epsilon_p}{\epsilon_f} = \frac{\int_0^\infty \eta^2 E_f(n)dn}{\int_0^\infty E_f(n)dn} \tag{13}$$

To calculate ϵ_p/ϵ_f as a function of Reynolds number we need information on the Lagrangian spectral energy distribution $E_f(n)$. Unfortunately this information is not directly obtainable from anemometer measurements which yield Eulerian spectra only. Basing his results on measurements obtained in the core region of turbulent pipe flow, Mickelsen [20] has shown that the curves of Eulerian and Lagrangian correlation coefficients have similar shapes, which suggests that the shapes of the energy spectra should also be similar. Although in the case under discussion flow is essentially two-dimensional and the application of Mickelsen's results represents a gross oversimplification, it is a simplification that must be made if any practical results are to be obtained.

Even then, information on Eulerian energy spectra is extremely sparse. The most reliable measurements are probably those of Comte-Bellot [11] who (Fig. IV-49, 51, 52,) gives plots of energy spectra of the v' component in two-dimensional flow at three different Reynolds numbers and at a distance $y/h = 0.45$ from the wall (where $2h$ is the height of the two-dimensional channel).

Using these figures and our Fig. 1 the product $\eta^2 E_f(n)$ can be obtained as a function of n and hence, by a numerical integration, equation (13) can be solved to yield ϵ_p/ϵ_f for the particles under consideration.

The results are plotted in Fig. 2 for 30μ lycopodium spores. The curve is admittedly not very accurate, being based on only three points measured at locations which differed somewhat in each of the three tests, but it does indicate that a fourfold increase in Reynolds number, which causes a more than fourfold increase in ϵ_f, results in less than a twofold increase in particle diffusivity, ϵ_p.

These results are based on measurements taken at a large distance from the wall ($1000 < y+ < 4000$). Near the wall, higher frequency oscillations contribute more to the value of $E_f(n)dn$ (Fig. IV-33 of reference [11]) and hence the amplitude ratio η and consequently ϵ_p/ϵ_f will be even smaller than calculated here.

With 1.7μ from particles, η is near unity for frequencies as high as 10^5 rad/sec. Fig. IV-33 of reference [11] shows that the whole energy spectrum of v' oscillations lies within these frequencies (even near the wall) and in this case in the assumption of $\epsilon_p/\epsilon_f = 1.0$ will not cause serious errors.

Particle Motion Within the Laminar Sublayer

Friedlander and Johnstone [3, 4] as well as Beal [2] had to resort to the use of unreasonably high radial velocities within the boundary layer when they calculated the stopping distance, in order to get their model to agree with experimental data. This suggests that pure inertial coasting may not be the only means by which particles are transported across the laminar sublayer.

In viscous motion through a stagnant fluid in the absence of external forces, the Stokes drag is indeed the only force acting on the particle and this forms the basis for the calculation of Stokes stopping distance.

The laminar sublayer, however, is anything but stagnant. On the contrary, it is characterized by very steep velocity gradients. Now while it is a well-known fact that a spinning sphere (or cylinder) in a moving fluid experiences a lateral lift force due to its rotation (Magnus effect) it is perhaps not so generally appreciated that a similar effect is present when a sphere moves through a viscous fluid in shear flow. Such effects were clearly demonstrated, however, by a number of investigators. Segre and Silberberg [12] observed that small, neutrally bouyant spheres in Poiseuille flow through a tube slowly migrated laterally away from the wall to a position 0.6 tube radii from the axis.

Karnis, Goldsmith, and Mason [13], Denson, Christiansen, and Salt [14], and Jeffrey and Pearson [15], all report a radial migration of particles, the latter stating that particles denser than the fluid migrate toward the wall in downward flow, and toward the center of the tube in upward flow.

Most researchers who considered the possibility of the shear-flow lift causing radial migration were reluctant to accept it on the grounds that the magnitude of the lift force was too small to produce such an effect.

Let us examine in more detail the magnitude of the forces involved. We shall use for this purpose the expression derived by Saffman [16] for the lift force experienced by a small sphere moving in an unbounded viscous shear flow

$$F_L = \frac{K\mu U a^2}{\nu^{1/2}} \left[\frac{du}{dy}\right]^{1/2} \tag{14}$$

where U is the difference between the velocity of the particle and the fluid, du/dy is the velocity gradient in the infinite shear flow, and $K = 81.2$ is a constant obtained from a numerical evaluation of an integral.

As a sufficient condition for validity of equation (14), Saffman stipulates

$$\mathrm{Re}_U \ll \mathrm{Re}_k^{1/2}, \qquad \mathrm{Re}_k \ll 1, \qquad \mathrm{Re}_\Omega \ll 1$$

where the three Reynolds numbers are defined as follows:

$$\mathrm{Re}_U = \frac{Ua}{\nu}, \qquad \mathrm{Re}_k = \frac{a^2}{\nu}\frac{du}{dy}, \qquad \mathrm{Re}_\Omega = \frac{\Omega a^2}{\nu}$$

(Ω is the rotational speed of the particle which, for free rotation, is equal to $\frac{1}{2}du/dy$).[3]

If we compare the magnitude of the shear flow lift force [equation (14)] to Stokes drag force ($F_s = 6\pi\mu aV$) we obtain

$$\frac{|F_L|}{|F_s|} = \frac{K}{6\pi}\left[\frac{a^2}{\nu}\frac{du}{dy}\right]^{1/2}\frac{U}{V} \tag{15}$$

Both U and V represent particle velocities relative to mean stream velocity and, if their ratio is taken as unity, equation (15) reduces to

$$\frac{|F_L|}{|F_s|} = \frac{K}{6\pi}\mathrm{Re}_k^{1/2} = 4.3\,\mathrm{Re}_k^{1/2}$$

For $\mathrm{Re}_k \ll 1$ which is one of the conditions of validity of equation (14), the lift force is indeed negligible compared to frictional drag, which is the conclusion reached by Soo, reference [6, p. 28].

If we apply the argument to the passage of the particle through the laminar sublayer, however, V will represent the transverse (radial) velocity which, very near the wall, must necessarily be very small and thus, even though the relative axial velocity U is not large in that region, the ratio U/V may be significant. Thus the lift force may have a measurable effect on particle motion.

To verify this contention, we write the equations of motion for a dense particle moving in the laminar sublayer when the main flow is directed vertically upward:

$$-6\pi\mu a(u_p - u_f) - \tfrac{4}{3}\pi a^3(\rho_p - \rho_f)g = \tfrac{4}{3}\pi\rho_p a^3\frac{du_p}{dt} \tag{16a}$$

$$-6\pi\mu a v_p - K\mu(u_p - u_f)\left(\frac{du_f}{dy}\right)^{1/2}\frac{a^2}{\nu^{1/2}} = \tfrac{4}{3}\pi\rho_p a^3\frac{dv_p}{dt} \tag{16b}$$

Equation (16a) is a force balance on the particle in the direction of flow (x-direction), x being taken as positive upward. Equation (16b) is the force balance in the y-direction, y being taken as zero at the wall, increasing positively toward the center line of the channel.

Subscripts p and f refer to particle and fluid, respectively. The first terms in both equations are Stokes friction force terms. The second term in equation (16a) is the gravitational term, negative for upward flow which was assumed here.

The second term in equation (16b) is Saffman's shear-flow lift term, which is negative (toward the wall) when the particle velocity in the x-direction (u_p) is greater than the local stream velocity u_f.

In the sublayer $u^+ = y^+$, so that

$$\frac{du_f}{dy} = \frac{U_{\mathrm{ave}}^2}{\nu}\cdot\frac{f}{2} = \kappa$$

where κ is the magnitude of the velocity gradient.

Equations (16) were solved numerically using a predictor corrector method described in reference [17]. Details of the program are given in reference [18].

It was assumed that the value of u_p at the edge of the sublayer

[3] Validity of application of equation (14) to the present case is discussed in Appendix B.

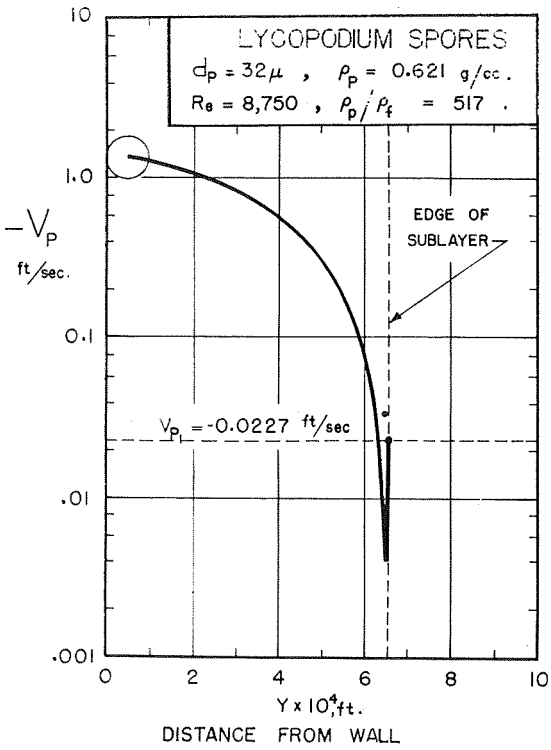

Fig. 3 Particle velocity in viscous sublayer

($y^+ = 5$) was equal to the local mean fluid velocity minus the velocity of gravitational settling, and different negative values of v_{p_1} were tried at $y^+ = 5$.

Since the flow is upward, u_p is lower than u_f and the lift force is directed toward the center line. Thus the particle, whose initial transverse velocity v_{p_1} causes it to start moving toward the wall, will decelerate because of the additive effect of lift and Stokes drag.

If the initial velocity v_{p_1} is low, the particle will soon reverse directions and start moving away from the wall.

If v_{p_1} is high enough, however, the particle will be carried sufficiently close to the wall, so that it enters the region in which its velocity in the direction of flow (u_p) becomes greater than the local fluid velocity u_f.

Under these conditions the lift force is directed toward the wall and the particle will start accelerating in that direction. This is vividly demonstrated in Fig. 3 where the transverse velocity v is plotted against the distance from the wall for the 32μ lycopodium particle.

For this particular flow condition, an initial velocity $v_{p_1} = -0.0227$ fps was sufficient to cause the particle to travel to the wall. This is a threshold value; a very small decrease in it would cause the particle to reverse directions and to return to the main stream.

By contrast, an initial velocity $v_{p_1} = -0.344$ fps (or about 15 times the previous value) would be required for the particle to reach the surface if Stokes drag was the only force acting on it in the sublayer.

With the initial velocity of $v_{p_1} = -0.0227$ fps, the Stokes stopping distance is 0.435×10^{-4} ft, so that the particle would be able to penetrate only about 7 percent of the laminar sublayer thickness if Stokes drag was the only force acting on it.

Thus it appears that in the laminar sublayer the assumption of negligible shear flow lift is not valid and therefore the whole concept of the Stokes stopping distance becomes questionable

The effect of the lift force was examined in some detail to determine its dependence on such factors as particle size and density and the flow Reynolds number. Results are presented for upflow of dense particles in terms of the following parameters:

1 Threshold velocity, v_{p_t}: The minimum velocity toward the wall which the particle must possess at the edge of the sublayer so that it will be deposited on the wall when the effect of the lift force is included.

2 Stokes-drag velocity, v_{p_s}: The minimum velocity toward the wall which the particle must possess at the edge of the sublayer so that it will be deposited on the wall when the effect of Stokes drag *only* is considered.

Effect of Particle Size

Fig. 4 shows a plot of both v_{p_t} and v_{p_s} for various particle sizes as a function of Reynolds numbers.

At *low Reynolds numbers* (Re < 4000) the threshold velocity is the same as the Stokes drag velocity for small particles, indicating that the effect of the lift force on the particles is indeed negligible. This is as expected since both the particle radius "a" and the velocity gradient du/dy are small so that F_L is very small (equation (14)). As the size of the particle increases, the lift force which varies as the radius squared, increases more rapidly than the drag which varies linearly with radius. The inertia of the particle increases even more rapidly, however (varying with the cube of the radius), so that the particle is able to penetrate sufficiently far into the boundary layer for the lift force to reverse its direction and to start accelerating the particle toward the wall. With the lift force now operating to assist deposition a lower velocity is needed than if Stokes drag was the only force acting on the particle and this is evident in Fig. 4 for particles greater than 8μ in diameter.

As the Reynolds number increases, du/dy becomes steeper and the particle reaches much more quickly the region where the direc-

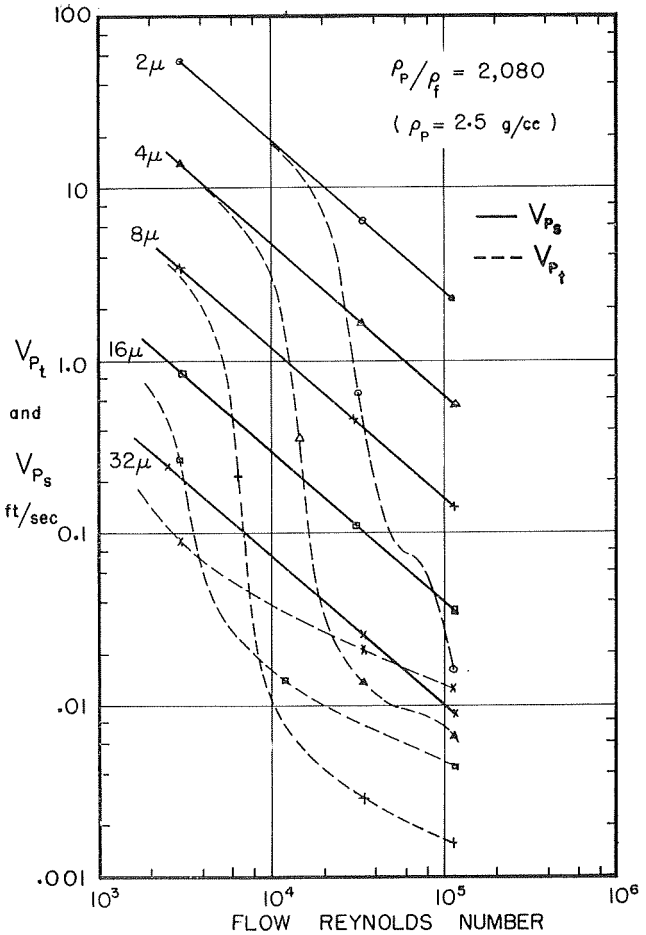

Fig. 4 Variation of threshold velocity and Stokes drag velocity with flow Reynolds number

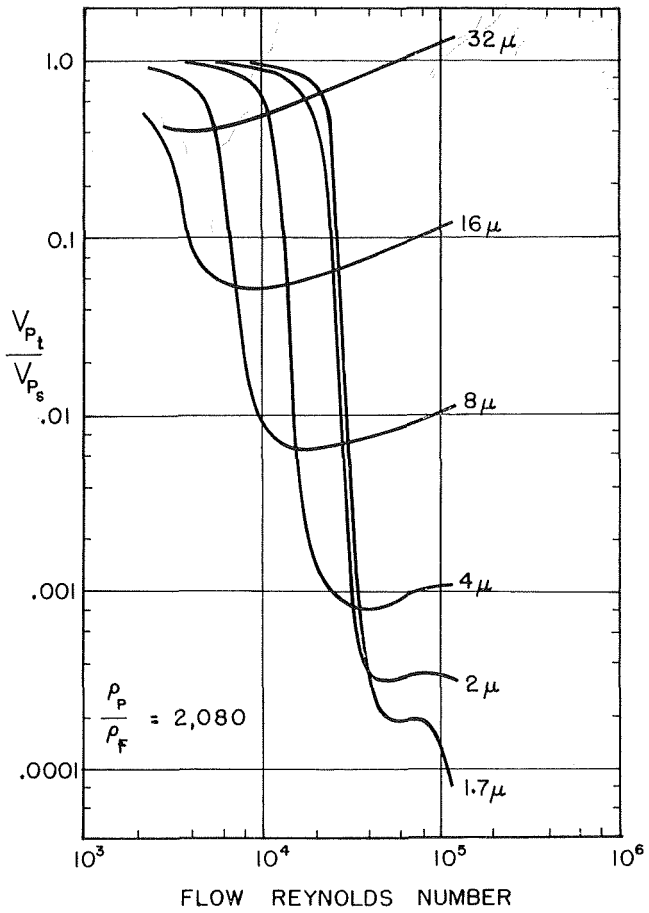

Fig. 5 Variation of ratio of threshold velocity to Stokes drag velocity with Reynolds number

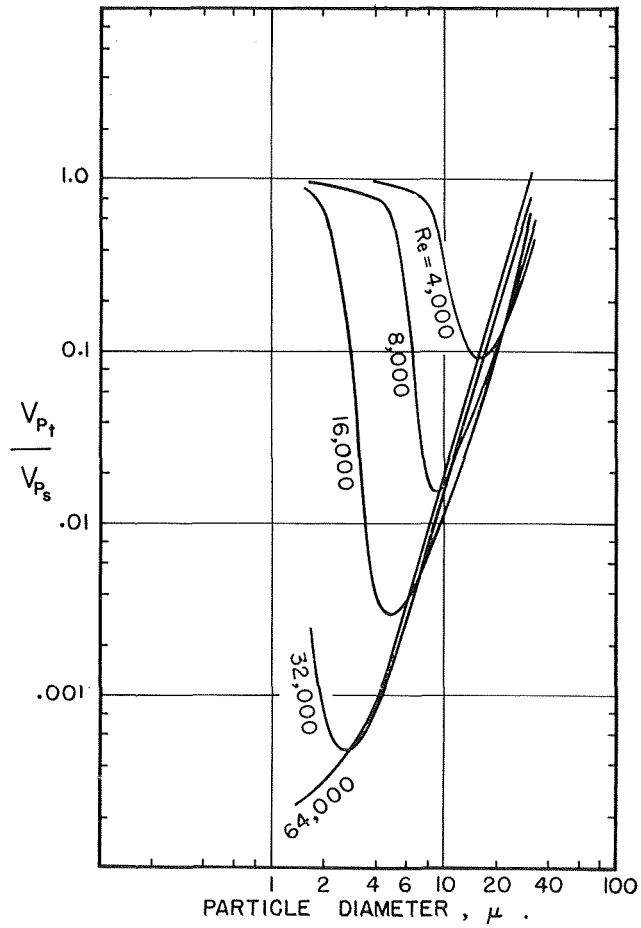

Fig. 6 Effect of particle size on ratio of threshold velocity to Stokes drag velocity

tion of the lift force is reversed. This helps deposition and thus the threshold velocity of small particles drops several orders of magnitude within a relatively narrow Reynolds number range. This effect is much less pronounced with larger particles and the curve for the 32μ particles suggests that it may disappear completely with larger sizes. This again is reasonable because with large particles their inertia becomes the dominant factor and although the lift force is operating its effect is relatively small so that there is not much difference between v_{p_t} and v_{p_s}.

At high Reynolds numbers the small particles benefit most from the effect of the lift force. Since the boundary layer is very thin, the distance that the particle must travel into the sublayer for the lift force to reverse directions is very small and although that force is not very large (a^2 being very small though $du/dy^{1/2}$ is large), the particle begins to accelerate toward the wall at a very early stage of its travel through the sublayer. Thus a very low threshold velocity is required for deposition, while a relatively high Stokes drag velocity would be needed because of the small inertia of the particle.

This most vividly demonstrated in Fig. 5 where the ratio of the threshold velocity to Stokes drag velocity is plotted. At high Reynolds numbers small particles need less than 1 percent of Stokes drag velocity in order to traverse the sublayer. Large particles, however, whose large inertia enables them to reach the wall without difficulty even without the assistance of the lift force, benefit but little from its presence. As a matter of fact, the ratio v_{p_t}/v_{p_s} exceeds unity for the 32μ particle at large Reynolds numbers. This again is logical, for both "a" and du/dy are now very large and the lift force acts so effectively that it tends to return the particle to the main stream, so that the threshold velocity must be increased considerably to prevent this from happening.

An interesting result is obtained when data of Fig. 5 are cross-plotted to show the dependence of v_{p_t}/v_{p_s} on particle diameter at constant Reynolds number. There appears to exist a definite particle size which is most affected by the action of the lift force at any given Reynolds number. (See Fig. 6.)

At low Reynolds numbers, this optimum size is fairly large ($\sim$16μ) because the large particle diameter produces a large lift force and the large inertia helps to overcome the initial deleterious effect of the lift.

At high Reynolds numbers, on the other hand, small particles benefit most from the action of the lift force because with their low inertia they would be stopped very quickly if drag force alone acted on them.

Effect of Particle Density

Fig. 7 shows the effect of particle density on the ratio v_{p_t}/v_{p_s}. It can be seen that, except at low Reynolds numbers, the light particles benefit most from the lift force.

This is understandable since, without the help of the lift force, the low inertia of these light particles prevents them from penetrating the sublayer to any great depth. This effect is not so pronounced at low Reynolds numbers, because here again, the magnitude of the lift force becomes small (because of small du/dy) and viscous drag predominates so that v_{p_t}/v_{p_s} will tend to approach unity.

Wall Impact

There is another conclusion which can be drawn from this analysis which is highly pertinent to the study of particle deposition from turbulent streams.

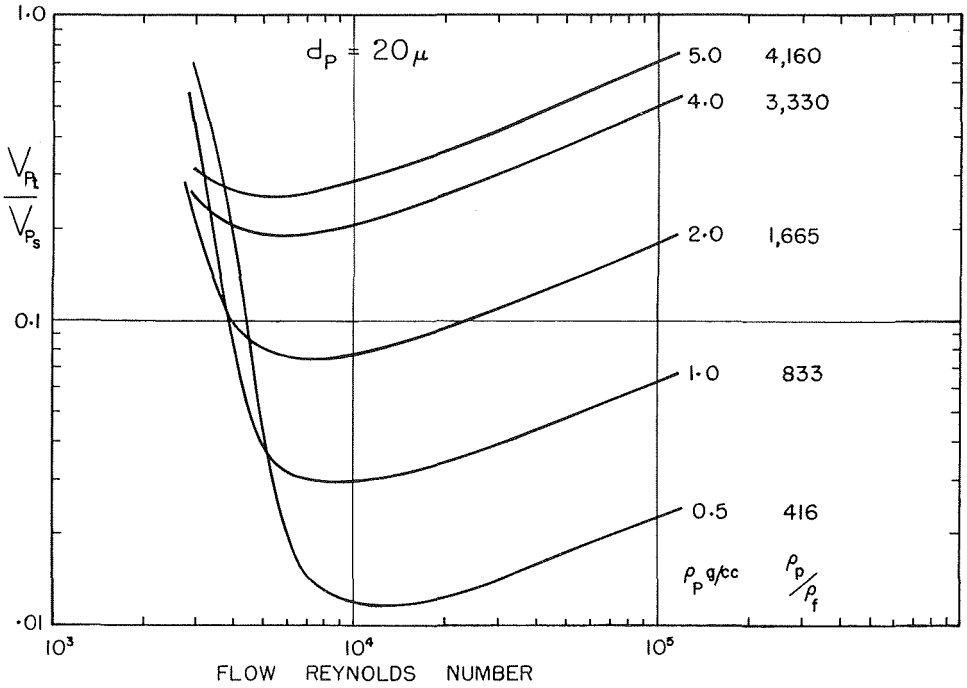

Fig. 7 Effect of particle density on ratio of threshold velocity to Stokes drag velocity

According to the Stokes stopping distance concept the particles approach the wall with an exponentially decaying transverse velocity, so that many of them would just barely reach the surface and might tend to skip or roll along it without being firmly deposited on it even at low stream velocities

Thus the efficiency of collection would become a problematic quantity. Most researchers, however, have not found this to be the case except at high Reynolds numbers, and not even then if the surface was coated with an adhesive substance. To verify this point, we observed under a microscope the surface on which particles were being deposited. The particles seemed to land with a definite impact and to embed themselves to a considerable depth in the adhesive with which the surface was coated. This behavior would not be likely with an exponentially decaying approach velocity.

A somewhat similar phenomenon was observed by Cousins and Hewitt [19] who report photographic studies in two-phase upflow which indicate that droplets "reach the surface with high velocities" without being "appreciably slowed as they enter the region of low gas velocity adjacent to the surface." They ascribe this to the fact that the stopping distance for the large droplet sizes they investigated is very large and therefore "the boundary sublayer is irrelevant in the type of mass transfer considered" by them. In many of their tests, however, the mean droplet diameter was no greater than 50μ, with 70 to 80 percent of the total number of droplets being less than 25μ in diameter. Since their photographic tests were made with water droplets suspended in air flowing at room temperature and pressure, the latter being also the conditions assumed for calculation of Fig. 7, the 1.0 gm/cc density curve in Fig. 7 (calculated for 20μ particles) can be used to obtain an estimate of the effect of lift on the particles photographed by Cousins and Hewitt. This effect is seen to be substantial, the threshold velocity being about an order of magnitude lower than the Stokes drag velocity for all Reynolds numbers, thus indicating that the lift force effect may well be responsible for the observed large velocities of at least the smaller droplets.

It is, of course, realized that the presence of a wavy liquid surface in this case renders the whole concept of a laminar sublayer even more questionable than it already is; it is remarkable nevertheless that in a study of deposition on solid wavy surfaces (to be published shortly) the authors have found that many of the observed deposition phenomena can be explained in terms of the effects of the Saffman lift force.

Conclusions

The foregoing discussion indicates clearly that the two fundamental assumptions (that of equality of particle and fluid diffusivity and that of purely inertial coasting within the viscous sublayer) on which existing deposition models are based can be completely invalid under most actual conditions.

A simple method of calculating the dependence of the ratio of particle to fluid diffusivity on Reynolds number is outlined, based on the integration of turbulent energy spectra.

The concept of Stokes stopping distance is shown to be invalid under most flow conditions, since the effect of shear flow induced transverse lift force, which heretofore has been disregarded, is not negligible when considering the passage of a dense particle through the viscous sublayer. Due to the action of this force much lower radial velocities are required at the edge of the sublayer to insure particle deposition on the wall than would be the case if Stokes drag were the only force present. This explains why deposition models based on Stokes stopping distance concept must resort to the use of unrealistically high radial velocities within the sublayer to insure agreement with experimental data.

The question that must be answered now is how to predict particle deposition, taking into account the presence of the lift force. Since the effect of lift force varies with the location of particle in the flow field it appears that in order to obtain the mass flux to the wall, trajectories of particles would have to be determined by solving the force-balance equations at incremental intervals in a manner similar to that employed by the authors.

As long as this procedure is restricted to the viscous (and possibly the buffer) layer, in which the motion of the fluid is assumed quasi-laminar, this presents no problem. As soon, however, as we move out into the turbulent core, velocity fluctuations of the main fluid cannot be neglected. Indeed, it is these fluctuations which cause the diffusion of particles toward the wall and it is these fluctuations which propel the particles sufficiently close to the wall to cause the reversal of the lift force (in upward flow) and eventual deposition.

Thus any realistic trajectory calculation would have to be based on a mathematical description of the turbulent motion of the fluid and in addition it should also include a proper assessment of the response of the particle to this motion. This is a formidable problem indeed but is one that must be solved before we can make realistic predictions of deposition of particles from turbulent streams.

Acknowledgments

The work reported in this paper was performed under an Atomic Energy of Canada Limited research contract.

APPENDIX A

Properties of Particle Used in Computation

	Lycopodium spores	Glass beads	Iron particles
Shape	Spherical	Spherical	Spherical
Size, microns	32	32	1.7
Specific gravity	0.621	2.5	7.8

Configuration of Channel Used in Computation

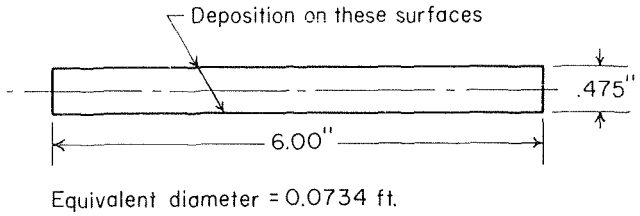

Equivalent diameter = 0.0734 ft.

APPENDIX B

(a) Proximity of Wall. Saffman derived this equation for a particle in an unbounded flow. Therefore the particle must be far enough from the wall if the equation is to hold. Fig. 3 shows the comparative thickness of the sublayer and of a 32μ particle. It also shows that the most crucial effects of the lift force occur near the edge of the laminar sublayer, or sufficiently far away from the wall, so that its effect may be neglected.

(b) Magnitude of Reynolds Number. As mentioned in the main text, the first condition is $\mathrm{Re}_u \ll \mathrm{Re}_k^{1/2}$ or in another form

$$\frac{u_p - u_f}{(\nu k)^{1/2}} \ll 1$$

This quantity was calculated for the case of lycopodium spores and for a mean air velocity of 20 fps at every step of the integration of equation (16).

It was found to have a maximum value of 0.05 at the edge of the sublayer, when v_{p_i} is near its threshold value. As the Reynolds number increases k increases also, reducing the value $(u_p - u_f)/(\nu k)^{1/2}$ even further. Thus the requirement of $\mathrm{Re}_u \ll \mathrm{Re}_k^{1/2}$ is well satisfied.

The second requirement was that $\mathrm{Re}_k \ll 1$ and $\mathrm{Re}_\Omega \ll 1$. Since for a freely rotating particle $\mathrm{Re}_\Omega = {}^1/_2\mathrm{Re}_k$ we shall examine the behavior of Re_k only.

Re_k was calculated for all types of particles used in this study. In Fig. 8 Re_k for 32μ and 1.7μ particles is plotted as a function of the duct Reynolds number. For the smaller particles, the Re_k requirement is well satisfied—for the larger ones, it holds reasonably well at lower Reynolds numbers.

(c) Constancy of Velocity Gradient. This assumption holds in the sublayer as far as mean flow velocity is concerned. Any velocity fluctuations which may be present there would tend to make the quantitative results inaccurate, but qualitative conclusions would remain the same.

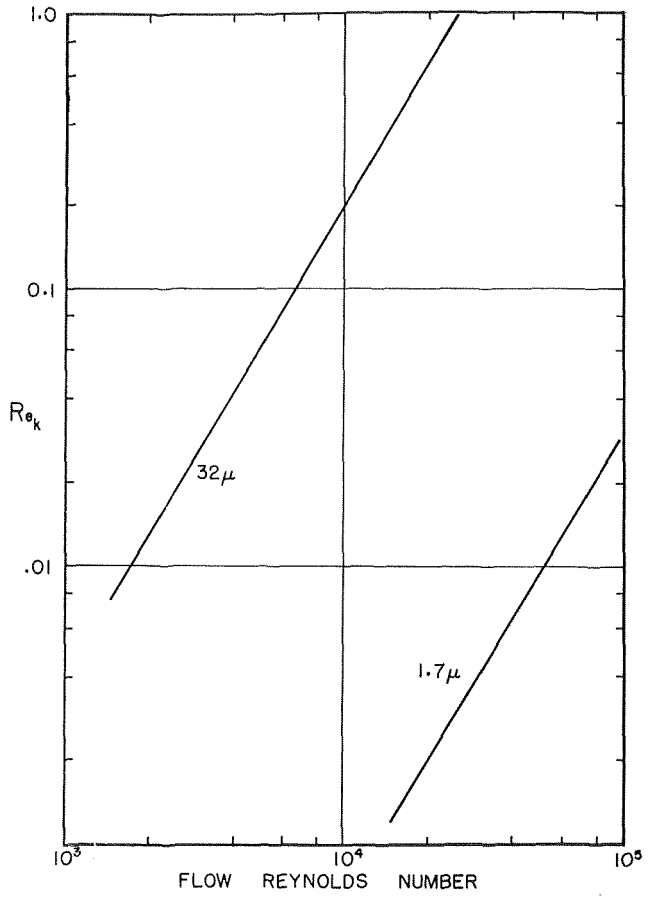

Fig. 8 Gradient Reynolds number in sublayer

References

1 Lin, C. S., Moulton, R. W., and Putnam, G. L., "Mass Transfer Between Solid Wall and Fluid Streams," *Industrial and Engineering Chemistry*, Vol. 45, 1953, p. 667.

2 Beal, S. K., "Transport of Particles in Turbulent Flow to Channel or Pipe Walls," Report WAPD-TM-765, 1968, Westinghouse Electric Corp., Bettis Atomic Power Laboratory, Pittsburgh, Pa.

3 Friedlander, S. K., "Deposition of Aerosol Particles From Turbulent Gases," PhD thesis, 1954, University of Illinois, Urbana, Ill.

4 Friedlander, S. K., and Johnstone, H. F., "Deposition of Suspended Particles From Turbulent Gas Streams," *Industrial and Engineering Chemistry*, Vol. 49, 1951, p. 1151.

5 Davies, C. N., "Deposition of Aerosols From Turbulent Flows Through Pipes," *Proceedings of the Royal Society*, London, Vol. 289, Series A, 1966, p. 235.

6 Soo, S. L., *Fluid Dynamics of Multiphase Systems*, Blaisdell Publishing Co., Waltham, Mass., 1967.

7 Hjelmfelt, A. T., Jr., and Mockros, L. F., "Particles in a Turbulent Fluid," *Applied Scientific Research*, Vol. 16, p. 149.

8 Tchen, C. M., "Mean Value and Correlation Problems Connected With the Motion of Small Particles Suspended in a Turbulent Field," PhD thesis, Delft, 1947.

9 Corrsin, S., and Lumley, J. L., "On the Equation of the Motion of a Particle in Turbulent Fluid," *Applied Scientific Research, Section A*, Vol. 6.

10 Hinze, J. O., *Turbulence*, McGraw-Hill, New York, 1959, p. 352.

11 Comte-Bellot, G., "Écoulement Turbulent Entre Deux Parois Paralleles," *Publications Scientifiques et Techniques du Ministère de l'Air*, No. 418, 1965.

12 Segre, G., and Silberberg, A., "Behaviour of Macroscopic Rigid Spheres in Poisseuille Flow," *Journal of Fluid Mechanics*, Vol. 14, 1962, Part 1, p. 115; Part 2, p. 136.

13 Karnis, A., Goldsmith, H. L., and Mason, S. G., "The Flow of Suspensions Through Tubes. V. Inertia Effects," *Canadian Journal of Chemical Engineering*, Aug. 1966.

14 Denson, C. D., Christiansen, E. B., and Salt, D. L., "Particle Migration in Shear Field," *AIChE Journal*, Vol. 12, No. 3, 1966, p. 589.

15 Jeffrey, R. C., and Pearson, J. R. A., "Particle Motion in Laminar Vertical Tube Flow," *Journal of Fluid Mechanics*, Vol. 22, 1965 Part 4, p. 721.

16 Saffman, P. Q., "The Lift on a Small Sphere in a Slow Shear Flow," *Journal of Fluid Mechanics*, Vol. 22, 1965, p. 385.

17 Ralston, A., and Wilf, H. S., *Mathematical Methods for Digital Computers*, Wiley, New York.

18 Rouhiainen, P. O., "Deposition of Airborne Particles on Walls of Two-Dimensional Channels," ME thesis, 1969, McGill University.

19 Cousins, L. B., and Hewitt, G. F., "Liquid Phase Mass Transfer in Annular Two-Phase Flow: Droplet Deposition and Liquid Entrainment," AERE-R 5657, 1968, U.K.A.E.A., Harwell.

20 Mickelsen, W. R., "An Experimental Comparison of the Lagrangian and Eulerian Correlation Coefficients in Homogeneous Isotropic Turbulence," NACA TN 3570, 1955.

journal of heat transfer

technical briefs

This section consists of contributions of 1500 words or less (about 2 1/2 double-spaced typewritten pages, including figures). Technical Briefs will be reviewed and approved by the specific division's reviewing committee prior to publication. After approval such contributions will be published as soon as possible, normally in the next issue of the Journal

A Note on the Radiative Interchange Among Nongray Surfaces

B. F. ARMALY[1] and C. L. TIEN[2]

Introduction

The calculation of the radiative interchange among nongray surfaces is complicated due to the dependence of the surface radiation properties on the wavelength. As a result, the gray-surface assumption is commonly employed to simplify the calculations. Several approximate methods, however, have been developed in order to take into account the nongray effect [1–4].[3] All these methods are common in their basic nature and are based on the band approximation, in which the important energy-containing wavelength region is subdivided into finite bands of wavelength-independent radiation properties. Mathematically, this approximation is equivalent to replacing the integration over wavelength by the summation over various bands. The purpose of the present Note is to present a basically different method for calculation of the radiative interchange among nongray surfaces. The primary advantage of this method is to have the formulation and solution procedure the same as that for gray surfaces. In this sense, the present approach is similar to the study of radiative transfer in nongray gases by use of appropriately defined mean absorption coefficients [5].

Analysis

The general formulation of the radiative interchange among nongray surfaces can be found in standard texts. For the case where each of the participating surfaces has uniform temperature and radiosity while emitting and reflecting diffusely at each wavelength, the governing equations can be expressed [1] as follows:

$$q_i = \int_{\lambda=0}^{\lambda=\infty} q_{i_\lambda} d\lambda = \sum_{j=1}^{N} (B_i - B_j) F_{ij} \tag{1}$$

and

$$B_i = \int_{\lambda=0}^{\lambda=\infty} B_{i_\lambda} d\lambda = \int_{\lambda=0}^{\lambda=\infty} \epsilon_{i_\lambda} e_{i_\lambda} d\lambda + \sum_{j=1}^{N} F_{ij} \int_{\lambda=0}^{\lambda=\infty} (1 - \epsilon_{i_\lambda}) B_{j_\lambda} d\lambda \tag{2}$$

where q is the heat flux, B the radiosity, F the angle factor, e the black-body emissive power, ϵ the emissivity, and N the total number of the participating surfaces. The subscripts i and j refer to surface i and j, while λ refers to spectral quantities. Equation (2) can be restated as

$$B_i = \epsilon_i e_i + \sum_{j=1}^{N} (1 - \alpha_{ij}) B_j F_{ij} \tag{3}$$

where

$$\epsilon_i = \int_{\lambda=0}^{\lambda=\infty} \epsilon_{i_\lambda} e_{i_\lambda} d\lambda / e_i \tag{4}$$

is the total emissivity and

$$\alpha_{ij} = \int_{\lambda=0}^{\lambda=\infty} \epsilon_{i_\lambda} B_{j_\lambda} d\lambda / B_j \tag{5}$$

is the total absorptivity.

Equation (3) reduces directly to the gray-surface equations [6] under the assumption that

$$\epsilon_i = \alpha_{ij} \tag{6}$$

This assumption is usually designated as the gray-surface assumption which is valid only when surface properties are independent of wavelength or when the surface is exchanging energy with a source having the same spectrally dependent emissive power; for example, another surface at the same temperature. This assumption is rarely valid and could result in a significant error when applied to actual situations.

For the development of the present method the spectral radiosity is expressed as:

$$B_{j_\lambda} = \epsilon_{j_\lambda} e_{j_\lambda} + (1 - \epsilon_{j_\lambda}) \left[\sum_{k=1}^{N} \epsilon_{k_\lambda} e_{k_\lambda} F_{jk} + \sum_{k=1}^{N} (1 - \epsilon_{k_\lambda}) F_{jk} \sum_{m=1}^{N} \epsilon_{m_\lambda} e_{m_\lambda} F_{km} + \sum_{k=1}^{N} (1 - \epsilon_{k_\lambda}) F_{jk} \sum_{m=1}^{N} (1 - \epsilon_{m_\lambda}) F_{km} \sum_{l=1}^{N} \epsilon_{l_\lambda} e_{l_\lambda} F_{ml} + \dots \right] \tag{7}$$

which represents the emitted and the reflected energy from the surface. The terms in the square brackets represent the energy incident on the surface due to emission and reflection of other surfaces. Each of the terms in the square brackets is equal to that portion of energy which arrives to the surface directly or after one or more reflections. This line of thought is similar to the one usually used for specular surfaces. The same equation can also be obtained by successively substituting the spectral radiosities of the participating surfaces in the expression for the spectral radiosity of surface j.

From the definition of the absorptivity, equation (5), and the use of equation (7) it is possible to express α_{ij} as a ratio of two infinite series. The resulting expression, however, is too complex

[1] Assistant Professor, Department of Mechanical and Aerospace Engineering, University of Missouri, Rolla, Mo.

[2] Professor, Department of Mechanical Engineering, University of California, Berkeley, Calif. Mem. ASME.

[3] Numbers in brackets designate References at end of Note.

Contributed by the Heat Transfer Division of The American Society of Mechanical Engineers.

Manuscript received at ASME Headquarters, May 26, 1969; revised manuscript received, September 17, 1969.

Table 1 Comparison of heat fluxes (subscripts 1, 2, and 3 refer to gray, approximate nongray, and exact nongray, respectively)

	Case 1	Case 2	Case 3	Case 4
Plate 1 at 800 deg K	equation (16)	equation (16)	equation (17)	equation (17)
Plate 2 at 100 deg K	equation (17)	equation (16)	equation (16)	equation (17)
q_2/q_3	0.876	1.014	1.011	1.005
q_1/q_3	0.358	1.326	1.055	0.408

to be of any practical value. For actual calculations, an approximate expression for the absorptivity can be obtained by terminating the infinite series after the second term. This can then be used to calculate the radiosity and the heat flux from equations (3) and (1), respectively. Thus

$$\alpha_{ij} = \frac{s_{ij}e_j + \sum_{k=1}^{N}(s_{ik} - s_{ijk})e_kF_{jk}}{\epsilon_je_j + \sum_{k=1}^{N}(\epsilon_k - s_{jk})e_kF_{jk}} \tag{8}$$

where

$$s_{ij} = \int_{\lambda=0}^{\lambda=\infty} \epsilon_{i_\lambda}\epsilon_{j_\lambda}e_{j_\lambda}d\lambda/e_j \tag{9}$$

$$s_{ijk} = \int_{\lambda=0}^{\lambda=\infty} \epsilon_{i_\lambda}\epsilon_{j_\lambda}\epsilon_{k_\lambda}e_{k_\lambda}d\lambda/e_k \tag{10}$$

The foregoing expression should be a good approximation when each of the participating surfaces sees all the others, since under this condition the absorptivity depends strongly on the spectral emittances of all the participating surfaces.

This method can be extended to include the case when some of the participating surfaces have specified heat fluxes instead of temperatures. For such a case it is more convenient to write

$$B_i = q_i + \sum_{j=1}^{N} B_jF_{ij} \qquad N_T + 1 \leq i \leq N \tag{11}$$

$$B_i = \epsilon_ie_i + \sum_{j=1}^{N}(1 - \alpha_{ij})B_jF_{ij} \qquad 1 \leq i \leq N_T \tag{12}$$

where N_T is the number of surfaces for which the temperature is specified. Following the same argument developed previously, there results when j is a member of N_T

$$\alpha_{ij} = \frac{s_{ij}e_j + \sum_{k=1}^{N_T}(s_{ik} - s_{ijk})e_kF_{jk} + \sum_{k=N_{T+1}}^{N} c_{ik}q_kF_{ik}}{\epsilon_je_j + \sum_{k=1}^{N_T}(\epsilon_k - s_{ik})e_kF_{jk} + \sum_{k=N_{T+1}}^{N} q_kF_{jk}} \tag{13}$$

and when j is not a member of N_T

$$\alpha_{ij} = \frac{c_{ij}q_j + \sum_{k=1}^{N_T} s_{ik}e_kF_{jk} + \sum_{k=N_{T+1}}^{N} c_{ik}q_kF_{jk}}{q_j + \sum_{k=1}^{N_T}\epsilon_ke_kF_{jk} + \sum_{k=N_{T+1}}^{N} q_kF_{jk}} \tag{14}$$

where

$$c_{ij} = \int_{\lambda=0}^{\lambda=\infty} \epsilon_{i_\lambda}q_{j_\lambda}d\lambda/q_j \tag{15}$$

Once the radiosities of the surfaces are determined the heat fluxes and the unknown surface temperatures can be calculated, respectively, from equations (1) and (12).

Example

In order to illustrate the proposed approximate method the radiative interchange between two nongray, infinite, parallel plates was analyzed. One plate was maintained at 800 deg K while the other was at 100 deg K. The heat flux was obtained on the basis of three different calculations: gray through equations (6), (3), and (1); approximate nongray through equations (8), (3), and (1); exact nongray through equations (2) and (1). The emissivities of the surfaces were taken as

$$\epsilon_\lambda = 0.05 + 0.95e^{-(3\times10^{-4}/\lambda)} \tag{16}$$

or

$$\epsilon_\lambda = 0.485(r/\lambda)^{1/2} \tag{17}$$

where λ is the wavelength in cm and r is the resistivity in ohm-cm. Equation (16) approximates the emission characteristics of a high emittance material such as electrical nonconductors [7], while equation (17) is the Hagen-Rubens relation approximating the behavior of low emittance materials such as metals. The results, as presented in Table 1, clearly demonstrate the good agreement between the approximate nongray and the exact nongray results, while the gray calculation could yield substantial errors. The surprisingly large errors involved in the gray solution for Case 1 and 4 are due to the fact that the larger reflectivity (or smaller emissivity) of Plate 2 (metal) at low temperature results in more bounces or rays and consequently more multiple errors.

In conclusion, an approximate method has been proposed which uses the model of the gray-surface analysis to predict with a reasonable accuracy the radiative interchange among nongray surfaces. The use of the gray assumption in the solution of a nongray problem could result in a large error.

References

1 Sparrow, E. M., and Cess, R. D., *Radiation Heat Transfer*, Brooks/Cole Publishing Company, 1966, p. 99.
2 Love, T. J., *Radiative Heat Transfer*, Merrill Publishing Company, 1968, 104 pp.
3 Wiebelt, J. A., *Engineering Radiation Heat Transfer*, Holt, Rinehart, and Winston Publishing Company, 1966, p. 128.
4 Hottel, H. C., and Sarofim, A. F., *Radiative Transfer*, McGraw-Hill, New York, 1967, p. 186.
5 Sparrow, E. M., and Cess, R. D., loc. cit., p. 214.
6 Sparrow, E. M., and Cess, R. D., loc. cit., p. 88.
7 Sparrow, E. M., and Cess, R. D., loc. cit., p. 37.

The Thermal Conductivities of Some 400 Series Stainless Steels

T. S. ASHLEY,[1] L. CARRUTH,[1] and H. A. BLUM[2]

Nomenclature

k = thermal conductivity (Btu/hr ft deg F)
t = temperature (deg F)

[1] Graduate Students, Thermal and Fluid Sciences Center, Institute of Technology, Southern Methodist University, Dallas, Texas.
[2] Chairman, Mechanical Engineering Department, Institute of Technology, Southern Methodist University, Dallas, Texas.

Contributed by the Heat Transfer Division of THE AMERICAN SOCIETY OF MECHANICAL ENGINEERS. Manuscript received at ASME Headquarters, June 5, 1969; revised manuscript received, September 18, 1969.

Table 1 Comparison of heat fluxes (subscripts 1, 2, and 3 refer to gray, approximate nongray, and exact nongray, respectively)

	Case 1	Case 2	Case 3	Case 4
Plate 1 at 800 deg K	equation (16)	equation (16)	equation (17)	equation (17)
Plate 2 at 100 deg K	equation (17)	equation (16)	equation (16)	equation (17)
q_2/q_3	0.876	1.014	1.011	1.005
q_1/q_3	0.358	1.326	1.055	0.408

to be of any practical value. For actual calculations, an approximate expression for the absorptivity can be obtained by terminating the infinite series after the second term. This can then be used to calculate the radiosity and the heat flux from equations (3) and (1), respectively. Thus

$$\alpha_{ij} = \frac{s_{ij}e_j + \sum_{k=1}^{N}(s_{ik} - s_{ijk})e_kF_{jk}}{\epsilon_je_j + \sum_{k=1}^{N}(\epsilon_k - s_{jk})e_kF_{jk}} \tag{8}$$

where

$$s_{ij} = \int_{\lambda=0}^{\lambda=\infty} \epsilon_{i_\lambda}\epsilon_{j_\lambda}e_{j_\lambda}d\lambda/e_j \tag{9}$$

$$s_{ijk} = \int_{\lambda=0}^{\lambda=\infty} \epsilon_{i_\lambda}\epsilon_{j_\lambda}\epsilon_{k_\lambda}e_{k_\lambda}d\lambda/e_k \tag{10}$$

The foregoing expression should be a good approximation when each of the participating surfaces sees all the others, since under this condition the absorptivity depends strongly on the spectral emittances of all the participating surfaces.

This method can be extended to include the case when some of the participating surfaces have specified heat fluxes instead of temperatures. For such a case it is more convenient to write

$$B_i = q_i + \sum_{j=1}^{N} B_jF_{ij} \qquad N_T + 1 \leq i \leq N \tag{11}$$

$$B_i = \epsilon_ie_i + \sum_{j=1}^{N}(1 - \alpha_{ij})B_jF_{ij} \qquad 1 \leq i \leq N_T \tag{12}$$

where N_T is the number of surfaces for which the temperature is specified. Following the same argument developed previously, there results when j is a member of N_T

$$\alpha_{ij} = \frac{s_{ij}e_j + \sum_{k=1}^{N_T}(s_{ik} - s_{ijk})e_kF_{jk} + \sum_{k=N_{T+1}}^{N} c_{ik}q_kF_{ik}}{\epsilon_je_j + \sum_{k=1}^{N_T}(\epsilon_k - s_{ik})e_kF_{jk} + \sum_{k=N_{T+1}}^{N} q_kF_{jk}} \tag{13}$$

and when j is not a member of N_T

$$\alpha_{ij} = \frac{c_{ij}q_j + \sum_{k=1}^{N_T} s_{ik}e_kF_{jk} + \sum_{k=N_{T+1}}^{N} c_{ik}q_kF_{jk}}{q_j + \sum_{k=1}^{N_T}\epsilon_ke_kF_{jk} + \sum_{k=N_{T+1}}^{N} q_kF_{jk}} \tag{14}$$

where

$$c_{ij} = \int_{\lambda=0}^{\lambda=\infty} \epsilon_{i_\lambda}q_{j_\lambda}d\lambda/q_j \tag{15}$$

Once the radiosities of the surfaces are determined the heat fluxes and the unknown surface temperatures can be calculated, respectively, from equations (1) and (12).

Example

In order to illustrate the proposed approximate method the radiative interchange between two nongray, infinite, parallel plates was analyzed. One plate was maintained at 800 deg K while the other was at 100 deg K. The heat flux was obtained on the basis of three different calculations: gray through equations (6), (3), and (1); approximate nongray through equations (8), (3), and (1); exact nongray through equations (2) and (1). The emissivities of the surfaces were taken as

$$\epsilon_\lambda = 0.05 + 0.95e^{-(3\times10^{-4}/\lambda)} \tag{16}$$

or

$$\epsilon_\lambda = 0.485(r/\lambda)^{1/2} \tag{17}$$

where λ is the wavelength in cm and r is the resistivity in ohm-cm. Equation (16) approximates the emission characteristics of a high emittance material such as electrical nonconductors [7], while equation (17) is the Hagen-Rubens relation approximating the behavior of low emittance materials such as metals. The results, as presented in Table 1, clearly demonstrate the good agreement between the approximate nongray and the exact nongray results, while the gray calculation could yield substantial errors. The surprisingly large errors involved in the gray solution for Case 1 and 4 are due to the fact that the larger reflectivity (or smaller emissivity) of Plate 2 (metal) at low temperature results in more bounces or rays and consequently more multiple errors.

In conclusion, an approximate method has been proposed which uses the model of the gray-surface analysis to predict with a reasonable accuracy the radiative interchange among nongray surfaces. The use of the gray assumption in the solution of a nongray problem could result in a large error.

References

1 Sparrow, E. M., and Cess, R. D., *Radiation Heat Transfer*, Brooks/Cole Publishing Company, 1966, p. 99.
2 Love, T. J., *Radiative Heat Transfer*, Merrill Publishing Company, 1968, 104 pp.
3 Wiebelt, J. A., *Engineering Radiation Heat Transfer*, Holt, Rinehart, and Winston Publishing Company, 1966, p. 128.
4 Hottel, H. C., and Sarofim, A. F., *Radiative Transfer*, McGraw-Hill, New York, 1967, p. 186.
5 Sparrow, E. M., and Cess, R. D., loc. cit., p. 214.
6 Sparrow, E. M., and Cess, R. D., loc. cit., p. 88.
7 Sparrow, E. M., and Cess, R. D., loc. cit., p. 37.

The Thermal Conductivities of Some 400 Series Stainless Steels

T. S. ASHLEY,[1] L. CARRUTH,[1] and H. A. BLUM[2]

Nomenclature

k = thermal conductivity (Btu/hr ft deg F)
t = temperature (deg F)

[1] Graduate Students, Thermal and Fluid Sciences Center, Institute of Technology, Southern Methodist University, Dallas, Texas.
[2] Chairman, Mechanical Engineering Department, Institute of Technology, Southern Methodist University, Dallas, Texas.

Contributed by the Heat Transfer Division of THE AMERICAN SOCIETY OF MECHANICAL ENGINEERS. Manuscript received at ASME Headquarters, June 5, 1969; revised manuscript received, September 18, 1969.

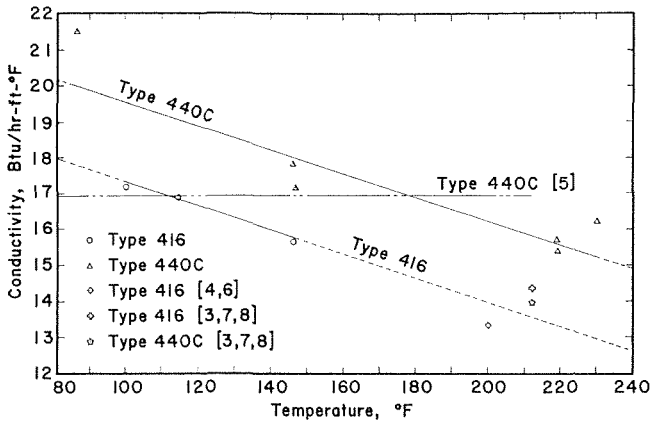

Fig. 1 Thermal conductivity of types 416 and 440c stainless steels

Introduction

A LOW heat-loss method developed by Williams and Blum [1][3] which employed an almost identical apparatus to that developed at the National Bureau of Standards [2] was used to obtain needed, but not available, thermal conductivities as a function of temperature of AISI types 416 and 440C vacuum-melt stainless steels in the unhardened condition. Equations are presented for straight lines which represent the data over the range from 80–240 deg F. Data points from several generally available references are presented for comparison purposes only and to indicate the type of data previously available. The results are considered to be accurate to within two percent.

Results

Three experiments were run using an AISI type 416 sample and six experiments were run using an AISI type 440C vacuum-melt sample. The results of these experiments are shown in Fig. 1 along with straight lines representing the data. The equation for the line representing the AISI type 416 is

$$k = -0.0336t + 20.7 \text{ (Btu/hr ft deg F)}$$

and, for the line represeuting the AISI type 440C vacuum-melt,

$$k = -0.0361t + 23.6 \text{ (Btu/hr ft deg F)}$$

It is interesting to note the decrease in thermal conductivity with increasing temperature (in this range) for these two types of stainless steel. This appears to be the general trend of the 400 series (no nickel) stainless steels whereas the reverse is true for the 300 series stainless steels [1].

References

1 Williams, D. R., and Blum, H. A., "The Thermal Conductivities of Several Metals: An Evaluation of a Method Employed by the National Bureau of Standards, Thermal Conductivity," *Proceedings of the Seventh Conference*, NBS Special Publication 302, pp. 349–354.

2 Watson, T. W., and Robinson, H. E., "Thermal Conductivity of Some Commercial Iron Nickel Alloys," JOURNAL OF HEAT TRANSFER, TRANS. ASME, Vol. 83, Series C, Nov. 1961.

3 *Materials Engineering*, Vol. 66, No. 5, Mid-Oct. 1967, pp. 77–78.

4 *Alloy Digest*, Nov. 1964.

5 *Alloy Digest*, Mar. 1960.

6 *Engineering Materials Manual*, ed. DuMond, T. C., Reinhold Publishing Corporation, New York, 1951.

7 *Metals Handbook*, 8th ed., Vol. 1, The American Society for Metals, Novelty, Ohio, pp. 422–423.

8 *Metals Properties*, ed. Hoyt, S. L., 1st ed., McGraw-Hill, New York, 1954, pp. 68–69.

[3] Numbers in brackets designate References at end of Note.

Transient Cooling of a Sphere in Space

D. L. AYERS[1]

A method is presented for determining the transient temperature distribution of a solid sphere cooling in space. The sphere is assumed initially to be at a uniform temperature and then instantaneously subjected to the radiation sink of space at time zero. This nonlinear problem was solved by using finite-difference computing techniques. Results are presented in dimensionless graphical form over a wide range of variables. This facilitates calculation of the transient temperature history at several points in the sphere.

Nomenclature

A = area, ft^2
C_p = specific heat, Btu/(lb deg R)
$\mathfrak{F}$ = radiation exchange factor between surface and environment, dimensionless
k = thermal conductivity, Btu/(hr ft deg R)
$N_{Fo} = \alpha\theta/R^2$ = Fourier number, dimensionless
$N_{rc} = k/\sigma\mathfrak{F}_i{}^3R$ = radiation number for cooling, dimensionless
r = radial coordinate, ft
R = outside radius, ft
T = absolute temperature, deg R
T_e = environmental temperature, deg R
T_i = original temperature of solid, deg R
T_R = surface temperature, deg R
$\alpha = k/\rho C_p$ = thermal diffusivity, sq ft/hr
ρ = density, lb/cu ft
σ = Steffan-Boltzman constant = 0.1714×10^{-8}, Btu/(hr ft^2 deg R^4)
θ = time, hr

Introduction

WITH the advent of space exploration and intensified research in plasmas and high-temperature technology, radiation heat transfer is becoming more important. There are few papers in this field, however, that enable the analyst to compute the transient temperature histories of nonisothermal solids. The difficulty in handling the nonlinear radiation boundary condition in the mathematical analysis explains the lack of available solutions.

There are various papers that deal with radiating semi-infinite solids or plates [1, 2, 7–14, 16, 18–21, 24, 25, 27, 28].[2] Cylindrical geometries are analyzed in [4, 8, 9, 11, 23]. The sphere is also analyzed in [1–3, 6, 8, 9, 11, 15, 20, 26], but unlike the plate and cylinder there are no dimensionless curves describing the thermal cooling of a sphere that are valid for long periods of time and a wide range of physical parameters. This paper presents curves of this nature which will enable the user to easily determine the temperature history of the sphere.

Statement of Problem

In solving for the transient temperature history of a radiating sphere, the following assumptions are made:

1 The sphere is composed of a homogeneous, opaque material whose thermal, physical properties are independent of temperature.

2 Radiation is the only mode of heat transfer between the surface and the space environment. At time zero the external surface of the sphere is exposed to a radiation environment of zero deg R.

[1] Senior Thermodynamic Engineer, Itek Corporation, Palo Alto, Calif.

[2] Numbers in brackets designate References at end of Note.

Contributed by the Heat Transfer Division of THE AMERICAN SOCIETY OF MECHANICAL ENGINEERS. Manuscript received at ASME Headquarters, May 14, 1969.

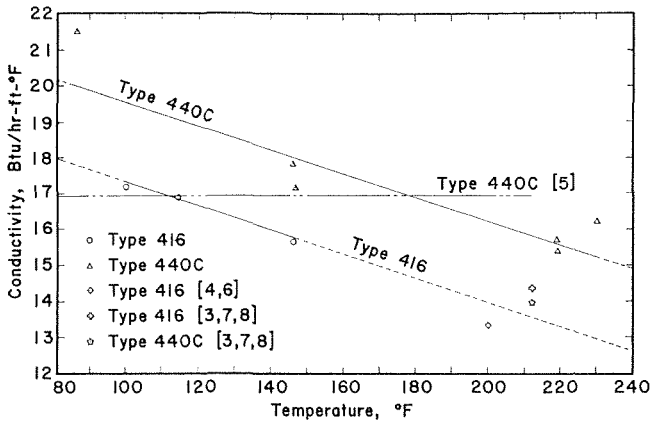

Fig. 1 Thermal conductivity of types 416 and 440c stainless steels

Introduction

A LOW heat-loss method developed by Williams and Blum [1][3] which employed an almost identical apparatus to that developed at the National Bureau of Standards [2] was used to obtain needed, but not available, thermal conductivities as a function of temperature of AISI types 416 and 440C vacuum-melt stainless steels in the unhardened condition. Equations are presented for straight lines which represent the data over the range from 80–240 deg F. Data points from several generally available references are presented for comparison purposes only and to indicate the type of data previously available. The results are considered to be accurate to within two percent.

Results

Three experiments were run using an AISI type 416 sample and six experiments were run using an AISI type 440C vacuum-melt sample. The results of these experiments are shown in Fig. 1 along with straight lines representing the data. The equation for the line representing the AISI type 416 is

$$k = -0.0336t + 20.7 \text{ (Btu/hr ft deg F)}$$

and, for the line represeuting the AISI type 440C vacuum-melt,

$$k = -0.0361t + 23.6 \text{ (Btu/hr ft deg F)}$$

It is interesting to note the decrease in thermal conductivity with increasing temperature (in this range) for these two types of stainless steel. This appears to be the general trend of the 400 series (no nickel) stainless steels whereas the reverse is true for the 300 series stainless steels [1].

References

1 Williams, D. R., and Blum, H. A., "The Thermal Conductivities of Several Metals: An Evaluation of a Method Employed by the National Bureau of Standards, Thermal Conductivity," *Proceedings of the Seventh Conference*, NBS Special Publication 302, pp. 349–354.

2 Watson, T. W., and Robinson, H. E., "Thermal Conductivity of Some Commercial Iron Nickel Alloys," JOURNAL OF HEAT TRANSFER, TRANS. ASME, Vol. 83, Series C, Nov. 1961.

3 *Materials Engineering*, Vol. 66, No. 5, Mid-Oct. 1967, pp. 77–78.

4 *Alloy Digest*, Nov. 1964.

5 *Alloy Digest*, Mar. 1960.

6 *Engineering Materials Manual*, ed. DuMond, T. C., Reinhold Publishing Corporation, New York, 1951.

7 *Metals Handbook*, 8th ed., Vol. 1, The American Society for Metals, Novelty, Ohio, pp. 422–423.

8 *Metals Properties*, ed. Hoyt, S. L., 1st ed., McGraw-Hill, New York, 1954, pp. 68–69.

[3] Numbers in brackets designate References at end of Note.

Transient Cooling of a Sphere in Space

D. L. AYERS[1]

A method is presented for determining the transient temperature distribution of a solid sphere cooling in space. The sphere is assumed initially to be at a uniform temperature and then instantaneously subjected to the radiation sink of space at time zero. This nonlinear problem was solved by using finite-difference computing techniques. Results are presented in dimensionless graphical form over a wide range of variables. This facilitates calculation of the transient temperature history at several points in the sphere.

Nomenclature

A = area, ft^2
C_p = specific heat, Btu/(lb deg R)
$\mathfrak{F}$ = radiation exchange factor between surface and environment, dimensionless
k = thermal conductivity, Btu/(hr ft deg R)
$N_{Fo} = \alpha\theta/R^2$ = Fourier number, dimensionless
$N_{rc} = k/\sigma\mathfrak{F}_i{}^3R$ = radiation number for cooling, dimensionless
r = radial coordinate, ft
R = outside radius, ft
T = absolute temperature, deg R
T_e = environmental temperature, deg R
T_i = original temperature of solid, deg R
T_R = surface temperature, deg R
$\alpha = k/\rho C_p$ = thermal diffusivity, sq ft/hr
ρ = density, lb/cu ft
σ = Steffan-Boltzman constant = 0.1714×10^{-8}, Btu/(hr ft^2 deg R^4)
θ = time, hr

Introduction

WITH the advent of space exploration and intensified research in plasmas and high-temperature technology, radiation heat transfer is becoming more important. There are few papers in this field, however, that enable the analyst to compute the transient temperature histories of nonisothermal solids. The difficulty in handling the nonlinear radiation boundary condition in the mathematical analysis explains the lack of available solutions.

There are various papers that deal with radiating semi-infinite solids or plates [1, 2, 7–14, 16, 18–21, 24, 25, 27, 28].[2] Cylindrical geometries are analyzed in [4, 8, 9, 11, 23]. The sphere is also analyzed in [1–3, 6, 8, 9, 11, 15, 20, 26], but unlike the plate and cylinder there are no dimensionless curves describing the thermal cooling of a sphere that are valid for long periods of time and a wide range of physical parameters. This paper presents curves of this nature which will enable the user to easily determine the temperature history of the sphere.

Statement of Problem

In solving for the transient temperature history of a radiating sphere, the following assumptions are made:

1 The sphere is composed of a homogeneous, opaque material whose thermal, physical properties are independent of temperature.

2 Radiation is the only mode of heat transfer between the surface and the space environment. At time zero the external surface of the sphere is exposed to a radiation environment of zero deg R.

[1] Senior Thermodynamic Engineer, Itek Corporation, Palo Alto, Calif.

[2] Numbers in brackets designate References at end of Note.

Contributed by the Heat Transfer Division of THE AMERICAN SOCIETY OF MECHANICAL ENGINEERS. Manuscript received at ASME Headquarters, May 14, 1969.

3 Heat flows only in the radial direction (end effects are negligible).

4 The radiation interchange factor $\bar{\mathfrak{F}}$ is independent of the sphere's surface temperature.

5 There is no heat generation within the sphere nor is there any internal cooling.

6 The sphere has a uniform initial temperature.

Mathematically, this problem is formulated as follows. The transient temperature distribution in the sphere must solve the Fourier equation for a sphere.

$$\frac{\partial^2 T}{\partial r^2} + \frac{2}{r}\frac{\partial T}{\partial r} = \frac{1}{\alpha}\frac{\partial T}{\partial \theta}, \qquad 0 \leq r \leq R,\ \theta \leq 0 \tag{1}$$

The solution to (1) must also satisfy the following initial and boundary conditions:

$$T(r, 0) = T_i \qquad 0 \leq r \leq R,\ \theta = 0 \tag{2}$$

$$\frac{\partial T_0}{\partial r} = 0 \qquad r = 0,\ \theta \geq 0 \tag{3}$$

$$\frac{\partial T_R}{\partial r} = \frac{\bar{\mathfrak{F}}\sigma}{k}\left[T_e^4 - T_R^4\right] \qquad r = R,\ \theta > 0 \tag{4}$$

Because of boundary condition (4), which includes the temperature to the fourth power, this problem is nonlinear. For this reason an analytical solution is not derived. Instead, a numerical solution is obtained.

Numerical Results

The numerical results were obtained using finite-difference computing techniques with a digital computer. In this numerical analysis, the sphere was divided into separate concentric spherical shells and each shell or node was assumed to be isothermal. The number of shells or nodes needed was determined by trial and error. The sphere was divided into finer and finer shells (or more and more nodes) until no difference in the computed results could be determined. For the case of the sphere whose surface is instantaneously reduced to the environmental temperature, an exact solution does exist, since eliminating the surface radiation also eliminates the problem of nonlinearity. A comparison of the digital results with the exact solution for this extreme case of cooling shows a maximum dimensionless temperature difference of 0.003 at the position of $r/R = 0.95$. This accuracy is quite adequate for a graphical presentation of the results. A comparison was also made where possible with the results of Crosbie [8] and there is agreement to within 0.003 in the dimensionless temperature.

The numerical results for the temperature distribution in a sphere are given in dimensionless form in Figs. 1–3. Five dimensionless parameters appear in these charts and are as follows:

Parameter	Expression	Values
Temperature	T/T_i	Continuous from 0–1.0
Time	$\alpha\theta/R^2$	Continuous from 0.001–100.0
Position	r/R	0, 0.5, 1.0
Radiation	$N_{rc} = k/\sigma\bar{\mathfrak{F}}T_i^3R$	0, 0.1, 0.3, 0.5, 1.0, 2.0, 3.0, 5.0, 10.0, 20.0, 30.0

Conclusions

The transient cooling of a sphere initially at a uniform temperature is presented graphically in Figs. 1–3. These charts cover the wide region of time where approximate solutions are not valid. These charts will enable the user to easily determine the temperature history of the cylinder. For cases not presented directly in the plots either chart interpolation is used, or approximate solutions valid for short or long times can be used.

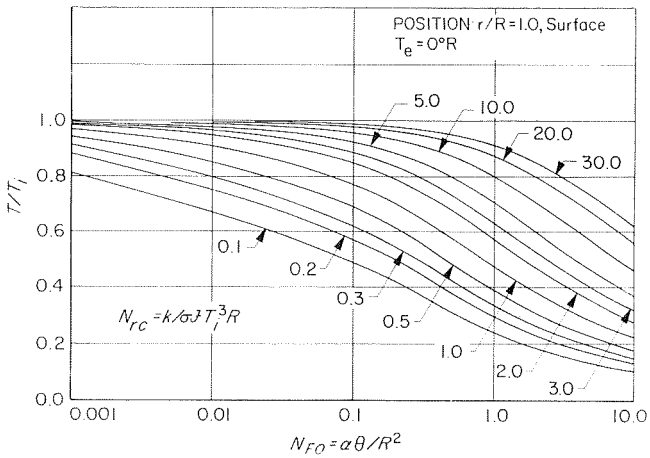

Fig. 1 Transient temperature of surface of a sphere subjected to radiation cooling; T_e = 0 deg R, r/R = 1.0

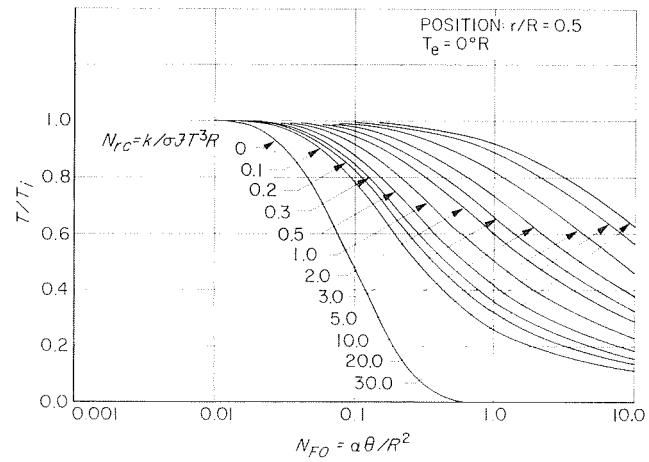

Fig. 2 Transient temperature of midplane of a sphere subjected to radiation cooling; T_e = 0 deg R, r/R = 0.5

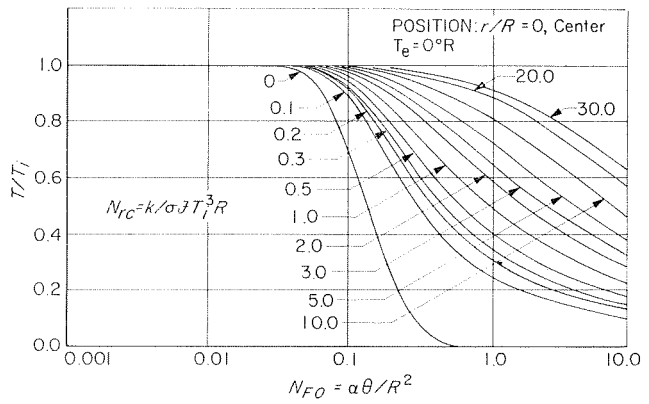

Fig. 3 Transient temperature of center of a sphere subjected to radiation cooling; T_e = 0 deg R, r/R = 0.0

If Fourier numbers less than $N_{F0} = 0.001$ are of interest, then the solutions presented in [1, 2, 14, 16, 18, 21, 24] will be valid if applied within the limitations stated. During this time, flat plate or infinite solid solutions can be applied to a sphere, because, for these very short times, only the very outermost region of the sphere has started to respond to the environment. If this response depth is small in comparison with the outer radius, then the sphere can be assumed to be a flat plate.

The graphs in this paper encompass a broad range and extend until the sphere is cooling in an isothermal manner. Cases beyond $N_{rc} = 30$ or $N_{F0} = 10.0$ are isothermal for all practical purposes. Once the sphere is cooling in an isothermal manner, the following exact solution can be used:

$$\frac{T}{T_i} = \left[1 + \frac{9N_{F0}}{N_{rc}}\right]^{-1/3} \tag{5}$$

The cooling of an isothermal solid is more thoroughly discussed in [5, 22].

References

1 Abarbanel, S. S., "On Some Problems in Radiative Heat Transfer," Massachusetts Institute of Technology, Fluid Dynamics Research Group, OSR Technical Report No. 59-531, Apr. 1959.

2 Abarbanel, S. S., "Time-Dependent Temperature Distribution in Radiating Solids," *Journal of Mathematics and Physics*, Vol. 39, No. 4, 1960, pp. 246–257.

3 Adams, E. W., and Spreuer, H., "Theoretical Solutions of the Nonlinear Problem of Transient Cooling of an Opaque Sphere in Space," Technical Note No. D-4046, National Aeronautics and Space Administration, Aug. 1967.

4 Ayers, D. L., "The Transient Temperature Distribution in a Radiating Cylinder," ASME Paper No. 67-HT-71, 1967.

5 Brogan, J. J., "Extensions to a Well-Known Heat Transfer Solution: The Thermal Response of a Thin Skin Exposed to a Constant Temperature Radiation Environment," AP1-8, Lockheed Aircraft Corporation, Missiles and Space Division, Sunnyvale, Calif., June 2, 1961.

6 Chadwick, P., "The Initial Stages of Cooling in a Nonhomogeneous Sphere," *Journal of the Institute of Mathematics and Its Applications*, Vol. 2, 1965, pp. 29–39.

7 Chambre, P. L., "Nonlinear Heat Transfer Problem," *Journal of Applied Physics*, Vol. 30, No. 11, 1959, pp. 1683–1688.

8 Crosbie, A. L., "Transient Heating or Cooling of One-Dimensional Solids Subjected to Nonlinear Boundary Conditions," MS thesis, Purdue University, 1966.

9 Crosbie, A. L., and Viskanta, R., "Transient Heating or Cooling of One-Dimensional Solids by Thermal Radiation," *Proceedings of the Third International Conference*, AIChE, Vol. 5, Aug. 1966, pp. 146–153.

10 Crosbie, A. L., and Viskanta, R., "Transient Heating or Cooling of a Plate by Combined Convection and Radiation," *International Journal of Heat Transfer*, Vol. 11, No. 2, Feb. 1968, pp. 305–317.

11 Crosbie, A. L., and Viskanta, R., "A Simplified Method for Solving Transient Heat-Conduction Problems With Nonlinear Boundary Conditions," JOURNAL OF HEAT TRANSFER, TRANS. ASME, Series C, Vol. 90, Aug. 1968, pp. 358–359.

12 Fairall, R. S., Wells, R. A., and Belcher, R. L., "Unsteady-State Heat Transfer in Solids With Radiation at One Boundary," JOURNAL OF HEAT TRANSFER, TRANS. ASME, Series C, Vol. 82, 1962, p. 226.

13 Friedman, A., "Generalized Heat Transfer Between Solids and Gases Under Nonlinear Boundary Conditions," *Journal of Applied Mathematics and Mechanics*, Vol. 8, No. 2, 1959, pp. 161–183.

14 Goodman, T. R., "The Heating of Slabs With Arbitrary Heat Inputs," *Forum, Journal of the Aero/Space Sciences*, Vol. 26, No. 3, 1959, pp. 187–188.

15 Heyda, J. F., "Temperature Distribution in an Orbiting Sphere With Alternate Heating and Cooling," General Electric Space Sciences Laboratory, Report No. R62SD61, June 1962.

16 Jaeger, J. C., "Conduction of Heat in a Solid With a Power Law of Heat Transfer at Its Surface," *Proceedings of the Cambridge Philosophical Society*, Vol. 46, 1950, pp. 634–641.

17 Jakob, M., *Heat Transfer*, Vol. 1, Wiley, New York, 1958, pp. 264.

18 Lardner, T. J., "Biot's Variational Principle in Heat Conduction," *AIAA Journal*, Vol. 1, No. 1, 1963, pp. 196–206.

19 Mann, R. W., and Wolf, F., "Heat Transfer Between Solids and Gases Under Nonlinear Boundary Conditions," *Quarterly of Applied Mathematics*, Vol. 9, No. 2, 1951, pp. 163–184.

20 Olson, F. C., and Schultz, O. T., "Temperatures in Solids During Heating or Cooling (Tables for the Numerical Solution of the Heating Equation)," *Industrial and Engineering Chemistry*, Vol. 34, July 1942, pp. 874–877.

21 Richardson, P. D., "Unsteady One-Dimensional Heat Conduction With a Nonlinear Boundary Condition," JOURNAL OF HEAT TRANSFER, TRANS. ASME, Series C, Vol. 86, 1964, pp. 298–299.

22 Robbins, W. H., "Analysis of the Transient Radiation Heat Transfer of an Uncooled Rocket Engine Operating Outside the Earth's Atmosphere," Technical Note D-62, National Aeronautics and Space Administration, Dec. 1959.

23 Roberts, A. F., "Heating of Cylinders by Radiation: An Approximate Formula for the Temperature Distribution," Paper No. 64-HT-39.

24 Schneider, P. J., "Radiation Cooling of Finite Heat Conducting Solids," *Journal of the Aero/Space Sciences*, Vol. 27, No. 7, 1960, pp. 547–548.

25 Schneider, P. J., *Temperature Response Charts*, Wiley, New York, 1963.

26 Schrober, G. E., "Transient Surface Temperature Distribution of a Thin-Walled Sphere Subjected to Radiation in Space," Technical Note D-2728, National Aeronautics and Space Administration, Apr. 1965.

27 Winter, D. F., "Transient Temperatures of Arrays of Plates and Cubes Radiating in a Vacuum," JOURNAL OF HEAT TRANSFER, TRANS. ASME, Series C, Vol. 89, No. 4, Nov. 1967, pp. 373–375.

28 Zerkle, R. D., and Sunderland, J. E., "The Transient Temperature Distribution in a Slab Subject to Thermal Radiation," JOURNAL OF HEAT TRANSFER, TRANS. ASME, Vol. 87, Series C, 1965, pp. 117–133.

Approximate Solution of Heat-Conduction Problems in Systems With Nonuniform Initial Temperature Distribution

H. H. BENGSTON[1] and F. KREITH[1]

AN integral method for the approximate solution of heat-conduction problems has been described by Goodman [1].[2] He applied the method to a variety of problems, including nonlinear ones, and obtained, with great savings in computational effort, solutions that agree well with exact solutions. It has been suggested [1] that the method of moments [2–4] may be suitable to solve the heat-conduction equation in systems with nonuniform initial temperature distribution, but so far it has only been used for problems with uniform initial conditions [5, 6]. Fujita [5] solved heat-conduction problems with temperature dependent thermal properties and Crank [6] solved diffusion problems with concentration dependent diffusivity. This Note illustrates application of the method of moments in the solution of a problem with nonuniform initial conditions.

The problem considered here is that of one-dimensional heat conduction in a finite slab without heat generation. The slab is insulated on one side but, on the other side, the heat flux, $-f(T_l, t)/k$, is specified. The initial temperature distribution, $g(x)$, is given. The mathematical statement of the problem to be solved is, therefore,

$$\frac{\partial^2 T}{\partial x^2} = \frac{1}{\alpha}\frac{\partial T}{\partial t}, \qquad 0 \le x \le l, \qquad t > 0$$

subject to

$$\frac{\partial T}{\partial x}(0, t) = 0, \qquad \frac{\partial T}{\partial x}(l, t) = -f(T_l, t) \tag{1}$$

$$T(x, 0) = g(x)$$

The method of solution assumes a profile, $T(x)$, which satisfies the boundary conditions and, in addition, contains n unknown parameters. Equations (2) and (3) are then used to determine these parameters:

$$\int_0^l x^j \left(\frac{\partial^2 T}{\partial x^2} - \frac{1}{\alpha}\frac{\partial T}{\partial t}\right) dx = 0, \qquad j = 0, 1, \ldots n - 1 \tag{2}$$

---

[1] Department of Chemical Engineering, University of Colorado, Boulder, Colo.

[2] Numbers in brackets designate References at end of Note.

Contributed by the Heat Transfer Division of THE AMERICAN SOCIETY OF MECHANICAL ENGINEERS. Manuscript received at ASME Headquarters, April 2, 1969; revised manuscript received, July 15, 1969.

The graphs in this paper encompass a broad range and extend until the sphere is cooling in an isothermal manner. Cases beyond $N_{rc} = 30$ or $N_{Fo} = 10.0$ are isothermal for all practical purposes. Once the sphere is cooling in an isothermal manner, the following exact solution can be used:

$$\frac{T}{T_i} = \left[1 + \frac{9N_{Fo}}{N_{rc}}\right]^{-1/3} \tag{5}$$

The cooling of an isothermal solid is more thoroughly discussed in [5, 22].

References

1 Abarbanel, S. S., "On Some Problems in Radiative Heat Transfer," Massachusetts Institute of Technology, Fluid Dynamics Research Group, OSR Technical Report No. 59-531, Apr. 1959.

2 Abarbanel, S. S., "Time-Dependent Temperature Distribution in Radiating Solids," *Journal of Mathematics and Physics*, Vol. 39, No. 4, 1960, pp. 246–257.

3 Adams, E. W., and Spreuer, H., "Theoretical Solutions of the Nonlinear Problem of Transient Cooling of an Opaque Sphere in Space," Technical Note No. D-4046, National Aeronautics and Space Administration, Aug. 1967.

4 Ayers, D. L., "The Transient Temperature Distribution in a Radiating Cylinder," ASME Paper No. 67-HT-71, 1967.

5 Brogan, J. J., "Extensions to a Well-Known Heat Transfer Solution: The Thermal Response of a Thin Skin Exposed to a Constant Temperature Radiation Environment," AP1-8, Lockheed Aircraft Corporation, Missiles and Space Division, Sunnyvale, Calif., June 2, 1961.

6 Chadwick, P., "The Initial Stages of Cooling in a Nonhomogeneous Sphere," *Journal of the Institute of Mathematics and Its Applications*, Vol. 2, 1965, pp. 29–39.

7 Chambre, P. L., "Nonlinear Heat Transfer Problem," *Journal of Applied Physics*, Vol. 30, No. 11, 1959, pp. 1683–1688.

8 Crosbie, A. L., "Transient Heating or Cooling of One-Dimensional Solids Subjected to Nonlinear Boundary Conditions," MS thesis, Purdue University, 1966.

9 Crosbie, A. L., and Viskanta, R., "Transient Heating or Cooling of One-Dimensional Solids by Thermal Radiation," *Proceedings of the Third International Conference*, AIChE, Vol. 5, Aug. 1966, pp. 146–153.

10 Crosbie, A. L., and Viskanta, R., "Transient Heating or Cooling of a Plate by Combined Convection and Radiation," *International Journal of Heat Transfer*, Vol. 11, No. 2, Feb. 1968, pp. 305–317.

11 Crosbie, A. L., and Viskanta, R., "A Simplified Method for Solving Transient Heat-Conduction Problems With Nonlinear Boundary Conditions," JOURNAL OF HEAT TRANSFER, TRANS. ASME, Series C, Vol. 90, Aug. 1968, pp. 358–359.

12 Fairall, R. S., Wells, R. A., and Belcher, R. L., "Unsteady-State Heat Transfer in Solids With Radiation at One Boundary," JOURNAL OF HEAT TRANSFER, TRANS. ASME, Series C, Vol. 82, 1962, p. 226.

13 Friedman, A., "Generalized Heat Transfer Between Solids and Gases Under Nonlinear Boundary Conditions," *Journal of Applied Mathematics and Mechanics*, Vol. 8, No. 2, 1959, pp. 161–183.

14 Goodman, T. R., "The Heating of Slabs With Arbitrary Heat Inputs," *Forum, Journal of the Aero/Space Sciences*, Vol. 26, No. 3, 1959, pp. 187–188.

15 Heyda, J. F., "Temperature Distribution in an Orbiting Sphere With Alternate Heating and Cooling," General Electric Space Sciences Laboratory, Report No. R62SD61, June 1962.

16 Jaeger, J. C., "Conduction of Heat in a Solid With a Power Law of Heat Transfer at Its Surface," *Proceedings of the Cambridge Philosophical Society*, Vol. 46, 1950, pp. 634–641.

17 Jakob, M., *Heat Transfer*, Vol. 1, Wiley, New York, 1958, pp. 264.

18 Lardner, T. J., "Biot's Variational Principle in Heat Conduction," *AIAA Journal*, Vol. 1, No. 1, 1963, pp. 196–206.

19 Mann, R. W., and Wolf, F., "Heat Transfer Between Solids and Gases Under Nonlinear Boundary Conditions," *Quarterly of Applied Mathematics*, Vol. 9, No. 2, 1951, pp. 163–184.

20 Olson, F. C., and Schultz, O. T., "Temperatures in Solids During Heating or Cooling (Tables for the Numerical Solution of the Heating Equation)," *Industrial and Engineering Chemistry*, Vol. 34, July 1942, pp. 874–877.

21 Richardson, P. D., "Unsteady One-Dimensional Heat Conduction With a Nonlinear Boundary Condition," JOURNAL OF HEAT TRANSFER, TRANS. ASME, Series C, Vol. 86, 1964, pp. 298–299.

22 Robbins, W. H., "Analysis of the Transient Radiation Heat Transfer of an Uncooled Rocket Engine Operating Outside the Earth's Atmosphere," Technical Note D-62, National Aeronautics and Space Administration, Dec. 1959.

23 Roberts, A. F., "Heating of Cylinders by Radiation: An Approximate Formula for the Temperature Distribution," Paper No. 64-HT-39.

24 Schneider, P. J., "Radiation Cooling of Finite Heat Conducting Solids," *Journal of the Aero/Space Sciences*, Vol. 27, No. 7, 1960, pp. 547–548.

25 Schneider, P. J., *Temperature Response Charts*, Wiley, New York, 1963.

26 Schrober, G. E., "Transient Surface Temperature Distribution of a Thin-Walled Sphere Subjected to Radiation in Space," Technical Note D-2728, National Aeronautics and Space Administration, Apr. 1965.

27 Winter, D. F., "Transient Temperatures of Arrays of Plates and Cubes Radiating in a Vacuum," JOURNAL OF HEAT TRANSFER, TRANS. ASME, Series C, Vol. 89, No. 4, Nov. 1967, pp. 373–375.

28 Zerkle, R. D., and Sunderland, J. E., "The Transient Temperature Distribution in a Slab Subject to Thermal Radiation," JOURNAL OF HEAT TRANSFER, TRANS. ASME, Vol. 87, Series C, 1965, pp. 117–133.

Approximate Solution of Heat-Conduction Problems in Systems With Nonuniform Initial Temperature Distribution

H. H. BENGSTON[1] and F. KREITH[1]

AN integral method for the approximate solution of heat-conduction problems has been described by Goodman [1].[2] He applied the method to a variety of problems, including nonlinear ones, and obtained, with great savings in computational effort, solutions that agree well with exact solutions. It has been suggested [1] that the method of moments [2–4] may be suitable to solve the heat-conduction equation in systems with nonuniform initial temperature distribution, but so far it has only been used for problems with uniform initial conditions [5, 6]. Fujita [5] solved heat-conduction problems with temperature dependent thermal properties and Crank [6] solved diffusion problems with concentration dependent diffusivity. This Note illustrates application of the method of moments in the solution of a problem with nonuniform initial conditions.

The problem considered here is that of one-dimensional heat conduction in a finite slab without heat generation. The slab is insulated on one side but, on the other side, the heat flux, $-f(T_l, t)/k$, is specified. The initial temperature distribution, $g(x)$, is given. The mathematical statement of the problem to be solved is, therefore,

$$\frac{\partial^2 T}{\partial x^2} = \frac{1}{\alpha}\frac{\partial T}{\partial t}, \qquad 0 \le x \le l, \qquad t > 0$$

subject to

$$\frac{\partial T}{\partial x}(0, t) = 0, \qquad \frac{\partial T}{\partial x}(l, t) = -f(T_l, t) \tag{1}$$

$$T(x, 0) = g(x)$$

The method of solution assumes a profile, $T(x)$, which satisfies the boundary conditions and, in addition, contains n unknown parameters. Equations (2) and (3) are then used to determine these parameters:

$$\int_0^l x^j \left(\frac{\partial^2 T}{\partial x^2} - \frac{1}{\alpha}\frac{\partial T}{\partial t}\right) dx = 0, \qquad j = 0, 1, \ldots n - 1 \tag{2}$$

---

[1] Department of Chemical Engineering, University of Colorado, Boulder, Colo.

[2] Numbers in brackets designate References at end of Note.

Contributed by the Heat Transfer Division of THE AMERICAN SOCIETY OF MECHANICAL ENGINEERS. Manuscript received at ASME Headquarters, April 2, 1969; revised manuscript received, July 15, 1969.

$$\int_0^l x^j T(x, 0)dx = \int_0^l x^j g(x)dx, \qquad j = 0, 1, \ldots n - 1 \quad (3)$$

Choosing a cubic profile, $T(x) = A + Bx + Cx^2 + Dx^3$, where A, B, C, and D are functions of t, and applying boundary conditions (1) yields

$$T(x, t, T_l) = A - [f(T_l, t) + 3Dl^2]x^2/2l + Dx^3 \quad (4)$$

Substituting equation (4) into equation (2) with $j = 0$ yields an ordinary differential equation. Solution of the differential equation subject to the initial conditions generated by equation (3) with $j = 0$ gives

$$A(T_l, t) = G_0(l)/l + l^3D/4 + lf(T_l, t)/6 - \frac{\alpha}{l}\int_0^t f(T_l, \tau)d\tau \quad (5)$$

where

$$G_0(l) = \int_0^l g(x)dx$$

A similar procedure using $j = 1$, followed by substituting equation (5) for $A(T_l, t)$, yields

$$l^3D(T_l, t) + 10\alpha l \int_0^t D(T_l, \tau)d\tau = 10G_0(l)/l - 20G_1(l)/l^2 - 5lf(T_l, t)/6 \quad (6)$$

where

$$G_1(l) = \int_0^l xg(x)dx$$

In order to continue the solution, more information must be given about $f(T_l, t)$. Three cases will be considered further:

1 f = constant.

2 $f = f(t)$.

3 $f = f(T_l)$.

Case 1: f = Const. For this case, equation (6) can be solved to give $D(t)$, and equation (5) specifies $A(t)$. Therefore, equation (4) becomes

$$T(x, t) = G_0(l)/l + lf/6 - x^2f/2l - \alpha ft/l + (5/2l)[G_0(l) - 2G_1(l)/l - fl^2/12]F(x/l)e^{-10\alpha t/l^2} \quad (7)$$

where

$$F(x/l) = 1 - 6(x/l)^2 + 4(x/l)^3$$

The exact solution for $f = 0$ is given by Carslaw and Jaeger [7]. The steady-state portion of the exact solution is the same as the steady-state portion of equation (7) with $f = 0$. The first eigenvalue of the exact solution is $\pi^2\alpha/l^2$ and is approximated in equation (7) by $10\alpha/l^2$. In order to compare equation (7) with the exact solution for a specific case, let $g(x) = x$. The approximate solution is then

$$T(x, t) = l/2 - (5l/12)F(x/l)e^{-10\alpha t/l^2} \quad (8)$$

The steady-state portion with the first eigenfunction of the exact solution is

$$T(x, t) = l/2 - (4l/\pi^2)\cos(\pi x/l)e^{-\pi^2\alpha t/l^2} \quad (9)$$

A graphical comparison of the solutions is presented in Fig. 1. The greatest deviation between the approximate solution and first eigenfunction of the exact solution is 12 percent at $t = 0$ and $x = 0$ or l. However, for $\alpha t/l^2 \geq 0.05$, they agree to within 2.0 percent over the entire slab, and for $0.2 \leq x \leq 0.8$, they agree to within 1.5 percent over the entire range of time. At extremely small values of time the first eigenfunction may not give a sufficiently close approximation of the complete exact solution. If

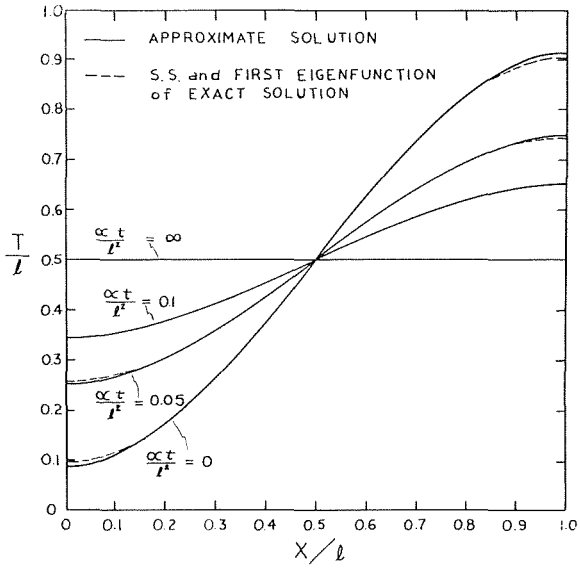

Fig. 1 Comparison of approximate and exact solution with f = const, $g(x) = x$

greater accuracy is required during the initial period, the approximate solution can be improved in that region by adding more terms to the assumed profile for $T(x)$; approximations for additional eigenfunctions can then be obtained. For example, if a quartic profile is assumed for $T(x)$ and a similar procedure is used to evaluate the three undetermined parameters, an approximation for the second eigenfunction is found in addition to the solution given by equation (7). The approximation found in this manner for $4\pi^2\alpha/l^2$, the second eigenvalue of the exact solution, was $42\ \alpha/l^2$.

Case 2: $f = f(t)$. In this case equation (6) can be solved readily to give $D(t)$, but since the actual solution for $D(t)$ depends upon the form of $f(t)$, no further generalizations will be made.

Case 3: $f = f(T_l)$. In this case equation (6) can be solved to give $D(T_l, t)$, and equation (4) becomes

$$T(x, t, T_l) = G_0(l)/l + (l/6 - x^2/2l)f(T_l) - \frac{\alpha}{l}\int_0^t f(T_l)dt + (5/2l)[G_0(l) - 2G_1(l)/l - (l^2/12)f(T_l)]F(x/l)e^{-10\alpha t/l^2} \quad (10)$$

If $T_l(t)$ is then substituted into equation (10), an expression for $T(x, t)$ is obtained but, if $f = f(T_l, t)$, it may not always be possible to obtain an analytical solution.

Ames [3, 4] discusses the value of using orthogonal polynomials, $P_j(x)$, rather than x^j as the weighting functions in equations (2) and (3). The problem under discussion was worked for f = const using the orthogonal polynomials, $P_0 = 1$ and $P_1 = 1 - x$, as weighting functions instead of x^j. The solution found was exactly the same as equation (7), the solution obtained using x^j as the weighting function. For other applications, there may be an advantage in using orthogonal polynomials as weighting functions. The main disadvantage of using orthogonal polynomials is the increased computational effort required.

The method of solution presented in this Note is suitable for many other heat-conduction problems with nonuniform initial conditions.

References

1 Goodman, T. R., "Application of Integral Methods to Transient Nonlinear Heat Transfer," *Advances in Heat Transfer*, Vol. 4, Academic Press, New York, 1964, pp. 52–120.

2 Crandall, S. H., *Engineering Analysis*, McGraw-Hill, New York, 1956, pp. 147–54.
3 Ames, W. F., *Nonlinear Partial Differential Equations in Engineering*, Academic Press, New York, 1965, pp. 243–262.
4 Ames, W. F., *Nonlinear Ordinary Differential Equations in Transport Processes*, Academic Press, New York, 1968, pp. 184–196.
5 Fujita, H., "On The Problem of Heat Conduction at High Temperature," *Memoirs of the College of Agriculture, Kyoto University*, Vol. 59, 1951, pp. 31–42.
6 Crank, J., *The Mathematics of Diffusion*, Oxford University Press., London, 1956, Chapter 9.
7 Carslaw, H. S., and Jaeger, J. C., *Conduction of Heat in Solids*, 2nd ed., Oxford University Press, London, 1959, p. 101.

Flow in the Entrance Region of a Concentric-Sphere Heat Exchanger

J. D. BOZEMAN[1] and C. DALTON[2]

Introduction

RUNDELL, et al. [1],[3] have examined the forced-convection concentric-sphere heat exchanger and indicate that a better understanding of the fluid mechanics is essential for a more complete understanding of the heat transfer problem. This Note is the result of a study to gain more knowledge of the fluid flow in the entrance region of the concentric spheres used in [1]. The concentric-sphere heat exchanger is described as follows: The fluid enters and leaves the annulus through diametrically opposed openings in the outer sphere. Fig. 1 describes the basic configuration and shows a simplified version of the inlet flow.

Ward [2] made a flow visualization study of the flow through the annular space, concentrating on the region between 60 and 120-deg downstream of the entrance, and drew certain conclusions from his observations. Some of Ward's visualization studies are contained in [1]. The results of Ward's study may be summarized as follows: All of the flow patterns indicated a higher velocity in the outer portion of the annulus than in the region near the inner sphere. A high degree of irregularity in the decelerating flow was indicated by the swirling vortical motions. Separation was observed to occur at approximately 45-deg downstream of the entrance and seemed to be independent of flow rate.

Ward's observations indicate that the entrance region (prior to separation) is the most significant heat transfer region. Separation of the entering fluid from the inner sphere past 45 deg causes more or less stagnant fluid to be in contact with the inner sphere over the region of maximum flow area, while the entrance region provides higher velocities at the inner sphere.

The flow in the exit region is characterized by a somewhat conventional accelerating velocity profile. Also, since the exit region flow should be at a higher bulk temperature than the entrance region, the entrance region would be more important as far as heat transfer rate is concerned.

Observation of Flow

The experimental setup used water as the working fluid. Fluorescein dye was used as the flow-visualization medium. The experimental apparatus was isothermal during the observations.

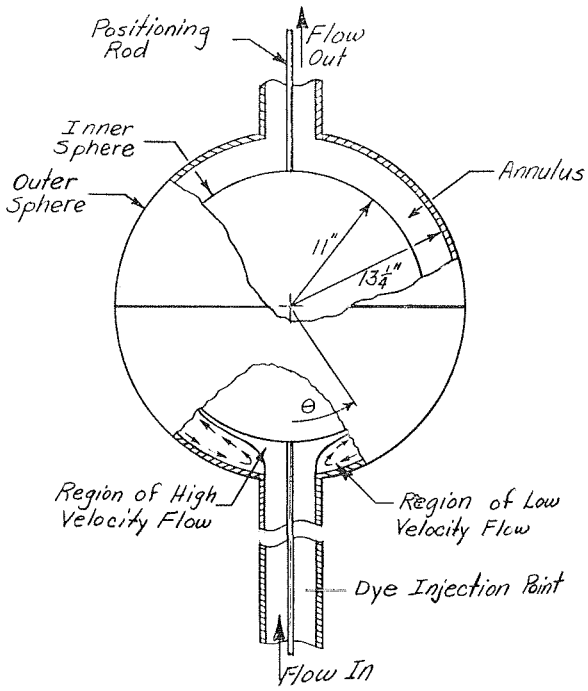

Fig. 1 Definition sketch

Fig. 2 Tracer element enters annulus with incoming fluid, Re = 411

Several phenomena were immediately apparent. First, the jetting of the entering flow developed an unstable free-shear layer which caused the development of a pair of toroidal vortices. This is shown in Fig. 2. Second, the flow is unsteady due to the downstream movement of the toroidal vortices which form a counterrotating pair of vortices. The development of the counterrotating vortices is shown in Fig. 3. These two phenomena were observed over a Reynolds number (of the flow in the approach pipe) range of 208–4020.

The location of the separation point was observed to be time-dependent. The entering flow separated from the inner sphere just upstream of the moving counterrotating vortices and moved downstream as the vortex pair moved downstream. This process continued until another vortex was formed at the surface of the inner sphere back upstream. Separation then occurred at the upstream vortex. Ward [2] and Rundell [1] had observed a fixed separation point.

For all of the Reynolds numbers observed, the regions of high

[1] NSF Trainee, University of Houston, Houston, Texas.
[2] Assistant Professor of Mechanical Engineering, University of Houston, Houston, Texas. Assoc. Mem. ASME.
[3] Numbers in brackets designate References at end of Note.
Contributed by the Heat Transfer Division of THE AMERICAN SOCIETY OF MECHANICAL ENGINEERS. Manuscript received at ASME Headquarters, June 9, 1969.

2 Crandall, S. H., *Engineering Analysis*, McGraw-Hill, New York, 1956, pp. 147–54.
3 Ames, W. F., *Nonlinear Partial Differential Equations in Engineering*, Academic Press, New York, 1965, pp. 243–262.
4 Ames, W. F., *Nonlinear Ordinary Differential Equations in Transport Processes*, Academic Press, New York, 1968, pp. 184–196.
5 Fujita, H., "On The Problem of Heat Conduction at High Temperature," *Memoirs of the College of Agriculture, Kyoto University*, Vol. 59, 1951, pp. 31–42.
6 Crank, J., *The Mathematics of Diffusion*, Oxford University Press., London, 1956, Chapter 9.
7 Carslaw, H. S., and Jaeger, J. C., *Conduction of Heat in Solids*, 2nd ed., Oxford University Press, London, 1959, p. 101.

Flow in the Entrance Region of a Concentric-Sphere Heat Exchanger

J. D. BOZEMAN[1] and C. DALTON[2]

Introduction

RUNDELL, et al. [1],[3] have examined the forced-convection concentric-sphere heat exchanger and indicate that a better understanding of the fluid mechanics is essential for a more complete understanding of the heat transfer problem. This Note is the result of a study to gain more knowledge of the fluid flow in the entrance region of the concentric spheres used in [1]. The concentric-sphere heat exchanger is described as follows: The fluid enters and leaves the annulus through diametrically opposed openings in the outer sphere. Fig. 1 describes the basic configuration and shows a simplified version of the inlet flow.

Ward [2] made a flow visualization study of the flow through the annular space, concentrating on the region between 60 and 120-deg downstream of the entrance, and drew certain conclusions from his observations. Some of Ward's visualization studies are contained in [1]. The results of Ward's study may be summarized as follows: All of the flow patterns indicated a higher velocity in the outer portion of the annulus than in the region near the inner sphere. A high degree of irregularity in the decelerating flow was indicated by the swirling vortical motions. Separation was observed to occur at approximately 45-deg downstream of the entrance and seemed to be independent of flow rate.

Ward's observations indicate that the entrance region (prior to separation) is the most significant heat transfer region. Separation of the entering fluid from the inner sphere past 45 deg causes more or less stagnant fluid to be in contact with the inner sphere over the region of maximum flow area, while the entrance region provides higher velocities at the inner sphere.

The flow in the exit region is characterized by a somewhat conventional accelerating velocity profile. Also, since the exit region flow should be at a higher bulk temperature than the entrance region, the entrance region would be more important as far as heat transfer rate is concerned.

Observation of Flow

The experimental setup used water as the working fluid. Fluorescein dye was used as the flow-visualization medium. The experimental apparatus was isothermal during the observations.

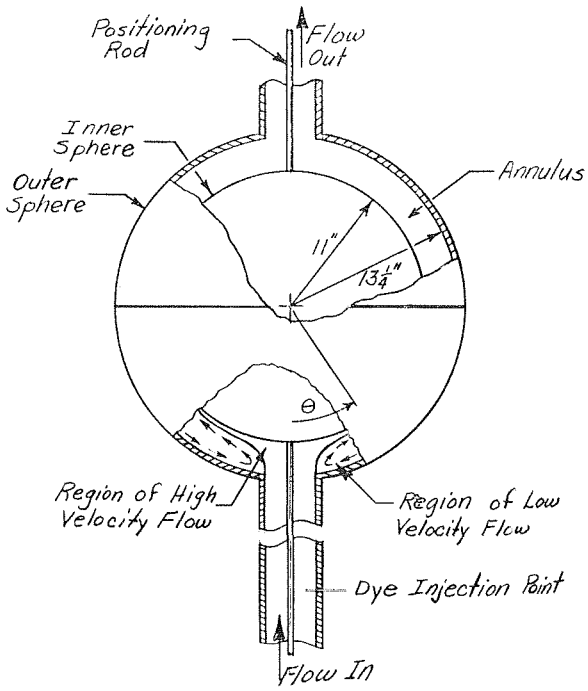

Fig. 1 Definition sketch

Fig. 2 Tracer element enters annulus with incoming fluid, Re = 411

Several phenomena were immediately apparent. First, the jetting of the entering flow developed an unstable free-shear layer which caused the development of a pair of toroidal vortices. This is shown in Fig. 2. Second, the flow is unsteady due to the downstream movement of the toroidal vortices which form a counterrotating pair of vortices. The development of the counterrotating vortices is shown in Fig. 3. These two phenomena were observed over a Reynolds number (of the flow in the approach pipe) range of 208–4020.

The location of the separation point was observed to be time-dependent. The entering flow separated from the inner sphere just upstream of the moving counterrotating vortices and moved downstream as the vortex pair moved downstream. This process continued until another vortex was formed at the surface of the inner sphere back upstream. Separation then occurred at the upstream vortex. Ward [2] and Rundell [1] had observed a fixed separation point.

For all of the Reynolds numbers observed, the regions of high

[1] NSF Trainee, University of Houston, Houston, Texas.
[2] Assistant Professor of Mechanical Engineering, University of Houston, Houston, Texas. Assoc. Mem. ASME.
[3] Numbers in brackets designate References at end of Note.
Contributed by the Heat Transfer Division of THE AMERICAN SOCIETY OF MECHANICAL ENGINEERS. Manuscript received at ASME Headquarters, June 9, 1969.

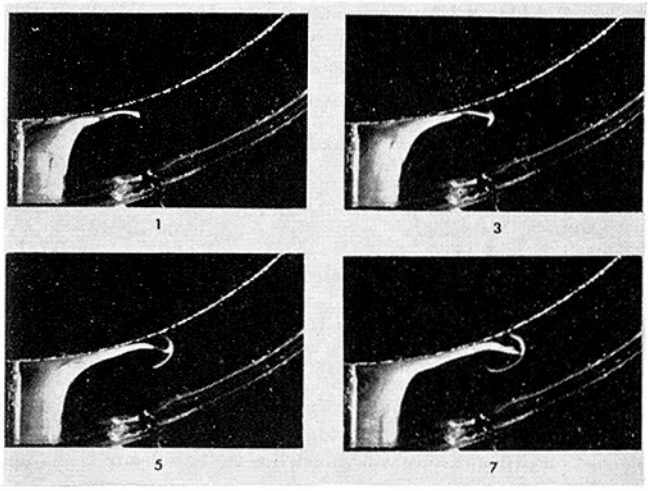

Fig. 3 Sequence showing entrainment of entering flow in a counter-rotating vortex pair, Re = 1584. The number appearing beneath photographs refers to frame number in film sequence to which photographs correspond (10 frames/sec).

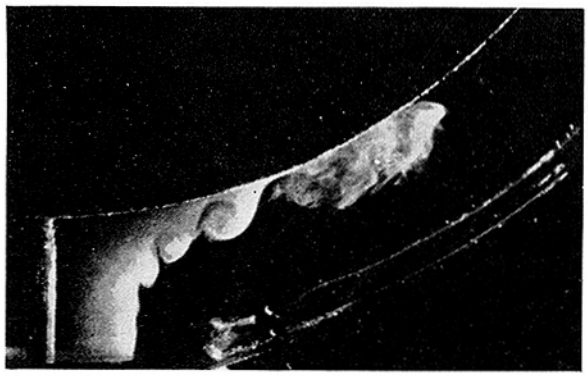

Fig. 4 Tracer element enters annulus, Re = 4020

and low-velocity flow remained in the same relative positions as shown in Fig. 1. Since this basic flow pattern arises due to the jetting of the entering flow against the inner sphere, it is strongly suggested that this pattern exists not only for the Reynolds number range observed, but is repeated at Reynolds numbers outside the range tested.

The free-shear layer at the boundary separating the high and low-velocity regions was observed to remain smooth for one or more annulus widths downstream of the inlet, for flow in the low Reynolds number range. The length of the smooth portion of the free-shear layer varied inversely with the Reynolds number, thus the rolling up of the free-shear layer occurred nearer and nearer to the inlet as the Reynolds number increased.

In the low Reynolds number range the flow was viscosity dominated, thus allowing the shear layer roll-ups to grow to the rather large sizes shown in Fig. 2. Also clearly visible in the flow pattern typified by Fig. 2 are large counterrotating roll-ups which accompany each of the large free-shear layer roll-ups. In some cases these roll-up pairs approached the width of the annulus. Thus large quantities of fluid were caught in the roll-up pairs such that small scale mixing of the entering flow with fluid already in the annulus was delayed until these large concentrations of vorticity were either diffused or broken up.

As the Reynolds number was increased through the lower range of values, shear-layer roll-ups appeared with increasing frequency, grew to much smaller size, appeared nearer the inlet, and were quickly transported downstream. This general flow pattern remained the same until observations were made at a Reynolds number of 1360. Differences in the structure of the free-shear layer roll-ups were observed at this Reynolds number. The shear-layer roll-ups no longer grew to the large sizes observed in the lower Reynolds number range, but quickly became disorganized and mixed with the fluid downstream.

For Reynolds numbers significantly higher than 1360, these flow pattern changes were intensified. The shear layer became increasingly irregular and disturbed near the inlet, followed quickly by the rolling up of the shear layer around the disturbances. The frequency of shear-layer roll-up increased with increasing Reynolds number, along with a corresponding decrease in roll-up smoothness and size. These energetic roll-ups move only a short distance downstream before breakup into turbulent mixing, as shown in Fig. 4. The frequent and irregular rolling up of the free-shear layer followed by a breakdown into turbulent mixing is expected to characterize the flow at Reynolds numbers even higher than those tested.

The majority of the flow visualization photographs appearing in [1, 2] were for flow at a Reynolds number of 2920. The remaining flow visualization photographs were either at Reynolds numbers of 4420 and 5550 or unidentified. However, all of the photographs identified by Reynolds number were of the region far downstream of the inlet, 45 deg $\leq \theta \leq$ 135 deg, therefore no direct comparison could be made with the present flow visualization photographs.

Conclusions

We can summarize the flow characteristics in the entrance region as follows:

1 Existence of an unstable free-shear layer at the boundary separating the high-velocity and low-velocity regions.

2 Roll-up of the unstable free-shear layer into regions of concentrated vorticity.

3 Formation of vortices adjacent to the inner sphere simultaneous with the rolling up of the free-shear layer to form counterrotating vortex pairs.

4 Growth of these vortices to large size for Reynolds numbers less than 1360.

5 Rapid breakdown of the counterrotating vortex pairs into turbulent mixing at higher Reynolds numbers.

6 Transient nature of the separation point.

Now that a better understanding of the fluid mechanics has been obtained, we can comment on its relevance to the high-exchanger application of the concentric-sphere geometry. Local heat transfer coefficients for the experimental configuration should be high in the region upstream of the separation point where the entering flow impinges on the inner sphere and then flows tangentially along the surface. The local heat-transfer coefficient would then decrease irregularly in the downstream region studied by Rundell [1], where the local heat-transfer coefficient would be relatively low. Local values of the heat-transfer coefficient would vary significantly and transiently, due to the nature of the flow pattern.

Ring baffles could be used to good advantage in improving the heat transfer coefficient. Select placement of baffles on the inside of the outer sphere would influence separation and cause the velocity near to the inner sphere to be greater. The local heat-transfer coefficient would be improved and, therefore, the overall heat transfer coefficient would also be improved.

References

1 Rundell, H., Ward, E. G., and Cox, J. E., Journal of Heat Transfer, Trans. ASME, Series C, Vol. 90, 1968, pp. 125–129.

2 Ward, E. G., Unpublished Master's thesis, University of Houston, Houston, Texas.

Convection in a Closed Rectangular Region: The Onset of Motion

IVAN CATTON[1]

Introduction

THE first investigator to consider a fully confined fluid was Davis [1].[2] Davis chose perfectly conducting walls and used the Galerkin method. In using the Galerkin method, however, he violated the Weierstrass theorem, and his set of trial functions were not complete within the region of interest. In the present work, Davis's problem [1] of perfectly conducting side walls is reexamined using a set of trial functions for the Galerkin method that do not violate the Weierstrass theorem. It is found that the results are not markedly different; however, in the region of small aspect ratios where Davis was unable to obtain meaningful results, the use of valid trial functions eliminates the problem. The results are discussed and compared with those of other investigators.

Analysis

In the initial state, a quasi-incompressible (Boussinesq) fluid fills a rectangular region. The base of the rectangle is fixed at a temperature higher than the top and a linear temperature gradient is established in the fluid in the direction of the body force (the negative z-axis). The initial velocity, temperature, and pressure distributions are given by

$$\mathbf{v}_0 = 0, \qquad \nabla T_0 = \beta\mathbf{k}, \qquad \nabla p_0 = \rho g(1 - \alpha\beta z)\mathbf{k} \tag{1}$$

where ρ is the mean fluid density, $\mathbf{k}$ a unit vector along the z-axis, β the mean temperature gradient, α the volumetric thermal expansion coefficient, and g the acceleration of gravity. In this particular problem, instability sets in via a marginal state and terms with time derivatives will not appear in the equations governing the perturbations. In dimensionless forms, the perturbation equations are [2]

$$\text{div } \mathbf{v} = 0 \tag{2}$$

$$\nabla^2\mathbf{v} + \mathrm{R}\theta\mathbf{k} - \text{grad } p = 0 \tag{3}$$

$$\nabla^2\theta + w = 0 \tag{4}$$

where $\mathbf{v}$, θ, and p are the velocity, temperature, and pressure disturbances measured in units of κ/L, βL, and $\rho\nu\kappa/L^2$, respectively. The characteristic length L is the height of the rectangular region, and ν and κ, the kinematic viscosity and thermal diffusivity. The horizontal coordinates, x and y, are measured in units of the rectangles height L. The Rayleigh number is defined

$$\mathrm{R} = \frac{\alpha g\beta L^4}{\nu\kappa} \tag{5}$$

The boundary conditions for this problem are

$$\mathbf{v} = 0 \text{ on } |z| = \tfrac{1}{2}, \qquad |x| = \tfrac{1}{2}H_1, \qquad |y| = \tfrac{1}{2}H_2 \tag{6}$$

$$\theta = 0 \text{ on } |z| = \tfrac{1}{2}, \qquad |x| = \tfrac{1}{2}H_1, \qquad |y| = \tfrac{1}{2}H_2 \tag{7}$$

Equations (2)–(4) and the boundary conditions given by equations (6) and (7) constitute an eigenvalue problem for the Rayleigh number. The smallest eigenvalue is the desired critical Rayleigh number.

The Galerkin method is readily adapted to problems of this type. The interior orthogonality relations are written for the equations of motion [3]

$$\sum_j^N \int_v (\nabla^2\mathbf{v} + \mathrm{R}\theta\mathbf{k} - \text{grad } p)_j \cdot \mathbf{v}_k dV = 0 \tag{8}$$

$$\sum_j^N \int_v (\nabla^2\theta + w)_j \theta_k dV = 0 \tag{9}$$

where $\mathbf{v}_j$, θ_j, and p_j are represented by

$$\mathbf{v}_j = a_j\mathbf{F}_j(x, y, z), \qquad \theta_j = b_jG_j(x, y, z), \qquad p_j = c_jH_j(x, y, z) \tag{10}$$

When the expressions given by equations (10) are substituted into equations (8) and (9) and the indicated integration is carried out, the pressure will vanish due to the solenoidal characteristic of $\mathbf{v}_j$ and there results

$$\sum_{j=1}^N \int_v |a_j\mathbf{F}_k \cdot \nabla^2\mathbf{F}_j + \mathrm{R}b_jG_j\mathbf{k}\cdot\mathbf{F}_k| dV = 0 \tag{11}$$

$$\sum_{j=1}^N \int_v |a_jG_k\mathbf{k}\cdot\mathbf{F}_j + b_jG_k\nabla^2G_j| dV = 0 \tag{12}$$

The requirement that equations (11) and (12) have nontrivial solutions (a_j and b_j nonzero) requires that the secular determinant be zero,

$$\det \begin{vmatrix} M_{11} & \mathrm{R} & M_{12} \\ M_{21} & & M_{22} \end{vmatrix} = 0 \tag{13}$$

where M_{11}, M_{12}, M_{21}, and M_{22} and $N \times N$ matrices defined as

$$M_{11} = \int_v \mathbf{F}_k \cdot \nabla^2\mathbf{F}_j dV, \qquad M_{12} = \int_v \mathbf{k}\cdot\mathbf{F}_kG_j dV$$
$$M_{21} = \int_v \mathbf{k}\cdot\mathbf{F}_jG_k dV, \qquad M_{22} = \int_v G_k\nabla^2G_j dV \tag{14}$$

By choosing suitable expansions for $\mathbf{v}$ and θ, it is possible to obtain good approximations for the lowest values of R by truncating the secular determinant (13) at some finite number of terms. The j and k in equations (14) each indicate some x, y, z dependence of a trial function. The trial functions used are the beam functions and sine and cosine functions. The method used in selecting trial functions for the velocity is that of Davis. Davis takes advantage of the fact that superposing two-dimensional motions (each satisfying continuity) can generate any three-dimensional motion if enough terms are incorporated into the expansion. For example, one might choose trial functions so that

$$\frac{\partial u}{\partial x} + \frac{\partial w_1}{\partial z} = 0 \quad \text{and} \quad \frac{\partial v}{\partial y} + \frac{\partial w_2}{\partial z} = 0$$

This yields

$$w = w_1 + w_2, \qquad u = u, \qquad v = v$$

which is fully three-dimensional motion and is the sum of two finite rolls. The various trial functions used to construct a solution are given in the Appendix.

The determinant given by equation (13) can be reduce to

$$\left| M_{22}^{-1}M_{21}M_{11}^{-1}M_{12} - \frac{1}{\mathrm{R}}I \right| = 0 \tag{15}$$

which is a $N \times N$ eigenvalue problem rather than a $2N \times 2N$ determinant whose zeros must be found.

The procedure used to solve the problem posed by equation

---

[1] Assistant Professor of Engineering, University of California, Los Angeles, Calif. Assoc. Mem. ASME.

[2] Numbers in brackets designate References at end of Note.

Contributed by the Heat Transfer Division of THE AMERICAN SOCIETY OF MECHANICAL ENGINEERS. Manuscript received at ASME Headquarters, January 17, 1969; final manuscript received, August 13, 1969.

Table 1 Critical Rayleigh number for the onset of natural convection for various aspect ratios

H_1	H_2 0.125	0.25	0.5	1.0	2.0	3.0	4.0	5.0	6.0
0.125	9802960.0	1554480.0	606001.0	469377.0	444995.0	444363.0	457007.0	473725.0	494742.0
0.25	1554480.0	638754.0	115596.0	64270.8	53529.7	50816.4	50136.1	50088.6	50410.1
0.50	606001.0	115596.0	48178.9	14615.3	11374.5	9831.6	9311.9	9099.4	8980.2
1.00	469377.0	64270.8	14615.3	6974.0	5137.9	3906.0	3633.6	3446.2	3357.9
2.00	444995.0	53529.7	11374.5	5138.2	3773.6	2753.6	2530.5	2359.5	2285.7
3.00	444363.0	50816.4	9831.6	3906.0	2753.6	2557.4	2337.2	2174.4	2100.9
4.00	457007.0	50136.1	9312.0	3633.6	2530.5	2337.2	2270.2	2110.9	2037.2
5.00	473725.0	50088.7	9099.4	3446.2	2359.5	2174.44	2110.9	2081.7	2007.8
6.00	494741.0	50410.1	8980.2	3358.0	2285.7	2101.0	2037.2	2007.8	1991.9

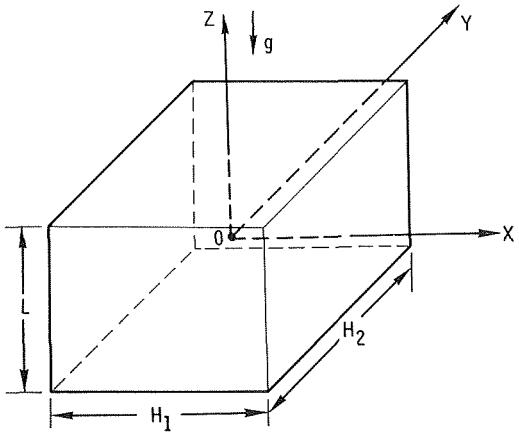

Fig. 1 Geometry and coordinate system of rectangular region

(15) was to use the trial functions given in the Appendix to generate the matrices, equations (14). The number of trial functions used (N) was increased until six significant figures of accuracy were obtained in R. This was done for each of the sets of functions given in the Appendix and for various combinations of sets of functions. The characteristic Rayleigh number being the minimum one found. This procedure was carried out for horizontal dimensions H/L from $^1/_8$ to 6 where L is the height of the perfectly conducting walls. The results are given in tabular form in Table 1 and in graphical form in Fig. 2.

Discussion of Results

The effect of confining perfectly conducting walls on the onset of natural convection has been determined for rectangular planforms of various aspect ratios. The Galerkin method was used with trial functions constructed from a linear combination of a complete set of orthogonal coordinate functions. The trial functions were selected to allow for the possibility of fully three-dimensional flow configurations. The minimum Rayleigh numbers were obtained for trial functions representing rolls whose axis are perpendicular to the longer dimension. The preferred orientation of rolls has been observed by Whitehead and Busse [4], and predicted by Davis [1].

The results of this analysis are presented in Table 1 for aspect ratios (H/L) from $^1/_8$ to 6. Selective results are presented graphically in Fig. 1. The stability curves, Fig. 1, obtained have a kink at some value of H_1/H_2 between 1 and 2. This kink is caused by flow going from a single roll to a multiple roll configuration. This was also observed by Davis [1] and Kurzweg [5]. The curve labeled $H_1 = 6.0$ in Fig. 2 is essentially a limit curve for large H_2. This would be equivalent to an infinite channel.

The upper-bound estimates of the critical Rayleigh number determined in this work are lower by 15 percent than the estimates found by Davis when one of the aspect ratios is less than unity and the kinks are almost nonexistent. If both aspect ratios are greater than unity, the results compare quite well. Davis used trial functions that were not a linear combination of a complete

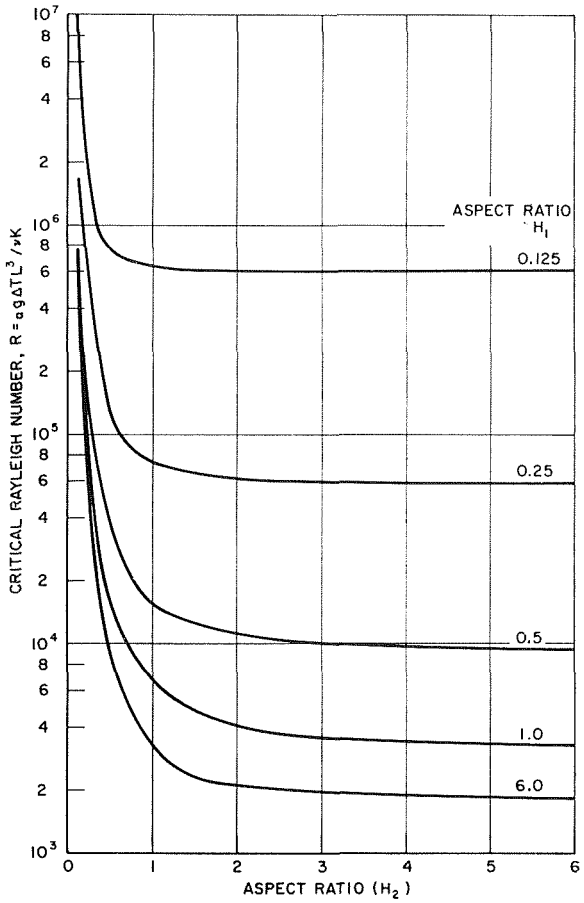

Fig. 2 Critical Rayleigh number for various aspect ratios

orthogonal set. This in itself is not a problem; however, his trial functions were constructed out of a set of equally spaced rolls. It is inconceivable that the walls would not affect the adjacent rolls. This, possibly, could be the reason that Davis could not obtain convergence when the aspect ratios were small. Davis [6] used these results to look at finite amplitude convection. It is suggested herein that his conclusions should be suspect. The present method does not have this difficulty and convergence is achieved very easily for small aspect ratios. As a matter of fact, the convergence improves the smaller the aspect ratio to the extent that a one-term approximation does a reasonable job in predicting the minimum Rayleigh number.

References

1 Davis, S. H., "Convection in a Box: Linear Theory," RAND Report No. RM-5251-PR, The RAND Corp., June 1967.

2 Chandrasekhar, S., *Hydrodynamic and Hydromagnetic Stability*, Oxford Clarendon Press, London, 1961, pp. 9–73.

3 Snyder, L. J., Spriggs, T. W., and Stewart, W. E., "Solution of the Equations of Change by Galerkins Method," *AIChE Journal*, Vol. 10, No. 4, 1964, pp. 535–540.

4 Whitehead, J. A., and Busse, F., Personal Communication, UCLA Institute of Geophysics.
5 Kurzweg, V., "Convective Instability of a Hydromagnetic Fluid Within an Enclosed Rectangular Cavity," *International Journal of Heat and Mass Transfer*, Vol. 8, 1965, pp. 35–41.
6 Davis, S. H., "Convection in a Box: The Dependence of Preferred Wave Number Upon the Rayleigh Number at Finite Amplitude," RAND Report No. RM-5504-PR, The RAND Corp., Aug. 1968.
7 Reid, W. H., and Harris, D. L., "On Orthogonal Functions Which Satisfy Four Boundary Conditions," *Astrophysics Journal Supplement Series*, Vol. 3, 1958, pp. 429–452.

APPENDIX

Trial Functions

The velocity components u, v, and w are expanded in terms of beam functions to satisfy two boundary conditions at each solid surface. The beam functions are

$$C_m(x) = \frac{\cosh(\lambda_m x)}{\cosh(\lambda_m/2)} - \frac{\cos(\lambda_m x)}{\cos(\lambda_m/2)} \tag{16}$$

and

$$S_m(x) = \frac{\sinh(\lambda_m x)}{\sinh(\lambda_m/2)} - \frac{\sin(\lambda_m x)}{\sin(\lambda_m/2)} \tag{17}$$

with

$$C_m(\tfrac{1}{2}) = C'_m(\tfrac{1}{2}) = S_m(\tfrac{1}{2}) = S'_m(\tfrac{1}{2}) = 0 \tag{18}$$

where the prime denotes differentiation with respect to the independent variable. These functions and integrals of various combinations of them are found in Harris and Reid [7].

The various sets of functions used are as follows:

1 Odd number of x rolls

$$w_{pqr} = \frac{C'_p\left(\frac{x}{H_1}\right)}{\lambda_p} \cos\left((2q-1)\pi\frac{y}{H_2}\right) C_r(z) \tag{19}$$

$$u_{pqr} = -\frac{H_1\lambda_r}{\lambda_p} C_p\left(\frac{x}{H_1}\right) \cos\left((2q-1)\pi\frac{y}{H_2}\right) \frac{C'_r(z)}{\lambda_r} \tag{20}$$

$$T_{pqr} = \sin\left(2p\pi\frac{x}{H_1}\right) \cos\left((2q-1)\pi\frac{y}{H_2}\right) \cos((2r-1)\pi z) \tag{21}$$

2 Even number of y rolls

$$w_{pqr} = \frac{S'_p\left(\frac{x}{H_1}\right)}{\mu_p} \cos\left((2q-1)\pi\frac{y}{H_2}\right) C_r(z) \tag{22}$$

$$u_{pqr} = -\frac{H_1\lambda_r}{\mu_p} S_p\left(\frac{x}{H_1}\right) \cos\left((2q-1)\pi\frac{y}{H_2}\right) \frac{C'_r(z)}{\lambda_r} \tag{23}$$

$$T_{pqr} = \cos\left((2p-1)\pi\frac{x}{H_1}\right) \times \cos\left((2q-1)\pi\frac{y}{H_2}\right) \cos((2r-1)\pi z) \tag{24}$$

3 Odd number of y rolls

$$w_{pqr} = \cos\left((2p-1)\pi\frac{x}{H_1}\right) \frac{C'_q\left(\frac{y}{H_2}\right)}{\lambda_q} C_r(z) \tag{25}$$

$$u_{pqr} = -\frac{H_2\lambda_r}{\lambda_q} \cos\left((2p-1)\pi\frac{x}{H_1}\right) C_q\left(\frac{y}{H_2}\right) \frac{C'_r(z)}{\lambda_r} \tag{26}$$

$$T_{pqr} = \cos\left((2p-1)\pi\frac{x}{H_1}\right) \sin\left(2q\pi\frac{y}{H_2}\right) \cos((2r-1)\pi z) \tag{27}$$

4 Even number of y rolls

$$w_{pqr} = \cos\left((2p-1)\pi\frac{x}{H_1}\right) \frac{S'_q\left(\frac{y}{H_2}\right)}{\mu_q} C_r(z) \tag{28}$$

$$u_{pqr} = -\frac{H_2\lambda_r}{\mu_p} \cos\left((2p-1)\pi\frac{x}{H_1}\right) Sq\left(\frac{y}{H_2}\right) \frac{C'_r(z)}{\lambda_r} \tag{29}$$

$$T_{pqr} = \cos\left((2p-1)\pi\frac{x}{H_1}\right) \times \cos\left((2q-1)\pi\frac{y}{H_2}\right) \cos((2r-1)\pi z) \tag{30}$$

Conduction to an Insulated Cylinder From a Semi-Infinite Region

S. W. CHURCHILL[1]

A complete analytical or numerical solution for conduction in the region outside an infinitely long, isothermal, insulated cylinder does not appear to have been developed. Furthermore, examination of the analytical solutions for the region outside an insulated sphere [1][2] and for the limiting cases of the cylinder described later suggests that a complete analytical solution would be so complex as to be impractical for computational purposes. The number of parameters in the problem magnifies the task of developing and presenting a sufficiently complete numerical solution. The general problem is, however, of considerable practical interest in the underground storage of cryogenic fluids, in buried pipelines, etc.

It is possible through the techniques described in [2, 3] to construct a complete solution of sufficient accuracy for all practical purposes from the available solutions for limiting cases. The construction of this solution is described herein and illustrative results are presented.

The solution for the transient heat flux density, q, from infinitely thick insulation at a uniform initial temperature, T_0, to an infinitely long cylinder of radius a, at constant temperature, T_s, is

$$\frac{qa}{k'(T_0 - T_s)} = \frac{4}{\pi^2}\int_0^\infty \frac{e^{-K't u^2/a^2} du}{u[J_0^2(u) + Y_0^2(u)]} \tag{1}$$

where t is time, k' and K' are the thermal conductivity and thermal diffusivity, respectively, of the insulation, and $J_0(u)$ and $Y_0(u)$ are Bessel functions of the first kind and zero order, and second and zero order, respectively.

Approximations for this integral for both large and small values of $K't/a^2$ are given on page 336 of [4] and numerical values are tabulated in [5]. The logarithm of the right side of equation (1) is plotted as the ordinate in Fig. 42, page 338 of [4] with the logarithm of $K't/a^2$ as the abscissa.

Substitution of thermal conductivity, k, and thermal diffusivity, K, of the external region for k' and K' in equation (1) produces a solution for no insulation.

For insulation of finite thickness, δ; an initial uniform temperature, T_0, in both the insulation and surroundings; and an infinite conductivity in the surroundings

[1] Carl V. S. Patterson, Professor of Chemical Engineering, University of Pennsylvania, Philadelphia, Pa.
[2] Numbers in brackets designate References at end of Note.
Contributed by the Heat Transfer Division of THE AMERICAN SOCIETY OF MECHANICAL ENGINEERS. Manuscript received at ASME Headquarters, June 23, 1969; revised manuscript received, August 25, 1969.

4 Whitehead, J. A., and Busse, F., Personal Communication, UCLA Institute of Geophysics.
5 Kurzweg, V., "Convective Instability of a Hydromagnetic Fluid Within an Enclosed Rectangular Cavity," *International Journal of Heat and Mass Transfer*, Vol. 8, 1965, pp. 35–41.
6 Davis, S. H., "Convection in a Box: The Dependence of Preferred Wave Number Upon the Rayleigh Number at Finite Amplitude," RAND Report No. RM-5504-PR, The RAND Corp., Aug. 1968.
7 Reid, W. H., and Harris, D. L., "On Orthogonal Functions Which Satisfy Four Boundary Conditions," *Astrophysics Journal Supplement Series*, Vol. 3, 1958, pp. 429–452.

APPENDIX

Trial Functions

The velocity components u, v, and w are expanded in terms of beam functions to satisfy two boundary conditions at each solid surface. The beam functions are

$$C_m(x) = \frac{\cosh(\lambda_m x)}{\cosh(\lambda_m/2)} - \frac{\cos(\lambda_m x)}{\cos(\lambda_m/2)} \tag{16}$$

and

$$S_m(x) = \frac{\sinh(\lambda_m x)}{\sinh(\lambda_m/2)} - \frac{\sin(\lambda_m x)}{\sin(\lambda_m/2)} \tag{17}$$

with

$$C_m(\tfrac{1}{2}) = C'_m(\tfrac{1}{2}) = S_m(\tfrac{1}{2}) = S'_m(\tfrac{1}{2}) = 0 \tag{18}$$

where the prime denotes differentiation with respect to the independent variable. These functions and integrals of various combinations of them are found in Harris and Reid [7].

The various sets of functions used are as follows:

1 Odd number of x rolls

$$w_{pqr} = \frac{C'_p\left(\frac{x}{H_1}\right)}{\lambda_p} \cos\left((2q-1)\pi\frac{y}{H_2}\right) C_r(z) \tag{19}$$

$$u_{pqr} = -\frac{H_1\lambda_r}{\lambda_p} C_p\left(\frac{x}{H_1}\right) \cos\left((2q-1)\pi\frac{y}{H_2}\right) \frac{C'_r(z)}{\lambda_r} \tag{20}$$

$$T_{pqr} = \sin\left(2p\pi\frac{x}{H_1}\right) \cos\left((2q-1)\pi\frac{y}{H_2}\right) \cos((2r-1)\pi z) \tag{21}$$

2 Even number of y rolls

$$w_{pqr} = \frac{S'_p\left(\frac{x}{H_1}\right)}{\mu_p} \cos\left((2q-1)\pi\frac{y}{H_2}\right) C_r(z) \tag{22}$$

$$u_{pqr} = -\frac{H_1\lambda_r}{\mu_p} S_p\left(\frac{x}{H_1}\right) \cos\left((2q-1)\pi\frac{y}{H_2}\right) \frac{C'_r(z)}{\lambda_r} \tag{23}$$

$$T_{pqr} = \cos\left((2p-1)\pi\frac{x}{H_1}\right) \times \cos\left((2q-1)\pi\frac{y}{H_2}\right) \cos((2r-1)\pi z) \tag{24}$$

3 Odd number of y rolls

$$w_{pqr} = \cos\left((2p-1)\pi\frac{x}{H_1}\right) \frac{C'_q\left(\frac{y}{H_2}\right)}{\lambda_q} C_r(z) \tag{25}$$

$$u_{pqr} = -\frac{H_2\lambda_r}{\lambda_q} \cos\left((2p-1)\pi\frac{x}{H_1}\right) C_q\left(\frac{y}{H_2}\right) \frac{C'_r(z)}{\lambda_r} \tag{26}$$

$$T_{pqr} = \cos\left((2p-1)\pi\frac{x}{H_1}\right) \sin\left(2q\pi\frac{y}{H_2}\right) \cos((2r-1)\pi z) \tag{27}$$

4 Even number of y rolls

$$w_{pqr} = \cos\left((2p-1)\pi\frac{x}{H_1}\right) \frac{S'_q\left(\frac{y}{H_2}\right)}{\mu_q} C_r(z) \tag{28}$$

$$u_{pqr} = -\frac{H_2\lambda_r}{\mu_p} \cos\left((2p-1)\pi\frac{x}{H_1}\right) S_q\left(\frac{y}{H_2}\right) \frac{C'_r(z)}{\lambda_r} \tag{29}$$

$$T_{pqr} = \cos\left((2p-1)\pi\frac{x}{H_1}\right) \times \cos\left((2q-1)\pi\frac{y}{H_2}\right) \cos((2r-1)\pi z) \tag{30}$$

Conduction to an Insulated Cylinder From a Semi-Infinite Region

S. W. CHURCHILL[1]

A complete analytical or numerical solution for conduction in the region outside an infinitely long, isothermal, insulated cylinder does not appear to have been developed. Furthermore, examination of the analytical solutions for the region outside an insulated sphere [1][2] and for the limiting cases of the cylinder described later suggests that a complete analytical solution would be so complex as to be impractical for computational purposes. The number of parameters in the problem magnifies the task of developing and presenting a sufficiently complete numerical solution. The general problem is, however, of considerable practical interest in the underground storage of cryogenic fluids, in buried pipelines, etc.

It is possible through the techniques described in [2, 3] to construct a complete solution of sufficient accuracy for all practical purposes from the available solutions for limiting cases. The construction of this solution is described herein and illustrative results are presented.

The solution for the transient heat flux density, q, from infinitely thick insulation at a uniform initial temperature, T_0, to an infinitely long cylinder of radius a, at constant temperature, T_s, is

$$\frac{qa}{k'(T_0 - T_s)} = \frac{4}{\pi^2}\int_0^\infty \frac{e^{-K't u^2/a^2}du}{u[J_0^2(u) + Y_0^2(u)]} \tag{1}$$

where t is time, k' and K' are the thermal conductivity and thermal diffusivity, respectively, of the insulation, and $J_0(u)$ and $Y_0(u)$ are Bessel functions of the first kind and zero order, and second and zero order, respectively.

Approximations for this integral for both large and small values of $K't/a^2$ are given on page 336 of [4] and numerical values are tabulated in [5]. The logarithm of the right side of equation (1) is plotted as the ordinate in Fig. 42, page 338 of [4] with the logarithm of $K't/a^2$ as the abscissa.

Substitution of thermal conductivity, k, and thermal diffusivity, K, of the external region for k' and K' in equation (1) produces a solution for no insulation.

For insulation of finite thickness, δ; an initial uniform temperature, T_0, in both the insulation and surroundings; and an infinite conductivity in the surroundings

[1] Carl V. S. Patterson, Professor of Chemical Engineering, University of Pennsylvania, Philadelphia, Pa.
[2] Numbers in brackets designate References at end of Note.
Contributed by the Heat Transfer Division of THE AMERICAN SOCIETY OF MECHANICAL ENGINEERS. Manuscript received at ASME Headquarters, June 23, 1969; revised manuscript received, August 25, 1969.

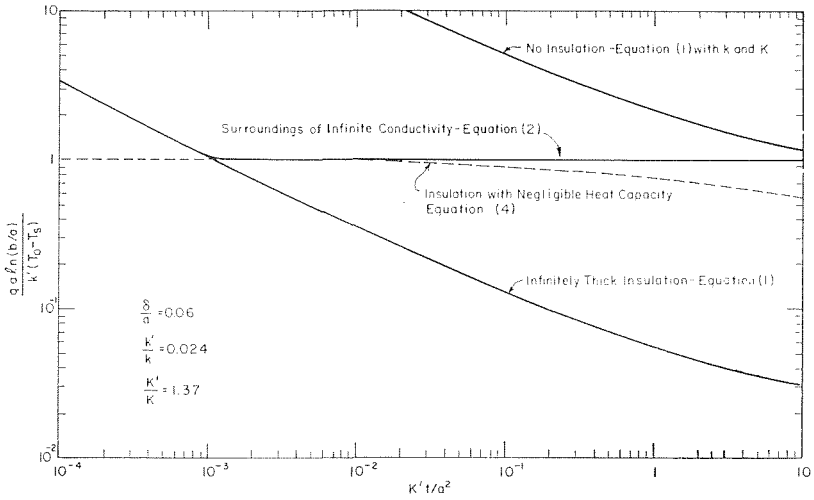

Fig. 1 Construction of solution by bounding

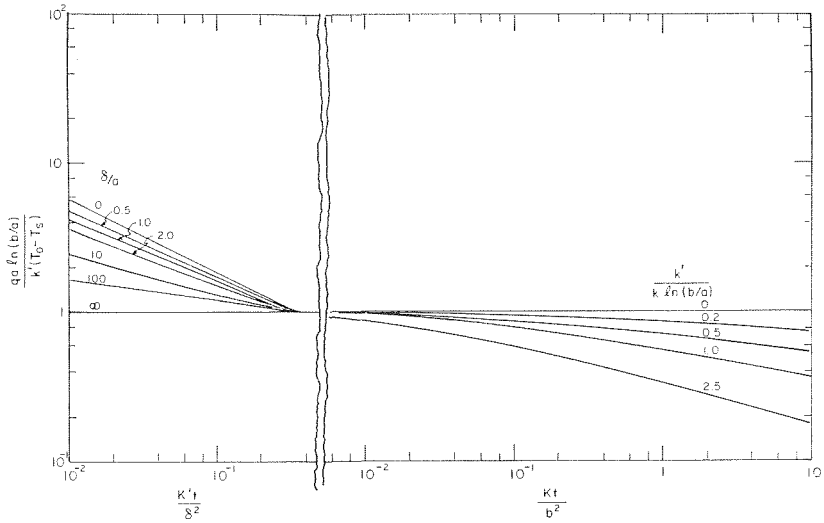

Fig. 2 Generalized solution for conduction to an insulated cylinder

$$\frac{qa \ln (b/a)}{k'(T_0 - T_s)} = 1 + 2 \ln \left(\frac{b}{a}\right) \sum_{n=1}^{\infty} \frac{J_0^2\left(\frac{b}{a}\alpha_n\right) e^{-K't\alpha_n^2/a^2}}{J_0^2(\alpha_n) - J_0^2\left(\frac{b}{a}\alpha_n\right)} \tag{2}$$

where $b = a + \delta$ is the outer radius of the insulation and α_n are the positive roots of

$$J_0(\alpha_n) \cdot Y_0(b\alpha_n/a) - J_0(b\alpha_n/a) \cdot Y_0(\alpha_n) = 0 \tag{3}$$

A few numerical values of the roots of equation (3) are given in Table IV of [4].

The solution for the general case, except for the assumption that the heat capacity of the insulation is negligible, is

$$\frac{qa \ln (b/a)}{k'(T_0 - T_s)} = \frac{2H}{\pi} \int_0^{\infty} \frac{\phi(u, H) e^{-Ktu^2/b^2}}{u} du \tag{4}$$

where $H = k'/k \ln (b/a)$,

$$\phi(u, H) = \frac{Y_0(u)[uJ_1(u) + HJ_0(u)] - J_0(u)[uY_1(u) + HY_0(u)]}{[uJ_1(u) + HJ_0(u)]^2 + [uY_1(u) + HY_0(u)]^2}, \tag{5}$$

and $J_1(u)$ and $Y_1(u)$ are Bessel functions of the first kind and first order and second kind and first order, respectively. Values of the right side of equation (4) are plotted as the ordinate in Fig. 43 of [4], with Kt/b^2 as the abscissa and H as the parameter.

These four limiting solutions are plotted in Fig. 1 for particular values of the three dimensionless parameters. From either physical or mathematical reasoning it is apparent that the heat-flux density must always be greater than that given by equation (1) and (4), and less than that given by equation (1) with k and K substituted for k' and K', and by equation (2). Furthermore, the difference between the general solution and equations (4) and (2) must decrease with increasing and decreasing times, respectively. Since equations (2) and (4) differ negligibly for intermediate times the general solution must differ negligibly from equation (2) for short and intermediate times and from equation

(4) for long and intermediate times. The simpler equation (1) is evidently a satisfactory approximation for short times. These conclusions are valid for other finite values of the three parameters. For the limiting values of the parameters, one of the limiting solutions becomes exact.

It might be presumed that the heat capacity of the insulation is always negligible and hence that equation (4) is sufficient for all practical purposes. The heat capacity of the insulation indeed does not affect the heat flux significantly after $t = \delta^2/\pi K'$, but approximately one half of the accumulative heat transfer up to that time is due to the sensible heat of the insulation.

Although a minimum of five dimensionless groups are required to describe the general solution, $qa \ln (b/a)k'(T_0 - T_s)$ is a significant function only of b/a and $K't/a^2$ for short times, essentially unity for intermediate times, and a significant function only of $k'/k \ln (b/a)$ and Kt/b^2 for the long times. Hence a complete graphical solution can be constructed, as illustrated in Fig. 2, with a split abscissa and a single parameter in each segment.

A complete solution for the transient temperature field in the insulation and outer region can be constructed by the technique just described above, although one additional independent variable is involved.

Acknowledgment

The criticisms and assistance of R. G. Rigg and the students in my heat transfer seminars at the University of Michigan and University of Pennsylvania are gratefully acknowledge.

References

1 Chen, Ja-Min, and Churchill, S. W., "Transient Heat Transfer From a Composite Sphere," unpublished report, University of Michigan.

2 Churchill, S. W., "Heat Transfer Rates and Temperature Fields for Underground Storage Tanks," *Society of Petroleum Engineers Journal*, Mar. 1962, pp. 28–32.

3 Churchill, S. W., "Bounded and Patched Solutions for Boundary Values Problems," *AIChE Journal*, Vol. 11, 1965, pp. 431–435.

4 Carslaw, H. S., and Jaeger, J. C., *Conduction of Heat in Solids*, 2nd ed., Oxford University Press, London, 1959.

5 Jaeger, J. C., and Clarke, M., *Proceedings, Royal Society of Edinburgh*, Series A, Vol. 61, 1942, pp. 229–230.

Stability of Natural Convection Within an Inclined Channel

U. H. KURZWEG[1]

Introduction

The authors, De Graaf and van der Held [1],[2] have found experimentally that the onset of convective heat transfer across an inclined air layer heated from below is characterized by the appearance of longitudinal convection rolls whose axes are parallel to the existing steady-state convection. We will show in the present Note that these longitudinal rolls are closely related to the well-known problem of convective instability between differentially heated horizontal surfaces and that the critical Grashof number at the onset of roll instability is directly obtainable from the known results of that problem. The resultant analytical relation between the critical Grashof number and the layer inclination to the vertical will be compared with our own observations on convection within a differentially heated inclined channel.

[1] Associate Professor, Department of Engineering Science and Mechanics, College of Engineering, University of Florida, Gainesville, Fla.

[2] Numbers in brackets designate References at end of Note.

Contributed by the Heat Transfer Division of The American Society of Mechanical Engineers. Manuscript received at ASME Headquarters, March 8, 1965; final revision, August 8, 1969.

Analysis

Consider natural convection within a plane channel of width δ inclined at angle θ with respect to the vertical. Let the lower and upper walls be maintained at temperature T_1 and T_2, respectively, and introduce a Cartesian coordinate system (x, y, z) such that the x-axis lies along the lower wall in direction of the flow and the z-axis is normal to the walls with the upward direction being positive. In terms of these coordinates, the stationary velocity and temperature profiles within the enclosed fluid layer are

$$V_x = U_0 f(z)(x), \qquad T = T_1 - \Delta T h(z)(x), \tag{1}$$

where U_0 is a representative velocity and $\Delta T = T_1 - T_2$. The lengths x, y, and z are expressed in units of δ and the dimensionless functions $f(z)$ and $h(z)$ remain unspecified for the time being. Equations governing the stability of these solutions are readily obtainable by the usual method of small disturbances. Without going into details of the derivation, we find that the growth rate for arbitrary infinitesimal, three-dimensional disturbances is governed (within the framework of the Boussinesq approximation) by the linear equations

$$\left[(\nabla^2 - L)\nabla^2 + \mathrm{Re}\,(D^2 f)\frac{\partial}{\partial x}\right] v_z = \mathrm{Gr}\left[\cos\theta\,\frac{\partial^2}{\partial x \partial z} - \sin\theta(\nabla^2 - D^2)\right]\tau \tag{2}$$

$$\left[L - \frac{1}{\mathrm{Pr}}\nabla^2\right]\tau = (Dh)v_z \tag{3}$$

where v_z is the nondimensional normal component of the velocity perturbation and τ the nondimensional temperature perturbation with

$$\mathrm{Re} = u_0\delta/\nu, \qquad \mathrm{Gr} = g\beta\frac{\Delta T}{\nu^2}\delta^3, \qquad \mathrm{Pr} = \frac{\nu}{\alpha}, \qquad D = \frac{\partial}{\partial z},$$

$$\nabla^2 = \frac{\partial^2}{\partial x^2} + \frac{\partial^2}{\partial y^2} + \frac{\partial^2}{\partial z^2}, \quad \text{and} \quad L = \frac{\partial}{\partial t} + \mathrm{Re}\, f\frac{\partial}{\partial x}.$$

The quantities g, ν, α, β, and t represent, respectively, the gravitational constant, kinematic viscosity, thermal diffusivity, coefficient of volume expansion, and the nondimensional time.

The secular relation corresponding to the onset of instability follows by solving equations (2) and (3) for an appropriate set of boundary conditions after introducing the normal mode relations $\partial/\partial x = ik_x$, $\partial/\partial y = ik_y$, and $\partial/\partial t = \omega_r + i\omega_i$ and equating the real part of the time variation to zero. The actual procedure of evaluating the resultant secular relation is quite involved unless certain simplifying assumptions concerning the form of the disturbances are made. One such simplification is to assume that the disturbances are transverse waves, in which case the foregoing equations reduce to the modified Orr-Sommerfeld form obtained by Plapp [2]. Here we consider a second limiting case, namely, that of longitudinal convection rolls as observed experimentally in reference [1]. These disturbances are independent of x and spatially periodic in y, with nondimensional wave number k_y. It follows from equations (2) and (3) that the growth rate of such disturbances is independent of $f(z)$ and that the equation governing the onset of nonoscillatory rolls is simply

$$(D^2 - k_y^2)^3 W = -k_y^2\,\mathrm{Gr}\,\mathrm{Pr}\sin\theta(Dh)W, \tag{4}$$

where W represents the z dependence of v_z. This equation will be recognized to be identical with that governing convective instability in a horizontal fluid layer with nonlinear vertical temperature distribution [3], provided the effective gravitational constant $g \sin\theta$ in equation (4) is replaced by g. The corresponding secular relation for the critical Grashof number is

$$\mathrm{Gr}_{\mathrm{crit}} = (\mathrm{const}/\mathrm{Pr})\csc\theta, \tag{5}$$

(4) for long and intermediate times. The simpler equation (1) is evidently a satisfactory approximation for short times. These conclusions are valid for other finite values of the three parameters. For the limiting values of the parameters, one of the limiting solutions becomes exact.

It might be presumed that the heat capacity of the insulation is always negligible and hence that equation (4) is sufficient for all practical purposes. The heat capacity of the insulation indeed does not affect the heat flux significantly after $t = \delta^2/\pi K'$, but approximately one half of the accumulative heat transfer up to that time is due to the sensible heat of the insulation.

Although a minimum of five dimensionless groups are required to describe the general solution, $qa \ln (b/a)k'(T_0 - T_s)$ is a significant function only of b/a and $K't/a^2$ for short times, essentially unity for intermediate times, and a significant function only of $k'/k \ln (b/a)$ and Kt/b^2 for the long times. Hence a complete graphical solution can be constructed, as illustrated in Fig. 2, with a split abscissa and a single parameter in each segment.

A complete solution for the transient temperature field in the insulation and outer region can be constructed by the technique just described above, although one additional independent variable is involved.

Acknowledgment

The criticisms and assistance of R. G. Rigg and the students in my heat transfer seminars at the University of Michigan and University of Pennsylvania are gratefully acknowledge.

References

1 Chen, Ja-Min, and Churchill, S. W., "Transient Heat Transfer From a Composite Sphere," unpublished report, University of Michigan.

2 Churchill, S. W., "Heat Transfer Rates and Temperature Fields for Underground Storage Tanks," *Society of Petroleum Engineers Journal*, Mar. 1962, pp. 28–32.

3 Churchill, S. W., "Bounded and Patched Solutions for Boundary Values Problems," *AIChE Journal*, Vol. 11, 1965, pp. 431–435.

4 Carslaw, H. S., and Jaeger, J. C., *Conduction of Heat in Solids*, 2nd ed., Oxford University Press, London, 1959.

5 Jaeger, J. C., and Clarke, M., *Proceedings, Royal Society of Edinburgh*, Series A, Vol. 61, 1942, pp. 229–230.

Stability of Natural Convection Within an Inclined Channel

U. H. KURZWEG[1]

Introduction

THE authors, De Graaf and van der Held [1],[2] have found experimentally that the onset of convective heat transfer across an inclined air layer heated from below is characterized by the appearance of longitudinal convection rolls whose axes are parallel to the existing steady-state convection. We will show in the present Note that these longitudinal rolls are closely related to the well-known problem of convective instability between differentially heated horizontal surfaces and that the critical Grashof number at the onset of roll instability is directly obtainable from the known results of that problem. The resultant analytical relation between the critical Grashof number and the layer inclination to the vertical will be compared with our own observations on convection within a differentially heated inclined channel.

[1] Associate Professor, Department of Engineering Science and Mechanics, College of Engineering, University of Florida, Gainesville, Fla.

[2] Numbers in brackets designate References at end of Note.

Contributed by the Heat Transfer Division of THE AMERICAN SOCIETY OF MECHANICAL ENGINEERS. Manuscript received at ASME Headquarters, March 8, 1965; final revision, August 8, 1969.

Analysis

Consider natural convection within a plane channel of width δ inclined at angle θ with respect to the vertical. Let the lower and upper walls be maintained at temperature T_1 and T_2, respectively, and introduce a Cartesian coordinate system (x, y, z) such that the x-axis lies along the lower wall in direction of the flow and the z-axis is normal to the walls with the upward direction being positive. In terms of these coordinates, the stationary velocity and temperature profiles within the enclosed fluid layer are

$$V_x = U_0 f(z)(x), \qquad T = T_1 - \Delta T h(z)(x), \tag{1}$$

where U_0 is a representative velocity and $\Delta T = T_1 - T_2$. The lengths x, y, and z are expressed in units of δ and the dimensionless functions $f(z)$ and $h(z)$ remain unspecified for the time being. Equations governing the stability of these solutions are readily obtainable by the usual method of small disturbances. Without going into details of the derivation, we find that the growth rate for arbitrary infinitesimal, three-dimensional disturbances is governed (within the framework of the Boussinesq approximation) by the linear equations

$$\left[(\nabla^2 - L)\nabla^2 + \mathrm{Re}\,(D^2 f)\frac{\partial}{\partial x}\right] v_z = \mathrm{Gr}\left[\cos\theta\,\frac{\partial^2}{\partial x \partial z} - \sin\theta(\nabla^2 - D^2)\right]\tau \tag{2}$$

$$\left[L - \frac{1}{\mathrm{Pr}}\nabla^2\right]\tau = (Dh)v_z \tag{3}$$

where v_z is the nondimensional normal component of the velocity perturbation and τ the nondimensional temperature perturbation with

$$\mathrm{Re} = u_0\delta/\nu, \qquad \mathrm{Gr} = g\beta\frac{\Delta T}{\nu^2}\delta^3, \qquad \mathrm{Pr} = \frac{\nu}{\alpha}, \qquad D = \frac{\partial}{\partial z},$$

$$\nabla^2 = \frac{\partial^2}{\partial x^2} + \frac{\partial^2}{\partial y^2} + \frac{\partial^2}{\partial z^2}, \quad \text{and} \quad L = \frac{\partial}{\partial t} + \mathrm{Re}\, f\frac{\partial}{\partial x}.$$

The quantities g, ν, α, β, and t represent, respectively, the gravitational constant, kinematic viscosity, thermal diffusivity, coefficient of volume expansion, and the nondimensional time.

The secular relation corresponding to the onset of instability follows by solving equations (2) and (3) for an appropriate set of boundary conditions after introducing the normal mode relations $\partial/\partial x = ik_x$, $\partial/\partial y = ik_y$, and $\partial/\partial t = \omega_r + i\omega_i$ and equating the real part of the time variation to zero. The actual procedure of evaluating the resultant secular relation is quite involved unless certain simplifying assumptions concerning the form of the disturbances are made. One such simplification is to assume that the disturbances are transverse waves, in which case the foregoing equations reduce to the modified Orr-Sommerfeld form obtained by Plapp [2]. Here we consider a second limiting case, namely, that of longitudinal convection rolls as observed experimentally in reference [1]. These disturbances are independent of x and spatially periodic in y, with nondimensional wave number k_y. It follows from equations (2) and (3) that the growth rate of such disturbances is independent of $f(z)$ and that the equation governing the onset of nonoscillatory rolls is simply

$$(D^2 - k_y^2)^3 W = -k_y^2\,\mathrm{Gr}\,\mathrm{Pr}\sin\theta(Dh)W, \tag{4}$$

where W represents the z dependence of v_z. This equation will be recognized to be identical with that governing convective instability in a horizontal fluid layer with nonlinear vertical temperature distribution [3], provided the effective gravitational constant $g \sin\theta$ in equation (4) is replaced by g. The corresponding secular relation for the critical Grashof number is

$$\mathrm{Gr}_{\mathrm{crit}} = (\mathrm{const}/\mathrm{Pr})\csc\theta, \tag{5}$$

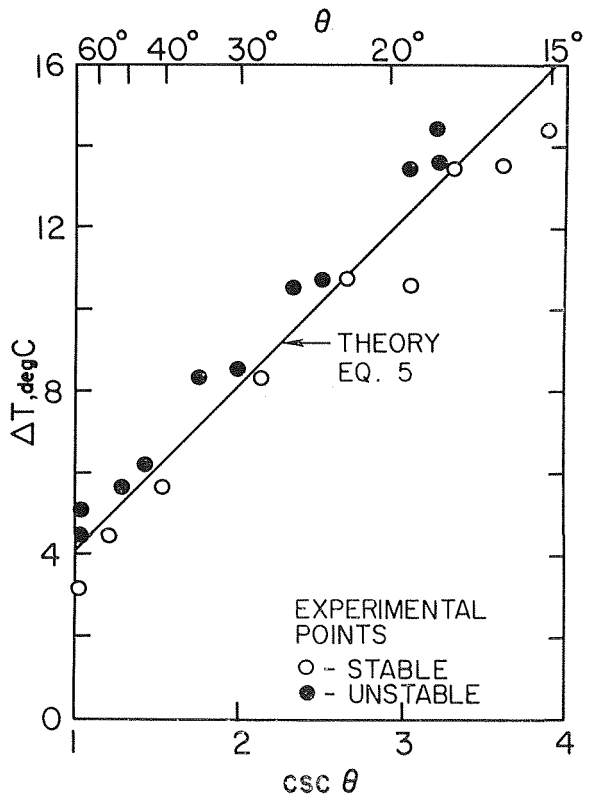

Fig. 1 Onset of longitudinal roll instability as function of layer inclination to vertical

where the value of the constant in this expression depends upon the temperature profile $h(z)$ and upon the boundary conditions. For the case of a linear temperature profile $h(z) = z$ in a channel whose walls are good thermal conductors, the value of this constant is 1707.8 and the associated critical wave number is $k_y = 3.12$.

Experiment

A series of experiments similar to those of reference [1] were undertaken to verify equation (5) for natural convection within an enclosed fluid layer. The apparatus consisted of an inclined plane channel of width $\delta = 0.61$ cm formed by two differentially heated copper plates. The mean temperature within the channel was maintained at 21 deg C, while the temperature difference ΔT between the heated lower and the cooled upper plate was adjustable from 0–20 deg C. Silicone oil (Dow-Corning 704), having the properties $\nu = 0.45$ cm^2/sec, $\alpha = 9.35 \times 10^{-4}$ cm^2/sec, and $\beta = 0.799 \times 10^{-3}$ (deg C)$^{-1}$ at 21 deg C, was chosen as the working fluid and convection within the fluid layer detected by the motion of suspended graphite particles. Results of the experimental observations are recorded in Fig. 1, together with the theoretical relation $\Delta T_{crit} = (4.04 \text{ deg C}) \csc \theta$ obtained from equation (5) upon substitution of the foregoing fluid properties and channel width. Agreement between theoretical predictions and the experimental results is seen to be excellent.

Concluding Remarks

The longitudinal roll disturbances considered here are also expected to occur in free convection along heated surfaces, such as inclined plates and horizontal cylinders. In these latter instances, equation (5) will no longer be a simple cosecant law since $h(z)$ is now a function of the surface inclination to the vertical. It would be of interest to solve the complete equations (2) and (3) for free convection along a nearly vertical plate, thereby determining how a slight fluid stratification affects Plapp's [2] theoretical results based upon the assumption of transverse disturbances of the Tollmien-Schlichting type.

References

1 De Graaf, J. G. A., and van der Held, E. F. M., "The Relation Between the Heat Transfer and the Convection Phenomena in Enclosed Plane Air Layers," *Applied Scientific Research*, Series A, Vol. 3, 1953, pp. 393–409.

2 Plapp, J. E., "The Analytic Study of Laminar Boundary-Layer Stability in Free Convection," *Journal of the Aeronautical Sciences*, Vol. 24, 1957, pp. 318–319.

3 Sparrow, E. M., Goldstein, R. J., and Jonsson, V. K., "Thermal Instability in a Horizontal Fluid Layer: Effect of Boundary Conditions and Nonlinear Temperature Profile," *Journal of Fluid Mechanics*, Vol. 18, 1964, pp. 513–528.

Laminar Free Convection From Vertical Cylinders With Uniform Heat Flux

H. R. NAGENDRA,[1] M. A. TIRUNARAYANAN,[2] and A. RAMACHANDRAN[3]

The boundary-layer analysis of free-convection heat transfer from a vertical cylinder with uniform heat flux at its surface is made. The transformed ordinary coupled equations form a two-parameter system (η_w and Pr). The two search type of equations is solved using an iterative scheme developed for the isothermal case. Numerical solutions obtained for parametric values of Pr and η_w indicate that the cylinders can be classified as short cylinders, long cylinders, and wires. Heat transfer correlations are presented and compared with experimental data. The results suggest that correlations for the isothermal case may be used for the present case also if a discrepancy of about 6 percent can be tolerated.

Nomenclature

D = diameter of cylinder
f = transformed stream function
g = acceleration due to gravity
Gr = Grashof number, equations (1)
k = thermal conductivity of fluid
L = length of cylinder
Nu = Nusselt number, (9)
Ns = shear stress number, equation (15)
Pr = Prandtl number, ν/α
q = rate of heat transfer per unit area
r, R = radial coordinates
Ra = Rayleigh number: Gr × Pr
t, T = temperature variable
u, U = vertical velocity component
v, V = radial velocity component
x, X = vertical coordinates
α = thermal diffusivity
β = coefficient of volume expansion
η = transformed independent variable
θ = transformed temperature variable
ν = kinematic viscosity
ψ = stream function
τ = shear stress

[1] Technical Assistant, Department of Mechanical Engineering, Indian Institute of Science, Bangalore, India.

[2] Professor-in-Charge, Department of Mechanical Engineering, Indian Institute of Science, Bangalore, India.

[3] Formerly, Professor, Department of Mechanical Engineering, Indian Institute of Science, Bangalore, India; presently, Director, Indian Institute of Technology, Madras, India.

Contributed by the Heat Transfer Division of THE AMERICAN SOCIETY OF MECHANICAL ENGINEERS. Manuscript received at ASME Headquarters, March 11, 1969; final manuscript received, October 13, 1969.

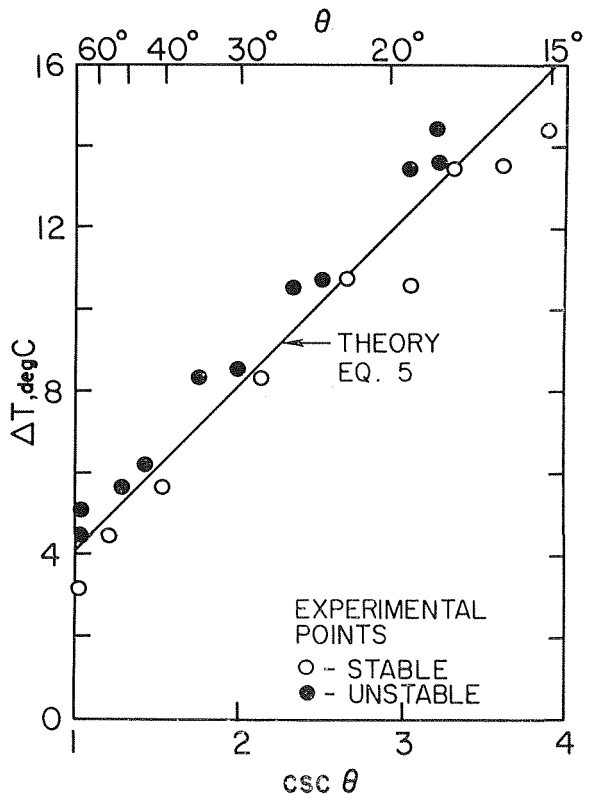

Fig. 1 Onset of longitudinal roll instability as function of layer inclination to vertical

where the value of the constant in this expression depends upon the temperature profile $h(z)$ and upon the boundary conditions. For the case of a linear temperature profile $h(z) = z$ in a channel whose walls are good thermal conductors, the value of this constant is 1707.8 and the associated critical wave number is $k_y = 3.12$.

Experiment

A series of experiments similar to those of reference [1] were undertaken to verify equation (5) for natural convection within an enclosed fluid layer. The apparatus consisted of an inclined plane channel of width $\delta = 0.61$ cm formed by two differentially heated copper plates. The mean temperature within the channel was maintained at 21 deg C, while the temperature difference ΔT between the heated lower and the cooled upper plate was adjustable from 0–20 deg C. Silicone oil (Dow-Corning 704), having the properties $\nu = 0.45$ cm²/sec, $\alpha = 9.35 \times 10^{-4}$ cm²/sec, and $\beta = 0.799 \times 10^{-3}$ (deg C)$^{-1}$ at 21 deg C, was chosen as the working fluid and convection within the fluid layer detected by the motion of suspended graphite particles. Results of the experimental observations are recorded in Fig. 1, together with the theoretical relation $\Delta T_{crit} = (4.04 \text{ deg C}) \csc \theta$ obtained from equation (5) upon substitution of the foregoing fluid properties and channel width. Agreement between theoretical predictions and the experimental results is seen to be excellent.

Concluding Remarks

The longitudinal roll disturbances considered here are also expected to occur in free convection along heated surfaces, such as inclined plates and horizontal cylinders. In these latter instances, equation (5) will no longer be a simple cosecant law since $h(z)$ is now a function of the surface inclination to the vertical. It would be of interest to solve the complete equations (2) and (3) for free convection along a nearly vertical plate, thereby determining how a slight fluid stratification affects Plapp's [2] theoretical results based upon the assumption of transverse disturbances of the Tollmien-Schlichting type.

References

1 De Graaf, J. G. A., and van der Held, E. F. M., "The Relation Between the Heat Transfer and the Convection Phenomena in Enclosed Plane Air Layers," *Applied Scientific Research*, Series A, Vol. 3, 1953, pp. 393–409.

2 Plapp, J. E., "The Analytic Study of Laminar Boundary-Layer Stability in Free Convection," *Journal of the Aeronautical Sciences*, Vol. 24, 1957, pp. 318–319.

3 Sparrow, E. M., Goldstein, R. J., and Jonsson, V. K., "Thermal Instability in a Horizontal Fluid Layer: Effect of Boundary Conditions and Nonlinear Temperature Profile," *Journal of Fluid Mechanics*, Vol. 18, 1964, pp. 513–528.

Laminar Free Convection From Vertical Cylinders With Uniform Heat Flux

H. R. NAGENDRA,[1] M. A. TIRUNARAYANAN,[2] and A. RAMACHANDRAN[3]

The boundary-layer analysis of free-convection heat transfer from a vertical cylinder with uniform heat flux at its surface is made. The transformed ordinary coupled equations form a two-parameter system (η_w and Pr). The two search type of equations is solved using an iterative scheme developed for the isothermal case. Numerical solutions obtained for parametric values of Pr and η_w indicate that the cylinders can be classified as short cylinders, long cylinders, and wires. Heat transfer correlations are presented and compared with experimental data. The results suggest that correlations for the isothermal case may be used for the present case also if a discrepancy of about 6 percent can be tolerated.

Nomenclature

D = diameter of cylinder
f = transformed stream function
g = acceleration due to gravity
Gr = Grashof number, equations (1)
k = thermal conductivity of fluid
L = length of cylinder
Nu = Nusselt number, (9)
Ns = shear stress number, equation (15)
Pr = Prandtl number, ν/α
q = rate of heat transfer per unit area
r, R = radial coordinates
Ra = Rayleigh number: Gr × Pr
t, T = temperature variable
u, U = vertical velocity component
v, V = radial velocity component
x, X = vertical coordinates
α = thermal diffusivity
β = coefficient of volume expansion
η = transformed independent variable
θ = transformed temperature variable
ν = kinematic viscosity
ψ = stream function
τ = shear stress

[1] Technical Assistant, Department of Mechanical Engineering, Indian Institute of Science, Bangalore, India.

[2] Professor-in-Charge, Department of Mechanical Engineering, Indian Institute of Science, Bangalore, India.

[3] Formerly, Professor, Department of Mechanical Engineering, Indian Institute of Science, Bangalore, India; presently, Director, Indian Institute of Technology, Madras, India.

Contributed by the Heat Transfer Division of THE AMERICAN SOCIETY OF MECHANICAL ENGINEERS. Manuscript received at ASME Headquarters, March 11, 1969; final manuscript received, October 13, 1969.

Superscripts

Prime = ordinary differentiation with respect to η
$*$ = value based on qL/k
$—$ = integrated mean value

Subscripts

D = value based on diameter of cylinder
L = value based on length of cylinder
∞ = value at a distance far away from cylinder
x = local value

Introduction

Free convection from vertical plates has been analyzed by several investigators under different boundary conditions [1–4].[4] The series solution of Sparrow and Gregg [5] for isothermal vertical cylinders, extension of the series solution by singular perturbation techniques by Kuiken [4], and similarity solution for a linearly varying surface temperature [6] are some of the investigations connected with vertical cylinders. Hama, Recesso, and Christiaens [7] report the results of the integral analysis and interferometric study of free convection from thin wires to air. The present authors used a new method of solution [8] which enabled to classify the complete family of cylinders into three categories—short cylinders, long cylinders, and wires. The foregoing method has been extended to the present case of vertical cylinders with uniform heat flux at the surface. The importance of this study lies in the fact that this type of boundary condition is commonly met with in practice. Electrical heating of cylinders and wires may be cited as examples.

Analysis

A vertical cylinder surrounded by a quiescent bulk fluid at a constant temperature T_∞ is heated such that the unit surface heat flux is constant. The assumptions made in the analysis and the basic boundary-layer equations are the same as those used by the authors in [8]. The transformation variables used in the present case to nondimensionalize the equations are

$$x = X/L;\ r = R/L;\ u = UL/\nu;\ v = VL/\nu;$$
$$t = (T_\infty - T)/(qL/k) \qquad (1)$$
$$\mathrm{Pr} = \nu/\alpha;\ \mathrm{Gr}_L{}^* = g\beta L^4 q/k\nu^2$$

Further, introducing the stream function ψ as

$$u = (1/r)\frac{\partial\psi}{\partial r};\qquad v = -(1/r)\frac{\partial\psi}{\partial x} \qquad (2)$$

and using the following transformation variables,

$$\eta = (\mathrm{Gr}_L{}^*/5)^{1/5}\, r/x^{1/5};\ t = (5/\mathrm{Gr}_L{}^*)^{1/5}x^{1/5}\,\theta(\eta, x);\ \psi = 5xf(\eta, x) \qquad (3)$$

the following set of nonlinear partial differential equations are obtained:

$$\eta^2 f_{\eta\eta\eta} + \eta f_{\eta\eta}(5f - 1) - f_\eta(3\eta f_\eta + 5f - 1) - \eta^3\theta = \eta_w(\eta f_\eta f_{\eta\eta w} + 5f_\eta f_{\eta w} - 5\eta f_{\eta\eta} f_{\eta w}). \qquad (4a)$$

$$\eta\theta_{\eta\eta} + \theta_\eta(1 + 5f\mathrm{Pr}) - \theta f_\eta \mathrm{Pr} = \eta_w(f_{\eta w}\theta_{\eta w} - \theta_\eta f_{\eta w})\mathrm{Pr} \qquad (4b)$$

where the subscripts denote partial differentiation with respect to the respective independent variables η and η_w. For the first approximation the RHS of equations (4a) and (4b) were neglected since they involve the unknown terms $f_{\eta w}$ and $f_{\eta\eta w}$. This simplification leads to a set of ordinary differential equations, viz.,

$$\eta^2 f''' + \eta f''(5f - 1) - f'(3\eta f' + 5f - 1) - \eta^3\theta = 0 \qquad (5a)$$

$$\eta\theta'' + \theta'(1 + 5f\mathrm{Pr}) - \theta f'\mathrm{Pr} = 0 \qquad (5b)$$

with boundary conditions,

$$f = f' = 0 \quad \text{and} \quad \theta' = 1 \text{ at } \eta = \eta_w$$
$$f' \to 0 \quad \text{and} \quad \theta \to 0 \text{ as } n \to \infty \qquad (5c)$$

[4] Numbers in brackets designate References at end of Note.

where η_w is defined as,

$$\eta_w = (\mathrm{Gr}_D{}^* D/160X)^{1/5} \qquad (6)$$

These set of ordinary differential equations (5a) and (5b) with boundary conditions, equation (5c), were solved numerically on a C.D.C. 3600 computer for parametric values of $\eta_w(10^{-3}$ to 10) to cover the entire range of cylinders and Pr(0.01, 0.1, 0.733 and 5) to encompass liquid metals gases and water using the iterative scheme developed by the authors [8].

On obtaining the solutions of the approximated equations, Eq. 5, the quantities on the RHS of equations (4) were calculated. It was found at this stage that introduction of RHS would bring in a variation of only 3% in the calculation of $f_{\eta\eta\eta}$ and $\theta_{\eta\eta}$ in the second approximation. It is to be noted that the quantity on RHS will vary with η and the variation mentioned was the maximum value. Substituting the values of RHS the set of equations (4a) and (4b) were solved to obtain the second approximation. It was observed that the final results with second approximation was only 2 per cent less than those with RHS neglected in equations (4a) and (4b). Hence only the first approximation will be used in the following calculations and discussions.

Heat Transfer and Fluid Flow Parameters

The temperature distribution at the wall can be found by the expression,

$$(T_W - T_\infty)/(qL/k) = (\mathrm{Gr}_L{}^*/5)^{-1/5}(X/L)^{1/5}\theta(\eta_W) \qquad (7)$$

If an average temperature difference is defined as

$$\overline{T_W - T_\infty} = (1/L)\int_0^L (T_W - T_\infty)dX \qquad (8)$$

and the corresponding average Nusselt number as

$$\mathrm{Nu}_D = (qD/k)/\overline{(T_W - T_\infty)} \qquad (9)$$

then the final expression for Nu_D will be

$$\mathrm{Nu}_D = (\mathrm{Gr}_L{}^* L/5D)\Big/\left[\int_0^L \left(\frac{X}{L}\right)^{1/5}\theta(\eta_W)dX\right] \qquad (10)$$

A similar analysis can also be done for fluid flow results. Under boundary-layer assumptions, the shear stress τ_x is given by

$$\frac{\tau_x}{\left(\dfrac{\mu\nu}{L^2}\right)} = f''(\eta_W) \qquad (11)$$

When an average shear stress is defined, equation (11) gives

$$\tau = (1/L)\int_0^L \tau_x dX = \left(\frac{\mu\nu}{L^2}\right)\frac{1}{L}\int_0^L f''(\eta_W)dX \qquad (12)$$

It is to be noted that $\theta(\eta_W)$ and $f''(\eta_W)$ are functions of x and hence their functional dependence with x is to be determined to evaluate the integrals in equations (10) and (12).

Results

Velocity and temperature distributions were obtained as the solution of equations (4) and (5) for parametric values of η_W and Pr. Table 1 gives the value of $\theta(\eta_W)$ for various values of Pr when $\eta_W = 1$ and the maximum value of f' attained with air (Pr = 0.733) for different η_W values to bring out the important features of the solution. It can be seen from the table that the values of $f_{\max}{}'$ decreases fast with decreasing values of η_W.

Table 1 Variation of $\theta(\eta_W)$ and $f_{\max}{}'(\eta_W)$

Pr	$\theta(\eta_W)$	η_W	$f_{\max}{}'(\eta_W)$
0.01	−0.9771	1.0	0.0926
0.10	−0.9414	0.1	1.061×10^{-4}
0.733	−0.8260	0.01	1.045×10^{-8}
5.000	−0.6718	0.001	1.045×10^{-12}

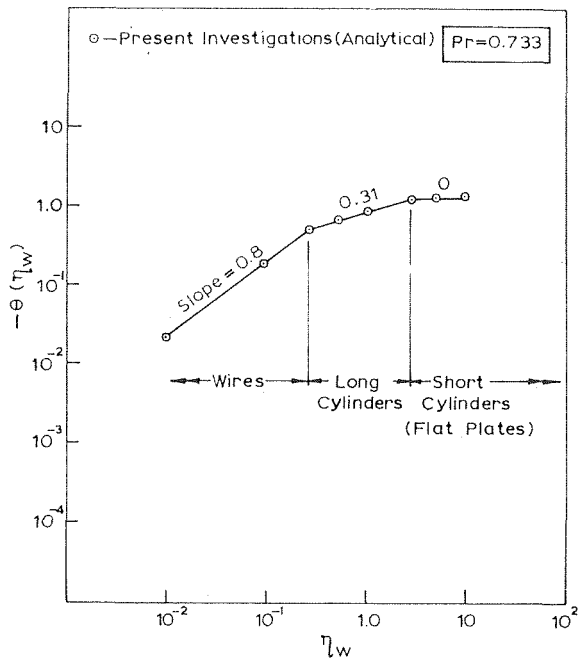

Fig. 1 Variation of $\theta(\eta_w)$ versus η_w

To develop heat transfer correlations, Figs. 1 and 2 are drawn. In Fig. 1 as η_W increases the value of $-\theta(\eta_W)$ increases reaching an asymptotic value of 1 for η_W greater than about 3. As seen from the figure, the results can be represented by

$$\theta(\eta_W) = -F(\eta_W)^a \tag{13}$$

for the 3 regimes where a and F are constants with respect to η_W but vary in different regimes. For $\eta_W \gtrsim 3$, the regime is designated as short cylinders since the results in this region do not vary by more than 8 percent of the values for flat plates. Further, the two regimes represented by $0.2 \lesssim \eta_W < 3$ and η_W less than 0.2 belong to the categories of long cylinders and wires. It may also be noted that the value of $\eta_W = 3$ in the uniform heat-flux case corresponds to a value of $\eta_W = 5$ in the isothermal case. It may be noted that the criterion that demarcates the short cylinders from the long ones in the isothermal case is $\eta_W = 5$.

For different Prandtl numbers the plots of $-\theta(\eta_W)$ versus η_W were similar to Fig. 1. It was observed from the study of these plots that the slopes of the straight lines in each regime were independent of Pr. However, F in equation (13) depends on Pr and is evaluated from the plot of $-\theta(\eta_W)$ versus Pr (see Fig. 2). Thus the final correlations can be simplified from equation (10) as

$$\mathrm{Nu}_D = C_1(\mathrm{Ra}_D{}^*D/L)^{C_2} \tag{14}$$

If, in the definition of $\mathrm{Gr}_L{}^*$ (equation (1)), qL/k is replaced by $\overline{T_W - T_\infty}$, then equation (14) simplifies to

$$\mathrm{Nu}_D = C_3(\mathrm{Ra}_D D/L)^{C_4} \tag{15}$$

The values of these constants are given in Table 2. It can be observed in Table 2 that the final values of $\mathrm{Ra}_D D/L$ which demarcate the different categories of cylinders are as follows:

1 Short cylinders: $\mathrm{Ra}_D D/L$ greater than 10^4.
2 Long cylinders: $\mathrm{Ra}_D D/L$ 0.05 to 10^4.
3 Wires: $\mathrm{Ra}_D D/L$ less than 0.05.

In the isothermal case, the values of $\mathrm{Ra}_D D/L$ were the same as in the foregoing for the respective categories [8].

The present analytical results are shown in Fig. 3, together with those for the isothermal case for comparison. The experimental results of the authors [9] are also plotted. In the regime of short cylinders, the straight line is above that for the isothermal case by about 5 percent. Thus the observation of Sparrow and Gregg

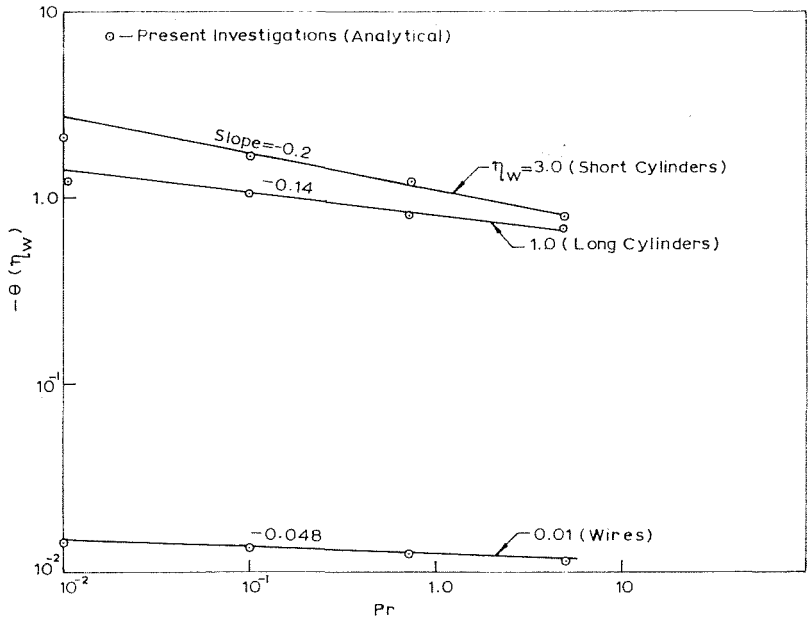

Fig. 2 Variation of $-\theta(\eta_w)$ wtih Pr for different η_w

Table 2

Category	C_1	C_2	C_3	C_4			Range of $\mathrm{Ra}_D D/L$
Short cylinders	0.55	0.20	0.60	0.25			above 10^4
Long cylinders	1.33	0.14	1.37	0.16			0.05 to 10^4
Wires	0.90	0.048	0.93	0.05			below 0.05
	A_1	A_2	A_3	A_4	A_5	A_6	
Short cylinders	1.36	0.60	−0.12	0.56	0.75	−0.10	Above 10^4
Long cylinders	1.52	0.63	−0.08	0.92	0.73	−0.14	0.05 to 10^4
Wires	1.26	0.66	−0.04	0.36	0.60	−0.19	below 0.05

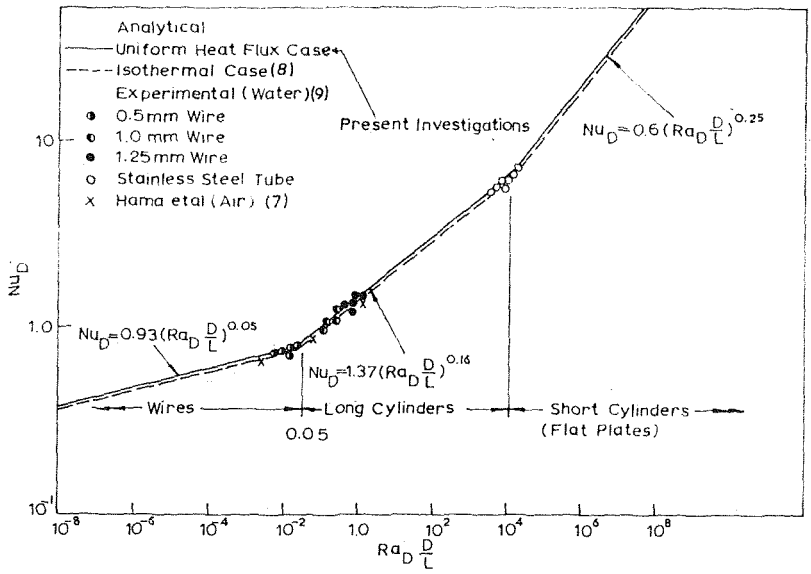

Fig. 3 Heat transfer correlations

[2], for flat plates that the results of uniform heat flux case do not vary by more than 10 percent of the isothermal case, seems justified. In fact, by the definition of modified Grashof number, the variation is still reduced.

When equation (7) is simplified, it gives the result that $(T_W - T_\infty)$ is proportional to $x^{(1-a)/5}$. In the regime of short cylinders (also flat plates) $a = 0$ (see Fig. 1 where slope $a = 0$) and hence $(T_W - T_\infty)$ is proportional to $x^{0.2}$, which is in conformity with the results of Sparrow and Gregg [2]. For long cylinders, the exponent of x reduces to 0.138 and for wires the exponent is 0.04. Thus, in the region of wires, the results of uniform heat flux and isothermal cases should be very nearly the same. The foregoing trend can be observed in Fig. 3; the results in the region of wires do not vary by more than 3 percent.

The analysis for fluid-flow results give the final correlations as

$$Ns_D = \tau/(\mu\nu L/D^3) = A_1(\mathrm{Pr})^{A_2}(\mathrm{Gr}_D{}^*D/L)^{A_3} \quad (16)$$

or

$$Ns_D = A_4(\mathrm{Pr})^{A_5}(\mathrm{Gr}_D D/L)^{A_6} \quad (17)$$

The values of these constants are also shown in Table 2.

Conclusions

1 The values of $\mathrm{Ra}_D D/L$ which demarcate the different category of cylinders in the isothermal case hold good for the present case also.

2 Heat transfer and fluid flow correlations are developed. Heat transfer correlations based on average surface temperature are developed to show that they do not vary by more than 5 percent of those for the isothermal case as one proceeds from short cylinders to wires. In general, higher heat transfer rates are countered.

3 For low Pr, the heat transfer correlations differ by about 10 percent.

4 Experimental results reported in [9] are in good agreement with the present results.

References

1 Ostrach, S., NACA 1111, 1953.

2 Sparrow, E. M., and Gregg, J. L., TRANS. ASME, Vol. 78, 1956, pp. 435.

3 Ibid, TRANS. ASME, Vol. 80, 1958, pp. 379.

4 Kuiken, H. K., Doctoral thesis, Delft, 1967.

5 Sparrow, E. M., and Gregg, J. L., TRANS. ASME, Vol. 78, 1956, pp. 1823.

6 Millsaps, K., and Pohlhausen, K., *Journal of the Aeronautical Sciences*, Vol. 25, 1958, pp. 357.

7 Hama, F. R., Recesso, J. V., and Christiaens, J., *Journal of the Aerospace Sciences*, Vol. 26, 1959, pp. 335.

8 Nagendra, H. R., Tirunarayanan, M. A., and Ramachandran, A., M. E. Report 2, II Sc, 1969.

9 Nagendra, H. R., Tirunarayanan, M. A., and Ramachandran, A., *Journal of the Chemical Engineering Society*, Vol. 24, 1969, pp. 1491.

Combined Convective Heat Transfer From Horizontal Cylinders in Air

P. H. OOSTHUIZEN[1] and S. MADAN[2]

Introduction

ALTHOUGH many thorough investigations of the heat transfer rates from horizontal, circular cylinders by free convection ($R_d \to 0$) alone and forced convection ($G_d \to 0$) alone have been undertaken, comparatively little attention has been given to the combined free and forced-convection region. The effect of the buoyancy forces on the heat transfer rate has, of course, been noted in a number of investigations, e.g., references [1, 2],[3] but the only specific investigations of the combined convection region for the horizontal cylinder case appear to be those of references [3, 4]. In both these investigations, however, only the case where the buoyancy forces were at right angles to the forced flow was studied.

In the present study, the heat transfer rates from a series of circular cylinders, so arranged that the forced flow and buoyancy forces were in the same direction, i.e., the forced flow was vertical, have been measured. In these tests the Reynolds number (R_d) varied, approximately, between 100 and 3000, and the Grashof number (G_d) approximately between 25,000 and 300,000.

[1] Assistant Professor, Department of Mechanical Engineering, Queen's University, Kingston, Canada.

[2] Graduate Student, Department of Mechanical Engineering, Queen's University, Kingston, Canada.

[3] Numbers in brackets designate References at end of Note.

Contributed by the Heat Transfer Division of THE AMERICAN SOCIETY OF MECHANICAL ENGINEERS. Manuscript received at ASME Headquarters, May 8, 1969; revised manuscript received, September 8, 1969.

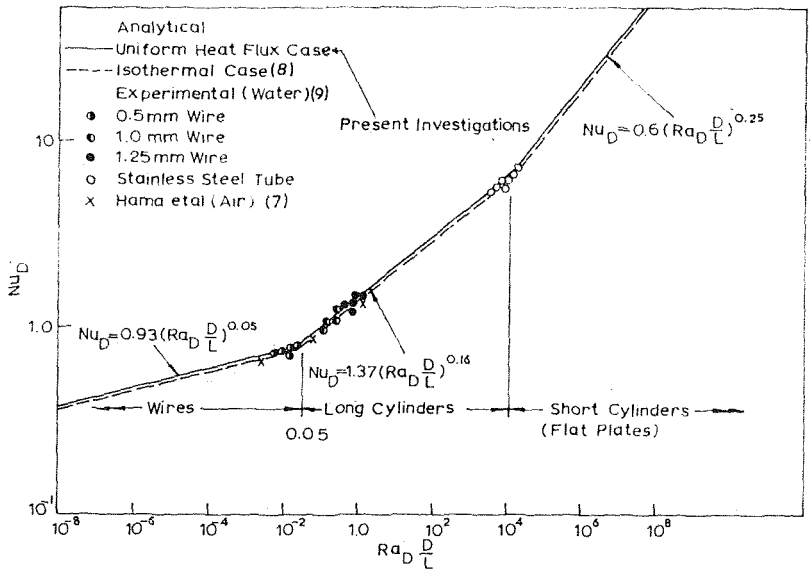

Fig. 3 Heat transfer correlations

[2], for flat plates that the results of uniform heat flux case do not vary by more than 10 percent of the isothermal case, seems justified. In fact, by the definition of modified Grashof number, the variation is still reduced.

When equation (7) is simplified, it gives the result that $(T_W - T_\infty)$ is proportional to $x^{(1-a)/5}$. In the regime of short cylinders (also flat plates) $a = 0$ (see Fig. 1 where slope $a = 0$) and hence $(T_W - T_\infty)$ is proportional to $x^{0.2}$, which is in conformity with the results of Sparrow and Gregg [2]. For long cylinders, the exponent of x reduces to 0.138 and for wires the exponent is 0.04. Thus, in the region of wires, the results of uniform heat flux and isothermal cases should be very nearly the same. The foregoing trend can be observed in Fig. 3; the results in the region of wires do not vary by more than 3 percent.

The analysis for fluid-flow results give the final correlations as

$$Ns_D = \tau/(\mu\nu L/D^3) = A_1(\mathrm{Pr})^{A_2}(\mathrm{Gr}_D{}^* D/L)^{A_3} \quad (16)$$

or

$$Ns_D = A_4(\mathrm{Pr})^{A_5}(\mathrm{Gr}_D D/L)^{A_6} \quad (17)$$

The values of these constants are also shown in Table 2.

Conclusions

1 The values of $\mathrm{Ra}_D D/L$ which demarcate the different category of cylinders in the isothermal case hold good for the present case also.

2 Heat transfer and fluid flow correlations are developed. Heat transfer correlations based on average surface temperature are developed to show that they do not vary by more than 5 percent of those for the isothermal case as one proceeds from short cylinders to wires. In general, higher heat transfer rates are countered.

3 For low Pr, the heat transfer correlations differ by about 10 percent.

4 Experimental results reported in [9] are in good agreement with the present results.

References

1 Ostrach, S., NACA 1111, 1953.

2 Sparrow, E. M., and Gregg, J. L., TRANS. ASME, Vol. 78, 1956, pp. 435.

3 Ibid, TRANS. ASME, Vol. 80, 1958, pp. 379.

4 Kuiken, H. K., Doctoral thesis, Delft, 1967.

5 Sparrow, E. M., and Gregg, J. L., TRANS. ASME, Vol. 78, 1956, pp. 1823.

6 Millsaps, K., and Pohlhausen, K., *Journal of the Aeronautical Sciences*, Vol. 25, 1958, pp. 357.

7 Hama, F. R., Recesso, J. V., and Christiaens, J., *Journal of the Aerospace Sciences*, Vol. 26, 1959, pp. 335.

8 Nagendra, H. R., Tirunarayanan, M. A., and Ramachandran, A., M. E. Report 2, II Sc, 1969.

9 Nagendra, H. R., Tirunarayanan, M. A., and Ramachandran, A., *Journal of the Chemical Engineering Society*, Vol. 24, 1969, pp. 1491.

Combined Convective Heat Transfer From Horizontal Cylinders in Air

P. H. OOSTHUIZEN[1] and S. MADAN[2]

Introduction

ALTHOUGH many thorough investigations of the heat transfer rates from horizontal, circular cylinders by free convection ($R_d \to 0$) alone and forced convection ($G_d \to 0$) alone have been undertaken, comparatively little attention has been given to the combined free and forced-convection region. The effect of the buoyancy forces on the heat transfer rate has, of course, been noted in a number of investigations, e.g., references [1, 2],[3] but the only specific investigations of the combined convection region for the horizontal cylinder case appear to be those of references [3, 4]. In both these investigations, however, only the case where the buoyancy forces were at right angles to the forced flow was studied.

In the present study, the heat transfer rates from a series of circular cylinders, so arranged that the forced flow and buoyancy forces were in the same direction, i.e., the forced flow was vertical, have been measured. In these tests the Reynolds number (R_d) varied, approximately, between 100 and 3000, and the Grashof number (G_d) approximately between 25,000 and 300,000.

[1] Assistant Professor, Department of Mechanical Engineering, Queen's University, Kingston, Canada.

[2] Graduate Student, Department of Mechanical Engineering, Queen's University, Kingston, Canada.

[3] Numbers in brackets designate References at end of Note.

Contributed by the Heat Transfer Division of THE AMERICAN SOCIETY OF MECHANICAL ENGINEERS. Manuscript received at ASME Headquarters, May 8, 1969; revised manuscript received, September 8, 1969.

Apparatus

Four models having diameters of 0.75, 1.00, 1.25, and 1.50 in. were used in the study. These models were mounted in a vertical, low-speed wind tunnel having a 16 in. × 16 in. working section. The velocities used ranged between approximately 0.4 and 5 fps, these velocities being measured by means of a Pitot tube at the higher values and a Disa low velocity anemometer at the lower values. The turbulence level in the tunnel was less than 0.7 percent.

The models were made of solid aluminum and were 12-in. long with a 2-in-long nylon insulating cap of the same diameter as the model on each end. The velocity in the tunnel was uniform across the model and, as far as could be determined, end effects were negligible.

Before a test, a model was uniformly heated to a temperature of about 300 deg F and then placed in the tunnel and the variation of temperature with time measured using a thermocouple, the test being terminated when the temperature had dropped to about 150 deg F. From this measured temperature-time history the heat transfer rate was determined, assuming, because of the extremely small Biot numbers, a uniform model temperature, in the following way. The total heat loss rate from the model is given by

$$Q = -MC \frac{dT_W}{dt} \tag{1}$$

where M is the mass of the cylinder, C its specific heat, and T_W its temperature. The heat transfer coefficient at any instant of time is, therefore, given in terms of the rate of temperature change, by

$$hA(T_W - T_1) = -MC \frac{dT_W}{dt} \tag{2}$$

The function A being the surface area of the cylinder and T_1 the free-stream air temperature. Thus using the measured variation of T_W with time t, h could be determined at any instant of time. The convective heat transfer coefficient was then determined by subtracting the relatively very small, radiant heat-loss coefficient.

The heat transfer rate from each model was also measured in the same way with zero forced velocity.

Results

In the present investigation, the ratio of model diameter to test section height (d/H) varied between 0.047 and 0.094 and thus some blockage effect was to be expected [2]. This effect resulted in the measured Nusselt numbers (N_d) for the four models at a given Reynolds number in the purely forced-convection region differing from each other, the Nusselt numbers for the 1.5-in-dia model being approximately 8 percent higher than those for the 0.75-in-dia model in this range. A Reynolds number correction factor was therefore determined by selecting a Nusselt number in the purely forced convection region, determining the Reynolds, number corresponding to this Nusselt number for each model, and then plotting the variation of this Reynolds number with d/H and extrapolating to find an equivalent Reynolds number corresponding to zero d/H. This correction factor remained approximately constant for each model over the entire Reynolds number range corresponding to purely forced convection and was thus assumed to be independent of Reynolds number for the values covered by the present tests, and the correction factors determined in this way were applied to all results.

The values of these blockage correction factors are shown in Table 1. They will be seen to be between the curves for blockage correction factor given in reference [2] and are also consistent with the results of reference [5].

Typical results for the four models, with the correction factor just discussed, applied are shown in Fig. 1. Since the model

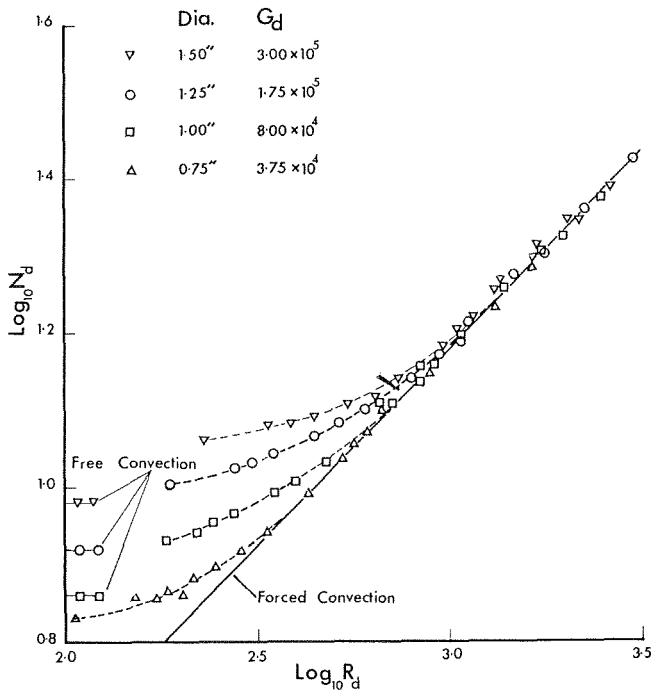

Fig. 1 Variation of Nusselt number with Reynolds number, corrected for blockage, for typical Grashof numbers

Table 1

Model diameter	Blockage (d/H)	Reynolds number correction factor
0.75 in.	0.047	1.03
1.00 in.	0.063	1.07
1.25 in.	0.078	1.10
1.50 in.	0.094	1.16

temperature varied during each run and since the fluid properties were evaluated at the film temperature, the Nusselt, Reynolds, and Grashof numbers all varied during a run. The results shown in Fig. 1 were thus obtained by interpolating to find the Nusselt and Reynolds numbers corresponding to the selected Grashof numbers. Also shown in Fig. 1 are some of the values of N_d, corresponding to the selected values of G_d, determined with zero forced velocity.

The results in the forced-convection region can be closely fitted by the equation

$$N_{dfor} = 0.464\ R_d^{0.5} + 0.0004\ R_d \tag{3}$$

which is an equation of the type proposed by Douglas and Churchill [2] and in good agreement with other forced flow results. The values of N_d given by this equation are indicated by the forced convection line in Fig. 1.

Now, for the unseparated portion of the flow over the cylinder, it can be analytically shown that the ratio of the actual local Nusselt number to the local Nusselt number that would exist with purely forced convection at the same position at the same Reynolds number will depend only on the parameter (G_d/R_d^2). Therefore, while it does not seem possible to analytically deduce this relation for the separated portion of the flow, it seems logical to attempt to correlate the measured mean Nusselt numbers in terms of this parameter, i.e., to assume

$$N_d/N_{dfor} = \text{function}\ (G_d/R_d^2) \tag{4}$$

where N_{dfor} is given by equation (3). The experimental results are therefore plotted in this form in Fig. 2 from which it will be

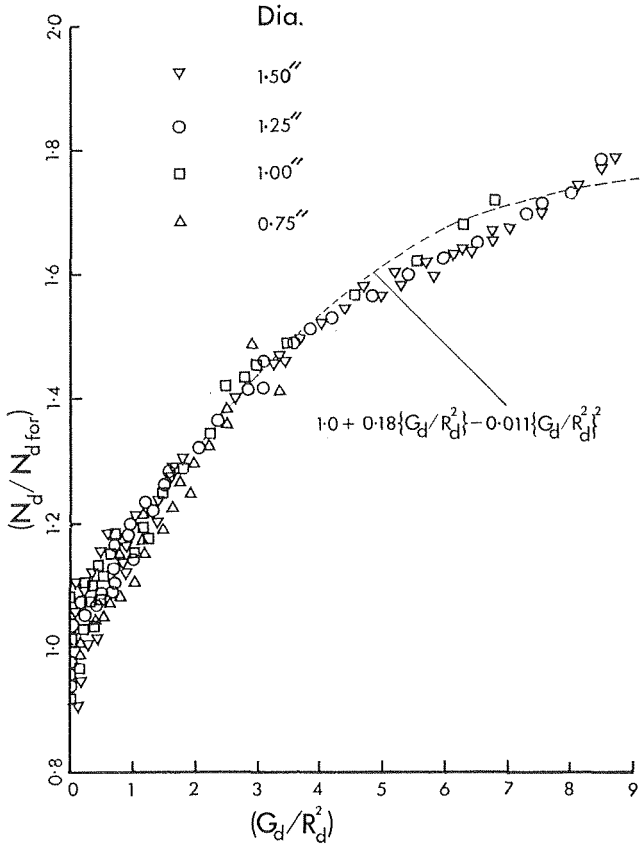

Fig. 2 Correlation of Nusselt numbers in terms of combined convection parameter

seen that the results can, indeed, be correlated in this manner.

Over the range of variables covered by the present tests, therefore, the heat transfer rates can be approximately expressed by

$$N_d/N_{dfor} = 1 + 0.18\,(G_d/R_d^2) - 0.011\,(G_d/R_d^2)^2 \qquad (5)$$

If forced convection is assumed to exist if N_d is within 5 percent of N_{dfor}, then this relation indicates that for forced convection $G_d/R_d^2 < 0.28$.

Acknowledgment

The financial assistance received from the National Research Council of Canada under Grant No. A5573 is gratefully acknowledged.

References

1 Deaver, F. K., Penney, W. R., and Jefferson, T. B., "Heat Transfer From an Oscillating Horizontal Wire to Water," JOURNAL OF HEAT TRANSFER, TRANS. ASME, Series C, Vol. 84, 1962, pp. 251–256.

2 Perkins, H. C., Jr., and Leppert, G., "Forced-Convection Heat Transfer From a Uniformly Heated Cylinder," JOURNAL OF HEAT TRANSFER, TRANS. ASME, Series C, Vol. 84, 1962, pp. 257–263.

3 Van Der Hegge Zijnen, B. G., "Modified Correlation Formulas for the Heat Transfers by Natural and by Forced Convection From Horizontal Cylinders," *Applied Scientific Research*, Series A, Vol. 6, 1956, pp. 129–140.

4 Collis, D. C., and Williams, M. J., "Two-Dimensional Convection From Heated Wires at Low Reynolds Numbers," *Journal of Fluid Mechanics*, Vol. 6, 1959, pp. 357–384.

5 Acrivos, A., et al., "The Steady Separated Flow Past a Circular Cylinder at Large Reynolds Numbers," *Journal of Fluid Mechanics*, Vol. 21, 1965, pp. 737–760.

Transient Response of Fin-Tube Space Radiators[1]

R. W. PALMQUIST,[2] L. J. MORIARTY,[3] and W. A. BECKMAN[4]

Nomenclature

c_p = specific heat of fin material
$\bar{c}_p$ = average specific heat of tube and coolant
2δ = fin thickness
E_f = fin energy storage rate per unit width of radiator
F_{dx-i} = view factor from element of fin to base i
k = thermal conductivity
$2L$ = distance between tubes
m = mass of base per unit width of radiator
M = $L\delta\rho c_p(m\bar{c}_p)^{-1}$, capacitance ratio
N = $\sigma L^2 T_{b0}^3/k\delta$, conductance parameter
Q_b = net radiant energy leaving surface of base per unit width of radiator
Q_c = energy conducted from base into fin per unit width of radiator
Q_f = net radiant energy leaving surface of fin per unit width of radiator
Q^* = $Q/\sigma L T_{b0}^4$, dimensionless heat flux
r = radius of tube
ρ = density of fin material
σ = Stefan-Boltzmann constant
T = absolute temperature of fin
T_b = absolute temperature of base
T_{b0} = initial temperature of base
T^* = T/T_{b0}, dimensionless temperature
t = time
τ = $t/(m\bar{c}_p/\sigma L T_{b0}^3)$, dimensionless time
x = distance along fin from tube
X = x/L, dimensionless length

DESIGN parameters for steady-state operation of minimum weight fin-tube radiators have been given in reference [1][5] and the transient response of minimum weight fin-tube radiators in reference [2]. The designer must consider the transient response of space radiators, since the liquid coolant may freeze if the power supply is temporarily cut off. This study considers the case where steady-state operation is suddenly halted and the system is allowed to cool. As in previous studies, all surfaces are assumed black and radiant interchange between tube and fin is taken into account, although radiation from an external source is not considered. The temperatures of the tubes and coolant are taken to be equal and uniform. Consequently, the results can be used by the designer to give a lower bound on the time which may elapse before freezing of the coolant begins.

As seen from Fig. 1, the symmetry of the fin-tube radiator allows analysis of a single base and fin system. The base is

---

[1] A publication of the Solar Energy Laboratory of the University of Wisconsin, Madison, Wis.

[2] Research Assistant, Department of Mechanical Engineering, University of Wisconsin, Madison, Wis.

[3] Presently at the General Electric Company, Cincinnati, Ohio.

[4] Associate Professor of Mechanical Engineering, University of Wisconsin, Madison, Wis. Assoc. Mem. ASME.

[5] Numbers in brackets designate References at end of Note.

Contributed by the Heat Transfer Division of THE AMERICAN SOCIETY OF MECHANICAL ENGINEERS. Manuscript received at ASME Headquarters, February 14, 1968; revised manuscript received, September 11, 1969.

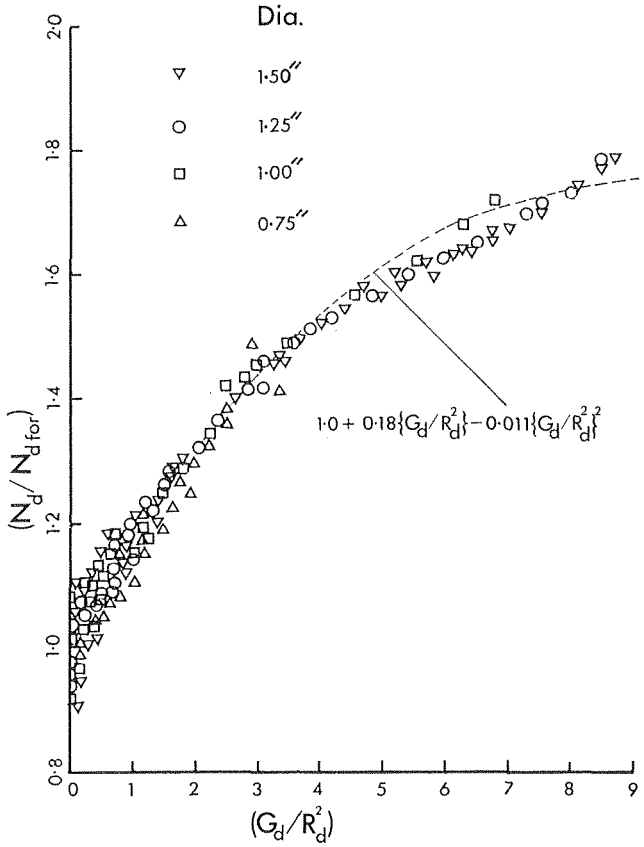

Fig. 2 Correlation of Nusselt numbers in terms of combined convection parameter

seen that the results can, indeed, be correlated in this manner.

Over the range of variables covered by the present tests, therefore, the heat transfer rates can be approximately expressed by

$$N_d/N_{dfor} = 1 + 0.18\ (G_d/R_d^2) - 0.011\ (G_d/R_d^2)^2 \qquad (5)$$

If forced convection is assumed to exist if N_d is within 5 percent of N_{dfor}, then this relation indicates that for forced convection $G_d/R_d^2 < 0.28$.

Acknowledgment

The financial assistance received from the National Research Council of Canada under Grant No. A5573 is gratefully acknowledged.

References

1 Deaver, F. K., Penney, W. R., and Jefferson, T. B., "Heat Transfer From an Oscillating Horizontal Wire to Water," JOURNAL OF HEAT TRANSFER, TRANS. ASME, Series C, Vol. 84, 1962, pp. 251–256.

2 Perkins, H. C., Jr., and Leppert, G., "Forced-Convection Heat Transfer From a Uniformly Heated Cylinder," JOURNAL OF HEAT TRANSFER, TRANS. ASME, Series C, Vol. 84, 1962, pp. 257–263.

3 Van Der Hegge Zijnen, B. G., "Modified Correlation Formulas for the Heat Transfers by Natural and by Forced Convection From Horizontal Cylinders," *Applied Scientific Research*, Series A, Vol. 6, 1956, pp. 129–140.

4 Collis, D. C., and Williams, M. J., "Two-Dimensional Convection From Heated Wires at Low Reynolds Numbers," *Journal of Fluid Mechanics*, Vol. 6, 1959, pp. 357–384.

5 Acrivos, A., et al., "The Steady Separated Flow Past a Circular Cylinder at Large Reynolds Numbers," *Journal of Fluid Mechanics*, Vol. 21, 1965, pp. 737–760.

Transient Response of Fin-Tube Space Radiators[1]

R. W. PALMQUIST,[2] L. J. MORIARTY,[3] and W. A. BECKMAN[4]

Nomenclature

c_p = specific heat of fin material
$\bar{c}_p$ = average specific heat of tube and coolant
2δ = fin thickness
E_f = fin energy storage rate per unit width of radiator
F_{dx-i} = view factor from element of fin to base i
k = thermal conductivity
$2L$ = distance between tubes
m = mass of base per unit width of radiator
M = $L\delta\rho c_p(m\bar{c}_p)^{-1}$, capacitance ratio
N = $\sigma L^2 T_{b0}^3/k\delta$, conductance parameter
Q_b = net radiant energy leaving surface of base per unit width of radiator
Q_c = energy conducted from base into fin per unit width of radiator
Q_f = net radiant energy leaving surface of fin per unit width of radiator
Q^* = $Q/\sigma L T_{b0}^4$, dimensionless heat flux
r = radius of tube
ρ = density of fin material
σ = Stefan-Boltzmann constant
T = absolute temperature of fin
T_b = absolute temperature of base
T_{b0} = initial temperature of base
T^* = T/T_{b0}, dimensionless temperature
t = time
τ = $t/(m\bar{c}_p/\sigma L T_{b0}^3)$, dimensionless time
x = distance along fin from tube
X = x/L, dimensionless length

DESIGN parameters for steady-state operation of minimum weight fin-tube radiators have been given in reference [1][5] and the transient response of minimum weight fin-tube radiators in reference [2]. The designer must consider the transient response of space radiators, since the liquid coolant may freeze if the power supply is temporarily cut off. This study considers the case where steady-state operation is suddenly halted and the system is allowed to cool. As in previous studies, all surfaces are assumed black and radiant interchange between tube and fin is taken into account, although radiation from an external source is not considered. The temperatures of the tubes and coolant are taken to be equal and uniform. Consequently, the results can be used by the designer to give a lower bound on the time which may elapse before freezing of the coolant begins.

As seen from Fig. 1, the symmetry of the fin-tube radiator allows analysis of a single base and fin system. The base is

---

[1] A publication of the Solar Energy Laboratory of the University of Wisconsin, Madison, Wis.

[2] Research Assistant, Department of Mechanical Engineering, University of Wisconsin, Madison, Wis.

[3] Presently at the General Electric Company, Cincinnati, Ohio.

[4] Associate Professor of Mechanical Engineering, University of Wisconsin, Madison, Wis. Assoc. Mem. ASME.

[5] Numbers in brackets designate References at end of Note.

Contributed by the Heat Transfer Division of THE AMERICAN SOCIETY OF MECHANICAL ENGINEERS. Manuscript received at ASME Headquarters, February 14, 1968; revised manuscript received, September 11, 1969.

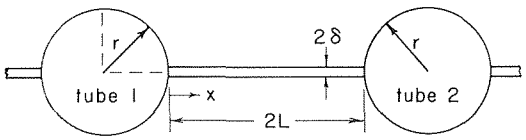

Fig. 1 Cross section of fin-tube radiator

taken to be a 90-deg arc of tube and the enclosed fluid, while the fin is of length L and thickness δ. The following analysis is based on a tube and fin of unit width.

An energy balance on the base yields

$$m\bar{c}_p \frac{dT_b}{dt} = -(Q_b + Q_c) \tag{1}$$

Since $Q_c = Q_f + E_f$, the equation may be written as

$$\frac{dT_b^*}{d\tau} = -(Q_b^* + Q_f^* + E_f^*) \tag{2}$$

where the dimensionless variables are

$$T_b^* = T_b/T_{b0} \qquad \tau = t/(mc_p/\sigma L T_{b0}^3)$$
$$Q^* = Q/\sigma L T_{b0}^4 \qquad E_f^* = E_f/\sigma L T_{b0}^4$$

Noting that the fin receives radiant energy from both tube 1 and tube 2, the net energy radiated from the fin is

$$Q_f^* = \int_0^1 [T^{*4} - T_b^{*4}(F_{dx-1} + F_{dx-2})]dX \tag{3}$$

where

$$T^* = T/T_{b0}, \qquad X = x/L.$$

As derived in reference [1], the net energy radiated from the base is

$$Q_b^* = (r/L)T_b^{*4} + \int_0^1 (2T_b^{*4} - T^{*4})(F_{dx-1} + F_{dx-2})dX \tag{4}$$

and the view factors are

$$F_{dx-1} = \frac{1}{2}\left\{1 - \frac{\sqrt{(r/L + X)^2 - (r/L)^2}}{(r/L) + X}\right\}$$
$$F_{dx-2} = \frac{1}{2}\left\{1 - \frac{\sqrt{(r/L + 2 - X)^2 - (r/L)^2}}{(r/L) + 2 - X}\right\} \tag{5}$$

The energy storage rate for the fin is given by

$$E_f^* = M \int_0^1 \frac{\partial T^*}{\partial \tau} dX \tag{6}$$

where $M = L\delta\rho c_p/m\bar{c}_p$. The parameter M is called the capacitance ratio since it is a ratio of the heat capacity of the fin to the heat capacity of the base.

Substituting equations (3), (4), and (6) into (2) yields the equation

$$-\frac{dT_b^*}{d\tau} = (r/L)T_b^{*4} + T_b^{*4}\int_0^1 (F_{dx-1} + F_{dx-2})dX + \int_0^1 T^{*4}[1 - (F_{dx-1} + F_{dx-2})]dX + M\int_0^1 \frac{\partial T^*}{\partial \tau} dX \tag{7}$$

which has the initial condition $T_b^*(0) = 1$.

The fin temperature profile is found by solving the equation

$$\frac{\partial^2 T^*}{\partial X^2} - N[T^{*4} - T_b^{*4}(F_{dx-1} + F_{dx-2})] = MN\frac{\partial T^*}{\partial \tau} \tag{8}$$

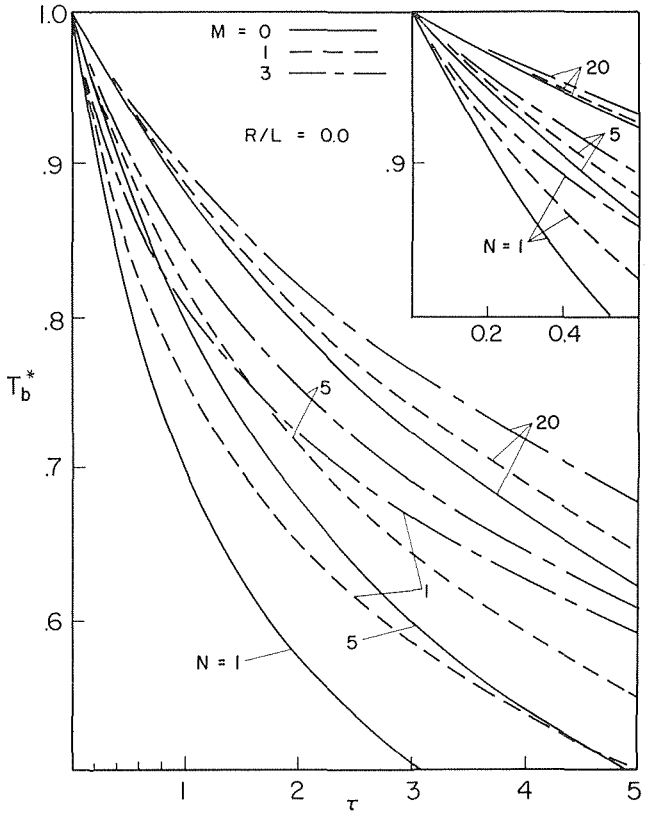

Fig. 2 Base temperature versus time for $r/L = 0$

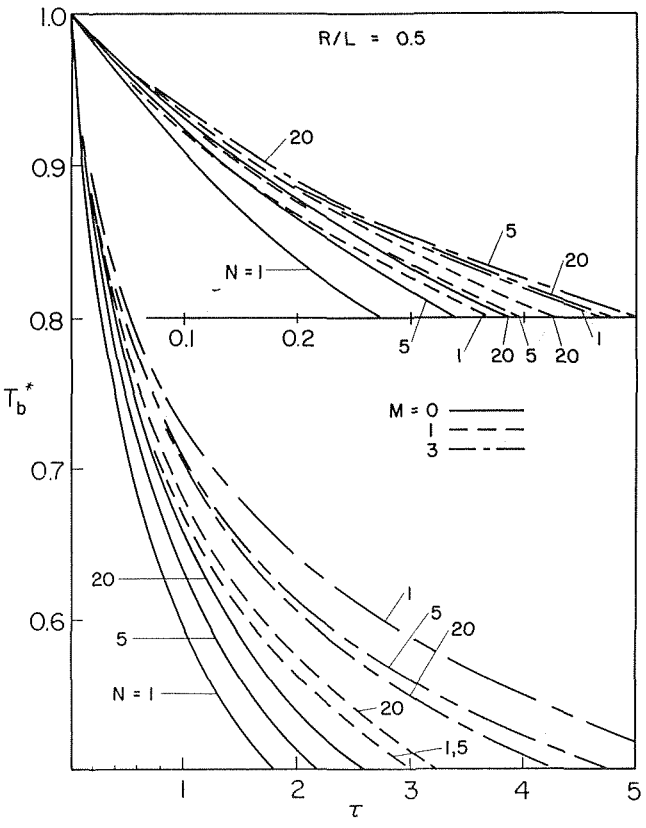

Fig. 3 Base temperature versus time for $r/L = 0.25$

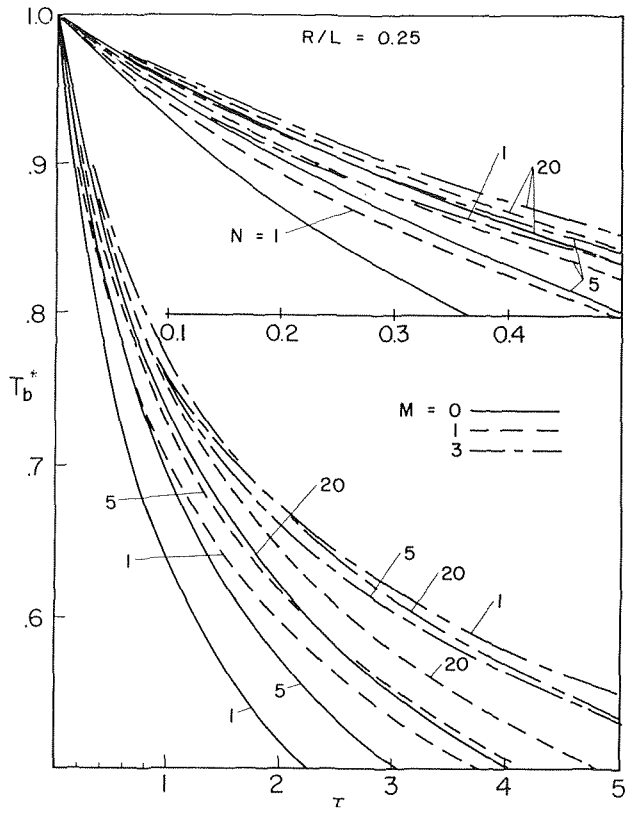

Fig. 4 Base temperature versus time for $r/L = 0.5$

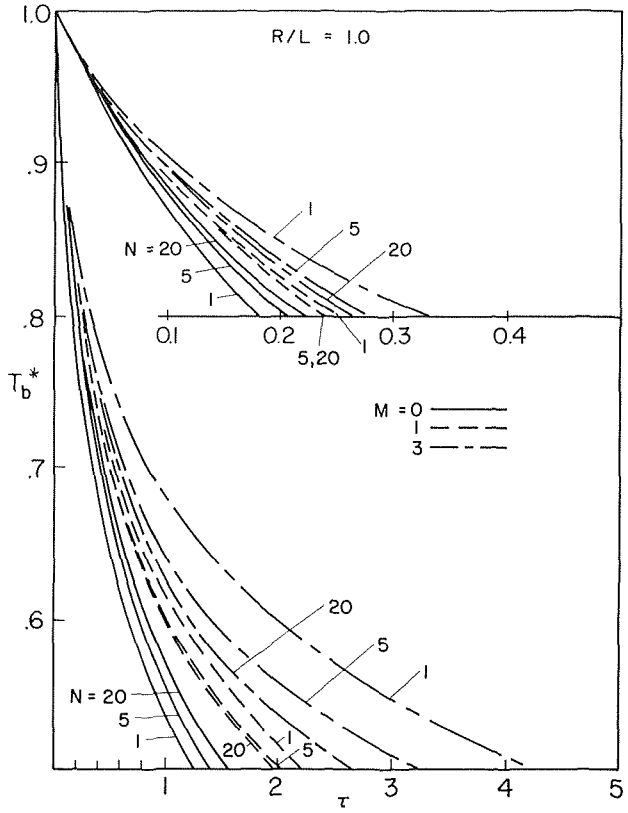

Fig. 5 Base temperature versus time for $r/L = 1.0$

where $N = \sigma L^2 T_{b0}^3 / k\delta$ is the conductance parameter. The initial and boundary conditions are

$$T^*(0, \tau) = T_b^*(\tau), \frac{\partial T^*}{\partial X}(1, \tau) = 0, T^*(X, 0) = T_{ss}^*(X)$$

where the steady-state solution T_{ss}^* is found from equation (8) $\partial T^*/\partial \tau = 0$ and the boundary conditions $T_{ss}^*(0) = 1$ and $\partial T_{ss}^*(1)/\partial X = 0$.

When $N = 0$ the fin is isothermal and transient is given simply by the following equation:

$$T_b = [1 + 3\tau(1 + r/L)/(1 + M)]^{-3} \quad (9)$$

Equations (7) and (8) were solved by finite-difference techniques on a digital computer. The base temperature, as a function of time, is given in Figs. 2–5 for $r/L = 0$, 0.25, 0.5, 1.0; $N = 1$, 5, 20; and $M = 0$, 1, 3. Equation (9) can be used to provide information for $N = 0$.

Since N is inversely proportional to the conductivity, one associates small values of N with efficient fins and hence it is expected that the base would cool more rapidly when N is small. This is always the case for $M = 0$, but not for $M > 0$. In Figs. 4 and 5, the curves for $M = 1$ and $M = 3$ show that the base cools more rapidly as N becomes larger. The reason for such anomalous behavior lies in the fact that the total amount of energy in the system is greater if the fin has a more uniform temperature distribution, as it does when N is small. When a small N is coupled with a large M, the energy stored in the fin is large compared to the energy in the base and the amount of energy conducted into the fin may be small or even negative.

References

1 Sparrow, E. M., and Eckert, E. R. G., "Radiant Interaction Between Fin and Base Surfaces," JOURNAL OF HEAT TRANSFER, TRANS. ASME, Vol. 84, Series C, Feb. 1962, pp. 12–18.

2 Moriarty, L. J., "Transient Analysis of Fin-Tube Space Radiator Systems," Master's thesis, Department of Mechanical Engineering, University of Wisconsin, Madison, Wis., 1966.

Absorption of Thermal Radiation in a Hemispherical Cavity

H. H. SAFWAT[1]

Nomenclature

A, B, c_1, c_2 = assumed constants in equation (12)

$dF_{(dA_j - dA_i)_t}$ = total view factor between area elements dA_j and dA_i

$f_0, f_1, f_2, \ldots$ = factors giving contributions of specular images in total view factor $dF_{(dA_j - dA_i)}$

$F_{dA_j - \text{circular opening}}$ = diffuse view factor between element dA_j and circular opening of cavity

H = diffuse irradiation streaming into cavity opening

R = radius of curvature of hemispherical cavity

S_s = specular hemispherical coefficient, given by equation (5)

[1] Mechanical Engineering Department, West Virginia University, Morgantown, W. Va.

Contributed by the Heat Transfer Division of THE AMERICAN SOCIETY OF MECHANICAL ENGINEERS. Manuscript received at ASME Headquarters, March 18, 1969; revised manuscript received, June 23, 1969.

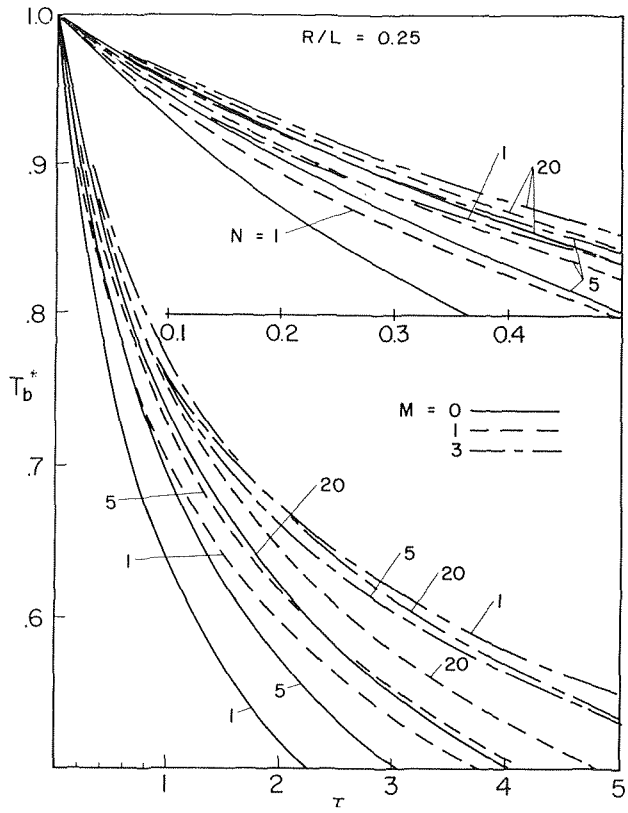

Fig. 4 Base temperature versus time for $r/L = 0.5$

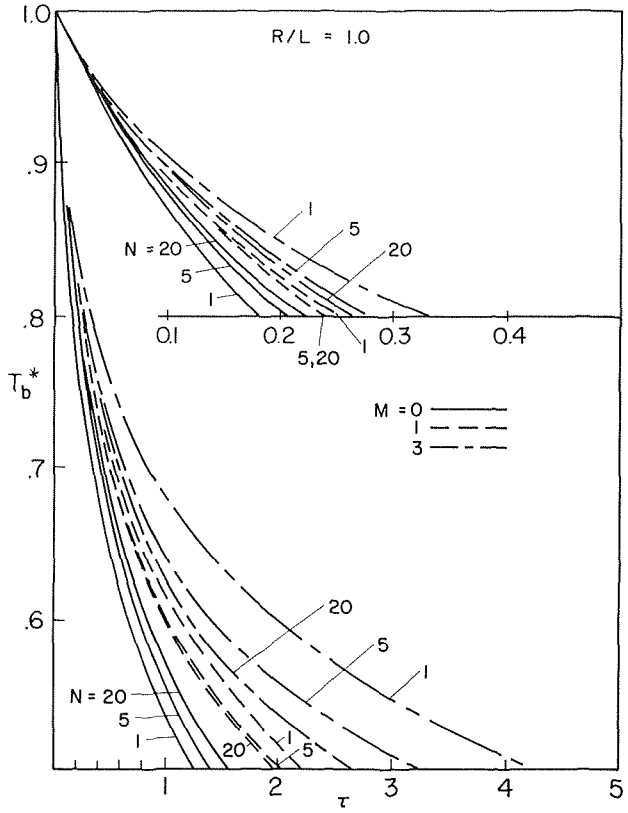

Fig. 5 Base temperature versus time for $r/L = 1.0$

where $N = \sigma L^2 T_{b0}^3 / k\delta$ is the conductance parameter. The initial and boundary conditions are

$$T^*(0, \tau) = T_b^*(\tau), \frac{\partial T^*}{\partial X}(1, \tau) = 0, T^*(X, 0) = T_{ss}^*(X)$$

where the steady-state solution T_{ss}^* is found from equation (8) $\partial T^*/\partial \tau = 0$ and the boundary conditions $T_{ss}^*(0) = 1$ and $\partial T_{ss}^*(1)/\partial X = 0$.

When $N = 0$ the fin is isothermal and transient is given simply by the following equation:

$$T_b = [1 + 3\tau(1 + r/L)/(1 + M)]^{-3} \quad (9)$$

Equations (7) and (8) were solved by finite-difference techniques on a digital computer. The base temperature, as a function of time, is given in Figs. 2–5 for $r/L = 0$, 0.25, 0.5, 1.0; $N = 1$, 5, 20; and $M = 0$, 1, 3. Equation (9) can be used to provide information for $N = 0$.

Since N is inversely proportional to the conductivity, one associates small values of N with efficient fins and hence it is expected that the base would cool more rapidly when N is small. This is always the case for $M = 0$, but not for $M > 0$. In Figs. 4 and 5, the curves for $M = 1$ and $M = 3$ show that the base cools more rapidly as N becomes larger. The reason for such anomalous behavior lies in the fact that the total amount of energy in the system is greater if the fin has a more uniform temperature distribution, as it does when N is small. When a small N is coupled with a large M, the energy stored in the fin is large compared to the energy in the base and the amount of energy conducted into the fin may be small or even negative.

References

1 Sparrow, E. M., and Eckert, E. R. G., "Radiant Interaction Between Fin and Base Surfaces," JOURNAL OF HEAT TRANSFER, TRANS. ASME, Vol. 84, Series C, Feb. 1962, pp. 12–18.

2 Moriarty, L. J., "Transient Analysis of Fin-Tube Space Radiator Systems," Master's thesis, Department of Mechanical Engineering, University of Wisconsin, Madison, Wis., 1966.

Absorption of Thermal Radiation in a Hemispherical Cavity

H. H. SAFWAT[1]

Nomenclature

A, B, c_1, c_2 = assumed constants in equation (12)

$dF_{(dA_j - dA_i)_t}$ = total view factor between area elements dA_j and dA_i

$f_0, f_1, f_2, \ldots$ = factors giving contributions of specular images in total view factor $dF_{(dA_j - dA_i)}$

$F_{dA_j - \text{circular opening}}$ = diffuse view factor between element dA_j and circular opening of cavity

H = diffuse irradiation streaming into cavity opening

R = radius of curvature of hemispherical cavity

S_s = specular hemispherical coefficient, given by equation (5)

[1] Mechanical Engineering Department, West Virginia University, Morgantown, W. Va.

Contributed by the Heat Transfer Division of THE AMERICAN SOCIETY OF MECHANICAL ENGINEERS. Manuscript received at ASME Headquarters, March 18, 1969; revised manuscript received, June 23, 1969.

S = power of incoming beam per unit area normal to it (in case of parallel bundle of rays incident on cavity opening)
W_j = diffuse radiosity of an elemental area dA_j
α = absorptance of surface material of the hemispherical cavity ($\alpha = 1 - \rho$)
α_a = apparent absorptivity of the hemispherical cavity
ρ = directional hemispherical reflectance
ρ_d = diffuse component of mixed reflectance
ρ_s = specular component of mixed reflectance
ϕ_n = angle shown in Fig. 4
ψ and ζ = angles shown in Fig. 3

THIS Note is concerned with the energy absorbed when radiation from an external source enters a hemispherical cavity. The apparent absorptivity of the hemispherical cavity α_a, defined as the ratio of the energy absorbed in the cavity to the energy entering the cavity, is found for two types of irradiation:

1 Diffuse irradiation streaming through the cavity opening.
2 Bundle of parallel beams entering the cavity in a direction normal to its opening plane.

The hemispherical cavity surface has a mixed reflectance ρ such that ($\rho = \rho_d + \rho_s$) [1].[2] ρ_s and ρ_d are the specular and diffuse reflectance components, respectively. ρ_s and ρ_d are assumed to be independent of the directional distribution of the incident radiant flux and the surface temperature.

A Hemispherical Cavity Whose Opening Is Irradiated With Diffuse Irradiation *H*

With reference to Fig. 1, the integral equation describing the radiation exchange in the cavity [2–4] is given by

$$W_j = (\rho_d + \rho_s)HF_{dA_j-\text{circular opening}} + \rho_d \int_{A_i} W_i dF_{(dA_j-dA_i)_t} \quad (1)$$

where

W_j = diffuse radiosity of an elemental dA_j
$F_{dA_j-\text{circular opening}}$ = diffuse view factor between element dA_j and circular opening of cavity
$dF_{(dA_j-dA_i)_t}$ = total view factor between elements dA_j and dA_i (including all specular images effect)

and

$$F_{dA_j-\text{circular opening}} = F_{dA_j-\text{topping hemisphere}} = 1/2, \text{ reference [5]} \quad (2)$$

and

$$dF_{(dA_j-dA_i)_t} = f_0 + \rho_s f_1 + \rho_s^2 f_2 + \rho_s^3 f_3 + \ldots . \quad (3)$$

f_0 coincides with diffuse view factor between dA_j and dA_i; $\rho_s f_1$ corresponds to radiant transport between dA_j and dA_i with one intervening specular reflection; $\rho_s^k f_k$ corresponds to radiant transport between dA_j and dA_i with k intervening specular reflections. With reference to Fig. 2,

$$dF_{(dA_j-dA_i)_t} = \frac{dA_i}{4\pi R^2}\cdot\left[1 + \frac{\rho_s}{2^2} + \frac{\rho_s^2}{3^2} + \frac{\rho_s^3}{4^2} \cdot \ldots .\right] = S_s \cdot \frac{dA_i}{4\pi R^2} \quad (4)$$

where R is the radius of curvature of the hemisphere and

$$S_s = 1 + \sum_{k=1}^{\infty} \frac{\rho_s^k}{(k+1)^2} \quad (5)$$

By substituting equations (2) and (4) into (1), W_j can be expressed as

[2] Numbers in brackets designate References at end of paper.

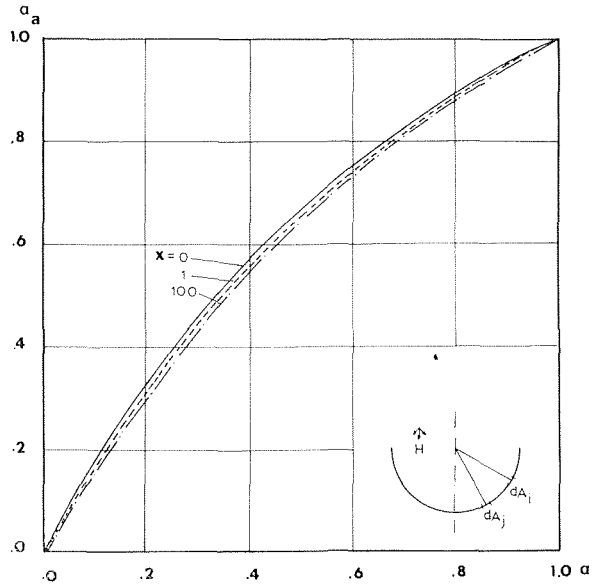

Fig. 1 Apparent absorptivity of a diffusely irradiated hemispherical cavity versus absorptance of cavity surface material ($x = \rho_s/\rho_d$)

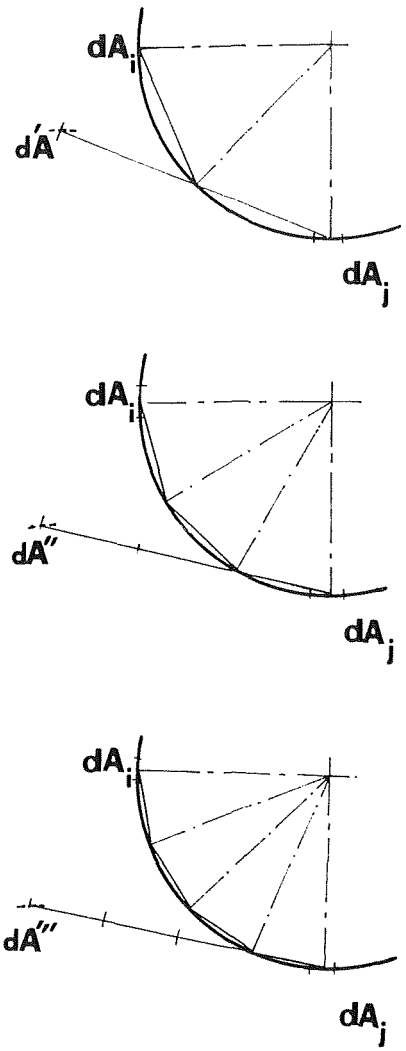

Fig. 2 Specular images of dA_i as seen by dA_j

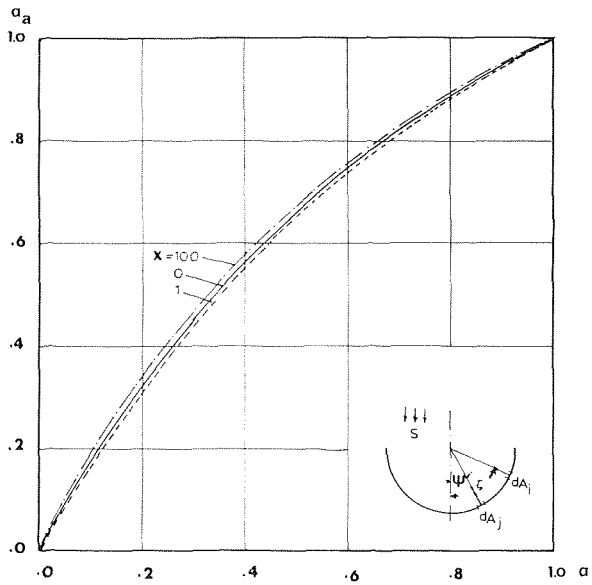

Fig. 3 Apparent absorptivity of a hemispherical cavity as irradiated with a parallel bundle of rays versus absorptance of cavity surface ($x = \rho_s/\rho_d$)

$$W_j = (\rho_s + \rho_d)\cdot\frac{H}{2} + \rho_d\frac{S_s}{4\pi R^2}\int_{A_i} W_i dA_i \tag{6}$$

and the solution of the foregoing equation is given by

$$W_j = \frac{(\rho_d + \rho_s)}{\left(1 - \dfrac{\rho_d S_s}{2}\right)}\cdot\frac{H}{2} \tag{7}$$

Thus, for this case,

$$\alpha_a = \frac{\left(1 + \dfrac{\rho_s S_s}{2}\right)}{\left(1 - \dfrac{\rho_d S_s}{2}\right)}\alpha \tag{8}$$

Fig. 1 shows plots of α_a versus α for different values of ($x = \rho_s/\rho_d$) as calculated from equation (8).

A Hemispherical Cavity Irradiated With a Bundle of Parallel Beams Incident Normal to Cavity's Opening

Let S be the power of the incoming beam per unit area normal to the beam. With reference to Fig. 3, the integral equation [2–4] describing the radiant exchange in the cavity is given by

$$W_j(\psi) = \rho_d\left[S\cos\psi + \int_{A_i} W_i(\zeta)dF_{(dA_j - dA_i)_t} + \sum_{n=1}^{\infty}\rho_s{}^n S\cos\phi_n\cdot\frac{dA_j}{dA_n}\right] \tag{9}$$

where

W_j = diffuse radiosity of an elemental area dA_j, Fig. 3
dA_n = an elemental area of spherical surface which is located at an angle ϕ_n, considering specular reflections only, (a beam incident on dA_n would reach dA_j after n specular reflections, Fig. 4)
$dF_{(dA_j - dA_i)_t}$ = total view factor between elements dA_j and dA_i, given by equation (4)
ψ and ζ = angles shown in Fig. 3
ϕ_n = an angle shown in Fig. 4

The first term in between the square brackets in equation (9) represents the radiation directly arriving at dA_j from outside the cavity through its opening. The second integral term gives the diffuse irradiation received by dA_j from all the surface of the cavity. The last summation term is the energy received

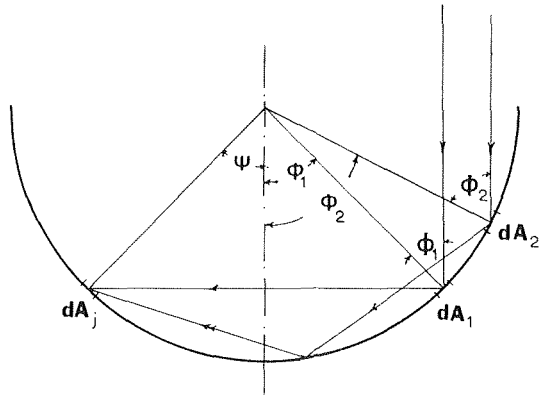

Fig. 4 Energy received by element dA_j which has undergone only specular reflections on hemisphere's wall before reaching dA_j

by the element dA_j which has undergone only specular reflections on the hemisphere's surface before reaching dA_j. With reference to Fig. 4, this energy reaches dA_j after one reflection from dA_1 and after n reflection from dA_n, where

$$\phi_n = \frac{n\pi - \psi}{2n + 1} \tag{10}$$

Using spherical geometry expressions for dA_j and dA_n together with equations (5) and (10), equation (9) can be written as

$$W_j(\psi) = \rho_d\left[S\cos\psi + \frac{S_s}{2}\int_0^{\pi/2} W_i(\zeta)\sin\zeta d\zeta + \sum_{n=1}^{\infty}\frac{\rho_s{}^n S}{(2n+1)}\cos\left(\frac{n\pi - \psi}{2n+1}\right)\cdot\frac{\sin\left(\dfrac{n\pi - \psi}{2n+1}\right)}{\sin\psi}\right] \tag{11}$$

To obtain a solution to equation (11), assume that

$$W_j(\psi) = \rho_d\left[A + B\cos\psi + \sum_{n=1}^{\infty} c_n\cos\left(\frac{n\pi - \psi}{2n+1}\right)\cdot\frac{\sin\left(\dfrac{n\pi - \psi}{2n+1}\right)}{\sin\psi}\right] \tag{12}$$

where $A, B, c_1, c_2, \ldots, c_n, \ldots$ are constants.

Substituting from equation (12) into (11), gives

$$B = S \tag{13}$$

$$c_n = \frac{\rho_s{}^n S}{(2n+1)} \tag{14}$$

$$A = \frac{\dfrac{\rho_s S_s}{2}\cdot\frac{S}{2}\cdot\left\{1 + \sum_{n=1}^{\infty}\rho_s{}^n\left(\cos^2\left(\frac{2n-1}{2n+1}\right)\frac{\pi}{2} - \cos^2\left(\frac{n\pi}{2n+1}\right)\right)\right\}}{\left(1 - \dfrac{\rho_d S_s}{2}\right)} \tag{15}$$

The energy absorbed inside the cavity is given by

$$\alpha\int_0^{\pi/2}\frac{1}{\rho_d}W(\psi)\cdot 2\pi R^2\sin\psi d\psi$$

Thus, for this case,

$$\alpha_a = \alpha\frac{\left\{1 + \sum_{n=1}^{\infty}\rho_s{}^n\left(\cos^2\left(\frac{2n-1}{2n+1}\right)\cdot\frac{\pi}{2} - \cos^2\left(\frac{n\pi}{2n+1}\right)\right)\right\}}{\left(1 - \dfrac{\rho_d S_s}{2}\right)} \tag{16}$$

Fig. 3 shows plots of α_a versus α for different values of ($x = \rho_s/\rho_d$) as calculated from equation (16).

For either the diffuse and parallel irradiation the apparent absorptivity of the hemispherical cavity is virtually insensitive to the relative amount of reflection that is specular, i.e. x from 0 to 100. This can be explained by the minimum surface to volume ratio characterizing spherical configurations.

In case of diffuse irradiation, a purely diffuse reflecting surface exhibits larger apparent absorptivity than a reflecting surface with large x. This is due to the escape of a large portion of the incoming irradiation upon the first specular reflections through the opening of the cavity.

On the other hand, in the case of the parallel bundle of rays the apparent absorptivity of a specular surface cavity is larger than that of a cavity having a diffuse surface but a cavity with a surface whose $x = 1$ still has smaller apparent absorptivity. This can be seen in view of the two counteracting factors of the multiple reflections of rays arriving near the outside edges of the cavity and the escape of specularly reflected rays arriving to the central part of the cavity.

The results show different effects for the value of x of the surface material of the cavity for the diffuse irradiation and the directional irradiation.

References

1 Seban, R. A., "Discussion," JOURNAL OF HEAT TRANSFER, TRANS. ASME, Series C, Vol. 84, No. 3, Nov. 1962, p. 299.

2 Sparrow, E. M., Eckert, E. R. G., and Jonsson, V. K., "An Enclosure Theory for Radiative Exchange Between Specularly and Diffusely Reflecting Surfaces," JOURNAL OF HEAT TRANSFER, TRANS. ASME, Series C, Vol. 84, No. 3, Nov. 1962, p. 294.

3 Lin, S. H., and Sparrow, E. M., "Radiant Interchange Among Curved Specularly Reflecting Surfaces, Application to Cylindrical and Conical Cavities," JOURNAL OF HEAT TRANSFER, TRANS. ASME, Series C, Vol. 87, No. 3, Nov. 1965, p. 299.

4 Sparrow, E. M., and Lin, S. H., "Radiation Heat Transfer at a Surface Having Both Specular and Diffuse Reflectance Components," *International Journal of Heat and Mass Transfer*, 1965, p. 769.

5 Sparrow, E. M., and Jonsson, V. K., "Absorption and Emission Characteristics of Diffuse Spherical Enclosures," JOURNAL OF HEAT TRANSFER, TRANS. ASME, Series C, Vol. 84, No. 2, Aug. 1962, p. 188.

Heat Flux Through a Strip-Heated Flat Plate

R. A. SCHMITZ[1]

Introduction

THIS Note concerns the problem of predicting the rate of heat conduction through a solid slab maintained at a constant temperature on one surface and heated (or cooled) by equally spaced strips which are at a constant temperature on the other. The space between the strips is assumed to be perfectly insulated. The situation is depicted in Fig. 1, which serves to define much of the notation to be used. The problem is closely akin to one recently studied by Van Sant [1].[2] In that study one side of the slab was supposed to be cooled by convection, and the focus was on the extent of the temperature variation on that surface when the other side was strip-heated. The case of a constant strip temperature was solved by a finite-difference scheme. No heat flux results were reported.

The present version of the problem came to my attention when it was required, in a certain application, to determine the conditions in terms of the geometric parameters of slab thickness, strip size, and strip spacing under which one could assume for practical purposes that the heat flux is given by one of the two simple extremes, namely:

1 Treating the strip-heated surface as being uniformly heated so that the heat flux q, termed q_m for this case, based on the total slab surface is given by $q_m = k(T_s - T_0)/\delta$, where k is the thermal conductivity of the slab material.

2 Considering the heat flux to be channeled through that portion of the solid lying above the strips so that $q/q_m = a/(a + b)$, where q again is based on the total slab surface area.

Method of Solution

The solution method employed here would seem to be applicable to a wide variety of heat-conduction problems for which the classical separation of variables approach cannot be used and apparently offers considerable computational advantage over finite-difference approaches. It has been employed previously [2–6] for problems described mathematically by Laplace's equation and applied in one of these cases [7] to a heat-conduction problem. Thus only a brief description is called for here.

The method is based on the observation that in each of regions I and II, shown in the sketch in Fig. 1, the solution for two-dimensional steady heat conduction can be expressed in terms of an infinite series by way of the usual separation of variables approach. Thus

$$t_{\mathrm{I}} = \sum_{n=1}^{\infty} A_n \sin\left(\frac{\pi n y}{\delta}\right) \cosh\left(\frac{\pi n x}{\delta}\right) \tag{1}$$

$$t_{\mathrm{II}} = 1 + \sum_{n=1}^{\infty} B_n \cos\left[\frac{\pi(2n-1)y}{2\delta}\right] \times \cosh\left[\frac{\pi(2n-1)}{4\delta}(a + b - 2x)\right] \tag{2}$$

where $t = (T - T_s)/(T_0 - T_s)$, and subscripts I and II refer to the regions in the slab identified in Fig. 1. A system of linear equations, infinite in number, for the unknown coefficients A_n and B_n results by matching the temperatures and heat fluxes at the boundary at $x = a/2$ and invoking the orthogonality property of the sine and cosine functions in the preceding equations. With

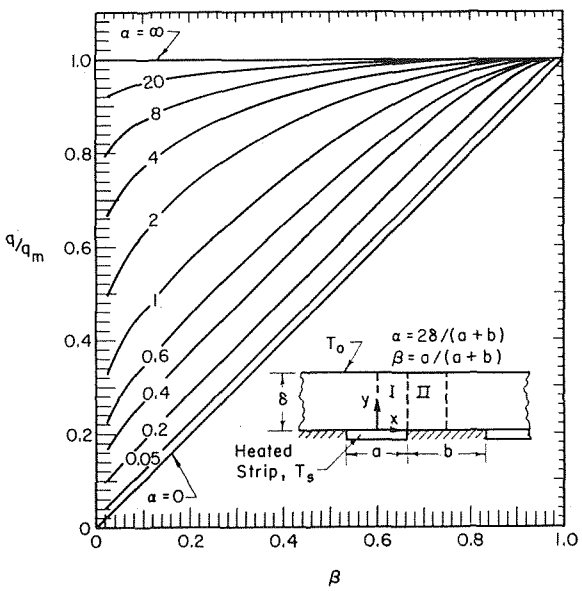

Fig. 1 Heat flux through slabs held at a uniform temperature on one surface and having equally spaced constant temperature strips on the other

[1] Department of Chemistry and Chemical Engineering, University of Illinois, Urbana, Ill.

[2] Numbers in brackets designate References at end of Note.

Contributed by the Heat Transfer Division of THE AMERICAN SOCIETY OF MECHANICAL ENGINEERS. Manuscript received at ASME Headquarters, August 29, 1969.

Fig. 3 shows plots of α_a versus α for different values of ($x = \rho_s/\rho_d$) as calculated from equation (16).

For either the diffuse and parallel irradiation the apparent absorptivity of the hemispherical cavity is virtually insensitive to the relative amount of reflection that is specular, i.e. x from 0 to 100. This can be explained by the minimum surface to volume ratio characterizing spherical configurations.

In case of diffuse irradiation, a purely diffuse reflecting surface exhibits larger apparent absorptivity than a reflecting surface with large x. This is due to the escape of a large portion of the incoming irradiation upon the first specular reflections through the opening of the cavity.

On the other hand, in the case of the parallel bundle of rays the apparent absorptivity of a specular surface cavity is larger than that of a cavity having a diffuse surface but a cavity with a surface whose $x = 1$ still has smaller apparent absorptivity. This can be seen in view of the two counteracting factors of the multiple reflections of rays arriving near the outside edges of the cavity and the escape of specularly reflected rays arriving to the central part of the cavity.

The results show different effects for the value of x of the surface material of the cavity for the diffuse irradiation and the directional irradiation.

References

1 Seban, R. A., "Discussion," JOURNAL OF HEAT TRANSFER, TRANS. ASME, Series C, Vol. 84, No. 3, Nov. 1962, p. 299.

2 Sparrow, E. M., Eckert, E. R. G., and Jonsson, V. K., "An Enclosure Theory for Radiative Exchange Between Specularly and Diffusely Reflecting Surfaces," JOURNAL OF HEAT TRANSFER, TRANS. ASME, Series C, Vol. 84, No. 3, Nov. 1962, p. 294.

3 Lin, S. H., and Sparrow, E. M., "Radiant Interchange Among Curved Specularly Reflecting Surfaces, Application to Cylindrical and Conical Cavities," JOURNAL OF HEAT TRANSFER, TRANS. ASME, Series C, Vol. 87, No. 3, Nov. 1965, p. 299.

4 Sparrow, E. M., and Lin, S. H., "Radiation Heat Transfer at a Surface Having Both Specular and Diffuse Reflectance Components," *International Journal of Heat and Mass Transfer*, 1965, p. 769.

5 Sparrow, E. M., and Jonsson, V. K., "Absorption and Emission Characteristics of Diffuse Spherical Enclosures," JOURNAL OF HEAT TRANSFER, TRANS. ASME, Series C, Vol. 84, No. 2, Aug. 1962, p. 188.

Heat Flux Through a Strip-Heated Flat Plate

R. A. SCHMITZ[1]

Introduction

THIS Note concerns the problem of predicting the rate of heat conduction through a solid slab maintained at a constant temperature on one surface and heated (or cooled) by equally spaced strips which are at a constant temperature on the other. The space between the strips is assumed to be perfectly insulated. The situation is depicted in Fig. 1, which serves to define much of the notation to be used. The problem is closely akin to one recently studied by Van Sant [1].[2] In that study one side of the slab was supposed to be cooled by convection, and the focus was on the extent of the temperature variation on that surface when the other side was strip-heated. The case of a constant strip temperature was solved by a finite-difference scheme. No heat flux results were reported.

The present version of the problem came to my attention when it was required, in a certain application, to determine the conditions in terms of the geometric parameters of slab thickness, strip size, and strip spacing under which one could assume for practical purposes that the heat flux is given by one of the two simple extremes, namely:

1 Treating the strip-heated surface as being uniformly heated so that the heat flux q, termed q_m for this case, based on the total slab surface is given by $q_m = k(T_s - T_0)/\delta$, where k is the thermal conductivity of the slab material.

2 Considering the heat flux to be channeled through that portion of the solid lying above the strips so that $q/q_m = a/(a + b)$, where q again is based on the total slab surface area.

Method of Solution

The solution method employed here would seem to be applicable to a wide variety of heat-conduction problems for which the classical separation of variables approach cannot be used and apparently offers considerable computational advantage over finite-difference approaches. It has been employed previously [2–6] for problems described mathematically by Laplace's equation and applied in one of these cases [7] to a heat-conduction problem. Thus only a brief description is called for here.

The method is based on the observation that in each of regions I and II, shown in the sketch in Fig. 1, the solution for two-dimensional steady heat conduction can be expressed in terms of an infinite series by way of the usual separation of variables approach. Thus

$$t_{\mathrm{I}} = \sum_{n=1}^{\infty} A_n \sin\left(\frac{\pi n y}{\delta}\right) \cosh\left(\frac{\pi n x}{\delta}\right) \tag{1}$$

$$t_{\mathrm{II}} = 1 + \sum_{n=1}^{\infty} B_n \cos\left[\frac{\pi(2n-1)y}{2\delta}\right] \times \cosh\left[\frac{\pi(2n-1)}{4\delta}(a + b - 2x)\right] \tag{2}$$

where $t = (T - T_s)/(T_0 - T_s)$, and subscripts I and II refer to the regions in the slab identified in Fig. 1. A system of linear equations, infinite in number, for the unknown coefficients A_n and B_n results by matching the temperatures and heat fluxes at the boundary at $x = a/2$ and invoking the orthogonality property of the sine and cosine functions in the preceding equations. With

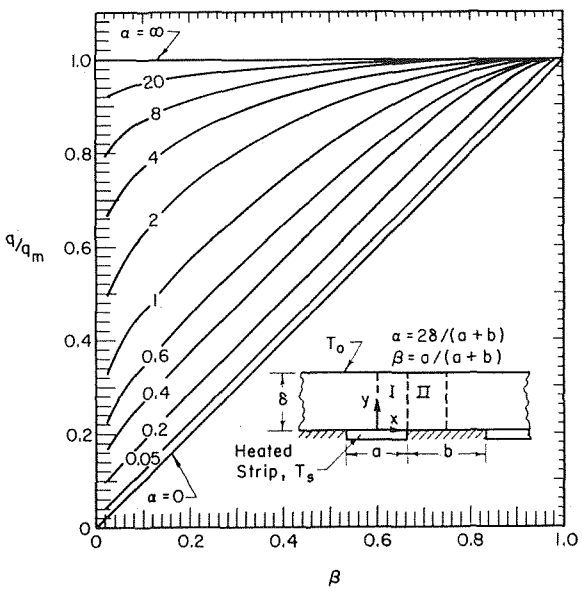

Fig. 1 Heat flux through slabs held at a uniform temperature on one surface and having equally spaced constant temperature strips on the other

[1] Department of Chemistry and Chemical Engineering, University of Illinois, Urbana, Ill.

[2] Numbers in brackets designate References at end of Note.

Contributed by the Heat Transfer Division of THE AMERICAN SOCIETY OF MECHANICAL ENGINEERS. Manuscript received at ASME Headquarters, August 29, 1969.

each of the foregoing series truncated at N terms, this system may be written as follows:

$$\sum_{n=1}^{N} \frac{n}{n^2 - (k - \frac{1}{2})^2} \left[\frac{1}{\tanh\left(\frac{\pi n a}{2\delta}\right)} + \frac{n A_n}{(k - \frac{1}{2}) \tanh\left[\frac{\pi(k - \frac{1}{2})b}{2\delta}\right]} \right] \times \sinh\left(\frac{\pi n a}{2\delta}\right) = \frac{1}{\pi(k - \frac{1}{2})^2} \quad (3)$$

$$B_k = \sum_{n=1}^{N} \frac{4n^2 \sinh A_n \left(\frac{\pi n a}{2\delta}\right)}{\pi(2k - 1)[(k - \frac{1}{2})^2 - n^2] \sinh\left[\frac{\pi b(2k - 1)}{4\delta}\right]} \qquad k = 1, 2, \ldots, N \quad (4)$$

Finally, the heat flux through the slab, expressed as q/q_m, is given by

$$q/q_m = \frac{2\delta}{a + b} \int_0^{a/2} \left(\frac{\partial t_1}{\partial y}\right)_{y=0} dx \quad (5)$$

which by means of equation (1) may be written as follows in terms of two parameter groups α and β:

$$\frac{q(N)}{q_m} = \beta + \alpha \sum_{n=1}^{N} A_n \sinh\left(\frac{\pi n \beta}{\alpha}\right) \quad (6)$$

where $\alpha = 2\delta/(a + b)$, and $\beta = a/(a + b)$. Thus, for given values of α and β, the computation of q/q_m essentially involves the solution of N simultaneous linear equations for N values of A_n from equation (3). Through subsequent solution of equation (4) for N values of B_k, one may compute the entire temperature field from equations (1) and (2). Presumably any desired accuracy can be achieved by taking N appropriately large. For all of the results to be presented here, an extrapolated value $q(\infty)/q_m$ was estimated from

$$\frac{q(N)}{q_m} = \frac{q(\infty)}{q_m} + \frac{a}{N} + \frac{b}{N^2}$$

The estimation required the computation of $q(N)/q_m$ for three values of N. Successively larger values of N were employed until two consecutive extrapolated answers were in agreement through the fourth decimal place. The number of terms in the series required to reach this level of accuracy varied from 4–56, depending on the parameter values.

Results

Results, shown in Fig. 1 illustrate the effect of the geometric parameters α and β. In the figure, q/q_m of course approaches zero as β approaches zero for all values of α. Computations were carried out only for $\beta > 0.025$. The results show that for $\alpha < 0.05$ the heat flow is channeled for the most part through that portion of the slab directly above the heated strips so that q/q_m approaches $a/(a + b)$. On the other hand, for $\alpha > 20$, $q/q_m \simeq 1.0$ for most values of β, so that the heat flux is nearly that for the case of a uniform temperature over the entire slab surface at $y = 0$.

One possible utilization of the results may be conveniently illustrated. Suppose that in a given application the total slab area and strip area are fixed at values such that $\beta = 0.6$. Then, according to Fig. 1, at least 95 percent of the maximum flux q_m may be achieved by sizing and spacing the strips uniformly in such a way that $\alpha \geq 4.0$.

It is worthwhile pointing out that the results also have meaning in certain diffusion problems. In these problems, the slab may represent a stagnant fluid or it may typify the so-called "diffusion layer" in simplified models of boundary-layer problems. If a diffusion-controlled chemical reaction occurs at the surface on $0 \leq x < a/2$ and if the surface is impervious and inactive for $a/2 < x \leq (a + b)/2$, then q/q_m in Fig. 1 gives the ratio of the actual mass flux to that which would be realized if the entire surface at $y = 0$ were active. The diffusion-controlled reaction may be caused either by highly active catalytic sites or by a polarized condition in electrolysis.

References

1 Van Sant, J. H., "Temperature Variations on the Surface of a Strip-Heated Flat Plate," JOURNAL OF HEAT TRANSFER, TRANS. ASME, Series C, Vol. 89, 1967, pp. 372–373.

2 Smythe, W. R., "Flow Over Thick Plate With Circular Hole," *Journal of Applied Physics*, Vol. 23, 1952, pp. 447–452.

3 Kirkham, D., "Potential and Capacity of Concentric Coaxial Capped Cylinders," *Journal of Applied Physics*, Vol. 28, 1957, pp. 724–731.

4 Kirkham, D., "Exact Theory of Flow Into a Partially Penetrating Well," *Journal of Geophysical Research*, Vol. 64, 1959, pp. 1317–1327.

5 Enfros, A. L., "Potential Distribution Near a Cylindrical Probe," *Soviet Physics, Technical Physics*, Vol. 5, 1961, pp. 954–959.

6 Kelman, R. B., "Axisymmetric Potentials in Composite Geometries: Finite Cylinder and Half Space," *Contributions to Differential Equations*, Vol. 2, 1963, pp. 421–440.

7 Kelman, R. B., "The Steady Temperature Interior to a Finite or Semi-Infinite Cylinder With a Discontinuous Radiation Condition," *Journal of Mathematics and Mechanics*, Vol. 14, 1965, pp. 881–902.

A Schlieren Interferometer Method for Heat Transfer Studies[1]

V. SERNAS[2] and L. S. FLETCHER[3]

THE main interferometric tool used in heat transfer studies has been the Mach-Zehnder interferometer, an instrument which produces fringe shifts proportional to the local temperature. The temperature profiles in thermal boundary layers may be obtained easily with this interferometer; however, local heat fluxes may be obtained only from extrapolated temperature profiles at the wall. A schlieren interferometer of the type reported by Merzkirch [1][4] produces fringe shifts proportional to the local temperature gradient. This instrument previously has been used in supersonic flow studies, but it will be shown that it can also be very useful in heat transfer studies. The local heat flux at a heated wall may be obtained with this instrument by a single measurement of a fringe shift at the wall, but the temperature profile need not be determined.

A standard single pass schlieren system can be converted into a schlieren interferometer by replacing the knife edge with a Wollaston prism which has polarizers on each side, as shown in Fig. 1. The polarizers must be oriented at 90 deg to each other and at 45 deg to the apex of the prism wedges. The fringe pat-

[1] Research sponsored in part by AFOSR, Office of Aerospace Research, U.S. Air Force, under Contract F 44620-68-C-0018.

[2] Assist. Prof. of Mechanical Engineering, Rutgers Univ., New Brunswick, N. J. Assoc. Mem. ASME.

[3] Assist. Prof. of Aerospace Engineering, Rutgers Univ., New Brunswick, N. J. Assoc. Mem. ASME.

[4] Numbers in brackets designate References at end of paper.

Contributed by the Heat Transfer Division of THE AMERICAN SOCIETY OF MECHANICAL ENGINEERS. Manuscript received by the Heat Transfer Division, April 15, 1969.

each of the foregoing series truncated at N terms, this system may be written as follows:

$$\sum_{n=1}^{N} \frac{n}{n^2 - (k - \frac{1}{2})^2} \left[\frac{1}{\tanh\left(\frac{\pi n a}{2\delta}\right)} + \frac{n A_n}{(k - \frac{1}{2}) \tanh\left[\frac{\pi(k - \frac{1}{2})b}{2\delta}\right]} \right] \times \sinh\left(\frac{\pi n a}{2\delta}\right) = \frac{1}{\pi(k - \frac{1}{2})^2} \quad (3)$$

$$B_k = \sum_{n=1}^{N} \frac{4n^2 \sinh A_n \left(\frac{\pi n a}{2\delta}\right)}{\pi(2k - 1)[(k - \frac{1}{2})^2 - n^2] \sinh\left[\frac{\pi b(2k - 1)}{4\delta}\right]} \qquad k = 1, 2, \ldots, N \quad (4)$$

Finally, the heat flux through the slab, expressed as q/q_m, is given by

$$q/q_m = \frac{2\delta}{a + b} \int_0^{a/2} \left(\frac{\partial t_1}{\partial y}\right)_{y=0} dx \quad (5)$$

which by means of equation (1) may be written as follows in terms of two parameter groups α and β:

$$\frac{q(N)}{q_m} = \beta + \alpha \sum_{n=1}^{N} A_n \sinh\left(\frac{\pi n \beta}{\alpha}\right) \quad (6)$$

where $\alpha = 2\delta/(a + b)$, and $\beta = a/(a + b)$. Thus, for given values of α and β, the computation of q/q_m essentially involves the solution of N simultaneous linear equations for N values of A_n from equation (3). Through subsequent solution of equation (4) for N values of B_k, one may compute the entire temperature field from equations (1) and (2). Presumably any desired accuracy can be achieved by taking N appropriately large. For all of the results to be presented here, an extrapolated value $q(\infty)/q_m$ was estimated from

$$\frac{q(N)}{q_m} = \frac{q(\infty)}{q_m} + \frac{a}{N} + \frac{b}{N^2}$$

The estimation required the computation of $q(N)/q_m$ for three values of N. Successively larger values of N were employed until two consecutive extrapolated answers were in agreement through the fourth decimal place. The number of terms in the series required to reach this level of accuracy varied from 4–56, depending on the parameter values.

Results

Results, shown in Fig. 1 illustrate the effect of the geometric parameters α and β. In the figure, q/q_m of course approaches zero as β approaches zero for all values of α. Computations were carried out only for $\beta > 0.025$. The results show that for $\alpha < 0.05$ the heat flow is channeled for the most part through that portion of the slab directly above the heated strips so that q/q_m approaches $a/(a + b)$. On the other hand, for $\alpha > 20$, $q/q_m \simeq 1.0$ for most values of β, so that the heat flux is nearly that for the case of a uniform temperature over the entire slab surface at $y = 0$.

One possible utilization of the results may be conveniently illustrated. Suppose that in a given application the total slab area and strip area are fixed at values such that $\beta = 0.6$. Then, according to Fig. 1, at least 95 percent of the maximum flux q_m may be achieved by sizing and spacing the strips uniformly in such a way that $\alpha \geq 4.0$.

It is worthwhile pointing out that the results also have meaning in certain diffusion problems. In these problems, the slab may represent a stagnant fluid or it may typify the so-called "diffusion layer" in simplified models of boundary-layer problems. If a diffusion-controlled chemical reaction occurs at the surface on $0 \leq x < a/2$ and if the surface is impervious and inactive for $a/2 < x \leq (a + b)/2$, then q/q_m in Fig. 1 gives the ratio of the actual mass flux to that which would be realized if the entire surface at $y = 0$ were active. The diffusion-controlled reaction may be caused either by highly active catalytic sites or by a polarized condition in electrolysis.

References

1 Van Sant, J. H., "Temperature Variations on the Surface of a Strip-Heated Flat Plate," JOURNAL OF HEAT TRANSFER, TRANS. ASME, Series C, Vol. 89, 1967, pp. 372–373.

2 Smythe, W. R., "Flow Over Thick Plate With Circular Hole," *Journal of Applied Physics*, Vol. 23, 1952, pp. 447–452.

3 Kirkham, D., "Potential and Capacity of Concentric Coaxial Capped Cylinders," *Journal of Applied Physics*, Vol. 28, 1957, pp. 724–731.

4 Kirkham, D., "Exact Theory of Flow Into a Partially Penetrating Well," *Journal of Geophysical Research*, Vol. 64, 1959, pp. 1317–1327.

5 Enfros, A. L., "Potential Distribution Near a Cylindrical Probe," *Soviet Physics, Technical Physics*, Vol. 5, 1961, pp. 954–959.

6 Kelman, R. B., "Axisymmetric Potentials in Composite Geometries: Finite Cylinder and Half Space," *Contributions to Differential Equations*, Vol. 2, 1963, pp. 421–440.

7 Kelman, R. B., "The Steady Temperature Interior to a Finite or Semi-Infinite Cylinder With a Discontinuous Radiation Condition," *Journal of Mathematics and Mechanics*, Vol. 14, 1965, pp. 881–902.

A Schlieren Interferometer Method for Heat Transfer Studies[1]

V. SERNAS[2] and L. S. FLETCHER[3]

THE main interferometric tool used in heat transfer studies has been the Mach-Zehnder interferometer, an instrument which produces fringe shifts proportional to the local temperature. The temperature profiles in thermal boundary layers may be obtained easily with this interferometer; however, local heat fluxes may be obtained only from extrapolated temperature profiles at the wall. A schlieren interferometer of the type reported by Merzkirch [1][4] produces fringe shifts proportional to the local temperature gradient. This instrument previously has been used in supersonic flow studies, but it will be shown that it can also be very useful in heat transfer studies. The local heat flux at a heated wall may be obtained with this instrument by a single measurement of a fringe shift at the wall, but the temperature profile need not be determined.

A standard single pass schlieren system can be converted into a schlieren interferometer by replacing the knife edge with a Wollaston prism which has polarizers on each side, as shown in Fig. 1. The polarizers must be oriented at 90 deg to each other and at 45 deg to the apex of the prism wedges. The fringe pat-

[1] Research sponsored in part by AFOSR, Office of Aerospace Research, U.S. Air Force, under Contract F 44620-68-C-0018.

[2] Assist. Prof. of Mechanical Engineering, Rutgers Univ., New Brunswick, N. J. Assoc. Mem. ASME.

[3] Assist. Prof. of Aerospace Engineering, Rutgers Univ., New Brunswick, N. J. Assoc. Mem. ASME.

[4] Numbers in brackets designate References at end of paper.

Contributed by the Heat Transfer Division of THE AMERICAN SOCIETY OF MECHANICAL ENGINEERS. Manuscript received by the Heat Transfer Division, April 15, 1969.

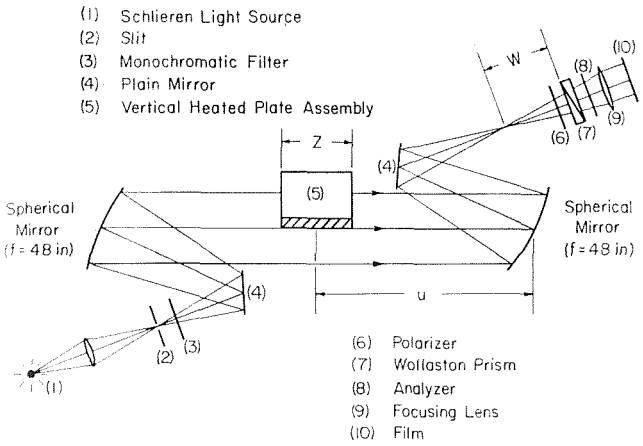

Fig. 1 Schlieren interferometer optical arrangement

terms obtained may be interpreted with the relationship presented by Sernas and Carlson [2], which is:

$$\frac{\partial T}{\partial \xi} = -\left(\frac{RT^2}{p}\right)\left[\frac{\lambda}{2KZ(n_0 - n_e)\tan\alpha\left(f + W - \frac{uW}{f}\right)}\right]\left(\frac{\Delta S}{S}\right) \tag{1}$$

where

$\frac{\partial T}{\partial \xi}$ = the local temperature gradient in the ξ direction (the direction normal to the fringes in any region in the test section where no density gradients exist)

$\frac{\Delta S}{S}$ = the fringe shift as defined in Fig. 2

R = the gas constant

T = the absolute temperature

p = the absolute pressure

λ = the wavelength of the monochromatic light used

K = the Gladstone-Dale constant

$(n_0 - n_e)$ = the difference in refractive index of an ordinary and extraordinary ray within the Wollaston prism

α = the wedge angle of the Wollaston prism

f = the focal length of the parabolic mirror on the Wollaston prism side of the test section

W = the distance between the centerline of the Wollaston prism and the focal point of the parabolic mirror closest to the prism, and

u = the distance between the center of the test section and the parabolic mirror closest to the Wollaston prism.

This expression differs from the one reported by Merzkirch (if his expression were written in terms of temperature instead of density) in that the temperature gradient is used instead of a temperature difference, and the proportionality constant appearing in the square brackets is slightly different.

An application for which the Wollaston prism schlieren interferometer is particularly suited is that of determining the local heat flux and the local heat transfer coefficient in two-dimensional thermal boundary layers. Experiments were conducted using a heated, constant temperature, vertical plate under atmospheric conditions to illustrate the use of the schlieren interferometer system in heat transfer studies.

A 7 in. by 7 in. vertical plate was constructed of 1/2 in. thick aluminum and instrumented with twelve 30 AWG copper constantan thermocouples imbedded from the back side. The plate was heated by a hot water pool in direct contact with the back side (Fig. 2). Measurements of the plate temperature on the free

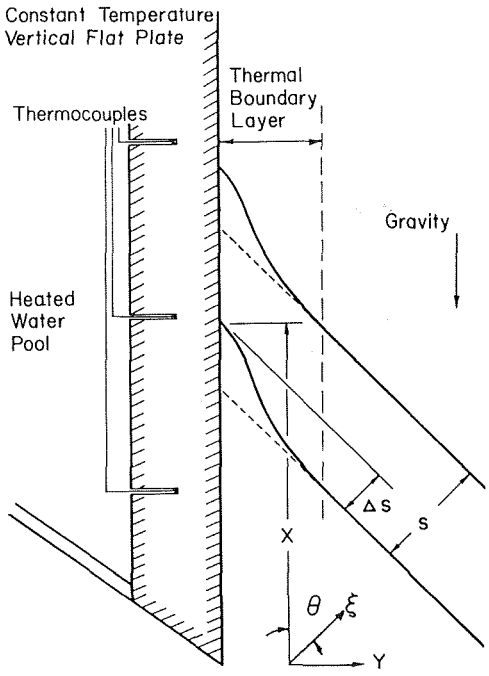

Fig. 2 Cross section of constant temperature plate and fringe shift interpretation

convection side could be made to within ±0.2 deg F, and it was found that the entire plate could easily be kept at a constant temperature within ±0.5 deg F. The major variation of temperature was observed in the vertical direction, while the temperature in the transverse direction was constant to within the temperature-measuring accuracy.

The heated plate was placed in the parallel beam of the schlieren system and aligned such that the plate surface was parallel to the light rays. A large cardboard shield was placed around four sides of the plate to reduce room air currents at the plate. A monochromatic filter of 5461Å with a band width of 70Å was placed in front of a mercury light source to produce monochromatic light, and a pair of calipers was suspended in front of the plate and in view of the camera to facilitate distance measuring on a photograph. The Wollaston prism was rotated to produce fringes in still air at about 45 deg to the plate surface normal, and photographs of the interference pattern were taken. Fig. 3 is a typical fringe pattern obtained when the fringes are oriented at about 70 deg to the surface normal.

When the prism is rotated to produce still air fringes normal to the plate, the fringe shifts in the thermal boundary layer are almost nonexistent because very little temperature gradient exists in a direction parallel to the wall. Interferograms taken with the still air fringes parallel to the plate generally do not show any fringes hitting the wall. As a consequence, it is difficult to measure the temperature gradient very close to the wall, but a temperature gradient profile in the thermal boundary layer away from the wall can be made readily with this orientation of the fringes. A 45 to 70 deg orientation of the fringes was found to be satisfactory for this study in that substantial fringe shifts could be observed, and the fringes terminated at the wall.

The heat dissipated by the heated plate in natural convection must first be transmitted to the air by conduction at the wall. The heat flux at the wall is thus a vector whose component in the ξ-direction is:

$$q'' \sin\theta = k_{\text{air}}\left(\frac{\partial T}{\partial \xi}\right)_{\text{wall}}. \tag{2}$$

The local heat transfer coefficient is then:

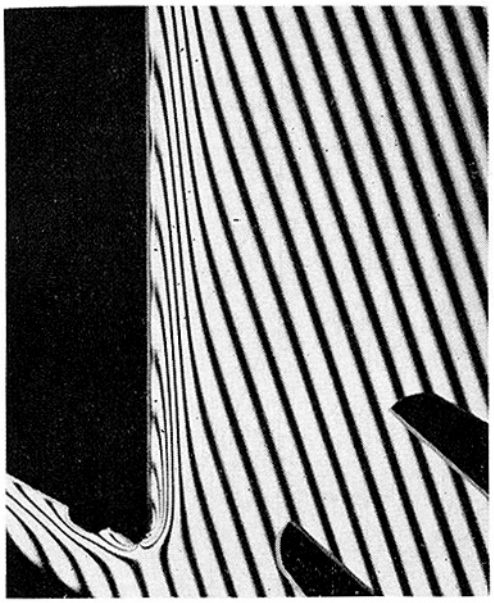

Fig. 3 Representative interferogram of heated vertical plate. Calipers are set at 1.0 in.

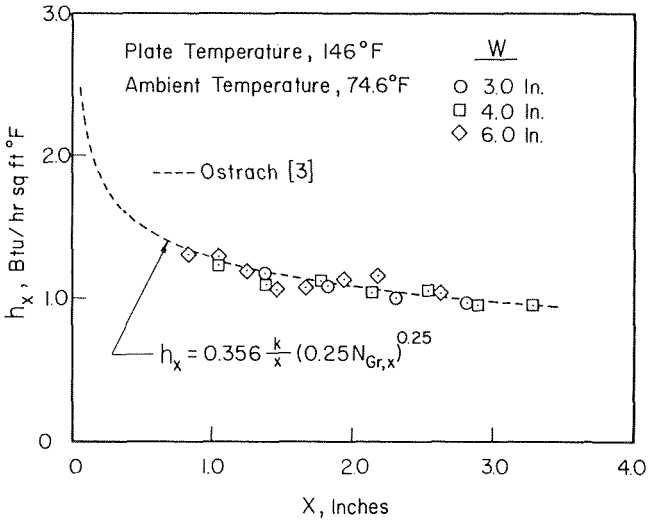

Fig. 4 Comparison of experimental heat transfer coefficients with those predicted by Ostrach [3]

$$h_x = \frac{k_{\text{air}}}{(T_w - T_\infty)\sin\theta} \left(\frac{\partial T}{\partial \xi}\right)_{\text{wall}} \tag{3}$$

where $\left(\frac{\partial T}{\partial \xi}\right)_{\text{wall}}$ is obtained from equation (1) with all variables evaluated at the wall. Only one fringe shift reading at the wall is required to obtain the local heat transfer coefficient. Fig. 4 shows a comparison between the heat transfer coefficients obtained from three different interferograms and the widely accepted correlation for h_x due to Ostrach [3]. The agreement is quite good even though the fringe deflections and fringe spacings were read by eye on an optical comparitor. Greater accuracy can be obtained by more sophisticated film reading devices and methods.

This method of measuring h_x can also be applied to heated walls whose temperature is unknown. The density of the air at the wall can be obtained from interferograms by numerical integration of the fringe shifts along ξ between the wall and a reference location where the density is known. The integration is best performed in terms of the density because when equation (1) is rewritten in terms of the density gradient, the right hand side is independent of the local temperature within the thermal boundary layer. By means of the perfect gas law, the density at the wall can be converted to the wall temperature which in turn can be used with equations (1) and (3) to find the local heat transfer coefficient at the wall.

Acknowledgments

The authors are grateful to Jack A. Jones for his assistance in developing the schlieren interferometer and to R. R. Perez and D. Dello-Stritto for their design and construction of the heated plate facility.

References

1 Merzkirch, W. F., "A Simple Schlieren Interferometer System," *AIAA Journal*, Vol. 3, Oct. 1965, pp. 1974–1976.

2 Sernas, V., and Carlson, C. R., "Density Gradient Measurements With a Wollaston Prism Schlieren Interferometer," Rutgers University, RU-TR 129-MAE-F, 1969.

3 Ostrach, S., "An Analysis of Laminar Free-Convection Flow and Heat Transfer About a Flat Plate Parallel to the Direction of the Generating Body Force," NACA Report 1111, 1953.

Temperature Depression at the Base of a Fin

E. M. SPARROW[1] and D. K. HENNECKE[1]

Introduction

In journal and textbook articles dealing with fins, the temperature at the fin base is generally treated as a known, spatially uniform quantity. This point of view is common to both one-dimensional and multidimensional analyses [1, 2].[2] Furthermore, the conventional definitions of effectiveness and efficiency imply that the base temperature is not affected by the presence of the fin, with the added inference that the temperature is the same as that which the base surface would have if it were without fins. On the other hand, physical reasoning suggests that the presence of the fin will act both to depress the level of the base temperature and to create spatial nonuniformities. This paper is concerned with a quantitative exploration of these effects which, to the best knowledge of the authors, have not been previously analyzed in the published literature.

Analysis, Solutions, and Results

The physical situation analyzed here is pictured schematically in Fig. 1, which shows an isolated fin of rectangular profile affixed to a thick wall. The exposed surfaces of the fin and of the wall lose heat by convection to the fluid environment. Specific consideration is given to the case in which the fin and the wall have the same thermal conductivity. Furthermore, it is assumed that the surface heat transfer coefficient is uniform and equal on all surfaces, and that $T = T(x, y)$. These conditions, as well as the geometry itself, were chosen with a view to minimizing the number of parameters while maintaining the essential features of the problem.

The temperature distribution along the fin base ($x = 0$, $-1/2 \leq y/t \leq 1/2$) remains unspecified, its determination awaiting the

[1] Department of Mechanical Engineering, University of Minnesota, Minneapolis, Minn.

[2] Numbers in brackets designate References at end of Note.

Contributed by the Heat Transfer Division of The American Society of Mechanical Engineers. Manuscript received at ASME Headquarters, July 24, 1969; revised manuscript received, September 12, 1969.

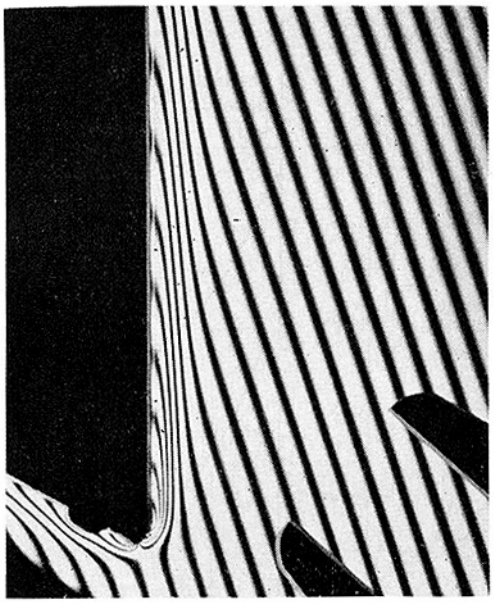

Fig. 3 Representative interferogram of heated vertical plate. Calipers are set at 1.0 in.

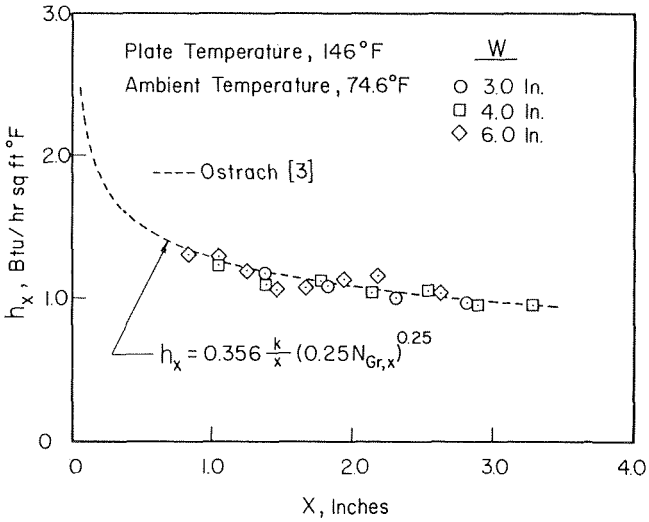

Fig. 4 Comparison of experimental heat transfer coefficients with those predicted by Ostrach [3]

$$h_x = \frac{k_{\text{air}}}{(T_w - T_\infty)\sin\theta}\left(\frac{\partial T}{\partial \xi}\right)_{\text{wall}} \tag{3}$$

where $\left(\frac{\partial T}{\partial \xi}\right)_{\text{wall}}$ is obtained from equation (1) with all variables evaluated at the wall. Only one fringe shift reading at the wall is required to obtain the local heat transfer coefficient. Fig. 4 shows a comparison between the heat transfer coefficients obtained from three different interferograms and the widely accepted correlation for h_x due to Ostrach [3]. The agreement is quite good even though the fringe deflections and fringe spacings were read by eye on an optical comparitor. Greater accuracy can be obtained by more sophisticated film reading devices and methods.

This method of measuring h_x can also be applied to heated walls whose temperature is unknown. The density of the air at the wall can be obtained from interferograms by numerical integration of the fringe shifts along ξ between the wall and a reference location where the density is known. The integration is best performed in terms of the density because when equation (1) is rewritten in terms of the density gradient, the right hand side is independent of the local temperature within the thermal boundary layer. By means of the perfect gas law, the density at the wall can be converted to the wall temperature which in turn can be used with equations (1) and (3) to find the local heat transfer coefficient at the wall.

Acknowledgments

The authors are grateful to Jack A. Jones for his assistance in developing the schlieren interferometer and to R. R. Perez and D. Dello-Stritto for their design and construction of the heated plate facility.

References

1 Merzkirch, W. F., "A Simple Schlieren Interferometer System," *AIAA Journal*, Vol. 3, Oct. 1965, pp. 1974–1976.

2 Sernas, V., and Carlson, C. R., "Density Gradient Measurements With a Wollaston Prism Schlieren Interferometer," Rutgers University, RU-TR 129-MAE-F, 1969.

3 Ostrach, S., "An Analysis of Laminar Free-Convection Flow and Heat Transfer About a Flat Plate Parallel to the Direction of the Generating Body Force," NACA Report 1111, 1953.

Temperature Depression at the Base of a Fin

E. M. SPARROW[1] and D. K. HENNECKE[1]

Introduction

In journal and textbook articles dealing with fins, the temperature at the fin base is generally treated as a known, spatially uniform quantity. This point of view is common to both one-dimensional and multidimensional analyses [1, 2].[2] Furthermore, the conventional definitions of effectiveness and efficiency imply that the base temperature is not affected by the presence of the fin, with the added inference that the temperature is the same as that which the base surface would have if it were without fins. On the other hand, physical reasoning suggests that the presence of the fin will act both to depress the level of the base temperature and to create spatial nonuniformities. This paper is concerned with a quantitative exploration of these effects which, to the best knowledge of the authors, have not been previously analyzed in the published literature.

Analysis, Solutions, and Results

The physical situation analyzed here is pictured schematically in Fig. 1, which shows an isolated fin of rectangular profile affixed to a thick wall. The exposed surfaces of the fin and of the wall lose heat by convection to the fluid environment. Specific consideration is given to the case in which the fin and the wall have the same thermal conductivity. Furthermore, it is assumed that the surface heat transfer coefficient is uniform and equal on all surfaces, and that $T = T(x, y)$. These conditions, as well as the geometry itself, were chosen with a view to minimizing the number of parameters while maintaining the essential features of the problem.

The temperature distribution along the fin base ($x = 0$, $-1/2 \leq y/t \leq 1/2$) remains unspecified, its determination awaiting the

[1] Department of Mechanical Engineering, University of Minnesota, Minneapolis, Minn.

[2] Numbers in brackets designate References at end of Note.

Contributed by the Heat Transfer Division of The American Society of Mechanical Engineers. Manuscript received at ASME Headquarters, July 24, 1969; revised manuscript received, September 12, 1969.

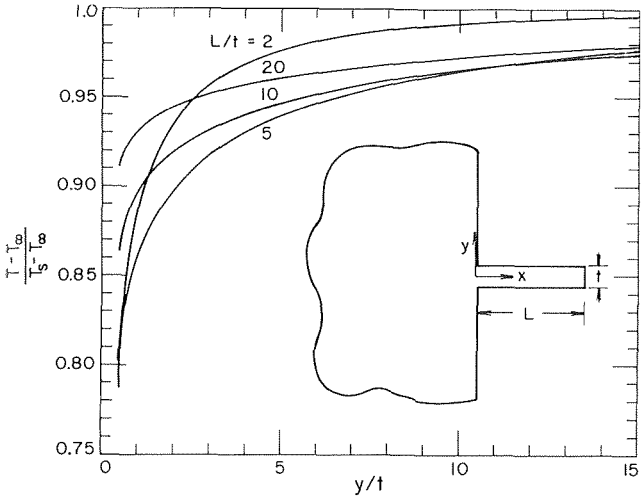

Fig. 1 Schematic of problem and distributions of wall surface temperature

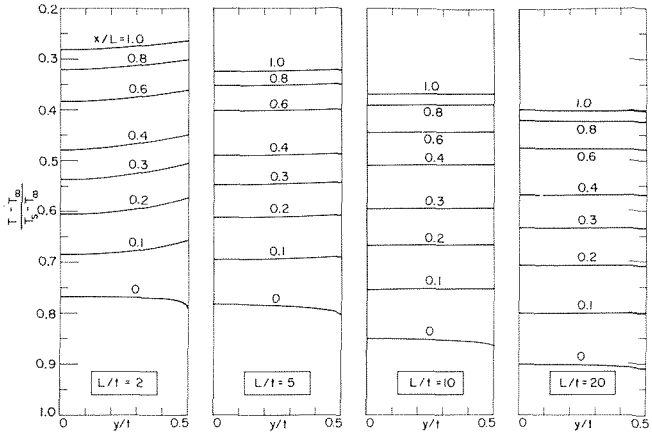

Fig. 2 Fin-temperature profiles

simultaneous solution of the temperature fields in the fin and in the wall.

Turning now to the analysis, it is convenient to introduce dimensionless variables in accordance with the definitions

$$\theta = \frac{T - T_\infty}{T_s - T_\infty}, \qquad X = \frac{x}{t}, \qquad Y = \frac{y}{t}, \quad \mathrm{Bi} = \frac{ht}{k} \tag{1}$$

in which T_s is the temperature of the exposed surface of the wall in the *absence* of the fin[3] and T_∞ is the fluid temperature. The temperature field in the fin and in the wall is governed by Laplace's equation $\partial^2\theta/\partial X^2 + \partial^2\theta/\partial Y^2 = 0$ subject to convective boundary conditions $\partial\theta/\partial n + \mathrm{Bi}\,\theta = 0$ on all exposed surfaces. Additionally, in the wall, at sufficiently large distances from the fin, the disturbance of the temperature field due to the fin must die away, so that $\theta = 1 - \mathrm{Bi}\,X$.

Solutions of the just-outlined problem depend on the values of two parameters, the fin aspect ratio L/t and the Biot number Bi. In fin design, it is customary to employ as a guideline the optimizing condition [1]

$$\mathrm{Bi}\,(L/t)^2 = 1 \tag{2}$$

Correspondingly, for the present solutions, the Biot numbers for preassigned values of L/t were evaluated from equation (2).

Solutions of the coupled two-dimensional heat-conduction problem encompassing the fin and the wall were carried out by finite differences, with due account taken of thermal symmetry about the line $y = 0$. A total of 777 nodal points were dispersed throughout the solid in the region $y \geq 0$, the distribution of the points being made to accommodate the rapidity of the temperature variations. The closure condition $\theta = 1 - \mathrm{Bi}\,X$ was imposed along the lines $y/t = 64$ and $x/t = -64$. Solutions were obtained with the aid of a CDC 6600 computer. The parameter L/t was assigned values of 2, 5, 10, and 20, with the corresponding Bi values from equation (2).

Fin temperature profiles taken from the numerical solutions are presented in Fig. 2. The figure contains four graphs corresponding, respectively, to the four values of the aspect ratio L/t. In each graph, the dimensionless temperature $(T - T_\infty)/(T_s - T_\infty)$ is plotted as a function of the dimensionless transverse coordinate y/t for parametric values of the axial position variable x/L.

Attention will first be focused on the temperature at the fin base; i.e., at $x/L = 0$. In the absence of the fin, the base temperature would be T_s, so that $(T - T_\infty)/(T_s - T_\infty) = 1$. Fig. 2 shows that the presence of the fin significantly reduces the base temperature. For instance, for $L/t = 2$, $(T - T_\infty)/(T_s - T_\infty) \cong 0.77$. Since the fin heat transfer is proportional to the base-to-fluid temperature difference, the base temperature depression for this case results in a heat transfer rate that is about 23 percent less than that reckoned using $T_s - T_\infty$ as the thermal driving force. Lesser base temperature depressions are in evidence as L/t increases.

The existence of the base temperature depression is physically plausible. That is, if the presence of the fin augments the heat transfer, then heat must be brought by conduction to the base from more remote regions of the wall, and this conductive transport necessitates a temperature drop.

Further inspection of Fig. 2 indicates that the base temperature varies somewhat with transverse position, being lowest at the center and highest at the edges. This implies that the lines of heat flow (normal to the isotherms) tend to converge as they enter the fin. On the other hand, at cross sections characterized by larger values of x/L, the transverse temperature variation is opposite to that at the base, implying a divergence of the heat flow lines. Thus, as in the analogous fluid flow case, there is a vena contracta effect with respect to heat flow lines entering a fin.

Fig. 2 shows that the transverse temperature variations are not very large and become almost nonexistent at large values of L/t. This suggests that if the base temperature were known, then the fin heat transfer could be calculated by applying the one-dimensional theory, for instance, equation (3–26) of [1]. To examine this matter, heat transfer rates were evaluated from the just-mentioned equation using the base-to-fluid temperature differences of Fig. 2. In all cases, these heat transfer rates were within a few percent of those given by the finite-difference solution.

The presence of the fin, in addition to depressing its own base temperature, also depresses the temperature of the adjacent wall surface, thereby reducing the heat transfer from the wall. Distributions of wall surface temperature are shown in Fig. 1 for parametric values of L/t. In the immediate neighborhood of the fin, the greatest depression of the wall surface temperature occurs at smaller values of L/t, which, in accordance with equation (2), correspond to larger values of the Biot number and, therefore, to high rates of heat transfer through the fin. On the other hand, at wall surface locations relatively remote from the fin, the temperature depression is least at the smaller L/t values, as is reasonable inasmuch as the surface Biot number is higher for these cases.

The results of this investigation demonstrate that fins cannot be properly designed without due consideration of the thermal interaction between the fin and the wall to which it is affixed. That is, consideration must be given to the depression of the temperature of the fin base and of the adjacent wall surface.

[3] With the fin in place, the wall surface temperature approaches T_s at large distances from the fin.

Furthermore, it is expected that the base temperature depression associated with an ensemble of fins would be greater than that calculated herein for the case of an isolated fin.

References

1 Eckert, E. R. G., and Drake, R. M., *Heat and Mass Transfer*, McGraw-Hill, New York, 1959.

2 Avrami, M., and Little, J. B., "Diffusion of Heat Through a Rectangular Bar and the Cooling and Insulating Effect of Fins," *Journal of Applied Physics*, Vol. 13, 1942, pp. 255–264.

Heat Transfer From the Rear of a Cylinder in Transverse Flow

P. S. VIRK[1]

Nomenclature

d = cylinder outside diameter, cm
D = diffusivity, cm²/sec
f = shedding frequency, hertz
h = heat transfer coefficient, watts/cm² C
k = thermal conductivity, watts/cm C
m = mass transfer coefficient, cm/sec
N_{Nu} = Nusselt number: (hd/k) for heat, (md/D) for mass
N_{Pe} = Peclet number: (Ud/α) for heat, (Ud/D) for mass
N_{Pr} = Prandtl number, (ν/α)
N_{Re} = Reynolds number, (Ud/ν)
N_{Sc} = Schmidt number, (ν/D)
N_{Sr} = Strouhal number, (fd/U)
q = heat flux, watts/cm²
T = shedding time period, $(= 1/f)$ sec
U = free stream velocity, cm/sec
ν = kinematic viscosity, cm²/sec
α = thermal diffusivity, cm²/sec
θ = temperature excess, C
ϕ = azimuthal angle from forward stagnation point
π = 3.14159 . . .

Subscript

$,R$ = indicates average over rear face of cylinder 90 deg $< \phi <$ 180 deg

THE object of this note is to present a model, hitherto unavailable, for the heat transfer from the trailing face of a cylinder. It has, of course, long been recognized [1][2] that this transfer depends upon the eddying flow that prevails aft of the separation point. A more direct connection between shedding and rear face heat transfer can be inferred from a problem encountered in hot wire anemometry when a hot wire is operated at $N_{Re} > 40$. In this case spectral analysis of the wire (electrical) signal shows a distinct "spike," unrelated to the free stream turbulence, at precisely the shedding frequency. Since the local heat transfer from the leading face of a cylinder is unlikely to be periodic, the spike most probably stems from the transfer in the rear.

The nature of eddy shedding, whereby discrete amounts of fluid break away periodically from the cylinder, and the indication that the heat transfer from the rear has the periodicity of the shedding suggest the "eddy penetration" model outlined next.

Consider a long cylinder maintained at a uniform temperature excess, θ, above a laminar, isothermal stream flowing transverse to it. Attention is limited to the subcritical, eddy shedding regime, $40 < N_{Re} < 2 \times 10^5$, in which the shedding behavior is well documented [2, 3] and separation occurs at $\phi \cong 90$ deg so that the shedding can be associated with the entire rear face, 90 deg $< \phi <$ 180 deg. It is now assumed that an eddy remains "attached" to the rear of a cylinder for a period of time equal to the reciprocal of the shedding frequency. During this period the eddy grows by the entrainment of fluid from the free stream while heat transfer from the cylinder occurs by the penetration of heat into the eddy. Thereafter the eddy sheds and moves downstream while the cycle is repeated with succeeding eddies. The time average heat flux from the rear face is, therefore, the average value obtained during a single shedding time period. Further, if this period is short enough for the penetration of heat into an eddy to be limited to distances small relative to eddy size, then the temperature of the eddy will remain essentially at the free stream value and the heat flux during a cycle might be calculated assuming conduction from the cylinder surface into an effectively infinite eddy.

From penetration theory, the time average heat flux per unit area in the time period from 0 to T is

$$q = 2k\theta/(\pi\alpha T)^{1/2} \tag{1}$$

which is twice the instantaneous value at T. Using the usual definition of a heat transfer coefficient, $h = (q/\theta)$, the time average Nusselt number for the rear face becomes

$$N_{Nu,R} = 2d/(\pi\alpha T)^{1/2} \tag{2}$$

where the time period, T, is the reciprocal of the shedding frequency f. The latter is available from a nondimensional Strouhal-Reynolds number relation (e.g. [2]); for our range, N_{Sr} is about 0.11 at $N_{Re} \simeq 40$, increases to 0.20 by $N_{Re} \simeq 200$ and remains constant at higher N_{Re}. Thus, while the complete N_{Re}-N_{Sr} relation is known, little error is incurred by using

$$N_{Sr} = (fd/U) = (d/TU) = 0.20 \tag{3}$$

Substitution for T in (2) then yields the final nondimensional Nusselt-Peclet relation for the time average heat transfer from the rear face:

$$N_{Nu,R} = 0.50 N_{Pe}^{1/2} \tag{4}$$

It is evident that the arguments presented for heat transfer would apply equally to mass transfer.

The major assumptions involved in the foregoing are considered briefly.

First, the use of penetration theory implies purely molecular transport. This assumption is, clearly, somewhat in error since the eddies shed possess an internal circulation and, for $N_{Re} > 500$, also contain portions of turbulent fluid. Thus some convective transport undoubtedly occurs and this would tend to make the transfer higher than that predicted by (4). By conventional reasoning, the actual ratio of convection to conduction from the rear face should be of order $[\delta u/\alpha]$, where u is a velocity characteristic of the region, thickness δ, penetrated in one shedding time period. Though one cannot be quantitative about this ratio (primarily for lack of information about the relevant velocity field), it should be noted that the velocity, u, in this recirculating "deadwater" region is much lower than free stream, U. Also, as shown below, the penetration distance, δ, is small compared to cylinder diameter, d. Therefore conduction is likely to dominate the transfer from the rear face upto values of the usual Peclet number, (dU/α), much greater than unity.

Second, penetration theory will apply when the ratio of eddy diameter, say $(d/2)$, to penetration distance, say $(4\sqrt{\alpha T})$ is large. Elimination of T via (3) shows that this will be so if

---

[1] Assistant Professor of Chemical Engineering, Massachusetts Institute of Technology, Cambridge, Mass.

[2] Numbers in brackets designate References at end of paper.

Contributed by the Heat Transfer Division of THE AMERICAN SOCIETY OF MECHANICAL ENGINEERS. Manuscript received by the Heat Transfer Division, August 8, 1967; revised manuscript received September 9, 1968.

Furthermore, it is expected that the base temperature depression associated with an ensemble of fins would be greater than that calculated herein for the case of an isolated fin.

References

1 Eckert, E. R. G., and Drake, R. M., *Heat and Mass Transfer*, McGraw-Hill, New York, 1959.

2 Avrami, M., and Little, J. B., "Diffusion of Heat Through a Rectangular Bar and the Cooling and Insulating Effect of Fins," *Journal of Applied Physics*, Vol. 13, 1942, pp. 255–264.

Heat Transfer From the Rear of a Cylinder in Transverse Flow

P. S. VIRK[1]

Nomenclature

d = cylinder outside diameter, cm
D = diffusivity, cm²/sec
f = shedding frequency, hertz
h = heat transfer coefficient, watts/cm² C
k = thermal conductivity, watts/cm C
m = mass transfer coefficient, cm/sec
N_{Nu} = Nusselt number: (hd/k) for heat, (md/D) for mass
N_{Pe} = Peclet number: (Ud/α) for heat, (Ud/D) for mass
N_{Pr} = Prandtl number, (ν/α)
N_{Re} = Reynolds number, (Ud/ν)
N_{Sc} = Schmidt number, (ν/D)
N_{Sr} = Strouhal number, (fd/U)
q = heat flux, watts/cm²
T = shedding time period, $(= 1/f)$ sec
U = free stream velocity, cm/sec
ν = kinematic viscosity, cm²/sec
α = thermal diffusivity, cm²/sec
θ = temperature excess, C
ϕ = azimuthal angle from forward stagnation point
π = 3.14159 . . .

Subscript

$,R$ = indicates average over rear face of cylinder 90 deg $< \phi <$ 180 deg

THE object of this note is to present a model, hitherto unavailable, for the heat transfer from the trailing face of a cylinder. It has, of course, long been recognized [1][2] that this transfer depends upon the eddying flow that prevails aft of the separation point. A more direct connection between shedding and rear face heat transfer can be inferred from a problem encountered in hot wire anemometry when a hot wire is operated at $N_{Re} > 40$. In this case spectral analysis of the wire (electrical) signal shows a distinct "spike," unrelated to the free stream turbulence, at precisely the shedding frequency. Since the local heat transfer from the leading face of a cylinder is unlikely to be periodic, the spike most probably stems from the transfer in the rear.

The nature of eddy shedding, whereby discrete amounts of fluid break away periodically from the cylinder, and the indication that the heat transfer from the rear has the periodicity of the shedding suggest the "eddy penetration" model outlined next.

Consider a long cylinder maintained at a uniform temperature excess, θ, above a laminar, isothermal stream flowing transverse to it. Attention is limited to the subcritical, eddy shedding regime, $40 < N_{Re} < 2 \times 10^5$, in which the shedding behavior is well documented [2, 3] and separation occurs at $\phi \cong 90$ deg so that the shedding can be associated with the entire rear face, 90 deg $< \phi <$ 180 deg. It is now assumed that an eddy remains "attached" to the rear of a cylinder for a period of time equal to the reciprocal of the shedding frequency. During this period the eddy grows by the entrainment of fluid from the free stream while heat transfer from the cylinder occurs by the penetration of heat into the eddy. Thereafter the eddy sheds and moves downstream while the cycle is repeated with succeeding eddies. The time average heat flux from the rear face is, therefore, the average value obtained during a single shedding time period. Further, if this period is short enough for the penetration of heat into an eddy to be limited to distances small relative to eddy size, then the temperature of the eddy will remain essentially at the free stream value and the heat flux during a cycle might be calculated assuming conduction from the cylinder surface into an effectively infinite eddy.

From penetration theory, the time average heat flux per unit area in the time period from 0 to T is

$$q = 2k\theta/(\pi\alpha T)^{1/2} \tag{1}$$

which is twice the instantaneous value at T. Using the usual definition of a heat transfer coefficient, $h = (q/\theta)$, the time average Nusselt number for the rear face becomes

$$N_{Nu,R} = 2d/(\pi\alpha T)^{1/2} \tag{2}$$

where the time period, T, is the reciprocal of the shedding frequency f. The latter is available from a nondimensional Strouhal-Reynolds number relation (e.g. [2]); for our range, N_{Sr} is about 0.11 at $N_{Re} \simeq 40$, increases to 0.20 by $N_{Re} \simeq 200$ and remains constant at higher N_{Re}. Thus, while the complete N_{Re}-N_{Sr} relation is known, little error is incurred by using

$$N_{Sr} = (fd/U) = (d/TU) = 0.20 \tag{3}$$

Substitution for T in (2) then yields the final nondimensional Nusselt-Peclet relation for the time average heat transfer from the rear face:

$$N_{Nu,R} = 0.50 N_{Pe}^{1/2} \tag{4}$$

It is evident that the arguments presented for heat transfer would apply equally to mass transfer.

The major assumptions involved in the foregoing are considered briefly.

First, the use of penetration theory implies purely molecular transport. This assumption is, clearly, somewhat in error since the eddies shed possess an internal circulation and, for $N_{Re} > 500$, also contain portions of turbulent fluid. Thus some convective transport undoubtedly occurs and this would tend to make the transfer higher than that predicted by (4). By conventional reasoning, the actual ratio of convection to conduction from the rear face should be of order $[\delta u/\alpha]$, where u is a velocity characteristic of the region, thickness δ, penetrated in one shedding time period. Though one cannot be quantitative about this ratio (primarily for lack of information about the relevant velocity field), it should be noted that the velocity, u, in this recirculating "deadwater" region is much lower than free stream, U. Also, as shown below, the penetration distance, δ, is small compared to cylinder diameter, d. Therefore conduction is likely to dominate the transfer from the rear face upto values of the usual Peclet number, (dU/α), much greater than unity.

Second, penetration theory will apply when the ratio of eddy diameter, say $(d/2)$, to penetration distance, say $(4\sqrt{\alpha T})$ is large. Elimination of T via (3) shows that this will be so if

---

[1] Assistant Professor of Chemical Engineering, Massachusetts Institute of Technology, Cambridge, Mass.

[2] Numbers in brackets designate References at end of paper.

Contributed by the Heat Transfer Division of THE AMERICAN SOCIETY OF MECHANICAL ENGINEERS. Manuscript received by the Heat Transfer Division, August 8, 1967; revised manuscript received September 9, 1968.

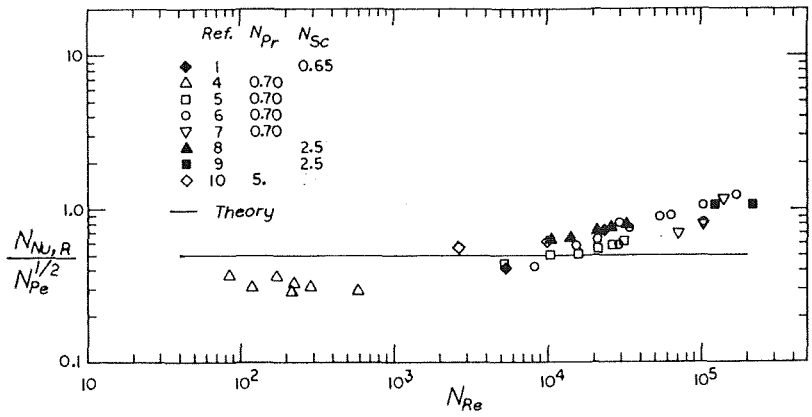

Fig. 1 Comparison of eddy penetration model with experimental data

$$N_{Pe} \gg 300 \tag{5}$$

Failure to satisfy (5) will result, physically, in a final eddy temperature that is significantly different from free stream; in which case the actual heat transfer will be poorer than predicted by equation (4).

Third, it should be pointed out that in equation (1) the expression for the time average heat flux from a plane surface into a semi-infinite medium was used directly for the cylinder surface. This causes negligible error at the short penetration times relevant to the present case.

Fourth, an eddy was assumed to shed without leaving any residual fluid adhering to the rear face; adhering fluid would result, in effect, in a stagnant film over the face, making the transfer poorer than predicted. Finally, it should be noted that the heat transfer from the rear of a cylinder is a function both of time and location, ϕ. The present model yields the time average transfer over the entire rear face but is unable to predict local variations.

Experimental measurements of heat and mass transfer coefficients around the periphery of cylinders in cross flow have been widely reported (e.g., [4–10]). Average rear face Nusselt numbers obtained from these are compared with the present theory in Fig. 1. The ordinate, $(N_{Nu,R}/N_{Pe}^{1/2})$, is suggested by the form of equation (4). The theory is within a factor of two of the experimental data over the entire range—nearly four decades—of Reynolds numbers. The physical property dependence cannot be tested adequately since (see legend of Fig. 1) all but one of the measurements involved transfer to air with Prandtl (or Schmidt) numbers of order unity.

The systematic trend of the data with respect to the theory is crudely consistent with the simplifying assumptions discussed earlier. Thus the air data meet the penetration criterion, (5), at $N_{Re} \simeq 3000$; at lower Reynolds numbers the experimentally measured transport is poorer than predicted. At the highest Reynolds numbers the actual transport is higher than predicted, presumably because of a significant convective contribution.

In summary, a mechanism has been proposed for the heat transfer from the rear of a cylinder in transverse flow. According to this the transfer occurs during the shedding process by the penetration of heat from the cylinder surface into an eddy during the time that the eddy stays attached. Thereafter the eddy sheds and the cycle is repeated with the frequency of shedding. The model yields the correct order of magnitude of the transfer—its predictions are within a factor of two of experimental data over the entire Reynolds number range, $40 < N_{Re} < 2 \times 10^5$, encompassed.

References

1 Lohrisch, W., "Bestimmung von Warmeubergangszahlen durch Diffusionversuche," *Mitt. Forschungsarb*, Vol. 322, 1929, p. 46.

2 Roshko, A., "On the Development of Turbulent Wakes from Vortex Streets," NACA Tech. Rept. No. 1191, 1955.

3 Roshko, A., "Experiments on the Flow Past a Circular Cylinder at Very High Reynolds Numbers," *Journal of Fluid Mechanics*, Vol. 10, 1961, pp. 345–356.

4 Eckert, E. R. G., and Soehngen, E., "Distribution of Heat-Transfer Coefficients Around Circular Cylinders in Crossflow at Reynolds Number from 20 to 550," TRANS. ASME, Vol. 74, 1952, pp. 343–347.

5 van Meel, D. A., "A Method for the Determination of Local Convective Heat Transfer from a Cylinder Placed Normal to an Air Stream," *International Journal of Heat and Mass Transfer*, Vol. 5, 1962, pp. 715–722.

6 Schmidt, E., and Wenner, K., "Heat Transfer Over the Circumference of a Heated Cylinder in Transverse Flow," NACA Tech. Mem. 1050, 1943.

7 Giedt, W. H., "Investigation of Variation of Point Unit Heat Transfer Coefficient Around a Cylinder Normal to an Air Stream," TRANS. ASME, Vol. 71, 1949, pp. 375–381.

8 Winding, C. C., and Cheney, A. J., "Mass and Heat Transfer in Tube Banks," *Industrial Engineering Chemistry*, Vol. 40, No. 6, 1948, pp. 1087–1093.

9 Sogin, H. H., and Subramanium, V. S., "Local Mass Transfer from Circular Cylinders in Cross Flow," JOURNAL OF HEAT TRANSFER, TRANS. ASME, Series C, Vol. 83, 1961, pp. 483–493.

10 Perkins, H. C., and Leppert, A., "Local Heat Transfer Coefficients on a Uniformly Heated Cylinder," *International Journal of Heat and Mass Transfer*, Vol. 7, 1964, pp. 143–158.

Time-Temperature Charts for One-Dimensional Conduction With Uniform Internal Heat Generation

F. M. YOUNG[1] and C. R. SAVINO[2]

CHARTS are presented here for the case of one-dimensional, unsteady conduction with suddenly applied, uniform internal heat

[1] Associate Professor of Mechanical Engineering, Lamar State College of Technology, Beaumont, Texas. Assoc. Mem. ASME.

[2] Propulsion Engineer, NASA-MSC, Houston, Texas. Assoc. Mem. ASME.

Contributed by the Heat Transfer Division of THE AMERICAN SOCIETY OF MECHANICAL ENGINEERS. Manuscript received at ASME Headquarters, June 13, 1969; revised manuscript received, September 9, 1969.

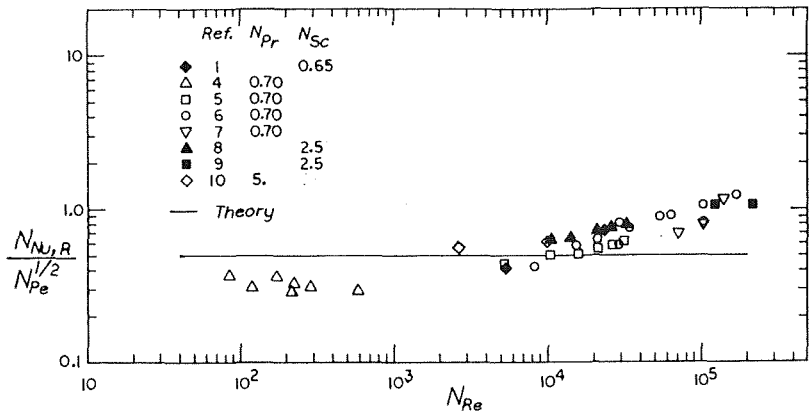

Fig. 1 Comparison of eddy penetration model with experimental data

$$N_{Pe} \gg 300 \tag{5}$$

Failure to satisfy (5) will result, physically, in a final eddy temperature that is significantly different from free stream; in which case the actual heat transfer will be poorer than predicted by equation (4).

Third, it should be pointed out that in equation (1) the expression for the time average heat flux from a plane surface into a semi-infinite medium was used directly for the cylinder surface. This causes negligible error at the short penetration times relevant to the present case.

Fourth, an eddy was assumed to shed without leaving any residual fluid adhering to the rear face; adhering fluid would result, in effect, in a stagnant film over the face, making the transfer poorer than predicted. Finally, it should be noted that the heat transfer from the rear of a cylinder is a function both of time and location, ϕ. The present model yields the time average transfer over the entire rear face but is unable to predict local variations.

Experimental measurements of heat and mass transfer coefficients around the periphery of cylinders in cross flow have been widely reported (e.g., [4–10]). Average rear face Nusselt numbers obtained from these are compared with the present theory in Fig. 1. The ordinate, $(N_{Nu,R}/N_{Pe}^{1/2})$, is suggested by the form of equation (4). The theory is within a factor of two of the experimental data over the entire range—nearly four decades—of Reynolds numbers. The physical property dependence cannot be tested adequately since (see legend of Fig. 1) all but one of the measurements involved transfer to air with Prandtl (or Schmidt) numbers of order unity.

The systematic trend of the data with respect to the theory is crudely consistent with the simplifying assumptions discussed earlier. Thus the air data meet the penetration criterion, (5), at $N_{Re} \simeq 3000$; at lower Reynolds numbers the experimentally measured transport is poorer than predicted. At the highest Reynolds numbers the actual transport is higher than predicted, presumably because of a significant convective contribution.

In summary, a mechanism has been proposed for the heat transfer from the rear of a cylinder in transverse flow. According to this the transfer occurs during the shedding process by the penetration of heat from the cylinder surface into an eddy during the time that the eddy stays attached. Thereafter the eddy sheds and the cycle is repeated with the frequency of shedding. The model yields the correct order of magnitude of the transfer—its predictions are within a factor of two of experimental data over the entire Reynolds number range, $40 < N_{Re} < 2 \times 10^5$, encompassed.

References

1 Lohrisch, W., "Bestimmung von Warmeubergangszahlen durch Diffusionversuche," *Mitt. Forschungsarb*, Vol. 322, 1929, p. 46.

2 Roshko, A., "On the Development of Turbulent Wakes from Vortex Streets," NACA Tech. Rept. No. 1191, 1955.

3 Roshko, A., "Experiments on the Flow Past a Circular Cylinder at Very High Reynolds Numbers," *Journal of Fluid Mechanics*, Vol. 10, 1961, pp. 345–356.

4 Eckert, E. R. G., and Soehngen, E., "Distribution of Heat-Transfer Coefficients Around Circular Cylinders in Crossflow at Reynolds Number from 20 to 550," TRANS. ASME, Vol. 74, 1952, pp. 343–347.

5 van Meel, D. A., "A Method for the Determination of Local Convective Heat Transfer from a Cylinder Placed Normal to an Air Stream," *International Journal of Heat and Mass Transfer*, Vol. 5, 1962, pp. 715–722.

6 Schmidt, E., and Wenner, K., "Heat Transfer Over the Circumference of a Heated Cylinder in Transverse Flow," NACA Tech. Mem. 1050, 1943.

7 Giedt, W. H., "Investigation of Variation of Point Unit Heat Transfer Coefficient Around a Cylinder Normal to an Air Stream," TRANS. ASME, Vol. 71, 1949, pp. 375–381.

8 Winding, C. C., and Cheney, A. J., "Mass and Heat Transfer in Tube Banks," *Industrial Engineering Chemistry*, Vol. 40, No. 6, 1948, pp. 1087–1093.

9 Sogin, H. H., and Subramanium, V. S., "Local Mass Transfer from Circular Cylinders in Cross Flow," JOURNAL OF HEAT TRANSFER, TRANS. ASME, Series C, Vol. 83, 1961, pp. 483–493.

10 Perkins, H. C., and Leppert, A., "Local Heat Transfer Coefficients on a Uniformly Heated Cylinder," *International Journal of Heat and Mass Transfer*, Vol. 7, 1964, pp. 143–158.

Time-Temperature Charts for One-Dimensional Conduction With Uniform Internal Heat Generation

F. M. YOUNG[1] and C. R. SAVINO[2]

CHARTS are presented here for the case of one-dimensional, unsteady conduction with suddenly applied, uniform internal heat

[1] Associate Professor of Mechanical Engineering, Lamar State College of Technology, Beaumont, Texas. Assoc. Mem. ASME.

[2] Propulsion Engineer, NASA-MSC, Houston, Texas. Assoc. Mem. ASME.

Contributed by the Heat Transfer Division of THE AMERICAN SOCIETY OF MECHANICAL ENGINEERS. Manuscript received at ASME Headquarters, June 13, 1969; revised manuscript received, September 9, 1969.

generation $\dot{q}$ and convective boundary conditions. Carslaw and Jaeger [1][3] present similar charts for the special case of an infinite Biot number. A range of Biot numbers of zero to infinity will be presented here for geometries of infinite plate, infinite cylinder, and sphere.

The boundary conditions for all cases are at time $\tau = 0$, for any position δ, the initial temperature is $T = T_i$; for $\delta = 0$, at any τ, $\dfrac{\partial T}{\partial \delta} = 0$; at the boundary $\delta = B$, at any τ, $-k\dfrac{\partial T}{\partial \delta} = h(T - T_\infty)$ where B is the half thickness L of the plate and the radius R of the cylinder or sphere. The solutions are found to be

Infinite Plate

$$T = T_i = (T_\infty - T_i)[1 - P(x, \tau)] - \frac{\dot{q}L^2}{k} QP(x, \tau) \quad (1)$$

Infinite Cylinder

$$T - T_i = (T_\infty - T_i)[1 - C(r, \tau)] + \frac{\dot{q}R^2}{k} QC(r, \tau) \quad (2)$$

Sphere

$$T - T_i = (T_\infty - T_i)[1 - S(r, \tau)] + \frac{\dot{q}R^2}{k} QS(r, \tau), \quad (3)$$

where $P(x, \tau)$, $C(r, \tau)$, and $S(r, \tau)$ are the solutions of the suddenly changed environmental temperature problem given by Heisler [2] and

$$QP(x, \tau) = \int_0^\tau [1 - P(x, \theta)]d\theta - \tau$$

$$QC(r, \tau) = \int_0^\tau [1 - C(r, \theta)]d\theta - \tau$$

$$QS(r, \tau) = \int_0^\tau [1 - S(r, \theta)]d\theta - \tau.$$

The solutions represented by equations (1)–(3) may be thought of as the sum of two temperature differences: (a) the temperature difference due to the suddenly changed environmental temperature $T_e - T_i$, and (b) the temperature difference due to the suddenly applied internal heat generation $T_Q - T_i$. The first temperature difference is found by looking up the appropriate value of $P(x, \tau)$, $C(r, \tau)$, or $S(r, \tau)$ from Heisler's charts and, since these functions are the ratio

$$\frac{T_e - T_\infty}{T_i - T_\infty}$$

the multiplication indicated in equations (1)–(3) give algebraically

$$(T_\infty - T_i)\left[1 - \frac{(T_e - T_\infty)}{(T_i - T_\infty)}\right] = T_e - T_i$$

where T_∞ is the environmental temperature. The second temperature difference $T_Q - T_i$ is given by Figs. 1–3 for an x/L or r/R of 0.0 and Fourier numbers from 0.1 to 1000. For positions other than 0.0 this temperature difference is found by looking up the central difference as given by Figs. 1–3 and the multiplicative position correction as employed by Heisler [2] could be used here in a more approximate sense. Since the position correction would be numerically the same as that plotted by Heisler it is not included here.

Example Calculation

A 0.1-in-dia, type 304 stainless-steel wire is suddenly subjected to uniform internal heat generation due to resistance heating. If the initial temperature of the wire were 32 deg F, the internal heat generation was found to be 10^6 Btu/hr ft^3, and the average heat transfer coefficient was estimated to be 192 Btu/hr ft^2 deg F. Find the temperature at the center of the wire after 9.25×10^{-5} hr.

The properties are taken as

$$k = 8.0 \text{ Btu/hr ft deg F}$$

$$\alpha = 0.15 \text{ ft}^2\text{/hr}$$

The Biot and Fourier numbers may be calculated.

$$\text{Bo} = \frac{hR}{k} = \frac{(192)(0.05)}{(8.0)(12)} = 0.1$$

$$1/\text{Bo} = 10$$

$$\frac{\alpha\tau}{R^2} = \frac{(0.15)(144)(9.25 \times 10^{-5})}{(0.05)^2} = 0.80$$

[3] Numbers in brackets designate References at end of Note.

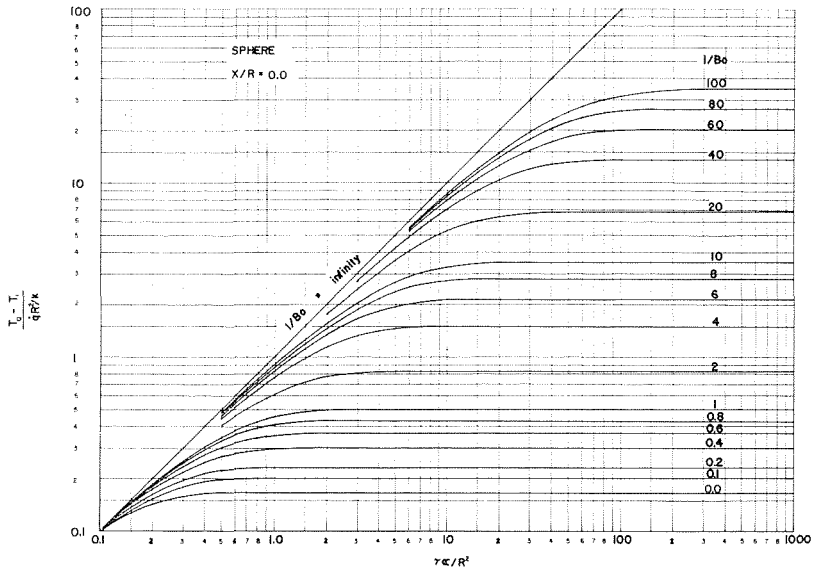

Fig. 1 Temperature difference in an infinite plate at $x/L = 0.0$ due to internal heat generation

From Fig. 2, $(T_Q - T_i)/qR^2/k$ is found to be 0.76 which gives,

$$T_Q - T_i = \frac{(10^6)(0.05)^2}{(144)(8.0)}(0.76)$$

$$T_Q - T_i = 16.5 \text{ deg F}$$

Since there was not an environmental temperature change,

$$T - T_i = T_Q - T_i = 16.5 \text{ deg F}$$

or

$$T = 48.5 \text{ deg F}.$$

A finite-difference technique was used to check the graphical results. Using 19 radius divisions, the temperature calculated by forward differences was 47.4 deg F. The entire line for 1/Bo = 10 was checked numerically with the result that the answers agreed as well as could be expected of the finite-difference technique used. Calculations were also made using similar examples for the 1/Bo = 10 line for both the plate and sphere with good agreement. The graphs were also checked against the plots of Carslaw and Jaeger [1] for 1/Bo = 0 with good agreement also. The accuracy of the line for 1/Bo = infinity is obvious.

Suppose we now desired to estimate the temperature at a radius ratio of 1.0 for the original problem. From Heisler [2], the position correction at $x/R = 1.0$ is found to be 0.955.

$$(T - T_i)_1 = (0.955)(16.5) = 15.8 \text{ deg F}$$

$$T_1 = 47.8 \text{ deg F}$$

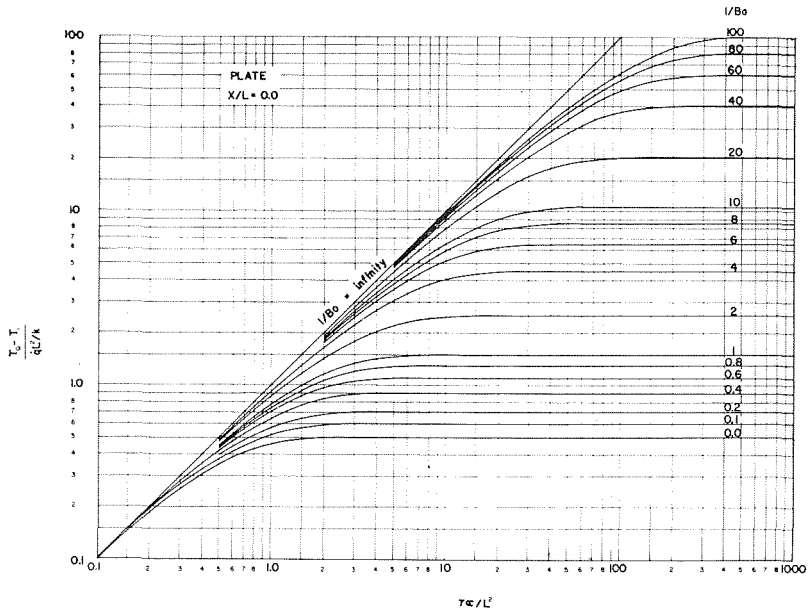

Fig. 2 Temperature difference in an infinite cylinder at $x/R = 0.0$ due to internal heat generation

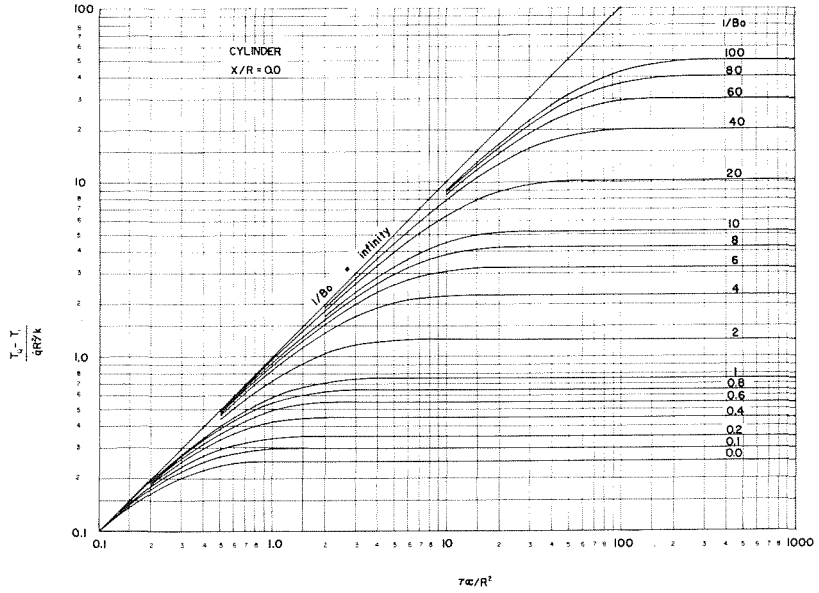

Fig. 3 Temperature difference in a sphere at $x/R = 0.0$ due to internal heat generation

If the environmental temperature had been changed to 0 deg F simultaneously with the application of internal heat generation, the central temperature change due to the sudden environmental temperature change may be found from Heisler [2] as:

$$C(0, 9.25 \times 10^{-5}) = 0.88$$

$$(T_e - T_i)_0 = (T_\infty - T_i)(1 - 0.88) = -3.8 \text{ deg F}$$

$$(T - T_i)_0 = (T_e - T_i)_0 + (T_Q - T_i)_0$$

$$(T - T_i)_0 = -3.8 \times 16.5 = 12.7 \text{ deg F}$$

$$T_0 = 44.7 \text{ deg F}.$$

The surface temperature may also be found in a similar manner.

$$C(1.0, 9.25 \times 10^{-5}) = C(0, 9.25 \times 10^{-5})(0.955) = 0.84$$

$$(T_e - T_i)_1 = (T_\infty - T_i)(1 - 0.84) = -5.1 \text{ deg F}$$

$$(T - T_i)_1 = (T_e - T_i)_1 + (T_Q - T_i)_1$$

$$(T - T_i)_1 = -5.1 + 15.8 = 10.7 \text{ deg F}$$

$$T_1 = 42.7 \text{ deg F}$$

Acknowledgment

The authors wish to express their appreciation to the Lamar Research Center for the sponsorship of Grant 466-68-14 for which these data were necessary in error analysis.

References

1 Carslaw, H. S., and Jaeger, J. C., *Conduction of Heat in Solids*, Oxford University Press, London, 1947, pp. 92–254.

2 Heisler, M. P., "Temperature Charts for Induction and Constant-Temperature Heating," TRANS. ASME, Vol. 69, Apr. 1947, pp. 227–236.

journal of heat transfer discussion

On Some Aspects of Steam Bubble Collapse[1]

T. G. Theofanous,[2] H. K. Fauske,[3] and H. S. Isbin.[4] Two factors stressed by the authors are the questioning of the thin thermal boundary-layer assumption previously used in other solutions and the effect of the vapor velocity. The authors are to be commended for their courageous attempt to resolve these factors by attempting to solve the heat diffusion equations numerically. In our independent treatment we have considered bubble growth nd collapse under constant and time-dependent pressure elds [7–9].[5] We have assumed a spatially uniform vapor, but with a time-dependent density which, with an overall mass and energy balance, yields an equation equivalent to (12), having the last term expressed on the basis of molecular kinetic considerations. A system of ordinary differential equations is obtained which is economical in use of computer time. We, too, have questioned the thin boundary-layer assumption (as used in the Plesset-Zwick analysis) and note that at a certain stage in the collapse case such an assumption breaks down. In our studies we have assumed a finite, but not necessarily a thin thermal boundary-layer, along with an appropriately defined, simple temperature distribution which is used to satisfy the overall energy balance.

For the heat transfer controlled experiments of Florschuetz and Chao, we illustrate an improved prediction as compared with the one achieved from their heat transfer solution. The improvement was uniform over all their experimental data obtained for both liquids (water, ethyl alcohol) and, in Fig. 5, we exhibit the three theoretical solutions and the experimental data for their bubble 8WA. No oscillations were observed in our solution and detailed information obtained from our solution shows that the bubble was very close to the saturation state and at a pressure very close to p_∞. No effect of vaporization coefficient on our solution was noted at this low subcooled condition. From this comparison we suggest that the oscillations observed in approach B of the authors are not peculiar to the inclusion of the "velocity of vapor," but that their source should probably be sought in numerical instabilities. The near adiabatic high-frequency oscillations are not surprising since in a sense they are forced through equation (12) and the uncertainties in guessing the heat transfer part in this equation.

At higher Jacob numbers, numerical solutions yield rebounding bubbles. We do not recommend extending our present solutions beyond the rebound point. Our solutions for rebounding bubbles gave in general much smaller rebound radii than those in the corresponding calculations of Florschuetz and Chao, thus agreeing with the trends of the authors' theory. This trend is illustrated in Fig. 6, a case similar to Fig. 2 of the authors' paper. A vaporization coefficient of $c = 10^{-2}$ was used in order to predict the data. If a value $c = 1$ were used, a case that would correspond to essentially the authors' equilibrium solution, an even smaller rebound radius would be obtained. We have shown that the effect of neglecting the variation of density of the vapor with time to be important near the rebound point, and this dependency is not included in the Florschuetz-Chao solutions.

Finally, we wish to point out that the character of the spatial temperature distribution (in both the liquid and in the vapor), presumably obtained by the authors as part of their calculations, at the growing portion of a rebounding bubble (for example, after the first rebound) would add information in evaluating numerical and other approximations.

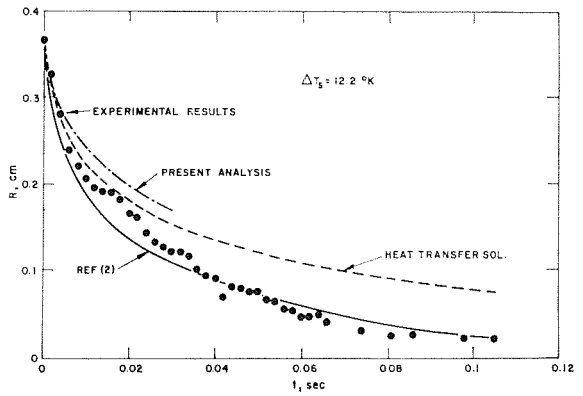

Fig. 5 Comparison of various theoretical solutions with experimental data of Florschuetz and Chao

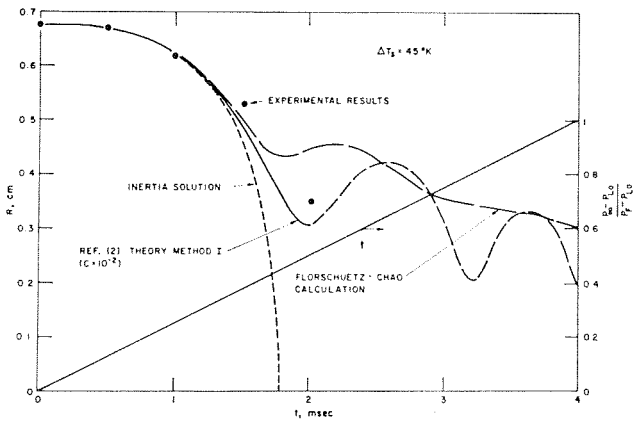

Fig. 6 Comparison of various theoretical solutions with experimental data of Florschuetz and Chao

---

[1] By S. M. Cho and R. A. Seban, published in the November, 1969, issue of the JOURNAL OF HEAT TRANSFER, TRANS. ASME, Vol. 91, No. 4, pp. 537–542.

[2] Assistant Professor, School of Chemical Engineering, Purdue University, Lafayette, Ind.

[3] Argonne National Laboratory, Reactor Engineering Division, Argonne, Ill.

[4] Professor, Chemical Engineering Department, University of Minnesota, Minneapolis, Minn.

[5] Numbers in brackets designate Additional References at end of Discussion.

Additional References

7 Theofanous, T., et al., "A Theoretical Study on Bubble Growth in Constant and Time-Dependent Pressure Fields," *Chemical Engineering Science*, Vol. 24, 1969, pp. 885–897.

8 Theofanous, T., et al., "Nonequilibrium Bubble Collapse—A Theoretical Study," Eleventh National Heat Transfer Conference, AIChE-ASME, Minneapolis, Minn., Aug. 3–6, 1969.

9 Theofanous, T., "The Dynamics of Spherical, Liquid-Vapor Phase Change in Constant and Time-Dependent Pressure Fields," PhD dissertation, University of Minnesota, 1969.

Authors' Closure

The authors appreciate the comments of the discussers. We would like to point out that runs with reduced increment size gave no indication of instability in the numerical solution. And we regret that we did not print out the spatial temperature distribution, so that this information cannot be provided.

Further theoretical studies as well as more experimental investigations are needed to better understand the behavior of collapsing bubbles.